202(3), 2025

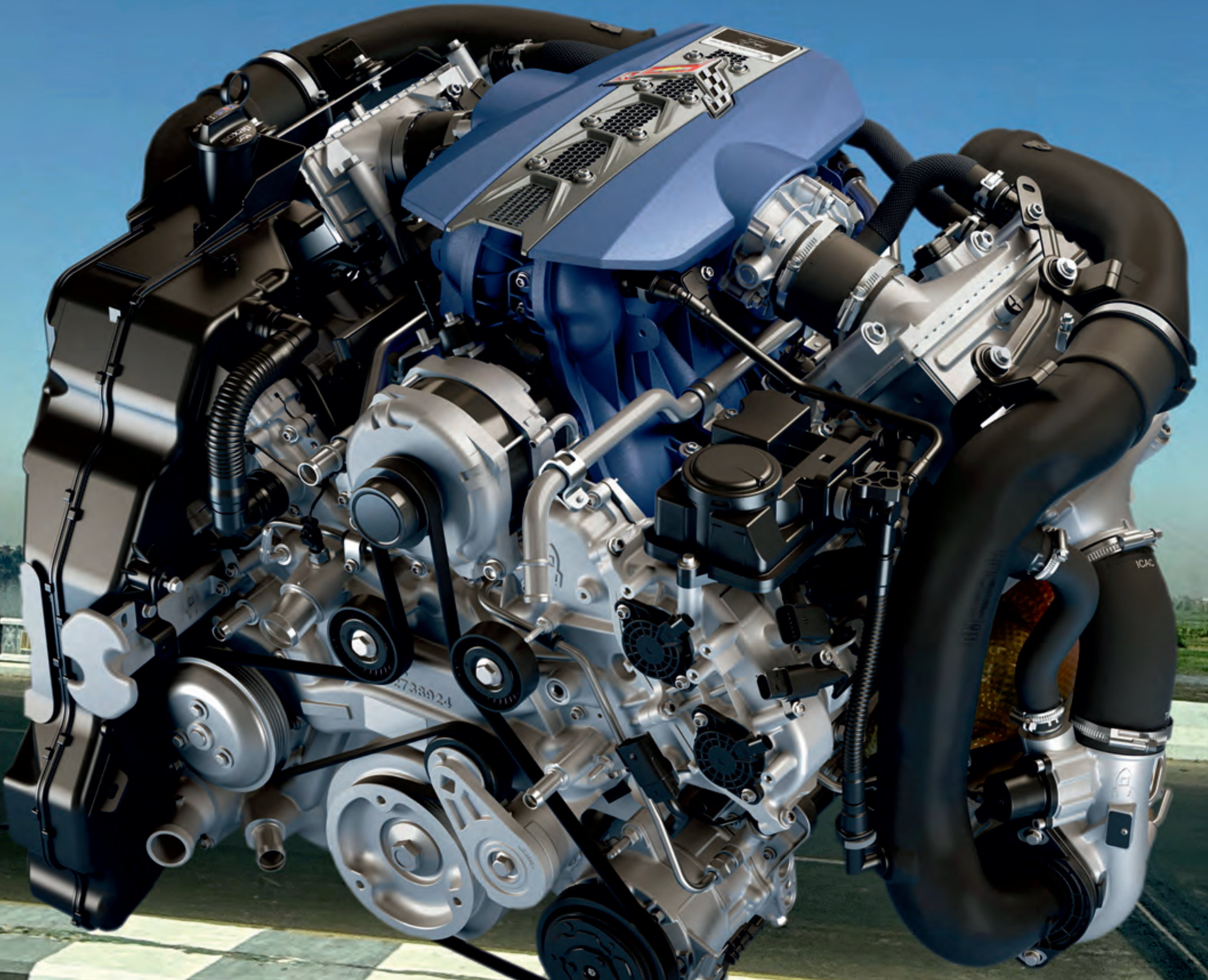

COMBUSTION ENGINES

AIR FORCE INSTITUTE OF TECHNOLOGY
INSTYTUT TECHNICZNY WOJSK LOTNICZYCH

ul. Księcia Bolesława 6, 01-494 Warszawa, Poland
tel.: +48 261 851 300; fax: +48 261 851 313
www.itwl.pl e-mail: poczta@itwl.pl

SUPPORTING OPERATIONS & MAINTENANCE OF AERONAUTICAL ENGINEERING:

- tribological diagnostics of lubrication systems in power units and hydraulic systems
- endoscopic examinations of power units
- measurements of operation parameters of power units using one's own and company systems and their analysis

DEVISING AND DEVELOPING NEW DIAGNOSTIC METHODS:

- CT examinations – V/tome/X CT system
- blade vibration measurements using the tip-timing method

NEW TECHNOLOGIES FOR UNMANNED AERIAL VEHICLES:

- technical condition monitoring system of mini jet engine
- hybrid drive of unmanned aerial vehicle

Due to the dynamic development of machine and vehicle powertrains, the "Combustion Engines" scientific journal, while retaining its historical title, currently publishes works related not only to internal combustion engines, but also other powertrains, including hybrid drives, electric drives and fuel cells.

PTNSS Supporting Members
Członkowie wspierający PTNSS

BOSMAL Automotive Research and Development Institute Ltd
Instytut Badań i Rozwoju
Motoryzacji BOSMAL Sp. z o.o

Motor Transport Institute
Instytut Transportu Samochodowego

Institute of Aviation
Sieć Badawcza Łukasiewicz
– Instytut Lotnictwa

Automotive Industry Institute
Sieć Badawcza Łukasiewicz
– Przemysłowy Instytut Motoryzacji

Sieć Badawcza Łukasiewicz
– Poznański Instytut Technologiczny

AVL List GmbH

Air Force Institute of Technology
Instytut Techniczny Wojsk Lotniczych

Military Institute of Armoured & Automotive Technology
Wojskowy Instytut Techniki Pancernej
i Samochodowej

Toyota Motor Poland Ltd. Sp. z o.o.

RADWAG Balances and Scales
RADWAG Wagi Elektroniczne

FOGO Sp. z o.o.

Horus Energia Sp. z o.o.

John Deere Polska Sp. z o.o.

COMBUSTION ENGINES

A Scientific Magazine
2025, 202(3)
Year LXIV
PL ISSN 2300-9896
PL eISSN 2658-1442

Publisher:
Polish Scientific Society of Combustion Engines
60-965 Poznan, pl. M. Skłodowskiej-Curie 5, Poland
tel.: +48 61 6475959, fax: +48 61 6652204
E-mail: sekretariat@ptnss.pl
WebSite: http://www.ptnss.pl
Papers available on-line: http://combustion-engines.eu

Scientific Board:

Krzysztof Wisłocki – chairman, Poland (*Poznan University of Technology*)

Yuzo Aoyagi – Japan (*Okayama University*)
Ewa Bardasz – USA (*National Academy of Engineering*)
Piotr Bielaczyc – Poland (*BOSMAL Automotive Research and Development Institute Ltd.*)
Zdzisław Chłopek – Poland (*Warsaw University of Technology*)
Tadeu Cordeiro de Melo – Brazil (*Petrobras*)
Jan Czerwinski – Switzerland (*CJ Consulting*)
Radostin Dimitrov – Bulgaria (*University of Varna*)
Friedrich Dinkelacker – Germany (*Leibniz Universität Hannover*)
Hubert Friedl – Austria (*AVL*)
Barouch Giechaskiel – Italy (*European Commission, JRC Italy*)
Leslie Hill – UK (*Horiba*)
Timothy Johnson – USA (*Corning Inc.*)
Kazimierz Lejda – Poland (*Rzeszow University of Technology*)
Hans Peter Lenz – Austria (*TU Wien*)
Helmut List – Austria (*AVL*)
Toni Kinnunen – Finland (*Proventia*)
David Kittelson – USA (*University of Minnesota*)
Christopher Kolodziej – USA (*Delphi Automotive Systems*)
Hu Li – UK (*University of Leeds*)
Vaselin Mihaylov – Bulgaria (*University of Varna*)
Federico Millo – Italy (*Politecnico Torino*)
Jeffrey D. Naber – USA (*Michigan Technological University*)
Andrzej Niewczas – Poland (*Motor Transport Institute*)
Marek Orkisz – Poland (*Rzeszow University of Technology*)
Dieter Peitsch – Germany (*TU Berlin*)
Stefan Pischinger – Germany (*FEV Germany*)
Andrzej Sobiesiak – Canada (*University of Windsor*)
Stanisław Szwaja – Poland (*Częstochowa University of Technology*)
Piotr Szymański – Nederlands (*European Commission, JRC*)
Leonid Tartakovsky – Israel (*Technion – Israel Institute of Technology*)
Andrzej Teodorczyk – Poland (*Warsaw University of Technology*)
Xin Wang – China (*Beijing Institute of Technology*)
Thomas Wallner – USA (*Argonne National Laboratory*)
Michael P. Walsh – USA (*International Council on Clean Transportation*)
Mirosław Wendeker – Poland (*Lublin University of Technology*)

Contents

Editorial:

Institute of Powertrains and Aviation
Poznan University of Technology
60-965 Poznan, Piotrowo 3 Street
tel.: +48 61 2244505, +48 61 2244502
E-mail: papers@ptnss.pl

Publisher:

Polish Scientific Society of Combustion Engines
60-965 Poznan, pl. M. Sklodowskiej-Curie 5, Poland
tel.: +48 61 6475959, fax: +48 61 6652204
E-mail: sekretariat@ptnss.pl
WebSite: http://www.ptnss.pl

Subscriptions
Send subscription requests to the Publisher's address.
Cost of a single issue PLN 100.

Preparation for print
ARS NOVA Publishing House
60-782 Poznan, ul. Grunwaldzka 17/10A

Circulation: 60 copies

Printing and binding

Zakład Poligraficzny Moś i Łuczak, sp. j.,
Poznań, ul. Piwna 1

The journal is under the patronage of the Transport Committee and the Machine Building Committee of the Polish Academy of Sciences

PAN
POLSKA AKADEMIA NAUK

The journal is registered and listed in the Polish and international database

Scopus®
INDEX COPERNICUS INTERNATIONAL
Crossref
EBSCO
DOAJ DIRECTORY OF OPEN ACCESS JOURNALS
POL-index Polska Baza Cytowań
SHERPA/RoMEO
ROAD
BazTech

Papers published in the

Combustion Engines

quarterly receive 70 points as stated by the Notification of the Minister of Science dated 5 January 2024.

Declaration of the original version
The original version of the Combustion Engines journal is the printed version.

Cover
I – 2025 Chevy Corvette ZR1 engine
(www.chevrolet.com)

IV – Mazda rotary engine
(newsroom.mazda.com)

Article citation info:
Zimakowska-Laskowska M, Kniaziewicz T. Analysis of methods for estimating pollutant emissions from marine engines in terms of their use for evaluating ambient air quality. Combustion Engines. 2025;202(3):3-10. https://doi.org/10.19206/CE-204922

Magdalena ZIMAKOWSKA-LASKOWSKA
Tomasz KNIAZIEWICZ

Combustion Engines
Polish Scientific Society of Combustion Engines

Analysis of methods for estimating pollutant emissions from marine engines in terms of their use for evaluating ambient air quality

ARTICLE INFO

Received: 13 February 2025
Revised: 6 April 2025
Accepted: 10 May 2025
Available online: 6 June 2025

This paper discusses a method for estimating pollutant emissions from the ICE of ships for air quality modelling. Three levels of emission estimation and methods for estimating ship pollutant emissions are divided into bottom-up and top-down approaches. The bottom-up approach is based on detailed ship operations and requires knowledge of many input parameters (a more accurate method, but is very time-consuming). The top-down approach is based on the value of the fuel consumed by the ship and is less precise but more accessible to apply. Various data sources are available for estimating pollutant emissions from ships, including studies commissioned by the IMO, which provide reliable emission estimates for different types of ships but lack geospatial information; the CEDS database, which optimises regional emissions information by scaling emissions from ships to national levels; CAMS-GLOB-SHIP, which provides emissions at a resolution of 0.25° × 0.25° for the following substances: CO, NO_x, VOC, EC, OC, BC, SO_x, SO_4; the EDGAR database, which provides annual emissions estimates at a resolution of 0.1° × 0.1°, but only covers the three main GHGs and F-gases; the Automatic Identification System (AIS), which provides high-resolution ship traffic data, allowing for a more realistic description of emitters. Many methods are available for estimating ship emissions, each with advantages and disadvantages. The choice of method depends on the available data and the level of accuracy required. The availability of AIS data allows for more accurate emission estimates, which are significant for a better understanding of the impact of shipping on air quality.

Key words: *ship, pollutant, IMO, emission modelling*

1. Introduction

With the swift growth of the global economy, increasing environmental protection requirements, and the rising demand for maritime transport, the issue of pollutant emissions from vessel internal combustion engines is becoming critically important. Combustion engines, regardless of their purpose (cars, aircraft, vessels, and other machines), are a source of pollutant emissions. The main pollutants emitted by vessel combustion engines operating on international routes and in ports include PM, VOCs and CO, which affect human health; SO_x and NO_x, which contribute to acid rain; and GHGs such as CO_2, CH_4 and N_2O, as well as BC, which, although not a GHG, has a strong climate-warming effect due to its ability to absorb solar radiation [1, 9, 28, 33, 35, 47]. Emissions from vessels' internal combustion engines do not just influence the local marine environment, but also the climate and air quality, therefore, precise comparative analysis of pollutant emission estimation methods is becoming increasingly important. In contrast to pollutant emissions from road vehicles, air pollutant emissions from vessels are much higher due to the amount of energy required to operate the vessels. In recent decades, emissions from global shipping have risen substantially, adding to anthropogenic pollution worldwide and significantly impacting air quality through their role in climate change, ozone layer depletion, and the formation of acid rain [30, 33, 40, 42]. Consequently, there are growing concerns about the impact of pollutant emissions from vessels on the environment and human health. Additionally, it is noteworthy that emissions from shipping were not included in the emission reductions discussed at the 21st annual COP because they do not occur within the borders of any specific country [33, 48].

The dispersion of pollutant emissions from ships poses a significant challenge, as research indicates that at least 70% of emissions from vessels on international routes occur within 400 kilometres of the coastline. These pollutants can travel hundreds of kilometres inland, leading to air quality issues even in distant coastal regions [5, 10, 33, 49]. As a major source of air pollution in cities and port areas, emissions from vessels have a harmful effect on the quality of ambient air and significantly contribute to the increase in the concentration of toxic substances in the surrounding areas. As a result, the shipping industry is responsible for higher concentrations of toxic substances in port areas than in inland municipalities. Emissions also arise when vessels are in ports, and most of the environmental impacts result from routine operations, such as their activities in port [30, 33, 42, 43]. These pollutants cause lung cancer, loss of lung function, cardiovascular and cardiopulmonary system, allergies and asthma, especially in coastal communities [9, 11, 29, 33].

Subsequently, a compelling approach technique is required to control the emission of pollutants from vessels into the environment, requiring strong forecasts in terms of observing, measurement, and localization, particularly within the zones with higher oceanic activity. To improve air quality management strategy, it is vital to prepare an emission inventory, which helps to identify significant sources of air pollutants, build up outflow patterns over time and direct administrative activities [45]. The emission inventory for air quality modelling purposes should start with a project plan: the main objective, the definition of pollutants and types of vessels to be analysed, the geographic resolution, the time resolution and the methodology for preparing the emission inventory, and the expected results [8].

In the context of global challenges related to reducing greenhouse gas emissions and air pollutants, understanding the effectiveness of different methods for estimating pollutant emissions from vessels' internal combustion engines becomes crucial. Proper emission estimation is not only essential for monitoring and enforcing environmental regulations, but also a fundamental step towards developing emission reduction strategies and improving energy efficiency in maritime transport and air quality [8, 13, 33, 45].

This article presents an overview of methods for estimating pollutant emissions from vessels' internal combustion engines with a view to using them for air quality modelling purposes. These considerations aim not only to present and compare different methodologies, but also to analyse their data requirements, accuracy levels, spatial and temporal resolution, and suitability for air quality modelling. This analytical perspective allows for identifying each method's trade-offs and practical implications in policy and scientific contexts.

2. Estimating exhaust emissions from ships

Because of their immediate and detrimental influences on human existence, emissions from pollution are frequently a key topic of study, as researchers consistently seek innovative methods to lessen their effects. To ensure the successful application of eco-friendly solutions, assessing pollutant emission inventories is essential, enabling targeted actions in the most critical and uncertain scenarios. Since measuring exhaust emissions from every vessel worldwide is impractical, comprehensive databases are developed, relying on various methods to estimate these emissions accurately.

In maritime transport, in contrast to land transport, where there are and are used emission models of pollutants, e.g. HBEFA [15] and COPERT [32], which take into account many factors influencing emissions (e.g. average speed, vehicle structure, traffic share), emission models are less developed and often focus on cumulative categories of ships, which makes it difficult to assess the impact of individual factors on emissions accurately. Estimating emissions from vessels is further complicated by the complexity of modelling GHG emissions and engine exhaust pollutants. The reliability of emission estimates largely depends on the adequacy of the applied engine models and the availability of validated empirical data, as shown in studies evaluating marine engine modelling frameworks [25]. This process demands detailed information, including vessel characteristics (such as length, width, draft, propulsion system condition, type and number of engines, and propellers), operational parameters (like speed and course), environmental factors (such as wind strength and direction, air and water temperature, atmospheric pressure, humidity, and sea conditions), as well as the number of vessels within various categories.

Although emissions from shipping activities have been discussed in many publications, which present different methods of estimating emissions [8, 14, 20, 33, 34] (Table 1), for the purpose however of modelling air quality (spread of pollutant emissions), not only the value of pollutant emissions but also geospatial information (division of emissions in the measurement grid) is needed. As mentioned earlier, there is a need for accurate and reliable data on the amount and distribution of emissions to effectively reduce emissions from ships and their negative impact on human health. Table 1 presents a comparison of the available methods of estimating pollutant emissions.

Table 1. Comparison of pollutant emission estimation methods [6]

Inventory	Scale	Pollutants	Method used
IMO	Global	PM2.5, CH_4, NO_x, N_2O, VOC	Bottom-up and Top-down
CEDS v_2021	National	NH_3, CO, BC, NMVOC, CH_4, N_2O, OC, NO_x, SO_2	Top-down
CAMS-GLOB-SHIP v3.1	0.25° × 0.25°	SO_x, SO_4, NO_x, EC, CO, VOC, OC, Ash	Bottom-up
EDGAR v7	0.1° × 0.1°	CH_4, F-gases, N_2O	Bottom-up and Top-down

IMO – International Maritime Organization
CEDS – Community Emissions Data System
CAMS-GLOB-SHIP – Copernicus Atmospheric Monitoring Service Global Shipping
EDGAR – Emissions Database for Global Atmospheric Research

As shown in Table 1, each method differs in scope and scale and data input structure, making their selection highly dependent on the available information and desired output resolution. This article analyses these differences to support appropriate method selection in various modelling contexts.

One notable emissions database is the IMO study, which offers reliable estimates for various vessel and engine types but does not include geospatial details. In contrast, the CEDS database enhances regional emissions data by increasing transportation emissions to national standards over an extended historical period. CEDS covers emissions of CO, BC, CO_2, CH_4, NH_3, NO_x, OC, NMVOC, N_2O, SO_2. The CAMS-GLOB-SHIP v3.1 database provides shipping emissions in a grid resolution of 0.25°×0.25° for pollutants such as NO_x, CO, SO_x, VOC, OC, EC, BC, and SO_4. Meanwhile, the EDGAR v7 database delivers annual emissions estimates in a finer-gridded resolution of 0.1°×0.1°, but it is limited to the three primary GHG (CO_2, CH_4, N_2O) and F-gases [6].

Given the above data, it becomes necessary to assess air pollutant emissions from ships as accurately as possible.

For all sources of pollutant emissions, including shipping, there are methods for estimating pollutant emissions from ships' internal combustion engines. The methodology for estimating GHG emissions is presented in the IPCC guidelines for national greenhouse gas inventories, while for pollutants in the EMEP/EEA air pollutant emission inventory guidebook [8].

Based on the methodology given in the guidelines, there are 3 levels of emission estimation, the choice depends on the availability of data.

The Tier 1 method, the most straightforward approach for creating national and international emission inventories, is employed when detailed data on vessel movements is unavailable [30, 33]. This method relies on information about marine fuel sales and emission factors associated with fuel consumption, expressed as the amount of pollutants per unit of fuel used [8].

The presented equations reflect the methodological framework in international guidelines such as the IPCC and EMEP/EEA. They are included to illustrate each estimation approach's underlying structure and assumptions. While this article does not aim to perform sample calculations, such examples can be found in national emission inventory reports or application-specific studies.

In this situation, the emission is determined using equation (1):

$$E_i = \sum_m (FC_m \cdot EF_{i,m}) \tag{1}$$

where: E_i – emission of pollutant i [kg]; FC_m – weight of m type marine fuel sales within the country [Mg]; $EF_{i,m}$ – emission factor of pollutant i for a specific fuel consumption and m type fuel [kg/Mg]; m – type of fuel (marine diesel oil (MDO), heavy fuel oil (HFO), LNG, petrol).

Marine fuel consumption data is typically obtained from statistical reports.

The Tier 1 method utilizes EFs for each pollutant and fuel type, with certain EFs, such as those for SO_2, being influenced by fuel quality.

Tier 2 assumes that data on fuel sales for shipping, categorized by fuel type, is available at the national level. Emissions are estimated according to a specific framework (see Fig. 1).

Tier 3, similar to Tier 1, relies on fuel consumption data categorized by fuel type. However, it also incorporates detailed, country-specific information on the distribution of fuel consumption based on engine type, whether low, medium, or high speed.

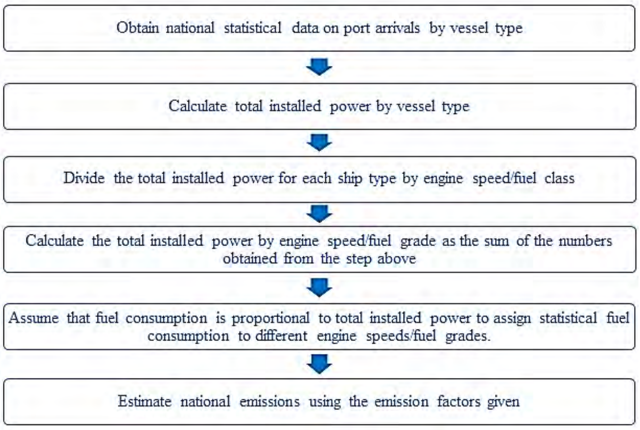

Fig. 1. Emission estimation scheme in Tier 2 method

Pollutant emission in Tier 2 is determined according to the equation:

$$E_i = \sum_m \left(\sum_j (FC_{m,j} \cdot EF_{i,m,j})\right) \tag{2}$$

where: E_i – emission of pollutant i [Mg]; $FC_{m,j}$ – weight of m type fuel consumed by vessels from j type vessels [Mg]; $EF_{i,m,j}$ – average emission factor of pollutant i by vessels with j type engine and using m type fuel [kg/Mg]; i – pollutant; j – engine type (gas turbine and steam turbine, slow, medium and high-speed, diesel oil); m – fuel type (marine diesel, heavy fuel oil (HFO), LNG, petrol).

In Tier 2, the indicators represent average conditions throughout the entire voyage. As a result, emission factors determined by taking a weighted total of the indicators across various operational points, where the weights represent the anticipated frequency of the ship's activity at each point throughout the typical journey.

The whole fuel allocation for domestic and foreign (HFO) vessels should be the focus of Tier 2. To apply emission factors more accurately, information on port arrivals must be gathered and categorized by engine type using national data and standard metrics of fuel kinds and ship operations.

The European Union's national port arrival data is gathered and submitted to Eurostat by every Member State by the Maritime Statistics Directive (Council Directive 96/64/EC). Quarterly data covering transportation, travellers, and cargo, classified by destination, collaborating party, and type of cargo, is available via Eurostat's Newcronos maritime database.

This data only covers major ports (but 90% of total traffic). Tiers 1 and 2 calculate emissions estimates by relying on the typical emission profiles of ships and consider fuel sales as the main indicator of activity. Individual vessel traffic data is the foundation of Tier 3 vessel traffic methodology.

This approach is recommended when detailed vessel traffic data and technical information about vessels (such as engine size, technology, installed power, fuel consumption, and operating hours) are available. This method is appropriate for gauging emissions on both a national and international, even though it may take a significant amount of time. To meet the country's overall reporting requirements, fuel adjustments must be made for other significant fuel-consuming divisions to preserve the national energy balance.

This methodology can calculate emissions based on the UNECE/EMEP domestic and international shipping definitions and alternative definitions (e.g., by flag, ownership, or geographical area).

Tier 3 calculates emissions from navigation for merchant vessels by summing the emissions for each voyage. For each trip, emissions can be expressed as:

$$E_{\text{Trip}} = E_{\text{Hotelling}} + E_{\text{Manouvering}} + E_{\text{Cruising}} \tag{3}$$

Total emissions are the sum of all trips made by all vessels over a year. Information can occasionally be collected from a typical selection of ships functioning in a designated time frame each year. In these scenarios, the estimated emissions for that selection must be adjusted to reflect the overall emissions from every journey and all ships over the entire year.

When the fuel consumption in each step is known, then the emission of pollutant *i* can be calculated for the entire trip via (4):

$$E_{\text{Trip},i,j,m} = \sum_p (FC_{j,m,p} \cdot EF_{i,j,m,p}) \tag{4}$$

where: E_{Trip} – emission during the entire trip [Mg]; $FC_{j,m,p}$ – fuel consumption [Mg]; $EF_{i,j,m,p}$ – emission factor [kg/Mg];

i – pollutant; m – fuel type (marine diesel oil (MDO/MGO), LNG, heavy fuel oil (HFO), petrol); j – engine type (slow, medium and high speed, gas turbine and steam turbine, diesel oil); p – other phase of the journey (cruise, hotelling, manoeuvring).

Suppose fuel consumption during different phases of the journey is unavailable. In that case, an alternative methodology for calculating emissions is suggested, which relies on the installed power and the time spent in each navigation phase.

Emissions can be estimated using straightforward information about the installed power of the main and auxiliary engines, the load factor, and the total time spent in each phase (in hours) by the following equation:

$$E_{Trip,i,j,m} = \sum_p \left[T_p \sum_e (P_e \cdot LF_e \cdot EF_{e,i,j,m,p})\right] \quad (5)$$

where: E_{Trip} – emission during the entire trip [Mg]; $EF_{e,i,j,m,p}$ – emission factor [kg/Mg], depends on the ship's type; L_{Fe} – engine load factor [%]; P_e – engine rated power [kW]; T_p – time [h]; e – engine category (main, auxiliary); i – pollutant; j – engine type (slow, medium and high speed, Diesel engine, gas turbine and steam turbine); m – fuel type (marine diesel oil (MDO), heavy fuel oil (HFO), LNG, petrol); p – other phase of the journey (cruise, hotelling, manoeuvring).

If the cruise time is not known, it can be calculated as follows:

$$T_{Cruising}\ (\text{hours}) = \frac{\text{Distance Cruised (km)}}{\text{Average Cruising Speed (km/hr)}} \quad (6)$$

Activity data, such as engine load factors and an estimate of annual usage hours, should be derived from population data for small boats, categorized by ship type, fuel type, engine type, and technology level. This will help estimate emissions from small vessels for which separated national activity statistics are unavailable. According to fuel type, emission and fuel consumption are calculated as follows (7):

$$E_{i,m} = \sum_b \sum_e \sum_z (N_{b,e,z} \cdot T_{b,e,z} \cdot P_{b,e,z} \cdot LF_{b,e,z} \cdot EF_{b,e,z}) \quad (7)$$

where: $E_{i,m}$ – emissions generated by small boats per year [Mg]; $N_{b,e,z}$ – number of ships [pcs.]; $T_{b,e,z}$ – average operating time of each ship per year [hours/ship]; $P_{b,e,z}$ – nominal engine power [kW]; $LF_{b,e,z}$ – engine load factor [%]; $EF_{b,e,z}$ – emission factor [g/kWh]; b – type of vessel (yawl, cabin boat, sailing, …); e – type of engine (inboard, outboard, 2S, 4S); i – pollutant (NMLZO, NO_x, NH_3, PM) or fuel consumption; m – type of fuel (petrol, diesel oil); z – technology layer (conventional, 2003/44/EC).

It is worth noting that if the navigation calculations are founded on samples, the effects should be scaled up to obtain an annual sum. A geographic information system (GIS) can be used to disaggregate the data spatially.

If the fuel consumption for a given phase of the journey is unknown, an alternative method of estimating pollutant emissions should be used based on the installed power and the time spent in the individual navigation stages. A thorough understanding of the power output of the installed main and auxiliary engines, the load factor, and the total time (hours) spent in each phase can be used to calculate pollutant emissions.

There are two main approaches used to calculate GHG and pollutant emissions for air quality modelling purposes from all emission sources including ships, which use the methods described above or models derived from them: the bottom-up approach (activity-based – Tier 3) and the top-down approach (fuel-based – Tier 1 and 2) [6, 26, 33]. The schematic of both modelling approaches is shown in Fig. 2.

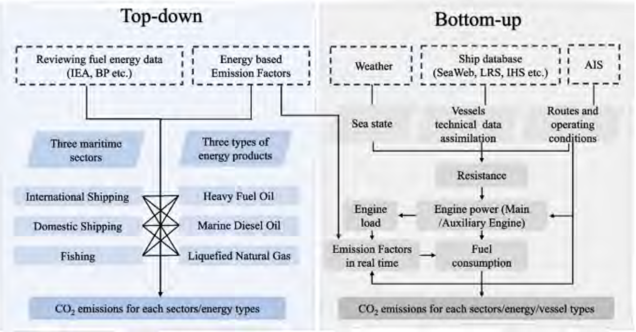

Fig. 2. Schematic approach to estimating emissions from ships [6]

The top-down method is based on the fuel consumption of the vessel [13], where the emission is calculated according to the Tier 1 or 2 method.

The bottom-up method is based on the vessel's activity (i.e. Tier 3), filling the shortcomings of the top-down method and improving the accuracy of the calculation of exhaust emissions from vessels [13]. Although a variety of data types are required, such as sailing time, vessel speed, navigational condition, engine power, load factors, emissions, etc., this method has made a detailed division of the vessel's activities, increasing the accuracy of the emission factor selection. Bottom-up approaches rely on data sources that provide each registered vessel's technical specifications in addition to worldwide shipping activity. In recent research, the AIS has been utilized to measure engine operating hours, instantaneous speeds, and the duration of journeys between locations at sea by analysing detailed vessel traffic data. Meanwhile, specific research from the ground up depends on fuel usage statistics submitted by operators for specific ships [4, 7, 12, 16, 26, 33].

The ambiguity surrounding fleet operations has decreased as a result of the more realistic description of emitters made possible by the availability of AIS data. AIS is an automated tracking system mandated by the SOLAS Convention for all passenger ships, all cargo ships above 500 GT, and all ships over 300 GT involved in international travel. At regular intervals, ships' AIS transceivers send vital information to shore stations and other vessels, including the ship's position, course, heading, speed, dimensions, type, draft, and destination. AIS data can be kept for later examination, making it a great resource for research, even if its main goal is to increase navigation safety. Numerous studies of maritime traffic have made advantage of the large datasets produced by AIS, particularly to describe maritime traffic patterns using unsupervised learning techniques [9, 34, 37–39], to detect maritime anomalies [36, 39], to assess the risk of ship collisions [37, 29, 41], maritime traffic and port management and to assess emissions [3, 22, 44]. Besides, with AIS information, it is conceivable to display high-resolution geological data on emissions and to examine the allotment of these emissions according to regularity, transport type, hail state, and transport routes. Once the specialized characteristics of the vessel are given, debilitated outflows can be demonstrated at exceptionally tall transient and spatial determination. The bottom-up approach permits the estimation of emissions by utilizing the information transmitted by AIS to calculate hourly fuel utilization and outflows for each vessel, where some vessels are distinguished as 'in operation' utilizing the IHS database. In this manner, the use of AIS and other vessel databases to gather information on vessel action and calculate GHG emissions from vessels utilizing the bottom-up strategy has become a common approach.

The AIS-based approach to ship emission inventories has found application in ship emission models. It was first proposed by Jalkanen et al. [16] who introduced the STEAM. Improvements in data assimilation and realistic performance modelling were then introduced, STEAM2 [18], STEAM3 [21], SENEM [31], and MariTEAM [26] models were subsequently published. The STEAM was developed by the FMI to accurately estimate pollutant emissions from maritime traffic. It is an advanced tool that allows dynamic modelling of gaseous and particulate emissions from vessels, taking into account real ship traffic data from the AIS system.

The STEAM model takes into account the type of fuel used to power both the main engines of the vessels and the auxiliary engines, as well as the fuel consumption indicator. The same value of the emission factors and fuel consumption was assumed for all engines. In order to estimate other emission indicators (SO_x and CO_2), the model is based on parameters describing fuel consumption (including the type of fuel and the type of engine). The emission profile of marine engines may vary significantly depending on fuel composition, as demonstrated in studies on the use of alternative fuel blends such as n-butanol and marine diesel oil [2]. NO_x emissions in the STEAM model are estimated based on the permissible values of unit emission from the engine speed described in Annex VI of the MARPOL Convention. Another simplification included in the model is the assumption that NOx emission indicators for all engines are the same regardless of their age, and they are independent of the actual fuel consumption. The STEAM model attempts to take into account the sulphur content in the fuel declared by the ship-owner [16]. If such data were not available, a 0.5% sulphur content in the fuel for the main engines and a 0.1% sulphur content for the auxiliary engines were assumed, in accordance with the requirements of Annex VI of the MARPOL Convention for Sulphur Emission Control Areas (SECA), including the Baltic Sea.

Another example is the secluded dispatch emission demonstrating framework (MoSES), which calculates toxin emissions in a spatial-temporal way, based on the ship's position information recorded from the programmed recognition system. MoSES is built in a secluded design, which ensures great extension and conceivable outcomes. A few transport type-specific strategies have been created to assess lost highlights that are vital for toxin emission displaying, such as net tonnage, fundamental or auxiliary motor control, motor control, or working speed, as these highlights are regularly not accessible at the show. In addition, the most recent emission factors for sulphates and particulate matter are taken from the literature on already ignored low-sulphur fuels. MoSES shows itself within the creation of an outflow stock for the North Ocean and Baltic Ocean locale, but it can be effectively connected to other districts as well [16–19].

Model of Emission From Ships At Sea (MEFSAS) is a predictive model and represents tool developed by the Polish Naval Academy in Gdynia, used to estimate emissions from vessels sailing on any stretch of water. This model uses a number of factors to calculate emissions, including the type of vessel, style of sailing (regular or tramp shipping), type and age of engine, type of fuel, and data on ship traffic obtained from the AIS system and meteorological information [23].

The input parameters to the model is information collected in a database created specifically for this purpose, containing [23]:

- vessel identification information (name, IMO number, type, displacement)
- information on the design of the vessel (hull dimensions, draft, year of construction, maximum speed)
- information on the main propulsion engine (engine type and its parameters, type of fuel used to power the engine, methods used to reduce toxic emissions from the engine)
- information on auxiliary engines.

To create this database, technical information on ships from databases including Lloyd's Register (LR) was used, supplemented by the data from ship-owners, local authorities and shipyards.

The MEFSAS model stands out from other approaches because it performs both retrospective and predictive emission assessments. Unlike models that focus solely on estimating historical emissions, MEFSAS enables simulation of emissions for any given period based on a combination of AIS data, vessel classification, engine characteristics, and meteorological information. It is particularly well suited for application in Baltic Sea regions, where detailed traffic and environmental data are available. Furthermore, MEFSAS introduces a division between regular and irregular shipping, using statistical methods (e.g., Monte Carlo simulations) to estimate movements of vessels with incomplete tracking data. This feature enhances the model's ability to provide temporally and spatially resolved emission estimates even in cases of limited AIS coverage.

3. Summary and conclusions

The presented methods were analysed comparatively regarding their methodological basis (top-down vs bottom-up), input data availability, resolution, and application potential. The analysis highlights that, while bottom-up methods offer higher precision, they demand significantly more detailed data and resources.

It is right now broadly acknowledged that the bottom-up approach is for the most part more exact than the top-down approach; however, extraordinary endeavours are required to diminish information gaps and peculiarities, particularly for large-scale studies [4, 27]. In truth, on a worldwide scale, the activity-based strategy postures challenges due to the utilize of normal input parameters such as motor stack components, time went through in operational modes, fuel utilization calculate and outflow variables, which depend on the measure, age, fuel sort, vessel sort course and advertise circumstance causing instability within the assessed emissions [9, 27].

Hence, the bottom-up outflow calculations will depend on the specialized data around the vessels (sort and/or category of the vessel; length of the vessel, GT, breadth, tallness; control of the most motor (ME) and assistant motor (AE); working speed of the vessel; particular fuel utilization of the motors), data on shipping and activity exercises (vessel speed and speeding up profile; arranged entry and flight times; motor operation data; AIS information) and other nitty gritty information such as fuel sort, day by day fuel utilization and outflow variables.

As for the technical information about the vessels, the best way to obtain the relevant data seems to be to combine data from the LRS database, engine manufacturers, local port authorities, and vessel owners, which allows for the collection of the most complete data for the studied fleet. However, data from commercial databases (e.g. LR) has to be purchased, which may be financially difficult.

As for the specialized information about the vessels, the perfect way to get the important information appears to be to combine information from the LRS database, motor producers, nearby harbour specialists, and vessel owners, which allows for the gathering of the most comprehensive data for the considered armada. Be that as it may, information from commercial databases (e.g. LR) must be obtained, which may be fiscally troublesome.

Displaying of destructive compounds emissions may be an exceptionally vital and at the same time exceptionally complex issue. Numerous endeavours are being made around the world to assess the outflow models of destructive compounds in the discharge of pollutants. Tragically, due to the reality that the structure of the demonstrate depends not as it were on its reason, but moreover, to a expansive degree, on the sum and quality of input information, and numerous considers are based on inadequately sum and quality of information, frequently gotten from numerous different sources and the have to be utilize rearrangements, this altogether influences the unwavering quality of the demonstrate. The models for evaluating toxin emissions displayed in this work are burdened with certain mistakes due to disentanglements constrained by down-to-earth reasons (e.g., a lack of information on the parameters of the vessel, motor, or outflow characteristics). To determine the activity and developments of ships, the use of AIS information appears to be the most solid and precise approach, since this information is much appreciated, it is possible to precisely model the operational profiles of ships. In spite of the focal points, it ought to be noted that AIS information may require filtering to remove irregularities caused by time gaps, which provide inaccurate positions and, thus, inaccurate speeds. Moreover, due to the extensive amount of information, calculations on this sort of information can be moderately complex. The basic difference between the described models, despite the apparent similarity in the general approach to the problem, is the way of approaching the input data. In the case of the STEAM model, an input database of vessels was created, and in the absence of information, it is assumed that it is a tugboat with specific parameters. The authors of the article adopted a different method of determining the vessel parameters and the movement of vessels. The division of vessels into regular shipping vessels (for which we have a database) and irregular shipping vessels was adopted, for which data is determined based on statistical data (using, among others, the Monte Carlo method) [23]. Therefore, MEFSAS can be considered a promising tool not only for reconstructing past emissions but also for forecasting emission scenarios in specific sea areas, thanks to its modular and data-driven structure.

It can therefore be stated that the MEFSAS model, unlike other models, allows not only for estimating the emission of toxic compounds in exhaust gases for the present or past, but also for forecasting emissions at any point in time.

Nomenclature

BC	black carbon
CAMS-GLOB-SHIP	Copernicus Atmospheric Monitoring Service Global Shipping
CEDS	Community Emissions Data System
CH_4	methane
CO	carbon monoxide
CO_2	carbon dioxide
COP21	Conference of the Parties
COPERT	Computer Programme to Calculate Emissions from Road Transport)
EDGAR	Emissions Database for Global Atmospheric Research
EF	emission factors
FMI	Finnish Meteorological Institute
GHG	greenhouse gas

GIS	geographic information system
HBEFA	Handbook Emission Factors for Road Transport
IMO	International Maritime Organization
IPCC	International Panel on Climate Change
MEFSAS	Model of Emission From Ships At Sea
N_2O	nitrous oxide
NH_3	ammonia
NMVOC	non-methane volatile organic compounds
NO_x	nitrogen oxides
OC	organic carbon
PM	particulate matter
SO_2	sulphur dioxide
SO_x	sulphur oxides
STEAM	Ship Traffic Emission Assessment Model
VOC	volatile organic compounds

Bibliography

[1] Beirle S, Platt U, von Glasow R, Wenig M, Wagner T. Estimate of nitrogen oxide emissions from shipping by satellite remote sensing. Geophys Res Lett. 2004;31(18). https://doi.org/10.1029/2004GL020312

[2] Bogdanowicz A, Kniaziewicz T, Zadrąg R. The emission of harmful compounds from the marine diesel engine fueled by a blend of n-butanol and marine fuel. Combustion Engines. 2021;187(4):90-95. https://doi.org/10.19206/CE-142031

[3] Bojić F, Gudelj A, Bošnjak R. An analytical model for estimating ship-related emissions in port areas. Journal of Marine Science and Engineering. 2023;11(12):2377. https://doi.org/10.3390/jmse11122377

[4] Browning L, Bailey K. Current methodologies and best practices for preparing port emission inventories. ICF Consulting Report to Environmental Protection Agency. 2006.

[5] Corbett JJ, Winebrake JJ, Green EH, Kasibhatla P, Eyring V, Lauer A. Mortality from ship emissions: a global assessment. Environ Sci Technol. 2007;41:8512-8518. https://doi.org/10.1021/es071686z

[6] Deng S, Mi Z. A review on carbon emissions of global shipping. Mar Dev. 2023;1(4). https://doi.org/10.1007/s44312-023-00001-2

[7] Deniz C, Kilic A. Estimation and assessment of shipping emissions in the region of Ambarlı Port, Turkey. Environ Prog Sustain. 2010;29:107-115. http://doi.org/10.1002/ep.10373

[8] European Environment Agency, EMEP/EEA air pollutant emission inventory guidebook 2013 – technical guidance to prepare national emission inventories, Publications Office. 2013. https://data.europa.eu/doi/10.2800/92722

[9] Etienne L, Devogele T, Bouju A. Spatio-temporal trajectory analysis of mobile objects following the same itinerary. Int Arch Photogramm. 2010;38:86-91.

[10] Goldsworthy L. Exhaust emissions from ship engines – significance, regulations, control technologies. Australian and New Zealand Maritime Law Journal. 2010;24:21-30.

[11] Goldsworthy L, Goldsworthy B. Modelling of ship engine exhaust emissions in ports and extensive coastal waters based on terrestrial AIS data- an Australian case study. Environ Modell Softw. 2015;63:45-60. https://doi.org/10.1016/j.envsoft.2014.09.009

[12] Howitt OJA, Revol VGN, Smith IJ, Rodger CJ. Carbon emissions from international cruise ship passengers' travel to and from New Zealand. Energ Policy. 2010;63:45-60. https://doi.org/10.1016/j.enpol.2009.12.050

[13] Huang L, Wen Y, Geng X, Zhou C, Xiao C, Zhang F. Estimation and spatio-temporal analysis of ship exhaust emission in a port area. Ocean Eng. 2017;140:401-411. https://doi.org/10.1016/j.oceaneng.2017.06.015

[14] IMO. Third IMO Greenhouse Gas Study 2014. International Maritime Organization: London 2014.

[15] INFRAS AG: HBEFA Handbook emission factors for road transport 4.2, INFRAS, Bern 2022.

[16] Jalkanen, JP, Brink A, Kalli J, Pettersson H, Kukkonen J, Stipa T. A modelling system for the exhaust emissions of marine traffic and its application in the Baltic Sea area. Atmos Chem Phys. 2009;9;23. https://doi.org/10.5194/acp-9-9209-2009

[17] Jalkanen JP, Johansson L, Kukkonen J. Comprehensive inventory of the ship traffic exhaust emissions in the Baltic Sea from 2006 to 2009. Ambio. 2014;43:311-324. http://doi.org/10.1007/s13280-013-0389-3

[18] Jalkanen JP, Brink A, Kalli J, Pettersson H, Kukkonen J, Stipa T. A modelling system for the exhaust emissions of marine traffic and its application in the Baltic Sea area. Atmos Chem Phys. 2009;9:9209-9223. https://doi.org/10.5194/acp-9-9209-2009

[19] Jalkanen, JP, Johansson L, Kukkonen J. A comprehensive inventory of ship traffic exhaust emissions in the European Sea areas in 2011. Atmos Chem Phys. 2016;16:71-84. https://doi.org/10.5194/acp-16-71-2016

[20] Johansson L. Emission estimation of marine traffic using vessel characteristics and AIS-data. Aalto University 2011.

[21] Johansson L, Jalkanen JP, Kukkonen J. Global assessment of shipping emissions in 2015 on a high spatial and temporal resolution. Atmos Environ. 2017;167:403-415. https://doi.org/10.1016/j.atmosenv.2017.08.042

[22] Kao SL, Chung WH, Chen CW. AIS-based scenario simulation for the control and improvement of ship emissions in ports. Journal of Marine Science and Engineering. 2022;10(2):129. https://doi.org/10.3390/jmse10020129

[23] Kim HS, Lee E, Lee EJ, Hyun JW, Gong IY, Kim K et al. A study on grid-cell-type maritime traffic distribution analysis based on AIS data for establishing a coastal maritime transportation network. Journal of Marine Science and Engineering. 2023;11(2):354. https://doi.org/10.3390/jmse11020354

[24] Kniaziewicz T. Using information from AIS system in the modelling of emission of toxic compounds in exhaust gas from marine Diesel engines. Maritime Transport. Technical, Innovation and Research. Barcelona 2012.

[25] Kniaziewicz T, Zacharewicz M. Evaluation of adequacy of a model of a marine diesel engine based upon empirical research. Combustion Engines. 2020;181(2):40-45. https://doi.org/10.19206/CE-2020-206

[26] Kramel D, Muri H, Kim Y, Lonka R, Nielsen JB. Ringvold AL. Global shipping emissions from a well-to-wake perspective: the MariTEAM Model. Environ Sci Technol. 2021;55(22):15040-15050. https://doi.org/10.1021/acs.est.1c03937

[27] Maragkogianni A, Papaefthimiou S, Zopounidis C. Mitigating Shipping Emissions in European ports: social and environmental benefits. Springer Cham. 2016. http://doi.org/10.1007/978-3-319-40150-8

[28] Matthias V, Bewersdorff I, Aulinger A, Quante M. The contribution of ship emissions to air pollution in the North Sea regions. Environ Pollut. 2010;158:2241-2250. http://doi.org/10.1016/j.envpol.2010.02.013

[29] Merico E, Donateo A, Gambaro A, Cesari D, Gregoris E, Barbaro E et. al. Influence of in-port ships emissions to gaseous atmospheric pollutants and to particulate matter of different sizes in a Mediterranean harbour in Italy. Atmos Environ. 2016;139:1-10. https://doi.org/10.1016/j.atmosenv.2016.05.024

[30] Merkisz J, Piaseczny L, Kniaziewicz T. Zagadnienia emisji spalin silników okrętowych (in Polish). Wydawnictwo Politechniki Poznańskiej. Poznań 2016.

[31] Moreno-Gutiérrez J, Durán-Grados V. Calculating ships' real emissions of pollutants and greenhouse gases: towards zero uncertainties. Sci Total Environ. 2021;750:141471. https://doi.org/10.1016/j.scitotenv.2020.141471

[32] Ntziachristos L, Gkatzoflias D, Kouridis C, Samaras Z, COPERT: A European Road Transport Emission Inventory Model. In: Athanasiadis IN, Rizzoli AE, Mitkas PA, Gómez JM (eds). Information Technologies in Environmental Engineering. Environmental Science and Engineering. Springer: Berlin/Heidelberg 2009. https://doi.org/10.1007/978-3-540-88351-7_37

[33] Nunes RAO, Alvim-Ferraz MCM, Martins FG, Sousa SIV. The activity-based methodology to assess ship emissions – a review. Environ Pollut. 2017;231(1):87-103. https://doi.org/10.1016/j.envpol.2017.07.099

[34] Ribeiro da Silva JN, Santos TA, Teixeira AP. Methodology for Predicting Maritime Traffic Ship Emissions Using Automatic Identification System Data. J Mar Sci Eng. 2024; 12:320. https://doi.org/10.3390/jmse12020320

[35] Richter A, Eyring V, Burrows JP, Bovensmann H, Lauer A, Sierk B et al. Satellite measurements of NO_2 from international shipping emissions. Geophys Res Lett. 2004; 31:1-4. http://doi.org/10.1029/2004GL020822

[36] Riveiro M, Pallotta G, Vespe M. Maritime anomaly detection: a review. Wiley Interdiscip Rev Data Min Knowl Discov. 2018;8:e1266. https://doi.org/10.1002/widm.1266

[37] Rong H, Teixeira AP, Guedes SC. Data mining approach to shipping route characterization and anomaly detection based on AIS data. Ocean Eng. 2020;198:106936. https://doi.org/10.1016/j.oceaneng.2020.106936

[38] Rong H, Teixeira AP, Guedes SC. Maritime traffic probabilistic prediction based on ship motion pattern extraction. Reliab Eng Syst Safe. 2022:217:108061. https://doi.org/10.1016/j.ress.2021.108061

[39] Rong H, Teixeira AP, Guedes SC. Spatial correlation analysis of near ship collision hotspots with local maritime traffic characteristics. Reliab Eng Syst Safe. 2021;209: 107463. https://doi.org/10.1016/j.ress.2021.107463

[40] Saraçoglu H, Deniz C, Kiliç A. An investigation on the effects of ship sourced emissions in Izmir Port, Turkey. Sci World J. 2013;3:218324. https://doi.org/10.1155/2013/218324

[41] Silveira PAM, Teixeira AP, Soares CG. Use of AIS data to characterise marine traffic patterns and ship collision risk off the coast of Portugal. J Navigation. 2013;66(6):879-898. https://doi.org/10.1017/S0373463313000519

[42] Song S. Ship emissions inventory, social cost and eco-efficiency in Shanghai Yangshan port. Atmos Environ. 2014;82:288-297. https://doi.org/10.1016/j.atmosenv.2013.10.006.

[43] Song SK, Shon ZH. Current and future emission estimates of exhaust gases and particles from shipping at the largest port in Korea. Environ Sci Pollut R. 2014;21:6612-6622. https://doi.org/10.1007/s11356-014-2569-5

[44] Svanberg M, Santén V, Hörteborn A, Holm H, Finnsgård C. AIS in maritime research. Mar Policy. 2019;106:103520. https://doi.org/10.1016/j.marpol.2019.103520

[45] Tu E, Zhang G, Rachmawati L, Rajabally E, Huang GB, Exploiting AIS data for intelligent maritime navigation: a comprehensive survey from data to methodology. IEEE T Intell Transp. 2018;19(5):1559-1582. https://doi.org/10.1109/TITS.2017.2724551

[46] Tzannatos E. Ship emissions and their externalities for the port of Piraeus – Greece. Atmos Environ. 2010;44(3):400-407. https://doi.org/10.1016/j.atmosenv.2009.10.024

[47] Vinken GCM, Boersma KF, Maasakkers JD, Adon M, Martin RV. Worldwide biogenic soil NO_x;emissions inferred from OMI NO_2 observations. Atmos Chem Phys. 2014;14(18):10363-10381. https://doi.org/10.5194/acp-14-10363-2014

[48] World Maritime News. COP21: Paris Remains Silent on Shipping and Aviation. 2016. http://worldmaritimenews.com/archives/178732/cop21-paris-remains-silenton-shipping-and-aviation/

[49] Wu G, Umar JA, Li T, Zhou X, Chen C, Li J, et al. Recent research progress on black carbon emissions from marine diesel engines. Atmosphere. 2024;15:22. https://doi.org/10.3390/atmos15010022

Magdalena Zimakowska-Laskowska, DEng. – Environment Protection Centre, Motor Transport Institute, Poland.

e-mail: *magdalena.zimakowska-laskowska@its.waw.pl*

Prof. Tomasz Kniaziewicz, DSc., DEng. – Faculty of Mechanical and Electrical Engineering, Polish Naval Academy, Poland.

e-mail: *t.kniaziewicz@amw.gdynia.pl*

Article citation info:
Kindler O, Królak S, Warguła Ł, Wieczorek B. Research on the design of a non-commercial impulse compressed air supply system for the turbocharger of a spark-ignition internal combustion engine. Combustion Engines. 2025;202(3):11-19. https://doi.org/10.19206/CE-205010

Oleg KINDLER
Szymon KRÓLAK
Łukasz WARGUŁA
Bartosz WIECZOREK

Combustion Engines
Polish Scientific Society of Combustion Engines

Research on the design of a non-commercial impulse compressed air supply system for the turbocharger of a spark-ignition internal combustion engine

ARTICLE INFO

Received: 29 April 2025
Revised: 8 May 2025
Accepted: 12 May 2025
Available online: 3 June 2025

A compressed air pulse directed to the turbocharger of an internal combustion engine can significantly improve the power and torque build-up characteristics. This article presents the design and testing of a universal compressed air delivery system for the turbine rotor on the exhaust side of a turbocharger, demonstrated using a Volvo V70 2.0 Turbo vehicle. The proposed solution offers a retrofit approach for older engine designs, inspired by the PowerPulse system, which was first introduced commercially by Volvo in 2016 in the S90 model. The non-commercial prototype tested in this study increased engine torque by up to 13% within a selected rotational speed range (1700 to 2400 rpm). Simultaneous changes were also observed in the manifold absolute pressure (MAP), lambda sensor readings, injection timing, and air mass flow in the intake manifold.

Key words: *Power Pulse system, reduction of turbo lag, improvement of torque and power characteristics, engine boosting with compressed air, enhancement of engine acceleration response*

1. Introduction

The phenomenon known as turbo lag refers to the delay between the demand for power and the actual increase in engine power output in turbocharged engines. This delay is primarily due to the time required for the turbocharger to spool up and provide the necessary boost pressure. Several key factors contribute to turbo lag. The design and efficiency of the turbocharger [19], including the turbine and compressor geometry, have a significant impact on transient response; for example, mixed flow turbines can improve efficiency at low velocity ratios [11], while variable geometry turbines (VGT) and variable diffuser vanes extend operating range and optimize torque delivery by adjusting flow conditions [9]. Turbochargers also operate under highly unsteady flow conditions due to the reciprocating nature of internal combustion engines, which affects overall performance [7, 13, 16]. The interaction between the turbocharger and the intake and exhaust systems [2], including pulsating flow dynamics, is critical to optimizing performance [13, 14]. Additionally, heat transfer within the turbocharger and aerodynamic aspects such as the shape of the turbine volute influence performance, especially under pulsating flow conditions [24], and deviations from expected behavior can occur at low engine loads due to heat transfer effects [17]. To address these challenges, advanced control strategies are employed, including computational fluid dynamics (CFD)-based optimization and genetic algorithms to improve design [10, 12, 15], as well as model-based control of fueling and valve timing to reduce cylinder-to-cylinder variation and improve performance [21, 25]. Mitigation techniques such as variable geometry turbochargers [9], turbo-discharging methods to recover exhaust energy [3], and the application of advanced materials and coatings to improve durability and efficiency under high-stress conditions are all helping to reduce turbo lag. While turbo lag remains a key challenge in turbocharged spark-ignition engines, ongoing advancements in turbocharger design, control systems, and materials continue to enhance engine response and overall performance.

One of the emerging solutions in the effort to improve engine response and reduce torque delay is the use of compressed air systems for turbochargers. Compressed air systems can help address this issue by providing an immediate supply of compressed air to the engine, thereby reducing the time required for the turbocharger to reach optimal performance levels [4]. Cieslar et al. in 2013 investigated two such systems: Air-Assist Systems and Exhaust Assist Systems. The Air-Assist System injects compressed air directly into the intake manifold, significantly enhancing the engine's transient response. This approach is relatively cost-effective compared to more complex technologies such as multi-stage turbocharging or electrically assisted turbochargers. However, its performance is often limited by the compressor surge margin. In contrast, the Exhaust Assist System represents a more innovative approach, where a compressed air reservoir, charged during braking, delivers air into the exhaust manifold. This technique helps overcome the surge limitation and substantially improves turbocharger acceleration, reducing the time required to generate torque by approximately 60% during gear shifts. Additionally, Song et al. in 2020 analyzed the Active Control Methodology (ACM), which involves extracting a portion of compressed air from the compressor outlet, heating it with fuel, and supplying it to the turbine inlet. This method aims to optimize turbocharger operating conditions by expanding the surge margin and enhancing instantaneous engine performance [18]. In 2008, Basu described hyperbar supercharging, also known as hyper-bar turbocharging, as a high-pressure turbocharging method primarily employed in applications demanding exceptionally high engine output. The technique utilizes turbochargers to dramatically increase intake air pressure, thereby boosting engine power density and overall performance [1]. In conclusion, compressed air-based systems present promising avenues for improving turbocharger dynamics and mitigating turbo lag. Each system offers distinct advantages and limitations, and further research is essential to refine these technologies for practical implementation in modern automotive engines.

The first commercially implemented compressed air system for turbocharger support was introduced by Volvo in 2016 in the D5 engine of the Volvo S90 under the name PowerPulse (Fig. 1). Developed in-house, this pneumatic system was designed to eliminate turbo lag and improve low-end engine response by injecting a pulse of compressed air directly into the exhaust manifold, accelerating the turbocharger turbine more rapidly. The system uses an electric compressor to pressurize a 2-liter air tank to 18 bar, releasing air through a solenoid valve when additional torque is requested, particularly enhancing responsiveness at engine speeds below 1500 rpm. Testing showed torque gains of up to 30% within one second of load application and improved acceleration in real-world driving conditions, such as stop-and-go traffic. Compared to competitors with larger diesel engines, the PowerPulse-equipped Volvo XC90 D5 delivered superior launch performance while maintaining fuel efficiency and low emissions [5, 6].

The aim of this article is to present the design of a universal compressed air pulse system for the turbocharger of a spark-ignition internal combustion engine, along with the results of experimental studies on its impact on torque, power output, manifold absolute pressure (MAP), intake air flow, injection duration, and lambda sensor readings. The research was conducted using a Volvo V70 2.0 Turbo as the test platform.

Fig. 1. Power-Pulse Volvo design [20]

2. Materials and methods

The concept involves designing a system that delivers compressed air to the turbine rotor on the exhaust side of the turbocharger, with the aim of increasing the air momentum. The primary actuator of the system is a pressure nozzle located in the exhaust manifold, aligned with the direction of exhaust gas flow (Fig. 2).

The subject of the study is a Volvo V70 2.0 Turbo equipped with a spark-ignition internal combustion engine designated as B5204T5. This 2004 engine is a five-cylinder unit with a displacement of 1984 cm³ (Table 1). It features Variable Valve Timing (VVT) on both camshafts and is fitted with 20 valves. According to the manufacturer's specifications, it delivers 180 HP and a maximum torque of 240 Nm. The compression ratio is 9.5:1, which is considered relatively low for modern turbocharged engines focused on reducing emissions. However, this ratio is relatively high in the context of modifications aimed at increasing boost pressure and engine output.

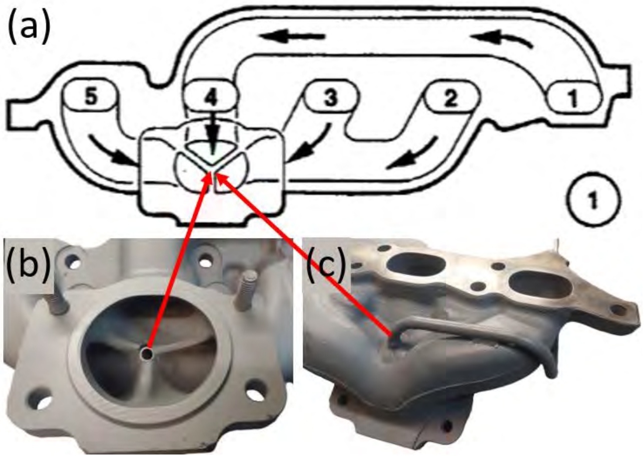

Fig. 2. Exhaust manifold of the Volvo V70 2.0 Turbo: (a) manufacturer's schematic, (b) additional channel for the compressed air impulse system (internal side), (c) additional channel for the compressed air impulse system (external side), where: 1–5 – cylinder numbers of the exhaust channels

Engine control is managed by the Bosch Motronic ME7 system, a series of control units developed by Bosch for spark-ignition engines with multi-point fuel injection. Fig. 3 illustrates the internal architecture of the controller, including the sensors and actuators it operates.

The engine's forced induction system features a Mitsubishi turbocharger from the TD04HL-20T family. On the intake side, it has a 47 mm inlet and a 58 mm outlet, while the exhaust side features a 52 mm inlet and a 45.6 mm outlet. This series of turbochargers is specifically designed for gasoline-powered engines. The rotor shaft is supported by journal bearings and is lubricated by oil supplied from the engine's main oil line. Additionally, the turbocharger core is cooled using a water jacket.

Table 1. Technical specifications of the B5204T5 engine

Parameter	Specifications
Type	Inline 5-cylinder
Displacement	1984 cm³
Power	180 hp (132 kW) at 5300 rpm
Torque	240 N·m (180 lb·ft) at 2000–5300 rpm
Bore	81 mm
Stroke	77 mm
Compression ratio	9.5:1
Type of supercharging	Turbocharged

To analyze the engine's operating parameters, the Volvo DICE diagnostic interface was used in combination with the Volvo VIDA software. Simulated engine load tests were conducted on a Dynomet ASP chassis dynamometer with active load control capabilities. The device is a load-type (brake) chassis dynamometer, capable of applying programmable resistance to simulate various driving conditions. The dynamometer allows for real-time measurement of wheel torque, engine output, and vehicle speed, with typical measurement accuracy of ±1% for power and torque, and ±0.2% for rotational speed. The system supports both steady-state and transient testing and can operate under automated load profiles for repeatable performance evaluations.

Measurements were carried out under three different scenarios involving the initiation of the compressed air impulse. In the first scenario, the system was activated at an engine speed of 1200 rpm; in the second, at 1700 rpm; and in the third, at 2000 rpm.

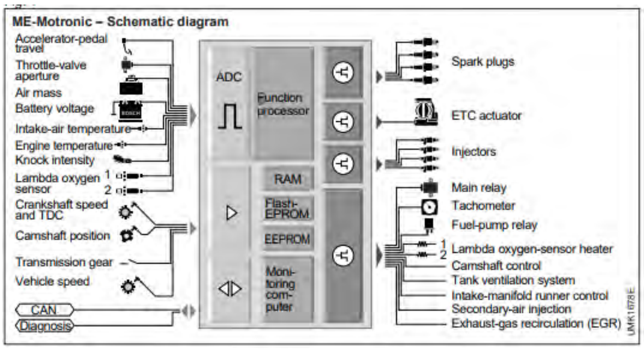

Fig. 3. Diagram of the BOSCH ME control unit with sensors and actuators [8]

3. Prototype design of the conceptual compressed air impulse delivery system

3.1. Concept of operating principle

The designed system is responsible for delivering a compressed air impulse to the turbocharger while maintaining full automation. This means that once installed and configured, the system operates autonomously, with all necessary actions managed and executed by the control unit.

The primary function of the system is to continuously monitor selected engine parameters that reflect the load on the power unit – specifically, the throttle opening degree, measured by the position sensor integrated into the original throttle body. At the same time, it monitors the pressure in the intake manifold, which, under high throttle opening, equals the pressure generated by the turbocharger. Another essential parameter for evaluating engine performance is engine speed.

Based on these inputs, the system compares real-time values with thresholds programmed by the installer. When specific conditions are met, the system decides to inject compressed air into the turbocharger. This injection is initiated by actuating a solenoid valve, and the supplied air accelerates the rotation of the turbocharger's rotors.

Due to the need for a constant supply of compressed air – something not typically available in passenger vehicles – the system includes a dedicated air preparation module. This module consists of a compressor and a storage tank. Its operation is supervised by the system's central control unit.

To allow both the user and the installer or technician to view system parameters and quickly deactivate the system if needed, a user interface panel is included. Designed for in-cabin installation via a single cable, the panel features an LCD display for real-time data and control buttons for manual input.

Ensuring system reliability and maintenance-free operation requires self-monitoring capabilities. For this purpose, the system includes additional temperature and pressure sensors. If any monitored parameter exceeds safe limits, the system automatically deactivates to prevent damage. Normal operation resumes automatically once the conditions return to a safe range.

3.2. Monitored parameters

Power demand assessment in gasoline engines is made possible by monitoring the Throttle Position Sensor (TPS). The standard output range for such built-in sensors is 0 to 5 V, which corresponds to an interpretable signal range for a microcontroller.

Intake manifold pressure in a turbocharged engine is a key parameter for the designed system, as it determines both the activation of the system and the correctness of its operation. This pressure is measured by a MAP sensor installed in the intake system. For optimal performance, the most suitable measurement location is in the intake manifold downstream of the throttle body, as this position includes vacuum values. In vehicles equipped with a MAF sensor, the MAP sensor is typically located in the intake before the throttle body. Therefore, in the new system, the MAP reading is taken from an auxiliary sensor, which may also be shared with an alternative fuel injection system (e.g., LPG or CNG). The pressure sensor used in the system must have a minimum operating range of –0.1 to 0.15 MPa.

Engine speed is a fundamental operating parameter of an internal combustion engine. It serves as the basis for functions that define other parameters. In the context of the designed system, it is essential for determining operational thresholds. The engine speed is determined in coordination with angular position detection, using a toothed ring rigidly connected to the crankshaft, in combination with an inductive or Hall-effect sensor.

Compressed air preparation would not be possible without monitoring the pressure inside the storage tank. It is necessary to maintain the desired pressure level via a compression unit, consisting of a compressor or a set of compressors controlled electronically by the system controller. For this reason, it is a critical parameter for overall system operation. The pressure is measured by a transducer mounted on and connected to the storage tank. The transducer's readings are processed by the control unit. The required sensor must have a measurement range of at least 0 to 0.8 MPa. However, considering that the system may require higher boost pressures for improved performance, a transducer with a wider operating range, such as up to 1.2 MPa, should be considered.

Temperature monitoring within the system is necessary due to the need for automation, self-diagnostics, and the challenging operating environment. The control unit is designed for installation in the engine bay and includes heat-generating components such as a step-down voltage converter supplying 5 V to digital circuits, power transistors for driving the solenoid valve, and a microcontroller. The controller is passively cooled without additional heat exchangers. A thermistor will be placed on its surface for temperature monitoring.

Another critical location requiring thermal management is the air compressor mounted in the vehicle's trunk. It is responsible for supplying significant volumes of compressed air. The electric motor generates considerable heat, and under the system's assumed working pressures, not all commercially available compressors support a 100% duty cycle. Additionally, the compression process itself generates heat that must be dissipated. As a result, the compressor is another potential overheating point and will also be equipped with a temperature sensor.

3.3. Actuators

The solenoid valve plays a crucial role in the designed system as the main actuator responsible for the precise delivery of compressed air. It operates by opening to allow airflow when the control unit detects the need for an air impulse, and closing to stop the flow when compressed air delivery is unnecessary or undesirable, such as in the case of system overheating. The valve's performance requirements include a fast response time to enable accurate activation and deactivation of the compressed air impulse, resistance to high pressure up to 0.8 MPa, and durability in harsh operating conditions such as elevated engine bay temperatures, moisture, and vibrations.

Equally important to the system's operation is the compressor, which is tasked with compressing air into a thin-walled storage tank essential for the system's functionality. In the proposed setup, the compressor is powered by a 12–14.4 V electric motor. It must meet several key requirements: it must generate compressed air at a target pressure of 0.8 MPa, have a compact design suitable for vehicle integration, and provide sufficient performance to pressurize the air tank efficiently in the shortest possible time. Additionally, the compressor must maintain power consumption at an acceptable level to ensure reliable and efficient operation within the vehicle's electrical system.

3.4. Control unit

The control unit serves as the central component of the system, responsible for analyzing sensor data, making real-time decisions to operate actuators, and ensuring communication with the vehicle driver through the user interface panel (Fig. 4). Its core functions include the analysis of input signals such as:

- MAP (Manifold Absolute Pressure): measuring intake manifold pressure in the internal combustion engine
- TPS (Throttle Position Sensor): detects the throttle opening angle
- TAP (Tank Air Pressure): monitoring the pressure of compressed air stored in the thin-walled tank
- RPM (Engine Speed): derived from the first fuel injector signal, allowing the system to determine the engine's crankshaft speed
- Compressor Temperature Sensor: monitoring the thermal condition of the compressor
- Control Unit Temperature Sensor: tracking the operating temperature of the control module itself
- Vehicle Electrical System Voltage: assessing power supply status
- User Panel Button States: detecting manual user inputs.

In terms of actuator control, the unit performs the following actions:

- Solenoid Valve Control: based on the analysis of selected engine parameters, the control unit determines when to open or close the valve
- Compressor Activation: it triggers the compressor when the pressure in the air tank drops below a preset threshold.

The user interface panel supports:

- Displaying system operating parameters
- Presenting predefined values for key variables
- Handling user input via buttons.

For safety and diagnostics, the control unit continuously monitors critical thresholds and deactivates the system if any parameter exceeds its safe limit. Once conditions return to normal, the system automatically resumes operation, ensuring reliability and minimizing the need for manual intervention.

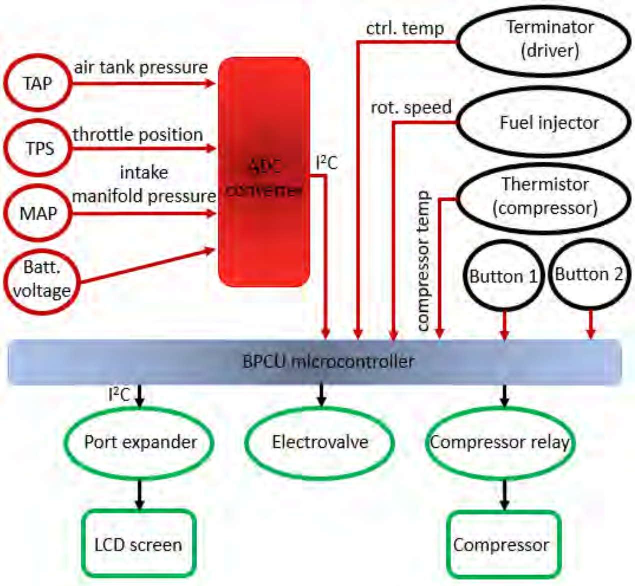

I^2C – a serial, bidirectional bus used for data transmission in electronic devices

Fig. 4. Schematic diagram of the control system

3.5. User panel

The user panel serves as the interface that allows the driver to monitor and manage, in real time, the operation of the system responsible for delivering compressed air impulses to the turbocharger. It is equipped with a 20×4 LCD screen and two buttons for system control.

Each button on the user panel has a distinct function. The first button enables system deactivation. Pressing it immediately shuts down the system, including the compressor. The driver can reactivate the system at any time by pressing the same button again. The second button is used to switch between different display screens, allowing the user to browse current operating parameters.

The first screen displays real-time engine and system parameters.

Displayed engine parameters include:
- Engine speed [rpm]
- Intake manifold pressure (MAP) [bar]
- Battery voltage (U.BAT.) [V].

Displayed system parameters include:
- Compressor activation status
- Compressed air pressure in the storage tank
- Compressor temperature
- Control unit temperature.

The second screen provides access to the preset values that define the system's activation conditions. The following data is shown:
- Boost pressure range (MAP) in the intake manifold at which the system is triggered
- Minimum throttle opening angle required to indicate power demand
- Maximum impulse duration, i.e., the maximum time compressed air is delivered into the intake or exhaust system.

When the system is deactivated, the screen displays a welcome message containing the project name and the authors' credits.

The electrical and pneumatic system components are shown in Fig. 5 and 6, respectively.

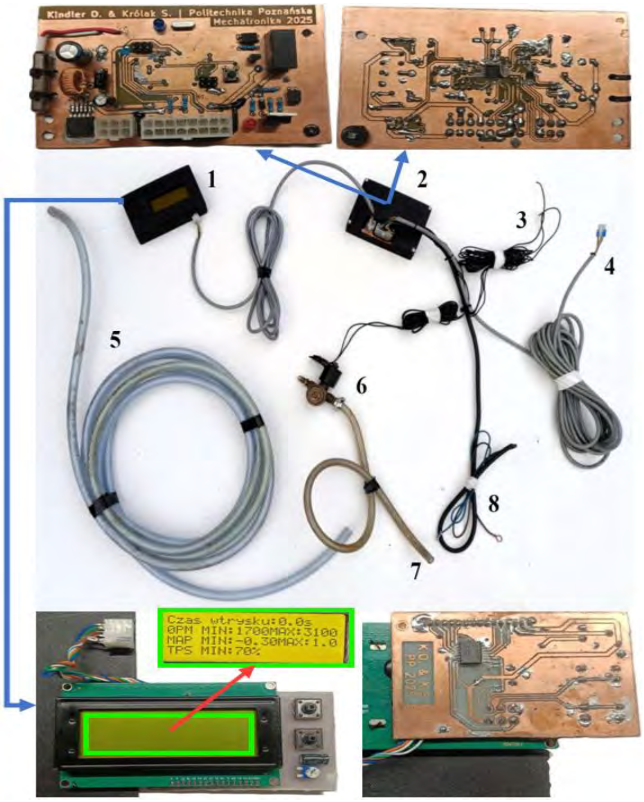

Fig. 5. Electrical system components, where: 1 – user panel, 2 – control unit, 3 – sensor signal inputs: MAP, TPS and rpm signal, 4 – air preparation module signal wire, 5 – air compressor wire, 6 – solenoid valve, 7 – air compressor output, 8 – power supply wires

4. Results and discussion

The tests conducted on the chassis dynamometer (Fig. 7) focus on the operating range of the designed system, which means the lower engine speed range—where, due to insufficient exhaust gas flow, the turbocharger cannot achieve the rotational speed necessary to generate the desired boost pressure. This type of testing enables a clear assessment of the system's effectiveness. The results for torque and power as a function of engine speed are presented for three tested activation ranges: starting from 1200 rpm (Fig. 8), 1700 rpm (Fig. 9), and 2000 rpm (Fig. 10).

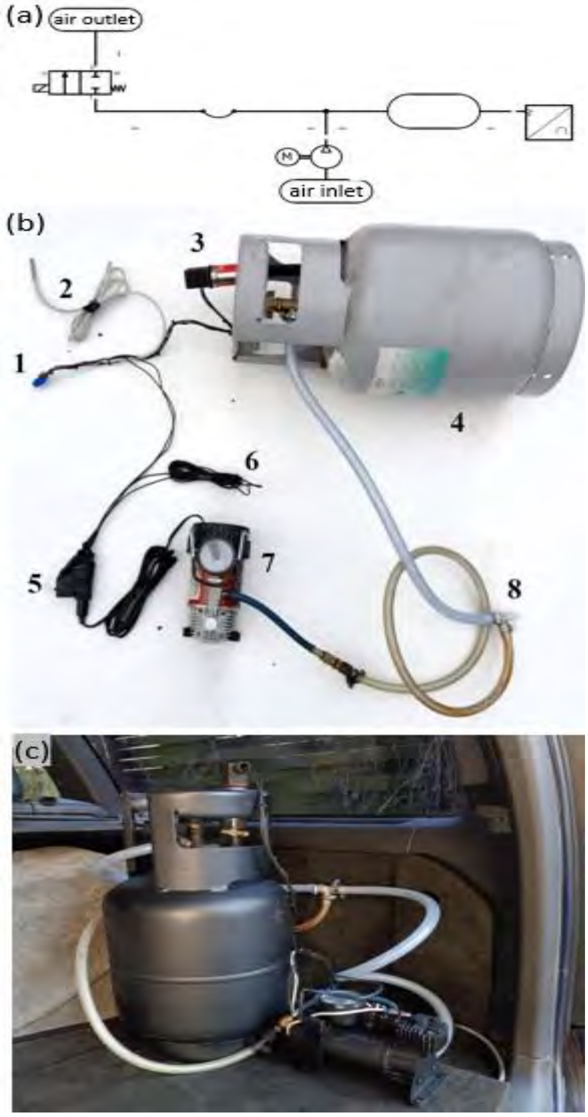

Fig. 6. Pneumatic system components (a) pneumatic diagram, (b) real parts, (c) air preparation system in the luggage compartment, where: 1 – air preparation module cable input, 2 – compressor temperature probe, 3 – tank pressure sensor (TAP), 4 – pressure tank, 5 – compressor relay, 6 – compressor power cables, 7 – electric compressor, 8 – air compressor output

The testing begins with a reference measurement across the full engine speed range to verify the proper functioning of the engine and control system. This reference serves as the baseline for evaluating the performance of the compressed air impulse system. By activating the system at different engine speeds, it becomes possible to determine the optimal timing for air injection in order to achieve the best performance gains. On the graphs, the operating range of the system is marked by two vertical lines indicating the beginning and end of the air impulse. The red curves on the graphs represent power output, while the green curves represent torque.

In the first test scenario, the system is activated at the lowest planned engine speed of 1200 rpm. Upon activation, a torque increase of approximately 6% is observed, lasting until the solenoid valve closes (Fig. 8).

The second test is carried out with a starting engine speed 500 rpm higher, at 1700 rpm – representing the mid-range of the tested speeds. Activating the compressed air impulse system at this point results in the performance shown in Fig. 9. A noticeable torque increase of approximately 25 Nm (around 9%) is recorded over a 400 rpm increase in engine speed. The engine responds immediately at the onset of the injection.

The third test is conducted with the system activation set at 2000 rpm. The results, shown in Fig. 10, reveal a significant torque increase of approximately 13%, equivalent to around 30 Nm. This improvement is substantial and would be clearly noticeable during real-world driving. However, it's important to note that the duration of the impulse is significantly shorter in this case. This is due to the control unit's programmed boost pressure limit of 0.06 MPa. Once this threshold is reached during injection, the system terminates the impulse after approximately 2 seconds. Increasing the activation speed any further would not yield additional benefits, as the MAP pressure limit would be exceeded, triggering the software's safety constraint and preventing further impulse generation.

Fig. 7. Vehicle tested on the chassis dynamometer

Testing on the chassis dynamometer confirms that the designed system is functional and has a measurable impact on engine power output. To objectively assess the influence on engine performance, additional parameters such as intake manifold pressure were also monitored (Fig. 11). In each scenario, an increase in boost pressure is observed during the system's operation. However, once the air injection ends, the pressure quickly returns to the baseline reference value. This indicates that the exhaust gas volume remains insufficient to drive the turbocharger effectively on its own in the low-speed range.

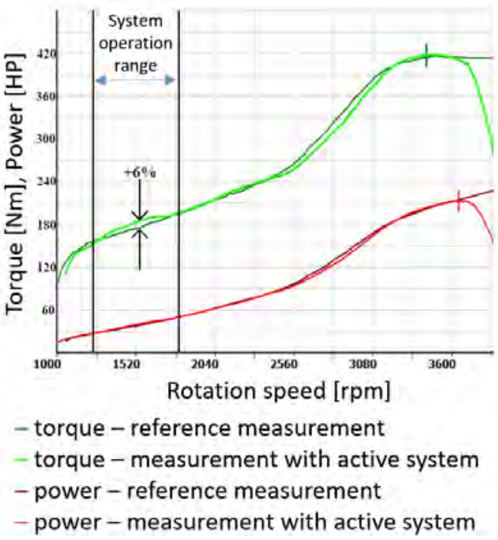

Fig. 8. Torque and power characteristics of the engine with the compressed air impulse system activated starting from 1200 rpm

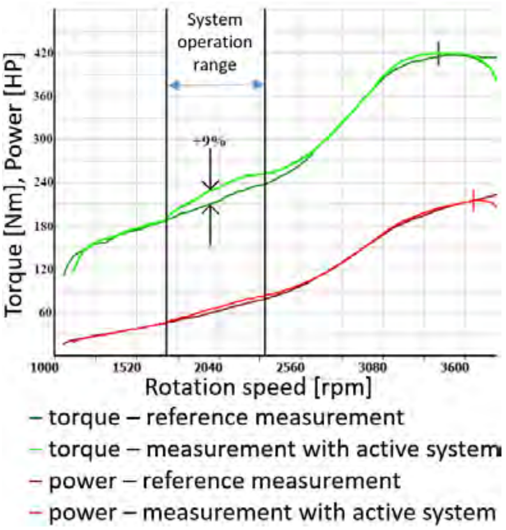

Fig. 9. Torque and power characteristics of the engine with the compressed air impulse system activated starting from 1700 rpm

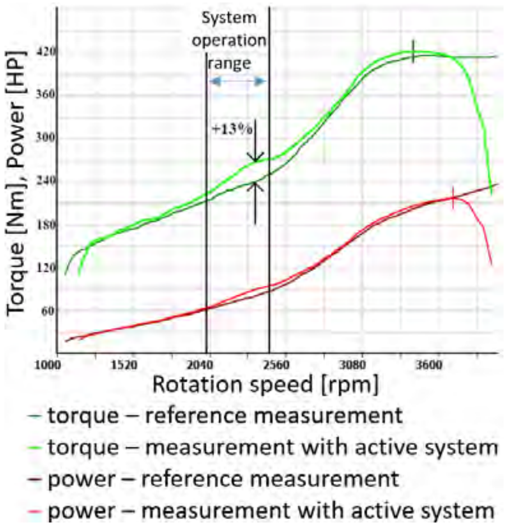

Fig. 10. Torque and power characteristics of the engine with the compressed air impulse system activated starting from 2000 rpm

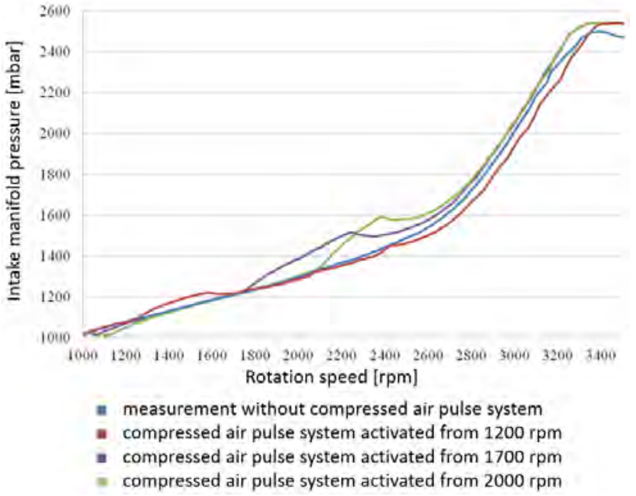

Fig. 11. Pressure in the intake manifold for different activation variants of the compressed air impulse system

The chart presents the Lambda sensor reading, which is directly influenced by the compressed air introduced into the system (Fig. 12). A Lambda value of 1 corresponds to a stoichiometric air-fuel mixture (14.7:1) [22, 23]. Values above 1 indicate an increased oxygen content in the exhaust gases, which the ECU interprets as a lean fuel mixture.

It is observed that, at the moment compressed air is delivered to the exhaust manifold, the Lambda value rises significantly. This prompts the ECU to apply a correction by increasing the fuel injection time in order to restore the proper mixture composition (Fig. 13). The extended injection duration is clearly visible in the chart (Fig. 13).

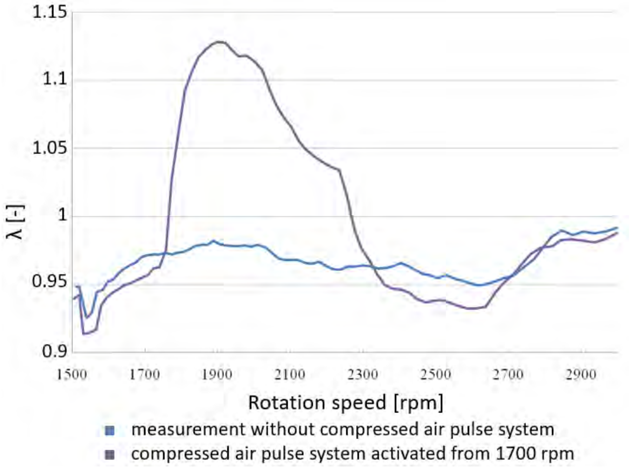

Fig. 12. Lambda value of the rotational speed function for with and without compressed air pulse system for exemplary system operating conditions, i.e. activation from 1700 rpm

The system's shutdown, i.e., the point when the air supply to the exhaust manifold is cut off, is marked by a sharp drop in the Lambda value (Fig. 12). This drop results from a sudden change in the oxygen content of the exhaust gases. At this moment, the Lambda value falls below that of the reference run, which is caused by a slight delay in the ECU's adjustment of the injection time.

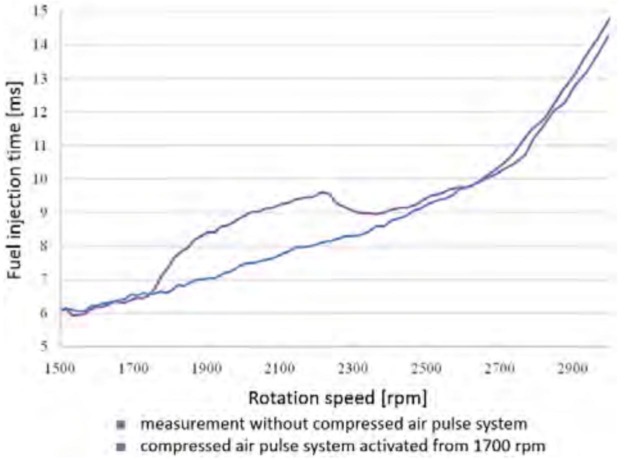

Fig. 13. Fuel injection time as a function of rotational speed for the system with and without compressed air pulse for exemplary system operating conditions, i.e. switching on from 1700 rpm

Figure 14 shows an increase in the mass of air delivered to the engine, indicating that the system has positively influenced turbocharger performance and reduced turbo lag – ultimately affecting the shape of the torque curve. Additionally, the enriched mixture, triggered by the Lambda sensor's initial misreading, may also enhance turbocharger function. A larger amount of fuel entering the combustion chamber leads to a higher exhaust gas volume, which helps drive the turbine rotor more effectively.

Despite the noticeable impact on the engine control system, the compressed air impulse system does not trigger any safety or protection algorithms built into the ECU. This confirms that the system is safe for engine operation and does not contribute to accelerated wear. Even if certain temporary deviations from ideal parameters may seem undesirable, their brief duration within the engine's full operating cycle is negligible.

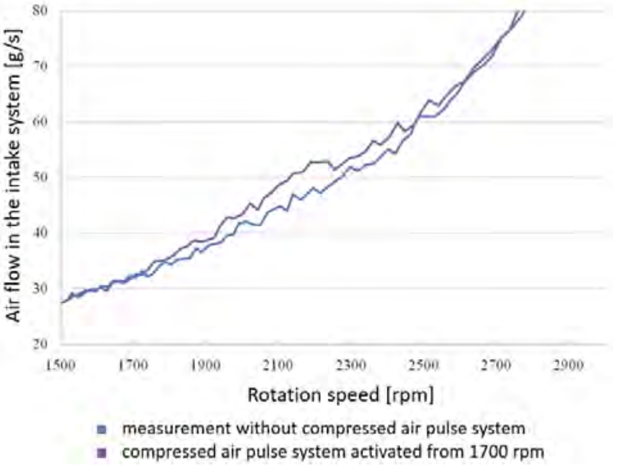

Fig. 14. Air flow in the intake system as a function of rotational speed for the system with and without compressed air pulse for exemplary system operating conditions, i.e., switching on from 1700 rpm

While commercial systems like Volvo's PowerPulse are tightly integrated into the vehicle's design and benefit from optimized software and hardware interactions, the presented prototype offers a modular and retrofittable alternative.

This makes it particularly relevant for aftermarket applications or for enhancing the performance of existing fleets without requiring significant modifications to the engine's core architecture.

One of the key insights from the testing phase is the system's immediate influence on engine control parameters, such as air-fuel mixture, fuel injection timing, and MAP readings. The observed increase in Lambda values at the onset of air injection, followed by rapid ECU correction through increased injection duration, demonstrates that the system operates within the expected logic of a spark-ignition control strategy. Importantly, no diagnostic faults or safety interventions were triggered, indicating that the system integrates safely with existing ECU routines.

The system also proved to have a positive effect on turbocharger performance by improving intake airflow and enhancing the transient response of the engine. Although brief fluctuations in mixture composition and MAP pressure were observed, their duration was minimal and did not lead to excessive deviations from reference operating conditions. These findings support the view that compressed air impulse systems – despite their simplicity – can provide substantial benefits in transient performance without compromising engine durability or efficiency.

However, certain limitations were also identified. For instance, the pressure threshold set within the control software constrained the duration of the impulse at higher engine speeds, reducing the effectiveness of the system as boost naturally increases. Future development should therefore consider dynamic boost thresholds or adaptive strategies to extend the usable operating window of the system.

Conclusion

The research presented in this study highlights the potential of non-commercial compressed air impulse systems as an effective solution to reduce turbo lag in spark-ignition engines, particularly in older vehicle platforms without modern turbocharger support technologies. The most important achievements of the study can be summarized as follows:

- Demonstrated up to 13% torque increase within a narrow engine speed range through the use of a compressed air impulse system
- Validated the concept of pneumatic turbo support as a viable retrofit solution for improving engine response
- Confirmed improvements in boost pressure characteristics and torque buildup at low engine speeds, where conventional turbochargers typically underperform
- Proved safe integration with the existing ECU without triggering diagnostic errors or protection algorithms
- Offered a cost-effective and modular alternative to factory-integrated systems like Volvo's PowerPulse, suitable for retrofitting
- Identified directions for further development, such as adaptive boost control and improved lambda signal interpretation under transient air injection conditions.

These results indicate that non-commercial compressed air impulse systems offer a promising approach for enhancing the performance and drivability of turbocharged spark-ignition engines, especially under low-speed, high-load conditions. Further development could extend their application in both performance tuning and emissions reduction for existing vehicle platforms.

Acknowledgements

The work on the prototype was financed from private funds of students of Mechatronics at the Faculty of Mechanical Engineering, Poznan University of Technology, Szymon Królak and Oleg Kindler. The tests on the chassis dynamometer at WSTR in Poznan were paid for by the Institute of Machine Design at Poznan University of Technology. Funding for publication of the article was provided by the subvention of the Ministry of Science and Higher Education.

Nomenclature

ACM	active control methodology
CFD	computational fluid dynamics
CNG	compressed natural gas
DICE	diagnostic communication equipment (Volvo)
ECU	engine control unit
LCD	liquid crystal display
LPG	liquefied petroleum gas
MAP	manifold absolute pressure
SI	spark ignition
TAP	tank air pressure
TPS	throttle position sensor
VIDA	vehicle information and diagnostics for aftersales
VGT	variable geometry turbines
VVT	variable valve timing

Bibliography

[1] Basu S. Modern marine turbocharger developments. J Inst Eng India Part MR Mar Eng Div. 2008;89:25-37.

[2] Bober B, Andrych-Zalewska M, Boguś P. Influence of exhaust manifold modification on engine power. Combustion Engines. 2024;196:54-65. https://doi.org/10.19206/CE-171389

[3] Caban J, Vrabel J, Górnicka D, Nowak R, Jankiewicz M, Matijošius J et al. Overview of energy harvesting technologies used in road vehicles. Energies. 2023;16:3787. https://doi.org/10.3390/en16093787

[4] Cieslar D, Collings N, Dickinson P, Glover K, Darlington A. A novel system for reducing turbo-lag by injection of compressed gas into the exhaust manifold. SAE Technical Paper. 2013-01-1310. 2013. https://doi.org/10.4271/2013-01-1310

[5] Fleiss M, Burenius R, Almkvist G, Björkholtz J. Das pneumatische Turbolader-Unterstützungssystem PowerPulse. MTZ Motortech Z. 2016;77:10-17. https://doi.org/10.1007/s35146-016-0044-1

[6] Fleiss M, Burenius R, Almkvist G, Björkholtz J. The Pneumatic Turbocharger Support System PowerPulse. MTZ Worldw. 2016;77:10-15. https://doi.org/10.1007/s38313-016-0042-1

[7] Galindo J, Serrano JR, De La Morena J, Samala V, Guilain S, Batard S. Evaluation of a double-entry turbine model coupled with a one-dimensional calibrated engine model at engine full load curves. Front Mech Eng. 2020;6. https://doi.org/10.3389/fmech.2020.601368

[8] Gerhardt J, Gollin W. Gasoline-engine management. ME-Motronic engine management – Technical Instruction BOSCH. Robert Bosch GmbH. Stuttgart 1999.

[9] Huang Q, Zheng X. Potential of variable diffuser vanes for extending the operating range of compressors and for improving the torque performance of turbocharged engines. Proc Inst Mech Eng Part J Automob Eng. 2017;231:555-566. https://doi.org/10.1177/0954407016661440

[10] Kaechele A, Chiodi M, Bargende M. Virtual full engine development: 3D-CFD simulations of turbocharged engines under transient load conditions. SAE Int J Engines. 2018;11:697-713. https://doi.org/10.4271/2018-01-0170

[11] Kamarudin MS, Zulkeflee M, Padzillah MH. Effect of tip clearance on the flow field of the mixed flow turbocharger turbine. J Teknol. 2017;79:97-103. https://doi.org/10.11113/jt.v79.11903

[12] Kisiel M, Szpica D. Determination of static flow characteristics of a prototypical differential valve using computational fluid dynamics. Acta Mech Autom. 2024;18:593-602. https://doi.org/10.2478/ama-2024-0063

[13] Marelli S, Carraro C, Capobianco M. Effect of pulsating flow characteristics on performance and surge limit of automotive turbocharger compressors. SAE Int J Engines. 2012;5:596-601. https://doi.org/10.4271/2012-01-0715

[14] Nannetti F, Usai V, Cordalonga C, Marelli S. Experimental analysis of the performance of a turbocharger compressor under pulsating flow condition. J Phys: Conf Ser. 2024; 2893:012099. https://doi.org/10.1088/1742-6596/2893/1/012099

[15] Padzillah MH, Rajoo S, Martinez-Botas RF. Numerical assessment of unsteady flow effects on a nozzled turbocharger turbine. Proceedings of the ASME Turbo Expo 2012: Turbine Technical Conference and Exposition. Volume 8: Turbomachinery, Parts A, B, and C. 2012;8:745-756. https://doi.org/10.1115/GT2012-69062

[16] Rao HKS, Raviteja S, Kumar GN. Computational analysis of unsteady flow in turbine part of turbocharger. Lect Notes Mech Eng. 2017:811-820. https://doi.org/10.1007/978-81-322-2743-4_76

[17] Shaaban S, Seume J. Impact of turbocharger non-adiabatic operation on engine volumetric efficiency and turbo lag. Int J Rotating Mach. 2012;2012. https://doi.org/10.1155/2012/625453

[18] Song Y, Ding S, Xu Z, Du F, Zhou Y. An active control methodology to improve pulsatile turbocharger operating conditions and performance. Proceedings of the ASME 2020 International Mechanical Engineering Congress and Exposition. 2020;11. https://doi.org/10.1115/IMECE2020-23209

[19] Sroka ZJ, Prakash S, Wlostowski R. Design of the turbocharger bearing arrangement to increase the overall efficiency of the combustion engine. Combustion Engines. 2022; 188:83-89. https://doi.org/10.19206/CE-142348

[20] Technologia Power Pulse w nowym Volvo S90 (in Polish) https://www.youtube.com/watch?v=ZpQu3uRy1jg (accessed on 05.01.2025).

[21] Voser C, Ott T, Dönitz C, Onder C, Guzzella L. In-cylinder boosting of turbocharged spark-ignited engines. Part 2: Control and experimental verification. Proc Inst Mech Eng Part J Automob Eng. 2012;226:1564-1574. https://doi.org/10.1177/0954407012443766

[22] Warguła Ł, Kaczmarzyk P, Wieczorek B, Gierz Ł, Małozięć D, Góral T et al. Identification of the problem in controlling the air–fuel mixture ratio (lambda coefficient λ) in small spark-ignition engines for positive pressure ventilators. Energies. 2024;17:4241. https://doi.org/10.3390/en17174241

[23] Warguła Ł, Wieczorek B, Gierz Ł, Karwat B. Critical concerns regarding the transition from E5 to E10 gasoline in the European Union, particularly in Poland in 2024 – a theoretical and experimental analysis of the problem of controlling the air–fuel mixture composition (AFR) and the λ coefficient. Energies. 2025;18:852. https://doi.org/10.3390/en18040852

[24] Yang M, Martinez-Botas R, Rajoo S, Yokoyama T, Ibaraki S. An investigation of volute cross-sectional shape on turbocharger turbine under pulsating conditions in internal combustion engine. Energy Convers Manag. 2015;105:167-177. https://doi.org/10.1016/j.enconman.2015.06.038

[25] Zsiga N, Voser C, Onder C, Guzzella L. Intake manifold boosting of turbocharged spark-ignited engines. Energies. 2013;6:1746-1763. https://doi.org/10.3390/en6031746

Oleg Kindler, MEng. – Faculty of Mechanical Engineering, Poznan University of Technology, Poland.

e-mail: *oleg.kindler@student.put.poznan.pl*

Szymon Królak, MEng. – Faculty of Mechanical Engineering, Poznan University of Technology, Poland.

e-mail: *szymon.krolak@student.put.poznan.pl*

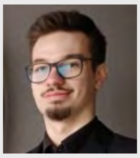

Łukasz Warguła, DSc., DEng., Prof. PUT – Faculty of Mechanical Engineering, Poznan University of Technology, Poland.

e-mail: *lukasz.wargula@put.poznan.pl*

Bartosz Wieczorek, DSc., DEng., Prof. PUT – Faculty of Mechanical Engineering, Poznan University of Technology, Poland.

e-mail: *bartosz.wieczorek@put.poznan.pl*

Article citation info:
Kropiwnicki J, Gawłas T. Energy efficiency of a car driving with regenerative braking. Combustion Engines. 2025;202(3):20-26. https://doi.org/10.19206/CE-207152

Jacek KROPIWNICKI
Tomasz GAWŁAS

Combustion Engines
Polish Scientific Society of Combustion Engines

Energy efficiency of a car driving with regenerative braking

ARTICLE INFO

Received: 16 May 2025
Revised: 13 June 2025
Accepted: 14 June 2025
Available online: 7 July 2025

Currently offered satellite navigation systems for cars are primarily focused on selecting the route with the shortest travel time. These systems also feature relatively simple models that allow the selection of the route with regard to minimizing fuel or electricity consumption, usually called the most ecological. Their effective use requires users to define basic vehicle data, such as drive type, maximum speed, etc. The paper presents an analysis of the impact of selected parameters characterizing vehicle properties and traffic conditions on energy consumption. The focus is mainly on parameters that can be technically used in car navigation systems to plan energy-saving routes. The analysis uses routes recorded in real traffic. The results of these analyses allowed the development of several guidelines for planning routes taking into account the EEC minimization criterion. One of the observations is that for roads with large changes in road height (> 20 m per km), a flat route with a length increased by 50% may be more energy-efficient than the original one. This is due to the efficiency of the regenerative braking system being significantly lower than 100%.

Key words: *electric vehicle, urban conditions, regenerative braking, energetic efficiency, route planning*

1. Introduction

As the global transition toward sustainable transportation accelerates, improving the energy efficiency of Internal Combustion Engine Vehicle (ICEV) [1, 7]. Especially electric vehicles (EVs) and hybrid electric vehicles (HEVs) have become a central research focus [6, 13]. Two major strategies for reducing vehicular energy consumption are the use of regenerative braking systems (RBS) and energy-aware route optimization algorithms [3, 4]. Together, these strategies enable smarter driving that aligns with the goals of energy efficiency, reduced emissions, and longer driving range [8]. Regenerative braking systems allow electric and hybrid vehicles to recapture kinetic energy during deceleration, converting it into electrical energy that is stored in the battery [11, 16]. Unlike conventional friction braking, which dissipates kinetic energy as heat, RBS contributes to energy reuse, thus improving overall vehicle efficiency. RBS can recuperate between 10% and 30% of the total energy consumed during urban driving, depending on various parameters such as driving patterns, traffic conditions, and terrain [9]. Urban driving, characterized by frequent acceleration and deceleration, offers ideal conditions for effective energy regeneration. The amount of recoverable energy depends on several dynamic factors: a) vehicle speed and deceleration rates: higher deceleration rates typically allow more energy to be harvested, though limitations exist based on battery charge rates and vehicle safety; b) battery state-of-charge (SOC): high SOC can limit energy recovery as the battery cannot accept more charge, potentially leading to reduced efficiency or increased use of mechanical brakes. Brake blending strategies: effective integration of regenerative and friction braking ensures driver safety while optimizing energy recovery. Adaptive control systems dynamically allocate braking torque between electric motors and hydraulic brakes to maximize regeneration without compromising stability [12]. Modern regenerative systems also incorporate predictive algorithms that estimate optimal braking force distribution in real time, accounting for the road slope, vehicle load, and traffic.

Traditional navigation systems prioritize time or distance minimization, but such objectives do not always align with energy efficiency. Energy-aware routing considers additional parameters, such as: a) elevation profiles (gradient): uphill roads increase energy consumption, while downhill roads offer potential for regenerative braking; b) traffic congestion: frequent stopping and idling increase energy usage and reduce regenerative opportunities; c) speed limits and driving behaviour: energy-efficient routes may involve smoother acceleration profiles and fewer stops. Researchers have proposed multiple routing algorithms focused on minimizing energy usage [2, 5]. Machine learning techniques have emerged as powerful tools in this domain. Although RBS and energy-aware routing have individually shown strong potential in reducing energy consumption, their combined use results in even greater efficiencies. Integrating regenerative braking potential into route planning allows vehicles to exploit downhill segments and frequent deceleration zones, which can be strategically selected to increase energy recovery. For example, a route that includes gentle downhill slopes with traffic lights can enhance energy regeneration without significant speed loss. These scenarios have inspired research into "eco-routing" or "green routing," where algorithms analyse the entire road profile for energy-optimal paths. The inclusion of regenerative braking factors into eco-routing decisions improved energy savings by an additional 7–10% over standard energy-optimized routing [10]. Moreover, vehicle-to-infrastructure (V2I) and vehicle-to-everything (V2X) communication technologies enhance this synergy by allowing real-time traffic signal prediction and adaptive speed control. The author [5] demonstrated a V2I-based cooperative control strategy that synchronized vehicle movement with signal phasing to avoid unnecessary stops and maximize regenerative braking potential.

Despite promising results, several challenges hinder the widespread adoption of integrated regenerative-route optimization systems. Real-time energy-optimal routing under uncertain traffic and environmental conditions requires high computational resources. Accurate road gradient, traffic, and SOC data are crucial but not always available. Aggressive driving can undermine energy savings, even on optimized routes. Energy recovery is constrained by battery acceptance rates, particularly in cold weather or near-full SOC levels [14]. Looking ahead, advancements in artificial intelligence, edge computing, and battery technologies are expected to mitigate these limitations [15]. Predictive analytics, cloud-based routing services, and real-time data integration will allow future EVs to self-optimize their routes and braking strategies based on continuous feedback from the environment and the vehicle's internal state.

This work presents an analysis of the impact of selected parameters characterizing vehicle properties and traffic conditions on energy consumption. The focus is mainly on parameters that can be technically used in car navigation systems to plan energy-saving routes. The analysis uses routes recorded in real traffic. The analysis included the impact of vehicle mass on electric energy consumption (EEC) and changes in the road gradient, by modifying the original height at which the vehicle is located, on EEC.

2. Traffic conditions

The main parameters characterizing the traffic conditions are defined below. The amount of energy expended to drive the vehicle will depend on the maximum speeds achieved, the number of acceleration cycles, their intensity, but also the vehicle mass and the distance travelled. In order to use the data in the analysis of the operation of drive systems of various vehicles, with different masses and covering different distances, it was decided to use specific energy consumption (SEC), in which the amount of energy expended is related to the vehicle mass and the distance travelled [9]:

$$\mathrm{SEC} = \frac{\mathrm{E}}{\mathrm{m} \cdot \mathrm{L}} \tag{1}$$

where: E – mechanical energy delivered to the wheels: L – distance covered, m –vehicle mass.

Mechanical energy delivered to the wheels can be calculated based on the following relationship:

$$\mathrm{E} = \int_{t=0}^{t=t_c} \left(k_p \cdot M \cdot \omega \cdot \eta_t\right) dt \tag{2}$$

where: M – engine torque, t_c – time of the cycle, ω – engine angular velocity, η_t –transmission system efficiency, k_p – positive tractive force factor:

$$k_p = \begin{cases} 1 \text{ for powered wheels} \\ 0 \text{ for idlling or braking} \end{cases} \tag{3}$$

Alternatively, the mechanical energy delivered to the wheels can be calculated as follows:

$$\mathrm{E} = \int_{t=0}^{t=t_c} \left(k_p \cdot P\right) dt \tag{4}$$

where: P – mechanical power,

$$P = F_t \cdot V \tag{5}$$

F_t – tractive force, V – vehicle velocity.

There are four types of driving resistances, which must be covered by the tractive force: aerodynamic drag, rolling resistance, gradient resistance, and acceleration resistance. With a constant time, step for measuring vehicle motion parameters, the following relationship can be used:

$$\mathrm{E} = \Delta t \cdot \sum_{i=1}^{N} \left(k_{p_i} \cdot P_i\right) \tag{6}$$

where: Δt – constant time step.

For the regeneration process, the regenerative braking energy can be calculated:

$$E_{reg} = \Delta t \cdot \sum_{i=1}^{N} \left(k_{reg_i} \cdot P_i\right) \tag{7}$$

where: k_{reg} – negative tractive force factor:

$$k_{reg} = \begin{cases} -1 \text{ for idlling or braking} \\ 0 \text{ for powered wheels} \end{cases} \tag{8}$$

Using negative tractive force factor when calculating regenerative braking energy, which is available for recovery system may cause some ambiguity in the research results, because the amount of available energy from the regeneration process depends not only on the speed profile and changes in height but also on the degree of aerodynamic perfection and quality of the driving wheels capable of generating lower or higher rolling resistance. In other words, a vehicle with low rolling and air resistance will have more energy available for the regeneration process than a vehicle of the same mass that generates higher rolling and air resistance.

Regenerative braking specific energy (RBSE) has been defined as follows:

$$\mathrm{RBSE} = \frac{E_{reg}}{m \cdot L} \tag{9}$$

Absolute electric energy delivered by the battery can be calculated as follows:

$$E_{battery} = m \cdot L \cdot \left(\mathrm{SEC} \cdot \frac{1}{\eta_{el}} - \mathrm{RBSE} \cdot \eta_{reg}\right) + P_{aux} \cdot t_c \tag{10}$$

where: η_{el} – efficiency of electric drive system (including: battery, inverter, motor and transmission), η_{reg} – efficiency of regenerative braking system (including: transmission, generator, inverter, battery), P_{aux} – auxiliary devices power consumption.

Electric energy consumption can be calculated as follows:

$$\mathrm{EEC} = m \cdot \left(\mathrm{SEC} \cdot \frac{1}{\eta_{el}} - \mathrm{RBSE} \cdot \eta_{reg}\right) + \frac{P_{aux} \cdot t_c}{L} \tag{11}$$

3. Specification of the testing conditions

The traffic conditions identification studies were carried out in the city of Gdynia (approx. 250,000 inhabitants), in regular city traffic, using a vehicle whose technical specifications are presented in Table 1. The vehicle was equipped with a GPS position recording system, which enabled both the determination of the vehicle's horizontal position and changes in height.

Table 1. Drive system parameters of the tested vehicle

Vehicle	Mass (driver inc.) [kg]	Power [kW]	Battery capacity [kWh]	η_{el} [%]	η_{reg} [%]	P_{aux} [W]
Mazda MX-30	1795	107	35	78	61	200

Figures 1 to 4 illustrate test routes with average driving speeds for 100-meter sections. The routes run through the city center, but due to the use of modern road infrastructure, some of them allow for a relatively high average speed (a small number of intersections with traffic lights, increased permissible driving speed). The routes were diversified in terms of the cross profile of the road so that the impact of the road gradient on the energy consumption to drive the vehicle could be taken into account in the tests.

Fig. 1. Average speed distribution on route 1 over 100 m sections

Fig. 2. Average speed distribution on route 2 over 100 m sections

Fig. 3. Average speed distribution on route 3 over 100 m sections

Table 2 presents the specification of the routes used in the tests. Their length is close to 3 km. The specification includes the highest and lowest height (Height max and Height min) at which the vehicle will be located and the relative change in height for the end and beginning of the route (Height difference). The parameter "Height difference" indicates the possibility of reducing or increasing the energy consumption for the drive due to gradient resistance. The routes were selected to ensure the widest possible variation in traffic conditions resulting from the hills overcome and traffic difficulties resulting in different average driving speeds.

Fig. 4. Average speed distribution on route 4 over 100 m sections

Table 2. Routes specification

Route No.	Length [m]	Av. speed km/h	SEC [kWh/ (t·100 km)]	RBSE [kWh/ (t·100 km)]	Height min [m]	Height max [m]	Height difference [m]
1	2762	16	10.7	5.3	41	88	20
2	2931	26	8.5	4.5	40	67	0
3	3117	35	6.6	1.9	45	57	–2
4	2891	45	6.2	3.6	33	59	–21

4. The influence analysis of vehicle properties and traffic conditions on energy consumption

The effect of vehicle mass, road gradient change, and traffic conditions on the amount of mechanical power required to drive the vehicle is presented below. This power was determined based on vehicle speeds and changes in height recorded during regular traffic for 4 selected routes, the specification of which was presented in the previous section. The power required to drive the vehicle (positive), the specification of which was included in Table 1, was calculated based on the vehicle motion resistance model that takes into account rolling resistance, air resistance, gradient resistance, and acceleration resistance. Similarly, the power that can be recovered in the energy recuperation system (negative) was calculated based on this model.

Figure 5 shows the speed and height at which the vehicle moves for route 1. This is the route with the lowest average speed of 16 km/h, but there are large changes in height; the difference between the highest and lowest height is 47 m, and the vehicle ends the route at a height 20 meters higher than it started. Figure 6 shows the profile of mechanical power supplied by the drive system or that can be delivered to the recuperation system (negative value) for a vehicle mass of 100%, 125% and 150% of the original vehicle mass, respectively. Figure 7 shows the effect of changing the road gradient, by modifying the original height at which the vehicle is located, on the mechanical power supplied or received by the drive system. Three levels of interference with height were considered: flat road (0%), original height (100%), and double height (200%).

Figures 8 to 10 show the results for route 2, which has a relatively low average driving speed of 26 km/h, while the height between the start and end of the route remains practically unchanged.

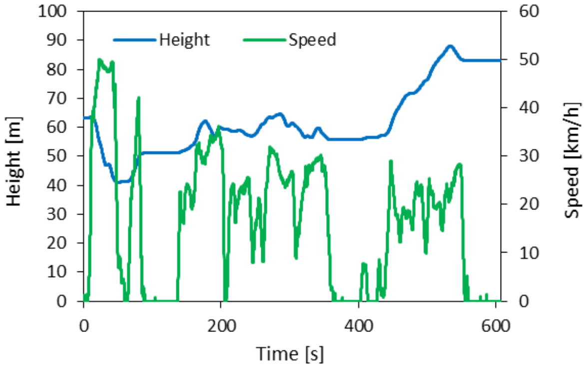

Fig. 5. Vehicle speed and height above sea level for route 1

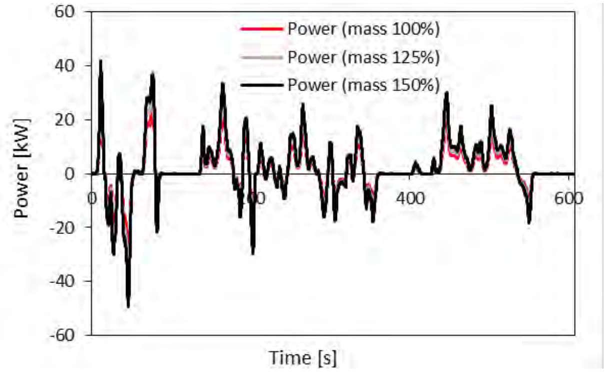

Fig. 6. Influence of vehicle mass on mechanical power supplied/received by the drive system for route 1

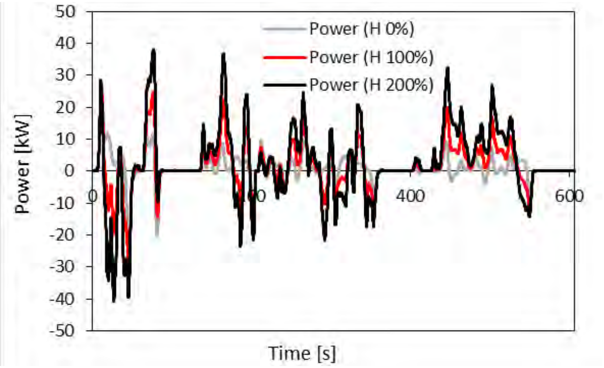

Fig. 7. Influence of road gradient (height multiplication) on mechanical power supplied/received by the drive system for route 1

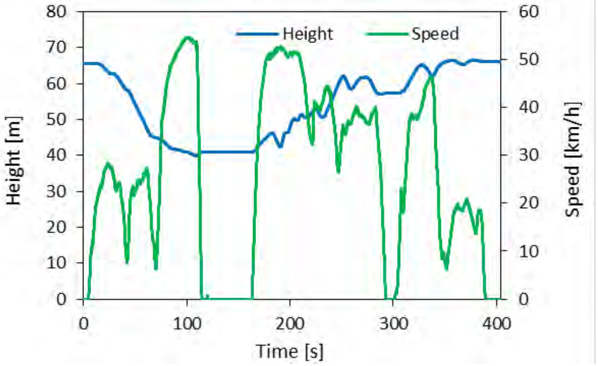

Fig. 8. Vehicle speed and height above sea level for route 2

Figures 11 to 13 show the results for route 3 (average speed 35 km/h), which has relatively few acceleration and braking cycles and is practically flat.

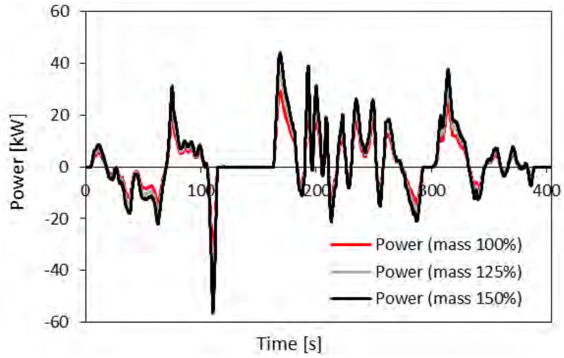

Fig. 9. Influence of vehicle mass on mechanical power supplied/received by the drive system for route 2

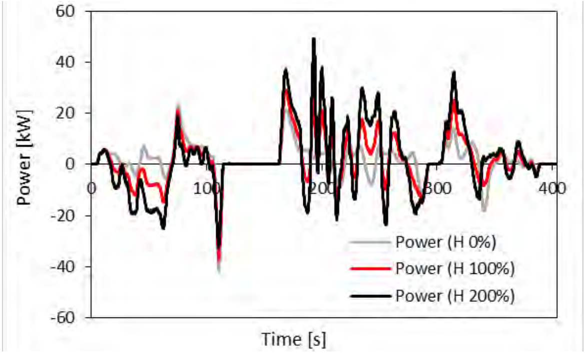

Fig. 10. Influence of road gradient (height multiplication) on mechanical power supplied/received by the drive system for route 2

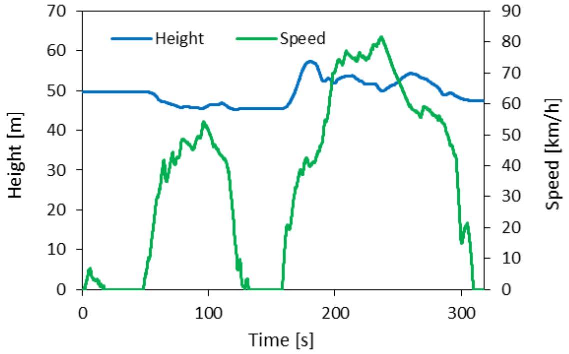

Fig. 11. Vehicle speed and height over the sea level for route 3

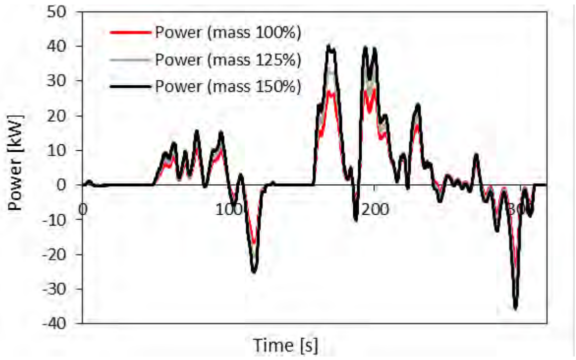

Fig. 12. Influence of vehicle mass on mechanical power supplied/received by the drive system for route 3

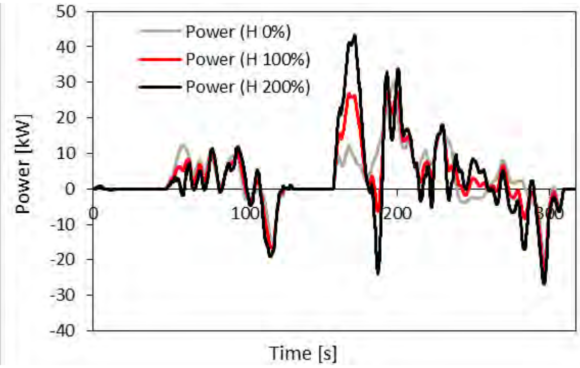

Fig. 13. Influence of road gradient (height multiplication) on mechanical power supplied/received by the drive system for route 3

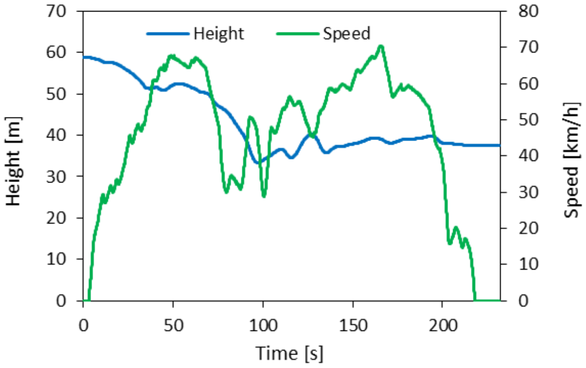

Fig. 14. Vehicle speed and height over the sea level for route 4

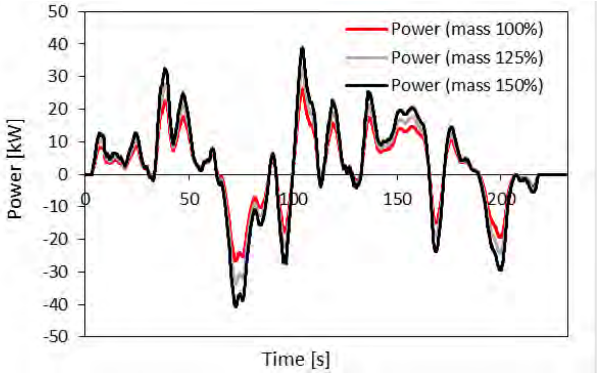

Fig. 15. Influence of vehicle mass on mechanical power supplied/received by the drive system for route 4

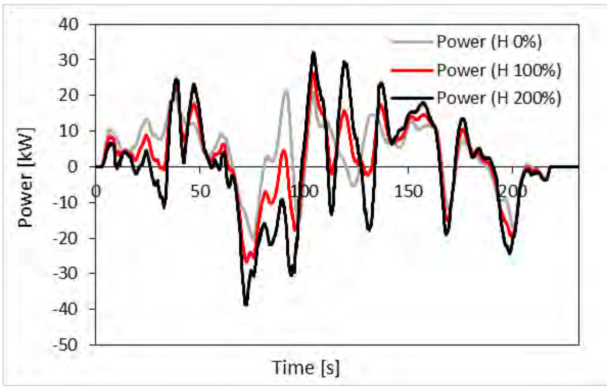

Fig. 16. Influence of road gradient (height multiplication) on mechanical power supplied/received by the drive system for route 4

Figures 14–16 show the results for route 4, which has the highest speed (45 km/h) and the fewest stops. At the same time, the road is sloping downwards; the end of the route is 21 m lower than the beginning.

Using the results presented in Fig. 5 to 16 and equations (1) to (11), the electric energy consumption (EEC) was determined for the analysed cases. While, based on findings from studies [10], this auxiliary power consumption was assumed to be constant at 200 W. The results of the effect of vehicle mass on EEC are presented in Fig. 17.

Fig. 17. Influence of vehicle mass on electric energy consumption

Based on the results obtained, it can be stated that route 1 is characterized by the highest EEC, despite the lowest average driving speed. The decisive factor in this situation turned out to be the necessity to overcome the difference in height of 20 m between the beginning and the end of the route. Similarly, the lowest EEC was recorded for route 4, where the speed variability is the lowest, and at the same time, the route leads downhill by 21 m. The influence of the vehicle mass on EEC is clearly visible for all routes, but it is not proportional to the increase in mass for all routes. For route 1, the increase in mass by 25% and 50% gives an increase in EEC by 22% and 45%, respectively, so it is almost proportional. For route 2, the EEC increases are 21% and 41%, respectively. For route 3, the EEC increases are 16% and 32%, respectively. For route 4, the EEC increases are 16% and 31%, respectively. It can therefore be concluded that for routes with a greater number of acceleration processes and their intensity, the impact of the mass increase on the EEC is greater. The regenerative braking process is therefore unable to compensate for the increased energy consumption resulting from the numerous acceleration processes and the increased mass. This is due to the efficiency of the regenerative braking system being significantly lower than 100%; usually, it is well below 80% [9].

Figure 18 shows the influence of road gradient (height multiplication) on the electric energy consumption.

Based on the obtained results, it can be stated that on flat roads (height 0%), the factor determining the EEC is the average driving speed; the lower it is, the lower the EEC. However, these differences are not large due to the occurrence of numerous acceleration processes at low average driving speeds and only their partial compensation during regenerative braking. On routes leading uphill, the increase in energy consumption is not proportional to the increase in gradient. For example, for route 1, doubling the gradient of the road causes an increase in EEC by 49%. It should be remembered that the resistance to the climb is only a part of the resistance to the vehicle's motion, which either does not depend on the road gradient (air resistance) or can decrease (rolling resistance). In the analysed cases, for a difference between maximum and minimum height of 27 m (route 2) with a route length of 2.9 km, the increase in energy consumption compared to a flat road is 16%, and with doubled elevation differences, 47%. This means that in the first analysed case, the flat route with a length greater by 16% (0.47 km) will require the same amount of energy as the original. For route 2, with double the height, the flat route can be as much as 47% (1.39 km) longer, giving the same energy consumption.

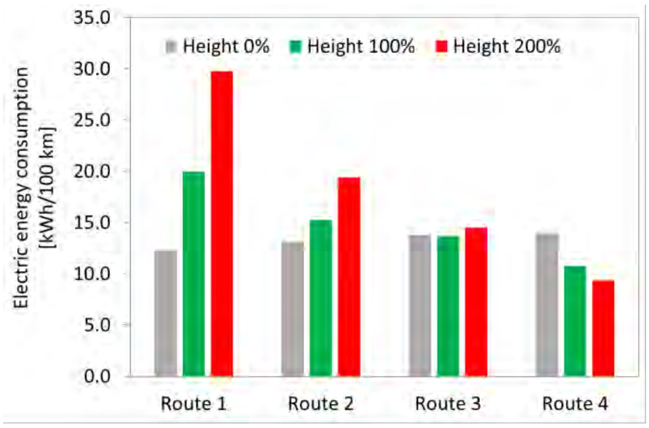

Fig. 18. influence of road gradient (height multiplication) on the electric energy consumption

5. Conclusions

Energy efficiency in vehicles is no longer confined to the powertrain design alone but extends to intelligent systems for energy regeneration and route optimization. Regenerative braking offers substantial energy savings by recapturing kinetic energy during braking, while energy-aware route optimization ensures that vehicle paths are aligned with energy conservation goals. Together, they provide a robust framework for enhancing vehicular efficiency, especially in EVs and HEVs. As energy efficiency becomes a competitive differentiator and environmental imperative, integrating regenerative braking and optimal routing will be key to the next generation of intelligent transportation systems.

This work presents an analysis of the impact of selected parameters characterizing vehicle properties and traffic conditions on energy consumption. The main focus was on parameters that can be technically used in car navigation systems to plan energy-efficient routes. The analysis used routes recorded in real traffic in the city of Gdynia. Four routes of similar length but different average speed and different cross-sectional road profiles were selected for testing. The analysis included the impact of vehicle mass on electric energy consumption (EEC) and changes in the road gradient, by modifying the original height at which the vehicle is located, on EEC. The results of these analyses allowed the development of several guidelines for planning routes taking into account the EEC minimization criterion:

- Vehicles should avoid routes with large changes in road height, as the increase in height causes an almost proportional increase in energy consumption, which is only slightly compensated by regenerative braking. This is due to the efficiency of the regenerative braking system being significantly lower than 100%; usually, it is well below 80%. On flat routes with an increase in mass, the increase in ECC is much smaller and can be almost twice as small as on routes with large changes in road height.
- Driving in a traffic jam gives a smaller EEC, due to the lower driving speed as long as the cross profile of the road is flat. A significant number of changes in road height causes an increase in EEC. Statistically, driving in traffic jams in terrain with changes in road height should therefore be avoided.
- Driving down and up to the same height causes additional energy consumption; the greater the changes in road height, the greater the increase in energy consumption. A road with a flat cross profile is therefore more energy-efficient.
- Driving a longer flat road can be more energy-efficient, especially with significant changes in road height (driving up–down–up). For roads with large changes in road height (over 20 m/1 km of route), a flat route with a length increased by 50% may be more energy-efficient than the original one.

Nomenclature

EEC	electric energy consumption	RBS	regenerative braking systems
EV	electric vehicle	RBSE	regenerative braking specific energy
HEV	hybrid electric vehicles	SEC	specific energy consumption
ICEV	internal combustion engine vehicle	SOC	state-of-charge

Bibliography

[1] Andrych-Zalewska M, Chłopek Z, Merkisz J, Pielecha J. Analysis of the operation states of internal combustion engine in the Real Driving Emissions test. Archives of Transport. 2022;61(1):71-88. https://doi.org/10.5604/01.3001.0015.8162

[2] Artmeier A, Haselmayr J, Leucker M, Sachenbacher M. The shortest path problem revisited: optimal routing for electric vehicles. In: Dillmann R, Beyerer J, Hanebeck UD, Schultz T. (eds) KI 2010: Advances in Artificial Intelligence. KI 2010. Lect Notes Comput Sc. 2010;6359. Springer, Berlin, Heidelberg. https://doi.org/10.1007/978-3-642-16111-7_35

[3] Chengqun Q, Wan X, Wang N, Cao S, Ji X, Wu K et al. A novel regenerative braking energy recuperation system for

electric vehicles based on driving style. Energy. 2023;283: 129055. https://doi.org/10.1016/j.energy.2023.129055

[4] Deptuła A, Natorska M, Mamala J, Prażnowski K, Urbanowicz K. Application of a decision classifier tree to evaluate energy consumption of an electric vehicle under real traffic conditions. Advances in Science and Technology Research Journal. 2025;19(4):91-108. https://doi.org/10.12913/22998624/199799

[5] Feng Y, Head KL, Khoshmagham S, Zamanipour M. A real-time adaptive signal control in a connected vehicle environment. Transport Res C-Emer. 2015;55:460-473. https://doi.org/10.1016/j.trc.2015.01.007

[6] Fiori C, Arcidiacono V, Fontaras G, Makridis M, Mattas K, Marzano V et al. The effect of electrified mobility on the relationship between traffic conditions and energy consumption. Transport Res D-Tr E. 2019;67:275-90. https://doi.org/10.1016/j.trd.2018.11.018

[7] Hunicz J, Yang L, Rybak A, Ji S, Gęca MS, Mikulski M. Comparison of diesel and hydrotreated vegetable oil as the high-reactivity fuel in reactivity-controlled compression ignition. Energ Convers Manage. 2025;323:119264. https://doi.org/10.1016/j.enconman.2024.119264

[8] Kropiwnicki J. A unified approach to the analysis of electric energy and fuel consumption of cars in city traffic. Energy. 2019;182:1045-1057. https://doi.org/10.1016/j.energy.2019.06.114

[9] Kropiwnicki J, Gawłas T. Estimation of the regenerative braking process efficiency in electric vehicles. Acta Mechanica et Automatica. 2023;17(2):303-310. https://doi.org/10.2478/ama-2023-0035

[10] Liu W, Qi H, Liu X, Wang Y. Evaluation of regenerative braking based on single-pedal control for electric vehicles. Front Mech Eng. 2020;15:166-179. https://doi.org/10.1007/s11465-019-0546-x

[11] Mamala J, Śmieja M, Prażnowski K. Analysis of the total unit energy consumption of a car with a hybrid drive system in real operating conditions. Energies. 2021;14(13):3966. https://doi.org/10.3390/en14133966

[12] Montoya A, Guéret C, Mendoza JE, Villegas JG. The electric vehicle routing problem with nonlinear charging function. Transport Res B-Meth. 2017;103:87-110. https://doi.org/10.1016/j.trb.2017.02.004

[13] Pielecha I, Cieślik W, Szałek A. The use of electric drive in urban driving conditions using a hydrogen powered vehicle – Toyota Mirai. Combustion Engines. 2018;172(1):51-58. https://doi.org/10.19206/CE-2018-106

[14] Qiu C, Wang G. New evaluation methodology of regenerative braking contribution to energy efficiency improvement of electric vehicles. Energ Convers Manage. 2016;119:389-398. https://doi.org/10.1016/j.enconman.2016.04.044

[15] Salari AH, Mirzaeinejad H, Mahani MF. A new control algorithm of regenerative braking management for energy efficiency and safety enhancement of electric vehicles. Energ Convers Manage. 2023;276:116564. https://doi.org/10.1016/j.enconman.2022.116564

[16] Yang C, Sun T, Wang W, Li Y, Zhang Y, Zha M. Regenerative braking system development and perspectives for electric vehicles: an overview. Renew Sust Energ Rev. 2024; 198:114389. https://doi.org/10.1016/j.rser.2024.114389

Prof. Jacek Kropiwnicki, DSc., DEng. – Faculty of Mechanical Engineering, Gdańsk University of Technology, Poland.

e-mail: *jkropiwn@pg.gda.pl*

Tomasz Gawłas, MEng. – BMG Goworowski sp. z o.o., Gdańsk, Poland.

e-mail: *tomasz.gawlas@bmg.mercedes-benz.pl*

Article citation info:
Pryciński P. Selected emissivity assessment issues for electric and hybrid vehicles. Combustion Engines. 2025;202(3):27-35.
https://doi.org/10.19206/CE-205274

Piotr PRYCIŃSKI

Combustion Engines
Polish Scientific Society of Combustion Engines

Selected emissivity assessment issues for electric and hybrid vehicles

ARTICLE INFO

This paper presents selected issues concerning the assessment of the emissivity of electric and hybrid vehicles, referred to as zero- or low-emission vehicles. This paper proposes an analytical method to determine air pollutant emissions generated by road electric vehicles and presents the results of air pollutant emissions measurements of hybrid vehicles obtained during real driving emissions tests (RDE). Air pollutant emissions measurements for hybrid vehicles were corrected for electricity consumption during operation and the pollutant emissions arising from electricity generation. The paper discusses the issue of air pollutant emissions of electric vehicles in relation to the changing sources of electricity generation in Poland over the past decade. It also presents the dynamics of change of in-use and newly registered electric and hybrid vehicles in Poland between 2022 and 2023. The aim of this paper is to compare the emissivity of electric vehicles, as well as hybrid vehicles, using the analytical method proposed in the paper to determine air pollutant emissions generated by electric vehicles.

Received: 11 April 2025
Revised: 12 May 2025
Accepted: 18 May 2025
Available online: 6 June 2025

Key words: *emissivity assessment, real driving emissions tests, electric, hybrid vehicles, exhaust emissions*

1. Introduction

Electricity production in Poland has been based on fossil fuels for many years. Air pollutant emissions accompanying this production change depend on the fuels used for electricity generation. Modern zero- or low-emission vehicles are equipped with electric motors. These are fully electric or hybrid vehicles. Their emissions, therefore depend on the sources used to generate electricity in Poland and worldwide. The main primary fossil fuels used in Poland for electricity production are hard coal, brown coal, natural gas, coalbed methane, and oils of all kinds. By classifying the above sources into two sets of conventional fuels, including hard coal, brown coal, natural gas, and RES fuels, including biomass, hydro, pumped-storage hydroelectricity, photovoltaics, and wind turbine plants, it is possible to track changes in the use of individual primary sources for electricity production in Poland. Poland has experienced significant developments in this regard over the last 10 years [26]. The substitution of primary materials for electricity production is shown in Fig. 1.

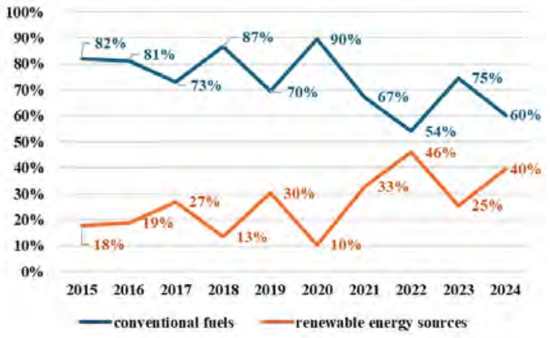

Fig. 1. Sources of electricity production in Poland 2015–2024 [26]

Noteworthy is the more than 20% decrease in the share of conventional fuels in electricity production in Poland [26] and the more than 22% increase in the share of renewable energy sources in electricity production. The decline in electricity produced from fossil fuels over the last decade has been dictated by the restructuring measures carried out in Poland in the area of the mining industry and the development of the renewable energy sector, particularly in wind, solar, and water production. The share of fossil fuels in electricity production in Poland is still high compared to the EU and to other countries in the EU [25]. When comparing Poland's results with those recorded in 2023 for other EU countries, it is noteworthy that only in Cyprus (79%) and Malta (87%) the share of electricity produced from fossil fuels is higher than in Poland. Higher shares of fossil fuels in electricity production in the EU are present in countries without deployed nuclear power. An example is Italy, where the share of electricity production from fossil sources was close to 55% in 2023. In terms of electricity production from conventional and renewable sources, Italian statistics are most similar to the Polish electricity production. Publicly available statistics [25] show a significant share of electricity produced from nuclear sources in the European Union. The share of nuclear power in the electricity production mix will reach more than 23% in 2023. The use of primary materials for electricity production in the EU is shown in Fig. 2.

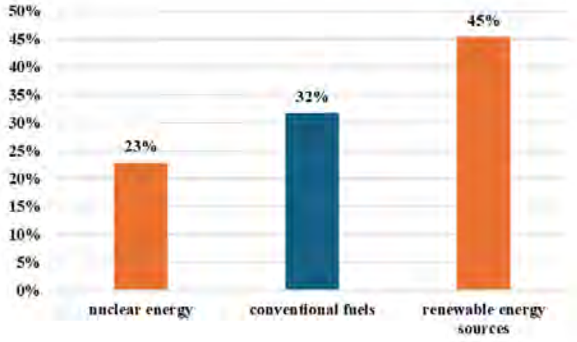

Fig. 2. Sources of electricity production in the European Union in 2023 [26]

The share of energy from renewable sources, on the other hand, was over 45%. Importantly, the share of electricity produced from renewables in the EU is close to the share of RES in Poland in 2024. Poland should achieve EU averages in the coming years, considering the growth dynamics of electricity production from RES.

Comparing the statistics of Poland and the EU, the share of renewable sources in electricity production in Poland nearly reached the EU average in 2024. The share of fossil fuels was unfortunately almost twice as high in Poland as in the EU. The reason for this may be the lack of nuclear power production and the ongoing restructuring processes in the mining industry. The functioning of the power system in Poland depends on regulatory changes and a number of legal conditions.

The Green Deal is the most important legal basis shaping the current and future industrial, transport and climate policy of Poland and Europe. At the European Union level, the technological trends associated with the electricity sector's decarbonisation, i.e., moving away from coal and reducing the role of natural gas, as well as the development of nuclear power, will play a fundamental role in the evolution of the power system and its surroundings in the near future. It is noteworthy that the development of renewable energy, energy storage, and the popularisation of zero-emission onsite transport means will continue to be supported. Moreover, a dynamic development of prosumer energy based mainly on photovoltaics is taking place in Poland. Solar-based energy, especially from 2020 onwards, has played a significant role in the national energy mix, as illustrated in Figure 1. There has been a marked development of large-scale photovoltaics, i.e., photovoltaic farms being established in larger suburban areas. Wind power plants are being built on land and in the Baltic Sea area [24]. Despite the high rate of change and new investments being undertaken, several key barriers to the wider development of renewable electricity production have been identified in Poland, which also has implications for electric vehicle emissions. One of the main barriers to the development of renewable energy is the issue of storing energy during periods of overproduction so that it can be used at times when generation from RES sources is not possible, i.e., during, for example, wind or sun shortages. The concept of energy storage is therefore being developed. Technological developments are favoured by falling component costs and the growth of commercial energy storage facilities for power system needs. However, regulatory support for the development of storage technologies is much less extensive than support for production technologies, and the rate of investment in new storage facilities is lower than for production technologies, which significantly limits the further integration of RES technologies into power systems. Another barrier related to transport is the rather slow pace of electromobility development. The widely heralded announcements of electromobility development are only partially reflected in the number of newly registered electric vehicles.

Nevertheless, initiatives are being taken to launch financial support and subsidies for the purchase of electric vehicles in Poland, e.g., the OurEvehicle programme. Announced in 2025 by the National Fund for Environmental Protection and Water Management and the Ministry of Climate and the Environment, the programme envisages a maximum funding amount of PLN 40,000. Only new M1-category electric vehicles that have not previously been registered and whose price does not exceed the net amount of PLN 225,000 are eligible for support [30]. At the same time, the development of infrastructure to ensure the efficient use of electric vehicles has been relatively slow, diverging significantly from plans to electrify road transport. In this respect, it is worth pointing out that at the end of July 2024, there were just over 70,000 passenger and commercial all-electric vehicles registered in Poland [3]. Between the beginning of the year and July 2024, the number of vehicles increased by 6% year-on-year. At the end of July 2024, there were 7,563 publicly accessible electric vehicle charging points in Poland, including 4,163 stations. As the number of electric vehicles has grown, so has the charging infrastructure. But the pace of development was too slow due to the condition of the power grids, among others. In July 2024, 308 new electric vehicle charging points were launched. Despite an inauspicious start in 2024, the International Energy Agency predicts that electric vehicles worldwide will reach a 20% market share by the end of 2024 [3]. Another barrier to the development of renewable energy is the price war among RES technologies and the competition between European players and the Chinese market. The production of components used in RES technologies in China, i.e., photovoltaic panels, batteries, energy storage, and electric vehicles, takes place on a large scale, making it unprofitable to produce for markets outside China. Such action results in a significant drop in component prices and the unprofitability of their production in European conditions, for example. This has resulted in the deepening monopolisation of many sectors, including, more recently, the EU's increasing dependence on Chinese supplies. The marked growth of Chinese capital in Europe is also evident in the transport sector. More new models and brands of Chinese-made vehicles are coming on sale, including SANY electric trucks [31] used in Poland for long-distance freight transport or service provision in the construction industry, for example. The above barriers inhibit the achievement of the green transition's goals, i.e. the European Union's energy autonomy and the reduction of air pollutant emissions also in the transport sector within the next decade. The commissioning date of the first nuclear units in Poland is 2035; the middle of the next decade will be crucial for the decarbonisation of energy and transport in Poland [24]. The larger-scale deployment of electric and hybrid vehicles is part of activities aimed at sustainability. Issues related to the modelling of sustainable transport systems [5], the search for air pollution emission reduction solutions [1] and scenarios with the development of electromobility [6] and risk analyses for the development of low-carbon transport and supply markets are widely published in the literature [8–10, 17]. In addition to the promotion of low- and zero-emission vehicles, strategies are being formulated to reduce emissions in urban areas, solutions to improve the cost-effectiveness of electric vehicle operation [4, 11] and studies in the field of air pollutant emission measurements of conventional, hybrid, electric [12–14, 18, 20, 33] and hydrogen vehicles [19].

2. Methodology

The paper proposes an analytical method to determine the air pollutant emissions generated by electric vehicles and presents the results of road tests measuring a hybrid vehicle's air pollutant emissions. Air pollutant emissions from vehicle operation usually boil down to determining the amount of air pollutants generated by a mode of transport during operation and affecting the external environment. Depending on the source of the pollution generated in the vehicles, this could be pollution coming directly from fuel combustion or from other sources. With regard to the issue of air pollutant emissions, different methods of measuring them are often pointed out. Common methods include the following:

- well to tank (WTT), understood as a method of measuring the amount of air pollutant emissions generated in the initial activity chain, e.g., involving extraction and production of the fuel used in a particular type of transport mode
- tank to wheel (TTW), understood as a method of measuring air pollutant emissions resulting from the direct consumption of fuel by a mode of transport
- well to wheel (WTW), understood as a method of measuring emissions along the entire chain, starting from the very source of an energy raw material in question to its use, i.e. from the extraction of the original propellant, e.g. oil, to the production and consumption of the fuels in the vehicle.

Measurements of air pollutant emissions should be selected depending on the mode of transport and the type of propellant used to power the vehicles. With regard to electric vehicles, on-site air pollutant emissions resulting from fuel combustion do not occur, so the TTW emissions measurement method is not applicable in this case. However, it is possible to use the WTT method to determine air pollutant emissions from electricity generation to power electric vehicles. In order to measure air pollutant emissions occurring during the vehicle operation phase, the focus should be on WTT emissions (electric vehicles, hybrid vehicles) and TTW emissions (conventional and hybrid vehicles).

For electric vehicles, the main air pollutant emission arising from electricity generation are applicable. These emissions are monitored and published by the National Centre for Emissions Management [22].

Table 1. Emission factors in [kg/MWh] for electricity end-users [22]

Year of measurements	Air pollutant type			
	CO_2	SO_2	NO_x	CO
2014	823	1.571	1.049	0.233
2015	798	1.516	0.954	0.234
2016	781	0.818	0.824	0.252
2017	778	0.729	0.741	0.265
2018	765	0.681	0.631	0.275
2019	719	0.511	0.576	0.233
2020	698	0.509	0.522	0.203
2021	708	0.505	0.505	0.237
2022	685	0.436	0.436	0.261
2023	597	0.363	0.392	0.222

Over the last decade, there has been a marked change in the emission factors for the main air pollutants from electricity production in Poland. The main air pollutants from electricity production in Poland are carbon dioxide, sulphur dioxide, nitrogen oxides, particulate matter, and carbon monoxide. Based on the data presented in Table 1, it can be concluded that over the last decade, the rate of CO_2 emissions during electricity generation in Poland has decreased by nearly 27%. The largest reduction in air pollutant emissions from electricity production in Poland was recorded for sulphur oxides (nearly 77%). In contrast, nitrogen oxides emissions in electricity production in Poland have dropped by nearly 63% in the last decade. The smallest reduction in air pollutant emissions in electricity production in Poland was recorded for carbon monoxide (5%). The reductions in air pollutant emissions in electricity production in Poland are directly related to Poland's energy mix and its significant change in the period from 2014 to 2024. The energy changes introduced in Poland are directly and positively reflected in air pollutant emissions generated in electricity production. The milestone for reducing emissions during electricity production in Poland will be the commissioning of the first nuclear power plant.

The emissions of electric vehicles in terms of propellant consumption come down to the determination of emissions during the operation of the mode of transport, in terms of the electric motor's electricity consumption, usually expressed as part of a combined cycle in terms of the power consumed per kilometre (Wh/km). Within the framework of the analytical method proposed in this paper, air pollutant emissions of electric vehicles can be determined based on emissivity factors published periodically by the National Centre for Emissions Management [22]. Moreover, air pollutant emissions of electric vehicles can be determined based on current and historical data, thereby making it possible to monitor changes in electric vehicle emissions in terms of changes to Poland's energy mix, as provided historically in Table 1. Using the KOBIZE values, the calculation of air pollutant emissions based on the proposed analytical method for electric vehicles, taking into account the variability of emissions over time due to changes in Poland's energy mix, is based on the following equations in mass units of each type of air pollutant per kilometre travelled by a specific type of electric vehicle.

$$E_{CO2} = P_k \times W_{1,y} \tag{1}$$

$$E_{SO2} = P_k \times W_{2,y} \tag{2}$$

$$E_{NOx} = P_k \times W_{3,y} \tag{3}$$

$$E_{CO} = P_k \times W_{4,y} \tag{4}$$

$$E_{T,y} = E_{CO2} + E_{SO2} + E_{NOx} + E_{CO} \tag{5}$$

where the individual symbols stand for specific air pollutant emissions, i.e.: $W_{1,y}$ – CO_2 emissions taken from Table 1 for k-th vehicle type and y-th assessment year; $W_{2,y}$ – SO_2 emissions taken from Table 1 for k-th vehicle type and y-th assessment year; $W_{3,y}$ – NO_x emissions taken from Table 1 for k-th vehicle type and y-th assessment year; $W_{4,y}$ – CO emissions taken from Table 1 for k-th vehicle type and y-th assessment year; $E_{T,y}$ – total emissions of main pollutants (CO_2, SO_2, CO, NO_x) for the k-th vehicle type in the y-th assessment year; P_k – energy consumption by the k-th electric vehicle type [kWh/km].

Air pollutant emissions from the operation of hybrid road vehicles, on the other hand, depend on the type of hybrid vehicle. As part of the paper, the RDE road test methodology was used to determine the emissions of hybrid vehicles. Air pollutant emissions were measured with the SEMTECH DS analyser, held by the Poznan University of Technology. The research was carried out under a discipline grant by the author. Warsaw University of Technology funded the grant.

The type of hybrid vehicle depends primarily on the configuration of the vehicle's power unit. Hybrid vehicles use an internal combustion engine and an electric motor for propulsion. Typically, the electric motor of a hybrid vehicle assists the internal combustion engine. There are three main types of hybrid vehicles, i.e., so-called full hybrids (HEVs), mild hybrids (mHEVs), and plug-in hybrids (PHEVs).

Considering the environmental impact issues of hybrid vehicles, the air pollutant emissions of hybrid vehicles are determined during real driving emissions tests (RDE). In addition, in terms of plug-in vehicles and MHEVs, it is possible to correct roadside measurements of air pollutant emissions by the value of air pollutant emissions that occur in the production of electricity consumed by the hybrid vehicle in the course of carrying out transport tasks. Thus, the emission results from road testing can be corrected (augmented) by the results of emissions generated by powering engines using electricity, based on the analytical method indicated earlier. The use of hybrid technologies in road vehicles is very common. As shown in Fig. 3 and Fig. 4, the popularity of electric and hybrid vehicles is significant.

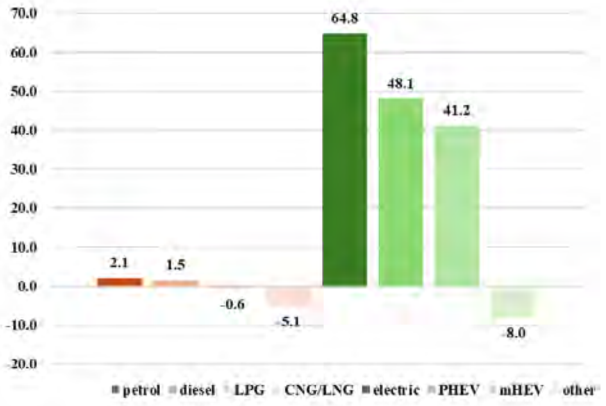

Fig. 3. Change in the number of registered vehicles in Poland, 2022/2023 [%] [23]

More than 48% more plug-in hybrid vehicles were registered in 2023 than in 2022. There was a similar increase in hybrid vehicle registrations in 2023 relative to 2022 for mHEVs (41%) [23]. The largest percentage increase in the number of vehicles registered year-on-year was for electric vehicles. Analysing new vehicle registrations, the highest increases of over 50% were also recorded for electric vehicles. Significantly, the year-on-year numbers of conventionally powered vehicles show little change, in favour of low- or zero-emission vehicles. Nevertheless, in absolute numbers, combustion vehicles are the largest group registered in Poland, which will not change in the coming years.

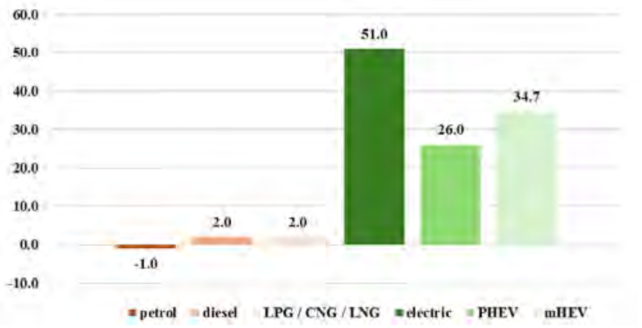

Fig. 4. Percentage change in the number of new registered vehicles in Poland 2022/2023 [23]

The measurement of air pollutant emissions of hybrid vehicles can be carried out in accordance with the real driving emissions (RDE). However, it should be mentioned that with the introduction of successive air pollutant emission standards, the methodologies for measuring air pollutant emissions have changed. Air pollutant emission measurements carried out under NEDC (New European Driving Cycle) or WLTP (Worldwide Harmonized Light-Duty Vehicles Test Procedure) laboratory conditions have been plagued by poor correlation between vehicle dynamic conditions on the dynamometer and in real traffic conditions. Manufacturers have often adapted combustion engines to meet all requirements only during laboratory tests. Hence, the measurement of exhaust gas emissions in real traffic conditions based on the RDE emission measurement test has been implemented [21]. Every car approved from 2017 onwards must meet RDE test requirements in addition to the WLTC test requirements. The compounds that appear in the exhaust gas when the vehicle is operated in urban, extra-urban, and motorway conditions are analysed during the road tests. The test route must be adjusted so that the test's continuity is not interrupted. Data should also be recorded without any interruption. The RDE test should be carried out on paved carriageways during working days. The regulations prohibit the excessive use of the neutral gear in the initial stage after starting the engine during the test. The route should run for a minimum of 16 km in urban, non-urban, and motorway conditions [14]. Hybrid vehicle tests were carried out in the Poznań agglomeration as part of this paper. Vehicle speeds in the urban area did not exceed 60 km/h, with average speeds between 15 and 45 km/h. The proportion of each section was approximately one-third of the length of the entire test route. Deviations of 10 percentage points were allowed, but the urban section should not represent less than 29% of the total test route. Moreover, stops, i.e., when the car is not moving faster than 1 km/h, should not account for more than 30% of the total route in the test's urban section. In the non-urban section, the vehicle travelled at least 16 km and travelled at speeds between 60 and 90 km/h. In the motorway section, the vehicle travelled at higher speeds, i.e., from 90 km/h, and the maximum speed did not exceed 145 km/h [14]. In terms of plug-in vehicles and MHEVs, the results of on-road air pollutant emissions tests can be further corrected, plus the value of air pollutant emissions that arise from the generation of electricity consumed by the vehicle in the course of its transport tasks.

3. Results

Given the analytical method described above for determining the air pollutant emissions generated by electric vehicles, as well as the air pollutant emissions published by KOBIZE [22], it is possible to determine TTW emissions for electric vehicles. The characteristics of the electric vehicles for which air pollutant emissions were determined are shown in Table 2.

Table 2. Characteristics of selected electric vehicles [28, 29, 32]

No.	Vehicle brand	Model	Energy consumption [Wh/km]	Maximum range [km]
1	Tesla	S Plaid	187	600
2	BMW	i5 eDrive40	159	582
3	Nissan	Leaf	166	285
4	VW	ID.3	152	388
5	Hyundai	IONIQ 6	139	429

Knowing the energy consumption during the electric vehicle's mixing cycle, it is possible to determine the air pollutant emissions generated during the electricity generation stage. In view of the issues involved in the life cycle analysis of road vehicles, including electric vehicles, it should be noted that electric vehicles have lower air pollutant emissions over their whole LCA (Life Cycle Analysis) compared to petrol and diesel vehicles [2]. The largest percentage of air pollutant emissions as CO_2-equivalent over a vehicle's life cycle is related to fuel production and fuel consumption for vehicle propulsion. For conventional road vehicles, the most relevant emissions component as part of the LCA assessment is the production of conventional fuels and the emissions from the combustion of petrol, diesel, or gas. With regard to electric vehicles in terms of air pollutant emissions, a key issue is related to electricity generation, as well as its sources. Figure 5–8 presents the results of the air pollutant emissions tests of the electric vehicles mentioned in Table 2 in 2023, determined using the analytical method presented earlier.

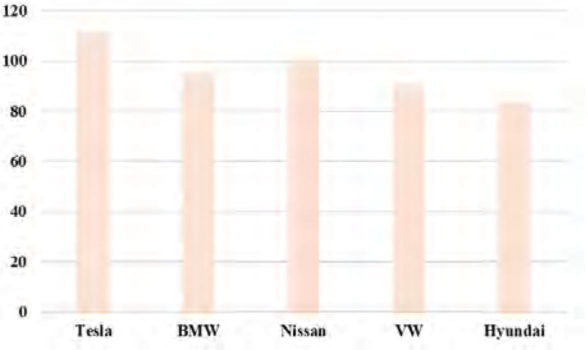

Fig. 5. CO_2 emissions of electric vehicles in 2023 [g/km]

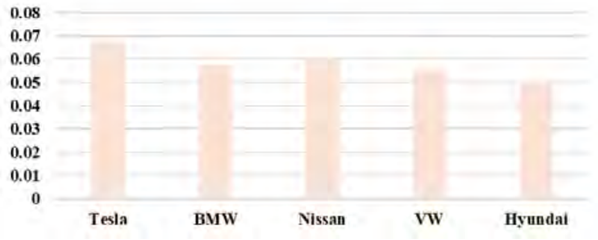

Fig. 6. SO_2 emissions of electric vehicles in 2023 [g/km]

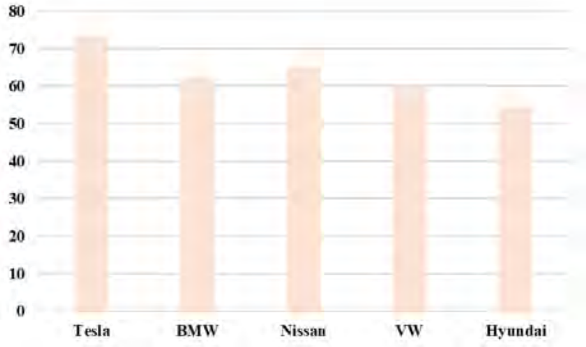

Fig. 7. NO_x emissions of electric vehicles in 2023 [g/km]

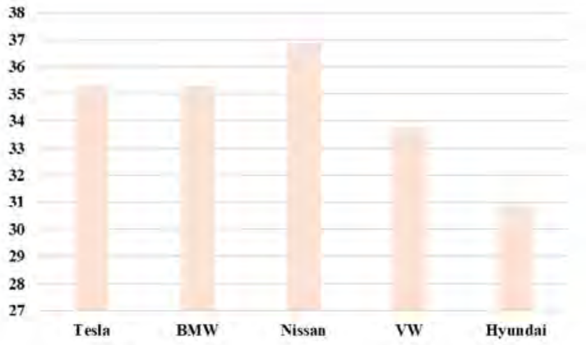

Fig. 8. CO emissions of electric vehicles in 2023 [g/km]

The CO_2 emissions are much higher than emissions of other compounds generated by vehicles, including NO_x and CO. However, the article presents CO and NO_x emissions due to the harmfulness of air pollutants generated in smaller quantities, and SO_2 emissions for electric vehicles.

The increasingly widespread use of electric vehicles in Poland and Europe represents an opportunity to reduce greenhouse gas emissions in the area of transport. Requirements for electric vehicles as well as charging stations are formulated to ensure safe use, monitoring of the charging process, and energy consumption [3]. In order for electric vehicles to be more widely used, charging stations on the TEN-T Trans-European Transport Network are required to be spaced at a maximum of every 60 km. The above can help reduce air pollutant emissions from road transport. An essential part of the infrastructure for powering electric vehicles is the power grids, of which, according to the Supreme Audit Office's reports, 90% of high-voltage power lines are more than 10 years old, with 43% – more than 40 years old. Low-voltage lines were in operation for the shortest time period, although still 32% of them had been in operation for more than 40 years [3]. In addition to lower air pollutant emissions, incentives for purchasing an electric vehicle can include lower insurance rates, lower electricity prices, attractive subsidy offers, concessions, and exemptions when driving in urban areas. In order to think about the widespread use of electric cars, the charging network needs to be increased by as much as six times by 2035 [3]. According to the IEA (International Energy Agency), if battery cars continue to develop at the current rate, their share of the global market should already reach 50% in the next decade.

As indicated earlier, due to the change in Poland's energy mix over recent years, the emissions of the individual compounds monitored by KOBIZE have changed. With emissions tables [22], it is possible to determine the rate of change of vehicle emissions over time for electric vehicles. To illustrate this phenomenon, two electric vehicles were used for the purpose of this paper, i.e., the VW ID.3 [32] and Nissan Leaf [29]. The power of the VW ID.3 vehicle was 170 kW, with a range of up to 388 km. Energy consumption was 152 Wh/km. The power of the Nissan Leaf vehicle was 150 kW, with a range of up to 285 km. Energy consumption was 166 Wh/km. The change in air pollutant emissions determined using the early analytical method described applies to carbon dioxide, nitrogen oxides and carbon monoxides are shown in Fig. 9 and Fig. 10.

Fig. 9. Change in air pollutant emissions of VW ID.3 from 2014 to 2023, own elaboration

Fig. 10. Change in air pollutant emissions of Nissan Leaf from 2014 to 2023

Analysing the historical KOBIZE emissions data, for the VW ID.3 and the Nissan Leaf, assuming the current technical parameters for energy consumption between 2014 and 2024 for the above-mentioned vehicles, it should be noted that in the past decade there has been a decrease of 27% in CO_2 emissions, 63% in nitrogen oxides and 5% in carbon monoxide. A change in Poland's energy mix is therefore responsible for reducing EV emissions. It can therefore be assumed that the transfer of electricity production in Poland to renewable energy sources or nuclear energy will allow for even more significant reductions in emissions. This will enable the operation of electric vehicles to be referred to as zero-emission vehicle operation. Until this happens, it is possible to refer to electric vehicles as low-emission vehicles.

As part of the emissions testing of hybrid vehicles, air pollutant emissions were measured for the Kia Niro, manufacturing year 2022, 1.6 petrol engine, plug-in type, with a total power of nearly 105 HP [28]. In terms of hybrid vehicles, the analysis of fuel consumption and energy requirements is also an important issue [27]. Cumulative fuel consumption increases with increasing mileage, but the increase is not a linear function. Similar observations were made in terms of air emissions of vehicles with diesel engines [15, 16]. Pollutant emissions increased with operating age, but this was not an increase that could be described by a linear function. Detailed results of RDE tests of air pollutants for the Kia Niro vehicle in urban, suburban, motorway, and RDE modes are shown in Fig. 11, Fig. 13, and Fig. 15.

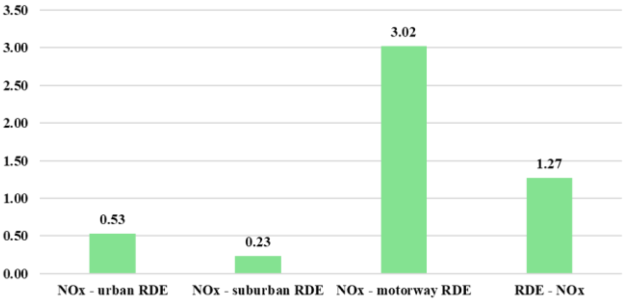

Fig. 11. NO_x emissions of the Kia Niro, RDE test [mg/km]

Fig. 12. NO_x emissions of the Kia Niro, RDE test and RDE + EN emissions [mg/km]

The air pollutant emissions of a hybrid vehicle are those from the combustion of fuel while the vehicle is running, shown in Fig. 11, Fig. 13, and Fig. 15, as well as emissions including air pollutants generated from electricity generation, designated RDE + EN in Fig. 12, Fig. 14, and Fig. 16. The emissions marked as RDE + EN on Fig. 12, 14, and 16 are the emissions generated by the hybrid vehicle during the road test from combustion fuel, plus the emissions resulting from the electricity consumed by the hybrid vehicle during the road test. The energy marked as EN in the figures indicates emissions from energy drawn from the electric network by the hybrid vehicle.

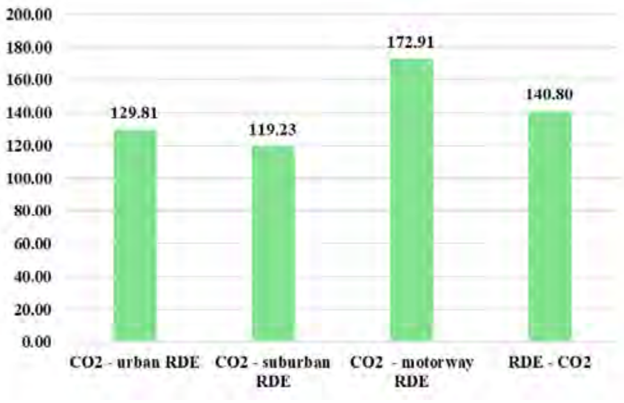

Fig. 13. CO_2 emissions of the Kia Niro, RDE test [mg/km]

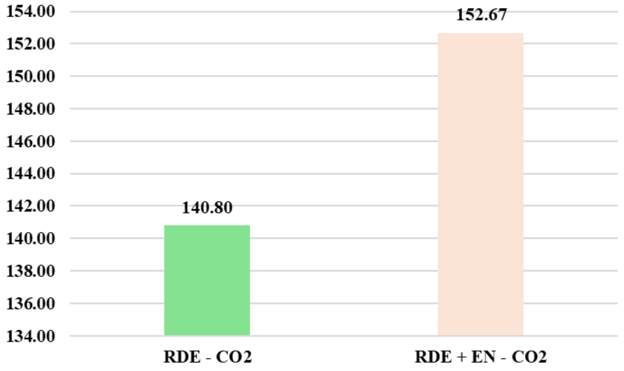

Fig. 14. CO_2 emissions of the Kia Niro, RDE test and RDE + EN emissions [mg/km]

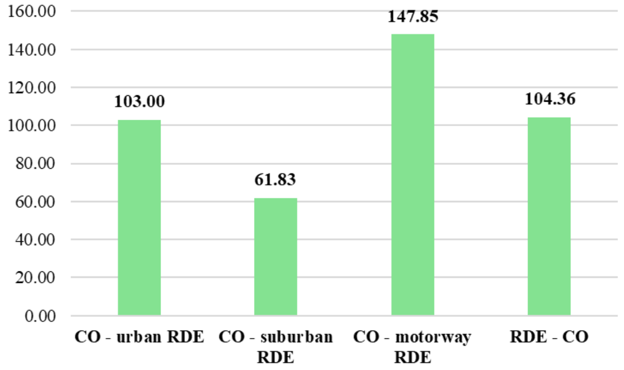

Fig. 15. CO emissions of the Kia Niro, RDE test [mg/km]

The air pollutant emissions of the hybrid vehicle, including those from electricity generation, contribute slightly to the higher total emissions found in the road tests. The above analyses related to determining the impact of emissions from electricity generation on the emissions of the hybrid vehicle were carried out using the analytical method indicated above and the air pollutant emissions from 2023 published by KOBIZE and shown in Table 1.

The Kia Niro hybrid vehicle's carbon dioxide emissions in the RDE road test were 140.80 g/km and, including emissions from electricity generation, amounted to 152.67 mg/km. This represents an increase in carbon dioxide emissions of around 8%. The nitrogen oxide emissions of the Kia Niro hybrid vehicle in the RDE road test were 1.27 mg/km and, including emissions from electricity generation, amounted to 1.28 mg/km. This represents an increase in nitrogen oxide emissions of around 1%. The carbon monoxide emissions of the Kia Niro hybrid vehicle in the RDE road test were 104.36 mg/km, and including emissions from electricity generation, also amounted to 104.36 mg/km.

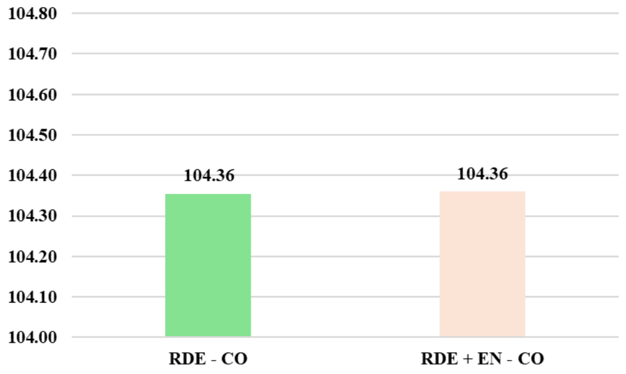

Fig. 16. CO emissions of the Kia Niro, RDE test, and RDE + EN emissions [mg/km]

4. Conclusions

The increasingly widespread use of electric vehicles in Poland and Europe represents an opportunity to reduce greenhouse gas emissions in the area of transport. An analytical method can be used to determine the emissions of electric vehicles, taking into account data from the general reports prepared by KOBIZE [22]. Knowing the energy consumption during the electric vehicle's mixing cycle, it is possible to determine the air pollutant emissions generated during the electricity generation stage. Analysing the historical KOBIZE emissions data, for the VW ID.3 and the Nissan Leaf, assuming the current technical parameters for energy consumption between 2014 and 2024 for the above-mentioned vehicles, it should be noted that the past decade featured a decrease of 27% in CO_2 emissions, 63% in nitrogen oxides and 5% in carbon monoxide. A change in Poland's energy mix is therefore responsible for reducing EV emissions. It can therefore be assumed that the transfer of electricity production in Poland to renewable energy sources or nuclear energy will allow for even more significant reductions in emissions. This will enable the operation of electric vehicles to be referred to as zero-emission vehicle operation. Until this happens, it is possible to refer to electric vehicles as low-emission vehicles. The proposed analytical method for determining the air pollutant emissions of electric vehicles makes it possible to observe changes in pollutant emissions over time, taking into account the changing electricity production mix in Poland and scenarios for organizing transport systems with electric vehicles [7].

For hybrid vehicles, RDE measurements of air pollutant emissions can be corrected using the analytical method to the extent that they relate to the measurement of emissions associated with electricity generation. The Kia Niro hybrid vehicle's carbon dioxide emissions in the RDE road test were 140.80 g/km and, including emissions from electricity generation, amounted to 152.67 mg/km. This represents an increase in carbon dioxide emissions of around 8%. The nitrogen oxide emissions of the Kia Niro hybrid vehicle in the RDE road test were 1.27 mg/km and, including emissions from electricity generation, amounted to 1.28 mg/km. This represents an increase in nitrogen oxide emissions of around 1%. The carbon monoxide emissions of the Kia Niro hybrid vehicle in the RDE road test were 104.36 mg/km, and including emissions from electricity generation, also amounted to 104.36 mg/km.

Acknowledgements

This paper was prepared as part of a research project in support of scientific activities in the discipline of Civil Engineering and Transport entitled "Investigating the phenomenon of ageing transport modes in the context of the environmental impact of vehicles".

Nomenclature

HEV	hybrid electric vehicle
IEA	International Energy Agency
KOBIZE	National Centre for Emissions Management
LCA	life cycle analysis
mHEV	mild hybrid electric vehicle
NEDC	New European Driving Cycle
PHEV	plug-in hybrid electric vehicle
RES	renewable energy sources
RDE	measurement of real driving emissions
TTW	tank to wheel
WLTP	Worldwide Harmonized Light-Duty Vehicles Test Procedure
WTT	well to tank

Bibliography

[1] Dziubak T, Ślęzak M. Characteristics of pollutants emitted by motor vehicles and their impact on the environment and engine operation. Combustion Engines. 2025;200(1):37-55. https://doi.org/10.19206/CE-194628

[2] Hill N. Determining the environmental impacts of conventional and alternatively fuelled vehicles through LCA. 2020. https://op.europa.eu/en/publication-detail/-/publication/1f494180-bc0e-11ea-811c-01aa75ed71a1

[3] Idzior M. Implications of power infrastructure development for the electromobility of the motor vehicle market in Poland. Logistics Systems in Theory and Practice 2024 Conference, Warsaw.

[4] Izdebski M, Jacyna M, Bogdański J. Minimisation of the energy expenditure of electric vehicles in municipal service companies, taking into account the uncertainty of charging point operation. Energies. 2024;17(9):2179. https://doi.org/10.3390/en17092179

[5] Jacyna M, Wasiak M, Lewczuk K, Kłodawski M. Simulation model of transport system of Poland as a tool for developing sustainable transport. Archives of Transport. 2014;31(3):23-35. https://doi.org/10.5604/08669546.1146982

[6] Jacyna M, Żochowska R, Sobota A, Wasiak M. Scenario analyses of exhaust emissions reduction through the introduction of electric vehicles into the city. Energies. 2021;14(7):2030. https://doi.org/10.3390/en14072030

[7] Jacyna M, Żochowska R, Sobota A, Wasiak M. Decision support for choosing a scenario for organizing urban transport system with share of electric vehicles. Scientific Journal of the Silesian University of Technology. Series Transport. 2022;117:69-89 https://doi.org/10.20858/sjsutst.2022.117.5

[8] Jacyna-Gołda I, Izdebski M, Szczepański E, Gołda P. The assessment of supply chain effectiveness. Archives of Transport. 2018;45(1):43-52. https://doi.org/10.5604/01.3001.0012.0966

[9] Lasota M, Zabielska A, Jacyna M, Gołębiowski P, Żochowska R, Wasiak M. Method for delivery planning in urban areas with environmental aspects. Sustainability. 2024;16(4):1571. https://doi.org/10.3390/su16041571

[10] Lasota M, Zabielska A, Jacyna M, Żak J. Research and analysis of the operation of vehicles with various propulsion systems, including costs and CO_2 emissions. Combustion Engines. 2023;4(195):3-13. https://doi.org/10.19206/CE-169845

[11] Mądziel M, Campisi T, Jaworski A, Tesoriere G. The development of strategies to reduce exhaust emissions from passenger cars in Rzeszow city – Poland, a preliminary assessment of the results produced by the increase of e-fleet. Energies. 2021;14(4):1046. https://doi.org/10.3390/en14041046

[12] Merkisz J, Sordyl A, Chłopek Z. Non-repeatability of the WLTP vehicle test results. Archives of Transport. 2024;71(3):25-49. https://doi.org/10.61089/aot2024.fjw8a575

[13] Pielecha J, Skobiej K, Kurtyka K. Exhaust emissions and energy consumption analysis of conventional, hybrid, and electric vehicles in real driving cycles. Energies. 2020;13(23):6423. https://doi.org/10.3390/en13236423

[14] Pryciński P, Pielecha P, Korzeb J, Pielecha J, Kostrzewski M, Eliwa A. Air pollutant emissions of passenger cars in Poland in terms of their environmental impact and type of energy consumption. Energies. 2024;17(21):5357. https://doi.org/10.3390/en17215357

[15] Pryciński P, Pielecha J, Korzeb J, Jachimowski R, Pielecha P. Impact of vehicle aging and mileage on air pollution emissions. Energies. 2025;18(4):939. https://doi.org/10.3390/en18040939

[16] Pryciński P, Korzeb J, Pielecha J: Research on the impact of vehicle aging on the amount of air pollution emissions. Journal of Konbin. 2025;55(1):105-120. https://doi.org/10.5604/01.3001.0055.0625

[17] Rudyk T, Szczepański E, Jacyna M. Safety factor in the sustainable fleet management model. Archives of Transport. 2019;49(1):103-114. https://doi.org/10.5604/01.3001.0013.2780

[18] Rymaniak Ł, Kamińska M, Szymlet N, Grzeszczyk R. Analysis of harmful exhaust gas concentrations in cloud behind a vehicle with a spark ignition engine. Energies. 2021;14(6):1769. https://doi.org/10.3390/en14061769

[19] Skobiej K. A review of hydrogen combustion and its impact on engine performance and emissions. Combustion Engines. 2025;200(1):64-70. https://doi.org/10.19206/CE-195470

[20] Suarez-Bertoa R, Astorga C, Franco V, Kregar Z, Valverde V, Clairotte M et al. Technical report by the Joint Research Centre (JRC). On-road vehicle emissions beyond RDE conditions. 2019. https://publications.jrc.ec.europa.eu/repository/handle/JRC115979

[21] Regulation of the Commission (EU) no. 2016/427 of 10 March 2016 amending Regulation (EC) no. 692/2008 as regards emissions from light passenger and commercial vehicles.

[22] Report: Air pollutant emissions from electricity production in Poland. 2025. KOBIZE. https://www.kobize.pl/pl/fileCategory/id/28/wskazniki-emisyjnosci

[23] Report: Automotive Industry 2024/2025. 2025. Polish Automotive Industry Association. https://www.pzpm.org.pl/en/Automotive-market/Reports/PZPM-Automotive-Industry-Report-2024-2025

[24] Report: Integrated Impact Report of Polskie Sieci Elektroenergetyczne S.A. 2025. PSE S.A. https://api-raport.pse.pl/uploads/PSE-Zintegrowany_Raport_Wplywu_2023.pdf

[25] Report: The structure of electricity production in the European Union. 2025. Council of the EU. https://www.consilium.europa.eu/pl/infographics/how-is-eu-electricity-produced-and-sold/#0

[26] Report: The structure of electricity production in Poland. 2025. CIRE. https://www.cire.pl/strony/struktura-i-produkcja-energii-elektrycznej-w-polsce

[27] Sitnik L, Ivanov Z, Sroka Z. Energy demand assessment for long term operation of hybrid electric vehicles. 2020 IOP Conf Ser: Mater Sci Eng. 2020;1002(1):012026. https://doi.org/10.1088/1757-899X/1002/1/012026

[28] Website: Motovolt. 2025. https://motorvolt.pl/baza-samochodow-elektrycznych

[29] Website: Nissan. 2025. https://www-europe.nissan-cdn.net/content/dam/Nissan/pl/brochures/Techdata/leaf-dane-techniczne.pdf

[30] Website: NFOSiGW. 2025. OurEvehicle programme. https://www.gov.pl/web/nfosigw/program-naszeauto-do-40-tys-zl-doplaty-do-samochodu-elektrycznego

[31] Website: Sany. 2025. https://www.sanyglobal.com/product/truck/semi-trailer_tractor/138/

[32] Website: Volkswagen. 2025. https://www.volkswagen.pl/

[33] Zimakowska-Laskowska M, Kozłowski E, Laskowski P, Wiśniowski P, Świderski A, Orynycz O. Vehicle exhaust emissions in the light of modern research tools: synergy of chassis dynamometers and computational models. Combustion Engines. 2025;200(1):145-154. https://doi.org/10.19206/CE-201224

Piotr Pryciński, DEng. – Faculty of Transport, Warsaw University of Technology, Poland.

e-mail: *piotr.prycinski@pw.edu.pl*

Article citation info:
Jakubowski M. Optimization of the cooling system in a prototype VCR engine using CFD analysis. Combustion Engines. 2025;202(3): 36-43. https://doi.org/10.19206/CE-205445

Mirosław JAKUBOWSKI

Combustion Engines
Polish Scientific Society of Combustion Engines

Optimization of the cooling system in a prototype VCR engine using CFD analysis

Article Info

Received: 5 May 2025
Revised: 18 May 2025
Accepted: 21 May 2025
Available online: 24 June 2025

The cooling system of an internal combustion engine affects various key parameters, including ignition delay, fuel evaporation, and the compression-expansion process. The geometry of its components impacts both cooling efficiency and the energy demand of the coolant pump. This paper presents CFD simulation results of coolant flow through selected elements of a modified cooling system in a prototype engine. Due to design changes in the power unit, the original coolant outlet manifold required redesign. Three manifold variants were analyzed under two coolant types and two back pressure levels. Flow patterns were evaluated using streamlines and velocity distributions in selected cross-sections. The applied manifold modification significantly increased coolant velocity. In the analyzed cases, the local resistance coefficient rose to values as high as 9. For version mod2, the risk of turbulence was higher with a water-glycol mixture than with water. For version mod1, turbulence sensitivity to coolant type was negligible.

Key words: *cooling system, internal combustion engine, CFD simulation, coolant flow, VCR engine*

1. Introduction

One of the fundamental conditions for the proper operation of internal combustion engines is maintaining adequate cooling intensity. Parameters of the cooling process, such as coolant flow rate, significantly influence heat exchange between the coolant and the heated walls of the cylinders and cylinder head. Additionally, cooling intensity affects pressure changes during the compression and expansion strokes, as well as the fuel evaporation process and ignition delay time in compression ignition engines. The thermal state of the engine also plays a crucial role in determining the quality of the air-fuel mixture.

In traction-type internal combustion engines, liquid cooling with forced circulation is almost universally applied. Approximately 30% of the heat generated during combustion is transferred to the coolant [23], representing a substantial thermal load. Ensuring proper coolant flow – achieved, for example, through the optimized geometry of cooling system components – is essential. For this purpose, commercial Computational Fluid Dynamics (CFD) software is commonly utilized [10].

Numerical analysis of coolant flow in internal combustion engine cooling systems must account for turbulence. The k–ε turbulence model is widely used due to its robustness and suitability for this application [2, 4, 13, 16]. CFD simulations typically consider both fluid dynamics and thermal interactions between the coolant and the walls of the flow passages [3, 17]. Phenomena such as cavitation [7, 12] and other flow disturbances are also relevant in such analyses. Since velocity distribution in coolant channels determines heat transfer efficiency, it is a critical aspect of CFD-based investigations.

The effect of the study [5] demonstrates that modifying the water jacket can reduce the volume of stagnant coolant by up to 75% and increase flow velocity by as much as 50%, compared to the original design. CFD simulations can also predict flow and thermal non-uniformities and identify zones of low velocity [19, 21, 22, 24]. These tools are increasingly applied in the thermal management of electric vehicle systems as well [6, 11].

Numerical flow analysis is also employed in the development and optimization of air-cooled engine systems. Simulations enable assessment of fin design with varying geometrical and material properties, and facilitate the estimation of thermal stresses [14, 15, 18, 20]. As shown in [20], simulation results exhibited good correlation with data obtained from wind tunnel experiments.

Cooling of internal combustion engines also involves heat dissipation through oil. Analyzing its flow using CFD offers benefits, such as reducing prototyping time, particularly in conditions of variable flow channel dynamics. This occurs, for instance, in connecting rods, where oil flows to cool the piston [8].

Designing modern internal combustion engines involves a wide array of requirements, including those pertaining to thermal management. The application of CFD tools facilitates rapid evaluation of various design configurations, enabling selection of appropriate geometries for manifolds, channels, hoses, and other components.

The subject of this study is a prototype diesel engine with a variable compression ratio, developed based on a commercially available four-stroke, inline four-cylinder engine. A distinguishing feature of the design is the lack of a permanent connection between the cylinders and the engine block housing the crankshaft, enabling variation in compression ratio by axial movement of the cylinder assembly.

The cylinder displacement mechanism consists of multiple components. The integration of these additional parts necessitated several design changes, including modifications to the engine's cooling system. The original coolant discharge system comprised a manifold with three segments connected by rubber hoses (Fig. 1).

The coolant manifold is mounted to the cylinders at the locations indicated in Fig. 2.

Fig. 1. Factory elements of the engine cooling system; manifold draining liquid from the cylinder block

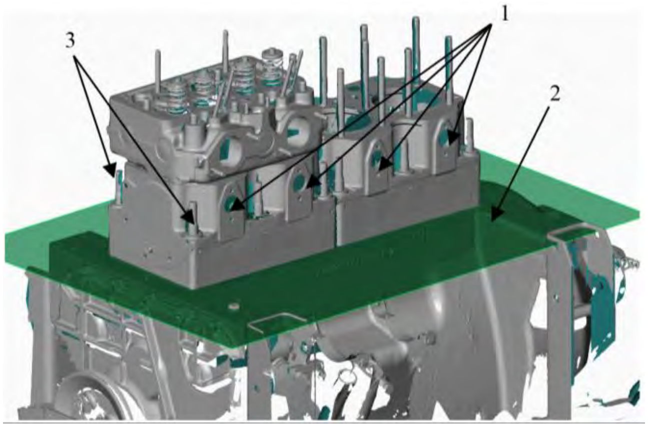

Fig. 2. 3D scan of the base engine: 1 – places for mounting the factory manifold, draining liquid from the cylinder block; 2 – the plane of division of the cylinder block and the engine block; 3 – pins on which the support plate is mounted

One of the key components of the cylinder displacement mechanism is the support plate, which is mounted on additional guide pins (Fig. 2). Unfortunately, the support plate interferes with the factory-installed coolant outlet manifold (Fig. 3). As a result, it was necessary to design new components to resolve this interference. The newly developed parts are flanges, which are mounted to the cylinder block prior to the installation of the support plate (Fig. 5).

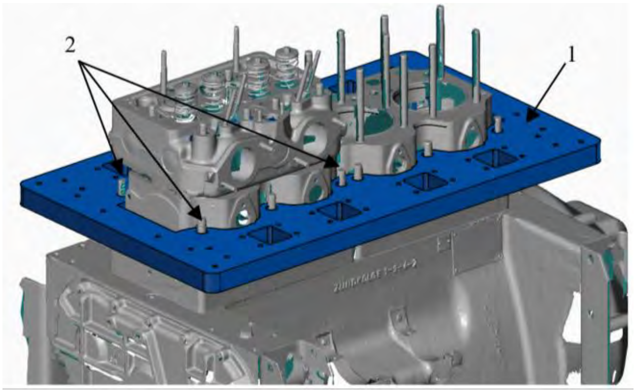

Fig. 3. 3D scan of the base engine with the CAD model of the main support plate of the cylinder block shift mechanism: 1 – support plate; 2 – threaded parts of the plate fixing pins (screwed with nuts)

After the support plate is mounted to the cylinder block, outlet pipes are screwed into the flanges and connected to the hoses. These modifications require additional changes – most importantly, the cross-sectional area of each of the four outlet channels coming from the cylinder block must be reduced. The cross-sectional area has been decreased by a factor of four. Applying the mass balance equation for fluid flow to the modified cross-sectional area yields:

$$\dot{m}_1 = \dot{m}_2 = \rho_1 \cdot v_1 \cdot A_1 = \rho_2 \cdot v_2 \cdot A_2 \tag{1}$$

where (indexes apply to sections 1 and 2): $\dot{m}$ – mass flow rate through cross-section A, ρ – fluid density, v – fluid velocity, A – cross-section area.

Since the coolant can be treated as an incompressible fluid, the density remains constant, i.e., $\rho_1 = \rho_2$. Consequently, a fourfold reduction in cross-sectional area requires a fourfold increase in fluid velocity to maintain the same mass flow rate, according to the principle of continuity. The continuity equation, expressed in Cartesian coordinates, takes the following form:

$$\frac{\partial \rho}{\partial t} + \frac{\partial \rho u}{\partial x} + \frac{\partial \rho v}{\partial y} + \frac{\partial \rho w}{\partial z} = 0 \tag{2}$$

where: ρ – fluid density, t – time, u, v, w – velocity component in, respectively, the x, y and z direction.

Many problems result from the increase in fluid velocity combined with cross-section changes and rapid flow direction changes. First of all, the value of local flow resistance increases and the flow character (laminar or turbulent) varies. Figure 4 shows the engine model with the mechanism for changing the compression ratio. The illustration shows the extent to which the space for the coolant manifold is limited.

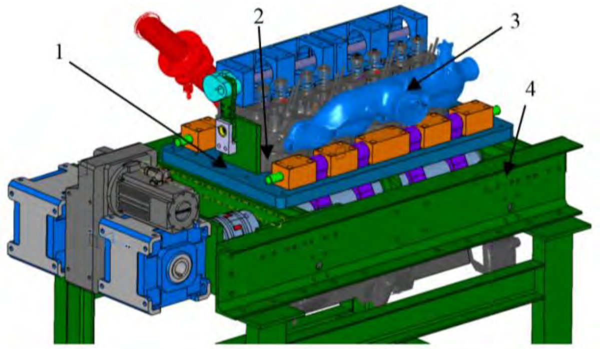

Fig. 4. VCR engine model with mechanism for changing the compression ratio: 1 – support plate; 2 – cylinder block; 3 – intake manifold; 4 – support structure element

The flanges described above with screw-in outlet pipes mounted on the engine are shown in Fig. 5 and 6.

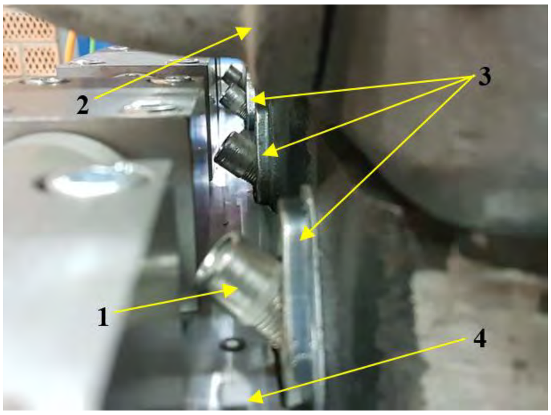

Fig. 5. Modified coolant outlet from the cylinder block (view along the axis of the engine shaft): 1 – outlet pipes; 2 – engine intake manifold; 3 – flanges; 4 – support plate

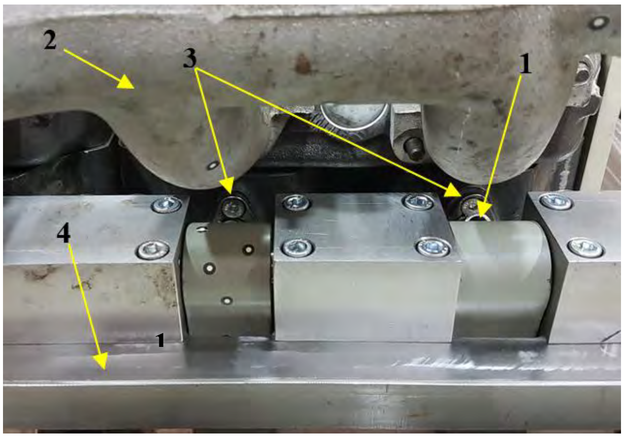

Fig. 6 Modified coolant outlet from the cylinder block (side view): 1 – outlet pipes; 2 – engine intake manifold; 3 – flanges; 4 – support plate

2. Research methodology

Based on the factors described above, outlet coolant manifolds were designed with geometries that accommodate the available space constraints. Figure 7 presents a comparison of the proposed models. These models were created using CATIA V5, exported in a standard CAD data exchange format (STEP), and then imported into the Autodesk CFD environment, where three-dimensional numerical flow analysis was performed.

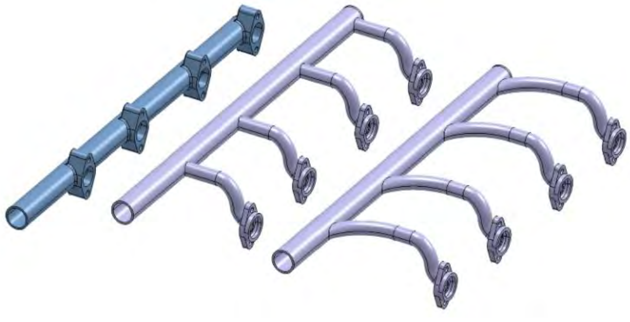

Fig. 7. Comparison of outlet coolant manifold models; from the left: factory manifold (mod0), modified version 1 (mod1), modified version 2 (mod2)

Figure 8 shows a comparison of coolant manifold models in version 1 (mod1) and 2 (mod2) mounted on the engine. A very small space is available for assembling them. It is mostly limited by the engine intake manifold and connecting rods of the cylinder block shifting system (used to change the compression ratio). An electric coolant pump was used in the construction of the prototype engine. The pump mass flow efficiency was calculated according to the formula (3) [9]:

$$\dot{m} = \frac{Q}{c_w \Delta T_w} \tag{3}$$

where: Q – heat taken from the engine, c_w – specific heat of the coolant, ΔT_w – temperature difference of the coolant flowing out and flowing in the engine.

According to formula (2) for the factory engine, the theoretical cooling mass flow $\dot{m}$ should be 1.9 kg/s (for water). Thus, the mass flow rate for each coolant manifold inlet is 0.48 kg/s. It was assumed that the total coolant stream is divided into four equal parts and its value is constant over time. For all tested manifolds, a simulation of the flow for two fluids – water and a mixture of ethylene glycol and water (50% by volume) – was carried out. During the analysis, it was assumed that the temperature, density, and dynamic viscosity of the coolant were constant. The simulations were carried out for two values of outlet back pressure (Fig. 8): 0 and 80 kPa [23].

The shape and size of the cross-sections at the manifold inlet were determined by the geometry of the openings in the cylinder block walls, while at the outlet, they were matched to the factory manifold in order to avoid the need for modifications to other components in the cooling system. It was also assumed that the factory flow channels upstream of the inlet and downstream of the outlet would perform their function properly, and their geometry was not considered in the simulation.

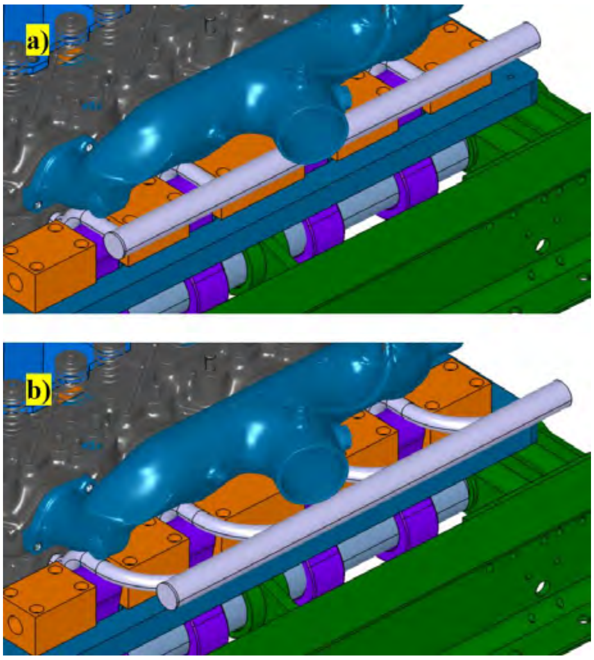

Fig. 8. Modified coolant manifolds on the engine: a) mod1, b) mod2

The symbolic names of individual simulations are presented in Table 1. The physical parameters of water and its mixtures with ethylene glycol at 20°C are given in Table 2.

Figure 9 shows the liquid inlets and outlet in the mod0 version. The back pressure is defined as overpressure relative to the ambient pressure.

The aim of the simulations was to compare the behavior of the coolant stream during flow through the different outlet manifold models. Research results play an auxiliary role in choosing the right design solution. It should be noted that the possibilities of obtaining significantly different versions of coolant manifolds are quite limited due to the very small available space. The work focused mainly on the analysis of trace lines and the distribution of coolant velocity at critical locations of manifold models. It is important to determine the areas or shapes of the channels in manifolds that can disturb the desired fluid flow. The heat transfer analysis was not included in the simulation. Therefore, no calculations for higher temperature values were carried out – this will be the subject of further studies.

Table 1. List of simulation names used in calculations

Outlet coolant manifold	Simulation name	Coolant	Back pressure [kPa]
	mod0-W-p0	Water	0
	mod0-W-p80		80
	mod0-WG-p0	Mixture of ethylene glycol and water (50% by volume)	0
	mod0-WG-p80		80
	mod1-W-p0	Water	0
	mod1-W-p80		80
	mod1-WG-p0	Mixture of ethylene glycol and water (50% by volume)	0
	mod1-WG-p80		80
	mod2-W-p0	Water	0
	mod2-W-p80		80
	mod2-WG-p0	Mixture of ethylene glycol and water (50% by volume)	0
	mod2-WG-p80		80

Table 2. Physical parameters of the analyzed coolants [1]

Parameter	Density [g/cm^3]	Dynamic viscosity [mPa·s]
Water	0.9982	1.00
Mixture of ethylene glycol and water (50% by volume)	1.0695	3.98

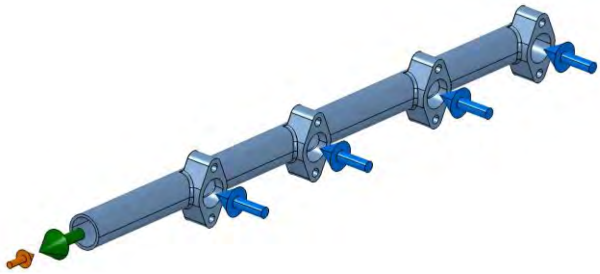

Fig. 9. Inlets (blue arrows) and outlet (green arrow) on the example of the factory manifold; the orange arrow symbolizes back pressure

3. Results and discussion

Due to the limited volume of the article, it was decided to present selected, representative forms of the results of the coolant flow simulation. Because a wider comparison of modified coolant manifolds (mod1 and mod2) is presented further on, only the results for water flow with 0 kPa back pressure for the factory manifold mod0 are presented here. The color scale for each visualization has been unified, so a given color indicates the same value in each figure. In Figs. 10 to 19, for better readability, the coolant trace lines are shown in individual illustrations.

Figures 12–26 show the results only for mod1 and mod2. The necessary modifications used in the mod1 and mod2 versions resulted in a rapid increase in fluid velocity (Fig. 12–19). Local reduction of the cross-section area also brings an increase in the value of the local resistance coefficient ξ. In the studied cases, the value of this coefficient is about 9.

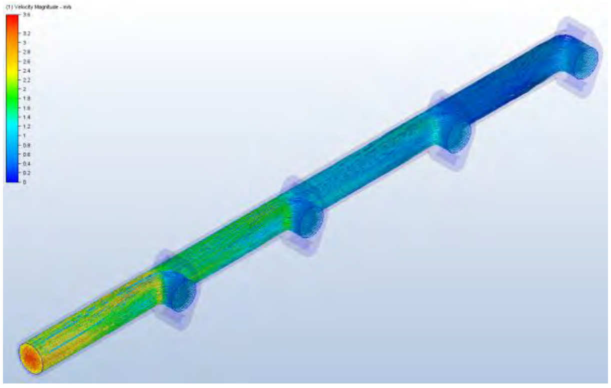

Fig. 10. Coolant trace lines with velocity distribution; mod0-W-0kPa

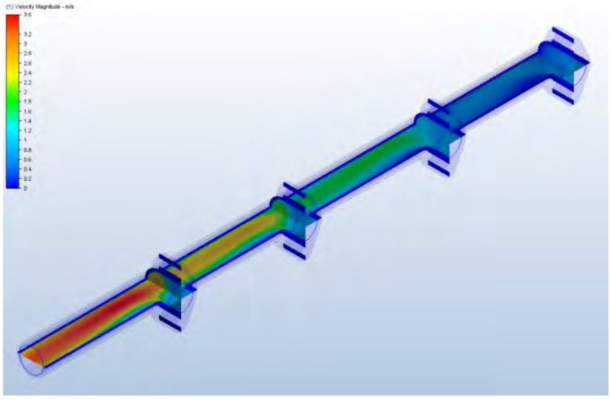

Fig. 11. Distribution of coolant velocity on selected planes; mod0-W-0kPa

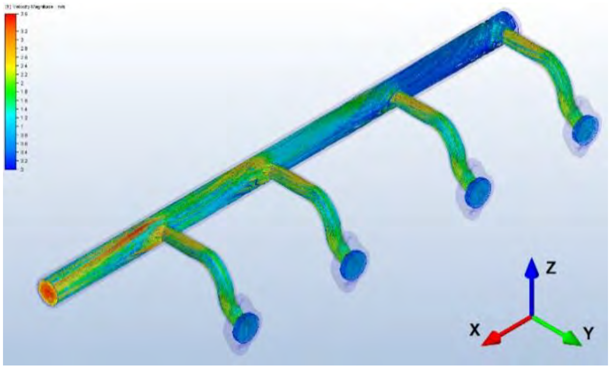

Fig. 12. Coolant trace lines with velocity distribution; mod1-W-0kPa

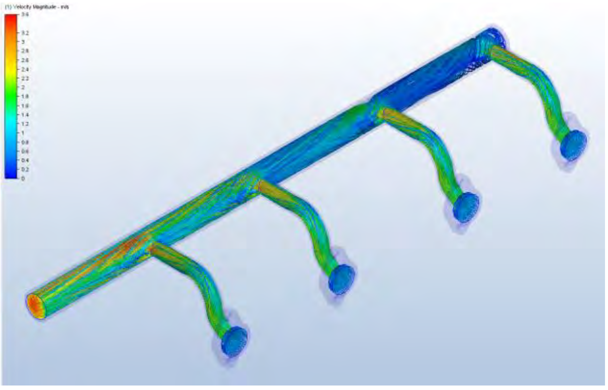

Fig. 13. Coolant trace lines with velocity distribution; mod1-WG-0kPa

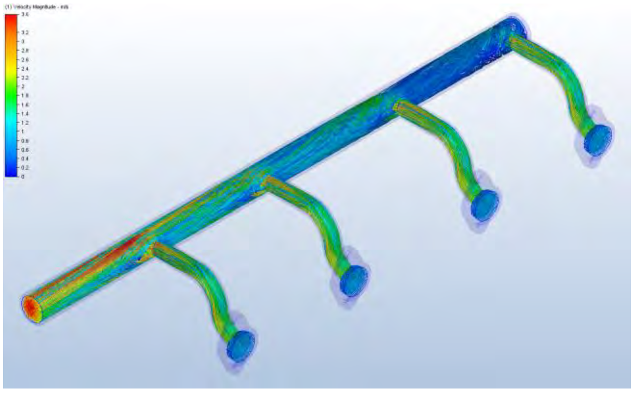

Fig. 14. Coolant trace lines with velocity distribution; mod1-W-80kPa

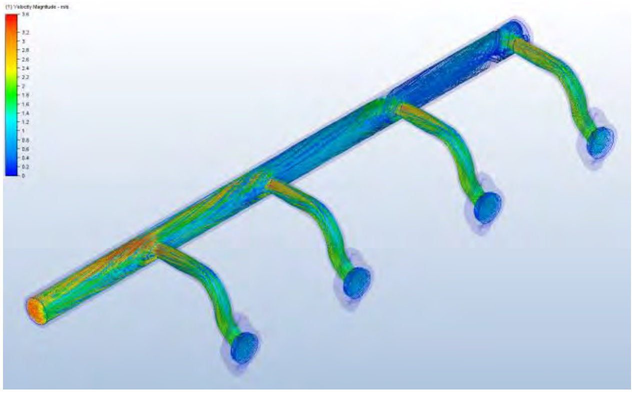

Fig. 15. Coolant trace lines with velocity distribution; mod1-WG-80kPa

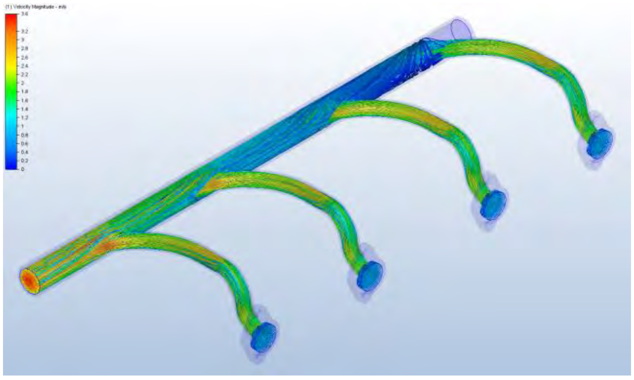

Fig.16. Coolant trace lines with velocity distribution; mod2-W-0kPa

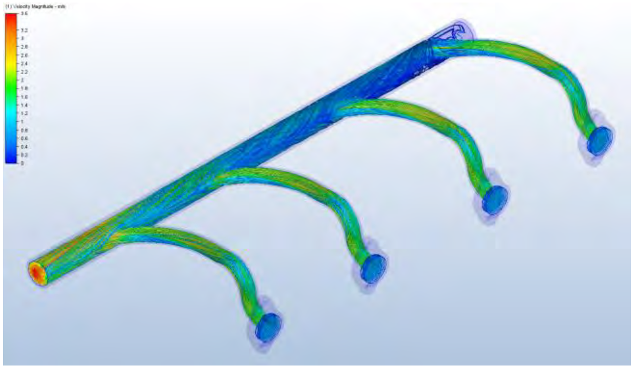

Fig. 17. Coolant trace lines with velocity distribution; mod2-WG-0kPa

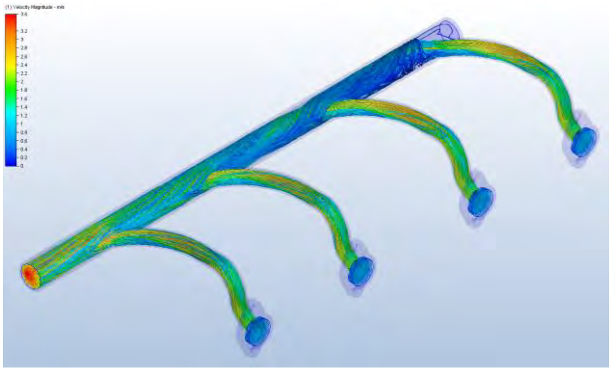

Fig. 18. Coolant trace lines with velocity distribution; mod2-W-80kPa

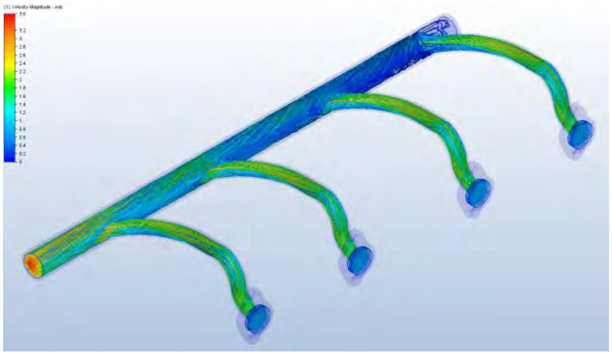

Fig. 19. Coolant trace lines with velocity distribution; mod2-WG-80kPa.

The velocity distribution (Fig. 20) shows that the water flow reaches higher values than that of the water–glycol mixture, and it occurs close to the manifold outlet pipe axis. This dependence is visible for both 0 and 80 kPa back pressure. In addition, in the considered plane (Fig. 20), the water flow at the outlet shows a more uniform velocity profile than that of the mixture of water with ethylene glycol.

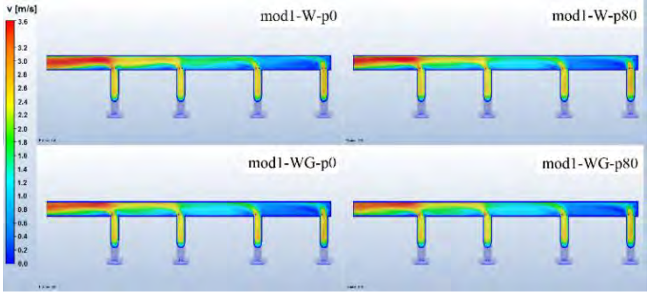

Fig. 20. Distribution of coolant velocity in the mod1 manifold on a plane passing through the axis of the outlet pipe of the manifold and parallel to the XY plane (Fig. 12)

Another undesirable feature of the modified manifolds is the space in which the trace lines are shown in Fig. 21 and 23. This volume is harmful from the point of view of the continuity of the coolant fluid stream. Its existence introduces the risk of local turbulence, which also increases the local flow resistance coefficient. For the mod1 version (Fig. 21), the formation of turbulent flow is slightly dependent on both the type of liquid and the back pressure value.

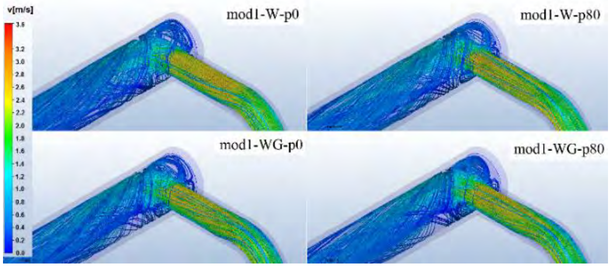

Fig. 21. Comparison of coolant trace lines for mod1

Each inlet channel of the mod1 manifold lies in one plane, which allowed for comparison of velocity distribution in individual sections (Fig. 22).

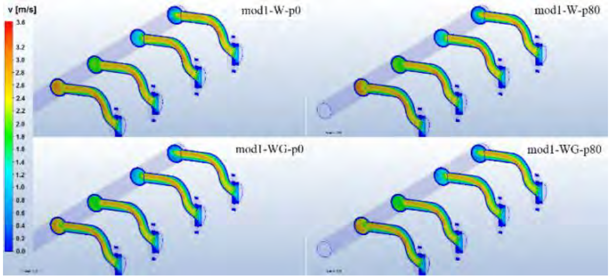

Fig. 22. Coolant velocity distributions in the planes passing through the inlet axes parallel to the YZ plane (Fig. 12); mod1

The considered space for the mod2 manifold causes a visible impact of the type of liquid on the risk of turbulent flow. The results (Fig. 23) show that this risk is greater for a glycol and water mixture than for water alone, both for 0 and 80 kPa back pressure.

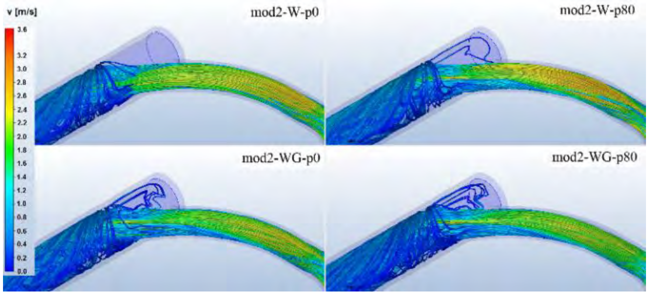

Fig. 23. Comparison of coolant trace lines for mod2

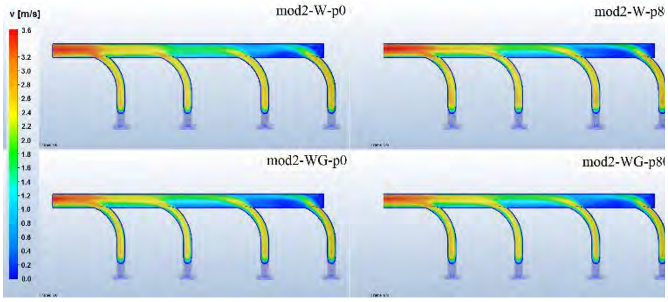

Fig. 24. Distribution of coolant velocity in the mod2 manifold on a plane passing through the axis of the outlet pipe of the manifold and parallel to the XY plane (Fig. 12)

Figures 25 and 26 show that using the mod1 version causes greater differences in velocity in the outlet axis for different simulation conditions than using the mod2 version. The differences reach 15% for water. For a water–glycol mixture, the differences are clearly smaller.

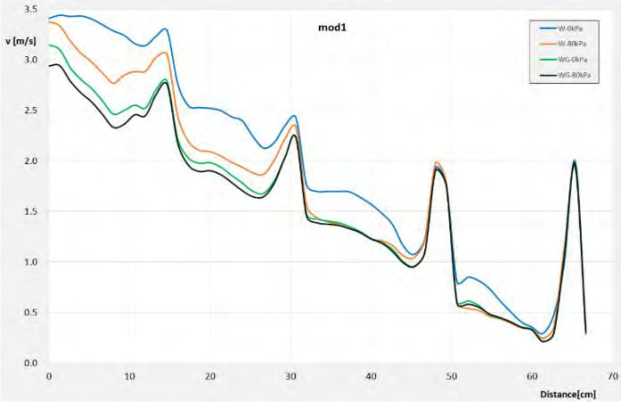

Fig. 25. Coolant velocity for mod1 in the axis shown in Fig. 27

For the mod2 version, the differences in coolant fluid velocity depending on the back pressure are noticeably smaller than for the mod1 version (Fig. 26).

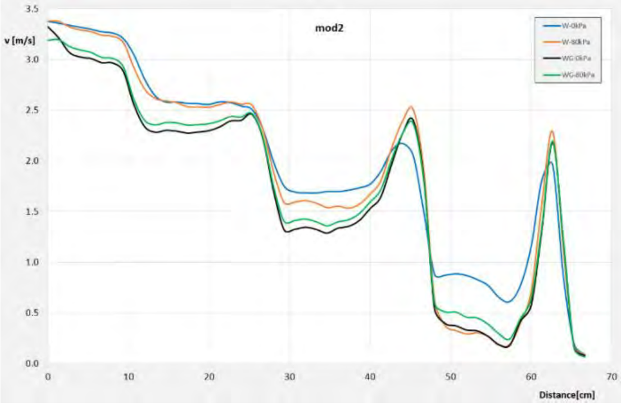

Fig. 26. Coolant velocity for mod2 in the axis shown in Fig. 26

For the mod2 version, the coolant velocity values for the first inlet channels (furthest from the outlet) to the main pipe area have a similar value – about 2.5 m/s. For mod1, the values are significantly different, in the range from 2.0 to 2.5 m/s.

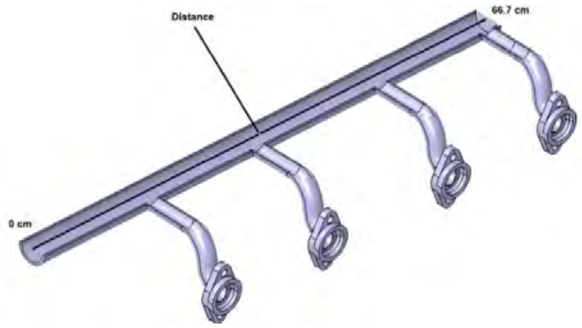

Fig. 27. Explanation of the "Distance" parameter using the example of the mod1 manifold (for charts in Fig. 25 and 26)

Conclusions

An important consideration is the behavior of the coolant streams in regions such as manifold inlet and outlet connectors, channel curvatures, and spaces that do not contribute to flow but are technologically necessary or difficult to eliminate.

During the design of the engine coolant manifold, it is essential to avoid unintended voids that could disrupt the flow.

The mod2 manifold exhibits a more favorable geometry for coolant flow. Its channel shapes help reduce the risk of turbulence. However, alternative geometrical configurations are also worth exploring.

The simulation was conducted for two different fluids and for manifolds with four inlets and one outlet. As a result, the Reynolds number varies significantly: from 17,900 to 72,900 for water, and from 4200 to 18,400 for a water–glycol mixture. Under actual operating conditions, the flow is considered turbulent across this entire range, due to factors inherent to such systems (e.g., uneven channel surface roughness, vibrations).

It is therefore reasonable to conduct further simulations to evaluate:

- the optimal channel curvature
- the effect of temperature on flow behavior
- heat transfer characteristics based on material selection.

Nomenclature

A	cross-sectional area
CFD	computational fluid dynamics
c_w	specific heat of the coolant
modx	name of the coolant manifold in simulation; x – number of manifold version (0 is for factory manifold); 1, 2 – modified versions
modx-W-p0	name of simulation for modx manifold with water flow and 0 kPa back pressure
modx-W-p80	name of simulation for modx manifold with water flow and 80 kPa back pressure
modx-WG-p0	name of simulation for modx manifold with mixture of ethylene glycol and water (50% by volume) flow and 0 kPa back pressure
modx-WG-p80	name of simulation for modx manifold with mixture of ethylene glycol and water (50% by volume), flow and 80 kPa back pressure
$\dot{m}$	mass flow rate, kg/s
Q	heat removed from the engine
ρ	fluid density
R_e	Reynolds number
ΔT_w	temperature differential between the engine coolant inlet and outlet
v	fluid velocity, m/s
VCR	variable compression ratio

Bibliography

[1] Anton Paar GmbH. Automotive antifreeze. https://wiki.anton-paar.com/en/automotive-antifreeze (accessed on 11.05.2025).

[2] Biały M, Pietrykowski K, Tulwin T, Magryta P. CFD numerical simulation of the indirect cooling system of an internal combustion engine. Combustion Engines. 2017; 170(3):8-18. https://doi.org/10.19206/CE-2017-302

[3] Brusiani F, Falfari S, Forte C, Cazzoli G Verziagi P, Ferrari M et al. Definition of a CFD methodology to evaluate the cylinder temperature distribution in two-stroke air cooled engines. Energy Proced. 2015;81:765-774. https://doi.org/10.1016/j.egypro.2015.12.082

[4] Coclite A, Faruoli M, Viggiano A, Caso P, Magi V. Liquid-cooling system of an aircraft compression ignition engine: A CFD analysis. Fluids. 2020;5(2):71. https://doi.org/10.3390/fluids5020071

[5] Ghare PP, Khalane H, Wakhure U, Khobragade T, Chaudhari S, Jahirabadkar A. Improving heat transfer in single cylinder DI engine through optimization of coolant flow distribution. SAE Technical Papers. 2015-01-1663. 2015. https://doi.org/10.4271/2015-01-1663

[6] Güçlüten GE, Tüccar G. Investigation of the effect of changing air flow velocities in electric vehicles on cylinder geometry battery based on computational fluid dynamics (CFD) analysis. Eur J Sci Technol. 2021;24:240-246. https://doi.org/10.31590/ejosat.899811

[7] Hemmatkhanloo R, Mohammadi A, Varmazyar M. Research on modification of cooling passage for a 4-cylinder turbocharged SI engine with precise cooling viewpoint. J Engine Res. 2016;41(Winter):31-39. https://civilica.com/doc/691372/

[8] Jaskiernik M, Buczek K, Walkowiak J. Simulation of the oil supply through the connecting rod to the piston cooling channels in medium speed engines. Combustion Engines. 2020;180(1):25-30. https://doi.org/10.19206/CE-2020-104

[9] Jędrzejowski J. Obliczanie tłokowego silnika spalinowego (in Polish). WNT. Warszawa 1984.

[10] Johansson A, Gunnarsson J. Predicting flow dynamics of an entire engine cooling system using 3D CFD. Master's thesis. Luleå University of Technology. Luleå 2017.

[11] Li A, Yuen ACY, Wang W, Weng J, Yeoh GH. Numerical investigation on the thermal management of lithium-ion battery system and cooling effect optimization. Appl Therm Eng. 2022;215:118966. https://doi.org/10.1016/j.applthermaleng.2022.118966

[12] Li W, Li E, Shi W, Li W, Xu X. Numerical simulation of cavitation performance in engine cooling water pump based on a corrected cavitation model. Processes. 2020;8(3):278. https://doi.org/10.3390/pr8030278

[13] Murakami Y, Kurosaka H, Kamiya H. Practical application of combustion simulation using CFD for small engine of two-wheeled vehicle. SAE Trans J Engines. 2004;113(3): 1732-1740. https://doi.org/10.4271/2004-32-0006

[14] Pietrykowski K, Tulwin T. Aircraft radial engine CFD cooling model. SAE Int J Engines. 2014;8(1):82-88. https://doi.org/10.4271/2014-01-2884

[15] Pradhan S, Kumari K, Barua A, Panicker RV, Singh H, Jeet S. Numerical simulation of heat transfer and design optimization of IC engine fins geometry using finite element analysis. Int J Interact Des Manuf. 2024;18(1):479-491. https://doi.org/10.1007/s12008-023-01602-3

[16] Shingare AP, Totla NB. Simulation of jacket cooling of a liner of four cylinder diesel engine for genset application. Int Eng Res J (IERJ). 2016:1276-1283. https://www.ijfeat.org/issuepage/august16.php

[17] Souza GR de, Pellegrini CC de, Ferreira SL, Soto Pau F, Armas O. Study of intake manifolds of an internal combustion engine: A new geometry based on experimental results and numerical simulations. Therm Sci Eng Prog. 2019;9: 248-258. https://doi.org/10.1016/j.tsep.2018.12.003

[18] Sroka ZJ, Sufe G, Kejela E. Improving heat transfer in an air-cooled engine by redesigning the fins. Combustion Engines. 2024. https://doi.org/10.19206/CE-195440

[19] Stanivuk T, Lalić B, Mikuličić JŽ, Šundov M. Simulation modelling of marine diesel engine cooling system. Trans Marit Sci. 2021;10(1):112-125. https://doi.org/10.7225/toms.v10.n01.008

[20] Takahashi Y, Yoshitsugu G. CFD air flow analysis for air-cooled motorcycle engines. Honda R&D Technical Review. 2018;18(2):140-147.

[21] Tan L, Yuan Y, Huang C. CFD modelling on flow field characteristics of engine cooling water jacket and its cooling performance improvement based on coolant transport path analysis method. Proc Inst Mech Eng A. 2023;237(2):385-401. https://doi.org/10.1177/09576509221116503

[22] Tang GZ, Zhang L, Jiao ZS. Design and improvement of engine cooling water jacket. Neiranji Gongcheng/Chinese Int Combust Eng Eng. 2014;35(4):91-96.

[23] Wajand JA, Wajand JT. Tłokowe silniki spalinowe (in Polish). WNT. Warszawa 2000.

[24] Zheng QP, Zhang HM, Li S. Flow analysis in cooling water jacket of engine based on three dimensional CFD technology. Neiranji Gongcheng/Chinese Int Combust Eng Eng. 2009;30(6).

Mirosław Jakubowski, DEng. – Department of Automotive Vehicles and Transport Engineering, Rzeszow University of Technology, Poland.

e-mail: *mjakubow@prz.edu.pl*

Article citation info:
Aoyagi T, Wakasugi T, Tsuru D, Tashima H. Effects of torch flame strength on the combustion process in medium-speed gas engines through pre-chamber orifice specifications. Combustion Engines. 2025;202(3):44-57. https://doi.org/10.19206/CE-205609

Takahide AOYAGI
Takuya WAKASUGI
Daisuke TSURU
Hiroshi TASHIMA

Combustion Engines
Polish Scientific Society of Combustion Engines

Effects of torch flame strength on the combustion process in medium-speed gas engines through pre-chamber orifice specifications

ARTICLE INFO

Received: 5 January 2025
Revised: 25 May 2025
Accepted: 27 May 2025
Available online: 10 July 2025

Gas engines are eagerly introduced for the moment to reduce GHG emissions from the marine sector, and could be used by green methane from the methanation process in the future. Pre-chamber-type gas engines burning lean premixture in a main chamber are the mainstream in the medium-speed engine range. Although the ejection behaviour of torch flames from the pre-chamber has a significant impact on the combustion in the main chamber, there are few research examples of confirming the effects of the pre-chamber specifications by actual observation of the combustion process. In this study, a constant-volume chamber was prepared to reproduce the combustion chamber near the top dead centre of a medium-speed gas engine, to visualize its whole combustion chamber, and to investigate the effects of the pre-chamber specifications. The validity of the CFD simulation based on the RANS turbulence model and the possibility of a design index for the ejection strength of torch flames were also examined.

Key words: *gas engine*, *pre-chamber*, *torch flame*, *combustion visualization*, *CFD simulation*, *jet intensity*

1. Introduction

Acceleration of global warming justifies the Paris Agreement to achieve the carbon neutrality target by 2050. As for the transportation sectors, radical progresses are being made in the development of electrification [29] and e-fuels [5, 16] to decarbonize prime movers in the field of land transportation, but more generous GHG reduction targets were once set for off-road power sources, such as industrial engines and marine engines, because of their long continuous operating time, and high average engine load, which results in the difficulty in electrification. At IMO/MEPC 80 in 2023 [12], however, it was announced that the marine industry would follow the same path as other sectors to accomplish the carbon neutrality by 2050, and mid-term measures were proposed to reduce GHG emissions by 20% to 30% by 2030 and 70% to 80% by 2040, while its target for the introduction of carbon-free marine fuels such as hydrogen and ammonia, which are essential to achieving the carbon neutrality, was set at a mere 5% to 10% of the fuel share by 2030. For the time being, therefore, it is expected that GHG emission reductions will be promoted by introducing low-speed and medium-speed gas engines with natural gas (NG) fuelled [2], and once the production of hydrogen, the raw material for carbon-free fuels, becomes widespread, it is also promising to continue utilising these gas engines using green methane (e-gas) synthesized through methanation [24].

Unlike low-speed marine gas engines, which operate in a two-stroke cycle with premixed or diffusion combustion mode and can be tolerated with modest mean effective pressure [8, 13], a lean-burn premixed combustion gas engine (LBGE, hereafter) has become mainstream [17] in the field of medium-speed range thanks to its less fuel gas compression work, better thermal efficiency by a high degree of constant-volume [15], and lower NO_x emissions. Nevertheless, medium-speed LBGEs' combustion chamber of c.a. 200 mm or more in bore exceeds the knock limit bore (≤ ~∅100 mm) of gasoline-fuelled SI engines and forces them to operate within a narrow range of air-to-fuel ratio (AFR) between the knock limit at richer AFR and the misfire limit at leaner AFR [23]. So, avoiding pre-ignition and knocking at higher engine loads, and misfiring at lower loads, has been the major challenge for LBGEs [18, 25, 28]. In addition, regardless of engine loads, excessive cycle-to-cycle variation and unburned fuel emissions are also worrying problems of LBGEs [9, 10].

After all, it is essential to enhance the ignition energy for the premixture in the combustion chamber of medium-speed LBGEs. Two ignition methods are the mainstream for that purpose. One is a spray flame by direct pilot injection of diesel fuel as seen in so-called "dual-fuel" engines [11], and the other is torch flames ejected through the orifices of a pre-combustion chamber (abbreviated as pre-chamber or PC in the study) mounted in the upper centre of the main combustion chamber (MC). The PC-type ignition is preferred for medium-speed LBGEs because it allows the usage of an ignition plug in the PC to realise mono-fuel operation and to be free from NO_x and soot emissions derived from diesel sprays [1]. More specifically, the PC with a dedicated supply path for fuel gas is called an Active PC (APC), and the one without the path is a passive PC. The former has a larger PC volume, realizes the mixture stratification from PC to MC, and strengthens the ignition potential and penetration of the torch flame. The APC is used exclusively for medium-speed LBGEs with a bore of over 200 mm, which requires higher ignition energy. In the APC, many factors such as the ignition energy, the PC volume, and the number and diameter of the orifice openings may affect the ejection behaviour of the torch flame, but these effects have not been clarified quantitatively enough because of a lack of full observations of in-cylinder phenomena of gas engines.

In the previous study [3], using a constant-volume chamber (CVC) that simulated a combustion chamber geometry near the top dead centre of an APC-type medium-speed LBGE, the authors visualized the ejection process of torch flames in detail and investigated the effects of the orifice specifications on the penetration and spreading angle of the torch flames. It was also shown that the measured results could be reasonably simulated by a 3D-CFD code implemented with a RANS-type turbulence model [22] and a detailed reaction scheme for methane [4]. All the experiments, however, were executed under incombustible MC gas conditions by filling the MC with pure nitrogen since the study focused on the correlation between the PC orifice specifications and the ejection behaviour of the torch flame. So, it is necessary to continue a comparative investigation both experimentally and numerically under combustible MC gas conditions by filling it with CH_4/air premixture to evaluate the effects of the torch flame ejection on the combustion process in the MC.

Considering many experimental and numerical results have accumulated for various types of medium-speed LBGEs [6, 7, 20, 21], it may be worth proposing a practical design index that estimates the ejection strength of the torch flames based on the PC specifications when designing the combustion chamber of an APC-type medium-speed LBGE.

An index for the ejection strength of the torch flame, so-called "jet intensity", has already been proposed for an APC-type small high-speed gas engine [19], but other than the engine dimensions and speeds, there are non-ignorable differences between APC-type medium-speed LBGEs and the relevant high-speed gas engine. Its fuel injector is located only in the PC instead of the separate fuel supply lines to both chambers, its ignition plug is located near the bottom of the PC instead of near the top of the PC, and so on. So, careful consideration is necessary before applying such an index.

Generally, the correlation between the torch flame ejection intensity and the pre-chamber specifications has not been fully clarified, especially for larger medium- or low-speed LBGEs. The reason can be that almost no studies have been made that have hierarchically classified the factors that can cause the problems of pre-chamber-type gas engines and investigated the true causes step by step. For example, possible causes of excessive cycle-to-cycle fluctuations include variations in the combustion speed due to excessive stretch of the lean premixed flame by the torch flame, excessive turbulence intensity of the pre-chamber flow excited by direct fuel injection and the inflow flux during the compression stroke, and asymmetry of the pre-chamber flow due to the eccentricity of the swirling flow in the main chamber and the above-mentioned complex flux in the pre-chamber. However, since these factors are combined in an actual engine, it is extremely difficult to identify the true cause. Therefore, it is important to first visualize the ejection behaviour of the torch flame in the entire combustion chamber under rather static conditions where there is no inflow flux due to compression or in-cylinder flow in the main chamber, and to understand the influence of the pre-chamber specifications and the presence or absence of cycle-to-cycle fluctuations.

In this study, from the above perspective, the correlation between the ejection behaviour of the torch flames and the combustion process in the MC was investigated both experimentally and numerically in the same manner as the previous study by filling the MC of the CVC with a CH_4/air premixture. The validity of the jet intensity index was examined by the observed ejection behaviours of the torch flame under comparative conditions with an APC-type medium-speed gas engine based on the PC orifice specifications.

2. Experimental and numerical procedures

2.1. Experimental apparatuses and procedures

Figure 1 and Table 1 show the central cross-section and main specifications of the constant-volume chamber (CVC) used in the study. It is the same as the one used in the authors' previous study [3], so its features are briefly summarised here. The CVC consists of a simple pancake-shaped main combustion chamber (MC) with a bore of ∅240 mm and a height of 30 mm. A pre-combustion chamber (PC) is mounted on the central axis of the CVC's top lid and protrudes to about half the height of the MC. The PC with orifices near its bottom houses an ignition plug and a high-pressure gas injection valve around its top. The configuration well reproduces the clearance volume of a medium-speed LBGE. The PC geometries, such as orifice diameter and the number of orifices, can be changed by replacing a PC tip part attached to the bottom of the PC. The details of the tested PC geometries will be explained later.

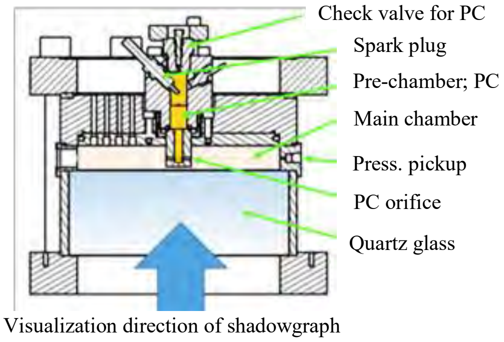

Fig. 1. Cross-sectional views of the CVC

Table 1. Main specifications of CVC

Main chamber (MC): $D_{MC} \times H_{MC}$	∅240 mm × 30 mm
Pre-chamber (PC): $D_{PC} \times H_{PC}$	∅20 mm × 65 mm (upper part of PC)
Optical window: $D_W \times H_W$	∅260 mm × 100 mm Fused quartz glass
Max. in-chamber press.	10 MPa
Ignition device in PC	Spark plug
Mixture supply system	PC and MC separated
Primary for artificial air	$O_2 + N_2$
Secondary for fuel gas	CH_4

Figure 2 shows a system diagram for blending and supplying the premixture for the MC and the PC of the CVC. Both chambers are independently controlled to simulate an

Active PC type (APC-type) medium-speed LBGE. The system consists of primary mixer tanks blending artificial air from pure O_2 and N_2, secondary mixer tanks adding methane (CH_4) to the artificial air to prepare a premixture of CH_4/air, and sets of a solenoid valve and a pressure regulator with a built-in pressure sensor before and after the tanks. The exit of the secondary mixer tank for the PC is connected to the high-pressure gas injection valve to realize the APC-type fuel supply, while the exit of the secondary mixer tank for the MC is connected to the MC directly through a set of solenoid valves and a pressure regulator. An exhaust/vacuum line is also connected to the MC to scavenge the burned gas into a sample bag for emission analysis and to evacuate the whole system for the next experiment. The experimental procedure is as follows. First, two combustion chambers, mixer tanks, and all connection pipes are evacuated. Second, the MC and PC are filled with the component gases up to the specified partial pressure. Third, a thyristor shuts off the current to an ignition coil, and spark ignition happens in the upper part of the PC. At last, after the combustion ends, the burned gas in the CVC is collected into a sample bag for emission analysis. A CPU electronically controls all the solenoid valves and pressure regulators with a specified time sequence. Each pressure regulator is optimized for pressure control accuracy according to the control range.

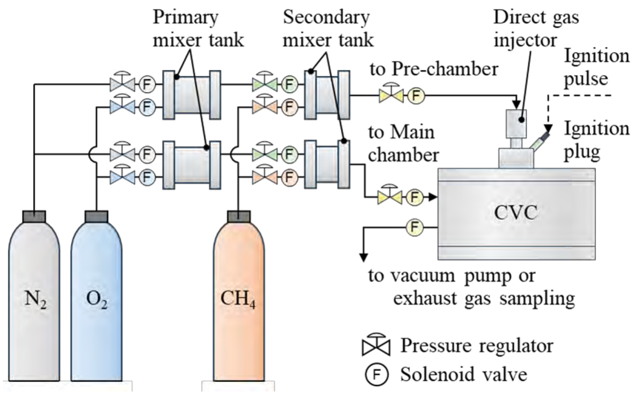

Fig. 2. System diagram for blending and supplying the premixture for the main chamber and the pre-chamber of the CVC

2.2. CFD sub-models and mesh setup

The 3D-CFD simulation by CONVERGE in the previous study by the authors [3] is continuously applied to reproduce the combustion phenomena in the CVC that simulated a chamber geometry of a PC-type medium-speed LBGE. A RANS turbulence scheme based on the RNG k-ε turbulence model is adopted to save computational load and time, considering the larger scale of medium-speed LBGEs and the practical CFD usage in the design phase. As for the combustion-related reactions, the SAGE detailed chemical kinetics solver by Senecal [22] is activated only in cells that pass threshold levels of temperature and HC mole fraction specified in CONVERGE. The multizone chemistry model by Babajimopoulos [4] was used to expedite the detailed chemistry calculations. The reaction mechanism is the reduced version of GRI-Mech1.2 by Kazakov [14] with an enhanced Zeldvich mechanism embedded and consists of 26 species and 107 reactions for methane. The spark ignition in the PC was numerically substituted by the energy source model. The jets of the unburned PC mixture were identified by setting the boundary concentration of marker PC gas to 1.0 mass%, and the torch flames, including the ignited MC mixture, were identified by setting the boundary cell temperature to 350 K or higher.

The meshing strategy was kept the same as the previous study [3], such as the usage of a rectangular Cartesian coordinate instead of a cylindrical coordinate concerning the constraint of axisymmetric alignment due to the central axis setting, but a finer mesh than the previous one was supposed to be necessary for better prediction of the ignition process of the MC premixture by the torch flame and the following flame propagation. The size and the number of the cells were changed as follows. The initial grid interval in the PC volume was halved from 1.0 mm to 0.5 mm. This reduction scheme was the same for a volume of a truncated-cone shape attached to the exit of orifices with a minimum diameter of about 8 mm and with a spread angle of about 30 degrees, while the grid interval in the PC orifices was reduced from 0.5 mm to 0.25 mm. The total number of cells is initially set to c.a. 1.0 million, about 4 times what it was in the previous study. As before, the Adaptive Mesh Refinement (AMR) was activated based on the local gradient in temperature and velocity between the cells, but the minimum grid interval was reduced from 0.5 mm to 0.25 mm and the maximum number of cells was increased from 1.5 million to 20 million, although both parameters were autonomously adjusted by the AMR. All the wall temperatures of the combustion chambers were set to 290 K. The heat loss to the wall surfaces was predicted by the turbulent heat transfer model using the boundary layer treatment based on the nondimensional distance y+ and the turbulent kinetic energy. For a better understanding of the calculation results, preceding jets of unburned PC mixture and following torch flames should be distinguished from the charge gas or the mixture in the MC. As before, the gas components originating from the PC mixture were identified as marker gases.

3. Experimental conditions

Table 2 lists the experimental conditions for both combustion tests and numerical simulations. Setups for photographing the combustion phenomena in the MC are included in the lower lines of the table.

Table 2. Experimental conditions

PC initial charge gas	CH_4/air premixture, $\lambda_{PC} = 1.0$
MC initial charge gas	Pure nitrogen ($\lambda_{MC} = 0/0$) Artificial air ($\lambda_{MC} = \infty$) CH_4/air premixture ($\lambda_{MC} = 1.7$)
Charged gas state	1.0 MPa, 290 K
PC geometry	PC1~PC5 on Table 3
Ignition device	Ignition plug in PC
Frame rate	20,000 fps
Resolution	1024×1024 pixels
Exposure time	10.0 μs

Table 3. Main specifications of the tested PC geometries

PC geometry	Orifice specifications					Throat diameter D_t [mm]	Chamber volume ratio V_{PC}/V_{MC} [%]
	Diameter Do [mm]	Length Lo [mm]	Aspect ratio L_o/D_o [-]	Number of holes N_o [-]	Total opening area A_o [cm^2]		
PC1	∅3.5	7.5	2.14	8	0.770	∅15	2.3
PC2	∅4.0	7.5	1.86	6	0.754	∅15	2.3
PC3	∅3.1	7.5	2.42	10	0.755	∅15	2.3
PC4	∅2.5	7.5	3.00	8	0.393	∅15	2.3
PC5	∅5.0	7.5	1.50	8	1.571	∅15	2.3

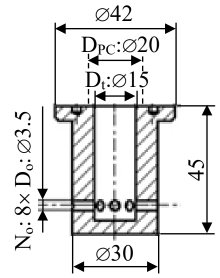

Fig. 3. Cross-sectional view of reference PC geometry (PC1)

Following the typical mixture formation in actual APC-type LBGEs, the PC was always filled with a stoichiometric ($\lambda_{PC} = 1.0$) CH_4/air mixture to secure stable ignition in the PC and to enhance torch flames, while MC gas conditions changed by the experimental requirements. In the previous study [3], the MC had been filled with pure nitrogen ($\lambda_{MC} = 0/0$) by shutting off a solenoid valve for supplying oxygen to the primary mixer tank and a corresponding valve for CH_4 to the secondary mixer tank. In the case of the combustible MC gas conditions, a CH_4/air mixture of an equivalence ratio; $\lambda_{MC} = 1.7$ was blended in the secondary mixer tank. Additionally, the artificial air was tried out as an MC charge gas to examine the effects of the continuation of the combustion reactions of the torch flame with a reference PC Since the detailed investigation had been already done under incombustible MC gas conditions, only the PC geometries for changing the number of orifices and the orifice diameter were selected in this study.

Table 3 summarizes the specifications of tested PC geometries identified as PC1~PC5. PC1 was selected as a reference PC geometry, in which the orifice diameter; D_o is ∅3.5 mm, and the number of orifices; N_o is set to 8.

Figure 3 shows a cross-sectional view of the reference PC (PC1). All the orifices of the PCs are horizontally bored to make it easy to measure the penetration and spread cone angle of the torch flame from the visualized flame images. PC2 and PC3 have N_o of 6 and 10, respectively, and their D_o is determined so that the total orifice opening area is almost the same as that of PC1. For PC4 and PC5, N_o is set constant at 8 and D_o is set to ∅2.5 mm and ∅5.0 mm, respectively.

4. Results and discussion

4.1. Comparison of torch flame developments in various MC in-chamber gas

Although already detailed in [27], it would be better to briefly mention the effects of the MC in-chamber gas's reactivity on the torch flame's development process.

Figure 4 compares the temporal changes in averaged L_f and θ_f of torch flames from the standard PC (PC1) by changing the MC in-chamber gas from nitrogen ($\lambda_{MC} = 0/0$) through air ($\lambda_{MC} = \infty$) to a premixture ($\lambda_{MC} = 1.7$). For reference, observation results of L_f under $\lambda_{MC} = 0/0$ conditions were well approximated to a steady gas jet regardless of the nozzle orifice specifications because it showed the relation of $L_f \propto t^{0.5}$ with time; t on the ASOE basis.

As shown in the figure, L_f was almost the same for $\lambda_{MC} = \infty$ and $\lambda_{MC} = 1.7$ except for the developing stage of the torch flame, and L_f for $\lambda_{MC} = 0/0$ was shorter than for other in-chamber gases. This suggests that the MC in-chamber gas was entrained into the torch flame immediately after the preceding unburned PC mixture jets out, that the increase in L_f was caused by the flame advance to the preceding tip unburned PC mixture [26], and that $\lambda_{MC} = \infty$ needed a longer time than $\lambda_{MC} = 1.7$ for the unburned premixture to ignite and merge with the torch flame. In addition, $\dot{L}_f$ at $\lambda_{MC} = 1.7$ was the highest at the start of the torch flame ejection, but it slowed down sharply as the flame developed and became the lowest near 10 ms ASOE.

θ_f was almost constant at around 20 deg. at $\lambda_{MC} = 0/0$ and $\lambda_{MC} = \infty$, whereas θ_f at $\lambda_{MC} = 1.7$ was consistently larger than other λ_{MC} conditions and increased with time, reaching 30 deg. at 10 ms ASOE. This indicates that the flame propagation in the main chamber occurs mainly in the spreading direction, not in the injection direction.

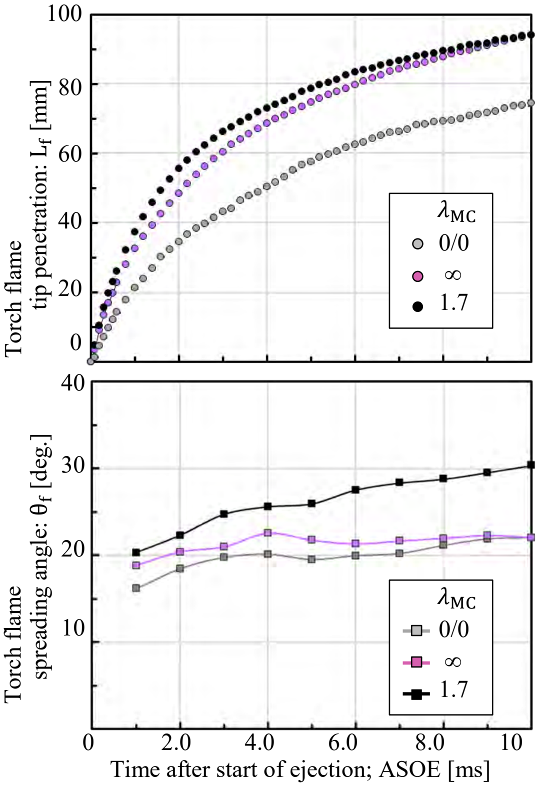

Fig. 4. Effects of the reactivity of the in-chamber gas of the MC on torch flame penetration: L_f (upper half) and its spreading angle: θ_f (lower half) by PC1 with $N_o = 8$ and $D_o = ∅3.5$ mm

Figure 5 exemplifies the shadowgraph images of the torch flame under the three MC in-chamber gas conditions at 4, 8, and 12 ms ASOE. Reflecting that the MC premixture was entrained in the torch jet and the flame propagation started into the unburned MC premixture, the difference in brightness between the burning region and the background of the shadowgraph was the largest at $\lambda_{MC} = 1.7$ of the three since the torch flame temperature was the highest in the area.

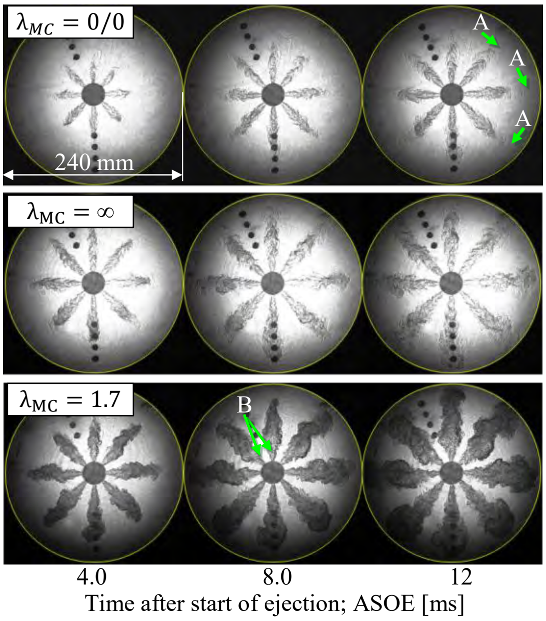

Fig. 5. Ejection behaviours of torch flames under different MC in-chamber gas conditions; $\lambda_{MC} = 0/0$: N_2 (top), $\lambda_{MC} = \infty$: air (middle), and $\lambda_{MC} = 1.7$: premixture of CH_4/air (bottom) with reference PC1 ($N_o = 8$, $D_o = \varnothing 3.5$ mm)

On the other hand, the difference was roughly negligible in $\lambda_{MC} = \infty$ and $\lambda_{MC} = 0/0$. It is inferred L_f at $\lambda_{MC} = 0/0$ was shortened by the ignition difficulty of the preceding pre-mixture jet originating from the PC that was indicated by the arrow "A"s in the figure. When the flame enhancement mentioned above, after τ_f reached the tip of the PC-originating jet, which included the preceding unburned PC mixture, the entire torch flame transitioned to a spindle-shaped or snake-head profile. It can also be seen that L_f at $\lambda_{MC} = 1.7$ was equivalent to that at $\lambda_{MC} = \infty$, but flame propagation to the MC premixture mainly progressed in the direction of increasing θ_f. In other words, the earlier combustion in the MC of the CVC, where the mixing and combustion promotion effects of in-chamber flow cannot be expected, is not a pure flame propagation from torch flame as an ignition source, but rather the entrainment and ignition of the premixed air-fuel mixture in the MC by the torch flame proceeds in parallel. Furthermore, as shown by the arrow "B", it can be noted that L_{fi} of 10~15 mm from the orifice exit was observed in the case of $\lambda_{MC} = 1.7$.

Figure 6 shows the prediction results of the progression of the preceding PC premixture and the following torch flame in the MC during 1~10 ms ASOE under two MC in-chamber gas conditions: $\lambda_{MC} = 0/0$ and $\lambda_{MC} = 1.7$. The unburned premixture from PC is painted in yellow, and the burning region in red. The tip penetration of the PC premixture was roughly the same in both conditions, but L_f at $\lambda_{MC} = 1.7$ was consistently longer than L_f at $\lambda_{MC} = 0/0$ from 1 ms ASOE, that is, immediately after the ejection start of the torch flame. The torch flame at $\lambda_{MC} = 1.7$ then quickly advanced to the tip of the PC-originating mixture, and θ_f also rapidly expanded, as shown in the figure. Although neither τ_{fi} nor L_{fi} was predicted by the simulation, it can be said that many of the considerations based on the observation results were well supported by the CFD, and L_f and θ_f in a combustible MC in-chamber gas were favourably reproduced just as a non-combustible MC in-chamber gas condition.

4.2. Effects of the number of PC orifices

The number of PC orifices: N_o is an important design factor related to the spatial distribution and total surface area of torch flames. PCs of $N_o = 6$ (PC2), $N_o = 8$ (PC1), and $N_o = 10$ (PC3) were selected to investigate the effects of N_o. Each PC geometry has a common V_{PC} and L_o, and its own D_o adjusted to have almost the same A_o. The orifice aspect ratio changes from 1.86 (PC2) through 2.14 (PC1) to 2.42 (PC3). In general, smaller N_o gives larger ejection momentum pre torch flame and longer L_f. The measurement results at $\lambda_{MC} = 0/0$ in the previous study by the authors [3] were consistent with the tendency.

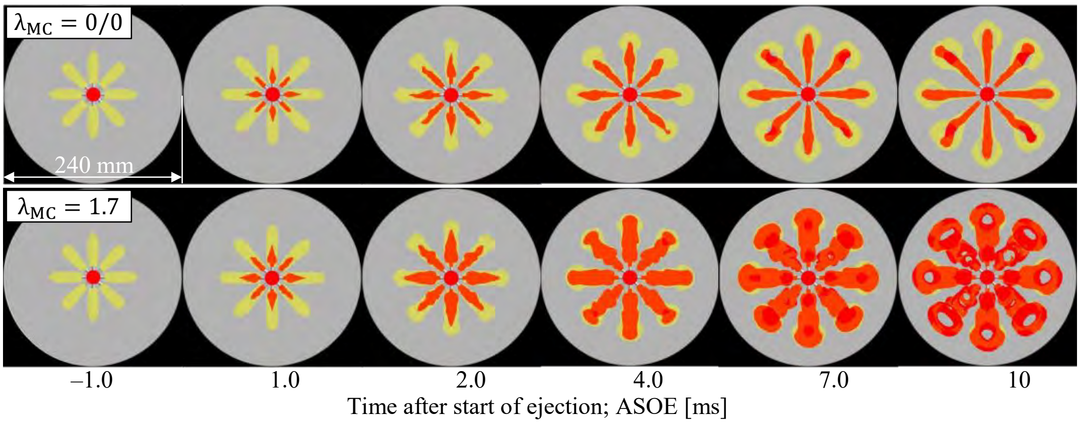

Fig. 6. Effects of MC in-chamber gas on developing process of PC-origin proceeding unburned gas jets and torch flame with reference PC1 ($N_o = 8$, $D_o = \varnothing 3.5$ mm) with $\lambda_{MC} = 0/0$ (N_2, upper row) and $\lambda_{MC} = 1.7$ (premixture of CH_4/air, lower row). Unburned premixture originating from PC painted in yellow and burning region painted in red

Figure 7 shows the temporal changes of L_f and θ_f observed in the tested PCs adding the corresponding changes for PC1 at $\lambda_{MC} = 0/0$ for comparison. The above-mentioned tendency of L_f versus $N_o$was confirmed again at $\lambda_{MC} = 1.7$. As pointed out in the previous section, $\dot{L}_f$ at the early ejection stage up to 2 ms ASOE was much higher at $\lambda_{MC} = 1.7$ than at $\lambda_{MC} = 0/0$. Still, it can be pointed out that $\dot{L}_f$ rapidly reduced in the later ejection stage around 10 ms ASOE and the effect of N_{ori} became relatively small when considering L_f at $N_o = 8$ and $N_o = 10$ are almost equal, and L_f at $N_o = 6$ slowed down to near stagnation in the later ejection stage. These can be recognized as the differences from the $\lambda_{MC} = 0/0$ case.

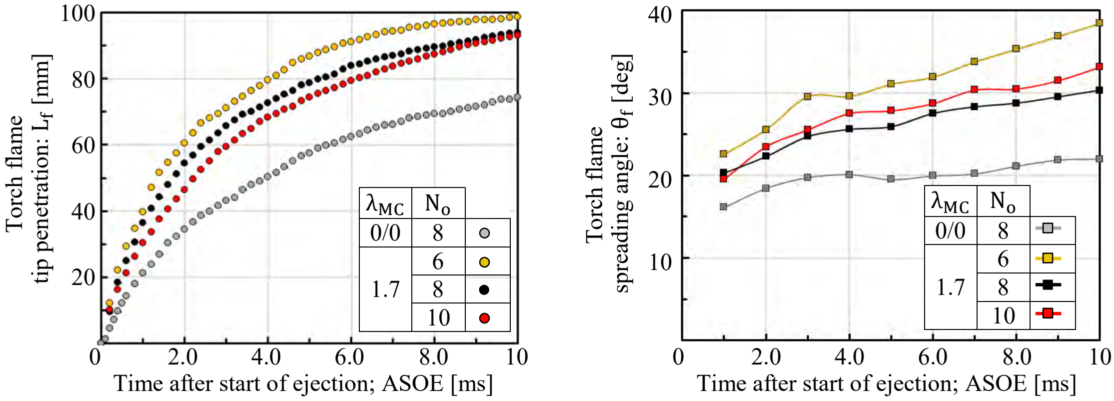

Fig. 7. Effects of number of PC orifices; N_o on torch flame penetration: L_f and its spreading angle: θ_f by PC2 ($N_o = 6$, $D_o = \varnothing 4.0$ mm), PC1 (8, ∅3.5 mm), and PC3 (10, ∅3.1 mm) respectively with ca. same A_o

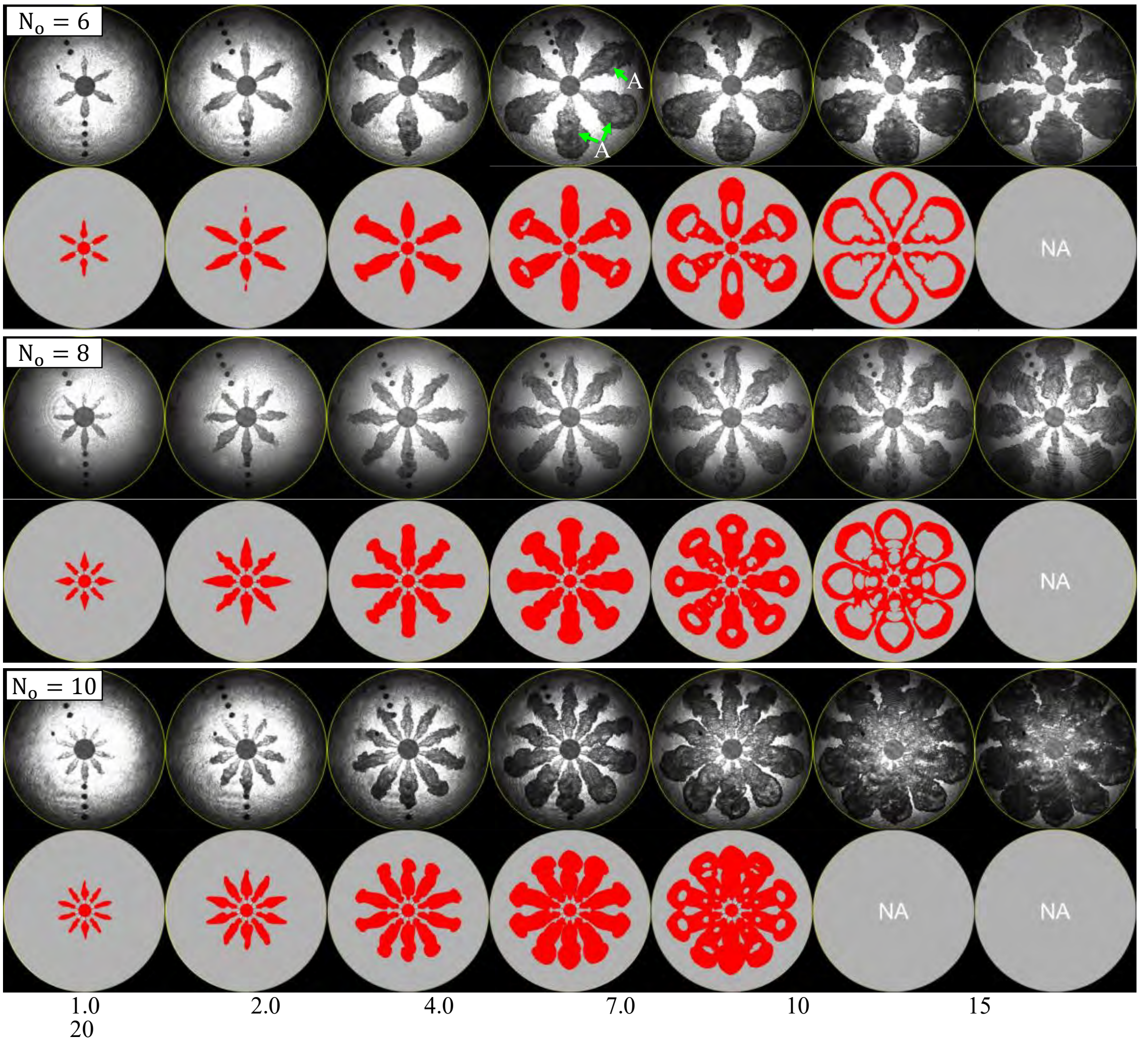

Fig. 8. Effects of the number of PC orifices; N_o on ejection behaviour of torch flame by PC2 ($N_o = 6$, $D_o = \varnothing 4.0$ mm), PC1 (8, ∅3.5 mm), and PC3 (10, ∅3.1 mm) respectively, with ca. same A_o. Shadowgraph images (upper row of each island) and simulation results (lower row of each island)

On the other hand, the measurement results for θ_f at $\lambda_{MC} = 1.7$ condition were rather different from those at $\lambda_{MC} = 0/0$. At $\lambda_{MC} = 0/0$, the correlation with N_o and the elapsed time in ASOE was weak, and it was found that θ_f was almost constant over time at around 20 degrees regardless of N_o. However, θ_f at $\lambda_{MC} = 1.7$ showed a monotonic increase over time in all N_o cases, and the differences among the tested N_o were more evident. Specifically, the torch flame expanded most rapidly in $\pm\theta_f$ direction in the $N_o = 6$ case, and except for just after the ejection start. θ_f at $N_o = 10$, where the torch flame momentum per PC orifice was the smallest of the three PCs, was slightly wider than θ_f at all N_o cases. In addition, it can be noted that the increase in θ_f at all N_o cases temporarily slowed down after 4 ms ASOE, and then it tended to increase again. This may mean that the torch flame expanded enough to contact the upper and lower walls of the MC as described below.

Figure 8 compares the shadowgraph images of torch flames with the predicted ones for the three N_o settings. To consider the correlation with the heat release process, the display period is set to 1~20 ms ASOE. In most of the prediction results after 15 ms ASOE, however, the flame image was not available because of the discontinuity of the isothermal surface of 350 K. The considerations of the shadowgraph images can be summarized as follows.

As a general trend, τ_{fi} was about 1~2 ms regardless of N_o, but τ_{fi} of each torch flame captured in a certain shadowgraph image at 1 ms ASOE indicated τ_{fi} variated among the torch flames. The unburned MC premixture between the torch flames seemed hard to burn up at any N_o even in the later combustion stage in the MC. As in the images at least after 10ms ASOE, when the tip of the torch flame came into contact with the upper and lower MC walls and flattened out, the apparent θ_f became overestimated.

The influence is stronger at $N_o = 6$, where the volume of the torch flame alone was the largest of the three cases, and there were flame images in which the original torch flame could be distinguished inside the flattened flame near the wall (arrow "A"s). By excluding this apparent expansion of θ_f, a smaller number of orifices such as $N_o = 6$ can increase both L_f and θ_f, but the total contact area between the MC premixture and the torch flames does not grow because of the limitation of the flame growth in $\pm\theta_f$ direction, while with a bigger number of orifices such as $N_o = 10$, the surface area of the torch flame can increase, but a decrease in the penetrating momentum of each flame presumably offsets this merit. Furthermore, at $N_o = 10$, the torch flames from the orifices in the upper half of the shadowgraph image had shorter τ_{fi} by about 1 ms than the orifices in the lower half, and in the downstream of L_{fi}, the torch flames made the immediate and discontinuous transition to the expanding flame profile. This is thought to be the reason why θ_f at $N_o = 10$ was evaluated to be larger than that at $N_o = 8$. Torch flames with shorter τ_{fi} at $N_o = 10$ also lost their penetrating momentum more quickly, and they did not seem to reach the inner sidewall of the MC and resulted in very slow flame propagation to the end gas zone of the MC.

In the CFD prediction, it should be pointed out that L_f is slightly underestimated, τ_{fi} and L_{fi} cannot be reproduced, so the torch flame expanded immediately after ejection from the PC, and the asymmetric flame development due to the rectangular mesh is particularly noticeable in the case of $N_o = 6$. However, the above-described effects of N_o on the ejection behaviour of the torch flame and the subsequent combustion process are qualitatively reproduced including the flame interconnection in the downstream of L_{fi} at $N_o = 10$. In addition, by the 10 ms ASOE, the holes in the background colour appeared around the flame tip in all N_o cases. This is because the torch flames being in contact with the upper and lower walls of the MC were cooled down and the isothermal surface of the burning area became discontinuous. It supports the wall contact and flattening of the torch flame described above.

Figure 9 shows the temporal change of the rate of heat release (ROHR) for the three N_o settings. The black curves are the estimated ROHRs based on the measured in-chamber pressure, and the red curves are the calculated ones based on the numerically predicted in-chamber pressure.

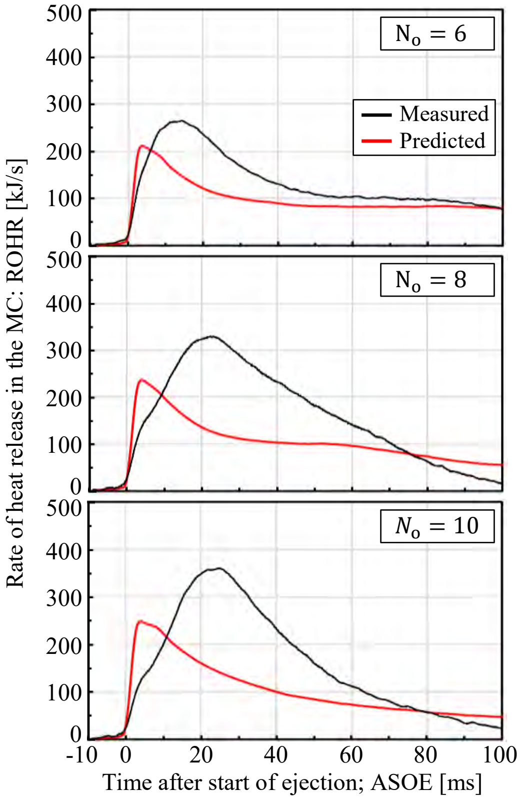

Fig. 9. Effects of the number of PC orifices; N_o on ROHR in the MC by PC2 ($N_o = 6$, $D_o = \varnothing 4.0$ mm), PC1 (8, ∅3.5 mm), and PC3 (10, ∅3.1 mm) respectively, with ca. same A_o. Measured ROHRs (black curves), and simulated ROHRs (red curves)

First, considering the measured ROHR under the condition of near constant A_o, it can be said that the effects of N_o on the heat release process in the MC was relatively small, and similar ROHR curves derived in all cases. When N_o increased from 6 to 10, the maximum value of the heat release rate increased from 270 kJ/s to around 360 kJ/s, and τ_{HRmax} was delayed from 15 ms ASOE to around 25 ms ASOE. Additionally, there was an inflection point in each

ROHR curve around 5 ms ASOE regardless of $\mathrm{N_o}$, which means the combustion in the MC may temporarily stagnate in the process of flame development. The smaller the number of orifices was, the higher the ROHR around 5 ms ASOE and the steeper the gradient of the ROHR were.

All in all, with a small number of nozzle holes, the increased penetrating momentum per torch flame can promote the early stage of the combustion in the MC, but the effect is not enough to compensate for the decrease in flame surface area and the enlargement of the gap between the torch flames from middle to late stage of the combustion in the MC. With a large number of nozzle holes, on the other hand, early-stage heat release in the MC slows down because of the slow ejection speed of torch flames, but the following heat release can be partially ensured thanks to an increase of the flame sur-face and a decrease of the gap between the torch flames. However, the penetrating momentum per torch flame seems crucial especially for the late stage of the combustion because the unburned premixture in the end gas zone needs a forcing ignition source to burn up fast instead of the slower flame propagation of the leaner CH_4-air mixture.

Next, comparing the predicted ROHRs with the measured ones, the tendency was consistent for the maximum ROHR to be proportional to $\mathrm{N_o}$, but the large discrepancy should be noted because the maximum value itself was significantly lower than the measured one and $\mathrm{t_{max}}$ advanced to about 4 ms ASOE. As for the total heat release, some trial calculations were executed up to several hundred milliseconds on ASOE, and the total amount of the predicted heat release was ensured to be almost equal to the accumulation of the measured values. The discrepancy may be due to the lack of implementation of appropriate submodels to reflect the effects of turbulent mixing of the torch flame and the MC premixture that can cause the quench of flame kernels and the resulting extension of $\mathrm{\tau_{fi}}$. Moreover, there was a lack of reproducibility of the instantaneous cooling loss around the torch flame including the inner wall of the orifice.

4.3. Effects of diameter of PC orifices

From the results of the previous section, it seems to be important for a large-scaled engine such as APC-type LBGEs, to secure the proper range of $\mathrm{N_o}$ so that the gap between adjacent torch flames is neither too broad to propagate nor too narrow to entrain the premixture, and the penetrating momentum of the torch flame to reach the torch flame to the end gas zone of the MC for rapid combustion completion.

In the section, three PCs having $\mathrm{N_o}(= 8)$ and $\mathrm{V_{PC}}$ in common, but different $\mathrm{D_o}$ were tested. Combinations of the PC geometry and $\mathrm{D_o}$ were PC4 ($\mathrm{D_o} = \varnothing 2.5$ mm), PC1 ($\varnothing 3.5$ mm), and PC5 ($\varnothing 5.0$ mm), respectively. The $\mathrm{A_o}$ ratio of PC4: PC1: PC5 was approximately 1:2:4 and the $\mathrm{L_o/D_o}$ ratio, which was found to have a positive correlation with the torch flame directionality at $\lambda_{\mathrm{MC}} = 0/0$, was set to 3.0, 2.14, and 1.5, respectively. The display range of the figures is the same as in the previous section unless otherwise specified.

Figure 10 shows the temporal changes in $\mathrm{L_f}$ and $\mathrm{\theta_f}$ for the tested PCs including those for PC1 at $\lambda_{\mathrm{MC}} = 0/0$. The previous measurements with the same PCs at $\lambda_{\mathrm{MC}} = 0/0$ showed that the smaller $\mathrm{D_o}$ was, the longer $\mathrm{L_f}$ and the narrower $\mathrm{\theta_f}$ were. The similar trend existed at $\lambda_{\mathrm{MC}} = 1.7$ in the early stage of torch flame ejection. However, $\mathrm{L_f}$ was approximately 1.6 times as long as that of $\lambda_{\mathrm{MC}} = 0/0$ at 2 ms ASOE and about 1.3 times at 10 ms ASOE.

The $\mathrm{L_f}$ elongation was particularly noticeable in $\mathrm{D_o} = \varnothing 2.5$ mm case, in which the torch flames collided with the inner circumferential wall of the MC around 6 ms ASOE, while the other $\mathrm{D_o}$ cases took much more time to reach the wall since the decrease in $\mathrm{\dot{L}_f}$ became clear around that timing. Specifically, $\mathrm{\dot{L}_f}$ in $\mathrm{D_o} = \varnothing 5.0$ mm case decreased rapidly after 3 ms ASOE, and $\mathrm{L_f}$ at 10 ms ASOE was the shortest compared to other PC geometries.

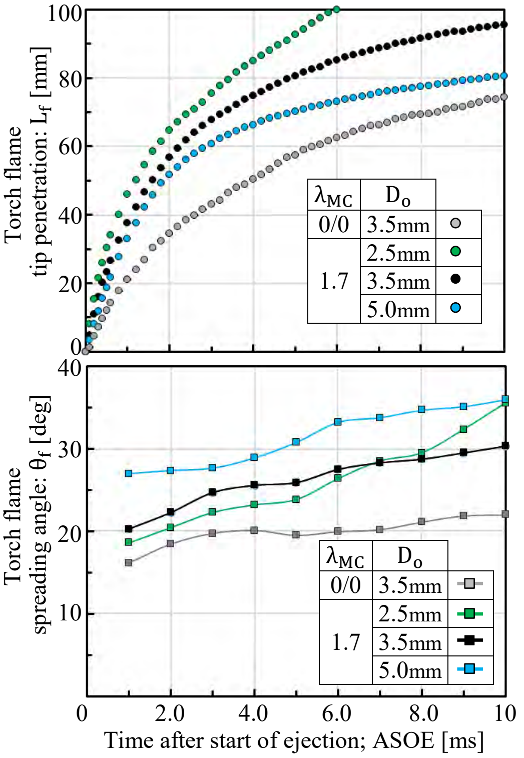

Fig. 10. Effects of diameter of PC orifices; $\mathrm{D_o}$ on torch flame penetration: $\mathrm{L_f}$ and spreading angle: $\mathrm{\theta_f}$ by PC4 ($\mathrm{D_o} = \varnothing 2.5$ mm), PC1 ($\varnothing 3.5$ mm), and PC5 ($\varnothing 5.0$ mm)

As for $\mathrm{\theta_f}$, the flame growth in $\mathrm{D_o} = \varnothing 2.5$ mm case was remarkable, too. Although the case showed the smallest $\mathrm{\theta_f}$ at the beginning of ejection, its $\mathrm{\theta_f}$ increased rapidly enough to surpass $\mathrm{\theta_f}$ in $\mathrm{D_o} = \varnothing 3.5$ mm case after 7 ms ASOE, when the torch flame in $\mathrm{D_o} = \varnothing 2.5$ mm case had already reached the MC inner wall, and to surpass $\mathrm{\theta_f}$ in $\mathrm{D_o} = \varnothing 5.0$ mm case after 10 ms ASOE. In $\mathrm{D_o} = \varnothing 5.0$ mm case, the initially large $\mathrm{\theta_f}$ showed a rapid increase during 4~6 ms ASOE, and it tended to transition to a gradual increase. All of these suggest that the combustion phase ignited by torch flames is greatly influenced by the ejection speed or strength of the torch flame.

Figure 11 compares the shadowgraph images of the torch flame with the predicted flame images for the three orifice number settings. Due to insufficient optical system adjustment in the case of $\mathrm{D_o} = \varnothing 2.5$ mm and $\mathrm{D_o} = \varnothing 5.0$ mm, false information was superimposed in the shadowgraph images as a darkened area of about twice the PC radius around the PC (arrow "A"s). It is clear from the shadowgraph images that the smaller D_o or the higher the torch flame ejection velocity, the longer L_{fi} is. In particular, $D_o = \varnothing 2.5$ mm case seems to be worth mentioning in detail.

In the $D_o = \varnothing 2.5$ mm case, ignition of the MC premixture entrained in the torch flame was first observed as late as after 3 ms ASOE, and τ_{fi} and L_{fi} were the longest among the three D_o parameters, but the variation in τ_{fi} and L_{fi} of each torch flame was also considerably large. For example, the τ_{fi} reached as long as 10 ms ASOE for the torch flame that ejected out vertically downwards in the images for $D_o = \varnothing 2.5$ mm case (arrow "B"). On the other hand, the initial value of L_{fi} from the orifices located in the upper half of the same images tended to be about half of L_f (arrow "C"s) rather than the vicinity of L_f like any PCs with other D_o or N_o (arrow "D"s). After τ_{fi}, the flame propagated rapidly from L_{fi} to the lower section of the torch flame, and the section including the entrained MC premixture expanded at the same time. After the ignition, the torch flame reached the inner circumferential wall of the MC by 10 ms ASOE, but even considering the change in the penetrating direction along the inner MC wall due to the collision, the growth of the torch flame to $\pm\theta_f$ direction accelerated in the middle combustion stage in the MC (arrow "E"). In summary, with an enhanced ejection speed of $D_o = \varnothing 2.5$ mm case, the MC premixture both in the gaps between the torch flames and in the end gas zone was able to be burned efficiently. The latter premixture is important to keep combustion efficiency high because of its large volume contribution in an MC. Upon closer observation, it is clear that L_f fluctuated over time even for torch flames from the same orifice. For example, the torch flame ejecting in the 45° direction to the lower right in the images showed $L_{fi} \approx 55$ mm at 4 ms ASOE but $L_{fi} \approx 68$ mm at 10 ms ASOE (arrow "F"s) when the pure torch flame seemed to push down the post-ignition premixed flame part to the lower side. The torch flame ejected vertically downward in the image had the longest L_f and τ_{fi} and the torch flames advancing to the lower left and right 45° bent upward after 7ms ASOE (arrow "G"s).

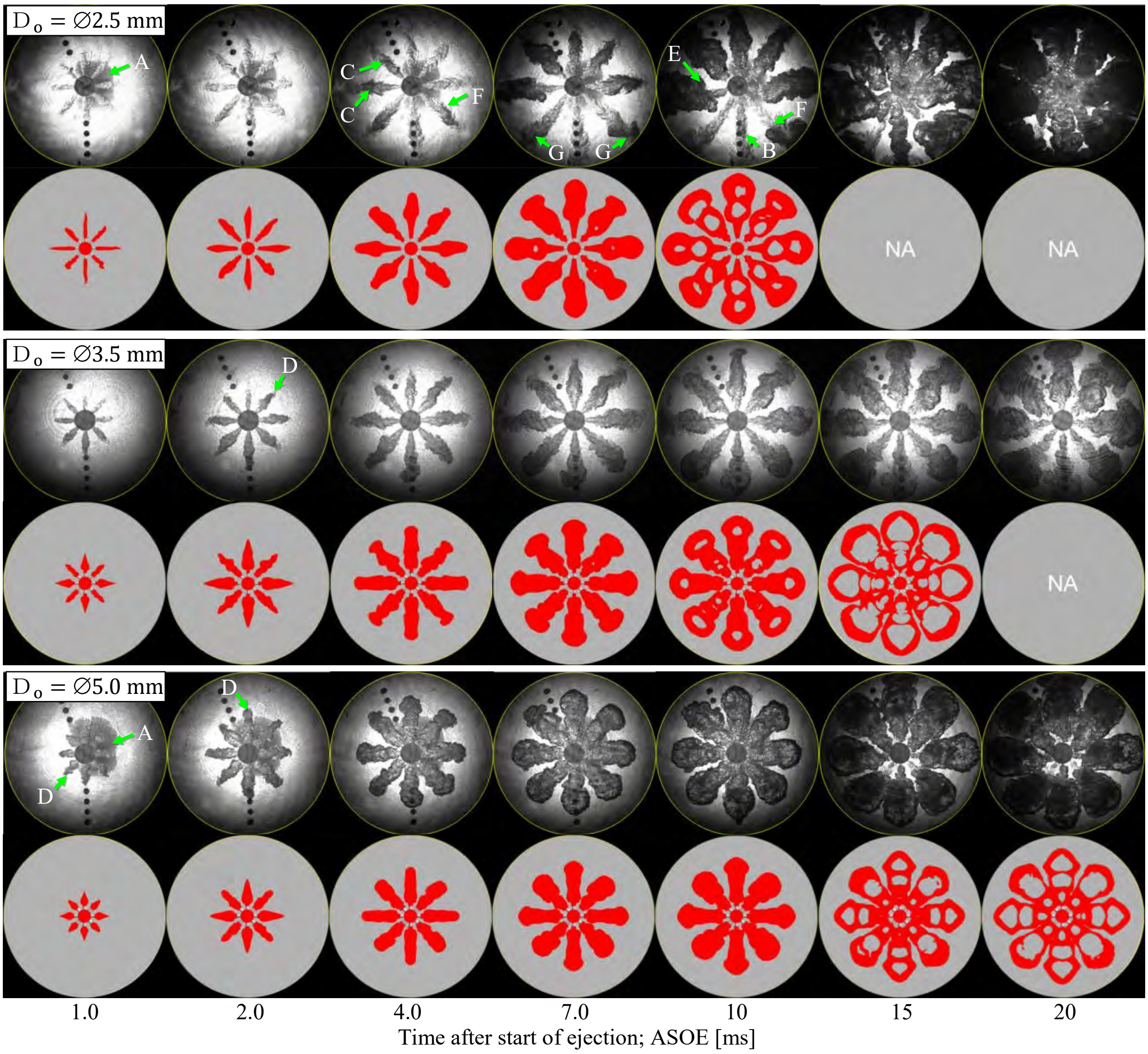

Fig. 11. Effects of diameter of orifices; D_o on ejection behaviour of torch flame by PC4 ($D_o = \varnothing 2.5$ mm), PC1 ($\varnothing 3.5$ mm), and PC5 ($\varnothing 5.0$ mm). Shadowgraph images (upper row of each island) and simulation results (lower row of each island)

One possible explanation goes below. In this experiment, the torch flames in the image's upper half ignited and grew more quickly than the ones in the lower half. A strong secondary in-chamber flow was induced from the upper to the lower half, passing through the MC centre. This downward flow reduced the relative speed between the torch flame and the MC premixture and resulted in the extension of the L_f and τ_{fi} of this torch flame. After the in-chamber flow collided with the peripheral MC wall, the flow split to the right and left and bent two torch flames.

On the other hand, at $D_o = \varnothing5.0$ mm, τ_{fi} and L_{fi} were extremely short compared to the other PC orifice specifications, and the flame expanded immediately after L_{fi}, and quickly transitioned to a turbulent jet flame with a snake-shaped tip. Overall, the flame development process was similar to that of $N_o = 10$, where the momentum per torch flame was small. However, compared with $N_o = 10$ case, the variation in τ_{fi}, L_{fi}, and development behaviour of the torch flame between each orifice were extremely small, and the decrease in $\dot{L}_f$ in the later stages of combustion was more evident due to the lowest ejection speed. Since the torch flame did not reach the peripheral inner MC wall or the premixture in the end gas zone, even at 20 ms ASOE, it can be inferred that combustion in the later stages was extremely slow.

Regarding the numerical prediction, it must first be pointed out that there was a large discrepancy between the observation results and the numerical prediction at $D_o = \varnothing2.5$ mm. For the reasons mentioned above about the CFD setup in this study, τ_{fi} and L_{fi} were configured to be zero regardless of the orifice specifications. This means the influence was greater in $D_o = \varnothing2.5$ mm case, where the absolute values of τ_{fi} and L_{fi} were long and varied depending on the nozzle hole and the elapsed time ASOE. There was also a clear tendency for L_f to be underestimated. On the other hand, at $D_o = \varnothing5.0$ mm, where τ_{fi} and L_{fi} were the shortest of all the cases, the behaviour of the torch flame ejection and its development was relatively well reproduced by the current CFD setups.

Figure 12 shows the temporal change in ROHR for the three D_o settings. The line type and legends are the same as in Fig. 9, but the scale for the ROHR is doubled. Considering the measured ROHRs, the impact of D_o on the combustion in the MC was considerably high with constant N_o. In $D_o = \varnothing2.5$ mm case with long τ_{fi} and L_{fi}, the ramp-up of ROHR was modest after the ejection started, but ROHR increased rapidly after τ_{fi} and t_{max} was reached at about 20 ms ASOE with the maximum value just over 1000 kJ/s, which was very high compared to other tested PC geometries.

However, there was also a local maximum value near 13 ms ASOE reflecting that the torch flames were divided into two groups, ones with relatively short τ_{fi} and the others with long τ_{fi}. In addition, the ROHR went negative after 50 ms ASOE, which suggested that the torch flame reached the peripheral inner MC wall at 10 ms ASOE causing the combustion of the entire MC including the end gas zone to be completed fast and that the heat loss through the wall surface increased due to the contact of torch flames with the inner wall.

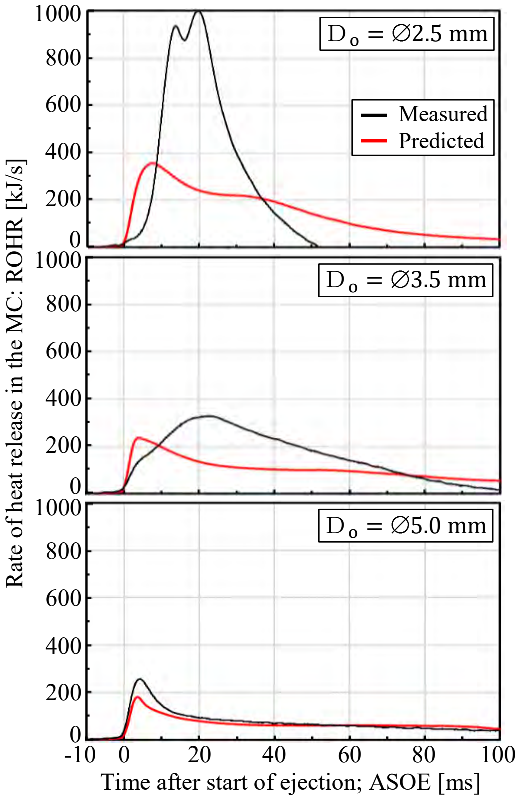

Fig. 12. Effects of diameter of PC orifices; D_o on ROHR in the MC by PC4 ($D_o = \varnothing2.5$ mm), PC1 (∅3.5 mm), and PC5 (∅5.0 mm). Measured ROHRs (black curves), and simulated ROHRs (red curves)

On the other hand, in $D_o = \varnothing5.0$ mm case, the ROHR rose fastest because of its short τ_{fi}, and t_{max} was reached at around 4.5 ms ASOE, which was significantly earlier than the PCs of other specifications, but the maximum ROHR was the lowest at just under 260 kJ/s. By comparing with the visualization results shown in Fig. 11, the quick rise of ROHR corresponded to the shortest τ_{fi} and the quick profile transitions to a snake-head shape, and the poor heat release in later stage combustion corresponded to the difficulty for the torch flame in reaching the inner MC wall due to insufficient penetrating momentum.

Next, considering the predicted ROHR, the smaller the D_o was, the lower the ROHR at the beginning of ejection and the higher the maximum ROHR were, both of which were consistent with the visualization results. However, the maximum ROHR was underestimated and t_{max} was overestimated, as in the results in the previous section. A discrepancy in both factors became large, especially in the case of $D_o = \varnothing2.5$ mm so it was hard to say the reproducibility of the combustion in the MC is appropriate. On the other hand, in $D_o = \varnothing5.0$ mm case, the discrepancy between the measured value and the predicted one was the smallest in the tested group of PCs, and the predicted ROHR followed a similar trajectory to the measured one, although the maximum ROHR was slightly underestimated. This suggests that the CFD setup applied in the study was capable of relatively good reproduction of the combustion process when the ejection velocity of torch flame was low and the effects of turbulent mixing were small, and that in APC-type methane-air premixed combustion including in actual engines, flame quenching or τ_{fi} extension due to turbulent mixing between the ejected torch flame and the MC premixture, and the following combustion promotion were essentially important matters.

4.4. Examination of the index for torch flame intensity

Nada et al. proposed the jet intensity: I_b expressed by the following formula [21] for the high-speed small gas engine. The variables in the formula conform to the notation adopted in this paper. The meanings of each factor are listed as follows: V_{PC}: Stored energy in PC (λ_{PC} is usually fixed around unity), $N_o \pi D_o^2/4$: Total opening area of PC orifices, D_{MC}: Distance to the end gas zone (relative evaluation factor).

$$I_b = \frac{V_{PC}}{D_{MC} N_o \pi D_o^2/4}\ [-] \tag{1}$$

The following can be inferred about the PC specifications of APC-type gas engines. As mentioned in the previous study [3], there are mechanical constraints on V_{PC} and D_t that are almost subordinate to D_{MC} [3]. N_o mainly determining the gap between the torch flames has little freedom to change between reducing the distance for flame propagation to the adjacent torch flame and yet securing space for the torch flame to entrain the MC lean premixture. Considering that V_{PC} is approximately proportional to the cube of D_{MC} and D_o is roughly proportional to D_{MC}, I_b can be regarded as an evaluation index not based on the engine scale.

Under these conditions, it is important to select proper D_o, so that the torch flame can have sufficient initial speed to reach the vicinity of the end gas zone during τ_{fi}, with which I_b is also thought to have positive correlation, and to promote combustion in the entire MC. In this study, for compensation of the change of the orifice aspect ratio that is accompanied with changes in N_o and D_o, the following torch flame intensity is used to confirm the correlation with the measurement results in the CVC.

$$TI = \frac{4V_{PC}(L_o/D_o)^{0.5}}{D_{MC} N_o \pi D_o^2}\ [-] \tag{2}$$

The term $(L_o/D_o)^{0.5}$ represents torch flame directionality. The evaluation of the effect is based on the measurement results of the ejection behaviour of torch flame under λ_{MC} = 0/0 conditions.

Figure 13a–f summarizes the investigation of the correlation between the above TI and the various combustion-relating characteristics in the MC obtained in the study.

First, the correlation between TI and the L_f at the ejection end was investigated. The end of ejection was identified as the timing when the differential pressure between them goes to zero. The timing was around 6 ms ASOE for most of the PCs except for 7 ms ASOE for PC4 (D_o = ∅2.5 mm) and 4 ms ASOE for PC5 (∅5.0 mm), of which L_f increased less than 7 mm even at 6 ms ASOE. As shown in (a), a linear correlation was found between TI and the L_f at the ejection end. This sustains the validity of the index to indicate the ejection strength of the torch flame.

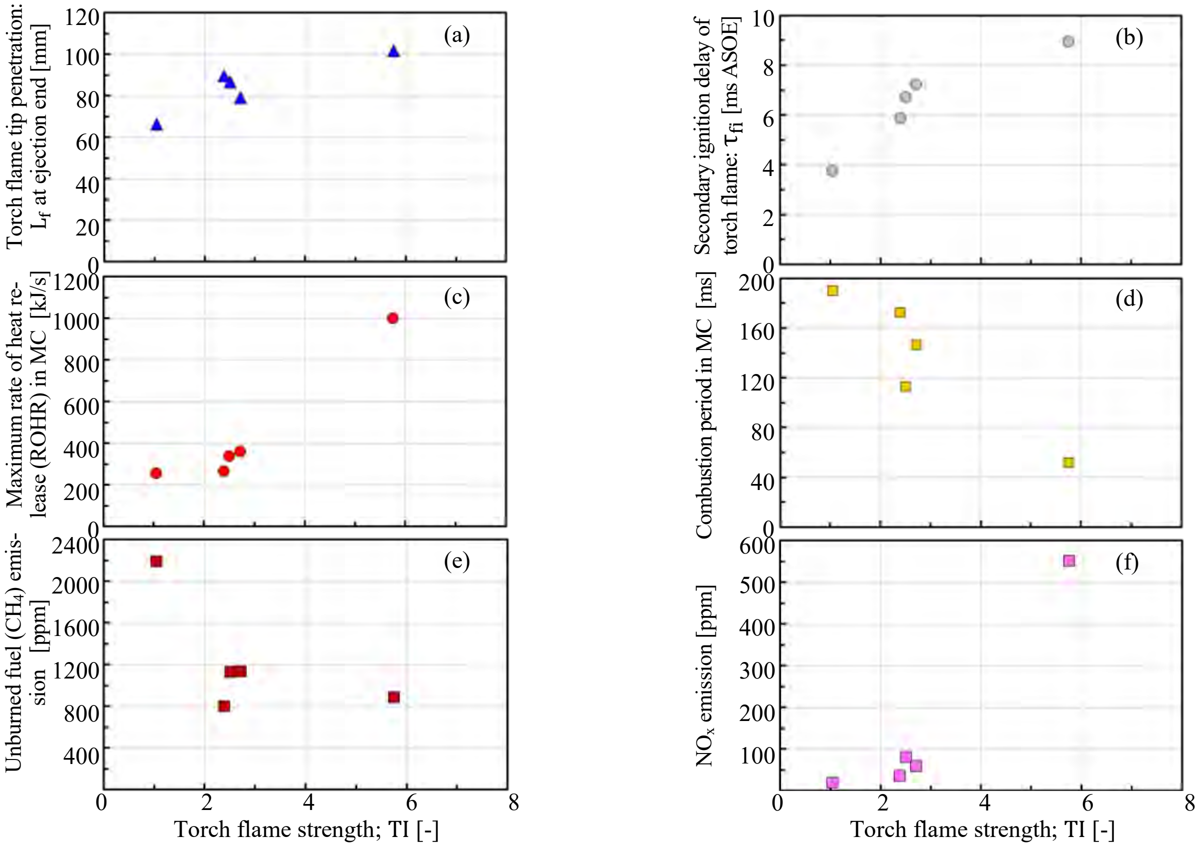

Fig. 13. Correlations between an index for torch flame strength; TI and several combustion and emission characteristics in the MC of the CVC. (a) penetration length of torch flame: L_f at ejection end, (b) secondary ignition delay of torch flame in the MC: τ_{fi}, (c) maximum rate of heat release: ROHR, (d) combustion period in the MC, (e) unburned fuel (CH_4) emissions, and (f) NO_x emissions

Second, the relationship between TI and combustion characteristics was examined. τ_{fi}, combustion period, and maximum ROHR were taken as the characteristics, and τ_{fi} was quantitively redefined here on ASOE basis as the time when 5% of supplied fuel energy released in the MC, and the combustion period is as the duration from τ_{fi} to the timing when 95% of supplied energy released. As shown in (b) and (c), strengthening TI leaded to a proportional increase in τ_{fi} and the maximum ROHR and to rather exponential shortening of the combustion period. So, TI is thought to be effective to quantify the extension of ignition delay due to turbulent mixing and the subsequent combustion promotion.

Finally, the unburned fuel component (CH_4) and NO_x in the MC residual gas were taken as the emission characteristics of the combustion in the MC. The unburned fuel emission was negatively correlated with TI and NO_x emission was positively and exponentially correlated with TI. Again, TI can indicate a degree of the combustion promotion by the ejecting strength of torch flames from a PC.

Overall, TI could be used to organize the combustion results in the CVC, but, before applying it to real engines, it is necessary to investigate the effects of engine speed and the trade-off between the combustion promotion and increased cooling loss caused by the torch flame impinging on the inner wall of the MC.

5. Conclusions

Combustion experiments were conducted by supplying methane-air premixture separately to the prechamber and main chamber of a constant-volume chamber simulating a prechamber-type medium-speed gas engine and changing the orifice specifications to investigate their effects on the combustion process in the main chamber and the effectiveness of the torch flame strength to organize the results. The following conclusions were derived.

(1) In the early stage of combustion after the premixture has ignited around the torch flame, the combustion of the premixture in the main chamber entrained into the torch flame is predominant. Flame propagation to the unburned premixture then becomes predominant from the middle to late stage.

(2) The ignition of the entrained premixture accompanies the secondary ignition delay in the main chamber from the torch flame to the premixture and the ignition delay distance that the torch flame penetrates alone from the orifice exit during that ignition delay. The combustion progresses mainly in a direction that increases the spreading angle of the torch flame instead of a direction that increases the torch flame penetration in the early stage of the combustion.

(3) A short ignition delay in the main chamber tends to transition the torch flame to a snake-head profile and cause the rapid decay of penetrating momentum, resulting in slow combustion in the end gas zone.

(4) When the total orifice opening area is kept constant, the number of orifices has little effect on the ignition delay in the main chamber nor the heat release process in the main chamber because of the trade-off between the combustion promotion by the increase in ejection momentum per torch flame and the hindrance by the decrease in flame surface area and the increase in the gap between torch flames. The appropriate number of orifices is limited to a narrow range.

(5) When the number of orifices and the prechamber volume are kept appropriate, with high ejection velocity of the torch flames by a small orifice diameter, the above-mentioned ignition delay and ignition delay length are elongated, but the following combustion promotion around the torch flame and in the end gas zone in the main chamber more than compensates for these drawbacks. Conversely, with very slow ejection velocity by a large orifice, as mentioned in (3), it has proven difficult to completely burn up the premixture in the end gas zone of the main combustion chamber.

(6) When the ignition delay in the main combustion chamber extends because of the high ejection velocity of the torch flame, the ignition position changes and the variation in ignition delay between torch flames increases. The latter may lead to the formation of a secondary in-chamber flow, which may increase the variation in the combustion process for each torch flame, which may be the cause of the large cyclic variation in actual gas engines.

(7) CFD incorporating a RANS-type turbulence model and detailed chemical reactions, which successfully reproduced the ejection behaviour of the torch flame when nitrogen was filled in the main chamber, is insufficient to reproduce the combustion process in the main chamber, except in cases where the torch flame ejection velocity is very low. The simulation for prechamber-type gas engines needs appropriate sub-models that reflect the quenching and ignition fluctuation due to turbulent mixing as well as the combustion-promotion by the torch flame jet.

(8) The existing formula proposed for estimating flame jet intensity in a high-speed small engine was applied to the measurement results of the study and found to have enough validity through checking the correlation with the penetration length of the torch flame, the heat release process in the main chamber, and the emission characteristics.

As a future task, additional measurements are necessary to verify the generality of these conclusions, as well as to investigate the effects of turbulent flow fields existing in an actual engine. For numerical predictions, it is necessary to reproduce the above-mentioned effects by turbulent mixing.

Nomenclature

A	total cross-sectional opening area of flow paths
AFR	air-to-fuel ratio
AMR	adaptive mesh refinement
APC	active pre-combustion chamber
ASOE	after the start of a torch flame ejection
CFD	computational fluid dynamics
CPU	central processing unit
CVC	constant-volume chamber
D	diameter of a chamber/window or a flow path
GRI	The Gas Research Institute

H	height of a chamber/window or a flow path
HG	greenhouse gas
I_b	jet intensity proposed by Nada et al. [19]
IMO	International Maritime Organization
L	length of a flow path, penetration of a gas jet or distance between ignition position of MC premixture on a torch flame and orifice exit of PC
$\dot{L}$	flow speed or penetration speed of a gas jet
LBGE	lean-burn premixed combustion gas engine
N	number of flow paths
MC	main combustion chamber, also used as a subfix
MEPC	Marine Environment Protection Committee
NG	natural gas
NO_x	nitrogen oxides
PC	pre-combustion chamber, also used as a subfix
RANS	Reynolds-Averaged Navier-Stokes equations
RNG	renormalization group
ROHR	rate of heat release
SAGE	structural adaptive grid embedding
TI	torch flame intensity
θ	spreading full angle of a gas jet
λ	global air excess ratio in a combustion chamber
t	elapsed time on ASOE basis (see the last item)
τ	delay time

Subfix:

f	torch flame
fi	ignition of MC premixture by torch flame
max	maximum of ROHR
o	PC orifice
t	PC throat
W	optical window

Bibliography

[1] Aakko-Saksa T, Lehtoranta K, Kuittinen N, Järvinen A, Jalkanen J, Johnson K et al. Reduction in greenhouse gas and other emissions from ship engines: current trends and future options. Prog Energ Combust. 2023;94:101055. https://doi.org/10.1016/j.pecs.2022.101055

[2] Al-Enazi A, Okonkwo EC, Bicer Y, Al-Ansari T. A review of cleaner alternative fuels for maritime transportation. Energy Reports. 2021;7:1962-1985. https://doi.org/10.1016/j.egyr.2021.03.036

[3] Aoyagi T, Wakasugi T, Tsuru D, Tashima H. Analysis of effects of pre-chamber orifices on torch flame behaviours in lean-burn gas engines. Combustion Engines. 2024;199(4):3-14. https://doi.org/10.19206/CE-188112

[4] Babajimopoulos A, Assanis DN, Flowers DL, Aceves SM, Hessel RP. A fully coupled computational fluid dynamics and multi-zone model with detailed chemical kinetics for the simulation of premixed charge compression ignition engine. Int J Engine Res. 2005;6:497-512. https://doi.org/10.1243/146808705X30503

[5] Brynolf S, Hansson J, Anderson JE, Skov IR, Wallington TJ, Grahn M et al. Review of electrofuel feasibility – prospects for road, ocean, and air transport. Prog Energ. 2022;4:4. https://doi.org/10.1088/2516-1083/ac8097

[6] Bueschke W, Skowron M, Szwajca F, Wisłocki K. Flame propagation velocity in 2-stage gas combustion system applied in SI engine. IOP Conf Ser: Mater Sci Eng. 2018; 421:042009. https://doi.org/10.1088/1757-899X/421/4/042009

[7] Bueschke W, Skowron M, Wisłocki K, Szwajca F. Comparative study on combustion characteristics of lean premixed CH_4/air mixtures in RCM using spark ignition and turbulent jet ignition in terms of orifices angular position change. Combustion Engines. 2019;176(1):36-41. https://doi.org/10.19206/CE-2019-105

[8] Cho HM, He BQ. Spark ignition natural gas engines – a review. Energ Convers Manage. 2007;48(2):608-618. https://doi.org/10.1016/j.enconman.2006.05.023

[9] Duan X, Deng B, Liu Y, Zou S, Liu J, Feng R. An experimental study the impact of the hydrogen enrichment on cycle-to-cycle variations of the large bore and lean burn natural gas spark-ignition engine. Fuel. 2020;282:118868. https://doi.org/10.1016/j.fuel.2020.118868

[10] Einewall P, Johansson B. Cylinder to cylinder and cycle to cycle variations in a six cylinder lean burn natural gas engine. SAE Technical Paper 2000-01-1941. 2000. https://doi.org/10.4271/2000-01-1941

[11] Guo H, Zhou S, Shreka M, Feng Y. Effect of pre-combustion chamber nozzle parameters on the performance of a marine 2-stroke dual fuel engine. Processes. 2019;7(12):876. https://doi.org/10.3390/pr7120876

[12] IMO HP MEPC80. https://www.imo.org/en/MediaCentre/PressBriefings/pages/Revised-GHG-reduction-strategy-for-global-shipping-adopted-.aspx

[13] Ishibashi R, Tsuru D. An optical investigation of combustion process of a direct high-pressure injection of natural gas. J Mar Sci Technol. 2017;22:447-458. https://doi.org/10.1007/s00773-016-0422-x

[14] Kazakov A, Frenklach M. GRI-Mech. University of California at Berkeley. http://combustion.berkeley.edu /drm/

[15] Korakianitis T, Namasivayam AM, Crookes RJ. Natural-gas fueled spark-ignition (SI) and compression-ignition (CI) engine performance and emissions. Prog Energ Combust. 2011;37(1):89-112. https://doi.org/10.1016/j.pecs.2010.04.002

[16] Kulzer AC. Sustainability & powertrain systems: from electrification to hydrogen and efuels (updated). Proc JSAE PEL Int Meeting, Technical Challenges for a Carbon Neutral Society by 2050. Keynote 4, Kyoto 2023.

[17] Liu J, Ulishney CJ, Dumitrescu CE. Experimental investigation of a heavy-duty natural gas engine performance operated at stoichiometric and lean operations. Energ Convers Manage. 2021;243(x):114401. https://doi.org/10.1016/j.enconman.2021.114401

[18] Liu L, Wu Y, Wang Y. Numerical investigation on knock characteristics and mechanism of large-bore natural gas dual-fuel marine engine. Fuel. 2022;310:122298. https://doi.org/10.1016/j.fuel.2021.122298

[19] Nada Y, Kidoguchi Y, Yamashita Y, Furukawa R, Kaya R, Nakamo H et al. Effects of sub-chamber configuration on heat release rate in a constant volume chamber simulating lean-burn natural gas engines. SAE Int J Adv & Curr Prac in Mobility. 2020;2(2):1032-1040. https://doi.org/10.4271/2019-32-0551

[20] Pielecha I. Analysis of mass transfer in marine engine with prechamber combustion spark ignition system. Bull Pol Ac: Tech. 2021;69(2):e136744. https://doi.org/10.24425/bpasts.2021.136744

[21] Pielecha I, Bueschke W, Skowron M, Fiedkiewicz Ł, Szwajca F, Cieślik W et al. Prechamber optimal selection for a two stage turbulent jet ignition type combustion system in

CNG-fuelled engine. Combustion Engines. 2019;176(1):16-26. https://doi.org/10.19206/CE-2019-103

[22] Senecal PK, Pomraning E, Richards KJ, Briggs TE, Choi CY, McDavid RM et al. Multi-dimensional modeling of direct-injection diesel spray liquid length and flame lift-off length using CFD and parallel detailed chemistry. Journal of Engines. 2003;112(3):1331-1351. http://www.jstor.org/stable/44741357

[23] Shapiro E, Tiney N, Kyrtatos P, Kotzagianni M, Bolla M, Boulouchos K et al. Experimental and numerical analysis of pre-chamber combustion systems for lean burn gas engines. SAE Technical Paper 2019-01-0260. 2019. https://doi.org/10.4271/2019-01-0260

[24] Shi J, Zhu Y, Feng Y, Yang J, Xia C. A prompt decarbonization pathway for shipping: green hydrogen, ammonia, and methanol production and utilization in marine engines. Atmosphere. 2023;14(3):584. https://doi.org/10.3390/atmos14030584

[25] Tashima H, Kunimitsu M, Sugiura K, Tsuru D. Development of high-efficiency gas engine through observation and simulation of knocking phenomena. Proc CIMAC Congress 10 Bergen. 2013; No. 213.

[26] Validi AA, Schock H, Jaberi F. Turbulent jet ignition assisted combustion in a rapid compression machine. Combust Flame. 2017;186:65-82. https://doi.org/10.1016/j.combustflame.2017.07.032

[27] Wakasugi T, Tsuru D, Tashima H. Influences of the pre-chamber orifices on the combustion behavior in a constant volume chamber simulating pre-chamber type medium-speed gas engines. Combustion Engines. 2022;191(4):66-76. https://doi.org/10.19206/CE-148171

[28] Yasueda S, Takasaki K, Tashima H. The abnormal combustion affected by lubricating oil ignition in premixed gas engine. Proc ASME 2012 ICES. 2012:29-36. https://doi.org/10.1115/ICES2012-81042

[29] Yuan M, Thellufsen JZ, Lund H, Liang Y. The electrification of transportation in energy transition. Energy. 2021; 236:121564. https://doi.org/10.1016/j.energy.2021.121564

Takahide Aoyagi, MEng. – Energy Conversion Group, Technology Platform Center, Technology & Intelligence Integration, IHI Corporation. Japan.

e-mail: *t.jr.aoyagi@gmail.com*

Takuya Wakasugi, MEng. – Interdisciplinary Graduate School of Engineering Sciences (IGSES), Kyushu University, Japan.

e-mail: *wakasugi.takuya.875@s.kyushu-u.ac.jp*

Daisuke Tsuru, DEng., Assoc. Prof. – Shipping Technology Department, National Institute of Technology (KOSEN), Oshima College, Japan.

e-mail: *tsuru.daisuke@oshima.kosen-ac.jp*

Hiroshi Tashima, DEng., Assoc. Prof. – Faculty of Arts and Sciences, Kyushu University, Japan.

e-mail: *tajima.hiroshi.539@m.kyushu-u.ac.jp*

Article citation info:
Puzdrowska P, Skobyłko K. Analysis of the possibility of using the Sankey diagram in the diagnosis of a partially loaded diesel engine. Combustion Engines. 2025;202(3):58-66. https://doi.org/10.19206/CE-205607

Patrycja PUZDROWSKA
Jakub SKOBYŁKO

Combustion Engines
Polish Scientific Society of Combustion Engines

Analysis of the possibility of using the Sankey diagram in the diagnosis of a partially loaded diesel engine

ARTICLE INFO

Received: 15 April 2025
Revised: 23 May 2025
Accepted: 27 May 2025
Available online: 13 June 2025

The purpose of this article is to determine if, in the case of inability to carry out diagnostic tests at engine operating loads in the range of 70–90%, engine functional systems can generate diagnostic signals in the form of changes in heat balance components. The motivation for working on the selected topic was the need to evaluate the effectiveness of graphical forms of heat balance representation, especially Sankey diagrams, in heat engine diagnostics, using a four-stroke diesel engine as an example. Interpretation of the results was carried out based on simulations performed using Blitz-PRO software and experimental tests carried out on a test bench. For the numerical simulations, the object under analysis was modeled, which was a single-cylinder, four-stroke diesel engine Andoria S320. Both numerical simulations and experimental tests were carried out for three engine operating states: the reference state and two malfunction states: in the air intake system and the fuel supply system. The analyses made it possible to draw conclusions. It was assessed that carrying out the analysis of the Sankey diagram for partial load doesn't bring significant diagnostic information.

Key words: *compression ignition engine, parametric diagnostics, Sankey diagram, numerical simulations, Blitz-PRO program*

1. Introduction

Maintaining stable operating parameters of a diesel engine and performing regular diagnostics is important, as it allows for the prevention of damage and degradation of entire functional systems and to operate the engine economically [7]. In IC engines, the most frequently diagnosed defects include the fuel supply system and the intake air system [3, 5]. Injector spring relaxation is indicated as one of the common failures of the fuel supply system. The consequence of this malfunction is incomplete combustion of fuel, which negatively affects the efficiency of engine operation. In turn, considering the air intake system, filter contamination can be a significant problem, restricting the free flow of air, thus reducing the efficiency of the engine's working processes [3, 12].

One of the diagnostic methods used in the analysis of IC engines is the evaluation of heat balances. Significant deviations from reference values, characteristic of a fully operational engine, can help indicate the functional system in which the malfunction has occurred [15]. Graphical tools such as Sankey charts are particularly useful for clearly interpreting the data obtained [4, 8, 11].

The purpose of the research presented in this article was to assess whether, under limited engine load conditions (less than 50%), engine functional systems generate diagnostic signals in the form of changes in heat balance components. The article presents some of the results obtained during the completion of the master's thesis for the energy technology faculty [13].

2. Description of the considered diagnostic method – Sankey's diagram

A diagnostic method based on the Sankey diagram involves graphically representing the flow of energy or mass within the system using a flow diagram [7]. In the case of a IC engine, the Sankey diagram illustrates the distribution of input energy $\dot{Q}_{fuel} + \dot{H}_{air}$ (energy contained in the fuel-air mixture) into several branches: indicated power P_i which can be separated into mechanical power Pm and effective power Pe), heat loss through exhaust gases $\dot{H}_{exh}$, s losses in lubricating oil $\dot{Q}_{oil}$, and cooling system $\dot{Q}_{cool}$, heat transferred to the environment $\dot{Q}_{amb}$, but also other forms of energy dissipation: residual heat dissipation stream $\dot{Q}_r$, which is a measure of energy losses not included in the energy balance (e.g. the stream of acoustic energy and mechanical vibration from the thermal-fluid and mechanical systems of the entire power unit) [7]. Formula (1) shows the relationship that allows the engine energy balance to be drawn up:

$$\dot{Q}_{fuel} + \dot{H}_{air} = \dot{H}_{exh} + \dot{Q}_{oil} + \dot{Q}_{cool} + \dot{Q}_{amb} + \dot{Q}_r + P_i \tag{1}$$

The thermal efficiency of the engine η_{th} is expressed as the ratio of the average indicated power P_i to the energy supplied to the engine (2):

$$\eta_{th} = \frac{P_i}{\dot{Q}_{fuel} + \dot{H}_{air}} \tag{2}$$

Visualization makes it possible to identify potential faults in functional systems. It also ensures the creation of a clear energy balance, assigning all input energy to useful work and its distribution to losses occurring in each engine's functional system. The measured data is used in the energy balance equations and then presented graphically in a Sankey diagram [1].

3. Obtained results of simulations and research

3.1. Numerical simulation in the Blitz-PRO program

The issues presented in this section were focused on the numerical analysis of thermodynamic processes occurring in an appropriately modeled Andoria S320 four-stroke, single-cylinder diesel engine.

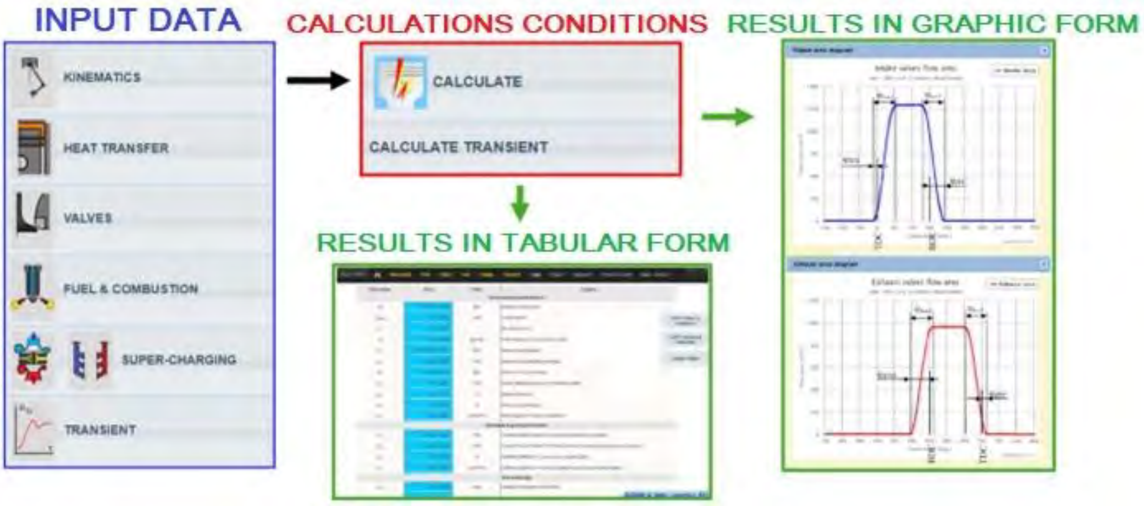

Fig. 1. Schematic of project management in Blitz-PRO software [2]

Numerical simulations in Blitz-PRO software were carried out in the first place, so it was possible to obtain results in a fast and non-invasive way. Based on the analysis of the simulation results, an assessment was made as to whether the implemented damage caused the expected effects, in the form of sufficiently noticeable changes in the values of parameters that could be recorded on the test bench. The second objective of the simulations carried out was to assess the correctness (validation) of the numerical tool's performance against the results of the tests carried out on the test bench.

Blitz-PRO simulation software makes it possible to analyze the thermodynamic cycle of internal combustion engines, including four-stroke IC engines. For each engine configuration, the basic approach remains the same: a division of the engine into several thermodynamic systems is made, interacting with each other through energy and mass exchange processes. The results of numerical simulations are compiled both in the form of a so-called report and diagrams representing the processes occurring during operation of the modeled engine [2,17].

Figure 1 presents a simplified form of the scheme for solving numerical simulations, taking into account the most important stages of project management.

According to the data shown in Fig. 1, proceeding to conduct numerical simulations must be preceded by the modeling of the engine under study, which involves implementing all the necessary parameters in such a way as to reproduce the structural and physical quantities of the various functional systems with the greatest possible precision [2].

The "Kinematics" tab allows configuration of the main geometric properties of the engine, i.e. cylinder diameter, piston stroke, number of cylinders and geometric compression ratio.

In the next section, the "Heat transfer" tab referring to frictional losses and heat transfer from the intake manifold, exhaust manifold and heat transferred due to piston motion to the boundary walls of the intra-cylinder space should be configured accordingly.

The next section, "Valves," refers to the valve components responsible for charge exchange in the combustion chamber. It mainly contains the geometric design parameters of the valve system, as well as the positions and durations of valve opening and closing [°CA].

The "Fuel & Combustion" section deals with the configuration of parameters related to the fuel injection system. It includes both information about the design of the injector and the characteristics of the fuel used.

The "Super-Charging" engine gas exchange system includes the selection of the configuration and geometric properties of the intake system and exhaust manifold, the method of cylinder charging, the type and number of compressors and their arrangement. It is possible to carry out calculations for a naturally aspirated engine (laboratory bench case) and supercharged engines.

With reference to the research objective of evaluating the effectiveness of using Sankey diagrams for diagnostics, a necessary step was to correctly model the engine located on the test bench. This was done by implementing the correct values in each of the described tabs.

Numerical simulations were carried out for three engine operating states. The reference state of the engine, which did not include any malfunction, was taken as the reference point for the analyses. The second state included a malfunction related to the engine's air intake system, while the third state was directly related to the fuel injection system into the combustion chamber. For all numerical operations, one engine operating point was selected for which the average value of fuel injection pressure was equal to the rated value of this parameter for the Andoria S320 engine $\left(p_{\text{inj}} = 14\ \text{MPa}\right)$. Simulations were carried out for an effective power, equal to $P_e = 10.8\ \text{kW}\ (0.82 \cdot P_N)$ and a crankshaft speed of 1200 min^{-1}. Analyses conducted for smaller loads indicated similar relationships to those whose results are presented in this article. The calorific value of the fuel used in the simulations was 42.5 MJ/kg. The temperature of the fuel was the same as the ambient temperature. Ambient conditions: $t_{amb} = 20^{\circ}\text{C}$, $p_{amb} = 101.3$ kPa, humidity 30%. Coolant temperatures were: at the inlet to the cylinder liner 358 K, at the inlet to the piston 368 K, at the inlet to the cylinder head 358 K. Intake valve opening was 23°CA before TDC, closing was 40°CA after BDC. Exhaust valve opening was 46°CA before BDC, closing was 17°CA after TDC. The injection advance angle was 32°CA before TDC, while the injection duration was 28°CA.

The output from the simulations made it possible to draw up energy balances for each engine operating condition, and consequently to graphically form them in the form of Sankey diagrams.

The first of the two faults implemented was to simulate fouling of the air filter feeding the cylinder section. The introduction of the malfunction into the intake system was done via changes made to the input parameters of the numerical simulator. For the reference condition, the internal area of the intake manifold was $A_{in} = 0.0035\ m^2$. In the case currently under consideration, this area was reduced by 80%, so this parameter was set at $A_{in} = 0.0007\ m^2$. The reduction in cross-sectional diameter also prompted a change in the value of pressure drop in the intake duct from $\Delta p_{in} = 1$ kPa (the value for the reference condition), to $\Delta p_{in} = 8$ kPa.

The second case of implemented failure represents a malfunction in the fuel injection system. This malfunction is directly related to the incorrect nature of the injector, so a component that, according to statistics in the literature, accounts for as much as 41% of all defects in the fuel supply system of diesel engines [3]. The malfunction in this system was implemented via changes in such parameters as the free-flight distance of the fuel jet and droplet diameters, for example. The result of such an action was, in effect, a reduction in the average fuel injection pressure p_{inj} by about 10% relative to the reference condition.

Table 1 summarizes the values of the component parameters of the energy balances, determined by numerical simulations. The green and red colors also indicate, in turn, the percentage increase or decrease in values relative to the reference condition. The data in Table 1 were also used to reflect the balances in graphical form, using Sankey diagrams, illustrated in Fig. 2.

For each of the analyzed cases, the highest loss in the balance was recorded in the form of heat flow absorbed by the engine cooling water $\dot{Q}_{cool}$, with the values of this parameter varying in magnitude. The throttling of the air intake contributed to an increase in the generated loss by 14.44%, while in the case of the second failure, the value decreased by 15.4% relative to the reference. The malfunction of the fuel supply system significantly reduced the loss associated with the heat flux absorbed by the engine oil, $\dot{Q}_{oil}$, by 17.27% relative to the condition representing a fully operational engine. The total value of the heat flux raised from the external surfaces of the engine to the environment by radiation and the flux of the rest of the heat dissipated $\left(\dot{Q}_{amb} + \dot{Q}_r\right)$ is the resulting value of the balance – the reports do not take these parameters into account.

In the great majority of the balance's component parameters, deviations from the reference values are within the limits of calculation error. The balances supplemented by the efficiencies (thermal η_{th}, mechanical η_m and overall η_o) showed that the reference condition in the overall comparison presented the worst, with the highest overall efficiency of the engine obtained for the condition taking into account the inefficiency of the fuel supply system: 25.91% (a 5.23% increase over the reference condition).

Reducing the cross-sectional area of the intake air duct by 80% resulted in about a 12% reduction in the heat delivered with the fuel. This is believed to be caused by a multiplicity of phenomena occurring simultaneously: throttling the airflow results in an increase in flow velocity, and consequently, losses of many types increase. In addition, the heat flow depends on the mass flow rate of the air flowing through. In turn, the mass flux depends on the cross-sectional area of the duct (which decreases) and the flow velocity (which increases). Less air always results in worse combustion conditions.

In the case of a noticeable increase in the enthalpy flux of the exhaust gas with a reduced injector opening pressure, it can be assumed that worse fuel atomization results in a decrease in the duration of combustion, and thus an increase in the temperature of the exhaust gas, which directly affects the enthalpy value. Reduced injector opening pressure always results in worse atomization and penetration of fuel particles in the combustion chamber.

Table 1. Components of the energy balance of the Andoria S320 engine (numerical simulations)

		Reference condition	Throttled air intake		Reduced injection pressure	
Parameter	Unit	Value	Value	δ_{REF} [%]	Parameter	Unit
$\dot{Q}_{fuel}$	[kW]	37.093	38.755	🟩 4.480	34.976	🟥 5.707
$\dot{H}_{air}$	[kW]	5.074	4.468	🟥 11.949	5.130	🟩 1.102
$\dot{H}_{exh}$	[kW]	7.425	7.082	🟥 4.619	7.629	🟩 2.746
$\dot{Q}_{cool}$	[kW]	11.714	13.406	🟩 14.440	9.910	🟥 15.403
$\dot{Q}_{oil}$	[kW]	4.128	4.258	🟩 3.151	3.415	🟥 17.270
$\dot{Q}_{amb} + \dot{Q}_r$	[kW]	5.125	4.726	🟥 7.774	5.531	🟩 7.937
P_i	[kW]	13.776	13.751	🟥 0.180	13.621	🟥 1.122
P_m	[kW]	2.998	2.939	🟥 1.982	2.822	🟥 5.862
P_e	[kW]	10.778	10.812	🟩 0.321	10.799	🟩 0.197
η_{th}	[%]	32.670	31.815	🟥 2.618	33.964	🟩 3.960
η_m	[%]	75.360	75.060	🟩 0.399	76.283	🟩 1.225
η_o	[%]	24.620	23.880	🟩 3.006	25.909	🟩 5.233

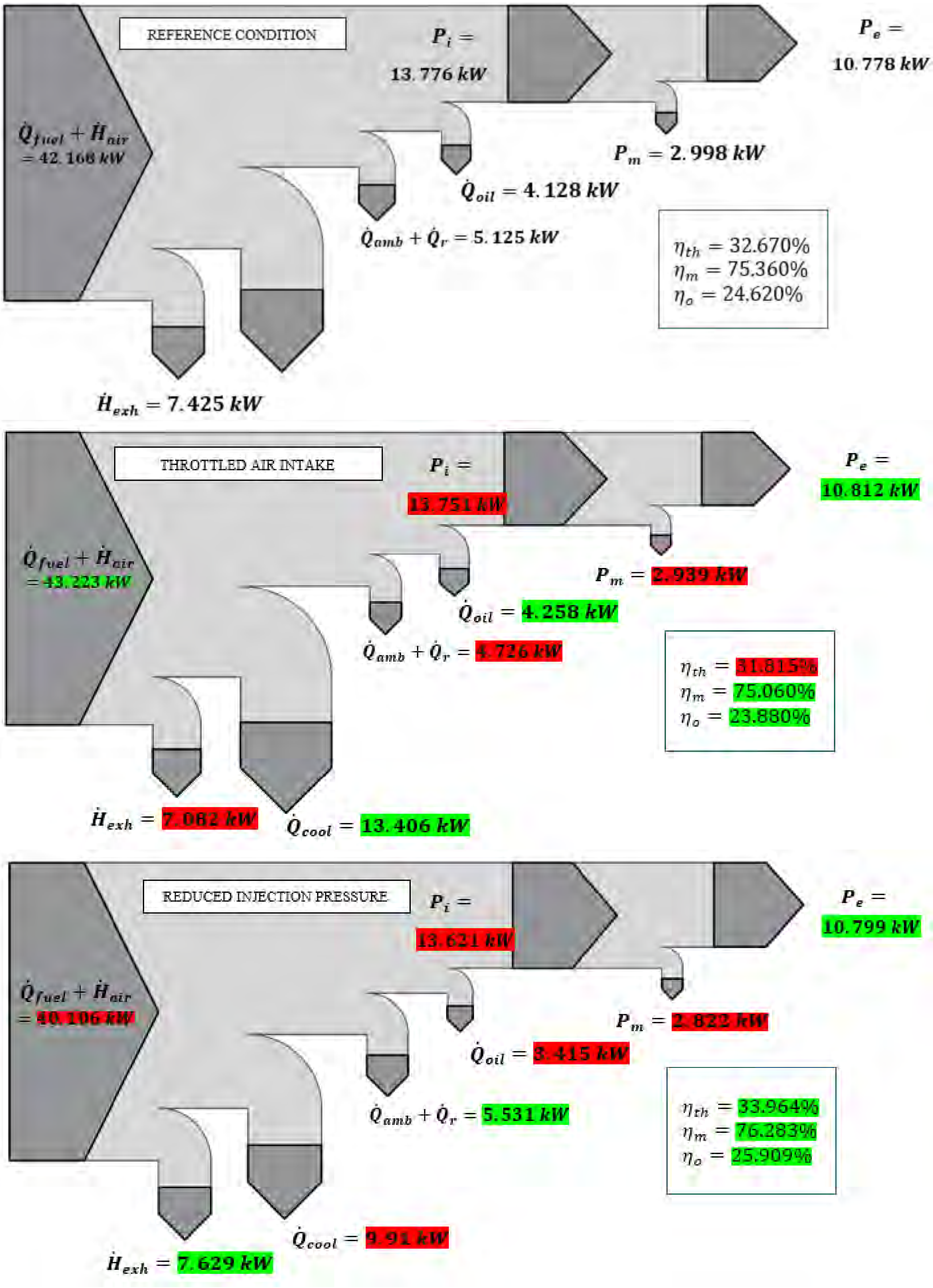

Fig. 2. Sankey diagrams – results of numerical simulations

The increase in the amount of heat received by the coolant and lubricating oil in the case of throttled air can be interpreted as a result of less oxygen in the combustion chamber, and thus an increase in the temperature of the circuit and an increase in the intensity of heat transfer.

With the changes introduced in the simulations, we are dealing with very complicated thermodynamic and flow phenomena. The mathematical algorithm of the software used is not fully known to the user, but it is treated as correct because of the publication support [9, 17].

3.2. Measurement results on the laboratory bench

The measurements were carried out on a test stand located in the Mechanical Engineering Laboratory of the Faculty of Mechanical Engineering and Ship Technology of Gdansk University of Technology. A single-cylinder, four-stroke IC engine powered by diesel fuel – Andoria S320 – was used (Fig. 3 and 4). The engine under study is characterized by a maximum power of 13.2 kW at a crankshaft speed of ,500 min^{-1} and a maximum torque of 84.4 Nm at 1200 min^{-1}. A summary of the most important values of the engine's technical parameters is presented in Table 2.

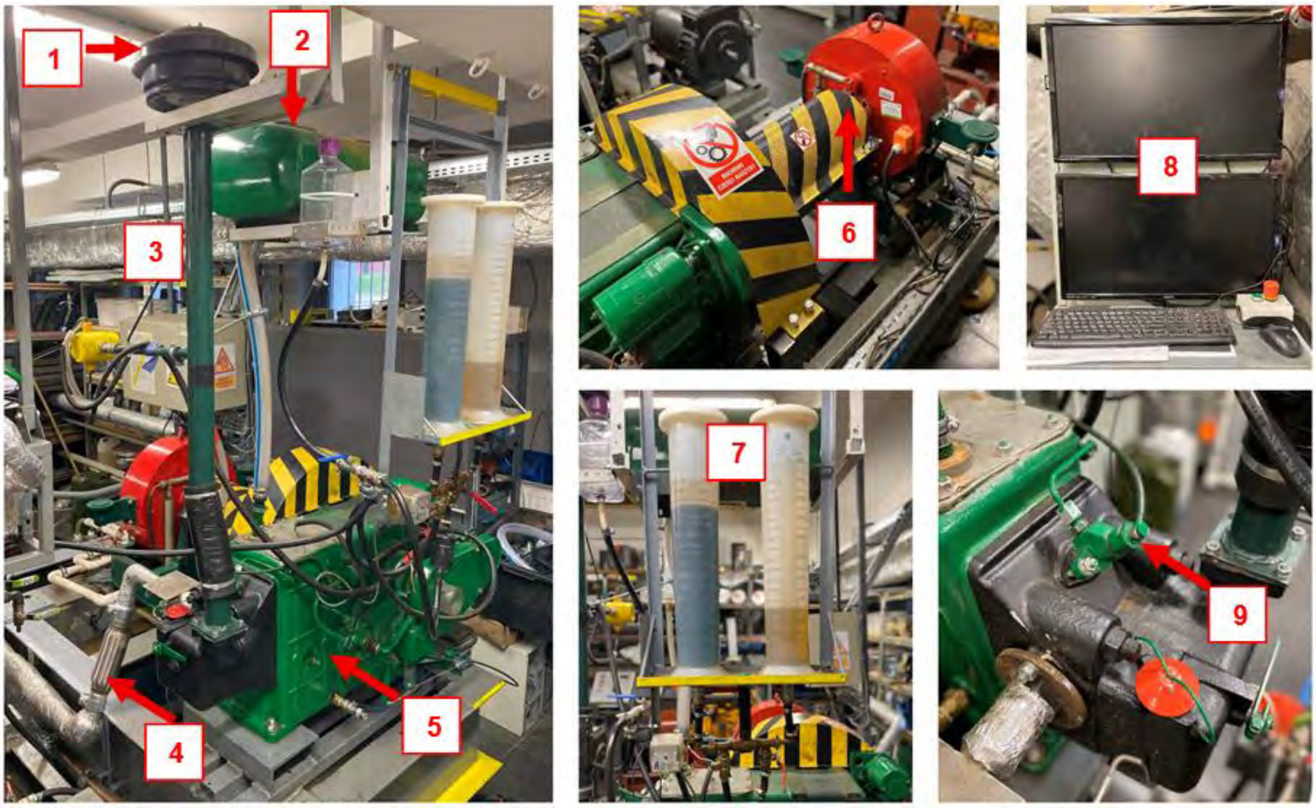

Fig. 3. Andoria S320 diesel engine test stand: 1 – air filter, 2 – engine cooling water tank, 3 – intake air duct, 4 – exhaust gas duct, 5 – Andoria S320 engine, 6 – water-cooled brake, 7 – supply fuel tanks, 8 – control and measurement software cabinet, 9 – injector

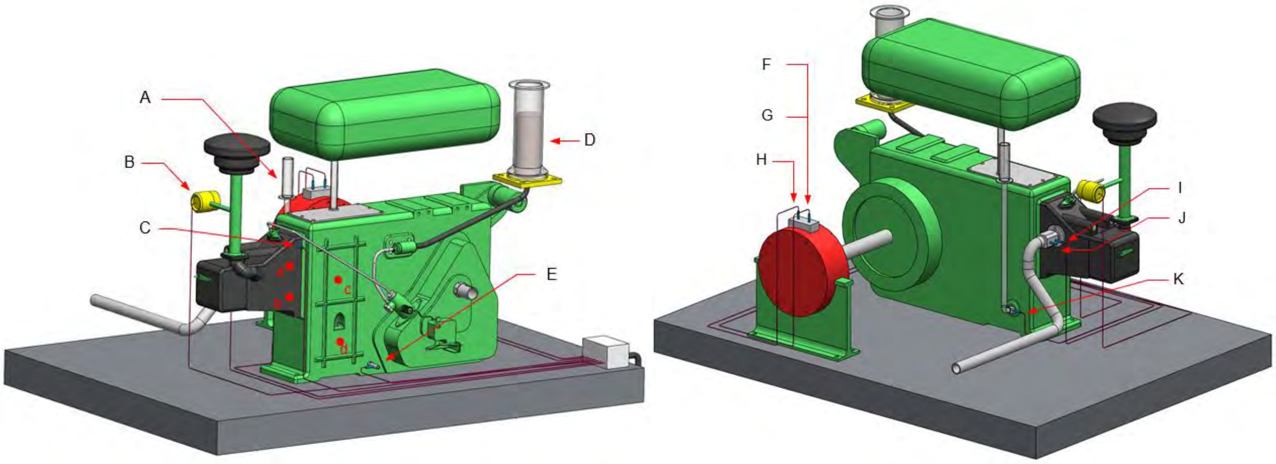

Fig. 4. Model of the test bench – front and back parts: A – cooling water level indicator, B – air flow rate meter, C –points for measuring the temperature of the surface of the engine, D – fuel level indicator, E –lubricating oil temperature measurement point, F – crankshaft rotational speed measurement, G – torque measurement, H – water-cooled brake, I – exhaust gas temperature measurement point, J – exhaust gas analyzer mounting point, K – cooling water temperature measurement

Table 2. Technical data of Andoria S320 engine

Parameter	Value	Unit
Displacement volume	1810	cm^3
Cylinder diameter	120	mm
Piston stroke	160	mm
Compression ratio	17	–
Injection advance angle	32	°CA
Injection pressure	17	MPa

Computer software provides both a live reading of sensor readings and smooth control of engine crankshaft speed and torque. The drive shaft is connected to a water-cooled brake, making it possible to conduct tests for preset engine loads.

Optrand D32294-Q sensor was used to measure the indicated software, it was possible to indicate the temperatures at the adopted measurement points and then calculate the $\dot{Q}_{amb}$ [14, 16].

Tests on the test bench were carried out in a similar manner to numerical simulations (three technical conditions). Regardless of the analyzed operating state, all measurements were made for a strictly defined crankshaft speed setting of 1200 min^{-1} and a torque of 40 Nm, consequently, the tests were carried out for an engine load equal to 38% of rated power. Malfunctions introduced into the intake air system were accomplished by restricting the flow area through the filter in such a way as to reduce the flow by about 50%. The impairment to the fuel supply system was introduced by means of a reduction in fuel injection pressure. This parameter was reduced from a reference value of 17 MPa to a value of 15 MPa, therefore by 12%.

During the laboratory test, the opening and closing angles of the intake and exhaust valves were the same as in the simulation. The same was the case with the injection timing advance angle. Water was cooling the engine by evaporation at 100°C. The tests were conducted at a lubricating oil temperature of 45°C. Summer diesel oil was used, the fuel temperature was the same as the ambient temperature. The ambient conditions were t_{amb} = 15°C, p_{amb} = 100.6 kPa, humidity 50%.

Table 3 presents the energy balances, in the form of energy input totals and energy losses, for each engine operating condition analyzed. Finally, Sankey diagrams for each engine operating condition are shown in Fig. 5.

By subjecting the presented Sankey diagrams (Fig. 5) to analysis for the three operating states of the Andoria S320 engine, it was found that there were no significant differences in the values of the heat balance components. The results obtained suggest a minimal effect of implemented damage on the efficiency of engine operation.

In the reference condition, which is the reference point for the analyses carried out, the input energy to the engine $(\dot{Q}_{fuel} + \dot{H}_{air})$ amounted to 21.468 kW, with the largest losses falling on the exhaust enthalpy stream $(\dot{H}_{exh} = 9.943\ \text{kW})$, while accounting for 46% of the total energy supplied to the engine. Obtained from thermal imaging camera measurements, the value of heat flow radiated from the engine's external surfaces to the environment was $\dot{Q}_{amb} = 1.760\ \text{kW}$. In the context of the analysis of the components of the heat balance, it is reasonable to note the almost negligibly small value of the heat flow taken up by the water in the coolant expansion tank $\dot{Q}_{cool}$, equal to 0.054 kW. For each of the other two engine operating states, values of the same order of magnitude were obtained. It is presumed that the obtained results related to this parameter, may be subject to some measurement error, resulting from the analog form of the reading.

Thus, significant differences were observed in the values of the results with respect to the results of numerical simulations, for which the heat flow extracted by water, in turn, was characterized by the dominant magnitude among all heat loss streams considered. The inconsistency of the values obtained through testing can also be confirmed by literature data, indicating that the average value of engine cooling losses is 26% [18]. Other component quantities of the energy balance obtained by numerical simulations also showed a significant deviation from the results of bench tests. Despite the noticeable differences for the two chosen paths (simulation and measurement), similar values of the overall efficiency of the engine η_o, were registered, with the numerical software taking the parameter to higher values, regardless of the engine's operating condition. In general, however, it should be borne in mind that the engine modeled in the Blitz-PRO numerical software represented values for a "new" engine, which in turn was not possible to verify the test object on the test bench.

Further analyzing the results obtained from the measurements, the component $\dot{Q}_r$, which is the residual heat dissipation stream (the stream of acoustic energy and mechanical vibration of the entire power unit), was juxtaposed as a summed value with the heat flow absorbed by the oil $\dot{Q}_{oil}$. This approach was used because the stream of residual heat dissipated is a measure of energy losses not included in the heat balance [7]. Then, for the reference condition, the value obtained was $\dot{Q}_{oil} + \dot{Q}_r = 1.527\ \text{kW}$. The value of the indicated power was $P_i = 8.104\ \text{kW}$, while the effective power was $P_e = 5.074\ \text{kW}$, with thermal efficiency $\eta_{th} = 37.748\ \%$, mechanical efficiency $\eta_m = 62.612\ \%$ and overall efficiency $\eta_o = 23.634\ \%$.

Table 3. Components of the energy balance of the Andoria S320 engine (test results)

		Reference condition	Throttled air intake		Reduced injection pressure	
Parameter	Unit	Value	Value	δ_{REF} [%]	Value	δ_{REF} [%]
$\dot{Q}_{fuel}$	[kW]	16.366	15.969	2.429	15.942	2.591
$\dot{H}_{air}$	[kW]	5.101	5.208	2.097	5.159	1.135
$\dot{H}_{exh}$	[kW]	9.943	9.971	0.290	9.825	1.179
$\dot{Q}_{cool}$	[kW]	0.054	0.046	14.865	0.057	5.405
$\dot{Q}_{amb}$	[kW]	1.760	1.764	0.255	1.784	1.368
$\dot{Q}_{oil} + \dot{Q}_r$	[kW]	1.608	1.527	5.049	1.230	23.492
P_i	[kW]	8.104	7.869	2.897	8.205	1.257
P_m	[kW]	3.030	2.836	6.381	3.147	3.853
P_e	[kW]	5.074	5.032	0.817	5.059	0.293
η_{th}	[%]	37.748	37.157	1.565	38.855	3.014
η_m	[%]	62.612	63.953	2.142	61.653	1.531
η_o	[%]	23.634	23.763	0.544	23.974	1.437

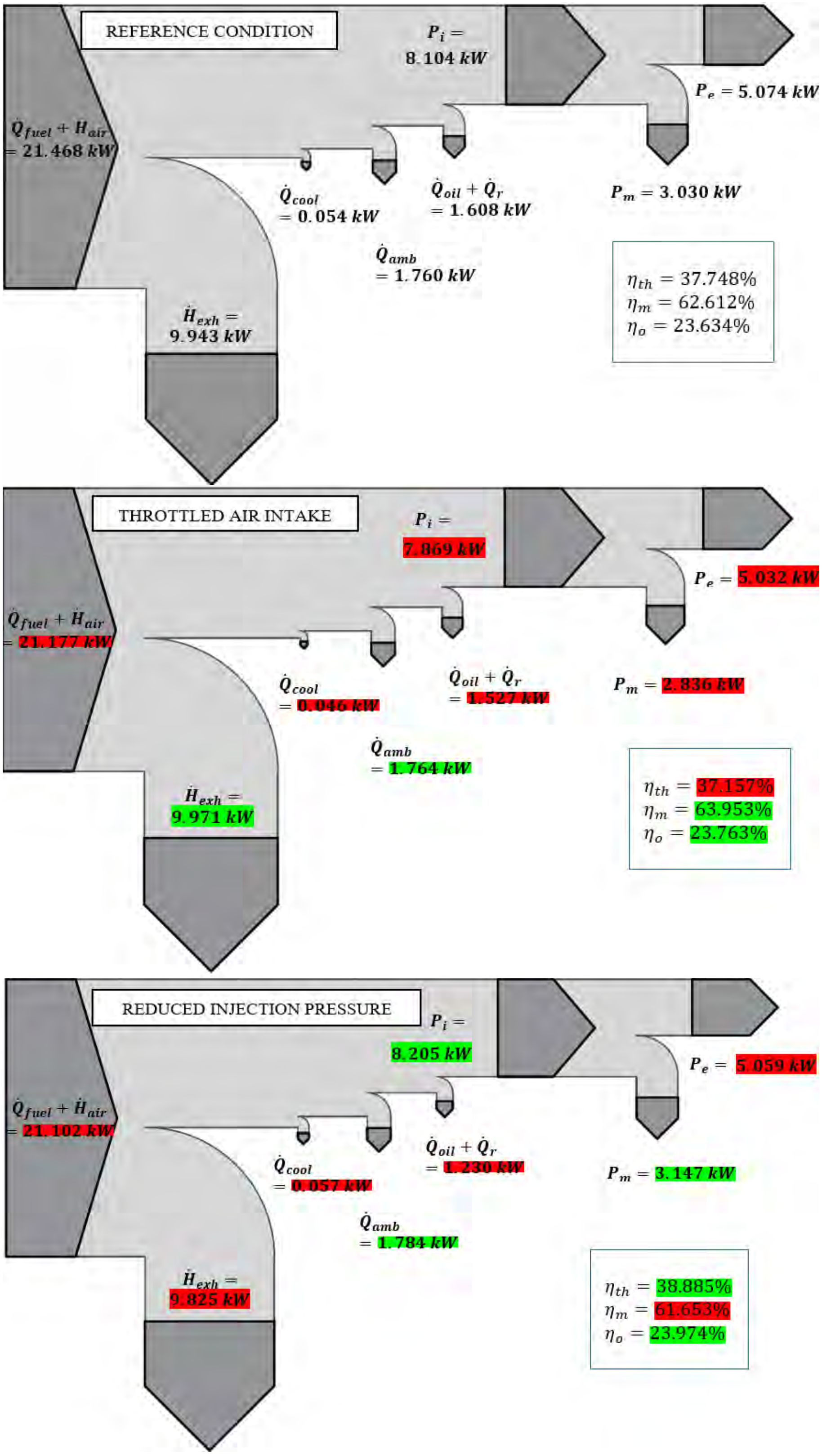

Fig. 5. Sankey diagrams – laboratory results

When the airflow through the filter was reduced by 50%, there was a slight deviation from the reference condition. The input power stream decreased slightly to a value of 21.177 kW (a decrease of 1.35%), indicating a minimal effect of this type of implemented damage on the considered parameter. There was also a 2.9% decrease in induced power P_i from 8.104 kW to 7.869 kW. The consequence of this was also a decrease in the thermal efficiency of the engine η_{th}. Since the mechanical loss power decreased from the reference condition by 6.38%, the overall benefit was observed with a minimal increase in mechanical efficiency η_m, equal to 2.14% (η_m = 63.953 %).

For the condition with reduced fuel injection pressure (17 MPa → 15 MPa), no significant changes were observed in the values of the components of the engine heat balance parameters. The largest deviation from the reference value (as much as 23.5%) was obtained for the heat flow extracted by oil $\dot{Q}_{oil}$, but since this is the resulting value of the other components, it proves difficult to adequately justify the possible reason for such a deviation. As a result of the small changes (relative to the reference condition) in the losses in the form of heat streams, the thermal, mechanical, and overall efficiencies also did not change significantly. Nevertheless, the overall efficiency η_o increased by 1.44% relative to the condition characterized by normal engine operation.

One of the reasons for the discrepancies in the results obtained by simulation and during laboratory testing may be different engine cooling conditions. While the simulation assumes the flow of coolant through the engine, the laboratory bench considers cooling by evaporation of water in the cooling tank. This and several smaller differences between the engine implemented in the program and that on the test bench can result in differences when validating both results.

4. Conclusions

Summarizing the research, calculations, and analyses carried out, the following conclusions were drawn:

- The assumption of carrying out numerical simulations was fulfilled, as changes were recorded in those values of the heat balance components that could be associated with the damage introduced into the model.
- Conducting tests under an engine load equal to 38% of rated power, was in line with the stated goal of verifying that, in a situation where testing at operating load is not possible, the engine's functional systems provide a diagnostic signal in the form of changes in the components of the energy balance. The results obtained confirmed consistency with existing literature conclusions, indicating that low-load tests are unable to provide a satisfactory result.
- It was shown that, regardless of the fault implemented, in the case of both the intake air system and the fuel supply system malfunctions, none of the balance components showed significant deviations from the reference condition. Variations of 2–3% are below the standard statistical error, caused, among other things, by the measurement accuracy of the instruments used, but also by the possibility of misreading analog readings.
- The following are considered to be the causes of incorrect (in relation to theoretical knowledge) increase/decrease in the value of the heat balance component: for simulations, inferior combustion conditions due to changes in the functional systems of the engine, for tests, insufficient water cooling. Different input data, such as technical condition, laboratory conditions, or a correct, but idealized calculation algorithm, are considered to be the reason for the lack of compatibility between the model and the tests.
- Engine load affects the way heat is released, as a higher fuel injection rate leads to faster injection and more intense combustion. An increase in injection speed causes the injection time to increase more slowly than the fuel dose, and combustion occurs more simultaneously. At a lower load, the auto-ignition delay lengthens, which reduces the maximum heat release rate in the initial phase of combustion. This phenomenon and others accompanying it simultaneously affect the various components of the engine's heat balance.
- On the test bench, it was not feasible to evaluate the mechanical and thermal condition of the engine's functional systems, even for the reference case. It was also not possible to input the engine's technical condition into the Blitz-PRO simulator. This may have had some impact on the results.
- The results obtained suggest continuing work on the development of the numerical software used, given its high potential.

Nomenclature

BDC	bottom dead center
$\dot{H}_{air}$	air enthalpy stream
$\dot{H}_{exh}$	exhaust gas enthalpy stream
IC	internal combustion
p_{amb}	ambient air pressure
P_e	effective power
P_i	indicted power
P_m	mechanical power
P_N	nominal power
$\dot{Q}_{amb}$	ambient heat stream
$\dot{Q}_{cool}$	cooling heat stream
$\dot{Q}_{fuel}$	fuel heat stream
$\dot{Q}_{oil}$	oil heat stream
$\dot{Q}_r$	residual heat stream
t_{amb}	ambient air temperature
TDC	top dead center
δ_{REF}	difference from the reference condition
η_m	mechanical efficiency
η_o	overall efficiency
η_{th}	thermal efficiency

Bibliography

[1] Baldi F, Gabrielli C, Andersson K. From energy flows to monetary flows – an innovative way of assessing ship performances through thermo-economic analysis. 2012. https://publications.lib.chalmers.se/records/fulltext/159874/local_159874.pdf

[2] Blitz-PRO Software Manual (accessed on 12.11.2024). http://blitzpro.zeddmalam.com/application/index/about

[3] Bocheński C, Janiszewski T. Diagnostyka silników wysokoprężnych (Diesel engine diagnostics). Wydawnictwo Komunikacji i Łączności. Warszawa 1996.

[4] Duda K, Wierzbicki S, Mikulski M. An experimental analysis of performance and exhaust emissions of a CRDI diesel engine operating on mixtures containing mineral and renewable components. Combustion Engines. 2019;179(4):27-31. https://doi.org/10.19206/CE-2019-404

[5] Jaichandar S, Samuelrai D, Sathish Kumar M. Effects of varying injector opening pressure on the performance of a B20 JOME biodiesel fueled engine. Journal of Mechanical Engineering. 2019;16(1). https://doi.org/10.24191/jmeche.v16i1.6031

[6] KIGAZ 310 Technical Specifications (accessed on 12.11.2024). https://www.metris.pl/produkt/kimo-kigaz-310-analizator-spalin-z-sond-z-wymiennymi-czujnikami/

[7] Korczewski Z. Metodyka testowania paliw żeglugowych w rzeczywistych warunkach pracy silnika o zapłonie samoczynnym (Methodology for testing marine fuels under real compression ignition engine operating conditions). Wydawnictwo Politechniki Gdańskiej. Gdańsk 2022.

[8] Korczewski Z. Thermal efficiency investigations on the self-ignition test engine fed with marine low sulfur diesel fuels. Combustion Engines. 2019;178(3):15-19. https://doi.org/10.19206/CE-2019-303

[9] Minchev D, Gogorenko O. Effect of thermal inertia on diesel engines transient performance. Internal Combustion Engines. 2020;1:68-72. https://doi.org/10.20998/0419-8719.2020.1.09

[10] Optrand D32294-Q Technical Specifications (accessed on 12.11.2024). https://www.optrand.com/apsis.htm

[11] Paszota Z. Losses and energy efficiency of drive motors and systems. Polish Maritime Research. 2013;20(1):3-10. https://doi.org/10.2478/pomr-2013-0001

[12] Puzdrowska P. Diagnosis of marine internal combustion engines by means of rapidly variable temperature and composition of exhaust gas as an alternative or support for currently used diagnostic methods. Combustion Engines. 2025; 200(1):19-30. https://doi.org/10.19206/CE-193951

[13] Skobyłko J. Analiza możliwości wykorzystania w diagnostyce silnika o ZS wykresu Sankey'a (Analysis of the possibility of using Sankey diagram in the diagnostics of the diesel engine) Master's thesis. Gdańsk University of Technology. Gdańsk 2025.

[14] Software specification InfReC Analyzer NS9500LT (accessed on 12.11.2024). https://www.infrared.avio.co.jp/en/support/thermo/download/ns9500lt-dl/

[15] Sroka ZJ, Prakash S, Wlostowski R. Design of the turbocharger bearing arrangement to increase the overall efficiency of the combustion engine. Combustion Engines. 2022; 188(1):83-89. https://doi.org/10.19206/CE-142348

[16] Technical specifications of NEC Thermo Gear G30 thermal imaging camera (accessed on 12.11.2024). https://www.infrared.avio.co.jp/en/products/ir-thermo/lineup/g30/index.html

[17] Varbanets R, Minchev D, Kucherenko Y, Zalozh V, Kyrylash O, Tarasenko T. Methods of real-time parametric diagnostics for marine diesel engines. Polish Maritime Research. 2024;31(3):71-84. https://doi.org/10.2478/pomr-2024-0037

[18] Włodarski JK, Witkowski K. Okrętowe silniki spalinowe. Podstawy teoretyczne. (Ship internal combustion engines. Theoretical fundamentals). Wydawnictwo Akademii Morskiej w Gdyni. Gdynia 2006.

Patrycja Puzdrowska, DEng. – Faculty of Mechanical Engineering and Ship Technology, Gdańsk University of Technology, Poland.

e-mail: *patpuzdr@pg.edu.pl*

Jakub Skobyłko, Eng. – Faculty of Mechanical Engineering and Ship Technology, Gdańsk University of Technology, Poland.

e-mail: *s182565@student.pg.edu.pl*

Article citation info:
Magdziak-Tokłowicz M, Biskup A, Grzyb M, Prowans M, Szymczyk J. The significance of telemetric data collection in electric motorcycles. Combustion Engines. 2025;202(3):67-73. https://doi.org/10.19206/CE-204322

Monika MAGDZIAK-TOKŁOWICZ
Aleksander BISKUP
Michał GRZYB
Mateusz PROWANS
Jędrzej SZYMCZYK

Combustion Engines
Polish Scientific Society of Combustion Engines

The significance of telemetric data collection in electric motorcycles

ARTICLE INFO

Received: 30 December 2024
Revised: 14 April 2025
Accepted: 23 April 2025
Available online: 13 June 2025

Motorsport is a branch of the automotive industry that requires constant research and testing to gain a competitive edge. A small change in a vehicle's suspension settings or engine management can make the difference between winning and losing in a particular competition. In order to ensure success, the vehicle is often pushed to its limits, however, while maintaining the driver's safety, all with the option of using vehicle telemetry, which collects, transmits, and analyses vehicle data during and after driving. Operational parameters measured in real time are analyzed for future corrections and improvements. This paper presents an analysis of telemetry testing of an electric motorbike, related to energy consumption, power output, torque, and thermal conditions to improve the efficiency of the drivetrain on the Aragón circuit in Spain at the MotoStudent competition. The article also demonstrates how to validate the values of individual parameters obtained during calculations and simulations, as well as the impact of minor changes on these parameters. It also describes how telemetry helps in assessing the skills of drivers.

Key words: *motorcycle, rider behavior, telemetry system, vehicle performance, data acquisition system*

1. Introduction

Electric motorcycles are rapidly advancing in both consumer and competitive markets, driven by sustainable energy solutions and the demand for high-performance vehicles. While consumer models emphasize range and affordability, racing models prioritize torque delivery, battery efficiency, and thermal management to enhance track performance. In racing, these motorcycles present unique challenges and opportunities due to factors such as torque delivery, battery management, and thermal regulation. Effective data-driven approaches are critical for optimizing performance on and off the track.

As electric motorcycles face distinct challenges in energy efficiency, thermal regulation, and torque delivery, telemetric data collection has become a fundamental tool in motorsports, providing real-time insights into vehicle behaviour and environmental conditions to address these issues effectively. It enables engineers and riders to refine strategies, enhance technical adjustments, and improve overall performance. While telemetry is well established in traditional motorsports, its application in electric motorcycle racing remains an emerging field with significant potential for innovation [12].

This study examines the significance of telemetric data acquisition in optimizing electric motorcycle performance by analysing data collected during the MotoStudent competition at the Aragón racetrack in Spain, an event that provides a controlled yet highly competitive environment for evaluating real-world racing conditions. Using an advanced data logger and a custom-built data acquisition system, key performance metrics – such as acceleration, speed, cornering dynamics, and load distribution – were monitored. Based on that data optimization opportunities were identified, contributing to a deeper understanding of how telemetry can shape electric motorcycle racing.

Telemetry systems are essential for real-time data collection during races. Professional teams in MotoGP use telemetry to monitor parameters like tire temperature, brake pressure, and throttle input, allowing precise adjustments to engine settings and suspension dynamics. In electric motorcycles, telemetry focuses on battery state, motor efficiency, and energy consumption – critical metrics for optimizing energy use and extending vehicle range [5, 11]. Unique challenges such as thermal management and regenerative braking are addressed through telemetry insights, ensuring performance consistency under varying conditions [2, 5, 13, 19].

Effective vehicle control is essential for achieving optimal performance in motorcycle racing, influencing stability, handling, and rider confidence. Beyond energy management, telemetry plays a key role in monitoring suspension dynamics and tire grip, factors that significantly impact stability and cornering performance [8, 20]. Advanced systems track suspension travel, damping forces, and tire contact patches, allowing teams to fine-tune settings for improved handling. For electric motorcycles, telemetry optimizes traction control and regenerative braking, balancing energy recovery without compromising stability [6, 8, 9, 15, 20, 21].

Telemetry is also instrumental in analysing rider behaviour and refining training methodologies. By tracking throttle position, braking force, and lean angles, teams can identify areas for technique and strategy improvements. This is particularly relevant for electric motorcycles, where riders must adapt to instant torque delivery and the absence of engine braking [1, 10, 14, 17].

The integration of artificial intelligence has further transformed telemetry by enabling predictive analytics. AI models process vast datasets to forecast vehicle performance under different track conditions, optimize throttle maps, and enhance energy management in electric motorcycles [18, 21]. AI-driven telemetry supports strategic decision-making, leading to better race outcomes for both electric and combustion-engine motorcycles.

Finally, telemetry plays a crucial role in vehicle design and race strategy. Data-driven insights guide chassis development, energy-efficient cooling systems, and aerodynamic enhancements. In real-time race scenarios, telemetry informs pit stop planning, tire wear assessment, and energy conservation strategies – factors that can determine podium finishes [3, 4, 7, 16, 19].

In summary, telemetry has revolutionized motorcycle racing, offering data-driven solutions for performance optimization, strategic planning, and vehicle innovation. The integration of AI with telemetry further enhances its impact, allowing for predictive analytics that refine energy management, optimize real-time adjustments, and improve overall race strategies. As technology advances, future research should focus on improving telemetry accuracy, integrating new sensor technologies, and expanding AI applications to enhance electric motorcycle racing further.

2. Subject and research location

The research was conducted based on a data acquisition system designed and implemented for the prototype racing electric motorcycle LEM Tachyon. This motorcycle was built by a student team as part of their participation in the MotoStudent competition, the world championship of student motorcycle designs, with the final race taking place at the Aragón circuit in Spain.

The LEM Tachyon project was designed and built by the LEM Wrocław Motorsport student team from Wrocław University of Science and Technology. During its design, all elements, except for brakes tires and brakes which competition officials provided, were modeled and then subjected to theoretical loads that could occur on them within the framework of Finite Element Method (FEM) simulations. However, since this is a project built from scratch with custom parts, a comprehensive telemetric data acquisition system was also created to enable the assessment of the applied solutions and identify the weaknesses of various systems, allowing improvements for the design of future motorcycles.

The vehicle was built in accordance with the stringent requirements of the competition regulations, where the motorcycle's dimensions are based on the Moto3 class. The materials and manufacturing methods for individual components were optional but had to meet strength requirements that were tested during the competition. The frame was made of chromium-molybdenum steel tubes, while the subframe and fairings were made entirely of carbon fiber composite. The motorcycle's swingarm was milled and then welded from 7020 aluminum. The design features a reduction gear with a ratio of 1.83 to reduce the rotational speed on the active wheel of the chain drive. According to the datasheet, the motor has 48 kW maximum power and 22 kW nominal power with a maximum of 7500 rpm. The front tire is 87 mm wide and 576 mm in diameter. The rear tire is 113 mm wide and 602 mm in diameter. The maximum speed of the motorcycle, as planned for calculations, was 200 km/h, while the highest speed measured on the track was 193 km/h.

Different sensors were mounted, as shown in Fig. 1. These allowed us to measure acceleration values, rotational speeds of the engine shaft and individual wheels, GPS position, suspension travel, braking forces, throttle level, temperatures of the engine, gearbox, radiator, and battery. The entire system is based on the LG-μCAN11_Moto2-211 logger, which is typically used in Moto2 category races. It allows data acquisition at frequencies up to 800 Hz, which was used for suspension and break pressure analysis. Other sensors operated at frequencies between 12.5 Hz and 200 Hz. To ensure clarity regarding the sensors used and their respective measurements, Table 1 summarizes the key parameters captured during the study, including measurement ranges, units, and sampling frequencies.

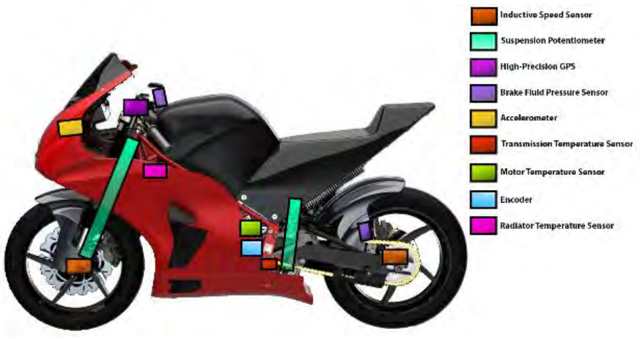

Fig. 1. Placement of sensors on the motorcycle

These sensors provided valuable insights into critical performance metrics such as braking forces, acceleration, and thermal behavior. All this data enabled us to improve the electric motor control to increase its efficiency, prevent failures of individual systems, and adapt the motorcycle to the specific rider. Thanks to this data and the changes applied based on their analysis, it was possible to prepare the motorcycle for the challenging conditions of the Aragón circuit.

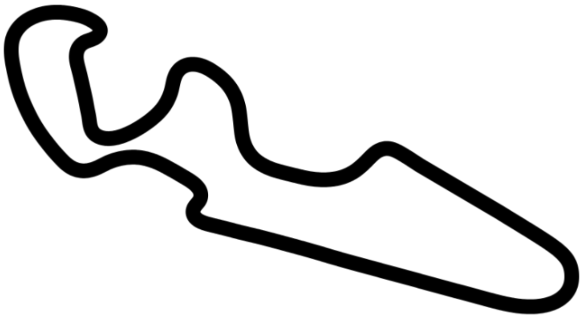

Fig. 2. Outline of the track shape of the Aragón Circuit

The Aragón circuit, shown in Fig. 2, is characterized by its complexity and presents many challenges for both riders and motorcycles during races. It features long straights, the longest being 1211 meters, as well as tight turns. Additionally, the total difference between the lowest and highest points of the track is 50 meters, with a maximum drop of 7.2%. The track length is 5.078 kilometers, and the width varies from 15 meters on the straights to 12 meters in other sections. Another aspect of this track is its heterogeneous surface throughout its length, resulting in changing traction conditions.

Table 1. Embedded sensors and data acquisition frequency

Name in data	Sensor	Measured parameter	Unit	Sampling frequency [Hz]	Notes
ACC_X, ACC_Y, ACC_Z	Accelerometer	Acceleration	m/s²	400	Used for analyzing vibrations and dynamics
BRAKE_F	Brake fluid pressure sensor (front)	Brake force of front system	Bar	800	Critical for managing high-speed braking stability
BRAKE_R	Brake fluid pressure sensor (rear)	Brake force of rear system	Bar	800	Used in sudden braking scenarios on straights
Latitude, Longitude	High-precision GPS	Geographic position	deg	12.5	
SV_Motor_Temperature	Motor temperature sensor	Motor temperature	°C	400	Evaluates drivetrain thermal management
SUSP_F	Suspension potentiometer (front)	Front suspension travel	mm	800	Provides data for optimizing front suspension behavior
SUSP_R	Suspension potentiometer (rear)	Rear suspension travel	mm	800	Tracks rear suspension response to braking and acceleration
V_Front	Inductive speed sensor (front)	Front wheel speed measurement	m/s	200	Used to estimate slip ratio and track braking performance at the front wheel
V_Rear	Inductive speed sensor (rear)	Rear wheel speed measurement	m/s	200	Used to analyze speed, traction and braking performance
TEMP_Transmission	Transmission temperature sensor	Transmission system temperature	°C	12.5	Monitors gearbox thermal performance
SV_RPM	Encoder	Rotational position of the motor	deg	200	Tracks angular displacement for motor rotation
SV_Heatsink_temp	Radiator temperature sensor	Coolant temperature in radiator	°C	50	Ensures cooling system operates within optimal limits

That imposes a unique challenge for both the rider and the motorcycle. The rider must adapt seamlessly to a variety of riding conditions, while the motorcycle needs to be highly adjustable to achieve the best settings for any scenario. A specialized data acquisition system plays a critical role in bridging the gap between on-track performance and the decision-making process, ensuring precision and efficiency in adjustments.

3. Studies conducted and results

The measurement tests were carried out at the MotoStudent competition in Spain during the main race. Data collection included six full laps on the Aragón circuit. Initially, parameters such as engine speed and torque were analyzed to see how the driver loads the electric motor during each lap. The motor load parameter is important because it gives us the answer to how energy is consumed during each lap, what times the driver achieves each time, and how the motor load affects the heating process of the motor and battery. Each lap was analyzed separately, and in Fig. 3, the full range of engine speeds can be seen during the run. The average engine speed for all runs was 4052.42 rpm. The driver was fastest on the second lap with a time of 2:27:594 with an average engine speed of 4268.90 rpm and a torque of 28.38 Nm – Fig. 4.

In Figure 4, the engine's operating range can be seen with load range and the cumulations in the middle operating range.

The fifth lap was the slowest, with a time 13 seconds longer. The engine workload was completely in the other work ranges, as can be seen in Fig. 5. The average speed was 3851.94 rpm with an average torque of 21.13 Nm. The results from each lap of the race are illustrated in Table 2.

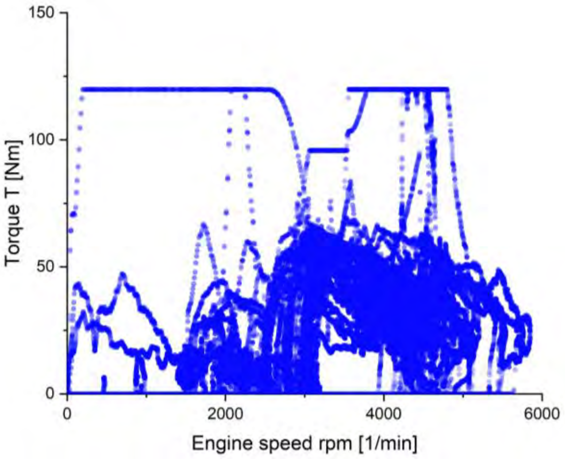

Fig. 3. Engine speed-to-torque graph for six laps

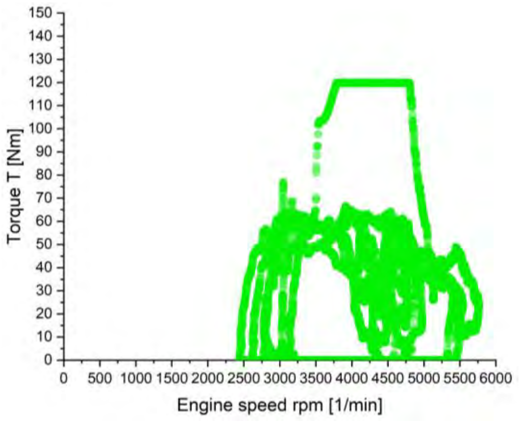

Fig. 4. Engine speed-to-torque graph for the fastest second lap

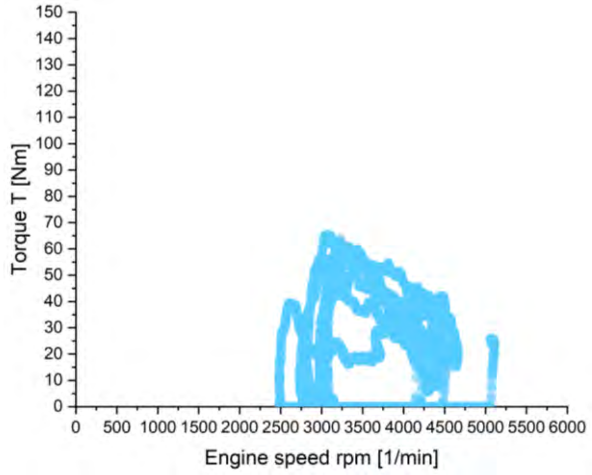

Fig. 5. Engine speed-to-torque graph for the slowest fifth lap

Table 2. Average engine parameters for each lap

Lap number	Average Torque T [Nm]	Average engine speed [rpm]	Lap time t [s]	Average speed V [m/s]
1	26,00	4183.34	2:29.911	33.35
2	28.38	4268.90	2:27.594	33.96
3	22.87	4037.05	2:34.474	32.42
4	23.03	4037.12	2:34.314	32.46
5	21.13	3851.94	2:40.715	31.31
6	26.91	3936.15	2:37.835	31.74

The important aspect that can be analyzed to improve performance and reduce lap times is the use of data from brake pressure sensors and throttle opening values. Analysis of these parameters allows for the development of more effective driver energy management tactics. Reducing the use of brakes in favor of driving using inertia enables a significant reduction in energy consumption, resulting in greater energy efficiency. In addition, less strain on the drivetrain leads to lower temperatures, preserving thermal reserves for moments requiring more power, for example, during dynamic acceleration on straight sections of the track.

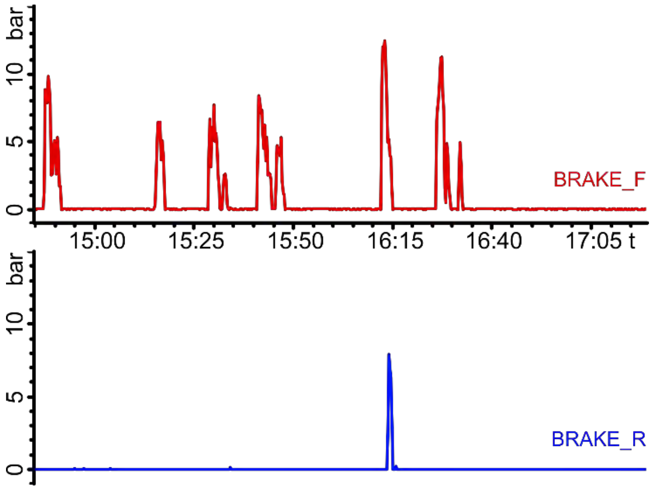

Fig. 6. Brake pressure plot for the fourth lap

In Figure 6, the brake pressure values are presented in correlation with the vehicle's position on the track. The inner curve, labelled BRAKE_R, represents the pressure in the rear brake system, while the outer curve, labelled BRAKE_F, illustrates the pressure in the front brake system at the same moments.

The analysis of the graph from Fig. 6 shows that the rear brake is rarely used, particularly during instances of sudden and intense braking. Conversely, the front brake is employed more frequently, indicating its critical role in managing speed and maintaining stability while navigating different sections of the track. The presented data reflects the expertise of an experienced rider who demonstrates a profound understanding of the dynamics of electric motorcycle handling.

Table 3. Min-max table for brake pressures for all laps

Lap ID	1	2	3	4	5	6
Total laps	1	2	3	4	5	6
Time [min]	2:29.9	2:27.6	2:34.5	2:34.3	2:40.7	2:37.8
Front brake pressure minimum brake_F [bar]	0	0	0	0	0	0
Front brake pressure maximum brake_F [bar]	14.8	13.5	14.2	13	14.2	11.9
Front brake pressure average brake_F [bar]	1.1	1.2	0.9	0.8	0.7	0.7
Rear brake pressure value minimum brake_R [bar]	0	0	0	0	0	0
Rear brake pressure value maximum brake_R [bar]	11	0	0	9	0	0
Rear brake pressure value average brake_R [bar]	0	0	0	0	0	0

Throughout all six laps, as Table 3 presents, brake pressure values range from 0 to 14.8 bars, highlighting a precise and deliberate approach to braking. Furthermore, Fig. 6 shows that the brakes are used almost exclusively before turns, underscoring a well-developed energy management strategy. This approach not only minimizes energy consumption but also optimizes the use of drivetrain reserves on straight segments of the track, constituting a fundamental aspect of efficient riding.

A crucial stage in the development and refinement of a motorbike lies in optimizing the suspension system, a fundamental component of any vehicle. The suspension must ensure optimal traction and stability throughout the lap, directly influencing performance and safety. By accurately acquiring suspension travel data, engineers can fine-tune the suspension settings with precision, enabling the motorbike to adapt seamlessly to both the rider's preferences and the specific conditions of the track.

Figure 7 shows suspension travel data overlaid over the Aragon track map. The inner curve represents front suspension travel values, while the outer curve represents rear suspension travel data. These values are highly correlated to braking data and acceleration data, as these are the main causes of changes in motorcycle dynamics.

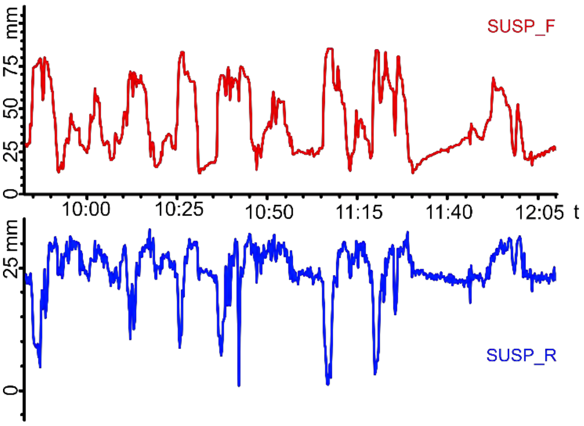

Fig. 7. Suspension plot, illustrating suspension behavior and dynamics across different sections of the circuit at second lap

Table 4. Minimum and maximum values of front and rear suspension travel recorded across all six laps of the race at the Aragón Circuit

Lap ID	1	2	3	4	5	6
Time [min]	2:29.9	2:27.5	2:34.4	2:34.3	2:40.7	2:37.8
Front suspension displacement minimum Susp_F [mm]	10.3	9.95	9.98	10.74	13.5	16.56
Front suspension displacement maximum Susp_F [mm]	88.8	85.39	89.55	84.04	82.55	80.64
Rear suspension displacement minimum Susp_R [mm]	0.69	0.7	0.73	0.74	1.6	2.56
Rear suspension displacement maximum Susp_R [mm]	33.66	33.87	32.97	33.45	33.81	33.31

Based on the suspension settings, the front suspension travel ranges from 9 mm to 90 mm, while the rear suspension travel varies between 0 mm and 40 mm. Table 4 illustrates the minimum and maximum suspension travel values recorded across all six laps of the race at the Aragón Circuit, providing a comprehensive overview of suspension dynamics throughout the event.

Additional visualizations, such as histograms and XY plots, can be generated to conduct a more precise analysis of the suspension system's behavior, providing more detailed insights for the engineering team. By correlating data from the linear suspension potentiometer with accelerometer readings, a comprehensive understanding of suspension dynamics and its interaction with external forces can be achieved. This data can then be used to fine-tune the suspension setup, optimizing it for specific track conditions and rider preferences. Such adjustments help enhance traction, stability, and overall performance, ultimately leading to faster lap times and improved vehicle handling.

In racing motorcycles, virtually all components are pushed to their limits, significantly affecting their operating conditions. In this regard, electric motorcycles are not fundamentally different from their combustion-engine counterparts. Continuous monitoring of key parameters such as temperature, pressure, displacement, and forces acting on components provides valuable information. This enables the full potential of each motorcycle component to be utilized while ensuring the highest level of safety.

The drivetrain, which is a fundamental factor in motorbike performance, is not exempt from this. In the case of the LEM Tachyon, the electric motor's thermal management was the main limiting factor in the overall performance. By being able to always analyze the motorcycle's condition with precision during the test sessions, drivetrain engineers were able to make data-driven decisions about motor controller settings, resulting in an exceptional level of efficiency.

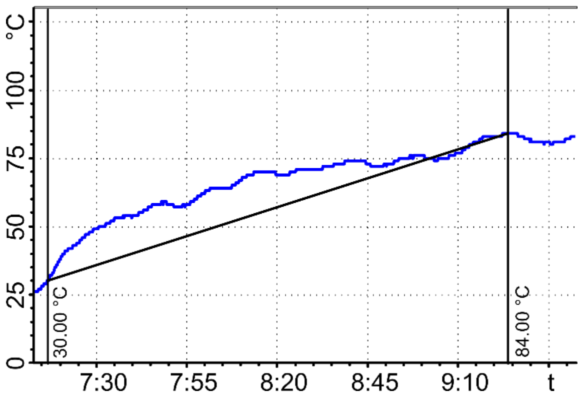

Fig. 8. Line plot of motor temperature over time in first lap

As illustrated in Fig. 8, despite the implementation of both on-board and external cooling systems to ensure the motor starts at the lowest possible temperature, the first lap sees a significant temperature increase of approximately 60 degrees Celsius. This rapid rise is attributed to the high current supplied by the motor controller to achieve the desired power output, which allows the vehicle to maintain a competitive edge. Furthermore, the motor's design limits the efficiency of heat transfer to the cooling system, thereby reducing its ability to regulate the drive unit's temperature effectively.

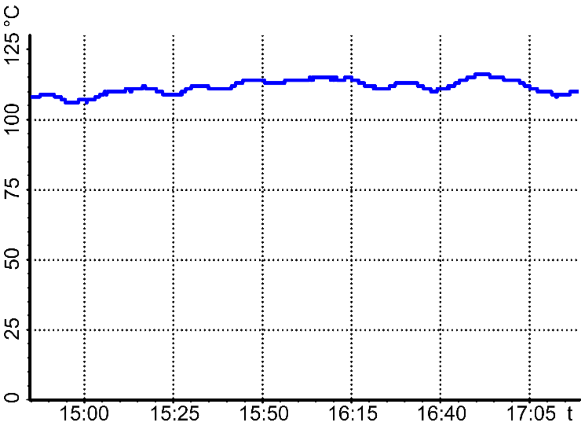

Fig. 9. Line plot of motor temperature over time in lap 4

In subsequent laps, as shown in Fig. 9, the temperature of the motor remains at a consistently elevated level. At this juncture, the onus shifts to the driver's ability to effectively manage the temperature through the utilization of available data, including motor temperature, coolant inlet and outlet temperatures, and other drivetrain performance metrics. This data provides a crucial foundation for the fine-tuning of the motor controller and the development of adaptive strategies. It offers evidence-based decision-making and immediate feedback on the efficacy of adjustments, thus enabling teams to optimize performance even under challenging thermal conditions.

4. Summary of results

The study underscores the significant role of telemetric data acquisition in enhancing the performance of electric motorcycles in competitive racing scenarios. Comprehensive telemetry data collected from the LEM Tachyon motorcycle during the MotoStudent competition at the Aragón circuit provided critical insights into various performance parameters, including engine speed, torque, suspension dynamics, braking forces, and thermal conditions. These data highlighted the intricate interplay between motor performance, energy efficiency, and thermal management.

The analysis revealed that optimal engine operation occurred at specific torque and rpm ranges, which varied across laps. The fastest lap was achieved at an average engine speed of 4268.90 rpm with a torque of 28.38 Nm, indicating the importance of precise load and energy management for competitive performance. Conversely, slower lap times were associated with higher drivetrain inefficiencies and suboptimal energy utilization. Data from brake pressure sensors and throttle usage demonstrated how strategic adjustments, such as reduced braking and inertia-based driving, contributed to improved energy efficiency and thermal control.

Suspension travel data emphasized the role of fine-tuning suspension settings to adapt to the track's unique characteristics. Front and rear suspension displacement patterns provided insights into load distribution and stability during braking and acceleration, enabling targeted improvements for handling and traction. Furthermore, drivetrain analysis highlighted thermal management as a limiting factor in maintaining consistent motor performance. The rapid rise in motor temperature during initial laps underscored the need for enhanced cooling systems and adaptive controller strategies.

The Aragón circuit's demanding conditions, characterized by its varying topography and traction levels, posed additional challenges for both the rider and the motorcycle. Telemetric data acquisition bridged the gap between on-track performance and decision-making processes, allowing engineers to apply data-driven refinements in real time.

5. Conclusion

The findings demonstrate that telemetric data acquisition is indispensable for the optimization of electric motorcycle performance in competitive settings. By capturing and analyzing data from a wide array of sensors, engineers and teams can identify performance bottlenecks, refine vehicle settings, and enhance energy efficiency. The study highlights several critical outcomes:

1. Energy and Thermal Management: Effective utilization of telemetric data enables the identification of optimal energy usage patterns and the mitigation of thermal inefficiencies, contributing to sustained motor performance during races.
2. Suspension Optimization: Detailed analysis of suspension dynamics facilitates precise adjustments to improve stability, traction, and rider comfort, enhancing overall vehicle handling.
3. Strategic Adjustments: Data-driven insights into braking and motorbike handle use support the development of adaptive strategies that optimize energy consumption and preserve drivetrain integrity.
4. Adaptability to Track Conditions: The ability to monitor and respond to the Aragón circuit's complex characteristics in real time showcases the versatility of telemetric systems in addressing diverse racing challenges.

The research confirms the potential of telemetric systems to drive innovation and efficiency in electric motorcycle racing. Future studies should focus on integrating advanced cooling technologies, refining sensor accuracy, and employing artificial intelligence for predictive analytics. These advancements will further unlock the capabilities of telemetric data, paving the way for more competitive, efficient, and sustainable racing solutions.

Acknowledgements

The article was written in cooperation with Autocomp Management Sp. z o.o. from Szczecin, Research and Development Center – Producer of simulators on the military and civilian market from Poland.

Bibliography

[1] Bartolozzi M, Boubezoul A, Bouaziz S, Savino G, Espie S. Data-driven methodology for the investigation of riding dynamics: A motorcycle case study. IEEE Trans Intell Transp Syst. 2023;24:10224-10237. https://doi.org/10.1109/TITS.2023.3271790

[2] Bonini F, Rivola A, Martini A. Braking torque estimation through machine learning algorithms. Materials Research Proceedings. 2023;26:213-218. https://doi.org/10.21741/9781644902431-35

[3] Calderón AG, Galbeño Ruiz G, Carlos A, Bohórquez G. GPRS telemetry system for high-efficiency electric competition vehicles. 2013 World Electric Vehicle Symposium and Exhibition (EVS27). Barcelona 2013. https://doi.org/10.1109/EVS.2013.6914788

[4] De Carlo M, Simeone E, Radano L, Carello M. A telemetry-driven architecture for the development of data-intensive race strategies. 2024 International Conference on Artificial Intelligence, Computer, Data Sciences and Applications (ACDSA), Victoria 2024. https://doi.org/10.1109/ACDSA59508.2024.10467558

[5] Cossalter V, Bellati A, Doria A, Peretto M. Analysis of racing motorcycle performance with additional considerations for the Mozzi axis. Veh Syst Dyn. 2008;46:815-826. https://doi.org/10.1080/00423110802037073

[6] Cossalter V, Doria A, Formentini M, Peretto M. Experimental and numerical analysis of the influence of tyres properties on the straight running stability of a sport-touring motorcycle. Veh Syst Dyn. 2012;50:357-375. https://doi.org/10.1080/00423114.2011.587520

[7] Cossalter V, Doria A, Garbin S, Lot R. Frequency-domain method for evaluating the ride comfort of a motorcycle. Veh Syst Dyn. 2006;44:339-355. https://doi.org/10.1080/00423110500420712

[8] Fouka M, Nehaoua L, Arioui H. Motorcycle state estimation and tire cornering stiffness identification applied to road safe-

ty: Using observer-based identifiers. IEEE Trans Intell Transp Syst. 2022;23:7017-7027. https://doi.org/10.1109/TITS.2021.3066417

[9] Fujii S, Shiozawa S, Shinagawa A, Kishi T. Steering characteristics of motorcycles. Veh Syst Dyn. 2012;50(8):1277-1295. https://doi.org/10.1080/00423114.2011.607900

[10] Katayama T, Aoki A, Nishimi T. Control behaviour of motorcycle riders. Veh Syst Dyn. 1988;17:211-229. https://doi.org/10.1080/00423118808968903

[11] Leonelli L, Limebeer DJN. Optimal control of a road racing motorcycle on a three-dimensional closed track. Veh Syst Dyn. 2020;58:1285-1309. https://doi.org/10.1080/00423114.2019.1617886

[12] Markowski M, Szczepan S, Zatoń M, Martin S, Michalik K. The importance of reaction time to the starting signal on race results in elite motorcycle speedway racing. PLoS One. 2023;18. https://doi.org/10.1371/journal.pone.0281138

[13] Moreno D, Mucchi E, Dalpiaz G, Rivola A, Mucchi E. Multibody analysis of the desmodromic valve train of the Ducati MotoGP engine. Multibody Dynamics 2007, ECCOMAS Thematic Conference. Milano 2007.

[14] Ruzicka J. 2020 Smart Cities Symposium Prague (SCSP): Prague, June 25th, 2020. IEEE.

[15] Sharp RS, Evangelou S, Limebeer DJN. Advances in the modelling of motorcycle dynamics. Kluwer Academic Publishers 2004.

[16] Stincescu T, Zhao R, Ballantyne EEF, Stone DA, Foster MP. MATLAB-based high-performance electric motorbike energy model, utilising video data. 16th International Conference on Ecological Vehicles and Renewable Energies, EVER 2021. Monte-Carlo 2021. https://doi.org/10.1109/EVER52347.2021.9456609

[17] Tobiáš M, Porteš P, Zháňal L, Fojtášek J. Measurement and analysis of dynamic riding behavior of a motorcycle. Engineering Mechanics 2020. Institute of Thermomechanics of the Czech Academy of Sciences, Prague; 2020:488-491.

[18] Venceslau de Souto JI, Barbosa da Rocha Á, Duarte RNC, de Moura Fernandes E. Design and implementation of an embedded data acquisition system for vehicle vertical dynamics analysis. Sensors. 2023;23. https://doi.org/10.3390/s23239491

[19] Villa-Salazar AF, Gomez-Miranda IN, Romero-Maya AF, Velásquez-Gómez JD, Lemmel-Vélez K. Optimizing electric racing car performance through telemetry-integrated battery charging: A response surface analysis approach. World Electr Veh J. 2024;15(7):317. https://doi.org/10.3390/wevj15070317

[20] Zhang XD, Chen CK. A study of a cornering braking control system for a motorcycle. Appl Sci. 2022;12(24|):12575. https://doi.org/10.3390/app122412575

[21] Zhu D, Pritchard E, Dadam SR, Kumar V, Xu Y. Optimization of rule-based energy management strategies for hybrid vehicles using dynamic programming. Combustion Engines. 2021;184(1):3-10. https://doi.org/10.19206/CE-131967

Monika Magdziak-Tokłowicz, DEng. – Faculty of Mechanical Engineering, Wrocław University of Science and Technology, Poland.

e-mail: *monika.magdziak-toklowicz@pwr.edu.pl*

Aleksander Biskup – Faculty of Electronics, Photonics and Microsystems, Wrocław University of Science and Technology, Poland.

e-mail: *aleksanderbiskup@icloud.com*

Michał Grzyb – Faculty of Mechanical Engineering, Wrocław University of Science and Technology, Poland.

e-mail: *m.grzyb.lemwroclaw@gmail.com*

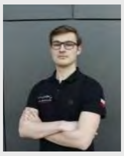

Mateusz Prowans – Faculty of Electronics, Photonics and Microsystems, Wrocław University of Science and Technology, Poland.

e-mail: *mateusz.prowans@gmail.com*

Jędrzej Szymczyk – Faculty of Information and Communication Technology, Wrocław University of Science and Technology, Poland.

e-mail: *jszymczyk99@gmail.com*

Article citation info:
Cebulska W, Hadrys D. Comparison of vibration emissions in electric and conventional cars. Combustion Engines. 2025;202(3):74-80. https://doi.org/10.19206/CE-204690

Wioletta CEBULSKA
Damian HADRYS

Combustion Engines
Polish Scientific Society of Combustion Engines

Comparison of vibration emissions in electric and conventional cars

ARTICLE INFO

Received: 22 November 2024
Revised: 5 May 2025
Accepted: 5 May 2025
Available online: 4 June 2025

Currently, great importance is attached to the issue of environmental protection, also in the context of the impact of transport on the environment. Limited fossil resources, climate change, and global warming are driving the automotive industry towards more efficient and sustainable solutions. These problems are driving car manufacturers to use new technologies and alternative drive systems. Examples of such vehicles are electric cars (EV) and hybrid cars (HEV or PHEV). The issue of the impact of using these means of transport on the emission of pollutants other than exhaust gases is important. An example of such emissions is vibrations. Cars with conventional drive generate vibrations from the operation of the combustion engine. All vehicles, both conventionally and alternatively driven, emit vibrations as a result of the operation of the drive system, suspension system, and interaction of tires with the road surface. Vibrations also arise from unevenness of the road surface. At first glance, it seems that vibrations are lower when driving an electric car. In this article, vibration measurements were performed inside an electric vehicle and a conventionally driven vehicle in urban and highway conditions.

Key words: *vibration emission, electric cars, electromobility, vibration measurements*

1. Introduction

Noise and mechanical vibrations accompany the operation of vehicles. Vibrations are a process in which physical quantities are variable as a function of time. Vibrations induced by a source are propagated by wave motion. These waves are transmitted through different media at different speeds, as a result of which kinetic energy (Ek) is converted into potential energy (Ep) and vice versa. Mechanical vibrations, the frequency band of which is in the range of 0.1–100 Hz, have an adverse effect on the human body. They are divided into shocks (changes in position to which the body reacts actively) and vibrations (the body reacts passively through the nervous system and organs). Exposure to vibrations can be short-term, in which the negative functional effects disappear after the vibrations cease, or long-term, causing health effects.

Vibration emissions in combustion cars are mainly due to the operation of the combustion engine, which generates vibrations during the combustion of the fuel mixture. These vibrations are transmitted by the drive system (gearbox, drive shaft) and the exhaust system. Vibrations can also be amplified by the operation of turbochargers, mufflers, and unevenness in the balance of moving elements, such as pistons and crankshaft.

In electric cars, vibration emissions are much lower because the electric engine operates more smoothly, without combustion processes and pistons. The lack of a gearbox eliminates jerks and additional sources of vibration. The main vibrations can come from small elements, such as engine bearings, cooling system fans, and road irregularities [1, 4, 11, 12].

2. Vibration measurements

Noise and mechanical vibrations accompany the operation of vehicles. Vibrations are a process in which physical quantities vary as a function of time. The basic quantities describing mechanical vibrations are displacement, vibration velocity, and vibration acceleration. The most common way to assess the effect of mechanical vibrations on the body is to use vibration acceleration values. A vibration signal may contain one component with a specific frequency (sinusoidal vibrations). However, complex vibrations consisting of many sinusoidal components are most common [7–9].

Due to the impact of vibrations, they can be divided into local vibrations (transmitted by limbs) and general vibrations (vibrations with a general effect). Whole-body vibrations refer to vibrations transmitted to the whole body. These vibrations can lead to health problems such as back pain, fatigue, and balance disorders. Reducing exposure to whole-body vibrations requires the use of appropriate shock-absorbing seats and ensuring an ergonomic work environment that minimizes the negative effects of mechanical vibrations. In local vibration measurements, based on the effective values of weighted vibration accelerations obtained by the meter during measurements, measured in all planes (x, y, z), the value of the vector sum of effective vibration accelerations is calculated according to formula (1):

$$a_{hvi} = \sqrt{a^2_{hwxi} + a^2_{hwyi} + a^2_{hwzi}} \qquad (1)$$

where: a^2_{hwxi}, $a\ ^2_{hwyi}$, $a\ ^2_{hwzi}$ – effective weighted vibration acceleration values, m/s^2, a_{hwi} – value of the vector sum of effective weighted vibration accelerations, m/s^2.

In the context of general vibrations, instead of the vector sum of the vibration acceleration, the dominant component is determined from the 3 planes x, y, and z. This means that the subsequent indices are determined for one dominant plane. Depending on which plane (x, y, or z) was selected as the value for evaluation, it should be multiplied by the appropriate factor: 1.4 for the x and y axes and 1 for the z axis. The calculation of the maximum value is determined by formula (2):

$$a_{wmax} = \max\{a_{wl1,}a_{wl2,} \dots a_{wln}\} \quad (2)$$

where: a_{wln} – selected highest value from 3 measurement planes (x, y or z), m/s^2, a_{max} – value of the vector sum of effective weighted vibration accelerations, m/s^2.

During vibration measurement, physical quantities are measured: acceleration, velocity and displacement of mechanical vibrations. For each of these values, the vibration amplitude can be given. This will be the difference between the lowest and highest momentary vibration level, half of this value. However, amplitude is not the most popular vibration measure. The most commonly used value is described as RMS. In the analysis of vibration signals, this is the most popular numerical value describing the average "vibration level" of a given machine, it is the so-called "effective value" of the signal.

The RMS indicator simply estimates the value of the vibration level independently of the amplitude value. The square of the signal value in the formulas for energy, power and RMS of the signal is important not only because of the negative values of the signals but also because of the possibility of analogous calculations in the frequency domain [5, 6, 14].

The interpretation of vibration data in the time domain (amplitude plotted against time) is limited to a few parameters in determining the vibration level: amplitude, peak value, and effective value, which are identified in the sinusoidal waveform. The RMS value is generally the most useful because it is directly related to the energy level of the vibration. Vibration is an oscillatory motion, so most vibration analyses aim to determine the rate of this oscillation or frequency. The number of times a full cycle of motion occurs in one second is the vibration frequency and is measured in Hz. For simple sinusoidal waves, the vibration frequency can be determined from observing the time domain waveform. When different frequency components and noise are added, spectrum analysis is necessary to obtain a clearer picture of the vibration frequency. In order to correctly determine the frequency spectrum, signal sampling is used. This is the number of samples taken in 1 second. The higher the sampling rate, the more accurately the signal is recorded [5, 6, 11, 16].

3. Impact of vibrations

Exposure to vibrations can be short-term, in which the negative functional effects disappear after the vibrations stop, and long-term, causing disease effects. Short-term exposure to vibrations can cause functional discomfort (e.g. motion sickness), irritation, excessive fatigue, insomnia and disruption of movement coordination. Research results show that exceeding 0.25 m/s^2 of the effective value of low-frequency vibration acceleration in the range of 0.1–0.315 Hz in the vertical direction causes undesirable symptoms [16, 18, 19, 21].

Prolonged exposure to vibrations can cause disorders of the organs and nervous centers. General fatigue, decreased efficiency, and reduced psychophysical efficiency occur. Disorders of the skeletal and joint systems in the cervical and lumbar spine, as well as shoulder, hip, and knee joints, occur. As a consequence, this can cause muscle and joint pain and spine ailments in all of its sections. Vibrations with frequencies corresponding to the natural vibration frequencies of internal organs are a major danger, as they can induce resonant vibrations of the organs, disturbing the temporary functioning of the body. Vibrations have a mechanical effect on the eyeballs, causing the image in the retina to shift, which manifests itself in the impression of a blurred image, deterioration of visual acuity, and difficulties in locating objects in space [2, 3, 6, 17]. The ISO 2631–1:1997 standard specifies comfort levels depending on the value of vibration acceleration in m/s^2 [16]:

- comfortable – below 0.315
- slightly uncomfortable – from 0.315 to 0.63
- quite uncomfortable – from 0.5 to 1
- uncomfortable – from 0.8 to 1.6
- very uncomfortable – from 1.25 to 2.5
- extremely uncomfortable – above 2.

3. Vibrations in electric vehicles

In vehicle operation, the greatest impact on vibrations during driving is the wheel contact with the road surface, with additional vibrations from the drive system and the drive unit. Factors inducing ground vibrations include changes in the contact forces between the vehicle wheel and the road surface, the reaction of the moving vehicle to geometric changes in the road surface, the vehicle's reaction to unevenness and momentary wheel lift-off states, forces resulting from wheel imbalance, as well as the air wave generated during vehicle movement [7–10]. Vibrations generated during driving are transferred to the person through the seat and platform, as well as through control elements such as the steering wheel. The excitations are transferred through the suspension to the vehicle body, then to the driver's and passenger seats. The seat should therefore provide adequate comfort and limit the impact of mechanical vibrations [10, 12, 14].

Vibrations emitted by a combustion engine vehicle seem to be greater than in the case of an electric vehicle, because they have an additional factor generating vibrations in the form of an internal combustion engine, as well as a gearbox and an exhaust system. It is believed that in electric vehicles, these vibrations are much smaller due to the lack of an internal combustion engine and other systems and rotating elements that emit vibrations. In the case of hybrid vehicles, the sources of vibrations are the same as in the case of internal combustion and electric vehicles. However, the issue of vibration emission while driving is different. These vibrations are caused by the work of the suspension system, shock absorption, and the cooperation of the tire with the road surface. They mainly depend on the type and construction, as well as the wear of the wishbones, shock absorbers, springs, wheel balance, and the type of tires and the condition of the road surface. It seems that vibrations in cars with conventional drives and with alternative drives while driving are similar [7–10, 19, 20]. The frequencies of vibrations emitted by electric and internal combustion engines differ depending on their design, rotational speed, and type of work. Combustion engines can emit vibrations in a wide range of frequencies, usually from a few Hz to several kHz. Lower frequencies (around 20–100 Hz) are associated with engine vibrations and vibrations resulting from the operation of the drive unit. Higher frequencies (up to several kHz) can occur as a result of various processes, e.g. exhaust system vibrations. Electric motors also emit vibrations in the range of several Hz to several kHz, but have different characteristics. The operating frequency of an electric motor is related to the supply frequency, for example, 50 Hz or 60 Hz for AC motors. Vibrations can be generated by the rotation of the rotor, which leads to vibrations in the range of about 20 Hz to 1 kHz [12, 13, 20–22].

4. Equipment and research subject

The vibration measurement system Simcenter SCADAS XS was used in the vibration tests. This is an analyzer that, thanks to the data acquisition template, can operate as a stand-alone device. Depending on the needs of the SCADAS XS, it can be wirelessly controlled from a tablet using the Simcenter Testlab Scope App. In these tests, this application was used to measure and record data. The application allows for configuration, starting, or stopping data acquisition [14]. The measuring device, together with the seat vibration transducer, is shown in Fig. 1, while the technical data are in Table 1.

Fig. 1. Siemens LMS SCADAS XS vibration measurement system with data acquisition device – left side, three-axis seat cushion – right side

Table 1. Technical parameters of the Siemens LMS SCADAS XS vibration measurement system [17]

Feature	Value
Control	Wireless from a tablet app
Sampling	50 kHz per channel
Sensitivity	For a seat-mounted vibration transducer: 100 mV/g
BNC connector	For microphones or single-axis accelerometers
LEMO connector	For single cables (with multiple cables inside) that allow three channels of a triaxial accelerometer to be connected
CAN-bus	Controller Area Network (CAN) for reading digital bus from built-in vehicle sensors

Fig. 2. Conventional drive car Dacia Sandero

The objects (Fig. 2) of the research are two passenger cars. A conventionally powered car of the Dacia Sandero III brand with a 1.0 Tce turbocharged petrol engine with an output of 67 kW. An electric car of the Dacia Spring brand with a synchronous motor with a permanent magnet, with an output of 33 kW. Both vehicles were manufactured in 2021 and had Crossover bodies.

Table 2. Technical data of the Dacia Sandero [13]

Model	Dacia Sandero III Hatchback
Drive	Conventional
Engine	1.0 Tce petrol turbocharged
Displacement	999 cm^3
Engine power	67 kW, 90 HP for 4600 rpm
Torque	160 Nm for 2100–3750 rpm
Drive	Front axle
Range	962 km
Current weight	1152 kg
Year of production	2021

Fig. 3. Electric drive car Dacia Spring

Table 3. Technical data of the Dacia Spring [13]

Model	Dacia Spring Crossover Electric
Drive	Electric
Engine	Permanent magnet synchronous
Engine power	33 kW, 45 HP for 3000–8200 rpm
Torque	125 Nm for 500–2500 rpm
Drive	Front axle
Battery	lithium-ion
Gross battery capacity	27 kWh
Charging time socket/fast	13 h/1h
Range	230 km
Own weight	920 kg
Year of production	2021

5. Research

5.1. Vibration measurements on site

Vibration measurements using the Siemens vibration measurement system were carried out in the vehicle operation laboratory at the Faculty of Transport and Aeronautical Engineering of the Silesian University of Technology. During the tests, the cars were placed on a lift. The measurements were taken using a seat transducer placed on the driver's seat (general vibrations) in three axes, X, Y, and Z. In the X axis, values were measured along the vehicle axis, in the Y axis transversely to the vehicle axis, while in the Z axis, vertical vibration values. During vibration measurements, the overall vibrations affecting the driver through the seat while driving were recorded. This measurement was based on an analysis in accordance with formula (2), which describes the method of assessing human exposure to vibrations in accordance with applicable standards. The tests were carried out in the vehicles while the driver was engaged at a speed of 20 km/h. Each time, 10 measurements were taken, each lasting 5 seconds. The sampling frequency was 51,200 Hz. Example time courses and frequency characteristics were presented in the form of graphs

4 to 5. The collective results of the effective value of vibration acceleration are presented in Fig. 6.

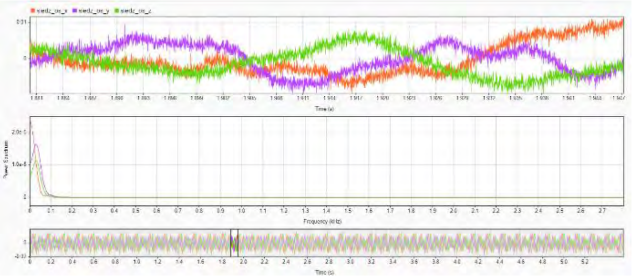

Fig. 4. Time course and frequency characteristics of the acceleration of vibrations of a conventionally driven car transferred to the driver (general vibrations) during tests at the test stand

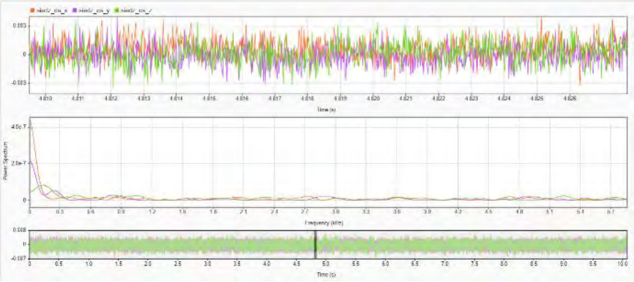

Fig. 5. Time course and frequency characteristics of vibration acceleration of an electric car transferred to the driver (general vibrations) during tests at the test stand

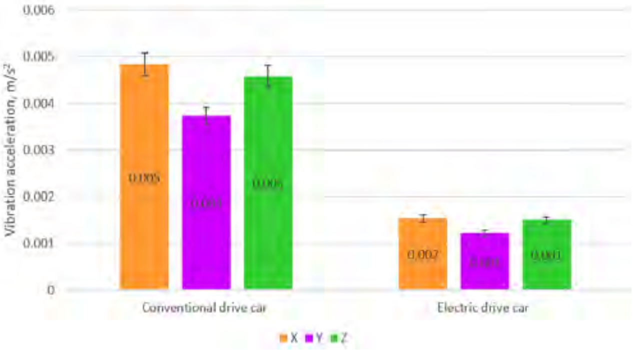

Fig. 6. Effective values of vibration acceleration in the X, Y, Z axes in vehicles measured on the driver's seat (general vibrations) during bench tests

Vibration measurements on the driver's seat showed that the lowest effective values of general vibration acceleration were recorded in the electric car (0.0021 m/s^2). General vibrations transferred to the driver during the operation of the combustion engine amounted to 0.0067 m/s^2. The vibration acceleration values were similar in all axes.

Vibrations in a combustion car have a higher level, with dominant frequencies below 0.5 kHz. They result mainly from the operation of the engine, drive system, and resonance of mechanical elements. In an electric car, vibrations are smaller, and their main band is below 0.4 kHz, which may be related to the operation of the electric engine and transmission. In short, combustion cars generate more complex vibrations, while electric cars are quieter, but have characteristic vibrations resulting from the electric drive.

5.2. Vibration measurements while driving

Vibration measurements inside the vehicle were taken in city and motorway traffic. The effective values of the acceleration of general vibrations were measured at speeds of 30 km/h and 50 km/h in city traffic and 100 km/h and 140 km/h in motorway traffic. The measurements were taken using a Siemens vibration measurement system with a seat measuring vibrations in three axes X, Y and Z, which was placed on the driver's seat. Each time, 10 measurements were taken, each lasting about 10 seconds. The temperature during the measurements was about 12°C, the weather was windless and without rain. The measurements were presented as an arithmetic mean of the collected results, rejecting the lowest and highest values. Examples of time histories of vibration amplitudes and frequencies prepared in MATLAB are shown in Fig. 7 and 8. The results are presented in the form of Fig. 9 to 12.

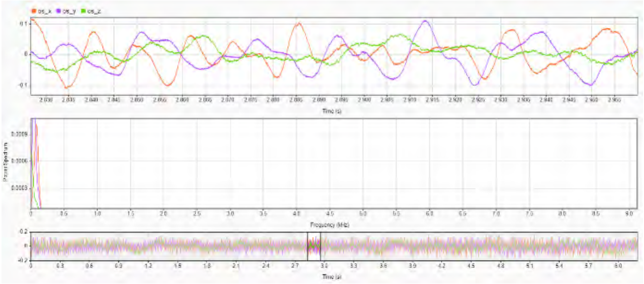

Fig. 7. Example of time course and frequency characteristics of vibration acceleration of an electric car

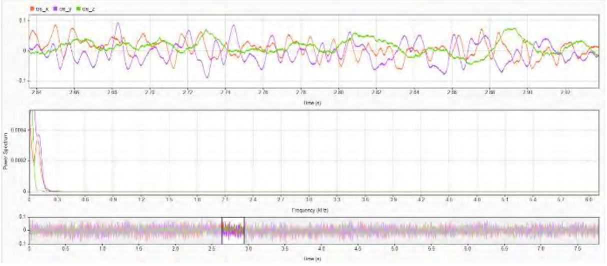

Fig. 8. Example of time course and frequency characteristics of vibration acceleration of a conventionally powered car

a) Vibration measurement in city traffic at a speed of 30 km/h

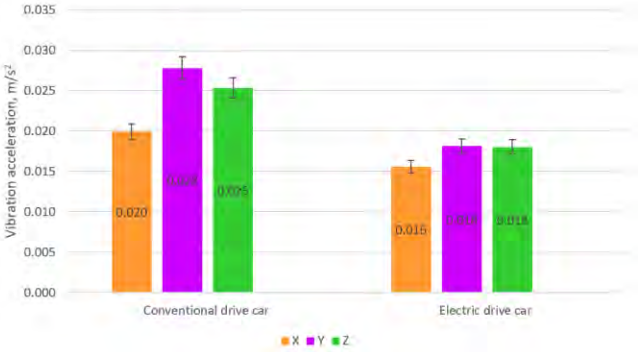

Fig. 9. Vibration acceleration in the X, Y, Z axes in vehicles at a speed of 30 km/h

During city driving at a speed of 30 km/h, electric cars were observed to generate lower levels of vibration in the Y-axis than conventionally powered cars. In the electric vehicle, the effective RMS (root mean square) values of the vibration acceleration in the Y-axis were 0.018 m/s², which means lower vibrations compared to the conventionally powered vehicle, which achieved 0.028 m/s². Higher vibrations in combustion cars may result from the operation of the drive system and additional sources of vibration typical of combustion engines.

b) Vibration measurement in city traffic at a speed of 50 km/h

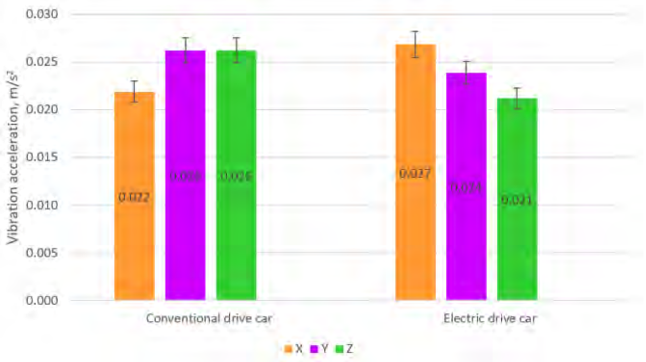

Fig. 10. Vibration acceleration in the X, Y, Z axes in vehicles at a speed of 50 km/h

At 50 km/h, vibration levels in conventional and electric cars were found to be very similar. In the conventional car, the effective vibration acceleration in the Y axis was 0.026 m/s², while in the electric car, it was 0.027 m/s² in the X axis. This means that at this speed, the differences in vibration levels between the drive types are minimal, suggesting that the effect of speed on the generated vibrations may be similar regardless of the drive type.

c) Vibration measurement in motorway traffic at a speed of 100 km/h

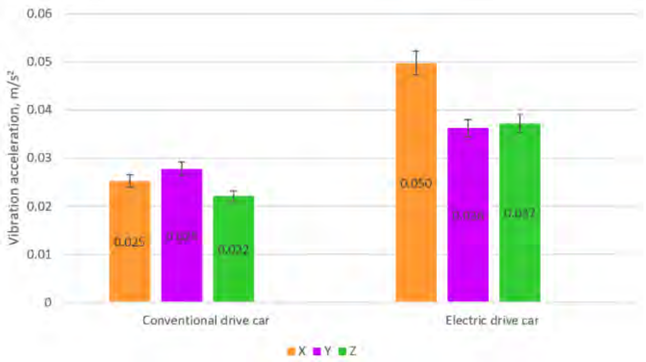

Fig. 11. Vibration acceleration in the X, Y, Z axes in vehicles at a speed of 100 km/h

While driving on the motorway at 100 km/h, an electric car experienced higher vibration levels than a vehicle with a combustion engine. In a vehicle with a conventional engine, the effective vibration acceleration was 0.028 m/s² in the Y axis, while in an electric car it was 0.05 m/s² in the X axis. Higher vibrations in an electric car may be due to several factors: poorer quality of workmanship, less sophisticated suspension and the lack of gear changes in the electric engine, which often operates at higher engine speeds. The lack of a gearbox in electric vehicles may cause increased vibrations transferred to the bodywork, because the engine operates more directly, without reducing vibrations during gear changes, which additionally affects driving comfort at high speeds.

d) Vibration measurement in motorway traffic at a speed of 140 km/h

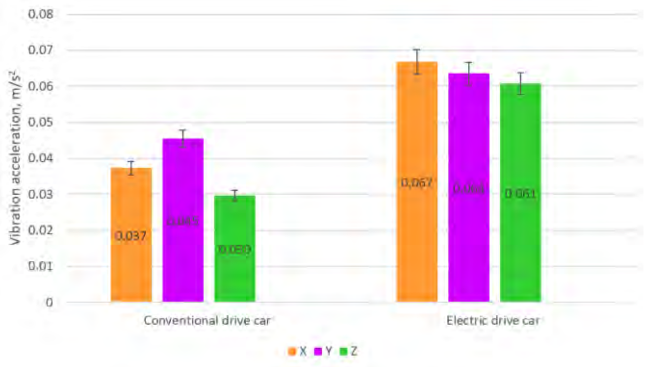

Fig. 12. Vibration acceleration in the X, Y, Z axes in vehicles at a speed of 140 km/h

When driving at a speed of 140 km/h, the highest vibration level was observed again in the electric car, where the effective vibration acceleration value was 0.097 m/s² in the X axis. In the vehicle with a conventional drive, the vibrations were lower, reaching 0.045 m/s² in the Y axis. The higher vibrations in the electric car may result from design limitations, such as simpler suspension, the lack of a gearbox, and a more direct transmission of driving forces without damping of gear changes. The lack of a mechanical gearbox means that the electric motor operates at a fixed gear ratio, which at high speeds can lead to increased vibrations transmitted to the body and reduced ride comfort.

The frequency range during driving in both vibration drives was from 10 Hz to 200 Hz in all axes for each drive type. Low and medium frequencies were related to road irregularities and vibrations, with vibrations caused by road irregularities and suspension system operation dominating.

The sampling frequency of 51,200 Hz was adopted at the measurement planning stage, before it was precisely determined which frequency bands would be most important in the analysis of vibrations in the vehicle. Initially, it was assumed that it would be worth using a high sampling frequency to avoid aliasing and to ensure the possibility of capturing also higher frequencies that could potentially appear in real driving conditions, e.g., as a result of resonances of suspension elements, engine, or drive system.

Only after conducting preliminary measurements and spectrum analysis did it turn out that the significant vibration band ends at around 200 Hz. Therefore, it can indeed be considered that the use of such a high sampling frequency was excessive in relation to the final needs of the analysis. However, from the perspective of data security and maintaining full measurement information, it was a prudent and justified decision.

It is also worth adding that modern data acquisition systems often operate by default with very high sampling rates, and limiting the signal bandwidth to the analyzed range (e.g., to 200 Hz) is done only at the data processing stage – e.g., by digital filtering. Therefore, a higher sampling rate does not necessarily mean increased noise, as long as the data is properly filtered and processed.

6. Conclusions

The results of the measurements of the effective values of vibration acceleration showed that the electric drive emits lower vibrations than the conventional drive during bench tests. In the vibration tests while driving for electric and conventional vehicles, the dominant frequencies were in the range from 10 Hz to 200 Hz, with lower and medium frequencies (10–100 Hz) present in all drives and resulting mainly from the unevenness of the road surface and the operation of the suspension system, while higher frequencies, particularly noticeable in vehicles with internal combustion engines, were related to the operation of the engine and its mechanical components. In the electric drive, the frequency range ended mainly at 100 Hz, because there were no additional vibrations generated by the internal combustion engine.

Measurements of vibrations affecting the driver and passengers while driving showed that the emission of vibrations increases with the increase in the speed of the vehicles. An increase in speed leads to an increase in the level of vibrations. The main source of vibrations while driving are vibrations resulting from the unevenness of the road surface and from the working suspension and shock absorption system of the vehicle and tires. The highest vibrations when driving at higher speeds were recorded for an electric car. An electric car shows very different vibration acceleration values depending on speed. At low speeds, vibrations are moderate, but at higher speeds (when driving on a motorway), vibration values increase significantly. This is due to the characteristics of electric motors, which, although they work smoothly, can generate vibrations resulting from higher revolutions at high speeds. The results suggest that in the case of a conventional vehicle, the vibration level depends on the driving speed, but the increase is not as pronounced as in an electric vehicle. In conventional cars, the use of a gearbox allows the torque to be adjusted to the driving conditions, which limits the increase in vibration at higher speeds. In electric vehicles, due to the direct drive and the lack of a gearbox, increasing the speed is associated with a proportional increase in the engine speed, which translates into higher vibration levels. This explains why the difference in vibration levels at different speeds is more noticeable in an electric vehicle than in a conventional one. Additionally, this vehicle had an uncomfortable suspension and a different mass distribution caused by the installed batteries, which also affects vibration emissions.

In practice, electric vehicle designers should pay special attention to ride comfort at higher speeds by appropriately tuning the suspension and vibration damping.

The results suggest that in the case of a conventional vehicle, the vibration level depends on the driving speed, but the increase is not as pronounced as in an electric vehicle. In conventional cars, the use of a gearbox allows the torque to be adjusted to the driving conditions, which limits the increase in vibration at higher speeds. In electric vehicles, due to the direct drive and the lack of a gearbox, increasing the speed is associated with a proportional increase in the engine speed, which translates into higher vibration levels. This explains why the difference in vibration levels at different speeds is more noticeable in an electric vehicle than in a conventional one.

The effective values of vibration acceleration considered comfortable, specified in the regulation [15], should not exceed 3.2 m/s^2 during short-term exposure and 0.8 m/s^2 during daily exposure. This means that the vibration acceleration values in all tested vehicles and on all drives affecting both the body and the driver and passengers meet the standard, do not pose a threat, and are considered comfortable.

The obtained vibration values are lower than the permissible limits specified in the standards, but this does not mean that the standards are excessive. The standards apply to a wide range of work environments, including those where the employee has direct contact with devices generating intense vibrations. An example would be a pneumatic hammer operator, where vibrations reach much higher levels than those occurring when driving a passenger car. In vehicles, however, driving comfort is an important factor, which is why the design of seats and suspension systems effectively dampens vibrations.

Nomenclature

a_{hvi}	vector sum of effective vibration accelerations
a_{hwxi}	effective weighted vibration acceleration values
a_{hwi}	value of the vector sum of effective weighted vibration accelerations
EV	electric cars
HEV	hybrid cars
RMS	root mean square

Bibliography

[1] Adamczyk J, Targosz J. Drgania drogowe (in Polish). Wydaw. KRIDM, AGH, Kraków 2003.

[2] Bhuiyan MHU, Fard M, Robinson SR. Effects of whole-body vibration on driver drowsiness: A review. J Safety Res. 2022;81:175-189. https://doi.org/10.1016/j.jsr.2022.02.009

[3] Bisu CF, Darnis P, Gerard A, K'nevez JY. Displacements analysis of self-excited vibrations in turning. Int J Adv Manuf Technol. 2009;44:1-16. https://doi.org/10.1007/s00170-008-1815-8

[4] Fiebig W. Drgania i hałas w inżynierii maszyn (in Polish). Wydawnictwo WNT. Warsaw 2020.
[5] Ghazali MHM, Rahiman W. Vibration analysis for machine monitoring and diagnosis: A systematic review. Shock Vib. 2021;2021(2):1-25. https://doi.org/10.1155/2021/9469318
[6] Greenblatt RE, Pflieger ME, Ossadtchi AE. Connectivity measures applied to human brain electrophysiological data. J Neurosci Methods. 2012;207(1):1-16. https://doi.org/10.1016/j.jneumeth.2012.02.025
[7] Horváth K, Zelei A. Simulating noise, vibration, and harshness advances in electric vehicle powertrains: strategies and challenges. World Electr Veh J. 2024;15(8):367. https://doi.org/10.3390/wevj15080367
[8] Kerber S, Fastl H. Prediction of perceptibility of vehicle exterior noise in background noise. Proc DAGA'08. Dresden 2008.
[9] Krishna K, Mahesha GT, Hegde S, Shenoy BS. A review on vibrations in electric and hybrid electric vehicles. J Inst Eng (India) Ser C. 2023;104(11):423-438. https://doi.org/10.1007/s40032-023-00930-3
[10] Mahdisoozani H, Mohsenizadeh M, Bahiraei M, Kasaeian A, Daneshvar A, Goodarzi M et al. Performance enhancement of internal combustion engines through vibration control: State of the art and challenges. Appl Sci. 2019;9(3): 406. https://doi.org/10.3390/app9030406
[11] Nader M. Drgania i hałas w transporcie (in Polish). Oficyna Wydawnicza Politechniki Warszawskiej. Warszawa 2016.
[12] Olabi AG, Abdelkareem MA, Wilberforce T, Alkhalidi A, Salameh T, Abo-Khalil AG et al. Battery electric vehicles: Progress, power electronic converters, strength (S), weakness (W), opportunity (O), and threats (T). Int J Thermofluids. 2022;16:100212. https://doi.org/10.1016/j.ijft.2022.100212
[13] Obsługa techniczna Dacia (in Polish). Dacia; 2024. https://www.dacia.pl/obsluga-techniczna.html (accessed on 6.04.2024).
[14] Qin Y, Tang X, Jia T, Duan Z, Zhang J, Li Y et al. Noise and vibration suppression in hybrid electric vehicles: state of the art and challenges. Renew Sustain Energy Rev. 2020; 124:109782. https://doi.org/10.1016/j.rser.2020.109782
[15] Reina G, Leanza A, Messina A. On the vibration analysis of off-road vehicles: influence of terrain deformation and irregularity. J Vib Control. 2018;24(22). https://doi.org/10.1177/1077546318754682
[16] Rozporządzenie Ministra Rodziny, Pracy i Polityki Społecznej z dnia 12 czerwca 2018 r. w sprawie najwyższych dopuszczalnych stężeń i natężeń czynników szkodliwych dla zdrowia w środowisku pracy, Dz.U. 2018 poz. 1286 (in Polish).
[17] Simcenter SCADAS XS: Wszystko co musisz wiedzieć (in Polish). ECTS 2024. https://www.ects.pl/artykul/simcenter-scadas-xs-wszystko-co-musisz-wiedziec/ (accessed on 10.09.2024).
[18] Tatsuno J, Maeda S. Effect of whole-body vibration exposure in vehicles on static standing balance after riding. Vibration. 2023;6(2):343-358. https://doi.org/10.3390/vibration6020021
[19] Verheijen ENG, Jabben J. Effect of electric cars on traffic noise and safety. National Institute for Public Health and the Environment 2010. Report 680300009/2010.
[20] Wang X, Osvalder A-L, Höstmad PBU. Influence of sound and vibration on perceived overall ride comfort – a comparison between an electric vehicle and a combustion engine vehicle. SAE Int J Veh Dyn Stab and NVH. 2023;7(2):1543-171. https://doi.org/10.4271/10-07-02-0010
[21] Wróblewski P, Drożdż W, Lewicki W, Miązek P. Methodology for assessing the impact of aperiodic phenomena on the energy balance of propulsion engines in vehicle electromobility systems for given areas. Energies. 2021;14(8): 2314. https://doi.org/10.3390/en14082314
[22] Yoshinaga H, Namikawa Y. Predicting noise reduction by electrification of automobiles. Inter-Noise 2009 Congress; Ottawa 2009.

Wioletta Cebulska, MEng. – Faculty of Transport and Aviation Engineering, Silesian University of Technology, Poland.
e-mail: *wioletta.cebulska@polsl.pl*

Damian Hadrys, DSc., DEng., Prof. PŚl. – Faculty of Transport and Aviation Engineering, Silesian University of Technology, Poland.
e-mail: *damian.hadrys@polsl.pl*

Article citation info:
Zacharewicz M, Bogdanowicz A, Socik P. Capacitance-based assessment of water content in lubricating oils for marine engines. Combustion Engines. 2025;202(3):81-87. https://doi.org/10.19206/CE-204692

Marcin ZACHAREWICZ
Artur BOGDANOWICZ
Paweł SOCIK

Combustion Engines
Polish Scientific Society of Combustion Engines

Capacitance-based assessment of water content in lubricating oils for marine engines

ARTICLE INFO

Received: 25 March 2025
Revised: 26 April 2025
Accepted: 5 May 2025
Available online: 29 May 2025

This article presents a method for assessing the water content in lubricating oils used in Navy ship marine engines, based on capacitance measurements. The method uses the dependence of capacitance on the permeability of the dielectric, which changes with water content and temperature. Real-time measurements are carried out using the Arduino Mega 2560 platform on samples with known water content. Experimental results show characteristic changes in capacitance and hysteresis effect due to water evaporation during heating. The proposed solution provides an effective online tool for oil condition monitoring, enabling early detection of engine damage and optimization of maintenance.

Key words: *marine diesel combustion engine, Arduino Mega 2560, dielectric analysis of lubricating oils, fault diagnosis of marine engines, water contamination*

1. Introduction

One of the primary causes of piston damage in internal combustion engines is the deterioration of the physicochemical properties of lubricating oil, which leads to the rupture of the oil film. Consequently, both mixed and dry friction phenomena occur, resulting in tribological damage to the engine's friction interfaces [8, 10, 19]. An example of such damage is shown in Fig. 1.

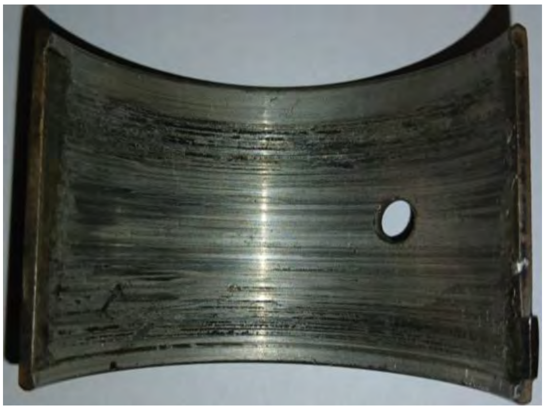

Fig. 1. Friction traces on the inner liner of the plain bearing

During engine operation, the physicochemical properties of the lubricating oil change, among which the most critical for engine reliability are:

- viscosity
- total base number
- total acid number
- flash point
- oxidation resistance and thermal stability
- lubricity
- the ability to wash away and disperse contaminants
- the ability to separate water.

Changes in the oil parameters typically occur gradually, following the curve shown in Fig. 2. The plotted curve denotes the functional dependence of the parameter on the measurement conditions. Its gradient may assume positive or negative values, indicating that, depending on the underlying physical sensitivity, the parameter can either increase or decrease as the conditions vary [14, 21].

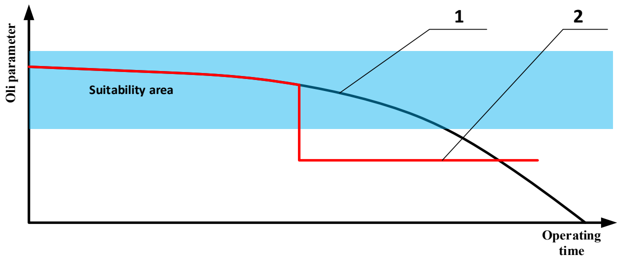

Fig. 2. An exemplary curve illustrating the change in an oil parameter as a function of its service time: 1 – natural degradation of oil parameters 2 – sudden change in oil parameters resulting from damage

In most cases, during engine operation, changes in the physicochemical parameters of lubricating oil occur in accordance with curve no. 1 and are predictable. Based on this, oils are utilized following a strategy that specifies a determined operating time (in line with the recommendations of both engine and oil manufacturers). Moreover, during the operation of marine engines, periodic inspections of the physicochemical parameters of the oils are conducted in specialized laboratories. This strategy generally prevents damage caused by the deterioration of the oil's physicochemical properties [15, 21].

However, there are instances during operation when the physicochemical parameters of the oils change suddenly in an unpredictable manner (contrary to the adopted strategy). Such a scenario is illustrated by curve no. 2 shown in Fig. 2. The most common cause of a sudden change in the oil's physicochemical parameters is engine damage, which results in the contamination of the oil with solid particles – usually metallic in nature (originating from its friction nodes) – as well as water or fuel. Contamination with fuel is typically accompanied by a decrease in viscosity and a reduction in flash point. Contamination with water, on the other hand, is accompanied by a rapid increase in oil density (in extreme cases, the oil transforms into an emulsion with a paste-like consistency), which drastically deteriorates its lubricating properties. The source of water contamination during engine operation is the cooling system. In the case of marine reciprocating engines, the oil may be contaminated with fresh water, which is primarily used to cool the cylinder liners and engine heads, or with water containing salt ions (seawater) employed to cool the turbocharged air and, occasionally, the lubricating oil [10, 14, 18].

From the perspective of piston engine operation, the early detection of both water contamination in the oil and oil contamination in the cooling water is of critical importance. During engine operation, the oil is subjected to a higher pressure than the cooling water. Consequently, in the event of a leak, oil is expected to enter the cooling water, whereas during engine downtime, the likelihood of water infiltrating the oil increases. Therefore, it is essential to develop an online detection method capable of identifying both water in the oil and oil in the cooling water [9, 11–13]. This task has been undertaken by a research team from the Institute of Ship Construction and Operation of the Naval Academy.

The proposed method is based on the use of a slot capacitor, in which the dielectric is provided by the lubricating oil (in the case of detecting water in oil) or by the cooling water (in the case of detecting oil in water). According to Equation 1, the capacitance of the capacitor depends directly on the plate surface area (S), the distance between the plates (d), and the relative permittivity (ε_0) of the dielectric between the plates. For the capacitor, the values of the plate separation and surface area are fixed and characteristic of its design, while the independent variable is the relative permittivity of the dielectric (i.e., the oil–water mixture) [3, 8, 18].

$$C = \varepsilon_0 \cdot \varepsilon_r \cdot \frac{S}{d} \tag{1}$$

2. Method assumptions

It is widely accepted that the oils used on ships are dielectrics whose dielectric properties may change during operation [2, 4, 15, 16, 20]. One source of these changes is the natural aging process of the oil (oxidation), during which the hydrocarbons in the oil are converted into esters with polar structures. During operation, the oil may become contaminated with solid particles, fresh water, or seawater. Both the oil's aging processes and its contamination with water (especially seawater) lead to changes in its dielectric properties. It is assumed that the relative permittivity of oil, ε, is approximately 2.5, whereas that of fresh water is close to 80. In the case of seawater, the relative permittivity is several times higher due to the presence of salt ions from elements such as sodium, magnesium, calcium, and potassium. It should be noted that the relative permittivity is highly dependent on temperature; for example, in distilled water it varies from 88 to 55.3 as the temperature changes from 0 to 100°C, as illustrated in Fig. 3.

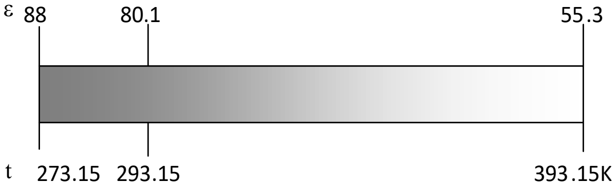

Fig. 3. The influence of water temperature on its relative electrical permittivity

In the case of oil contaminated with water, it can be assumed that the relative electric permittivity of the oil-water mixture is proportional to the relative water content (Fig. 4).

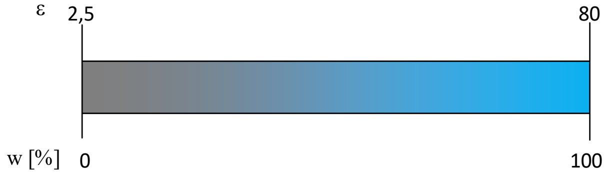

Fig. 4. The likely dependence of relative permittivity as a function of water content in oil

Direct determination of the relative permittivity is impossible. Therefore, indirect methods are typically used. The most common approach utilizes the dependence of the capacitance of a parallel-plate capacitor (Eq. 1). To determine the theoretical value of the relative electrical permittivity of mixtures, a linear or nearly linear model is usually employed, as described by the following relationship [1, 3, 21]:

$$\varepsilon_r(\omega) = \varepsilon_{r,oil} + k \cdot w \tag{2}$$

where: $\varepsilon_{r,oil}$ – the relative permittivity of pure oil (without water), w – the water content (e.g., in ppm or %), k – the calibration coefficient quantifying the influence of water content on the permittivity.

In practical studies, the sensor (capacitor) must be calibrated by measuring its capacitance for oil samples with known water content, and on that basis, a correction function is derived:

$$C(w) = C_0 + a_1 w + a_2 w^2 + \cdots \tag{3}$$

In order to determine the coefficients C_0 and a_1, capacitance measurements are performed for various known values of water content, w_i. Then, using the least squares method, the model parameters are determined[1, 3, 21]:

$$\begin{bmatrix} C_1 \\ C_2 \\ \vdots \\ C_n \end{bmatrix} = \begin{bmatrix} 1 & w_1 \\ 1 & w_2 \\ \vdots & \vdots \\ 1 & w_3 \end{bmatrix} \begin{bmatrix} C_0 \\ a_1 \end{bmatrix} \tag{4}$$

The solution is:

$$\begin{bmatrix} C_0 \\ a_1 \end{bmatrix} = (W^T W)^{-1} W^T C \tag{5}$$

where w is the matrix of water content, and C is the vector of measured capacitances.

In the conducted research, various methods for measuring the capacitance of a capacitor were considered, ranging from utilizing the resonance phenomenon of currents and voltages in RLC circuits to determining the time constant of a capacitor-resistor circuit with known capacitance [1, 3, 21].

The first method examined was based on the resonance phenomenon in RLC circuits, where the capacitor, with the oil or water under investigation serving as the dielectric, represents the capacitance C. In practice, either series or parallel resonance is employed, with elements such as the capacitor, inductor, and resistor connected either in series (Fig. 5a) or in parallel (Fig. 5b) [1, 3, 17, 21]:

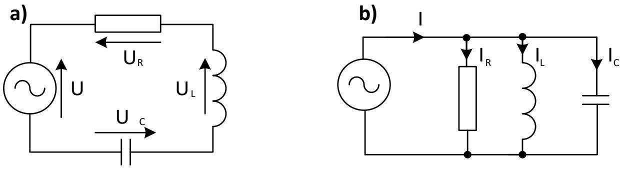

Fig. 5. RLC resonance circuit: a) series, b) parallel

In the case of the series resonance circuit (Fig. 5a), voltage resonance occurs, which in practice means that the amplitude of the voltage across the individual passive components UL, UR, and UC reaches its maximum when the resonance phenomenon occurs. The voltage across the passive elements is described by the following relationship [1, 3, 21]:

$$U_L = I \cdot L \cdot \omega_r = \frac{U}{R} \cdot \sqrt{\frac{L}{C}} \tag{6}$$

At the resonant frequency, the voltage across the inductor and the capacitor is described by the following relationship:

$$|U_L| = -|U_C| \tag{7}$$

Conversely, the resonant frequency is determined according to the following expression:

$$f_r = \frac{1}{2 \cdot \pi \cdot \sqrt{LC}} \tag{8}$$

In situations where the objective is to determine the capacitor's capacitance, the source frequency must be adjusted so that the voltage across the passive components is maximized. The resonant frequency is thereby a function of the capacitor's capacitance.

In the case of a parallel resonance circuit (Fig. 5b), the phenomenon is termed current resonance. The principle for determining the capacitor's capacitance is fundamentally analogous to that employed in the series resonance scenario. However, a key difference from a measurement perspective is that the circuit current is monitored, and the generator frequency at which this current reaches its maximum is identified. The resonant frequency in a parallel RLC circuit is described by the following relationship [1, 3, 21]:

$$f_r = \frac{R}{\sqrt{\frac{L}{C}}} \tag{9}$$

The resonant frequency value is also a function of the capacitor's capacitance. The methods described for determining the capacitor's capacitance (which is a function of the dielectric permittivity of the insulator) can be successfully employed in the construction of a measurement system. However, the drawbacks of such a measurement system include the duration of the measurement process and the need to utilize a sinusoidal voltage generator with an adjustable frequency. The measurement time is influenced by the necessity to scan a wide frequency range, which is both problematic and time-consuming in practice. Consequently, the authors have opted for an alternative method for measuring the capacitor's capacitance. They decided to construct a measurement system based on determining the time constant of a circuit composed of a capacitor and a resistor with a known resistance. The RC circuit time constant is defined as the time required for the voltage measured across the capacitor to reach 63.2% of its fully charged voltage. The capacitor's capacitance in the RC circuit is related to the time constant according to the following relationship [1, 3, 10, 19, 21]:

$$T_C = R \cdot C \tag{10}$$

Based on Equation 10, the capacitor's capacitance was calculated:

$$C = \frac{T_C}{R} \tag{11}$$

A graphical illustration of the principle of determining the capacitor's capacitance based on the RC circuit's time constant is shown in Fig. 6.

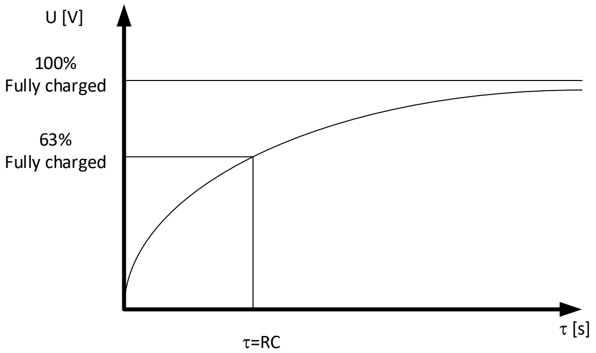

Fig. 6. Illustration of the principle for determining the time constant of an RC circuit

The constructed measurement system is based on the Arduino Mega 2560 microcontroller. This system enables the measurement of the charging time of a capacitor connected in series with a resistor (which reduces the charging current and, consequently, increases the circuit's time constant). This approach enhances the accuracy of the time measurement (i.e., the number of microcontroller clock cycles), thereby improving the precision of the capacitor's capacitance determination. In the conducted studies, two types of capacitors were utilized, both employing oil with variable water content as the dielectric. A slot capacitor and a specially fabricated cylindrical capacitor were used for this purpose. An illustration of the measurement system employing the slot capacitor is shown in Fig. 7.

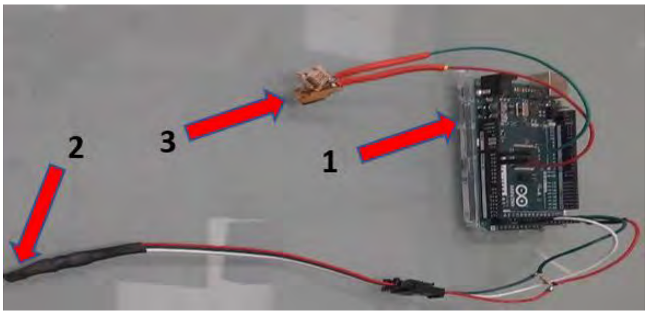

Fig. 7. Measurement system used in the studies: 1 – Arduino Mega 2560 microcontroller, 2 – slot capacitor, 3 – 18B20 temperature sensor

Additionally, the measurement system has been equipped with an 18B20 temperature sensor, which enables real-time monitoring of the temperature of the investigated medium. Temperature measurement is critical because there is a dependency between the temperature of the liquid (the dielectric of the liquid capacitor) and its capacitance. This relationship is characterized by the temperature capacitance coefficient T_{WC} [1, 3, 21]:

$$T_{WC} = \frac{1}{C} \cdot \frac{\delta C}{\delta T} \tag{12}$$

Conversely, the impact of temperature is delineated by the following relationship:

$$C(T) = C(T_0) \cdot [1 + T_{WC} \cdot (T - T_0)] \tag{13}$$

3. Research plan

The foundation of this research is the development of a method for detecting engine damage that results in the mixing of lubricating oil with cooling water. It is essential to measure the water content in the lubricating oil as well as the oil content in the cooling water, and the proposed method must support real-time (online) measurements.

It was determined that the optimal approach would be to measure the electrical capacitance of a capacitor, whose dielectric is constituted by the lubricating oil and cooling water under investigation. According to Eq. (1) and (13), the capacitance of the capacitor is a function of its temperature and the relative dielectric constant of the insulator forming the gap between its electrodes. The capacitance value depends on the oil temperature (see Fig. 3) and its water content (see Fig. 4). The geometric properties of the capacitor are assumed to remain constant throughout the experiments (thermal expansion of its components is neglected).

Experimental investigations were carried out by measuring the capacitance of a slot capacitor (immersed in the test liquid) as a function of water content and temperature. For this purpose, an apparatus based on the Arduino Mega 2560 platform was developed, enabling continuous measurement and transmission of both the capacitor's capacitance and the liquid's temperature to a computer. The measurements are performed with a sampling frequency of 1 Hz and a resolution of 12 bits.

During the experiment, the sample under investigation is placed on a magnetic stirrer equipped with a heating function. The sample contains the slot capacitor as well as a temperature sensor. Continuous measurements of temperature and capacitance are recorded while the sample is stirred and heated. The sample is heated from ambient temperature until it reaches 95°C – a value that approximates the standard operating temperature of lubricating oil in marine engines (80–95°C). Once the target temperature is attained, the heater is turned off. Measurements continue from the onset of heating until the sample cools back to ambient temperature (typically around 20°C). Additionally, samples are periodically collected and analyzed microscopically (see Fig. 8) to assess the homogeneity of the mixture [5, 6].

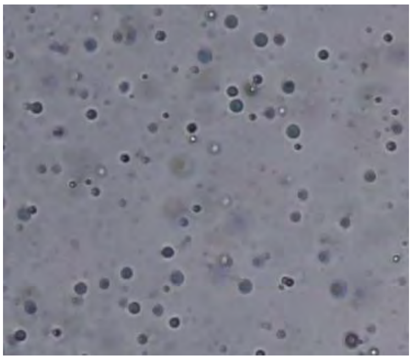

Fig. 8. Microscopic view of an oil sample with a water content of 0.5%

Under laboratory conditions, the water content in the sample decreases during measurement due to evaporation caused by heating. This is evidenced by the irreproducibility of the measurement results obtained during the heating and cooling phases of the sample. Furthermore, the foaming of the mixture's surface at elevated temperatures indicates the occurrence of water evaporation.

The study was conducted in accordance with a completely randomized statistical design. This design enables a more precise evaluation of the effect of a single factor – in this case, the water content in the oil – than would be possible using traditional statistical hypothesis testing. The investigated factor can assume values at each level p, limited solely by the technical conditions of the experiment. The null hypothesis, assumed a priori, postulates that the analyzed input factor has no effect on the output variable. A factor is deemed significant if the computed value of the test statistic is equal to or greater than the critical value specified in the relevant statistical tables. For a completely randomized design, it is most advantageous to use the Fisher-Snedecor F statistic [6, 7].

The planning matrix for the completely randomized statistical design, which is used to assess the impact of the single input factor on the output variable, is presented in Table 1.

The F test statistic is calculated according to the following relationship:

$$F = \frac{\sum_{i=0}^{p} n_i \, (\bar{y}_i - \bar{y})^2 (n - p)}{[\sum_{i=1}^{p} \sum_{j=1}^{q} n_i \, (y_{ij} - \bar{y})^2 - \sum_{i=1}^{p} n_i \, (\bar{y}_i - \bar{y})^2](p - 1)} \tag{14}$$

where: n_i – the number of measurements of the input factor at a given level, n – the total number of measurements, $\bar{y}_i$ – the mean measurement result in the i-th row, $\bar{y}$ – the overall mean of all measurement results, y_{ij} – denotes the value of the j-th output factor at level i, p – the number of levels of the input factor variability.

Table 1. Planning Matrix for the Completely Randomized Statistical Design [6, 7]

Input factor level	Number of experiments		
	1	…	q
1	y_{11}	…	y_{1q}
⋮	⋮	⋮	⋮
p	Y_{p1}	…	y_{pq}

The calculated F test statistic should be compared with the critical value determined from the table (for the chosen significance level α and for the degrees of freedom for the numerator calculated according to the following relationship:

$$f_1 = f_1 = p - 1 \tag{15}$$

and for the denominator according to the formula:

$$f_2 = f_m = n - p \tag{16}$$

If the computed F value is greater than or equal to the critical value F_{kr} $F \geq F_{kr} = F_{(\alpha;f_1;f_2)}$, the effect of the investigated factor is deemed significant. Conversely, if $F \leq F_{kr}$, this indicates that within the examined range of variability, the input factor does not influence the output variable [6, 7].

In the experimental studies, measurements were conducted over mass concentrations of water in oil at 0%, 0.5%, and 1%. All experiments were repeated five times, which facilitated a comprehensive statistical analysis of the results.

4. Results

As a result of the conducted studies, the capacitance values of a capacitor immersed in the test sample were obtained as a function of the mass fraction of water in the oil. The empirical results are presented graphically, illustrating the recorded variation in the capacitor's capacitance as a function of temperature (ranging from 80°C to 100°C, which corresponds to the typical operating temperature of the oil) for different water mass fractions (Fig. 9). Each plot displays the results of five experiments (for each concentration), as indicated by the colors of the data points. In Figure 9, for water concentrations of 0.5% and 1%, a characteristic hysteresis loop is observed, evidenced by the non-overlapping data points recorded during the heating and cooling phases of the mixture. This behavior is attributed to the water evaporation process, which consequently alters the sample composition. Therefore, only the data corresponding to the heating phase were used for further analysis. Due to water evaporation, a new sample with a predetermined water content was required for each repetition of the measurement at a given concentration.

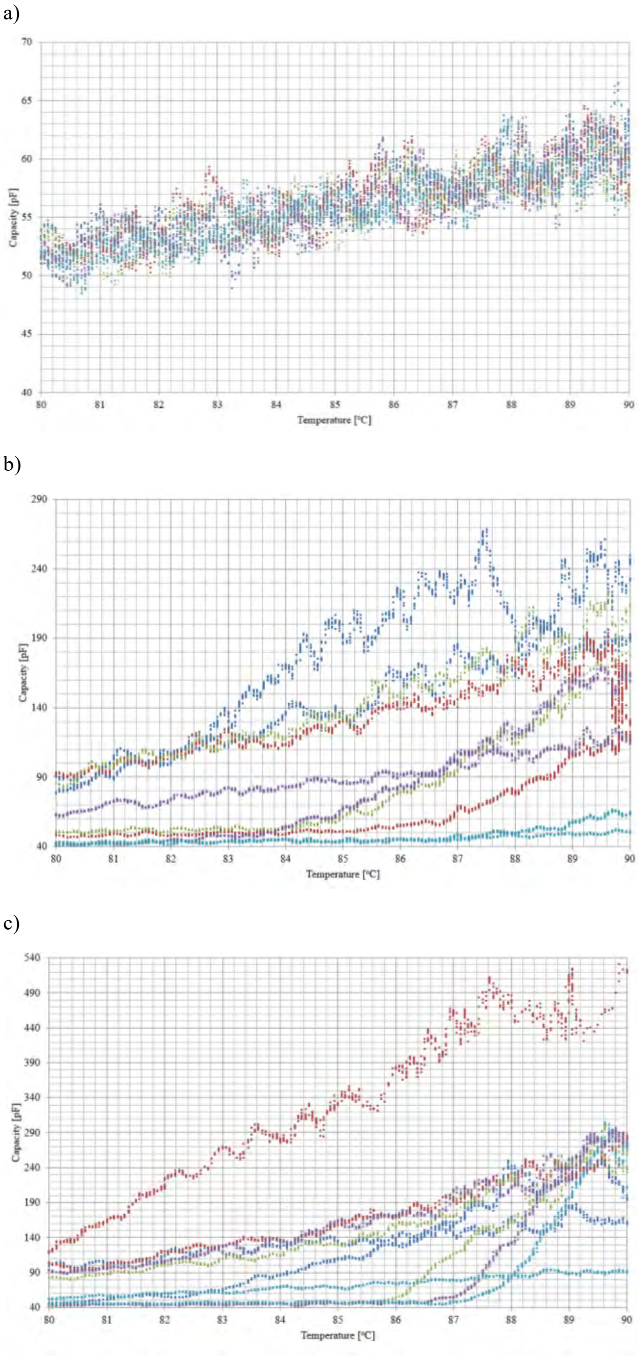

Fig. 9. Recorded capacitor capacitance curves as a function of the temperature of the oil-water mixture for the respective mass fractions: a) pure oil, b) 0.5% water, c) 1% water

Measurements were conducted with a constant time step of 1 Hz, so that the resulting data (temperature and capacitor capacitance) were functions of time. Consequently, it was necessary to derive capacitance curves as a function of the dielectric temperature. To this end, the measured capacitance values were averaged for each temperature value, with a resolution of 0.1°C. Subsequently, for each considered temperature (for each concentration), a single capacitance value was computed as the arithmetic mean of all five repeated measurements. The resulting data are presented in Fig. 10.

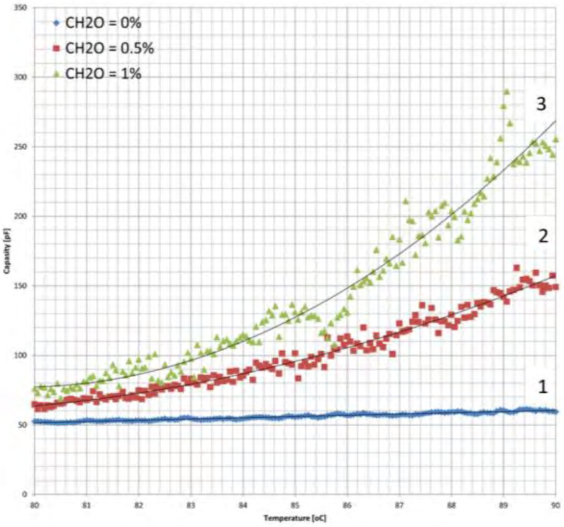

Fig. 10. Capacitance variation curves as a function of the dielectric temperature for the respective mass fractions of water in oil: 1 – oil, 2 – a mixture of 0.5% water and 99.5% oil, 3 – a mixture of 1% water and 99% oil

5. Conclusion

The conducted studies demonstrated that the proposed method for detecting and quantifying the mass fraction of water in engine oil is effective. It enables the real-time (online) acquisition of clear information regarding engine damage that results in the contamination of lubricating oil with water. The developed method is sufficiently sensitive to allow operators to take measures that minimize – practically, to prevent – the occurrence of secondary damage stemming from the deterioration of the oil's lubricating properties. Furthermore, by employing the capacitance-based approach, it is possible to detect metallic contaminants with a diameter equal to or greater than the distance between the capacitor plates. Such contamination will cause a short-circuit in the capacitor, which unequivocally indicates damage to the engine's friction components.

A significant drawback of the proposed method is the necessity of obtaining a homogeneous mixture of water and oil. However, in the case of internal combustion engines, the oil is intensely mixed with any water present during operation.

The proposed method can also be utilized for detecting engine oil contamination in water and for determining the proportions of individual components in mixtures and emulsions of liquids with differing dielectric properties. Currently, the research team is investigating the determination of the mass fractions of oil in both seawater and freshwater, as well as the quantification of biocomponents in marine fuels.

Nomenclature

C	electric capacitance, vector of measured capacitance values [F]
$C(T_0)$	capacitance of the capacitor at the initial temperature [F]
d	distance between the capacitor plates [m]
I	current [A]
k	calibration coefficient defining the influence of water content on capacitance [-]
L	inductance [H]
R	resistance [Ω]
S	surface area of the capacitor plates [m²]
T	temperature [K]
T_c	time constant of the RC circuit [s]
T_{WC}	temperature capacitance coefficient
U	electric voltage [V]
W	mass concentration of water in the mixture [%]
ε_0	permittivity of free space [F/m]
ε_r	relative permittivity of the dielectric [F/m]
$\varepsilon_{r,oil}$	relative permittivity of pure oil [F/m]

Bibliography

[1] Hambley AR, Pułka AK. Wprowadzenie do elektroniki i elektrotechniki. T. 2: Systemy cyfrowe (in Polish). PWN. Warszawa 2023.

[2] Eidi A. Fabricated electromechanical resonator sensor for liquid viscosity measurement. Metrol Meas Syst. 2023:30: 223-234. https://doi.org/10.24425/mms.2023.144868

[3] Floyd TL, Buchla DM. Principles of electric circuits: conventional current. Tenth edition, global edition. Pearson Education Limited. Harlow 2022.

[4] Gomółka L, Augustynowicz A. Evaluation of applicability of dielectric constant in monitoring aging processes in engine oils. Eksploat Niezawodn. 2019;21(2):177-185. https://doi.org/10.17531/ein.2019.2.1

[5] Idros MFM, Hashim H, Islam S, Ali SH. Capability of optical approach in condition based monitoring of lubricant oil. Sensors and Transducers. 2012;17:125-134. https://sensorsportal.com/HTML/ST_JOURNAL/PDF_Files/P_SI_272.pdf

[6] Kokot F, Hyla-Klekot L, Kokot S. Badania laboratoryjne: zakres norm i interpretacja (in Polish). Wyd. 5 uakt. i rozsz. Wydawnictwo Lekarskie PZWL. Warszawa 2011.

[7] Korzyński M. Metodyka eksperymentu: planowanie, realizacja i statystyczne opracowanie wyników eksperymentów technologicznych (in Polish). Wydawnictwa Naukowo-Techniczne. Warszawa 2006.

[8] Kozak M. A comparison of thermogravimetric characteristics of fresh and used engine oils. Combustion Engines. 2019;178(3):289-292. https://doi.org/10.19206/CE-2019-350

[9] Kozak M, Siejka P. Soot contamination of engine oil – the case of a small turbocharged spark-ignition engine. Combustion Engines. 2020;182(3):28-32. https://doi.org/10.19206/CE-2020-305

[10] Macián V, Tormos B, Olmeda P, Montoro L. Analytical approach to wear rate determination for internal combustion engine condition monitoring based on oil analysis. Tribol Int. 2003;36(10):771-776. https://doi.org/10.1016/S0301-679X(03)00060-4

[11] Malinowska M, Zera D. The oil engine lubricity variation analysis of engine oil applied in Cegielski-Sulzer motor 3AL25/30. Zeszyty Naukowe Akademii Morskiej w Gdyni. 2016;96:93-104. https://sj.umg.edu.pl/artykul-466.html

[12] Molenda J, Wolak A, Zając G, Cieloch P, Chudy D. Assessment of the suitability of paper chromatography for quick diagnostics of the operating condition of engine oil. Eksploat Niezawodn. 2023;25(2):162912. https://doi.org/10.17531/ein/162912

[13] Olszewski W. The possibility of estimate quality state of using motor oil by measuring dielectrical properties. Journal of Kones. 2001;8(3-4). https://yadda.icm.edu.pl/baztech/element/bwmeta1.element.baztech-article-BUJ7-0005-0011

[14] Shinde H, Bewoor A. Analyzing the relationship between the deterioration of engine oil in terms of change in viscosity, conductivity and transmittance. 2017 International Conference on Advances in Mechanical, Industrial, Automation and Management Systems (AMIAMS). https://doi.org/10.1109/AMIAMS.2017.8069185

[15] Shinde H, Bewoor A. Capacitive sensor for engine oil deterioration measurement. AIP Conf. Proc. 2018;1943:020099. https://doi.org/10.1063/1.5029675

[16] Shinde HM, Bewoor AK, Kumar R, Elsheikh, Singh DV, Shanmugan S et al. Engine oil quality deterioration estimation using an integrated sensory system. Proc Inst Mech Eng Part E J Process Mech Eng. 2023;237(6):2257-2267. https://doi.org/10.1177/09544089221135629

[17] Wolak A, Zając G, Kumbár W. Evaluation of engine oil foaming tendency under urban driving conditions. Eksploat Niezawodn. 2018;20(2):229-235. https://doi.org/10.17531/ein.2018.2.07

[18] Zhang Z, Ouyang W, Liang X, Yan X, Yuan C, Zhou X et al. Review of the evolution and prevention of friction, wear, and noise for water-lubricated bearings used in ships. Friction. 2024;12(1):1-38. https://doi.org/10.1007/s40544-022-0707-5

[19] Zhou F, Yang K, Wang L. The effect of water content on engine oil monitoring based on physical and chemical indicators. Sensors. 2024;24(4):1289. https://doi.org/10.3390/s24041289

[20] Zhu Q. Nonlinear systems: dynamics, control, optimization and applications to the science and engineering. Mathematics. 2022;10:4837. https://doi.org/10.3390/math10244837

[21] Żółtowski B, Ćwik Z. Leksykon diagnostyki technicznej (in Polish). ATR. Bydgoszcz 1996.

Prof. Marcin Zacharewicz, DSc., DEng. – Faculty of Mechanical and Electrical Engineering, Polish Naval Academy, Poland.

e-mail: *m.zacharewicz@amw.gdynia.pl*

Artur Bogdanowicz, DEng. – Faculty of Mechanical and Electrical Engineering, Polish Naval Academy, Poland.

e-mail: *a.bogdanowicz@amw.gdynia.pl*

Paweł Socik, MEng. – Faculty of Mechanical and Electrical Engineering, Polish Naval Academy, Poland.

e-mail: *p.socik@amw.gdynia.pl*

Article citation info:
Stoeck T. Enhanced diagnostics of common rail piezoelectric injectors using the box method. Combustion Engines. 2025;202(3):88-93. https://doi.org/10.19206/CE-205812

Tomasz STOECK

Combustion Engines
Polish Scientific Society of Combustion Engines

Enhanced diagnostics of common rail piezoelectric injectors using the box method

ARTICLE INFO

Received: 11 April 2025
Revised: 26 May 2025
Accepted: 2 June 2025
Available online: 13 June 2025

The article presents one of the techniques of analytic geometry, referred to as the box method or the Minimum Bounding Rectangle (MBR) approach, which was applied in the diagnostics of a common rail piezoelectric injector. By extending the standard test procedure with a computational phase, it was possible to estimate the fuel dosing surface areas and compare them with reference values. It was demonstrated that the proposed method is particularly useful in situations where a clear assessment of the injector's technical condition is difficult to obtain. This approach eliminates the need for additional measurements during the active testing phase, without increasing the final costs or the time required for the regeneration process.

Key words: *common rail system, piezoelectric fuel injector, box method, regeneration process*

1. Introduction

For many years, test benches have been used for the precise assessment of the technical condition of common rail injectors. These are universal, stationary diagnostic stations where service tests are conducted according to strictly defined procedures. This is made possible by dedicated software as well as databases that are periodically updated by the manufacturers. Among the various test plans performed automatically, a key role in injector diagnostics is played by Injector Volume Metering (IVM) tests. These typically involve evaluating fuel injection at four operating points, corresponding to the following injection quantities: full-load, part-load (emission), pre-injection, and idle [8, 9, 11]. Additional diagnostic information is provided by the backflow values, which are especially useful in assessing the proper functioning of the valve group [6, 10]. The obtained results are compared against threshold ranges, i.e., the fuel delivery tolerances stored in the test bench memory, and are then printed as a measurement protocol.

Unfortunately, problematic cases sometimes occur in which injectors fail to operate correctly, even though they meet the requirements defined in the test plans. In extended diagnostics, the number of measurement points is typically increased, which raises costs and prolongs the experimental phase [1, 5]. For this reason, an entirely different approach was adopted, based on identifying hidden dysfunctions using computational methods. It was assumed that the reference points from the standard procedure would be located within a Cartesian coordinate system and then connected to form an irregular quadrilateral. A similar process was applied to a reference injector, which allowed for the estimation and comparison of the surface areas of the resulting figures. Discrepancies in the calculated areas served as the basis for evaluating the technical condition of the tested injector. Examples of this approach in practical applications have been presented in publications [17, 18, 20].

The proposed box method offers an interesting alternative to previously employed computational techniques based on classical Gaussian and Newton-Cotes formulas. The analytical process is sufficiently simple to be carried out manually, which makes it particularly suitable for use under typical workshop conditions. At the same time, repeatability and automation can be achieved in a digital environment, since the formulas implemented in a spreadsheet provide a ready-to-use tool for performing future analyses.

2. Methods

2.1. Test object

The study was conducted on a Siemens VDO Continental 2.3 PCR injector (part number 5WS40156), taken from a 2.0 TDCi engine of a Ford Galaxy vehicle with a mileage of 278,000 km.

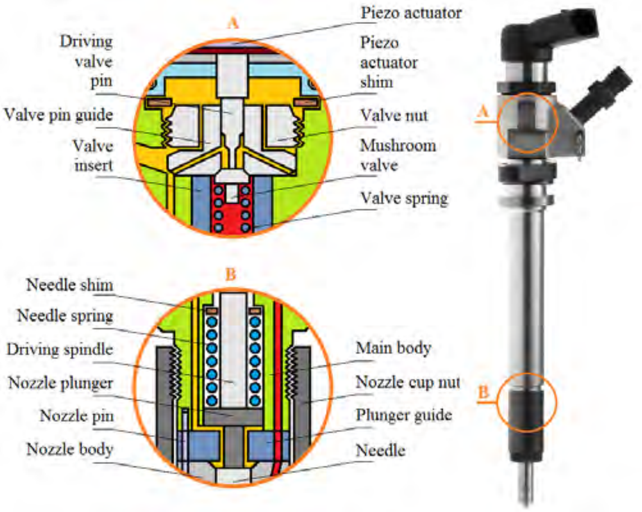

Fig. 1. Siemens VDO Continental PCR 2.3 fuel injector design [19]

This is a second-generation injector, operating at a maximum working pressure of 160 MPa [21]. In contrast to solutions offered by other manufacturers (e.g., Bosch, Denso), the piezoelectric actuator is positioned outside the main body, which allows for its straightforward replacement in the event of failure (Fig. 1). Moreover, this placement is also practically convenient, as it facilitates routine service operations, particularly: disassembly of the injector into individual components, ultrasonic cleaning, calibration, and reassembly after repair.

2.2. Test bench

The experimental phase was conducted on a Stardex Nova Ultima test bench, which included a simulator, flow meter, and a cooling, filtering, and damping module (Fig. 2). The test bench was complemented by a 12PSB drive table, as well as a PC-class computer with an Ubuntu Linux operating system installed.

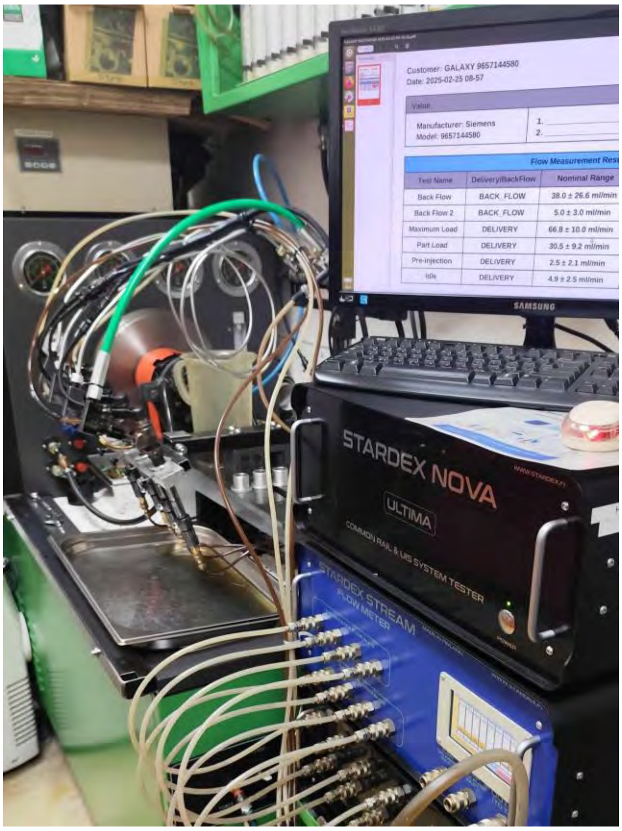

Fig. 2. General view of the Stardex Nova Ultima test bench

Additional equipment and tools were also used, which enabled the testing and comprehensive regeneration of the injector under investigation. The most important ones include:

- Mega Tester V3 electrical parameter measurement device
- Yizhan 13MP HDMI VGA industrial camera
- Bene YesWeCan 3L ultrasonic cleaner
- Facom E.316A200S torque wrench.

2.3. Research plan

Table 1 presents the test plan, which, in the measurement and operational parts, largely aligned with the manufacturer's procedure. The only exception was the comprehensive electrical parameter testing of the injector using the Mega Tester V3 device. Additionally, the extended diagnostics required the introduction of a computational phase, which was carried out on a station equipped with a PC-class computer. This computer is typically also used for visualizing and recording images transmitted from an industrial camera or laboratory microscope.

Table 1. Research plan with division into stages and workstations

Workplace	Stage I	Stage II
Mega Tester V3	Electrical test	Calibration
Stardex Nova Ultima	Internal cleaning	Main flow tests
	Preliminary flow tests	Injector coding
Personal computer	Calculation phase	Calculation phase
Tool stand	Disassembly into parts	Final acceptance
	Microscopic examination	
	Ultrasonic washing	
	Part drying	
	Parts exchange	
	Assembly	

2.4. Box method

In the Cartesian coordinate system, the points corresponding to the fuel delivery of the reference injector were located. After connecting them, an irregular quadrilateral with vertices 1-2-3-4 was obtained (Fig. 3). To calculate the area of the figure, the box method was applied, which involves embedding the figure in a rectangle with sides parallel to the coordinate axes and dividing the considered area into smaller parts [7, 15, 16]. The final result can be obtained from the following formula:

$$A_{VII} = A_{box} - A_I - A_{II} - A_{III} - A_{IV} - A_V - A_{VI} \qquad (1)$$

The use of the box method, also referred to as the Minimum Bounding Rectangle (MBR), is practically convenient, as in the component calculations of AI-AVII, only elementary mathematical formulas for the area of a rectangle (length × width) and a right triangle (½ × base × height) are considered [3, 4, 23].

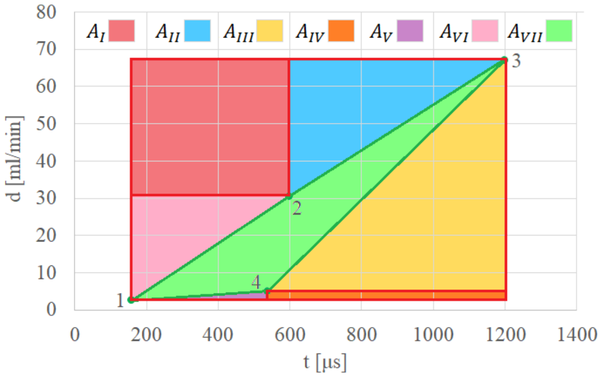

Fig. 3. Interpretation of the box method for the reference injector

Table 2 presents the results obtained for the input data, namely the nozzle opening times (t) and the corresponding fuel doses (d): pre-injection (1), part-load (2), full-load (3), idle (4).

Table 2. Results of surface area calculations for the reference figure

Input data		
Point	t	d
1	160	2.5
2	600	30.5
3	1200	66.8
4	540	4.9

Calculation result						
A_{box}	A_I	A_{II}	A_{III}	A_{IV}	A_V	A_{VI}
66,872	15,972	10,890	20,427	1584	456	6160
A_{VII}						
11,383						

3. Analysis results and discussion

3.1. Preliminary tests

The injector testing began with comprehensive electrical measurements using the Mega Tester V3. Based on these measurements, the failure of the piezoelectric stack was ruled out, as the obtained values met the requirements specified by the manufacturer, i.e., capacitance C = 3.4 μF (min. 2.8 μF), resistance R = 186 kΩ (160–220 kΩ) [22]. Furthermore, no damage to the actuator insulation was found, and a positive result was obtained in the continuous load test under the operating voltage of U = 200 V [11] (Fig. 4). For these reasons, the injector was cleared for flow measurements (IVM) on the Stardex Nova Ultima test bench (Fig. 5).

Fig. 4. Correct result of the continuous load test

Table 3. Results of preliminary IVM flow tests

Test name	p_{inj} [MPa]	t [μs]	d [ml/min]
Fuel doses			
Pre-injection	80	160	[2.5 ±2.1] 0.7
Part load	120	600	[30.5 ±9.2] 25.1
Maximum load	160	1200	[66.8 ±10.0] 56.9
Idle	25	540	[4.9 ±2.5] 4.4
Fuel returns			
Test name	p_{inj} [MPa]	t [μs]	r [ml/min]
Back flow	135	810	[38.0 ±26.6] 11.7
Back flow 2	25	540	[5.0 ±3.0] 3.6

Tables 3 and 4 present the measurement and calculation results obtained during the preliminary test. Although the fuel doses fell within the manufacturer's specified ranges, their values deviated from the accepted reference patterns. This was especially the case for points 2` and 3`, which were obtained under part-load and full-load conditions. As a result, the area of the tested injector was not only shifted but also 20% smaller compared to the quadrilateral 1-2-3-4 (Fig. 6).

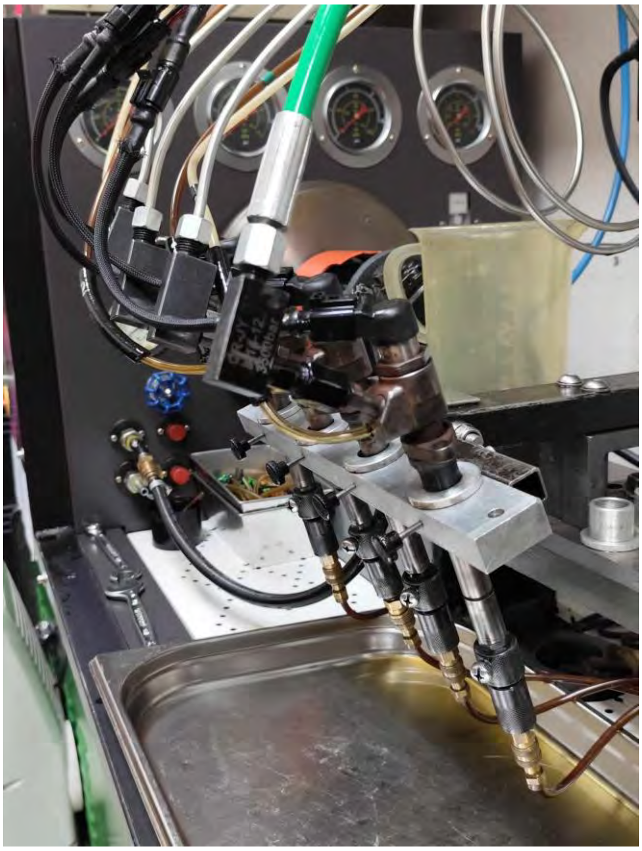

Fig. 5. Injector testing on the Stardex Nova Ultima test bench

Table 4. Results of surface area calculations for the figure 1`-2`-3`-4`

Input data						
Point	t			d		
1`	160			0.7		
2`	600			25.1		
3`	1200			56.9		
4`	540			4.4		
Calculation results						
A_{box}	A_{I}	A_{II}	A_{III}	A_{IV}	A_{V}	A_{VI}
58,448	13,992	9540	17,325	2442	703	5368
A_{VII}						
9078						

The cause can be attributed to the improper functioning of the precision pair (needle, nozzle), which, given the current operating conditions, should be replaced without delay [14]. It is also worth noting that the valve group operated correctly, maintaining its sealing regardless of the pressure set on the test bench. This is evidenced by the low values of return fuel flows.

Microscopic examinations revealed corrosion on many components that had direct contact with diesel fuel. Additionally, erosive wear was detected near the needle tip (Fig. 7). As a result, the decision to replace the precision pair was upheld, and the remaining components were directed for thorough cleaning in an ultrasonic cleaner. This process allows for the removal of deposits and contaminants that were not caught by the fuel filter. It is also possible to remove corrosion traces in cases where the pits are not extensive and are not deep [2, 13]. The piezoelectric actuator was excluded from this stage, as its insulation could have been permanently damaged.

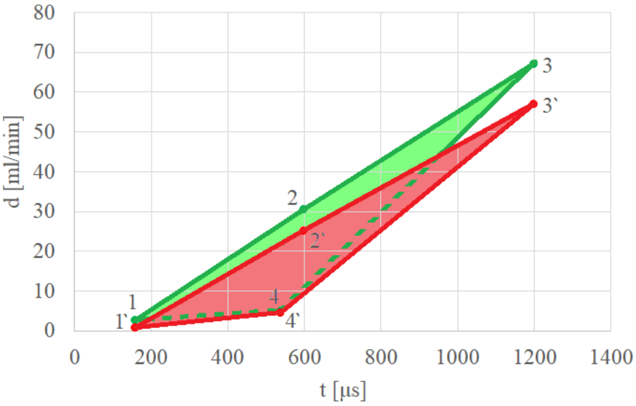

Fig. 6. Graphical interpretation of the results of preliminary tests

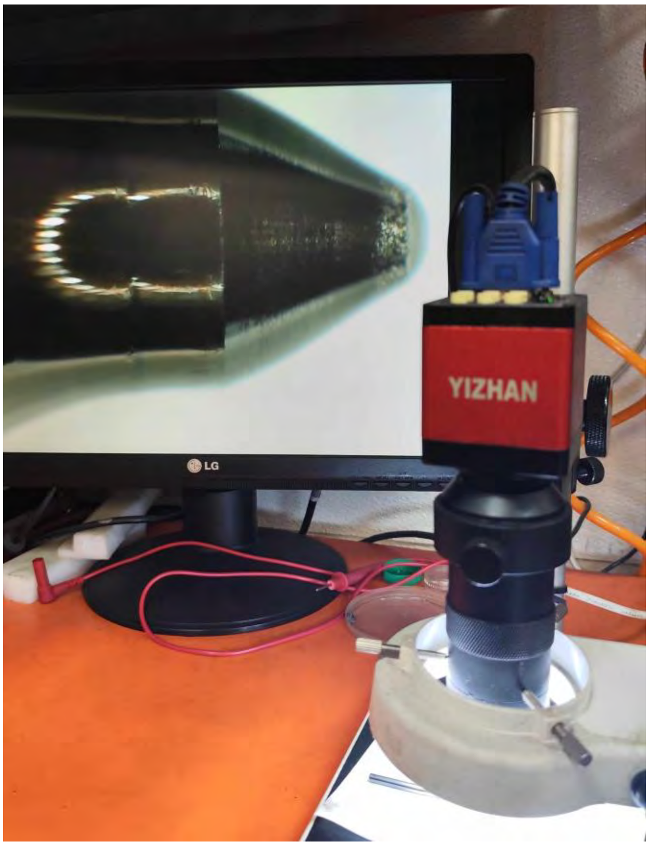

Fig. 7. Observation of corrosion traces and wear on the needle tip

To correct the fuel dosing by the injector, a shim from a lower selection group was used during the assembly of its upper part (Fig. 8). Additionally, the distance between the piezoelectric actuator and the valve pushrod was slightly reduced, setting the value of GAP = 1.7 µm. The calibration process using the Mega Tester V3 device is shown in Fig. 9.

Fig. 8. GAP calibration during the tightening of the piezoelectric actuator

3.2. Main tests

Tables 5 and 6 present a summary of the final results obtained in the main tests.

Table 5. Results of the main IVM flow tests

Test name	p_{inj} [MPa]	t [µs]	d [ml/min]
Fuel doses			
Pre-injection	80	160	[2.5 ±2.1] 1.8
Part load	120	600	[30.5 ±9.2] 31.2
Maximum load	160	1200	[66.8 ±10.0] 66.1
Idle	25	540	[4.9 ±2.5] 5.3
Fuel returns			
Test name	p_{inj} [MPa]	t [µs]	r [ml/min]
Back flow	135	810	[38.0 ±26.6] 13.4
Back flow 2	25	540	[5.0 ±3.0] 3.9

The regeneration process can be considered successful, as the surface areas of the tested and reference injectors were nearly identical, with a size difference of only 1.4% (Fig. 9). This improvement resulted from an increase in the individual fuel dose values compared to the initial condition, which affected the position of the quadrilateral vertices 1``-2``-3``-4``. At the same time, despite not replacing the valve group, the back fuel flow values remained very similar to those obtained in the preliminary test. It is also worth noting that the coding phase was carried out on the same test bench used for all IVM flow tests. This step is essential before the final installation of the injector in the engine.

Table 6. Results of surface area calculations for the figure 1``-2``-3``-4``

Input data						
Point	t			d		
1``	160			1.8		
2``	600			31.2		
3``	1200			66.1		
4``	540			5.3		
Calculation results						
A_{box}	A_{I}	A_{II}	A_{III}	A_{IV}	A_{V}	A_{VI}
66,872	15,356	10,470	20,064	2310	665	6468
A_{VII}						
11,539						

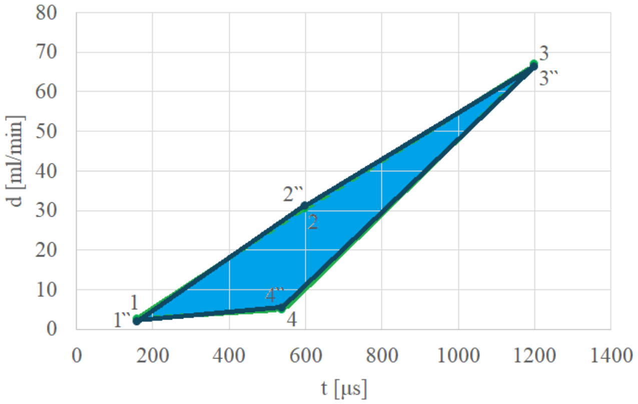

Fig. 9. Graphical interpretation of the results of the main tests

4. Conclusions

The proposed box method enables the use of advanced diagnostics for common rail injectors, whose operation raises concerns despite meeting the requirements set by the manufacturer. Its main advantages include:

1. The use of reference points eliminates the need for additional measurements during the experimental phase. As a result, the entire testing procedure is automated and does not require switching to manual mode or modifying the test bench software.
2. The positioning of the vertices affects the size of the surface areas of the analysed shapes and indicates possible causes of injector dysfunction.
3. The analytical process poses no significant difficulties, as elementary mathematical formulas are used in the calculations. Their correctness can be verified using other mathematical methods, such as Gauss or Newton-Cotes formulas.
4. In workshop and laboratory practice, cases were considered where 3 out of 4 vertices of the irregular quadrilateral were directly located along the sides of the rectangle. This allowed simplifying equation (1) due to a smaller number of components.
5. Input data for the calculations can come from any test bench where IVM flow tests are conducted.

It should be emphasized that the use of the box method becomes ineffective when the manufacturer's standard procedure assumes a greater number of measurement points. An example of this is the electromagnetic injectors from Delphi, which on the Stardex Nova Ultima test bench are checked for 15 fuel doses and 1 return fuel flow. This process is advanced and precise enough that the use of extended diagnostics becomes unnecessary.

It should also be noted that the calculated fuel delivery surface areas should be treated as purely hypothetical, as they may not reflect the actual performance of the injector outside the base (standard) operating points. Nevertheless, the proposed solution has proven applicable in practical settings, and the presented implementation method has no direct equivalent in the existing technical literature.

Acknowledgements

All research was conducted at the Szczecin-based company AUTO NEXT SERWIS, which provided the specialized equipment and tools necessary for the injector regeneration process.

Nomenclature

A	surface area of the quadrilateral (indices): 1-2-3-4 – reference 1`-2`-3`-4` – in preliminary tests 1``-2``-3``-4`` – in main tests
$A_{I\text{-}VII}$	surface areas of the box's components
A_{box}	surface area of the box
d	injection dosage
C	piezo actuator capacitance
GAP	space between the piezo actuator and the valve pusher
IVM	injector volume metering
MBR	minimum bounding rectangle
PC	personal computer
PCR	piezo common rail
p_{inj}	injection pressure
R	piezo actuator resistance
t	nozzle opening time
TDCi	turbo diesel common rail injection
U	continuous load test voltage

Bibliography

[1] Abramek KF, Osipowicz T, Mozga Ł. The use of neural network algorithms for modeling injection doses of modern fuel injectors. Combustion Engines. 2021;185(2):10-14. https://doi.org/10.19206/CE-137959

[2] Abramek KF, Stoeck T, Osipowicz T. Statistical evaluation of the corrosive wear of fuel injector elements used in comon rail systems. Strojniški vestnik – Journal of Mechanical Engineering. 2015;61(2):91-98. https://doi.org/10.5545/sv-jme.2014.1687

[3] Alexander DC, Koeberlein GM. Elementary geometry for college students. 5th ed. Belmont: Brooks/Cole, Cengage Learning. 2011.

[4] Bremigan EG, Bremigan RJ, Lorch JD. Mathematics for secondary school teachers. Washington: The Mathematical Association of America 2011.

[5] Busz W, Walaszyk A. Optimize the testing process common rail fuel injectors. Combustion Engines. 2015;162(3):978-981.

[6] Chomik Z, Łagowski P. The analysis of mechanical damage of Common Rail injectors. Journal of Research and Applications in Agricultural Engineering. 2019;64(1):13-20.

[7] Cuoco A, Waterman K, Kerins B, Kaczorowski E, Manes M. Linear algebra and geometry. Providence, Rhode Island: MAA Press; 2019;46.

[8] Karpiuk W, Bor W, Smolec R. Possibilities of analysis of condition and repair of common-rail system injectors. Journal of KONES Powertrain and Transport. 2018;23(4):209-216. https://doi.org/10.5604/12314005.1217208

[9] Kneba Z, Straszak P, Jakóbczyk K. The effectiveness of fault detection in common rail injectors examination methods. Combustion Engines. 2017;170(3):49-56. https://doi.org/10.19206/CE-2017-308

[10] Longwic R, Sander P, Lotko W, Gielniewski R, Gardyński L. Wear and tear problems used injectors in common rail systems. TTS. 2013;20(10):1709-1718.

[11] Mazanek A. The evaluation of the parameters of the Common Rail injection system supplied with fuels of various bio-component content. Nafta-Gaz. 2012;8:540-544.

[12] Mega Tester V3. Software instruction. Manual version 3.0. Khmelnitsky: The private company "Open System"; 2019.

[13] Osipowicz T, Lisowski M. The influence of corrosion phenomena on operational parameters of modern fuel injectors CI-engines. Combustion Engines. 2017;171(4):17-23. https://doi.org/10.19206/CE-2017-403

[14] Puzdrowska P. Adoption of the F-statistic of Fisher-Snedecor distribution to analyze importance of impact of modifications of injector opening pressure of a compression ignition engine on specific enthalpy value of exhaust gas flow. Combustion Engines. 2024;196(1):37-45. https://doi.org/10.19206/CE-168520

[15] Serra M. Discovering geometry. An investigative approach. 3rd ed. Emeryville. Key Curriculum Press 2003.

[16] Stewart J, Redlin L, Watson S. Precalculus. Mathematics for calculus. 5th ed. Belmont: Brooks/Cole Cengage Learning 2009.

[17] Stoeck T. Analytical methodology for testing Common Rail fuel injectors in problematic cases. Diagnostyka. 2021; 22(3):47-52. https://doi.org/10.29354/diag/135999

[18] Stoeck T. Diagnostic method for a piezoelectric injector using the Newton-Cotes formula. Combustion Engines. 2024;197(2):106-111. https://doi.org/10.19206/CE-177132

[19] Stoeck T. Method for testing modern common rail piezoelectric fuel injectors. Combustion Engines. 2021;186(3):31-36. https://doi.org/10.19206/CE-140246

[20] Stoeck T. Methodology of testing common rail fuel injectors with the use of Gauss's formulas. Combustion Engines. 2021;184(1):11-15. https://doi.org/10.19206/CE-133505

[21] Urban J. Study of the car fifth TDI-PCR-2L diesel engine with selective catalytic reduction medial load. Journal of KONES Internal Combustion Engines. 2005;12(3-4):343-354.

[22] VDO. CR injector test and repair. Manual version 1.21. Schwalbach: Continental Trading GmbH 2014.

[23] Vince J. Mathematics for computer graphics. 5th ed. London: Springer-Verlag London Ltd. 2017. https://doi.org/10.1007/978-1-4471-7336-6

Tomasz Stoeck, DEng. – Faculty of Mechanical Engineering and Mechatronics, West Pomeranian University of Technology in Szczecin, Poland.

e-mail: *tstoeck@wp.pl*

Article citation info
Grzywna M. Evaluation of the reliability of a heavy diesel locomotive. Combustion Engines. 2025;202(3):94-99.
https://doi.org/10.19206/CE-205974

Maciej GRZYWNA

Combustion Engines
Polish Scientific Society of Combustion Engines

Evaluation of the reliability of a heavy diesel locomotive

ARTICLE INFO

Received: 6 May 2025
Revised: 2 June 2025
Accepted: 5 June 2025
Available online: 16 June 2025

The article addresses the evaluation of the operational process of a heavy diesel locomotive type 15D/A, which was developed through the modernization of the TEM2 locomotive. The primary goal of the modernization was to improve technical and operational parameters while keeping investment costs low. The paper discusses the failure structure, causes of inefficiency and breakdowns, and calculates failure intensity parameters in relation to operational and transport performance. The determined indicators show relatively low failure rates for the analysed group of vehicles. Technical availability indicators – both operational and actual – were also evaluated. The research results demonstrate that the modernization reduced the locomotive's failure rate compared to other diesel traction vehicles, confirming the investment's rationale.

Key words: *heavy diesel locomotive, reliability, modernization, operational efficiency, maintenance*

1. Introduction

Contemporary challenges related to the sustainable development of railway transport are driving intensive modernization efforts of rolling stock, particularly locomotives. As the fleet ages, environmental requirements increase, and the need to improve energy efficiency grows, the modernization of existing vehicles becomes a key element of the railway sector's development strategy. In Poland, the average age of diesel locomotives exceeds 40 years, resulting in increased fuel consumption and the emission of harmful substances [4]. Similar issues are observed in other countries, where modernization not only involves the replacement of the drive system but also the implementation of modern control and energy management systems [6].

The modernization of locomotives aims not only to reduce operating costs but also to adapt vehicles to increasingly stringent emission standards. An example is the replacement of traditional two-stroke engines with modern power units, which allows for a significant reduction in fuel consumption and CO_2 emissions [4]. Additionally, the introduction of hybrid systems and the use of energy recovered during braking contribute to improved energy efficiency [3]. In the article [5], contemporary powertrain systems of rail vehicles were analyzed, including internal combustion engines, hybrid systems, and bi-mode propulsion systems. Attention was drawn to the increasing importance of energy storage, for example, through the use of ultracapacitors or fuel cells, which allows for an improvement in powertrain efficiency and adaptation to various operational conditions. For electric locomotives, optimizing traction systems, including the use of thyristor inverters and automatic control systems, is of key importance [9].

Another important aspect of modernization is improving reliability and operational safety. The introduction of online diagnostic systems and artificial intelligence algorithms enables early fault detection, which translates into reduced downtime and repair costs [14]. In the article [11], the use of thermal imaging for thermal analysis of the braking system and drivetrain of an electric locomotive under real operating conditions was presented. These studies enable the identification of potential operational issues and the assessment of the effectiveness of cooling and lubrication systems, which is crucial for ensuring the safety and reliability of rail vehicles.

Undoubtedly, an important aspect of the operation of internal combustion engines in locomotives is the wear of mechanical components, such as piston rings. The article [8] presents a study on the wear of modern sets of piston rings in a locomotive diesel engine. The analysis of the wear of these components is of key importance for evaluating engine durability and for planning maintenance and overhauls, which directly affect the reliability and operating costs of locomotives.

At the same time, rolling stock modernization must take into account the specifics of regional operating conditions, such as terrain configuration and infrastructure availability [1].

Due to the approaching deadline obliging the vehicle owner to perform P5-level repairs (major overhauls) to the SM48 series locomotives operated by them, taking into account the lack of planned changes in the vehicle components that could significantly increase the reliability of the traction means in question after the repair, and the financial factor related to the costs of carrying out such repair, it was planned to discontinue their operation.

The vehicles withdrawn from operation, taking into account the need to maintain a sufficient number of available locomotives in order to perform the planned operational work, had to be replaced with traction resources.

The lack of funds for the purchase of new rolling stock became a reason for developing a concept for the modernization of this series of locomotives, thanks to which the costs of obtaining vehicles with technical and operational parameters similar to those obtained by newly built vehicles amounted to approx. half of the value of brand new locomotives.

This modernization decision allowed the acquisition of about twice as many traction vehicles compared to purchasing new ones. This solution, considering earlier modernization decisions for other locomotive series, was well-received and helped maintain the operational fleet size.

2. Description of the analysed subject

The 15D/A locomotive is classified as a heavy diesel locomotive designed for freight train operations. Due to its layout of components typical for vehicles intended for shunting work – a single driver's cab and walkways on both sides of the engine compartment – the traction vehicle is suitable for heavy shunting work as well as for leading transfer and line trains. The traction characteristics also allow for double-traction operation.

The design resulted from a comprehensive modernization of the TEM2 locomotive, retaining the frame, bogies, fuel tanks, and traction motors. The original Soviet-made diesel engine was replaced with a modern American-made propulsion unit compliant with UIC 624 Annex A (Stage IIIa) emission requirements. The rated power of the TEM2 locomotive is 882 kW (1200 HP), while the modernized 15D/A locomotive has nearly double the power – 1550 kW (2107 HP). As a result, the original shunting characteristics were replaced by those of a line freight locomotive, while retaining the functionality of a shunting locomotive.

The locomotive consists of 11 main components arranged in such a way as to ensure proper weight distribution of wheelset pressures on the track. These components meet current national and EU standards. Access for maintenance personnel complies with the maintainability requirements of the vehicle, thanks to which inspection and repair activities can be performed in a shorter time, compared to the original, non-modernized version of the vehicle.

Figure 1 shows the location of the main components of the 15D/A locomotive, and Table 1 provides their descriptions.

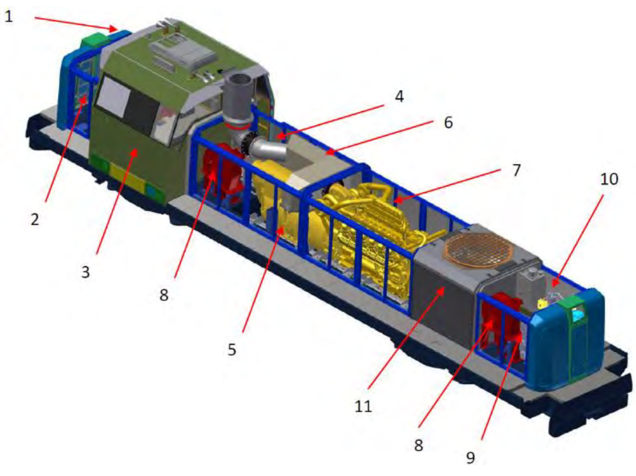

Fig. 1. Location of the main components of the 15D/A locomotive

Table 1. Main components of the 15D/A locomotive

No.	Component
1	Battery compartment
2	Electrical compartment – medium and high-voltage cabinets
3	Driver's cab
4	Main rectifiers of the locomotive
5	Main generator and auxiliary generator
6	Exhaust silencer
7	Diesel engine
8	Traction motor fans
9	Pneumatic panel
10	Compressor unit
11	Cooling unit

Table 2 presents the basic technical and operational characteristics of the analysed locomotives.

Table 2. Basic technical and operational characteristics of the 15D/A loco

Parameter	Value
Manufacturer	ŁTZ, BMZ, NEWAG (modernization)
Type	15D/A
Purpose	Shunting, freight train operations
Gauge	UIC 505-1
Axle arrangement	Co'Co'
Total length	16,970 mm
Maximum width	3084 mm
Maximum height from railhead	4553 mm
Distance between extreme axles	12,800 mm
Tare weight	110,000 kg ±3%
Service weight	116,000 kg ±3%
Fuel capacity	5400 kg (6000 dm^3)
Cooling system fluid volume	680 dm^3
Sand capacity	800 kg
Control multiplicity	Control of two locomotives from one cab
Locomotive control	Microprocessor controller
Transmission type	Electric
Brake system	Knorr-Bremse
Chassis type	Bogie
Connection to bogie	Pivot pin and spherical supports
Distance between pivot pins	8,600 mm
Number of bogies	2
Number of traction motors	6
Number of driving axles	6
Coupling type	Screw coupling

3. Analysis of recorded failures

Failure data were collected over a two-year period for a group of more than a dozen locomotives, based on operational logs and maintenance reports documenting the service and repair processes. These documents include:

- The railway vehicle logbook
- The periodic inspection logbook for traction vehicles
- The current repair logbook for traction vehicles.

These records contain detailed information such as:

- Series and vehicle number
- Date of failure identification
- Cause of failure
- Duration of maintenance tasks
- Type of work (maintenance level)
- Work description
- Labor intensity of repairs
- Diagnostic parameter values before and after repairs
- Quantity and value of materials and spare parts used
- Repair technology.

3.1. Recorded failures

The failure structure of the analyzed group of 15D/A locomotives is shown in Fig. 2. Table 3 explains the work order code fragments used in the chart labels (Fig. 2).

The fault coding system uses digits separated by dots. Each subsequent section of the code corresponds to the subsequent levels of decomposition of the system into subsystems. The method of the cited coding system assumes the division of the locomotive into units, subassemblies and elements, which to some extent corresponds to the classification of the coding method of the position-group method described in [2]. Table 3 presents the highest level of decomposition of the system into units.

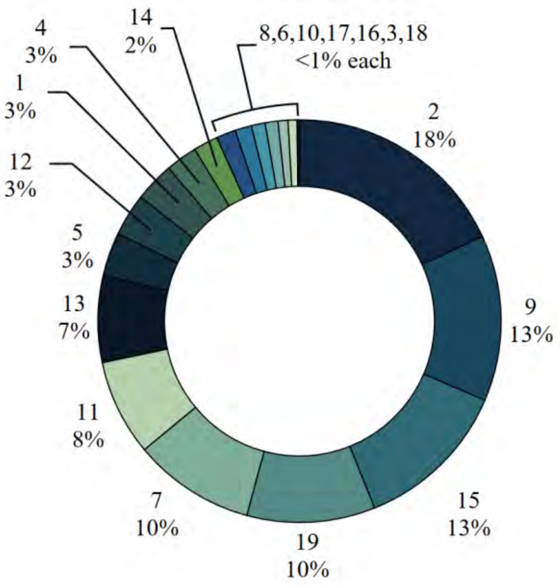

Fig. 2. Failure structure of the analysed locomotive group

Table 3. Explanation of work order code fragments

Code	Component	Code	Component
1	Others	10	Radiotelephone
2	Pneumatic system	11	Electric machines
3	Suspension	12	Batteries
4	Brake mechanical part	13	Lighting
5	Wheelsets	14	Diesel engine
6	Brake pneumatic part	15	Cooling system
7	Coupling and pneumatic couplers	16	Lubrication system
		17	Fuel system
8	Sandboxes	18	Turbocharger
9	Electrical equipment	19	Driver's cab

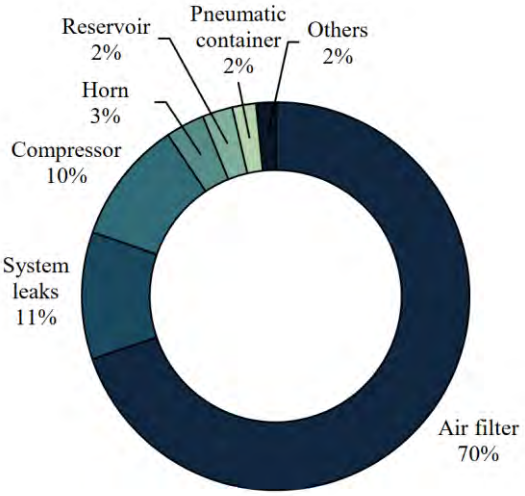

Fig. 3. Failure structure of the pneumatic system

The most common causes of failures in the analyzed group of 15D/A locomotives include:

- Pneumatic system failures – 18%
- Electrical equipment failures – 13%
- Cooling system failures – 13%
- Driver's cab component failures – 10%.

Failures in these components account for nearly half of all recorded inefficiencies.

Figure 3 shows the failure structure of the pneumatic system – the most unreliable component of the analyzed locomotive group.

The most common causes of pneumatic system failures are:

- Air filter failures – 70%
- System leaks – 11%
- Air compressor failures – 10%.

The most unreliable component in the pneumatic system is the air filters, accounting for approximately 14% of all recorded failures. In most cases, the issue is caused by membrane clogging, which disrupts airflow. The membrane must be cleared using compressed air, and if this is ineffective, the component must be replaced.

About 11% of pneumatic system failures result from leaks, primarily at joints and pneumatic valves.

One in ten pneumatic system failures is related to compressor unit damage, often due to oil shortages, clogged filters, or leaks affecting the component's performance.

Figure 4 shows the failure structure of the electrical equipment in the analyzed locomotive group. The main causes of electrical equipment failures are:

- Contactor failures – 31%
- Engine controller failures – 22%
- CAN bus and software issues – 11%
- GPS system failures – 8%.

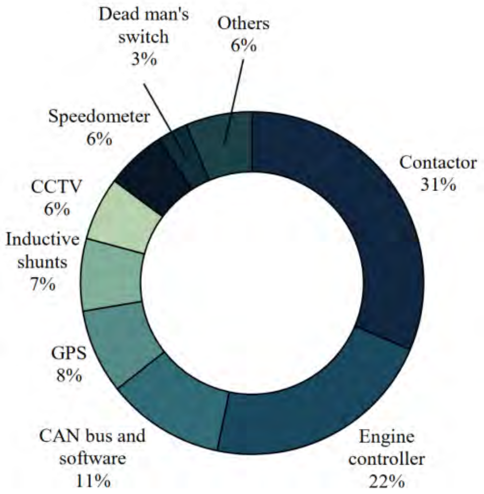

Fig. 4. Failure structure of the electrical equipment

Approximately one-third of failures are caused by contactor damage, primarily line contactors, excitation contactors, shunting contactors, and traction motor contactors. These failures are mainly due to power supply issues and errors.

Every fifth failure of electrical equipment results from damage to the combustion engine controller, which results in the inability to start it.

About 11% of failures are related to errors in the software of the traction vehicle's on-board computer and damage to the CAN bus. As a result, there is a loss of connection and a lack of communication between important components of the locomotive, preventing its proper use.

In 8% of cases, electrical equipment failures occur as a result of incorrect operation of the GPS device. This has an impact on the difficult work of the department responsible for planning vehicle maintenance – due to the lack of possibility of obtaining actual data on the number of hours of operation of the combustion engine until its next inspection, and the dispatch, because the positioning of the locomotive can be predicted only on the basis of processed information from the train timetable sent by the IT systems of the railway infrastructure manager. The GPS positioning system, using a fuel probe, also allows for monitoring the fuel tank filling level and any accelerated volume or mass losses.

3.2. In-service failures

Among the registered damages causing the unsuitability of a traction vehicle considered as a technical object, it is necessary to distinguish those occurring during train operation, light running, or shunting work were distinguished and resulted in the need to replace it with a replacement vehicle or to call another traction vehicle to pull the damaged traction means from the railway line – a section of the line between two signalling posts – to the nearest station for repair or sending it to a workshop.

In order to facilitate the classification and analysis of information relating to faults, damage codes are used that uniquely identify the damaged component (subassembly).

Failures can be categorized by their cause, such as damage to a component (subassembly). The causes include unfavourable weather conditions, improper vehicle operation by the traction team, use of improper material or material with improper properties, contamination or improper fuel composition, and improperly performed repairs by the maintenance department or guarantor.

Figure 5 shows the structure of recorded failures.

The most failure-prone components include electrical circuit devices and apparatuses, accounting for 30% of all failures, the internal combustion engine, responsible for 17% of all failures, and elements of the vehicle's pneumatic system, constituting 9% of total failures. A significant proportion of incidents involve locomotive breakdowns without the identification of a specific faulty component, representing 21% of all reported failures. This may result from specific operational conditions at the time, temporary malfunction of a component or subsystem that later returned to normal operation without showing signs of damage, or improper handling by the train crew, which, while not causing physical damage, temporarily impedes proper vehicle operation.

Based on statistical data concerning operational and transport activity, it is possible to determine the failure rate parameter [12] – an index associated with maintainability, characterizing the reliability of the analyzed locomotive group. In the given case, this parameter defines the number of failures requiring the deployment of a replacement vehicle or the towing of the damaged locomotive off the railway track, in relation to operational output expressed in vehicle-kilometers and gross ton-kilometers performed by the given vehicle population.

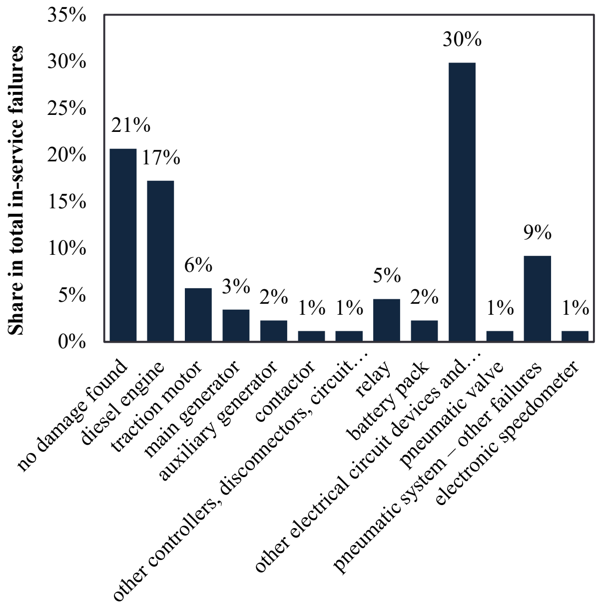

Fig. 5. In-service failure structure of the analysed locomotive group

The failure rate for operational performance is given by (1):

$$z_l = \frac{N(l)}{N_O \cdot l} = 25.06 \left[\frac{\text{failures}}{\text{million vehicle−km}}\right] \quad (1)$$

where: N(l) – number of failures during operational work l, N_O – population size, l – operational work.

The failure rate for transport performance is given by (2):

$$z_m = \frac{N(m)}{N_O \cdot m} = 2.73 \left[\frac{\text{failures}}{\text{100 million gross ton−km}}\right], \quad (2)$$

where: N(m) – number of failures during transport work m, m – transport work, other markings – as above.

Appropriate processing of the collected operational data made it possible to determine the failure rate parameter for other types of diesel traction vehicles in relation to operational performance – see Fig. 6, and transport performance – see Fig. 7.

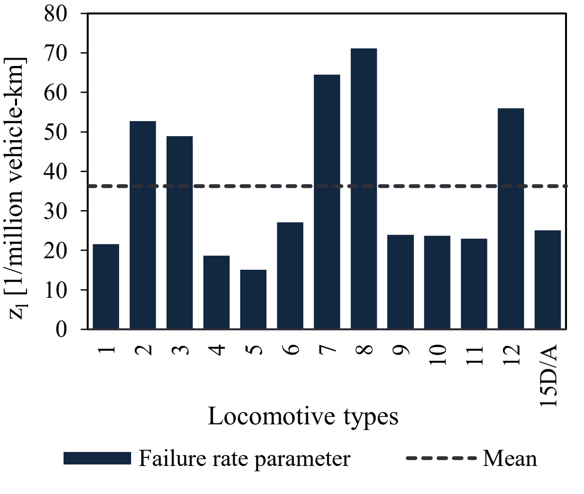

Fig. 6. Failure rate parameter in relation to operational performance

Data for the remaining vehicles, as with the analysed locomotives, were collected over the same two-year operational period. The dashed lines in the graphs indicate the average indicator values for all types of locomotives. The remaining locomotives are diesel-powered, comprising both line-haul (freight) and shunting types, with several units (more than a dozen in each group) included in the analysis.

The failure rate parameter related to operational performance, calculated for the studied group of traction vehicles, amounts to 25.06. This value represents approximately 69% of the average value of the parameters determined for other types of diesel locomotives. Such a value indicates a relatively low failure rate for the 15D/A vehicle population, consistent with modernization expectations and assumptions.

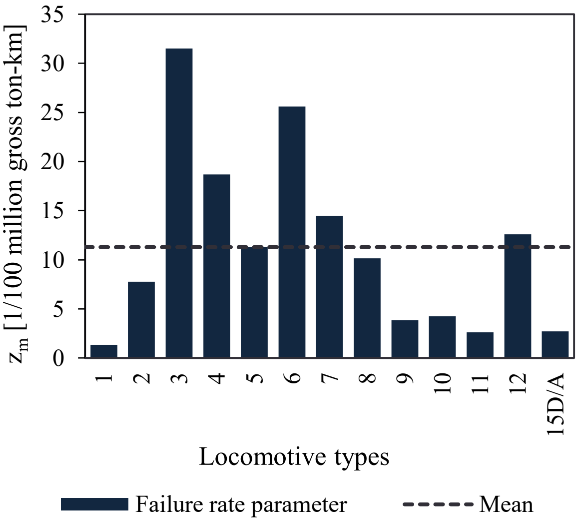

Fig. 7. Failure rate parameter in relation to transport performance

The failure rate intensity parameter relative to transport performance, calculated for the analyzed population of traction vehicles, amounts to 2.73, which constitutes approximately 24% of the average value of the parameters determined for other types of diesel traction locomotives. These low values of failure rate intensity indicators support the conclusion that this type of locomotive is characterized by low unreliability.

3.3. Availability

Availability is defined as the ability of a given system to remain in a state that allows it to perform its required functions under specified conditions, at a specified time or within a given time interval, assuming the required external resources are provided [13]. Availability depends not only on maintenance-related unserviceability but also on the probability of unserviceability that prevents the system from fulfilling its assigned functions (known as the effect of unavailability) [10].

The availability index is understood as the probability that the traction vehicle is in an operational state at time t. Therefore, the technical availability index must satisfy eq. (3):

$$A(t) = 1 - F(t) + \int_0^t [1 - F(t - \tau)]\, h(\tau) d\tau \tag{3}$$

where: $h(t)$ – renewal density function: $h(t) = \frac{H(t)}{dt}$.

In practice, equation (3) is not applicable due to the fact that the very concept of the technical availability coefficient is understood as a stationary value that the function A(t) tends to approach with increasing time [7] – equation (4):

$$A = \frac{T_0}{T_0 + U_0} \tag{4}$$

where: T_0 – mean time the locomotive remains in an operational (serviceable) state, U_0 – mean time the locomotive remains in an unserviceable state.

According to [2], the technical availability index is synonymous with the term "availability" and is classified as a fundamental reliability characteristic of renewable systems, taking into account the failure rate and maintainability of the vehicle.

The analysed group of vehicles undergoes both corrective repairs and preventive maintenance. Consequently, two types of technical availability have been distinguished: operational availability and actual availability.

Operational availability (A_o) is calculated by considering the time the traction vehicle remains in an unserviceable state due to a failure.

Actual availability (A_r) is calculated by considering both the time the traction vehicle is unserviceable due to a failure and the time it is undergoing preventive maintenance as specified in the Maintenance System Documentation.

To assess the technical availability of the analysed group of locomotives over a specific time interval (0, t), the operational availability A_o should be calculated using eq. (5):

$$A_O = \frac{\sum_{i=1}^{N} TZ_i}{\sum_{i=1}^{N} TZ_i + \sum_{i=1}^{N} TN_i} = 0.8609 \tag{5}$$

where: TZ_i – time the locomotive (i) remains in a serviceable state, TN_i – time the locomotive (i) remains in an unserviceable state, N – population size.

The actual availability A_R can be determined using equation (6):

$$A_R = \frac{\sum_{i=1}^{N} TZ_i}{\sum_{i=1}^{N} TZ_i + \sum_{i=1}^{N} TN_i + \sum_{i=1}^{N} TO_i} = 0.7784 \tag{6}$$

where: TO_i – time the locomotive (i) remains in an unserviceable state due to preventive maintenance, other symbols – as previously defined.

Considering the short, two-year service period of the analysed group of traction vehicles, the relatively low values of the indicators may be attributed to the initial phase of vehicle operation – the so-called run-in period.

4. Conclusions

The modernization of the TEM2 locomotive to the 15D/A version has resulted in the acquisition of vehicles with favourable operational characteristics, including nearly a twofold increase in power output, while maintaining reasonable investment costs – approximately 50% of the price of new locomotives.

The most common causes of vehicle failureability include failure of the pneumatic system (especially air filters), electrical equipment, cooling and cab driver components. It is therefore essential to review the range and capability of preventive maintenance tasks for the mentioned components.

The failure rate intensity parameter for the analysed vehicle population, in relation to operational performance, is 25.06 failures per million vehicle-kilometers, and in relation to transport performance, 2.73 failures per 100 million gross ton-kilometers. These values indicate a lower failure rate compared to other types of diesel locomotives – 69% and 24% of the average values for these parameters, respectively.

The operation and actual technical availability indicator values are below expectation for the modernized units because of the initial phase of operation – so-called running-in period. Monitoring and viewing the indicators at subsequent operation years is recommended..

The conducted analysis validates the justifications of modernization decisions as an excellent method of extending the lifespan of rolling stock and improving its operability with a low budget..

The results of the research can serve as a basis for developing the best maintenance and modernization strategies for other similar vehicles.

Upon completion of the criterion in view of calendar time to perform preventive activities at the P4 level, the entire inter-repair time could need to be thoroughly analyzed for reliability along with the test described above. The analysis would also need to include other RAMS parameters (reliability, availability, susceptibility and maintenance and safety) so as to have the entire view of how the entire system operates. Use of such a method allows one to make an overall estimation of the technical condition and life of modernized locomotives. Further developing the examination of traditional indicators, one can identify patterns and trends of failure modes, estimate the efficiency of the selected maintenance strategy, and define the reliability growth or degradation in time.

It may be a solution for providing support in the decision-making process regarding the continuation, modification or abandonment of some practices that are functioning within the maintenance system. In addition, using the RAMS indicators within the system evaluation allows for the identification of the most likely failing parts within the locomotive. This then enables the scheduling of design or operation-based action that aims to eliminate weak links, increase system reliability and extend the inter-repair cycles. Implementation of such a method not only allows for the achievement of high values of technical availability indicators that give the opportunity to ensure continuity of operations, but also facilitates the optimization of costs and affects the estimation of the effectiveness of investments in rolling stock modernization.

Bibliography

[1] Ablyalimov O, Rajibaev DO. Research of fuel and energy indicators of modernized diesel locomotives. E3S Web Conf. 2024;477:00084. https://doi.org/10.1051/e3sconf/202447700084

[2] Adamkiewicz W, Hempel L, Podsiadło A, Śliwiński R. Badania i ocena niezawodności maszyny w systemie transportowym (in Polish). WKiŁ. Warsaw 1983.

[3] Ahsan N, Hewage K, Razi F, Hussain SA, Sadiq R. A critical review of sustainable rail technologies based on environmental, economic, social, and technical perspectives to achieve net zero emissions. Renew Sust Energ Rev. 2023; 185:113621. https://doi.org/10.1016/j.rser.2023.113621

[4] Andrzejewski M, Daszkiewicz P, Urbański P et al. Impact of a locomotive engine modernization on fuel consumption. MATEC Web Conf. 2021;338:01001. https://doi.org/10.1051/matecconf/202133801001

[5] Daszkiewicz P, Kołodziejek D. Comparison and analysis of modern combustion powertrain systems of rail vehicles. Combustion Engines 2024;196(1):46-53. https://doi.org/10.19206/CE-171385

[6] Florentsev S, Polyukhovych V, Evpakov V. Modernization of industrial shunting diesel locomotives. International Ural Conference on Electrical Power Engineering (UralCon). 2022. https://ieeexplore.ieee.org/document/9906764

[7] Gniedenko BW, Bielajew JK, Sołowiew AD. Metody matematyczne w teorii niezawodności (in Polish). Wydawnictwa Naukowo-Techniczne. Warszawa 1968.

[8] Kaźmierczak AR. Research on the wear of novel sets of piston rings in a diesel locomotive engine. Combustion Engines 2023;195(4):56-62. https://doi.org/10.19206/CE-168518

[9] Hetman H, Visyn MH, Vlasenko BT, Kyiko OI. Modernization of freight electric locomotives VL80T and VL80S on the Railways of Ukraine. Science and Transport Progress. 2005;9:51-60. https://doi.org/10.15802/stp2005/19960

[10] Martorell S, Villanueva JF, Carlos S, Nebot Y, Sanchez A, Pitarch JL et al. RAMS+C informed decision-making with application to multi-objective optimization of technical specifications and maintenance using genetic algorithms. Reliab Eng Syst Safe. 2005;87(1):65-75. https://doi.org/10.1016/j.ress.2004.04.009

[11] Sawczuk W, Rilo Cañás AM, Kołodziejski S. Thermal imaging of the disc brake and drive train in an electric locomotive in field conditions. Combustion Engines. 2024; 196(1):161-168. https://doi.org/10.19206/CE-174320

[12] Szkoda M. Wskaźniki niezawodności środków transportu szynowego (in Polish). Logistyka. 2012;3. https://yadda.icm.edu.pl/baztech/element/bwmeta1.element.baztech-9093e1bc-e32c-4961-b875-a913438a847a

[13] Szkoda M. Assessment of reliability, availability and ma intainability of rail gauge change systems. Eksploat Niezawodn. 2014;16(3):422-432. https://archive.ein.org.pl/pl-2014-03-11

[14] Zvolenský P, Barta D, Grenčík J, Droździel P, Kašiar Ľ. Improved method of processing the output parameters of the diesel locomotive engine for more efficient maintenance. Eksploat Niezawodn. 2021;23(2):315-23. https://doi.org/10.17531/ein.2021.2.11

Maciej Grzywna, MEng. – Faculty of Mechanical Engineering, CUT Doctoral School, Cracow University of Technology, Poland.

e-mail: *maciej.grzywna@pk.edu.pl*

Article citation info:
Hennek K, Mamala J, Bieniek A, Kołodziej S. Analysis of the acceleration process of a passenger vehicle under variable load conditions. Combustion Engines. 2025;202(3):100-108. https://doi.org/10.19206/CE-205975

Krystian HENNEK
Jarosław MAMALA
Andrzej BIENIEK
Szymon KOŁODZIEJ

Combustion Engines
Polish Scientific Society of Combustion Engines

Analysis of the acceleration process of a passenger vehicle under variable load conditions

ARTICLE INFO

Received: 16 April 2025
Revised: 3 June 2025
Accepted: 5 June 2025
Available online: 29 June 2025

The study contains an analysis of the acceleration process of a passenger vehicle equipped with an IC powertrain, aimed at determining a throttle control strategy that minimizes fuel consumption during acceleration while maintaining adequate dynamic performance. The first stage involved measuring traction parameters for a constant assumed engine power. The second stage focused on determining a control trajectory that would ensure minimal fuel consumption during acceleration.

To achieve this the acceleration process was examined during a flexibility test in the speed range from 12.5 to 35 m/s, following an acceleration pedal control line related to the crankshaft rotation speed. Implementing the acceleration process along this control line resulted in a reduction in acceleration dynamics, accompanied by a decrease in fuel consumption per distance traveled by nearly 51%. An analysis of the average acceleration values for a given drivetrain gear ratio revealed that exceeding an acceleration pedal position of 70% yields no significant improvement in vehicle dynamics. The optimal acceleration pedal positions during acceleration were found to be within the range of 25% to 70%.

Key words: *acceleration, variable load, chassis dynamometer, fuel consumption, acceleration elasticity*

1. Introduction

Instantaneous values of indicators determining the dynamics and energy intensity of vehicle motion depend on their design, external conditions, traffic intensity, and driver behavior. Regardless of the energy source used, vehicle powertrains consist of propulsion units cooperating with drivetrain systems. This configuration results in the energetic complexity of powertrain systems, which complicates comparative analysis, especially between internal combustion, electric, and hybrid solutions.

At the same time, vehicle movement is powered by energy supplied to the drivetrain from an energy storage system, which directly contributes to the emission of substances into the atmosphere, including carbon dioxide (CO_2), recognized as a greenhouse gas. This issue affects every vehicle with an internal combustion powertrain, while in the case of BEVs (Battery Electric Vehicles), it depends on the method of electric energy generation. For PHEV (Plug-In Hybrid Vehicle) solutions, the overall CO_2 emission is also influenced by the share of different energy types stored in the energy reservoirs – fuel tank and battery packs – as well as the method of energy replenishment (grid charging, regenerative braking) [17].

The need to reduce the negative environmental impact of the automotive sector has two dimensions. The first is local, directly linked to the emission of toxic components into the atmosphere, and is addressed through successive emission standards. In the European Union, these are defined by successive iterations of the Euro standards, from Euro 1 to Euro 7. Since Euro 4 (implemented in 2006), there have been no significant changes in the permissible limits for nitrogen oxides (NO_x), carbon monoxide (CO), and hydrocarbons (HC).

A significantly greater challenge is reducing the environmental impact caused by emissions of non-toxic exhaust components, such as carbon dioxide (CO_2), and the mass and number of particulate matter emitted from the exhaust system, which unequivocally affects global emissions.

In 2021, the successive iterations of emission standards abandoned synthetic test cycles like NEDC (New European Driving Cycle) in favor of real-world driving measurements, through the implementation of the RDE (Real Driving Emissions) procedure. Numerous scientific studies have since been published describing indicators such as fuel consumption and emissions of harmful substances during RDE tests [4, 11, 12].

The rate at which carbon dioxide emissions are being reduced in passenger vehicle exhaust differs across global regions, as illustrated in Fig. 1. The most effective method for reducing CO_2 emissions in exhaust gases is decreasing the consumption of fossil fuels within the TTW (Tank to Wheels) energy chain.

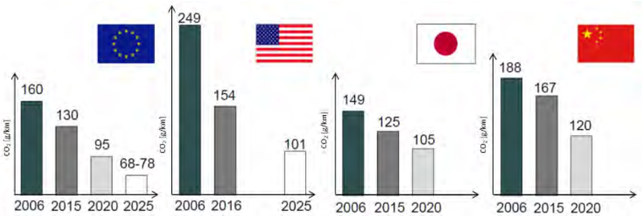

Fig. 1. Trend of carbon dioxide emission reduction in exhaust gases across different regions of the world in g/km [19]

According to report [7], in which global carbon dioxide emissions were presented and was published by scientists from over 90 institutions, the total projected CO_2 emissions for the year 2024 are expected to reach nearly 40 billion tons, indicating a continued upward trend, despite reductions achieved by the EU and the USA (Fig. 2).

The widespread drive to reduce carbon dioxide emissions is the primary motivation behind the continuous efforts of vehicle engineers to improve powertrain systems, including propulsion units. These improvements encompass aspects of design, control strategies, and driver support methods that promote environmentally conscious driving in accordance with the principles of so-called "Eco-Driving."

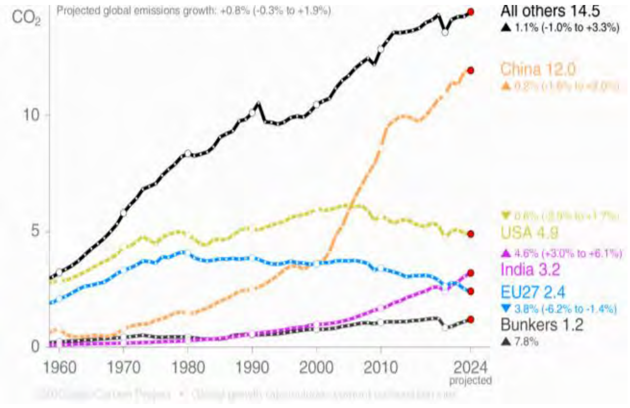

Fig. 2. Annual carbon dioxide (CO_2) emissions forecast for 2024 [7]

In many vehicle brands, driver support for ecological vehicle operation is limited to suggesting optimal instantaneous operating parameters of the powertrain. A common feature is the gear shift indicator displayed on the dashboard, which is mainly used in internal combustion vehicles with manual transmissions. An alternative approach is applied in some vehicles (e.g., Renault), where driving style is evaluated by awarding points on a scale from 0 to 100. This method particularly assesses the driver's behavior regarding the selection of driving speed, driving dynamics, and the use of the brake pedal. Frequent braking and aggressive use of the accelerator may result from high traffic density or a desire to achieve high driving dynamics, thus increasing the load on the powertrain.

Consequently, this leads to high variability in the speed profile, increasing the frequency and intensity of acceleration and braking phases. According to a study [13], eco-driving reduces fuel consumption by 12–37%, with only a minor drop in average driving speed of approximately 3% compared to dynamic driving. In study [14], it was shown that driving style significantly affects energy consumption in electric vehicles, while study [15] demonstrated a considerable impact of driving style, road conditions, and infrastructure on the efficiency of electric vehicles.

Literature source [2] defines moderate vehicle acceleration as acceleration up to approximately 0.85 m/s^2. Achieving higher acceleration rates involves a significant increase in power demand from the powertrain.

The fuel-optimal constant driving speed depends on the specific drivetrain type and vehicle characteristics. According to [6], the optimal speed for minimizing fuel consumption in engines compliant with Euro 5 is 70–75 km/h. On the other hand, publication [16] indicates that minimum fuel consumption occurs while following another vehicle at a speed of approximately 40 mph (65 km/h). Research shows that, for vehicles operating in electric mode or for electric vehicles, the optimal constant speed varies depending on the model and lies within the range of 37 to 60 km/h [18]. Another source [10] confirms an optimal speed of 60 km/h for several different electric vehicles.

Referring to the author's own research on an urban internal combustion vehicle (Fig. 3), the lowest fuel consumption per distance traveled was observed at speeds between 35 and 60 km/h.

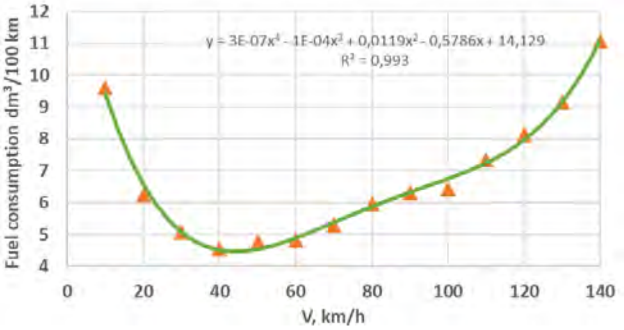

Fig. 3. Distance-specific fuel consumption at constant driving speed for an internal combustion powertrain

Minimizing fuel consumption directly reduces carbon dioxide emissions. By converting the distance-specific fuel consumption of 0.01 dm^3/km (equivalent to 1 dm^3/100 km), the corresponding CO_2 emission values are:

- Gasoline: 23.3 g/km
- Diesel: 26.3 g/km.

The impact of vehicle dynamics (acceleration intensity) on fuel consumption has been the subject of numerous scientific studies. In study [3], the authors analyzed the distribution of driving phases within urban and non-urban cycles, noting that over 20% of accelerations fall within the range of 0–1 m/s^2, and over 15% within 1–4 m/s^2. Despite the relatively small share of acceleration phases (approx. 5%) in the total driving cycle, the acceleration intensity significantly influences fuel consumption.

Fontaras et al. [5] demonstrated a 5% increase in fuel consumption in non-urban traffic and up to 70% in urban traffic. Simultaneously, study [9] analyzed the possibility of optimizing engine load and gear ratios, indicating that extending the acceleration time to 2 s in the 0–40 km/h range may reduce fuel consumption by more than 5%.

In study [2], the acceleration values for different vehicle groups were identified in the range of 0.45–2.87 m/s^2, highlighting their effect on fuel usage depending on driving style and road type. Research presented in [1] showed that higher driving dynamics increase fuel consumption by 40% outside urban areas and by 45% in city traffic.

Ultimately, the dynamics of the acceleration process and the energy demand of vehicle motion depend mainly on how the driver controls the powertrain. Regardless of how advanced the powertrain is – including hybrid or electric configurations – the driver can always operate the vehicle in a non-ecological manner. Therefore, the acceleration phase is the primary factor influencing the energy consumption of vehicle motion. This behavior does not always stem from the driver's intention – it can be forced by traffic conditions, e.g., performing maneuvers in public road traffic that require high dynamics to avoid hazards. Hence, the present analysis of the acceleration process is an attempt to establish a compromise between driving dynamics and energy intensity, aiming to enable dynamic acceleration using an economical operation line within the drivetrain system.

2. Identification studies

2.1. Vehicle acceleration under constant power

The first stage of the study involved performing an acceleration test of a passenger car on a chassis dynamometer with a predefined constant power input in the powertrain. The tested vehicle was equipped with a spark-ignition engine featuring port fuel injection and a manual transmission. The technical specifications of the tested vehicle are presented in Table 1.

Table 1. Basic parameters of the tested vehicle

Manufacturer	Volkswagen
Engine designation	AWT
Displacement	1781 cm^3
Maximum power	110 kW
Crankshaft rotational speed at maximum power	5700 rpm
Maximum torque	210 Nm
Crankshaft rotational speed at maximum torque	1750 rpm
Charging method	turbocharger
Compression ratio	9.5:1
Measurement gear number	4
Measurement gear ratio	1.029

In the acceleration test, a flexibility trial of the vehicle acceleration process was conducted for a selected, constant gear ratio in the drivetrain system. The flexibility test was carried out within the speed range from 45 km/h (12.5 m/s) to 120 km/h (35 m/s) using a MAHA MSR500 chassis dynamometer. The acceleration trials were performed under constant excitation conditions, resulting from a fixed power level in the drivetrain, which in turn was determined by a predefined throttle pedal position. The individual throttle pedal positions and the corresponding vehicle speed profiles during the tests are presented in Fig. 4.

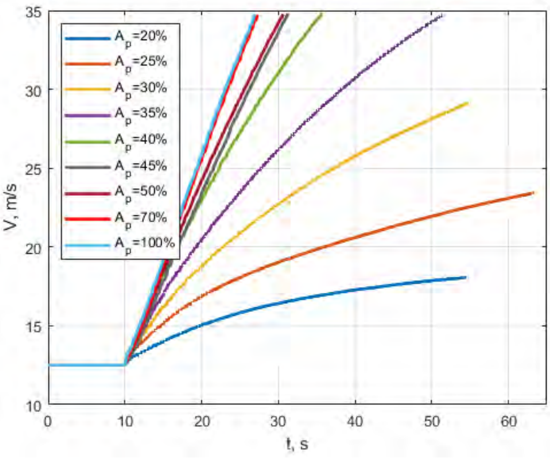

Fig. 4. Time profiles of vehicle speed measured during acceleration tests

Each acceleration test was initiated by reaching and stabilizing the minimum vehicle speed of 12.5 m/s for at least 10 seconds. Subsequently, the accelerator pedal was rapidly depressed to the target position, which was maintained until the vehicle reached the maximum speed or exceeded 35 m/s. In the initial trials, due to low throttle positions, the vehicle did not reach the target maximum speed, as the resistive forces exceeded the available wheel power. This situation occurred at throttle pedal positions (A_p) of 20%, 25%, and 30%, where the intended final speed was not achieved.

In Fig. 5, the vehicle speed profiles obtained from all acceleration trials are presented and indicated as 'Dane'. These profiles were then subjected to linear interpolation, denoted as V(t). The tolerance field of the interpolated results is also marked in Fig. 5 and reflects the repeatability of measurements at a given power level. A linear equation was selected as the interpolation function. The quality of this approximation was described using the coefficient of determination (R^2), and the standard deviation (σ) was calculated.

The instantaneous vehicle speed as a function of time reveals differences in acceleration dynamics, which increase with engine power. A higher power level also improves measurement repeatability, due to the progressively more stable operation of the powertrain. For maximum power, the correlation coefficients approach 1, and the standard deviation is three times lower than for the lowest throttle positions, amounting to 0.11.

In Table 2, the parameters of the correlation functions for the analyzed vehicle acceleration trials are presented. The argument value of the regression function corresponds directly to the slope coefficient of the linear function and provides information on the average acceleration achieved in a given test. The average acceleration values range from 0.112 m/s^2 to 1.328 m/s^2.

Table 2. Correlation functions and their parameters comparison

A_p, %	V(t)	R^2	σ
20	$V(t) = 0.112 \cdot t + 13.765$	0.9347	0.38
25	$V(t) = 0.178 \cdot t + 14.871$	0.9559	0.58
30	$V(t) = 0.347 \cdot t + 15.025$	0.9722	0.75
35	$V(t) = 0.521 \cdot t + 14.926$	0.9824	0.82
40	$V(t) = 0.866 \cdot t + 13.900$	0.9938	0.49
45	$V(t) = 1.080 \cdot t + 12.484$	0.9992	0.18
50	$V(t) = 1.097 \cdot t + 12.997$	0.9981	0.27
70	$V(t) = 1.319 \cdot t + 12.409$	0.9995	0.13
100	$V(t) = 1.328 \cdot t + 12.651$	0.9997	0.11

In Fig. 6, the average acceleration values during the acceleration process are presented. The average acceleration increases significantly for the initial power levels in the range of A_p from 20% to 45%. Subsequently, the values stabilize and remain similar for 45% and 50% throttle positions, then increase further to reach maximum values at 70% and 100% throttle pedal deflection.

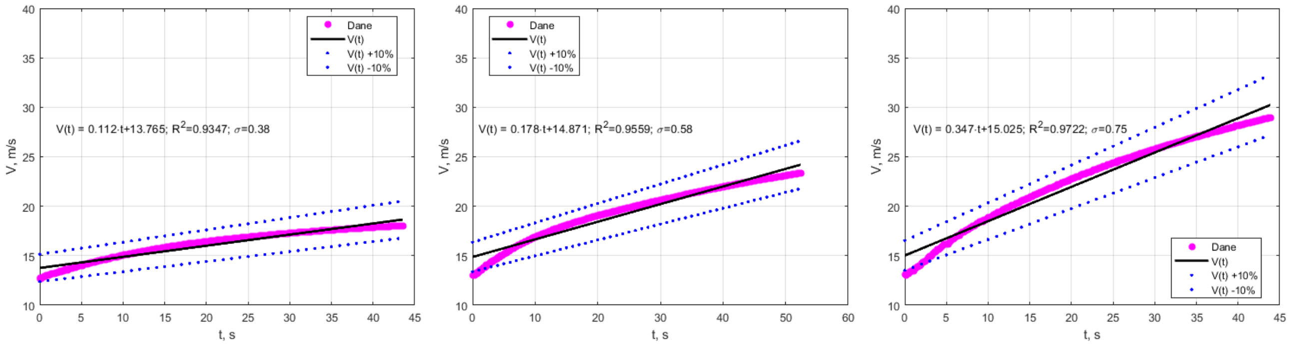

a) $A_p = 20\%$ b) $A_p = 25\%$ c) $A_p = 30\%$

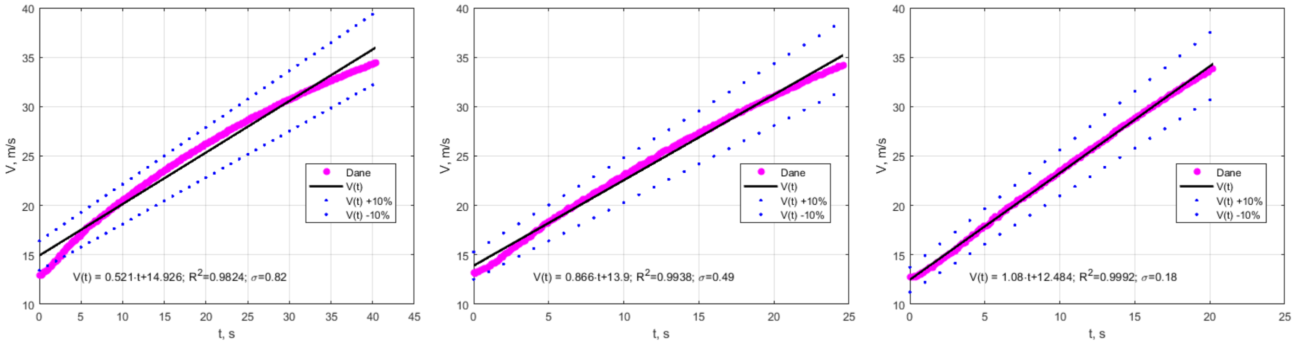

d) $A_p = 35\%$ e) $A_p = 40\%$ f) $A_p = 45\%$

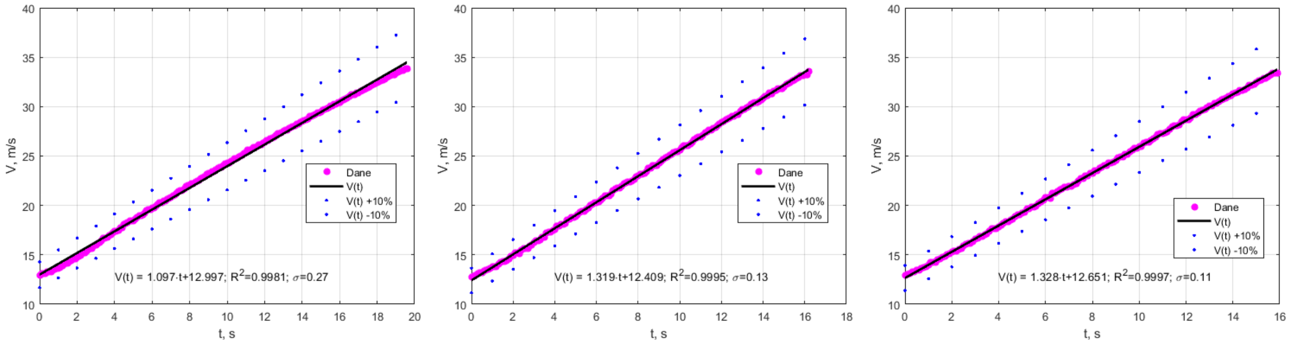

g) $A_p = 50\%$ h) $A_p = 70\%$ i) $A_p = 100\%$

Fig. 5. Velocity profile as a result of constant acceleration pedal position A_p

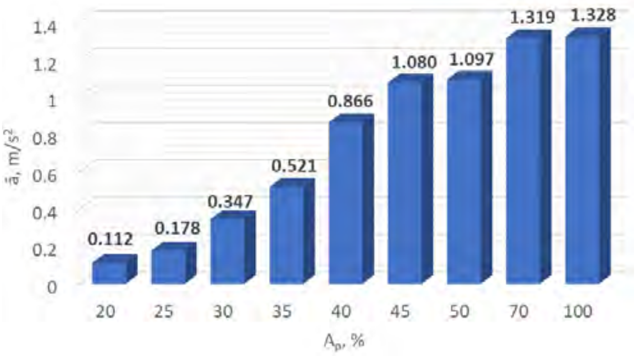

Fig. 6. Mean acceleration interpolation results

The primary factors determining the acceleration dynamics of a vehicle under constant power conditions are the vehicle's motion resistances. To determine their instantaneous and cumulative impact on the acceleration profile on a chassis dynamometer at constant drivetrain power, the percentage contributions of the main resistance components were calculated as a function of linear speed (Fig. 7). The profiles of the contributions from aerodynamic drag, rolling resistance, and inertial resistance, determined for each test, are presented in the left column of Fig. 7.

The profiles of the main components of motion resistance confirm the increasing contribution of inertial resistance to the total resistance force as the acceleration intensity rises. For averaged values, the share of power required to overcome vehicle inertia increases from 39.5% to 83.4%. Under conditions of maximum acceleration dynamics, 83.4% of the drivetrain power is irreversibly dissipated for accelerating the vehicle, thereby reducing the relative impact of rolling resistance and aerodynamic drag.

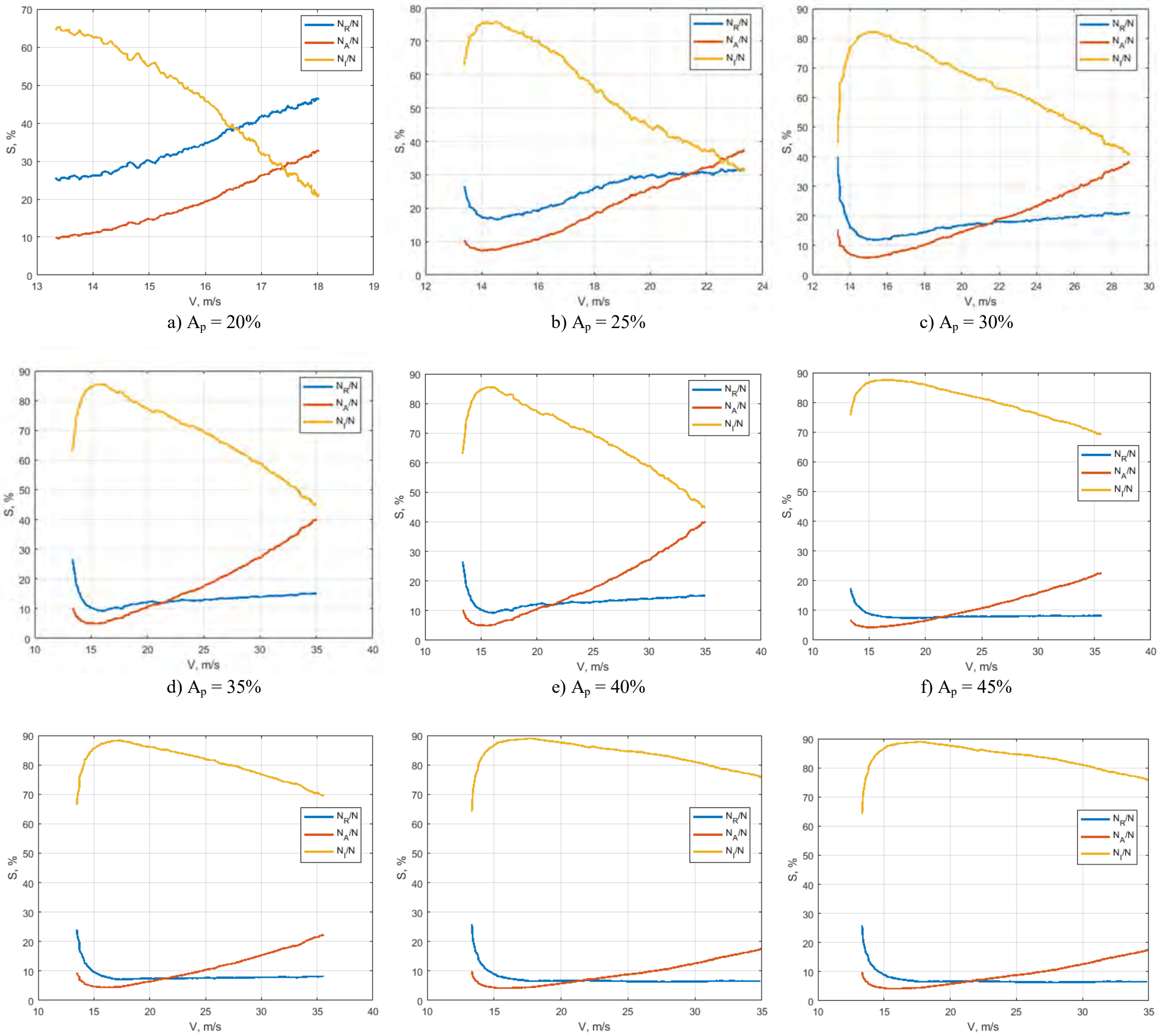

a) $A_p = 20\%$ b) $A_p = 25\%$ c) $A_p = 30\%$

d) $A_p = 35\%$ e) $A_p = 40\%$ f) $A_p = 45\%$

g) $A_p = 50\%$ h) $A_p = 70\%$ i) $A_p = 100\%$

Fig. 7. Percentage contribution (S) of motion resistance components as a function of the linear speed of the test vehicle during the acceleration trial (N_R – rolling resistance, N_A – aerodynamic drag, N_I – inertial resistance, N – wheel power)

When comparing these profiles across individual tests, it can be observed that in the initial speed range (up to approximately 20 m/s), the power share of rolling resistance is greater than that of aerodynamic drag. However, in the speed range between 20 and 25 m/s, the respective curves intersect, and from this point on, the aerodynamic drag power share exceeds that of rolling resistance.

$$N_I = m\delta\bar{a}\int_{t_s}^{t_e}\frac{ds}{dt} \tag{1}$$

where: N_I – inertial resistance, m – vehicle mass, δ – rotating mass factor, $\bar{a}$ – mean acceleration, t_s and t_e – start and end time, t – time, s – distance.

However, in each trial, the highest values are recorded for the average inertial power, which directly depends on the average acceleration and velocity over time, in accordance with Equation (1).

2.2. Fuel consumption during the acceleration process of a vehicle under constant power

Distance-specific fuel consumption (G_e) serves as an indirect indicator of the energy demand required to provide the power during the analyzed acceleration trial at constant drivetrain power (Fig. 8). At the same time, the power output of the drivetrain directly depends on the instantaneous speed and acceleration, under given motion resistance conditions.

In Fig. 9, the aggregate characteristics of specific fuel consumption (g_e) are presented. This parameter is a derivative of distance-specific fuel consumption (G_e) and drivetrain power (N), as defined by Equation (2).

$$g_e = \frac{G_e}{N} \tag{2}$$

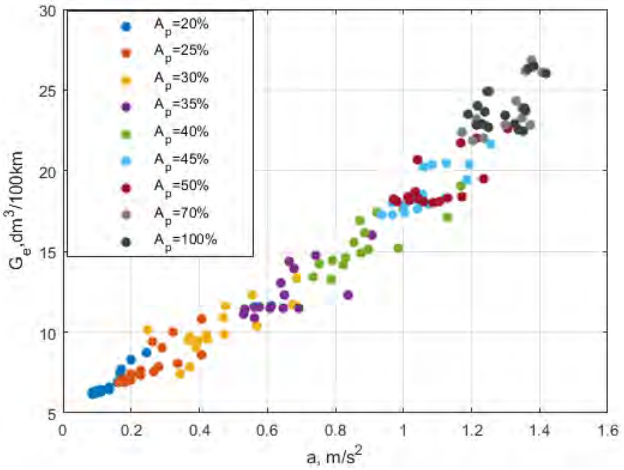

Fig. 8. Total distance-specific energy consumption as a function of mean acceleration in acceleration flexibility tests at constant throttle positions [8]

Taking into account the accuracy of the components that allow the calculation of fuel consumption, that is, the measurements of fuel pressure, the flow performance of injectors from the manufacturer's catalog, and time, the measurement error was calculated by the method of the complete differential, which is 3.3%.

To establish guidelines for the power control process during vehicle acceleration, attention was focused on the profile of the minimum specific fuel consumption line for each power input condition (Fig. 9).

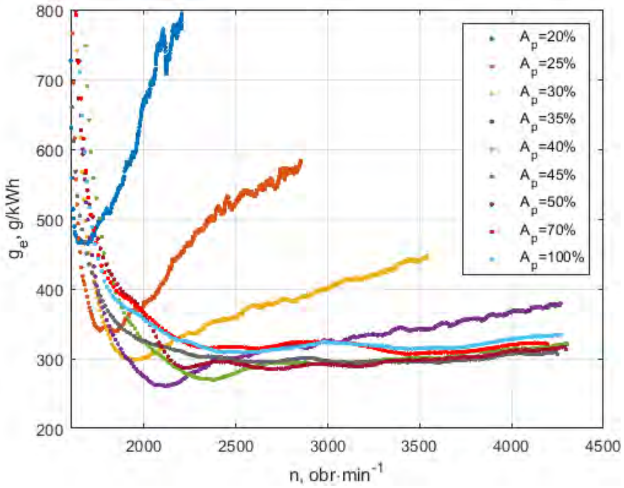

Fig. 9. Specific fuel consumption characteristics of the research passenger vehicle

For each curve, it is possible to determine the points of minimum specific fuel consumption across the full range of crankshaft rotational speed. The points obtained in this manner can be associated with the throttle pedal deflection and the speed range at which maximum drivetrain efficiency is achieved, in accordance with Equation (3).

$$\eta_{UN} = \frac{1}{g_e \cdot W_d} \tag{3}$$

where: η_{UN} – powertrain efficiency, W_d – lower heating value.

The determined points are presented in Table 3.

Since the values for A_p = 70% and 100% overlap above the crankshaft rotational speed of 3500 rpm, and considering the data from Table 3, it was decided to limit the throttle pedal deflection to 70%.

Table 3. Determined power control ranges for the efficient optimal line in the drivetrain system as a function of throttle pedal position and crankshaft rotational speed

Parameter	Value						
n, rpm	from 900 to 1650	from 1651 to 1800	from 1801 to 1900	from 1901 to 2250	from 2251 to 2600	from 2601 to 3320	from 3321 to 6500
A_p, %	20	25	30	35	40	50	45

In this way, it becomes possible to determine the theoretical power control line, referred to as the Efficient Optimal Line (EOL), within the drivetrain system under variable load conditions during the acceleration process.

2.3. Vehicle acceleration under variable power conditions in the flexibility test

For the defined range of variable speeds and throttle pedal positions, flexibility tests were carried out for vehicle acceleration under the same measurement conditions (Fig. 10).

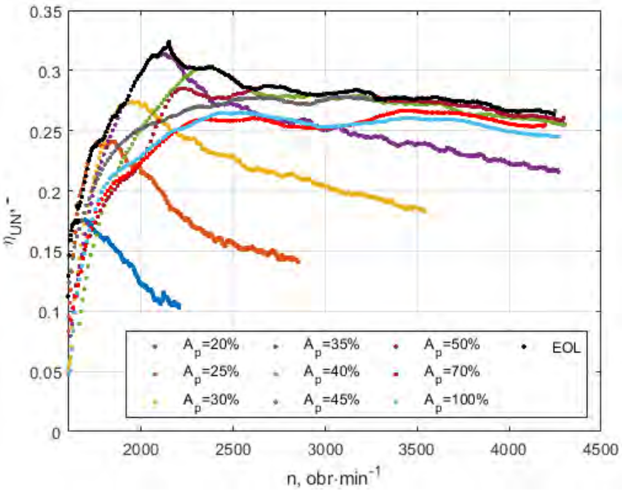

Fig. 10. Powertrain efficiencies for the defined control points

The drivetrain efficiency is a measure of the effectiveness in utilizing the energy contained in a given volume of fuel. The highest efficiency was achieved at A_p = 35% throttle pedal deflection and a crankshaft rotational speed of 2110 rpm. As anticipated, starting the acceleration process with variable and increasing throttle excitation is highly advantageous, closely following the acceleration intensity of A_p = 100%. However, as the crankshaft rotational speed increases, a decline in the overall drivetrain efficiency is observed.

Therefore, it was proposed to develop a physical acceleration trajectory based on the EOL, taking into account the objective of achieving high drivetrain efficiency. The trajectory was constructed by selecting individual points corresponding to the maximum drivetrain efficiency values, which define its course (Fig. 10).

The electrical characteristics of the factory throttle pedal position was determined and saved in a National Instruments (NI) software. The course of the characteristics depended on the engine's crankshaft speed. Using a NI control card and the programmed acceleration pedal position control trajectory made it possible to obtain external and repeatable control of the acceleration pedal.

Direct application of EOL in the process of controlling the throttle position of the test car yielded unsatisfactory results regarding the car's acceleration dynamics. The defined segments represent the highest instantaneous overall drivetrain efficiency, which in the initial phase is identical for $A_p = 20\%$ and $A_p = 25\%$ lines. This resulted in excessively slow initial vehicle acceleration, and therefore, it was decided to initiate the tests from a throttle deflection of 25%. This is related to the method of determining the EOL, which does not take into account the excess power in the drivetrain necessary for the acceleration process, and is only based on the efficiency of the drivetrain. In order to obtain sufficient surplus power, the accelerator pedal override range was increased while maintaining the engine crankshaft speed ranges specified in the EOL. The result was a control line, laboriously named T8. Its characteristics are given in Table 4.

In Fig. 11, a comparison of the results of speed curves during the acceleration flexibility test is presented. It should be noted that the newly defined acceleration trajectory T8 resulted in the vehicle reaching a speed of 120 km/h in a time 0.1 s shorter than that of the EOL, but 7.7 s longer compared to the 100% pedal deflection test. The parameters of the acceleration process are presented in Fig. 12.

Table 4. Determined power control ranges for the T8 strategy as a function of throttle pedal position and crankshaft rotational speed

Parameter	Value						
n, rpm	from 900 to 1650	from 1651 to 1800	from 1801 to 1900	from 1901 to 2250	from 2251 to 2600	from 2601 to 3320	from 3321 to 6500
A_p, %	25	30	35	40	45	50	70

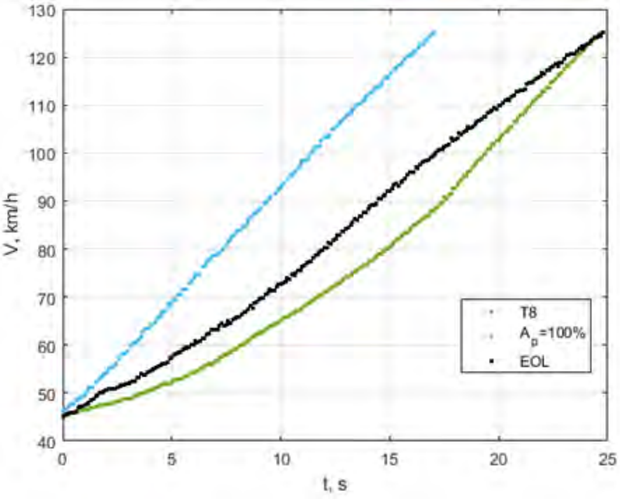

Fig. 11. Powertrain efficiencies for the defined control points according to: ● – the theoretical efficient optimal line (EOL), ● – full load at 100% throttle pedal deflection, ● – the physical implementation of the T8 control strategy

A reduction in vehicle acceleration dynamics resulted in a decrease in mean distance-specific fuel consumption from 21.68 $dm^3/100$ km to 10.71 $dm^3/100$ km, representing an almost 51% reduction in fuel usage (Fig. 13). Simultaneously, the acceleration distance increased by approximately 151 m, which corresponds to a 32.9% increase. Such an increase in distance is unacceptable in critical situations that determine the safety of vehicle occupants. On the other hand, under non-critical acceleration conditions, there is a possibility of significantly reducing fuel consumption at the expense of reduced acceleration performance.

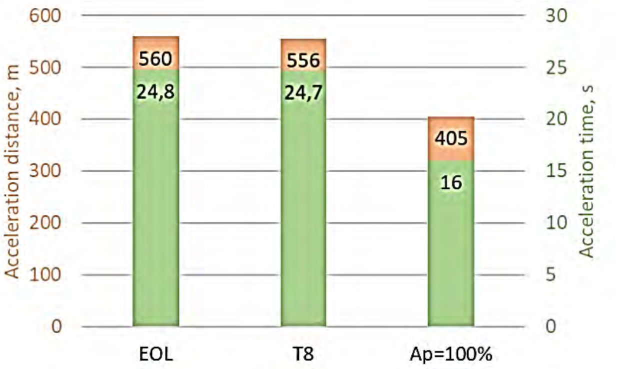

Fig. 12. Comparison of vehicle acceleration dynamics and distance travelled during acceleration from 45 to 120 km/h at 100% power utilization and according to the EOL and T8 control trajectories

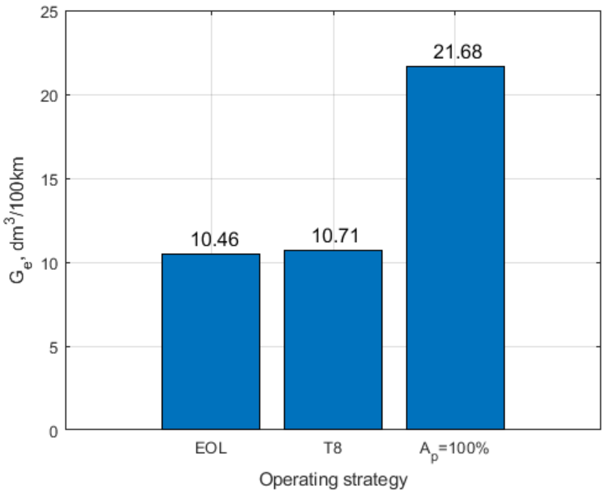

Fig. 13. Comparison of mean distance-related fuel consumption at 100% power utilization and according to the EOL and T8 control trajectories

3. Conclusion

For several years, there has been ongoing discussion regarding the decline of internal combustion engines (ICEs) used in passenger vehicles. However, until at least 2050, they are expected to remain the predominant propulsion systems. Internal combustion powertrains will continue to serve as the primary mode of transport, fulfilling the principles of sustainable mobility – meeting user demands while achieving economic and environmental stability, as well as ensuring driving range, which is a standard expectation for today's vehicles. Within this framework of sustainable development, the internal combustion engine still plays a vital role, and further advancements are expected in the coming years, as reflected in current development trends.

As a result, the power demand and fuel consumption of passenger vehicles are evolving, both of which are significantly influenced by the energy intensity of the acceleration process.

Broadly speaking, regardless of the type of power unit – whether internal combustion or electric – the challenge of efficient energy utilization under variable load conditions remains a relevant research issue, since the driver remains the final link in the power control process. Through the driver's subjective decisions, the instantaneous operating point of the drivetrain is determined, often unfavorably from both economic and ecological perspectives.

The powertrain control method proposed in this study for the acceleration process represents a compromise between fuel economy and vehicle dynamics, leading to a 51% reduction in fuel consumption. Using the T8 control line resulted in a drop in mileage-related CO_2 emission from 505 g/km to 250 g/km. Like any compromise, this one also requires certain concessions, among which dynamic performance should unquestionably yield to economic and environmental considerations. In this context, reduced fuel consumption (for ICEs) and lower energy usage (for electric drivetrains) result in lower CO_2 emissions, whether considered as direct (on-site) emissions or indirect (off-site) emissions, depending on the energy composition, which in many cases still includes fossil fuel-based electricity generation. As part of the research on the dependence of the accelerator pedal position on the crankshaft rotational speed, meeting the EOL assumptions, it was shown that in the acceleration process from a speed of 12.5 m/s to 35 m/s it is appropriate to use the acceleration pedal position range from 25% to 70%. Although the research was performed on one object, this range may prove adequate for other vehicles.

It is important to emphasize that such a reduction in vehicle dynamics contributes not only to environmental sustainability, but also to favorable operating conditions, reducing wear on drivetrain components, while still enabling dynamic acceleration within the scope of an economic power control line.

On the other hand, it must be recognized that in critical situations impacting occupant safety, the driver should always have full access to the drivetrain's maximum power output.

Nomenclature

BEV	battery electric vehicle	ICE	internal combustion engine
EOL	efficient optimal line	PHEV	plug-in hybrid electric vehicle
NEDC	New European Driving Cycle	RDE	real driving emissions
IC	internal combustion	TTW	tank to wheels

Bibliography

[1] Barth M, Boriboonsomsin K. Real-world carbon dioxide impacts of traffic congestion. Transp Res Record. 2008; 2058(1):163-171. https://doi.org/10.3141/2058-20

[2] Bokare PS, Maurya AK. Acceleration-deceleration behaviour of various vehicle types. Transp Res Proc. 2017;25: 4733-4749. https://doi.org/10.1016/j.trpro.2017.05.486

[3] Eisele WL, Turner SM, Benz RJ. Using acceleration characteristics in air quality and energy consumption analyses. Texas Transportation Institute 1996.

[4] Engelmann D, Zimmerli Y, Czerwinski J, Bonsack P. Real driving emissions in extended driving conditions. Energies. 2021;14:7310. https://doi.org/10.3390/en14217310

[5] Fontaras G, Zacharof NG, Ciuffo B. Fuel consumption and CO_2 emissions from passenger cars in Europe – laboratory versus real-world emissions. Prog Energ Combust. 2017;60: 97-131. https://doi.org/10.1016/j.pecs.2016.12.004

[6] Fontaras G, Franco V, Dilara P, Martini G, Manfredi U. Development and review of Euro 5 passenger car emission factors based on experimental results over various driving cycles. Sci Total Environ. 2014;468-469:1034-1042. https://doi.org/10.1016/j.scitotenv.2013.09.043

[7] Global Carbon Project, Key Messages from GCB 2025. globalcarbon.org

[8] Graba M, Bieniek A, Prażnowski K, Hennek K, Mamala J, Burdzik R et al. Analysis of energy efficiency and dynamics during car acceleration. Eksploat Niezawodn. 2023;25(1): 17. https://doi.org/10.17531/ein.2023.1.17

[9] He H, Cao J, Cui X. Energy optimization of electric vehicle's acceleration process based on reinforcement learning. J Clean Prod. 2020;248:119302. https://doi.org/10.1016/j.jclepro.2019.119302

[10] He Y, Sui S, Wang Q, Jin Y, Zhang L, Wang J. Super-high speed AMT shifting strategy and energy consumption optimization for electric vehicle. Energy. 2025;322:135489. https://doi.org/10.1016/j.energy.2025.135489

[11] Huang Y, Surawski N, Organ B, Zhou J, Tang O, Chan E. Fuel consumption and emission performance under real driving: comparison between hybrid and conventional vehicles. Sci Total Environ. 2018;659:275-282. https://doi.org/10.1016/j.scitotenv.2018.12.349

[12] Huang Y, Ng ECY, Zhou JL, Surawski NC, Lu X, Du B et al. Impact of drivers on real-driving fuel consumption and emissions performance. Sci Total Environ. 2021;798: 149297. https://doi.org/10.1016/j.scitotenv.2021.149297

[13] Lee J, Nelson D J, Lohse-Busch H. Vehicle inertia impact on fuel consumption of conventional and hybrid electric vehicles using acceleration and coast driving strategy. SAE Technical Papers. 2009. 2009-01-1322. https://doi.org/10.4271/2009-01-1322

[14] Li Q, Chen W, Li Y, Liu S, Huang J. Energy management strategy for fuel cell/battery/ultracapacitor hybrid vehicle based on fuzzy logic. Int J Elec Power. 2012;43(1):514-525. https://doi.org/10.1016/j.ijepes.2012.06.026

[15] Limblici C. Investigation of engine concepts with regard to their potential to meet the Euro 7 emission standard using 1D-CFD software. 2020. https://webthesis.biblio.polito.it/16275/

[16] McDonough K, Kolmanovsky I, Filev D, Yanakiev D, Szwabowski S, Michelini J. Stochastic dynamic programming control policies for fuel efficient vehicle following. 2013 American Control Conference (ACC) Washington June 17-19, 2013. https://doi.org/10.1109/ACC.2013.6580024

[17] Mamala J, Graba M, Bieniek A, Prażnowski K, Augustynowicz A, Śmieja M. Study of energy consumption of a hybrid vehicle in real-world conditions. Eksploat Niezawodn. 2021;23(4):636-645. https://doi.org/10.17531/ein.2021.4.6

[18] Mamala J, Graba M, Mitrovic J, Prażnowski K, Stasiak P. Analysis of speed limit and energy consumption in electric vehicles. Combustion Engines. 2023;195(4):83-89. https://doi.org/10.19206/CE-169370

[19] Pielecha J, Merkisz J. Selection of a particulate filter for a gasoline-powered vehicle engine in static and dynamic conditions. Energies. 2023;16(23):7777. https://doi.org/10.3390/en16237777

Krystian Hennek, DEng. – Department of Vehicle and Machine Mechatronics, Opole University of Technology, Poland.

e-mail: *k.hennek@po.edu.pl*

Prof. Jarosław Mamala, DSc., DEng. – Department of Vehicle and Machine Mechatronics, Opole University of Technology, Poland.

e-mail: *j.mamala@po.opole.pl*

Andrzej Bieniek, DEng. – Department of Vehicle and Machine Mechatronics, Opole University of Technology, Poland.

e-mail: *a.bieniek@po.edu.pl*

Szymon Kołodziej, DEng. – Department of Vehicle and Machine Mechatronics, Opole University of Technology, Poland.

e-mail: *s.kolodziej@po.opole.pl*

Article citation info:
Szpica D, Gęca MS, Hunicz J, Jakubowski M, Krzemiński A. Mieczkowski G. Cycle-by-cycle performance evaluation of a diesel engine fueled with a mixture of hydrotreated vegetable oil mixed with waste plastic pyrolysis oils. Combustion Engines. 2025;202(3):109-117. https://doi.org/10.19206/CE-207383

Dariusz SZPICA
Michał S. GĘCA
Jacek HUNICZ
Mirosław JAKUBOWSKI
Artur KRZEMIŃSKI
Grzegorz MIECZKOWSKI

Combustion Engines
Polish Scientific Society of Combustion Engines

Cycle-by-cycle performance evaluation of a diesel engine fueled with a mixture of hydrotreated vegetable oil mixed with waste plastic pyrolysis oils

ARTICLE INFO

Received: 28 April 2025
Revised: 14 June 2025
Accepted: 20 June 2025
Available online: 7 July 2025

Changing regulations on emissions from propulsion sources used in transportation and closed-loop resource management are intensifying the search for substitute fuels, especially for compression-ignition engines. In the study, three fuels were tested for comparison: conventional diesel fuel (DF), hydrotreated vegetable oil (HVO), and a mixture of HVO with waste pyrolytic oils from polypropylene (PPO) and polypropylene (PSO) in 60/20/20 weight ratios (HVO + WPPO). Tests were conducted on a specialized platform with an AVL 5402 engine, analyzing their combustion and operating stability under two different load and speed conditions. The results showed that HVO and the HVO + WPPO mixture exhibit similar or even better combustion performance compared to DF. Some differences were found in cylinder pressure traces, indicated mean effective pressure and heat release. Statistical analyses, including ANOVA and Levene's tests, confirmed significant differences between the fuels, indicating the potential of the HVO + WPPO mixture as an environmentally friendly alternative. The determined coefficients of variation allowed an assessment of the stability of engine operation. In conclusion, the research suggests that both HVO and its mixture with PPO and PSO can be effective and environmentally friendly solutions for diesel engines, with the possibility of wide application in the future.

Key words: *alternative fuel supply, hydrotreated vegetable oil, waste plastic pyrolytic oils, combustion, research*

1. Introduction

A very popular source of propulsion for motor vehicles and work machinery is the compression-ignition engine because of its relatively high efficiency, reliability, low fuel consumption, and ease of adaptation [10, 16, 29, 30]. However, the disadvantage of this type of propulsion is the emission of pollutants, including CO, NO_x, and PM. In addition, fossil fuels account for 85% of CO_2 emissions and 64% of total greenhouse gas emissions [5, 25]. Therefore, internal combustion engines are subject to increasingly stringent rules and regulations regarding the emission of toxic compounds from exhaust [11, 15].

One method for reducing toxic compounds and CO_2 emissions is to develop alternative waste-derived fuels. This group of fuels includes HVO and TPO, which are combinations of aromatic and aliphatic compounds, and plastic fuels (PPO and PSO) obtained by pyrolysis [4, 13, 14].

HVO can be produced from waste biomass, such as animal fats and vegetable oils. This fuel did not contain sulfur or aromatic hydrocarbons. HVO, compared to conventional diesel, has a higher cetane number and lower viscosity and density compared to conventional diesel. The high cetane number of hydrogenated vegetable oils accelerates the onset of combustion, particularly at low and medium loads [17]. The use of HVO to power a compression-ignition engine results in a 40% reduction in NO_x and PM emissions compared with diesel [12, 18].

To date, engine tests have been conducted on HVO alone and diesel mixtures with 30% and 7% v/v HVO [26]. Engine tests on mixtures of diesel, HVO, rapeseed methyl ether, and n-octanol isomers have also been conducted [20].

The authors of [21] showed a reduction in CO emissions by more than 50% when feeding the engine during the cold start phase with a mixture of DF and HVO (30%). No significant differences were observed in NO_x emissions compared to DF, whereas PM was reduced by 5.2–11.8%, depending on the test conditions.

Fuel obtained from waste plastic oil can be used in a compression-ignition engines at a higher compression ratio than that obtained from DF without any modifications to the power unit [1].

The results of ongoing research indicate that the use of fuels with the addition of plastic waste oil in a compression-ignition engine decreases the thermal efficiency by more than 2% compared with pure DF [7].

In [3], the authors demonstrated a positive or neutral effect of HVO on most of the measured emission components and engine operating parameters. Decreases of several tens of percent were observed in CO, THC, PM, and smoke emissions. NO_x and CO_2 emissions decreased, and the power output increased by a few percent.

In the case of using plastic pyrolytic oil (PPO), the results obtained by researchers are divergent, particularly in the context of NO_x emissions, with some studies reporting a reduction of more than 63%, whereas others reported an increase of more than 44% compared to running on pure DF [8].

Studies on mixtures of PPO with DF at concentrations of 10, 20% and 30% PPO showed that at 20%, the engine achieved a slightly higher thermal efficiency than that of pure DF [6]. It was further shown that NO_x and HC emissions were lower at low loads and increased with increasing load compared with DF.

Researchers [24] used a mixture of PPO and DF in proportions up to 50% PPO and showed that a higher concentration of PPO in the mixture increased the engine thermal efficiency and reduced the specific fuel consumption.

In the literature, one can find a PPO designation associated with pyrolytic oil extracted from plastic or made from polypropylene. The above data related to PPO oil refers to the first meaning. With regard to pyrolytic oil extracted from polypropylene, the authors of [22] showed that the addition of 20% PPO in a mixture with DF had no significant effect on HC and CO emissions, whereas the admixture of PSO increased them.

TPO can be used in fuel compression ignition engines as a mixture with diesel fuel (from 10% to 90%) without changing the engine design.

Combustion stability is crucial to overall engine performance because a mixture of fuels with different auto-ignition properties can increase the variability of the combustion cycle [23]. The available literature lacks studies on the combustion stability of HVO mixtures containing PPO and PSO. The research gap has directed efforts to develop an alternative fuel that is a mixture of these fuels. This type of activity is contained within a closed loop of raw materials. An important feature of the developed mixture is the similarity of its ignition and combustion characteristics to those of DF. The scientific contribution of such an activity is the evaluation of the preservation of the stability of the engine operation fueled by the developed mixture, which guarantees the functional continuity of the propulsion source.

2. Materials and methods

2.1. Tested fuels

In this study, three diesel fuels were tested.

- conventional diesel fuel (DF)
- hydrotreated vegetable oil (HVO)
- a mixture containing 60 wt% HVO, 20 wt% PPO and 20 wt% PSO (HVO + WPPO).

Table 1. Basic technical parameters of the tested fuels

Property	Unit	Diesel	HVO	PPO	PSO
Density at 15°C	kg/m^3	828	778	761	937
Kinematic viscosity (40°C)	mm^2/s	2.94	2.86	1.77	1.70
Lower heating value	MJ/kg	43.6	44	42.4	41
Flash point	°C	66	68	29	< 19
Cetane number	–	55	90	28	≈0
Composition by mass:					
Carbon	%	86.7	84.5	87.8	91
Hydrogen	%	13.1	15.2	12.2	8.2
Oxygen	%	0.05	–	–	–
Aromatic	%	17	< 1	–	98
FAME	%	6.3	–	–	1
Sulfur	ppm	5.2	–	56	3

The DF used as the base fuel was an EN 590-compliant conventional fuel from the ORLEN distribution network. HVO was a fuel derived from the hydrotreatment of vegetable oil and was distributed by NESTE. PPO was derived from the pyrolysis of polypropylene, whereas PSO was derived from the pyrolysis of polystyrene. The HVO + WPPO mixture was developed to achieve a similar ignition delay, volatility, and viscosity to DF. All component fuels were subjected to detailed physicochemical analyses to aid in mixture formation (Table 1).

2.2. Test equipment

Experiments were conducted using a single-cylinder AVL 5402 research engine. The primary operating parameters are listed in Table 2. A schematic of the test bench, detailing the air and fuel flow paths, is shown in Fig. 1.

Table 2. Research engine specifications

Parameter	Value/specification
Engine model	AVL 5402
Operating cycle	single-cylinder, four-stroke
Cylinder bore	85 mm
Piston stroke	90 mm
Connecting rod length	138 mm
Total displacement	510.5 cm^3
Compression ratio	17:1
Number of valves	4
Swirl number	1.7
Fuel delivery method	direct injection
Injection system	Bosch CP4.1, common rail
Injector type	electromagnetic, 8-hole, 0.12 mm orifice, 151 deg spray angle
Max. injection pressure	180 MPa
Natural gas supply	M+W D-6300 mass flow controller
Boost system	Eaton M45, electrically powered
EGR configuration	high-pressure loop, with cooling
ECU and control system	Bosch ETK7 with AVL-RPEMS
Intake valve opens at	712 CAD
Intake valve closes at	226 CAD
Exhaust valve opens at	488 CAD
Exhaust valve closes at	18 CAD
Max. IMEP	2.4 MPa

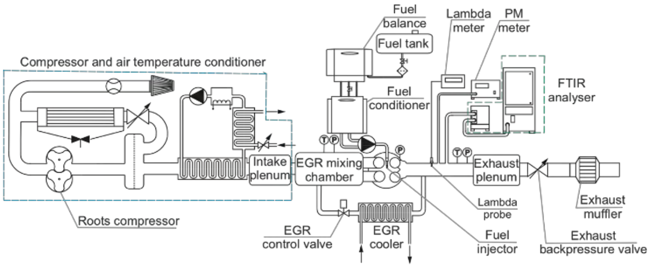

Fig. 1. Diagram of the engine air and fuel paths

The engine incorporated a four-valve cylinder head and a toroidal combustion chamber formed within the piston. The fuel was delivered using a Bosch CP 4.1 high-pressure pump to an eight-hole solenoid injector with a spray angle of 151 deg. The injection process was managed using ETAS INCA software and an open Bosch electronic control unit (ECU).

The fuel temperature and flow were regulated using an AVL 753C temperature controller and an AVL 733S dynamic flow meter. The boost pressure was generated using an Eaton M45 Roots-type supercharger powered by an 11 kW electric motor. The compressed intake air was thermally stabilized using a system of heat exchangers and a mixing valve.

An exhaust backpressure valve was used to emulate the effect of a turbocharger, facilitating high-pressure exhaust gas recirculation (EGR) and preventing the scavenging of natural gas during valve overlap.

The coolant and engine oil temperatures were maintained with ±0.5°C accuracy using a dedicated thermal management system. The air-fuel ratio was measured using a Bosch LSU 4.2 lambda sensor and an ETAS LA4 lambda meter with pressure compensation.

Combustion diagnostics relied on in-cylinder pressure data obtained from an AVL GU22C piezoelectric pressure sensor, synchronized with an optical encoder providing 0.1 CAD resolution.

Exhaust gas analysis of both the regulated and unregulated compounds was performed using an AVL FTIR spectrometer. The size distribution of particulate matter was measured using a TSI EEPS 3090 spectrometer operating on the principle of electrical mobility, covering the (5.6…560) nm range across 32 size bins. The key parameters of the measurement system are presented in Table 3.

Table 3. Engine test bench measurement equipment and accuracy

Parameter measured	Device	Meas. range	Accuracy
In-cylinder pressure	AVL GU22C	0…25 MPa	±0.25…1.0%
Liquid fuel consumpt.	AVL 733S	0…1.25 kg/h	±0.12%
Gaseous fuel flow	M+W D-6300	0…120 NL/min	±2%
Lambda (AFR)	Bosch LSU 4.2/ETAS LA4	0.7…2.8	±1.5%
Air mass flow rate	E+E EE741	2.6…1000 kg/h	±3%
Pressure (int./exh.)	WIKA A-10	0…4 bar	±0.5%
Temperature	TP-361	–40…400 degC	±0.2%
Exhaust gas temp.	TP-204	0…1200 degC	±0.8%
CO emissions	AVL FTIR	1…10000 ppm	±0.36%
UHC emissions	AVL FTIR	1…1000 ppm	±0.1…0.49%
NOx emissions	AVL FTIR	1…4000 ppm	±0.31%
Particulate matter/ number	TSI EEPS 3090	5.6…560 nm	-

2.2. Research and inference methodology

DF, HVO, and HVO + WPPO tests were conducted on a test platform with an AVL 5402 engine at two World Harmonized Stationary Cycle (WHSC) operating points. Low load and low speed were represented by the 1100/25 point, whereas high speed and high load were represented by the 1800/70 point. The first component of the test point designation was the engine crankshaft speed, while the second was the percentage of maximum load, which in this case was 2.2 MPa (BMEP). In the cases analyzed, the averaged BMEP value was 1100/25 – 0.5 MPa, 1800/70 – 1.4 MPa, respectively. In total, 100 consecutive cycles were performed.

In all tests, the 8-hole injector along the common-rail system was controlled using an open control unit in accordance with the modern EPA Tier IV emission standards.

In the first stage of the analysis, the cylinder pressure traces were recorded as functions of the crankshaft angle (CAD). The pressure changes represent the result of a number of input factors and form the basis for evaluating the self-ignition of fuels, the course of their combustion, and other factors determining the engine's energy, environmental, or economic capabilities.

Furthermore, based on the pressure traces and information on the changes in cylinder geometry, the IMEP (Eq. (1)) was calculated, which is the quotient of the volumetric work of the circuit and displacement volume of the cylinder.

$$\mathrm{IMEP} = \frac{W}{V_{sc}} = \frac{1}{V_{sc}} \int p\,dV_{sc} \tag{1}$$

where W is the volume work of the cycle; V_{sc} is the swept volume per cylinder; p is the cylinder pressure.

The data used for the IMEP calculations allowed us to assess the heat release (Eq. (2)).

$$q = \frac{\kappa}{\kappa-1} p\,dV + \frac{\kappa}{\kappa-1} V\,dp \tag{2}$$

where κ is the adiabatic exponent, which is the quotient of the specific heat at constant pressure to the specific heat at constant volume (c_p/c_v) determined by considering the effect of temperature and the chemical composition of the charge in the cylinder.

The stability of the cycle-by-cycle engine operation was evaluated using the coefficient of variation (Eq. (3)) [2, 19, 27].

$$\mathrm{COV} = \left(\frac{\sigma}{\bar{x}}\right) \times 100\% \tag{3}$$

where σ is the standard deviation; $\bar{x}$ is the mean value of the parameter under study.

The standard deviation was calculated using Eq. (4).

$$\sigma = \sqrt{\frac{1}{N-1} \sum_{i=1}^{N} (x_i - \bar{x})^2} \tag{4}$$

The average value of the parameter according to Eq. (5).

$$\bar{x} = \frac{1}{N} \sum_{i=1}^{N} x_i \tag{5}$$

where N is the number of points assessed; x_i is the value in each i-point.

The following values were considered for the engine stability analysis:

- maximum pressure in the cylinder – p_{max}
- indicated mean effective pressure – IMEP
- maximum heat exerted in the cylinder – q_{max}.

For each of these parameters, the coefficient of variation was determined from the standard deviation and mean value (Eq. (6)–(8)).

$$\mathrm{COV}_{p_{max}} = \left(\frac{\sigma}{\bar{x}}\right)_{p_{max}} \times 100\% \tag{6}$$

$$\mathrm{COV}_{\mathrm{IMEP}} = \left(\frac{\sigma}{\bar{x}}\right)_{\mathrm{IMEP}} \times 100\% \tag{7}$$

$$\mathrm{COV}_{q_{max}} = \left(\frac{\sigma}{\bar{x}}\right)_{q_{max}} \times 100\% \tag{8}$$

3. Results and analysis

By compiling the sample pressure traces at the first 1100/25 test points (Fig. 2a), the difference in shape between HVO + WPPO relative to DF and HVO was apparent. The reasons for the differences in the pressure traces were correlated with heat evolution (Fig. 2b). It should be noted that the high reactivity of HVO affects the combustion of pilot doses of 1 and 2. The heat evolution process developed 1°CA in advance relative to the DF with a similar gradient. This is different for HVO + WPPO, which lagged by approximately 2°CA behind the DF. The separation of pilot doses was evident in the cases of DF and HVO. A possible reason for this could be that the temperature in the cylinder increased after pilot injection 1, which promoted immediate ignition of the next dose. The burning of pilot fuel 1 increased the temperature and left active radicals, which caused immediate ignition of the next fuel dose. For the combustion of the main DF and HVO fuel doses, although there is mostly overlap, HVO starts at a lower q value, similar to that of HVO + WPPO. There was a noticeable angular shift in the heat release when the main dose of the HVO + WPPO fuel was burned, as can be seen in the pressure trace (Fig. 2a). The angular shift can affect the IMEP values.

The situation was different at the second 1800/70 test point (Fig. 3a). The exemplary DF pressure trace was below the HVO and HVO + WPPO. The heat development at test point 1800/70 (Fig. 3b) showed a much higher reactivity of HVO, especially at pilot dose 1, where in this particular case it exceeded the value achieved when burning the main dose. Increasing the speed and load of the engine highlighted the separation of pilot doses resulting from the higher brake drag torque, which determines the acceleration of the engine's crank-piston system in addition to the inertia of the mechanical system.

The averaged values from 100 cycles of $\bar{p}_{max}$ (Fig. 4) were 7.848, 7.781 MPa, and 7.556 MPa for DF, HVO, and HVO + WPPO, respectively (Table 4). This represents a 0.85% lower value for HVO and a 3.72% lower value for HVO + WPPO relative to the reference fuel DF. The calculated average values from 100 cycles $\overline{IMEP}$ of (Fig. 4) reached values for DF, of 0.667 MPa, for HVO of 0.659 MPa and for HVO + WPPO of 0.668 MPa, respectively (Table 4). In this case, the percentage difference in HVO relative to the reference DF was 1.26%. HVO+WPPO showed IMPE compliance with DF, with a difference of only 0.07% compared to the disadvantage of DF. The averaged maximum heat discharge $\bar{q}_{max}$ from 100 cycles was 2.05% lower for HVO (56.61 J/deg) and 12.68% lower for HVO + WPPO (50.47 J/deg) relative to DF (57.80 J/deg).

At the second 1800/70 test point, the highest value averaged over 100 cycles of $\bar{p}_{max}$ (Fig. 5) was recorded for HVO + WPPO, it was 12.42 MPa (4.28% higher than the DF reference fuel, 11.906 MPa) (Table 4). HVO showed 12.13 MPa (1.88% higher than that of DF). The 100-cycle averaged value $\overline{IMEP}$ of 1.636 MPa showed HVO + WPPO's advantage over DF (3.28% increase). HVO achieved an IMEP of 1.628 MPa, which was above the 1.584 MPa achieved by DF (2.79% difference). A significant difference from the 1100/25 test point was the change in the main fuel combustion dose. At the 1800/70 point, the highest values averaged over 100 cycles of exerted heat $\bar{q}_{max}$ (Fig. 5) were recorded for HVO (68.20 J/deg, 11.48% increase over DF, 61.18 J/deg). HVO + WPPO also showed an advantage over DF (66.74 J/deg, 9.09% increase) – Table 4.

Table 4. Comparative values of the analyzed parameters at both operating points

Fuel	DF	HVO	HVO + WPPO	DF	HVO	HVO + WPPO
RPM/load	1100/20			1800/70		
$\bar{p}_{max}$, MPa	7.848	7.781	7.556	11.906	12.131	12.416
$\sigma_{p_{max}}$, MPa	0.047	0.045	0.059	0.058	0.136	0.095
$COV_{p_{max}}$, %	0.604	0.573	0.785	0.491	1.122	0.767
$\overline{IMEP}$, MPa	0.667	0.659	0.668	1.584	1.628	1.636
σ_{IMEP}, MPa	0.008	0.007	0.013	0.012	0.033	0.018
COV_{IMEP}, %	1.117	1.101	1.905	0.781	2.006	1.125
$\bar{q}_{max}$, J/deg	57.799	56.612	50.467	61.181	68.203	66.743
$\sigma_{q_{max}}$, J/deg	1.679	1.430	1.520	1.615	2.631	2.076
$COV_{q_{max}}$, %	2.904	2.526	3.011	2.640	3.858	3.110

The highest values of pressure coefficient of variation $COV_{p_{max}}$ at the first test point (1100/25) were recorded for HVO and amounted to 0.573%, which represented a 5.19% increase relative to DF (0.604%) (Table 4). HVO + WPPO showed an increase in the coefficient of variation relative to DF of 29.84% (0.785%). COV_{IMEP} variability differences relative to DF appeared in a similar pattern (1.117%). HVO obtained a value that was 1.48% lower (1.101%), whereas that of HVO + WPPO was 70.49% higher (1.905%). Also, the coefficient of variation $COV_{q_{max}}$ reached the lowest value for HVO (2.526%), 13.00% lower than DF (2.904%). HVO + WPPO had a 3.70% (3.011%) higher rate than that of the DF.

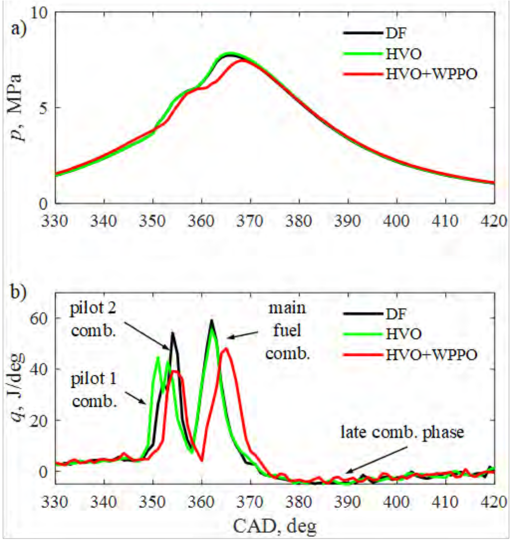

Fig. 2. Examples of in-cylinder pressure traces (a) and heat release (b) at operating point 1100/25

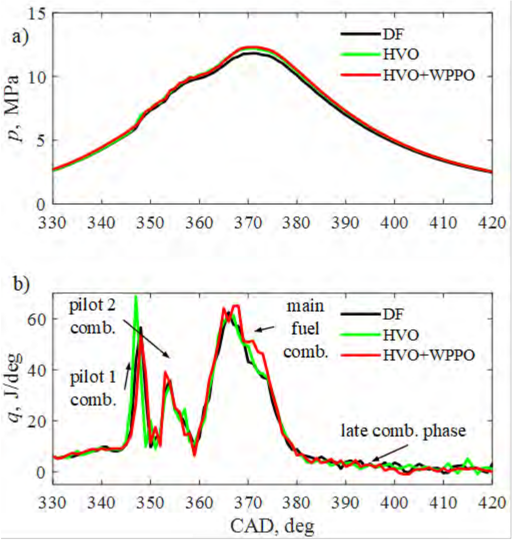

Fig. 3. Examples of in-cylinder pressure traces (a) and heat release (b) at test operating 1800/70

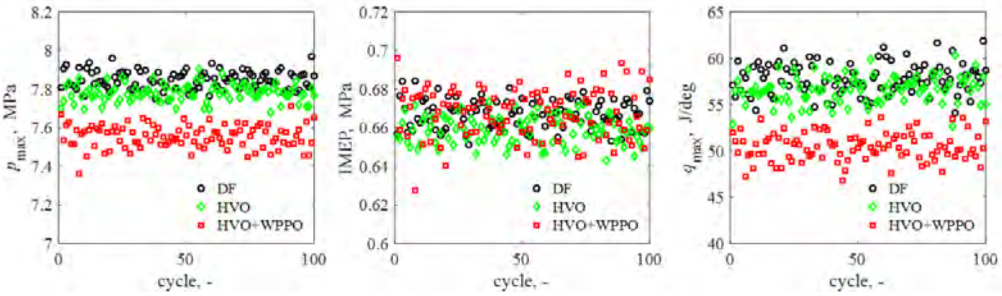

Fig. 4. Comparative values of analyzed parameters at operating point 1100/25

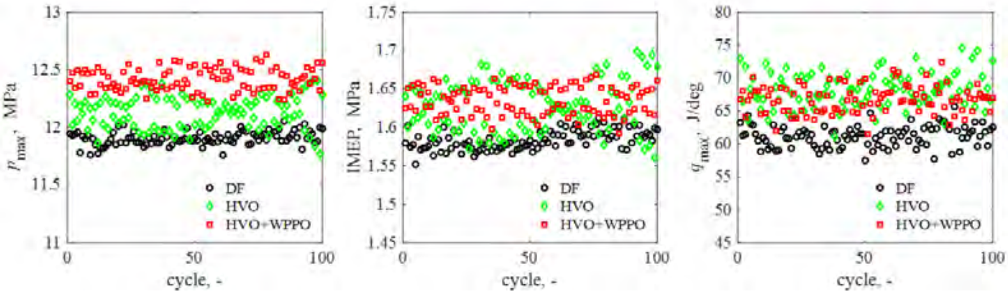

Fig. 5. Comparative values of analyzed parameters at operating point 1800/70

At the second test point (1800/70), where DF achieved lower average values of the compared parameters than the other tested fuels, it also exhibited the smallest variation in these parameters (Table 4). They amounted to $\mathrm{COV}_{p_{max}}$ 0.491%, COV_{IMEP} 0.781%, and $\mathrm{COV}_{q_{max}}$ 2.640%, respectively, which were lower than those obtained at point 1100/25. At the 1800/70 point, HVO showed an increase in $\mathrm{COV}_{p_{max}}$ relative to DF by 128.78% (1.122%), whereas HVO + WPPO showed an increase of 56.23% (0.767%). For COV_{IMEP}, the differences were, respectively, 156.88% increase for HVO (2.006%) and 44.06% increase for HVO + WPPO (1.125%). The smallest differences relative to DF were observed for $\mathrm{COV}_{q_{max}}$. For HVO, there was an increase of 46.12% (3.858%), whereas for HVO + WPPO it increased by 17.81% (3.110%). It is noteworthy that all analyzed parameters showed a coefficient of variation of less than 4% for $\mathrm{COV}_{q_{max}}$, to about 2% for COV_IMEP, and less than 1.15% for the most analyzed parameter $\mathrm{COV}_{p_{max}}$. Although the tests at the two points in the WHSC cycle showed differences in the average values and their coefficients of variation, they were not sufficiently large to exclude the proposed fuel from use in the engine. Owing to the lack of literature in the area covering this study, the results of other researchers were not referenced.

Because of the small number of analyzed values (100 points) for each test point, 10 classes were used in the distribution analysis. A non-parametric kernel-smoothing distribution was used for the analysis. Histograms were plotted to fit the density function, which could indicate multimodality in addition to asymmetry (Fig. 6 and Fig. 7). Although for the most part the distributions were close to normal, a few slightly bi-modal distributions also became apparent (e.g., p_{max} at HVO and HVO + WPPO feeds and IMEP for HVO + WPPO).

In the statistical analysis, kurtosis values κ were determined using MATLAB software (Table 5), and the distributions of the analyzed values were compared to a normal distribution. The lowest κ value 1.87 was found for q_{max} when the HVO was fed at test point 1800/70. This indicates the presence of a platykurtic. The vast majority of kurtosis values for both test points of operation were close to 3, which is the reference value of a normal distribution.

The second parameter used to assess the shape of the distribution of the analyzed values was the skewness s. In this case, the reference value was zero, indicating the normality of the distribution. In the analyzed cases (Table 5), the values were variably located in both the left and right areas, with small deformations. The maximum value of the skewness of the distribution (–0.32) was found for the IMEP at the HVO + WPPO feed at test point 1100/25. In addition, in the case of p_{max} itself, s was shown at –0.23, which confirms the asymmetry of the distribution.

One-way ANOVA [28] was used for the final statistical evaluation. The resulting groups were divided with respect to the fuels and study points, and MATLAB was used for the calculations. The null hypothesis was accepted, according to which the mean values in each group at each test point were derived from a population with the same mean value (Eq. (9))

$$H_0: \quad \bar{x}_{DF} = \bar{x}_{HVO} = \bar{x}_{HVO+WPPO} \tag{9}$$

According to the null hypothesis, the alternative hypothesis assumes that the averages of the analyzed populations are not equal (Eq. (10)).

$$H_1: \quad \bar{x}_{DF} \neq \bar{x}_{HVO} \neq \bar{x}_{HVO+WPPO} \tag{10}$$

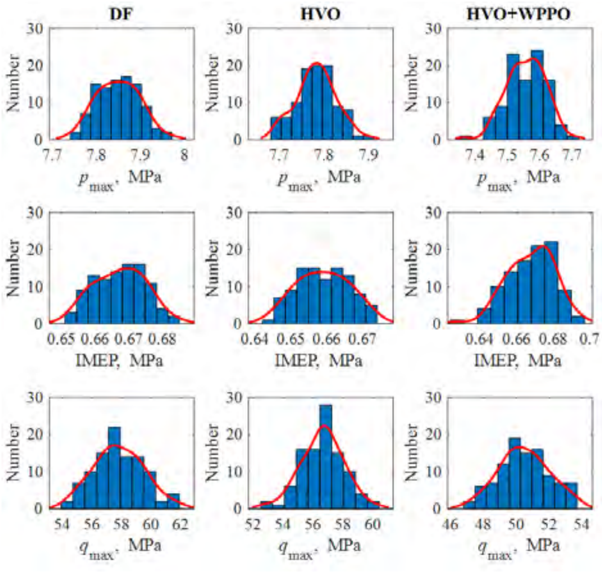

Fig. 6. Distributions of analyzed parameters at operating point 1100/25

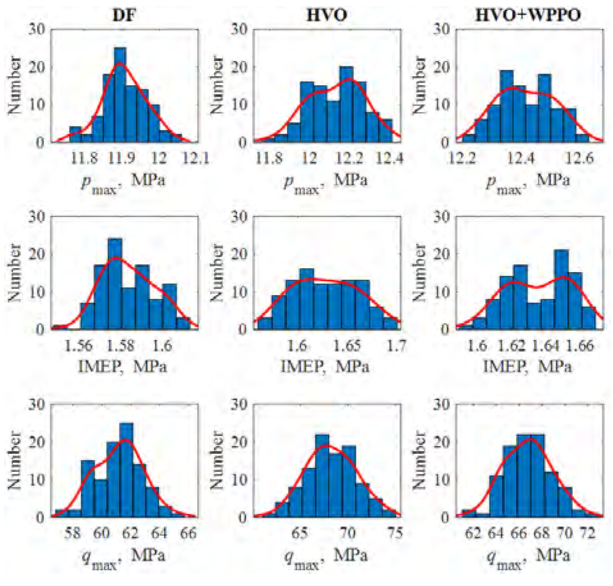

Fig. 7. Distributions of analyzed parameters at test operating 1800/70

Table 5. Comparative values of the kurtosis (κ) and skewness (s) at both operating points

operat. point		1100/25			1800/70		
fuel/ parameter		DF	HVO	HVO + WPPO	DF	HVO	HVO + WPPO
κ	p_{max}	2.5201	2.2559	2.6085	3.0940	2.4435	2.7119
	IMEP	2.8825	2.1528	3.1978	2.4370	2.1043	2.7506
	q_{max}	3.1465	2.9538	2.5597	2.0869	1.8698	2.8415
s	p_{max}	0.1041	0.0311	–0.2306	–0.0463	–0.1781	0.0677
	IMEP	–0.0080	–0.0039	–0.3209	0.2053	0.1232	–0.1693
	q_{max}	0.1117	–0.1392	0.0373	0.0686	0.0392	0.0932

Box plots (Fig. 8 and Fig. 9) highlighted differences in the location of mean values, clustering (25th and 75th percentile), and whiskers resulting from the spread of the analyzed values. A summary of the ANOVA is presented in Table 6, which includes the variance. SS represents the sum of squares, and df represents the degrees of freedom. The values of the mean square error MS clearly indicate low values relative to the mean values of the analyzed parameters. The statistic F was the quotient of the mean squares. The final probability values prob > F for all analyzed values and test points clearly indicate that the sample statistics did not reach the accepted threshold F. The highest value was reached for the IMEP at test point 1100/20 and was 1.01×10^{-11}, which is very low in relation to the limit derived from the 95% confidence threshold, which is 0.05. The remaining values prob > F were well below those indicated for the IMEP. This means that, in all the cases analyzed, the hypothesis H_0 (Eq. (9)) showing agreement of mean values, should be rejected in favor of the alternative hypothesis H_1 (Eq. (10)) indicating that the population means were different.

Because the distributions shown in (Fig. 6 and Fig. 7) showed possible discrepancies from the normal distribution, an additional statistical test was performed. In such cases, it was expedient to use Levene, Brown-Forsythe and O'Brien absolute tests [9]. As with the ANOVA, MATLAB software was used. The essence of the test is to show that the probability p of the test (f_{stat}) is in the range (0...1), with a value of 1 indicating acceptance of the hypothesis H_0 (Eq. (9)). All the p values determined in the course of the analysis, shown in Table 7, show small values, which indicates the fact that the alternative hypothesis H_1 has been accepted as valid, indicating the significance of the differences in the mean values of the analyzed parameters at the test points.

Based on the results of the calculations and analyses presented in this paper, it was concluded that this goal was achieved. The proposed HVO + WPPO alternative fuel has slightly different ignition and combustion characteristics and engine stability compared with DF. Tests at two points in the WHSC cycle showed differences in the average values of p_{max}, IMEP, q_{max}, and their COV coefficients of variation, but they were not large enough to exclude the proposed fuel from use in the engine. The dependence of the differences in the analyzed parameters on the load and engine speed was also determined. These findings highlight the need for further research in this area.

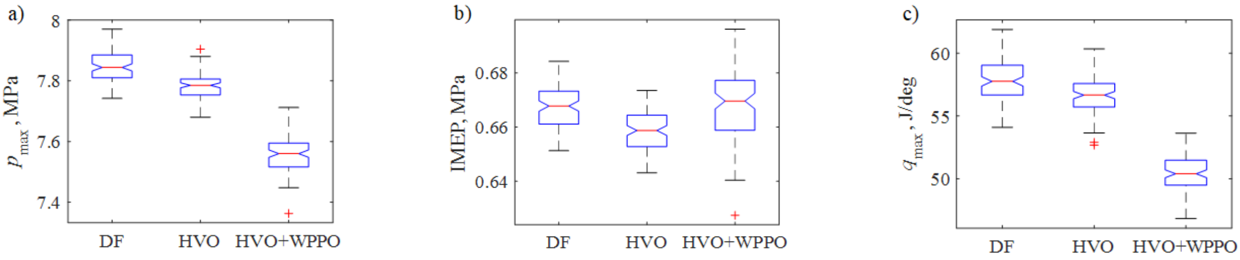

Fig. 8. Box plots indicating the location of the analyzed values at operating point 1100/25

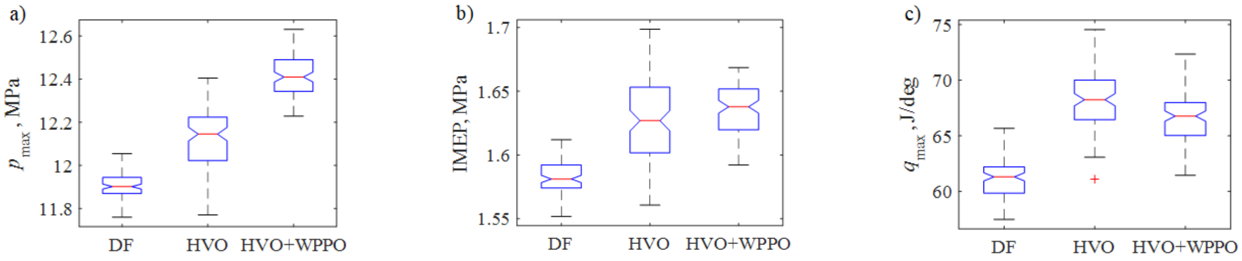

Fig. 9. Box plots indicating the location of the analyzed values at operating point 1800/70

Table 6. Summary ANOVA statistics of the values analyzed at both operating points

RPM/load	1100/25						1800/70				
Parameter	Source	SS	df	MS	F	Prob > F	SS	df	MS	F	Prob > F
p_{max}	Columns	4.68900	2	2.3445	907.46	3.09×10^{-127}	13.04260	2	6.5213	631.00	1.17×10^{-107}
	Error	0.76732	297	0.00258			3.06950	297	0.01034		
	Total	5.45630	299				16.11210	299			
IMEP	Columns	0.00497	2	0.00248	27.60	1.01×10^{-11}	0.15672	2	0.07836	150.89	6.03×10^{-46}
	Error	0.02672	297	9.00×10^{-5}			0.15424	297	5.20×10^{-4}		
	Total	0.03169	299				0.31097	299			
q_{max}	Columns	3097.50	2	1548.75	647.79	4.92×10^{-109}	2745.75	2	1372.88	297.58	1.16×10^{-71}
	Error	710.07	297	2.3908			1370.20	297	4.6135		
	Total	3807.57	299				4115.96	299			

Table 7. Summary Levene'a, Browna-Forsythe'a and O'Briena tests of the values analyzed at both operating points

Parameter		1100/25	1800/70
p_{max}	p	0.0049	1.1059×10^{-15}
	f_{stat}	5.4099	38.7588
IMEP	p	6.6987×10^{-10}	1.0665×10^{-21}
	f_{stat}	22.7002	57.0665
q_{max}	p	0.1436	4.5403×10^{-5}
	f_{stat}	1.9535	10.3443

4. Conclusions

In this study, three types of diesel fuel were compared: conventional diesel fuel (DF), hydrotreated vegetable oil (HVO), and a mixture of HVO with PPO and PSO additives (HVO + WPPO). Measurements were carried out on a special platform with a research engine at two points of the World Harmonized Stationary Cycle (WHSC) 1100/25 and 1800/70. Based on the measurements, calculations, and analysis, the following conclusions were drawn.

1. HVO and HVO + WPPO have slightly different combustion patterns than the conventional DF. In the case of HVO, this may be due to the higher reactivity of the fuel, which affects engine performance. HVO + WPPO has shown similar performance to DF, which is the rationale for its use in engines.
2. The average maximum pressure values at the 1100/25 point were 7.848, 7.781, and 7.556 MPa for DF, HVO, and HVO + WPPO, respectively. In contrast, at test point 1800/70, DF 11.906 MPa HVO 12.13MPa, HVO + WPPO 12.42 MPa. The values obtained were not significantly different.
3. The average values of the indicated mean effective pressure at the 1100/25 point were 0.667, 0.659, and 0.668 MPa for DF, HVO, and HVO + WPPO, respectively. However, at test points 1800/70, DF was 1.584 MPa, HVO was 1.628 MPa, and HVO + WPPO was 1.636 MPa. The values obtained were not significantly different.
4. The averaged maximum heat release values at the 1100/25 point were for DF 57.80 J/deg, HVO 56.61 J/deg MPa, and with HVO + WPPO 50.47 J/deg. In contrast, at test point 1800/70, DF 61.18 J/deg HVO 68.203 J/deg, HVO + WPPO 66.74 J/deg. The values obtained also do not provide a basis for rejecting HVO + WPPO from use in the engine.
5. The coefficients of variation of the analyzed parameters indicate the stability of the engine's operation, only in the case of heat generation approaching 4%, in other cases, they rarely reached 2%. Based on the small values of the coefficients of variation, the percentage differences often exceeded 50%.
6. 6 Statistical analyses, including ANOVA and Levene's tests, confirmed significant differences between the fuels, indicating the potential of the HVO + WPPO mixture as an environmentally friendly alternative to DF, especially at higher speeds and loads.

Acknowledgements

The research leading to these results has received funding from the commissioned task entitled “Polytechnic Network VIA CARPATIA named after President of the Republic of Poland Lech Kaczynski”, financed by a special purpose grant from the Minister of Science and Higher Education contract no: MEiN/2022/DPI/2575, MEiN/2022/DPI/2577, MEiN/2022/DPI/2578, activity “ISKRA – building inter-university research teams”.

Nomenclature

BMEP	brake mean effective pressure
CAD	crank angle degree
CO	carbon monoxide
CO_2	carbon dioxide

COV	cycle-by-cycle variations
DF	diesel fuel
FTIR	Fourier-transform infrared
HC	hydrocarbon
HVO	hydrotreated vegetable oil
IMEP	indicated mean effective pressure
NO_x	nitrogen oxides
PM	particulate matter
PPO	polypropylene oil
PSO	polystyrene oil
THC	total hydrocarbon
TPO	automobile tire oil
WHSC	World Harmonized Stationary Cycle
WPPO	waste plastic pyrolysis oils
$\bar{x}$	mean value of the parameter under study
κ	kurtosis
p	maximum pressure in the cylinder
q	heat released in the cylinder
s	skewness
σ	standard deviation

Bibliography

[1] Ananthakumar S, Jayabal S, Thirumal P. Investigation on performance, emission and combustion characteristics of variable compression engine fuelled with diesel, waste plastics oil blends. J Brazilian Soc Mech Sci Eng. 2017;39(1):19-28. https://doi.org/10.1007/s40430-016-0518-6

[2] Azeem N, Beatrice C, Vassallo A, Pesce F, Gessaroli D, Biet C et al. Experimental study of cycle-by-cycle variations in a spark ignition internal combustion engine fueled with hydrogen. Int J Hydrogen Energy. 2024;60:1224-1238. https://doi.org/10.1016/j.ijhydene.2024.02.182

[3] Bortel I, Vávra J, Takáts M. Effect of HVO fuel mixtures on emissions and performance of a passenger car size diesel engine. Renew Energy. 2019;140:680-691. https://doi.org/10.1016/j.renene.2019.03.067

[4] Budsaereechai S, Hunt AJ, Ngernyen Y. Catalytic pyrolysis of plastic waste for the production of liquid fuels for engines. RSC Adv. 2019;9(10):5844-5857. https://doi.org/10.1039/C8RA10058F

[5] Channappagoudra M, Ramesh K, Manavendra G. Comparative study of standard engine and modified engine with different piston bowl geometries operated with B20 fuel blend. Renew Energy. 2019;133:216-232. https://doi.org/10.1016/j.renene.2018.10.027

[6] Das AK, Hansdah D, Mohapatra AK, Panda AK. Energy, exergy and emission analysis on a DI single cylinder diesel engine using pyrolytic waste plastic oil diesel blend. J Energy Inst. 2020;93(4):1624-1633. https://doi.org/10.1016/j.joei.2020.01.024

[7] Devi DS, Kumar R, Rajak U. Experimental investigation of performance, emission and combustion characteristics of a CI engine fuelled by blends of waste plastic oil with diesel. Energy Sources, Part A Recover Util Environ Eff. 2022;44:7693-7708. https://doi.org/10.1080/15567036.2022.2115582

[8] Faisal F, Rasul MG, Jahirul MI, Chowdhury AA. Waste plastics pyrolytic oil is a source of diesel fuel: A recent review on diesel engine performance, emissions, and combustion characteristics. Sci Total Environ. 2023;886:163756. https://doi.org/10.1016/j.scitotenv.2023.163756

[9] Gastwirth JL, Gel YR, Miao W. The impact of Levene's Test of equality of variances on statistical theory and practice. Stat Sci. 2009;24(3):343-360. https://doi.org/10.1214/09-STS301

[10] Heng Teoh Y, Geok How H, Wen Lee S, Lin Loo D, Danh Le T, Tho Nguyen H et al. Optimization of engine out responses with different biodiesel fuel blends for energy transition. Fuel. 2022;318:123706. https://doi.org/10.1016/j.fuel.2022.123706

[11] Huang Z, Huang J, Luo J, Hu D, Yin Z. Performance enhancement and emission reduction of a diesel engine fueled with different biodiesel-diesel blending fuel based on the multi-parameter optimization theory. Fuel. 2022;314:122753. https://doi.org/10.1016/j.fuel.2021.122753

[12] Hunicz J, Krzaczek P, Gęca M, Rybak A, Mikulski M. Comparative study of combustion and emissions of diesel engine fuelled with FAME and HVO. Combustion Engines. 2021;184(1):72-78. https://doi.org/10.19206/ce-135066

[13] Jakubowski M, Jaworski A, Kuszewski H, Balawender K. Performance of a diesel engine fueled by blends of diesel fuel and synthetic fuel derived from waste car tires. Sustain. 2024;16(15):6404. https://doi.org/10.3390/su16156404

[14] Januszewicz K, Hunicz J, Kazimierski P, Rybak A, Suchocki T, Duda K et al. An experimental assessment on a diesel engine powered by blends of waste-plastic-derived pyrolysis oil with diesel. Energy. 2023;281:128330. https://doi.org/10.1016/j.energy.2023.128330

[15] Krzemiński A, Ustrzycki A. Visualisation testing of the vertex angle of the spray formed by injected diesel–ethanol fuel blends. Energies. 2024;17(12):3012. https://doi.org/10.3390/en17123012

[16] Li X, Liu Q, Ma Y, Wu G, Yang Z, Fu Q. Simulation study on the combustion and emissions of a diesel engine with different oxygenated blended fuels. Sustain. 2024;16(2):631. https://doi.org/10.3390/su16020631

[17] McCaffery C, Zhu H, Sabbir Ahmed CM, Canchola A, Chen JY, Li C et al. Effects of hydrogenated vegetable oil (HVO) and HVO/biodiesel blends on the physicochemical and toxicological properties of emissions from an off-road heavy-duty diesel engine. Fuel. 2022;323:124283. https://doi.org/10.1016/j.fuel.2022.124283

[18] Mussa NS, Toshtay K, Capron M. Catalytic applications in the production of hydrotreated vegetable oil (HVO) as a renewable fuel: a review. Catalysts. 2024;14(7):452. https://doi.org/10.3390/catal14070452

[19] Pietras D, Stelmasiak Z, Pietras P. Comparison of operational parameters and stability of performance of an automotive SI engine powered by methyl and ethyl alcohols. Combustion Engines. 2023;194(3):129-140. https://doi.org/10.19206/CE-169136

[20] Preuß J, Munch K, Denbratt I. Performance and emissions of renewable blends with OME3-5 and HVO in heavy duty and light duty compression ignition engines. Fuel. 2021;303:121275. https://doi.org/10.1016/j.fuel.2021.121275

[21] Prokopowicz A, Zaciera M, Sobczak A, Bielaczyc P, Woodburn J. The effects of neat biodiesel and biodiesel and HVO blends in diesel fuel on exhaust emissions from a light duty vehicle with a diesel engine. Environ Sci Technol. 2015;49(12):7473-7482. https://doi.org/10.1021/acs.est.5b00648

[22] Rybak A, Hunicz J, Szpica D, Mikulski M, Gęca M, Woś P. Comparative analysis of waste-derived pyrolytic fuels applied in a contemporary compression ignition engine. Combustion Engines. 2024;198(3):74-81. https://doi.org/10.19206/CE-186697

[23] Sharma P, Dhar A. Effect of hydrogen fumigation on combustion stability and unregulated emissions in a diesel fuelled compression ignition engine. Appl Energy. 2019; 253:113620. https://doi.org/10.1016/j.apenergy.2019.113620

[24] Singh RK, Ruj B, Sadhukhan AK, Gupta P, Tigga VP. Waste plastic to pyrolytic oil and its utilization in CI engine: performance analysis and combustion characteristics. Fuel. 2020;262:116539. https://doi.org/10.1016/j.fuel.2019.116539

[25] Sitnik LJ, Sroka ZJ, Andrych-Zalewska M. The impact on emissions when an engine is run on fuel with a high heavy alcohol content. Energies. 2021;14(1):41. https://doi.org/10.3390/en14010041

[26] Suarez-Bertoa R, Kousoulidou M, Clairotte M, Giechaskiel B, Nuottimäki J, Sarjovaara T et al. Impact of HVO blends on modern diesel passenger cars emissions during real world operation. Fuel. 2019;235:1427-1435. https://doi.org/10.1016/j.fuel.2018.08.031

[27] Tutak W, Jamrozik A, Pyrc M. Experimental investigations on combustion, performance and emissions characteristics of compression ignition engine powered by B100/ethanol blend. E3S Web of Conferences. EDP Sciences 2017;14: 02019. https://doi.org/10.1051/e3sconf/20171402019

[28] Vural E, Özer S, Özel S, Binici M. Analyzing the effects of hexane and water blended diesel fuels on emissions and performance in a ceramic-coated diesel engine by Taguchi optimization method. Fuel. 2023;344:128105. https://doi.org/10.1016/j.fuel.2023.128105

[29] Zhang Z, Li J, Tian J, Dong R, Zou Z, Gao S et al. Performance, combustion and emission characteristics investigations on a diesel engine fueled with diesel/ethanol/n-butanol blends. Energy. 2022;249:123733. https://doi.org/10.1016/j.energy.2022.123733

[30] Zhang Z, Ye J, Tan D, Feng Z, Luo J, Tan Y et al. The effects of Fe_2O_3 based DOC and SCR catalyst on the combustion and emission characteristics of a diesel engine fueled with biodiesel. Fuel. 2021;290:120039. https://doi.org/10.1016/j.fuel.2020.120039

Dariusz Szpica, DSc., DEng. – Faculty of Mechanical Engineering, Bialystok University of Technology, Poland.
e-mail: *d.szpica@pb.edu.pl*

Mirosław Jakubowski, DEng. – Faculty of Mechanical Engineering and Aeronautics, Rzeszow University of Technology, Poland.
e-mail: *mjakubow@prz.edu.pl*

Michał S. Gęca, DSc., DEng. – Faculty of Mechanical Engineering, Lublin University of Technology, Poland.
e-mail: *michal.geca@pollub.pl*

Artur Krzemiński, DEng. – Faculty of Mechanical Engineering and Aeronautics, Rzeszow University of Technology, Poland.
e-mail: *akrzeminski@prz.edu.pl*

Prof. Jacek Hunicz, DSc., DEng. – Faculty of Mechanical Engineering, Lublin University of Technology, Poland.
e-mail: *j.hunicz@pollub.pl*

Grzegorz Mieczkowski, DSc., DEng. – Faculty of Mechanical Engineering, Bialystok University of Technology, Poland.
e-mail: *g.mieczkowski@pb.edu.pl*

Article citation info:
Wróblewski P, Bratkowski P. Effect of using a combination of coatings on reducing structural defects in the working area of the combustion chamber and on the energy efficiency of a reciprocating internal combustion engine. Combustion Engines. 2025;202(3):118-130. https://doi.org/10.19206/CE-207651

Piotr WRÓBLEWSKI
Przemysław BRATKOWSKI

Combustion Engines
Polish Scientific Society of Combustion Engines

Effect of using a combination of coatings on reducing structural defects in the working area of the combustion chamber and on the energy efficiency of a reciprocating internal combustion engine

ARTICLE INFO

Received: 4 March 2025
Revised: 12 June 2025
Accepted: 27 June 2025
Available online: 28 July 2025

This article has reviewed the latest test results in the use of multi-layer thermal coatings in the combustion chambers of piston combustion engines. The work emphasized mainly their role in reducing the structural defects of thermal materials and their impact on improving the energy efficiency of engines. Two, three, or more layers of thermal coating systems reduce the consumption of material in areas undergoing the highest thermal load. Initially, significant disadvantages such as microcracks, corrosion and erosion of working components of engine combustion chambers have been excluded. This construction approach using multi-layer coatings leads to an increase in durability and reliability of piston internal combustion engines. This reduces the costs of engine operation.

The article compares various experimental and simulation results for different thermal coating systems. Companies such as ceramics, metal oxides, and nanostructural composites were analyzed. The authors emphasize in this work the increasing interest in these coatings in order to achieve a significant reduction of fuel consumption and greenhouse gas emissions. The conditions for the correct heat conduction, maintenance of thermal stability, and the ability to self-heal the coating in extreme conditions were analyzed in great detail. The summary and detailed analysis of the current state of knowledge in this area is certainly very valuable for engine designers and technologists in the automotive industry.

Key words: *thermal barrier coatings, multilayer coatings, structural defect reduction, energy efficiency, reciprocating internal combustion engines*

1. Introduction

Modern reciprocating internal combustion engines achieve high effective power through high rotational speed of the engine crankshaft and high value of mean effective pressure in the working chamber of the engine. The energy requirements imposed on modern engines necessitate new research into the use of materials for thermal and anti-wear coatings. The search for new solutions enforces studies on the possibility of applying multilayer coatings in the engine chamber. Such solutions allow for limiting the phenomenon of thermal microcrack formation, erosive and corrosive damage [15]. The use of these coatings also enables achieving higher thermal efficiency of internal combustion engines. This article presents a summary of the most important experimental and simulation studies on the use of multilayer coatings in internal combustion engines, significantly loaded mechanically and thermally. Most current research focuses on single-layer coatings. There are very few experimental studies involving piston components of internal combustion engines directed at multilayer coating systems. The authors point to the potential of this solution and the need for further research and analysis.

Preliminary studies on the possibility of using coatings as a thermal barrier included thick ceramic layers applied by plasma spraying or flame spraying [29]. In such configurations, it was often shown that these coatings, when applied to components of a reciprocating internal combustion engine, have limited crack resistance under dynamic temperature changes, e.g., in the engine combustion chamber [33, 35]. In contrast, very thin coating layers applied using these methods on turbine surfaces or deposited using PVD, CVD, and ion implantation methods exhibit better wear resistance. This allows for better thermal insulation, greater control over the coating structure, and its surface roughness. Coatings with a thickness greater than (> 0.5 mm) have significant disadvantages: low resistance to mechanical damage, reduced volumetric efficiency due to high thermal expansion, limited ability to form an oil film at elevated temperatures, and limited applicability in spark-ignition engines (in certain operating conditions, they cause knocking combustion). The research results presented in this study indicate very diverse problems related to the use of these coatings.

Some studies report up to an 8% increase in engine power and a 9% reduction in fuel consumption [46]. In other words, increased fuel consumption is observed, attributed to prolonged combustion time in the combustion chamber, dependent on the fuel dose [41]. This study proposes adjusting the fuel injection timing to counteract this effect. Moreover, the limited ability of ceramic coatings to radiate in the infrared range reduces their effectiveness in lowering radiative heat transfer, which accounts for 40% of the total heat flux in compression-ignition engines [9]. Results for spark-ignition engines appear more consistent, with some studies reporting a 6% reduction in fuel consumption. The same studies report increased hydrocarbon emissions due to the surface structure of the coatings [10, 20].

The main problem is the repeatability of results in different testing environments. In a comparative study [16], fatigue tests on six coatings conducted in three laboratories produced divergent results. The discrepancy in test results was attributed to different test conditions and the varying surface structure of the selected coatings. These studies demonstrate how strongly the geometry of the coatings and their chemical composition depend on engine operating parameters, such as combustion temperature, crankshaft rotational speed, and hydrodynamic pressure between selected kinematic pairs of the engine.

In response to these limitations, recent studies have shown that multilayer coatings with appropriate thickness and layer distribution of selected cooperating coatings can form systems with good mechanical and thermal properties. Proper selection of layers allows for meeting complex functional parameters. This primarily concerns the function of thermal insulation and the prevention of microcracks. Such complex systems of various coatings enable the formation of a highly efficient structure operating within the combustion chamber area, which translates into increased durability of the main piston mechanism of the internal combustion engine. Moreover, appropriate control of coating thickness and thermodiffusion parameters allows for the adjustment of their functional parameters to the operating conditions of selected components of the reciprocating internal combustion engine. Advanced numerical models presented in this study confirm the behavior of selected coatings under extreme engine operating conditions. These actions allow for the adoption of appropriate strategies in engine design. The literature review shows that multilayer coating systems are becoming increasingly advanced and are capable of meeting ever more demanding engine operating conditions.

Despite research challenges related to limitations in reproducibility and the application of various coatings, these systems offer a wide range of solutions aimed at achieving high engine power, reduced fuel consumption, and lower emissions of harmful exhaust substances [30]. Future research should focus on long-term durability tests under real engine operating conditions and should include studies on further improvement of materials and coating deposition technologies. In particular, this should concern the area of the engine combustion chamber.

2. Thermal loads of internal combustion engines

Computer simulation of the engine work cycle, combined with models of unknown heat exchange in individual components, can be used to forecast the temperature of the combustion chamber surface with and without insulation coating. Such a model was presented at work [47]. In the case of a combustion chamber with an insulation layer, two basic issues are distinguished [47]: the average temperature of the insulated element increases with the coating thickness and the amplitude of cyclical temperature fluctuations around this average is almost the same for thin and thick layers; In fact, the highest difference between peak and minimal values occurs for the thinnest tested layer (0.5 mm).

Thermal capacity, thermal conductivity, and thermal expansion are three key thermophysical features that determine the properties of the TBC coating. The heat capacity (C) expresses the amount of energy needed to increase the temperature of the material by one degree. It is primarily shaped by vibrations and rotation of atoms, electrons' transitions between energy levels, and changes in atom position. In porous materials, which contain less solid substance per unit of volume, heating or cooling occurs faster than in non-porous materials. In insulation, where rapid temperature changes are important, low thermal capacity is crucial. In most cases, thermal capacity is not a fixed value – it depends on the temperature, pressure, and volume. The thermal capacity at a constant pressure (C_P) and a constant volume (C_V) is most often considered. The change in internal energy along with a change in temperature at a constant volume is described by the C_V, while at constant pressure – C_P [47].

Thermal conductivity (K) determines how quickly heat flows through the material and is expressed in W/(M×K). This size depends on the energy stored in the material (i.e. the volume of heat capacity C), on heat carriers (electrons or phonons), and the heat wave distortion. The lower C, the speed of the media (V), and the average free road (λ), the lower the thermal conductivity. In ceramics, the range of values K can be very different, and at the same time, it should not be assumed that all ceramics conduct heat worse than metals. The highest K values are observed in dense, well-ordered structures, while the introduction of admixtures or foreign atoms reduces conductivity by distracting phonons [40].

In crystalline ceramics, the main mechanism of heat transport is vibrations of the crystalline network (Phonons), and the average free path (λ) decreases as the temperature increases, which increases thermal conductivity at low temperatures. However, in glass (disordered structure) λ depends less on the temperature, so the conductivity increases mainly due to increasing thermal capacity [40].

The importance of heat radiation also increases at higher temperatures. According to data at work [2], about 75% of radiation appears at frequencies above 3.1 kT/h (e.g. approx. 8.1×10^{13} Hz at 1300 K). The impact of inclusions and porosity on radiation absorption was also examined – point defects and oxygen gaps distract high-frequency network vibrations, reducing conductivity. To effectively disperse the waves with a frequency of 8.1×10^{13} Hz (at 12% porosity), spherical pores must have a radius of approximately. 0.45 μm. Additional porosity on a nanometric scale further reduces thermal conductivity, but does not affect radiation. Ultimately, low conductivity and heat capacity are desirable in ceramic barrier coatings (TBC), as well as good adhesion to the ground, high stability at elevated temperatures, and resistance to oxidation. Such rules should be strictly observed when designing coatings intended for work in piston combustion chambers of internal combustion engines.

The study [7] showed that temperature fluctuations (ΔT_s) on the surface of the engine combustion chamber are inversely proportional to the square element from the product of thermal conductivity (k), density (ρ), and specific heat (c).

$$\Delta T_s \sim \frac{1}{k\rho c}^{\frac{1}{2}} \tag{1}$$

The next key aspect is the heat wave penetration into the material. The depth of penetration (δ) is often referred to as a distance from the surface where the amplitude of temperature fluctuations drops to 1% of the initial value on the surface, is proportional to the square element from the thermal conductivity quotient (α) to the engine speed (N), which can be saved [7]:

$$\delta \sim \left(\frac{\alpha}{N}\right)^{\frac{1}{2}} \tag{2}$$

where:

$$\alpha = \frac{k}{\rho c} \tag{3}$$

Based on the analysis, it can be stated that thin insulating coatings demonstrate significant benefits compared to thick insulating layers in multilayer coating systems. This is particularly applicable in reciprocating internal combustion engines. Owing to their low thermal inertia, they enable surfaces to respond rapidly to varying gas temperatures. Thin coatings can also be successfully applied in spark-ignition engines. In these engines, a reduction in unburned hydrocarbon emissions is observed due to the flame-quenching effect, which also leads to accelerated heating of the catalytic converter. Additional advantages of thin coatings include less friction, better immunity for erosion and corrosion, increased life of components, and greater reliability. Therefore, thin insulation coatings allow for various possibilities to improve the durability of the engine, eliminating problems associated with thicker layers of insulation coatings. In the case of multi-layer coatings, it is possible to effectively use the properties of each coating and achieve a decisive reduction of erosion consumption resulting from the propagation of the flame in the combustion chamber.

3. Tests of single-layer coatings applied to the piston bottom and the space of the combustion chamber

Based on the analysis, it can be concluded that thin thermal-barrier coatings exhibit significant advantages over thick thermal-barrier layers in multilayer coating systems. This is particularly applicable in reciprocating internal combustion engines. Thanks to their low thermal inertia, they enable surfaces to respond quickly to changing gas temperatures. Thin coatings can also be successfully applied in spark-ignition engines. In these engines, a reduction in unburned hydrocarbon emissions is observed due to the flame-quenching effect, which also leads to accelerated heating of the catalytic converter.

3.1. Metal-based coatings

In the context of piston combustion engines and their combustion chambers, metallic coatings play an important role, especially in areas with increased temperatures and exposed to combustion gases. The use of such a protective layer allows: protecting elements against corrosion, protection against temperature increases, increasing chemical resistance, surface hardening, increasing the durability of components, and reducing the friction coefficient, which helps reduce the consumption of parts of selected cinematic pairs of the engine [50]. Large heat conduction, characteristic of most metals. For this reason, metallic coatings are rarely used as insulation coatings in the chambers. The use of basic metal single-layer coatings of chromium, nickel, and molybdenum has many significant defects. These disadvantages limit the further development of these solutions for designing heat flow in the combustion chamber.

3.2. Polymer coatings

In piston combustion engines, polymer coverings are found less often directly in the combustion chamber, but they are used, e.g. in seals or anti-corrosion coatings in areas with a lower heat load. The latest research focuses on polymer coatings, which can autonomously repair their microtasus and thus prevent further corrosion of the substrate. The main idea is that during operation, when the layer is outlined or damaged, active substances are released to enable partial regeneration of the coating.

Polymer coatings can also be used in anti-corrosion protection – they are found in many industrial sectors, including tank protection [1]. In [12], a compilation of self-healing materials based on polydimethylsiloxane was presented, in which phase-separated droplets of HOPDMS and PDES undergo polycondensation catalyzed by di-n-butyltin dilaurate. In this system, the healing agent remains as separate droplets, while the catalyst is encapsulated in polyurethane microcapsules that rupture under mechanical damage, releasing DBTL. This solution enables chemical stability even in humid and high-temperature conditions. Tests using a double-supported beam method showed the recovery of a significant portion of the original crack resistance, especially after the addition of an adhesion promoter [12]. The self-healing mechanism works such that when an external factor (e.g., a crack or scratch) disrupts the capsule structure, contact occurs between the particles of the active components (previously phase-separated). As a result of the reaction, a new polymer layer is formed, filling the damage and restoring the coating's original protective properties. This significantly extends the coating's service life [13].

In the context of piston internal combustion engines and their combustion chambers, polymers are used much less frequently than metallic and ceramic coatings, mainly due to their reduced thermal resistance and lower mechanical strength compared to metals and ceramics. Nevertheless, polymer coatings are sometimes employed on components that experience lower thermal loads or serve as lubricating layers, helping to reduce friction between engine parts. While the use of these coatings in the combustion chambers of piston engines seems unlikely, combining the unique characteristics of these materials may contribute to the development of thermal coatings for engine components that are less thermally stressed.

3.3. Functional properties of ceramic coatings in the use of an engine

Ceramics are non-metallic solid materials that can have a crystalline, partially crystalline, or amorphous structure. A wide range of ceramic coatings is available on the market. These materials are characterized by very low thermal and electrical conductivity, corrosion resistance, the ability to operate at higher temperatures than most other materials, resistance to rapid temperature changes, and high wear resistance. Before applying a ceramic coating to the components of internal combustion engine chambers, it is necessary to verify the compatibility between the ceramic and the metallic substrate. One of the most important aspects is the coefficient of thermal expansion. If the difference between the thermal expansion of the coating and the substrate is too great, tensile and compressive stresses resulting from the thermal cycles of a four-stroke engine may cause cracks to develop.

3.3.1. The use of TBC coatings in automatic and spark ignition engines

Studies [45] show that the use of coatings (TBC) based on stabilized zirconia on the surface of the bottom of the piston affects the emissions of the engine and its thermal efficiency. The 100 µm thick coating was tested. However, the advantages of these coatings depend largely on the engine load and changes in operating conditions. Although the engine efficiency increased from 1.14% to 8.84% with 50% engine load, the characteristics of these changes are non-linear. These studies indicate that the given energy benefits do not necessarily have to translate into such energy gains in real conditions of the piston internal combustion engine.

The introduction of TBC coatings into the combustion engines reduces fuel consumption [45]. Fuel consumption decreases by approximately 3.38% in full load conditions, up to 28.59% at partial load (25%) of the engine. The work [45] presents a reduction in HC emissions by a value of 35.27% and a reduction of emissions by 2.7%. An increase in CO_2 emissions was observed by about 5.27%. These studies indicate an improvement in the combustion process. The work also indicates the appropriate disadvantages of emissions. Experimental research and results largely depend on the conditions of the experiment and the engine itself. Therefore, the problem should be considered on the basis of other research data in other works.

Although most of the test results indicate the great potential to use TBC coatings, the practical possibility of using them requires further research. Such tests should take into account net energy balance, material stability in the longer period of engine operation, resistance to dynamic thermal load changes, and emissions to the environment. All these activities are closely related and require experimental tests, especially in terms of the durability of coatings.

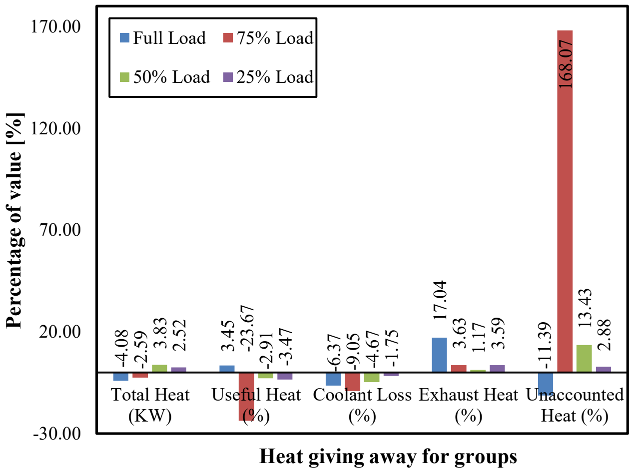

Fig. 1. Graph showing the percentage change in the application of the YSZ coating compared to no coating for various engine loads. The graph is based on selected data from the study [45]

The basic coating presented in the study [45] comprises an outer layer of zirconium dioxide (ZrO_2) partially stabilized with approximately 7% yttria (Y_2O_3). The MCrAlY (CoNiCrAlY) bond coat is applied using the HVOF method. The top coat is mainly applied by plasma spraying in an air atmosphere or by the EB-PVD method. Due to the high oxygen permeability in ceramic materials, corrosion protection relies on an intermediate layer capable of forming a dense, well-adhering oxide layer. The top coat is exposed to various types of damage caused by the penetration of foreign bodies, the effect of high temperatures that destabilize ceramic materials, and erosion induced by solid particles in the exhaust gas stream. This work suggests that the best process repeatability is achieved with the SIFCO (vapor phase) and HVOF methods; the APS method requires manual control of the coating thickness to maintain process stability. Current solutions include, among others, the use of new compositions for outer coatings (with additives of rare earth metal oxides), two-layer intermediate coatings, and the use of the HVOF spray technique [56].

In study [34], a thermal barrier coating (TBC) was applied to the cylinder head and valves of a spark-ignition engine by first removing a layer of material from the head, and then applying a 100 µm thick layer of NiCrAl (bond coat) and a 200 µm thick layer of yttria-stabilized zirconia (ZrO_2 with 8 wt.% Y_2O_3) using the atmospheric plasma spray (APS) method. The spraying specifications included a particle velocity of 500–550 mm/s, porosity of 1–8%, and a spraying distance of 100 mm. A single-cylinder Briggs & Stratton engine (10 HP, air-cooled) operating at a constant speed of 3000 rpm on gasoline and gasoline–n-butanol mixtures (GNB10 and GNB15) was used for the tests. In the engine with the TBC, a higher maximum cylinder pressure (by 2–8 bar) and a shift in the maximum heat release closer to TDC by approximately 10°CA were observed. Improved thermal insulation resulted in a reduction in specific fuel consumption (SFC) and an increase in thermal efficiency – up to 6% higher on gasoline and 7.4% higher on the GNB10 mixture compared to the uncoated engine. Better thermal insulation also led to higher exhaust gas temperatures. Emission analysis showed that, thanks to the TBC and the addition of n-butanol, the concentrations of CO and HC decreased (aided by higher combustion temperatures and the oxygen content in the fuel), whereas the concentration of NO_x increased due to the higher temperatures in the combustion chamber. Additionally, the ceramic layer protects the chamber components from damage caused by high temperatures, thereby enhancing the durability of that engine part.

In study [27], a thin ceramic coating was applied to a direct-injection diesel engine. The piston and cylinder head were coated with a 100-micrometer-thick thermal barrier coating based on yttria-stabilized zirconia, while the cylinder liner was protected with a 500-micrometer-thick coating of the same material. A reduction in fuel consumption of 6% at full load and 2600 rpm, and 3.5% at 1600 rpm, was achieved compared to a standard engine without protective coatings. These positive results were obtained thanks to the use of delayed injection timing along with high fuel injection pressure and speed. The introduction of a modern high-pressure fuel injection system enabled the desired heat release characteristics during the premixed combustion phase to be achieved. The thermal barrier coating contributed to an increased rate of heat release compared to the standard engine, confirming the quality and reliability of the obtained data relative to other studies.

In study [38], a 250-micrometer (0.25 mm) zirconia coating partially stabilized with yttria was applied to the combustion chamber surface and piston crown of an internal combustion engine. This enabled the operating temperature to increase from 350–400°C to 850–900°C and reduced heat losses to the external environment. As a result, thermal efficiency improved and the combustion process shifted from a premixed phase to diffusive combustion. The exhaust gas temperature changed from 410°C to 428°C. A significant reduction in emissions was also measured: CO lowered from 0.085% to 0.069%, HC lowered from 22 ppm to 14 ppm, and smoke levels from 4.4 to 4.13 BSU (bosch smoke unit).

3.3.2. Advanced TBC materials in automatic ignition engines

In the study [51], thermal barrier coatings (TBC) made of lanthanum zirconate ($La_2Zr_2O_7$) were applied to the piston, cylinder head, and valves of a single-cylinder diesel engine using APS plasma spray technology. The coatings had a total thickness of 500 µm, of which 150 µm was the bond coat (NiCrAlY) and 350 µm was the LZ layer. The spray process parameters included an arc current of 660 A, a primary gas (Ar) flow rate of 30 l/min, a secondary gas (H_2) flow rate of 15 l/min, a spray distance of 130 mm, and a powder feed rate of 40 g/min. The application of the TBC coatings resulted in significant energy and operational benefits. In the TBC-coated engine, fuel consumption was reduced by 4.16% for diesel, 2.9% for the B20 blend (20% biodiesel, 80% diesel), and 9.5% for B100 compared to the B100 engine without the coating [51]. At the same time, brake thermal efficiency (BTE) increased by 4% for diesel, 8.55% for B20, and 10.7% for B100 compared to the engine without the coating. CO emissions were reduced by 18% for diesel, 27.7% for B20, and 43.75% for B100, while HC emissions decreased by 11.68% for diesel, 40.98% for B20, and 62.26% for B100 [51]. However, NO_x emissions increased by 3.5% for diesel, 12% for B20, and 15% for B100 due to the higher combustion temperature of the fuel–air mixture in the combustion chamber [51]. Thanks to its low thermal conductivity (1.56 W/m·K compared to 2.5 W/m·K in PSZ) and the stability of its pyrochlore structure up to 2300°C, this material is characterized by high resistance to sintering and favorable catalytic properties, which translates into reduced HC, CO, and soot emissions [51].

The use of ceramic coatings, especially the type ($La_2Zr_2O_7$) coatings, indicates great advantages in the scope of their application on the elements of piston internal combustion engines. In diesel-powered engines, a reduction in fuel consumption is observed [28]. The tests were carried out on the components of the piston internal combustion engine after applying the coating and without applying the coating, fuel mixtures B20–B100 were used [28]. It has been shown that engines with these coatings produce a smaller amount. The coating ($La_2Zr_2O_7$) has low thermal conductivity and shows temperature stability to 2573 K [28]. Higher combustion temperature of the fuel-air mixture and catalytic properties allow the reduction of toxic exhaust components. The coating also plays a very important role [28].

Table 1. A summary of research findings regarding the application of TBC coatings in compression ignition and spark ignition engines

No.	Engine type/research object	Coating material and thickness	Application method	Key results (efficiency, fuel consumption, emissions)
[45]	Compression ignition engine, coating on the bottom of the piston	Yttria-stabilized zirconia (YSZ), thickness 100 µm	plasma spray coating	– Increase in brake thermal efficiency: +1.14% to +8.84% (at 50% load) – Decrease in fuel consumption: up to –28.59% (at 25% load) – Reduction in HC emissions: –35.27% – Reduction in CO: –2.7% – Increase in CO_2: +5.27%
[56]	General solutions for TBC coatings in spark ignition and compression ignition internal combustion engines	Surface coatings of ZrO_2–Y_2O_3 (approx. 7% Y_2O_3) + MCrAlY layers (CoNiCrAlY)	Gł. HVOF, EB-PVD, APS, SIFCO (vapor phase)	– New surface coating compositions (with additions of rare earth metal oxides) – Bilayer intermediate coatings – Superior repeatability of the SIFCO and HVOF methods – Necessity for precise thickness control in APS
[34]	Spark ignition engine (SI), single-cylinder Briggs & Stratton 10 HP	NiCrAl layer (100 µm) + ZrO_2–8%Y_2O_3 (200 µm)	APS (Atmospheric Plasma Spraying)	– Increase in maximum cylinder pressure (by 2–8 bar) – Higher thermal efficiency: up to +6% (gasoline), +7.4% (GNB10) – Reduction in SFC (specific fuel consumption) – Lower CO and HC emissions, increase in NO_x (due to higher combustion temperatures)
[27]	Compression ignition engine	ZrO_2–Y_2O_3 (100 µm on the piston and cylinder head, 500 µm on the cylinder liner)	APS (Atmospheric Plasma Spraying)	– Reduction in fuel consumption: +6% at 2600 rpm (full load) and +3.5% at 1600 rpm – Retardation of the injection timing along with high injection pressure and velocity – Higher rate of heat release compared to an engine without a coating
[38]	Compression ignition engine, coating on the combustion chamber and the bottom of the piston	Partially yttria-stabilized zirconia (250 µm)	–	At 75% rated load: – Increase in operating temperature from 350–400°C to 850–900°C – Increase in thermal efficiency (shift of combustion toward the diffusion phase) – Mitigations: CO emissions (–) 18.82%, HC (–) 36.3%, and smoke (–) 6.14%

In work [6, 39] the thermal diffusivity of modified materials is stable to a certain range of temperature. This parameter worsens with the increasing damage to the graphite coatings used in research. The use of platinum-based coatings caused more accurate test results. The thermal capacity (CP) of these materials was studied to 1400°C. In these studies, high stability for most samples was shown, except for $Eu_2Zr_2O_7$, where significant surface defects occurred. The lower value of the young module ($La_2Zr_2O_7$) partly equalizes defects in the form of thermal differences. In this way, the stress decreases, which causes less damage to the coating during engine operation.

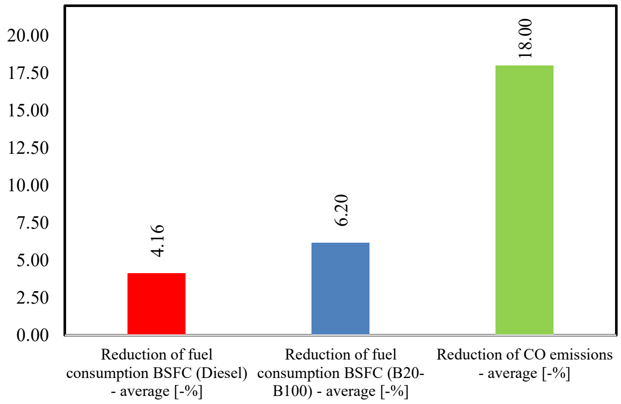

Fig. 2. The impact of $La_2Zr_2O_7$ ceramic coatings on reducing fuel consumption and CO emissions in internal combustion engines. The chart was created based on studies [6, 28, 39]

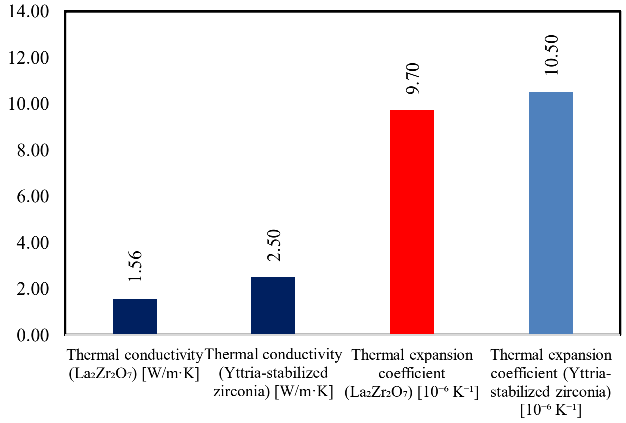

Fig. 3. The impact of $La_2Zr_2O_7$ ceramic coatings on thermal conductivity and thermal expansion coefficient in internal combustion engines. Chart created based on studies [6, 28, 39]

Similarly, the modifications described in [42] confirm the beneficial impact of coatings serving as thermal barriers on the operation of a spark ignition (SI) engine. After removing the appropriate thickness of the combustion chamber material to maintain the compression ratio, a bonding layer of NiCrAl (160 μm) and a layer of $MgZrO_3$ (320 μm) were applied to the piston, cylinder head, and valves, with the simultaneous use of an inert gas (argon) [42]. The application of TBC – with NiCrAl, $CaZrO_3$, and $MgZrO_3$ coatings on the piston, cylinder head, and valves – contributed to a change in the engine's operating parameters. In the standard engine (SE), an increase in energy efficiency of 9.93% was observed (from 81.3% at 0% Ar to 91.23% at 15% Ar), resulting from a higher mixture density and increased air mass flow [42]. However, in the TBC engine (TBCE), a decrease in efficiency of 3.89% (at 9% Ar) was noted compared to the SE, which was due to an increase in the combustion chamber wall temperature. The use of TBC also influenced fuel consumption (BSFC). In the SE, a reduction in BSFC of 17 g/kWh was measured with an increase in argon concentration from 0% to 15%, while in the TBCE, the reduction amounted to 18.2 g/kWh [42]. In the engine with TBC, the lower fuel consumption was a result of the higher combustion chamber wall temperatures, which enhanced the engine's load-bearing capacity. The maximum difference in BSFC between the TBCE and SE was 3 g/kWh in favor of the TBCE [42]. Exhaust gas temperatures decreased in both cases with increasing argon concentration. In the SE, the exhaust gas temperature dropped from 725°C (at 0% Ar) to 661°C (at 15% Ar), a decrease of 34°C [42]. In the TBCE, the exhaust gas temperature was 21°C higher compared to the SE, due to the adiabatic effect of the ceramic coatings. Regarding emissions, it was observed that introducing argon into the air mixture resulted in a 55% reduction in NO_x emissions in both the SE and TBCE compared to standard operating conditions without argon. However, NO_x emissions in the TBCE were higher than in the SE due to the higher exhaust gas temperatures and a faster combustion process. CO emissions increased with rising argon concentrations, reaching 91.2 g/kgf (at 15% Ar) in the SE, which was due to the limited availability of oxygen in the combustion process [42]. In the TBCE, CO emissions were lower because of the conversion of CO to CO_2 at higher exhaust gas temperatures. CO_2 emissions increased at lower argon concentrations (3–6%) due to greater oxygen availability, but decreased at higher argon concentrations [42]. With increasing engine speed (from 2100 rpm to 3300 rpm), an increase in exhaust gas temperature was observed in both cases; however, in the TBCE, it was on average 25°C (at 0% Ar) and 28°C (at 15% Ar) higher compared to the SE [42].

In the study [43], a CI engine with an LHR coating and one without was compared, powered by CSOME, NKOME, and diesel. The coating was applied using thermal plasma spraying, with several metal-ceramic layers on a Ni-Cr substrate. The thermal efficiency for CSOME and NKOME in the LHR engine was lower than that for diesel, and fuel consumption increased at full load. In the engine fueled by CSOME and NKOME, higher exhaust gas temperatures were recorded, along with increased emissions of unburned HC and CO. NO_x levels were also higher compared to diesel, as was smoke. The maximum cylinder pressure at partial load was highest for diesel, with a slightly lower rate of pressure increase observed for the methyl esters [43]. Thermal barrier coatings reduce heat losses, increase combustion temperatures, and improve fuel efficiency, while advanced filtration systems provide cleaner intake air, which reduces wear and stabilizes combustion conditions; together, they contribute to improved engine performance, lower emissions, and increased durability of components [27]. The use of thermal insulation in the combustion chamber raised the combustion temperature by approximately 300–350°C compared to a conventional diesel engine, which unfortunately led to higher NO_x emissions [6].

In study [52] and its co-authors, heat flow was analyzed at crank angles of 320°, 360°, and 410° for four models: the base model (without coatings), a model with a coating on the piston, one with a coating on the cylinder head and liner, and one with coatings on the piston, cylinder head, and liner simultaneously. It was demonstrated that ceramic materials (e.g., zirconia, silicon nitride) with low thermal conductivity reduce heat loss to the coolant and increase thermal efficiency. When the cylinder head and liner were insulated, heat conduction was significantly reduced, and energy transfer to the coolant was minimal. It was determined that isolating only the piston is less effective than full insulation of the piston, cylinder head, and liner. In contrast, study [58] conducted numerical investigations of an HCCI engine with catalytic combustion by coating the piston with platinum. This accelerated the ignition timing, slightly increased the maximum cylinder pressure and temperature, reduced CO and HC emissions by 9% and 4%, respectively, but increased NO_x by 5%. The indicated mean effective pressure increased by 5% and combustion efficiency by 7%. Additionally, the combustion duration was prolonged by 9%, without affecting the later phase of the process.

3.3.3. Coatings with additions of platinum and precious metals

Studies [17] showed that coating the piston of a diesel engine powered by diesel fuel with a platinum layer reduces soot emissions by 40%. However, within 8 hours of operation, the coating wore out due to poor adhesion and the formation of iron oxide deposits on the piston. In [49], a combustion engine burning methanol in a prechamber with an incandescent glow plug and a platinum mesh was described – this engine achieved low fuel consumption at light loads and lower HC emissions. Studies [24] and [25] demonstrated that coating the piston of a spark ignition (SI) engine with a Pt-Rh coating reduced unburned HC by 20%. In [27], an increase in thermal efficiency of 5–6% was achieved by using an engine with a thin thermal barrier coating. The authors of [5] reported fuel savings of 16–37%, while [54] showed an efficiency improvement of 14% under fully adiabatic conditions and 7% under partially adiabatic conditions. In [21], an improvement of 5–9% in specific fuel consumption was observed in the insulated engine compared to the standard engine. The influence of the combination of thermal conductivity and coating thickness on fuel consumption was also investigated [21]. The best results were obtained with a coating thickness of approximately 100 μm (yielding greater fuel savings), whereas thicknesses above 300 μm resulted in losses. However, thermal insulation of the engine can increase the combustion temperature by 300–350 °C compared to a conventional engine [57], which leads to a significant increase in NO_x emissions. Moreover, catalytic coatings may induce the phenomenon known as catalytic flame quenching, which negatively affects HC emissions [27].

3.3.4. Characteristics of damage and the life of coatings

Protective coatings (TBC) based on $ZrO_2–Y_2O_3$, applied using the APS plasma spray method, are characterized by good resistance to thermal fatigue [26]. Erosion tests complement thermal load tests, enabling additional assessment of top-layer damage caused by thermal fatigue. The greatest stress changes occur at the substrate/bond coat interface and the bond coat/top coat interface. Flame tests have been developed to simulate engine start-stop cycles, while furnace tests can be used to control the quality of the coating manufacturing process [23]. This represents an interesting alternative to bench tests using a piston internal combustion engine.

Table 2. Summary of the results of research on the use of TBC coatings in internal combustion engines

No.	TBC coating (material/ thickness)	Results (relative to the standard variant)	Key conclusions
[51]	$La_2Zr_2O_7$ (350 μm) Total TBC thickness: 500 μm	- BSFC: decrease by 4.16% (ON), 2.9% (B20), 9.5% (B100) - BTE: increase by 4% (ON), 8.55% (B20), 10.7% (B100) - CO: decrease by 18% (ON), 27.7% (B20), 43.75% (B100) - HC: decrease by 11.68% (ON), 40.98% (B20), 62.26% (B100) - NO_x: increase by 3.5% (ON), 12% (B20), 15% (B100)	– Higher combustion temperature and favorable catalytic properties ($La_2Zr_2O_7$) contribute to the reduction of CO, HC, and soot – Lower thermal conductivity (1.56 W/m·K) enables reduced heat losses – The increase in NO_x is due to the higher temperature in the chamber
[6], [28], [39]	($La_2Zr_2O_7$) and other pyrochlore TBC ($Eu_2Zr_2O_7$, $Gd_2Zr_2O_7$) with varied structural stability.	- Thermal conductivity ($La_2Zr_2O_7$): 1.56 W/m·K - Pyrochlore structural stability: up to 2300 °C (or up to 2573 K) - Thermal expansion coefficient: 9.7×10^{-6} K^{-1} ($La_2Zr_2O_7$) vs. 10.5×10^{-6} K^{-1} (YSZ) - Heat capacity (Cp) stable up to 1400°C (exception: $Eu_2Zr_2O_7$) - Lower Young's modulus reduces stresses	– Low thermal conductivity and pyrochlore stability promote thermal insulation – Matching the thermal expansion coefficient with the substrate is key – A lower Young's modulus minimizes the risk of coating cracking
[43]	(320 μm) + bonding layer (e.g., NiCrAl, $CaZrO_3$)	- Volumetric efficiency: decrease of approximately 3.89% in the TBC engine (TBCE) at 9% Ar (compared to the standard engine, SE) - BSFC: reduction of 18.2 g/kWh in TBCE with Ar increased to 15% (in SE: 17 g/kWh) - Exhaust gas temperature: in TBCE, on average 21°C higher (adiabatic effect) - NO_x emissions in TBCE are higher than in SE, but NO_x decreases with the addition of Ar	– High combustion chamber wall temperature in the TBCE reduces fuel consumption – The addition of Ar to the mixture decreases NO_x (due to less oxygen and exhaust gas cooling) but increases CO emissions – Higher exhaust gas temperature in the TBCE promotes the conversion of CO to CO_2, thereby reducing CO emissions compared to the SE

3.3.5. Issues of heat exchange in ceramic coatings

Article [36] presents the results of heat transfer studies through surfaces covered with a thin ceramic coating. The theoretical analysis showed that the ceramic coating reduces the heat flux density at a constant heat transfer coefficient. The experiments were conducted on three types of thin thermal insulation coatings: zirconium oxide (ZrO_2) partially stabilized with either yttria (Y_2O_3) or lanthana (Ln_2O_3), which were plasma-sprayed onto an aluminum alloy. The heat flux density, heat transfer coefficient, and thermal resistance of the coating were determined. It was demonstrated that heat transfer in such systems is strongly influenced by the coating's porosity, roughness, and emissivity, and that knowledge of only the coating thickness and thermal conductivity is insufficient for accurate calculations. In such cases, heat transfer must be investigated experimentally, particularly in piston internal combustion engines.

3.3.6. Popular oxides in protective coatings

Aluminum oxide (Al_2O_3) is one of the most commonly used ceramic materials in the protective coatings industry. Its high hardness, chemical inertness, wear resistance, and a melting temperature of 2072°C make it a good choice for applications in the harsh operating conditions of piston internal combustion engines. The maximum operating temperature of this material is 1650°C, which further enhances its versatility. It can be combined with TiO_2 to improve fracture toughness, although this decreases its hardness [22, 48].

In other studies, the use of Cr_2O_3 coatings is suggested. This material is characterized by high hardness, wear resistance, and chemical inertness, with a maximum operating temperature of 540°C. Its properties can be further enhanced by adding SiO_2 and TiO_2 [8, 48]. Cr_2O_3 is applied on the inner surfaces of air and gas cylinders, mechanical seals, and components in textile machinery.

Another material is LSM – $(La_{00.8}Sr_{0.2})$ $0.98MnO_3$, an advanced ceramic material used in solid oxide fuel cells (SOFC) based on YSZ electrolyte. Thanks to its thermal expansion coefficient, which is close to that of doped zirconia, and a maximum operating temperature of 1500°C, this material is indispensable for limiting the evaporation of chromite components in SOFCs, as well as for catalysts and sensors [48]. Its application in internal combustion engines is possible, but it is limited to selected components exposed to high thermal loads.

In work [48], the use of titanium oxide (TiO_2) is also suggested. Naturally occurring titanium oxide is characterized by low roughness and a dense coating structure. Its conductive properties enable its application as a conductive coating, for example, in architectural and automotive glass. With appropriate spraying parameters, both hard, dense coatings and more porous, thick layers can be achieved while avoiding cracking and delamination. The addition of Cr_2O_3 increases hardness as well as wear and corrosion resistance. TiO_2 coatings are used, among other applications, in cutting tools for CNC machines.

4. Multi-layer systems of coatings are used for combustion chambers

In thick TBC layers, a low thermal expansion coefficient (TEC) at the hot surface is essential to reduce thermal stresses and resistance to thermal shocks. However, a large TEC mismatch between the metal substrate and the coating hinders adhesion. Multilayer systems can help reconcile these opposing demands. A group of chemically compatible materials with varied TEC values and suitable thermal conductivity has been identified. Current research focuses on analyzing temperature and stress distributions within the coating to evaluate stress levels during deposition and under operational conditions. The aim is to optimize layer thicknesses to minimize operational stresses.

4.1. Multi-layered TBC coatings – concepts and materials

In the following works, the results and design ideas of multilayer TBC coatings are presented, along with the role of various materials (including intermetallic, ceramic, and metallic layers) and the need to take into account conflicting mechanical and thermal requirements.

In work [8], the use of a layered TBC MMC structure contributes to improved thermal barrier properties. Nonetheless, the high thermal conductivity of the aluminum layers limits the effectiveness of the intermetallic Fe-Al layers that form during the reactive sintering of the multilayer structure. To reduce the thermal conductivity of the aluminum layers, their reinforcement with ceramic phases of low thermal conductivity, such as YSZ (yttria-stabilized zirconia), is proposed. Such a design, consisting of intermetallic layers and Al-YSZ layers, enables the achievement of high mechanical strength and mitigates the negative impact of aluminum on the overall thermal barrier properties. Thus, the concept of a three-phase multilayer structure is justified. Enhancing the crack resistance of thermal coatings, especially under conditions of intense mechanical and thermal loading, is crucial for their durability.

In work [31], LPCS (Low-Pressure Cold Spraying) technology combined with thermal treatment enables the production of multilayer TBC coatings with excellent thermal and mechanical properties. These coatings are partly based on the addition of yttria-stabilized zirconia, aluminum, and stainless steel, combining the superior thermal insulation properties of ceramic materials with the high resistance of metals to thermal shocks. The composition of the multilayer ceramic-metal composite deposited by the LPCS method can be modified by incorporating catalytically active layers. This helps reduce the emission of harmful substances into the environment and improves the thermal efficiency of engines. Studies have shown that multilayer TBC coatings of the (Al-ZrO_2)-SHS 717 type, consisting of layers 40–50 μm thick, provide adequate insulating properties both during the spraying process and after sintering [31]. The sintering process of the Al-SHS 717 composite leads to interphase reactions and the formation of intermetallics, which results in reducing the effective thermal conductivity to about 6.0 W/mK, comparable to that of yttria-stabilized zirconia (YSZ) [31]. Depositing mixtures of Al-ZrO_2 powders causes ZrO_2 particles to fracture upon impact with the substrate, leading to the formation of a homogeneous structure with ZrO_2 particles sized 3–10 µm [31]. These coatings provide a temperature difference of about 55°C between the top surface and the substrate at a test temperature of approximately 530°C [31]. The developed TBCs demonstrate the ability to reduce thermal fatigue of component surfaces [31].

At work [3], a multi-layered coating was used to increase the strength of HFB_2 ceramic materials. Such an addition is widely used in single-layer coatings. This solution concerns the strengthening of the coating structure to avoid additional cracks. However, more advanced systems consisting of several coatings require more difficult technological procedures. Combining various ingredients, such as metals, ceramics, and intermetallic particles, allows you to obtain a coating that fulfills various functions in internal combustion engines. TBC coatings are very complex multi-material systems. These coatings must meet thermal and functional requirements. They should also achieve high hardness and bending resistance. Their appropriate design and selection of materials increase the thermal efficiency of the engine, reduce fuel consumption, and contribute to reducing the emission of harmful fumes.

Experimental studies on mechanical behavior are essential for understanding failure mechanisms. The strength of multilayer three-phase composites depends on both individual layer properties and the interactions between them. A key obstacle is the limited availability of detailed data on such structures. Current research focuses on two main strategies: metal-matrix composites and multilayer systems with enhanced barrier performance and crack resistance.

4.2. Catalytic layers in TBC and impact on the emission of toxic substances

The standard thermal-barrier coatings (TBC) with a thickness of about 300 µm presented in [11] are insufficient to achieve a significant improvement in energy efficiency and to reduce harmful exhaust emissions. In this case, selected parameters of these coatings must be enhanced. For example, in [50], the TBC material applied to the surfaces of selected engine components caused a 12% increase in exhaust-gas temperature. That study also reported a 28% decrease in CO and a 21% increase in NO_x emissions. Introducing catalytic layers into these coatings can help reduce NO_x emissions. In oxygen-deficient zones, such as a piston crown coated with a catalytic layer, the NO_x-reduction process can be supported. This process can be promoted by catalysts such as Cu-Zn/Ni-Zeolite [37], $MoSi_2/Mo_2C$, or Cr_2O_3 [4].

The temperatures prevailing in the engine working space during combustion are higher than in the exhaust gases, which increases catalyst activity. Nevertheless, the development of TBC with catalytic layers is not widely described in the literature.

4.3. Methods of manufacturing and the properties of multi-layer TBC coatings

Standard deposition methods, such as APS, HVOF, LPPS, or plasma techniques, enable precise control of coating parameters [14]. In the case of intermetallic coatings, for example, MCrAlY, controlling the thermodynamic and kinetic processes is crucial [18].

In [53], the research focused on multilayer thermal-barrier coatings (TBC) produced by APS in order to increase the durability of the coating system and improve its performance characteristics. The material used was 8% yttria-stabilized zirconia in powder form. These particles exhibited two distinct morphologies: hollow spherical particles (HOSP) and fused-and-crushed particles (FC). The powder particle diameters ranged from D10 = 6 µm to D90 = 105 µm for HOSP and to 77 µm for FC [53]. The coatings were deposited on the nickel-based superalloy Rene 80 with a NiCoCrAlY bond coat and on aluminum for mechanical and thermal measurements. Single-layer coatings (C1–C6) with thicknesses of approximately 400 µm displayed varying densities and porosities [53]. Denser coatings, such as C4, achieved a fracture toughness of K_IC = 2.24 MPa√m and an elastic modulus E = 35.2 GPa, whereas more porous coatings, for example, C1, exhibited K_IC = 1.84 MPa√m and E = 22.4 GPa [53]. Furnace cyclic tests (FCT) at 1100°C demonstrated that the single-layer coatings could endure between 600 and 800 cycles [53]. The two-layer coatings (B1–B7) with a total thickness of 300 µm were designed so that the inner layer (30–90 µm) was dense and robust, while the outer layer was porous to promote low thermal conductivity [53]. Coatings B6 and B7 showed durability beyond 1200 cycles – more than twice that of the single-layer coatings. In particular, coating B6, with an inner layer thickness of 60 µm, achieved the best compromise between durability and low thermal conductivity [53].

In studies [19] concerning 38MnSiVS5 steel, NiCoCrAlY coatings (applied via APS/HVAF) were used as the bonding layer, together with YSZ/GZO ceramics (via SPS). Additional sealing layers – both metallic and ceramic – improved tightness but reduced mechanical durability. SPS-GZO exhibited the best thermal insulation properties (thermal conductivity 0.7–0.8 W/m·K, porosity 10–15%), while APS offered high insulation efficiency but lower resistance to thermal cycling [19]. In thermal fatigue tests, SPS-GZO with ceramic sealing endured 4000 cycles, and without sealing, 6000 cycles, whereas coatings with metallic sealing suffered damage after only a few hundred cycles. These results indicate the need for a compromise between thermal insulation, durability, and resistance to thermal cycles. In studies [32], single-layer YSZ was compared with two- and three-layer GZ/YSZ coatings (applied by SPS) on Hastelloy-X and IN-738 alloys. The multilayer TBCs demonstrated lower thermal conductivity across the entire temperature range of 25–1190°C and higher durability at 1300°C (395 cycles for GZ/YSZ, 521 cycles for GZ_dense/GZ/YSZ), while single-layer YSZ survived only 43 cycles. The lower fracture toughness of GZ (1.02 ±0.11 $MPa \cdot m^{0.5}$) promoted crack formation at the GZ/YSZ interface, and the sintering of GZ led to pore closure [32]. The tetragonal phase of YSZ remained stable up to 1200°C, while the cubic phase of GZ (with a fluorite defect) was stable above 1400°C [32]. Thus, multilayer GZ/YSZ coatings offer higher durability and lower thermal conductivity under extreme conditions [32].

In work [55], residual stresses in a two-layer $La_2Zr_2O_7$/8YSZ (DCL TBC) coating applied by APS were analyzed. The coating system comprised a NiCoCrAlY bond coat (100 μm), 8YSZ (240 μm), and an LZ layer (60 μm). A finite element "birth and death element" method was used to simulate the spraying and cooling processes. The results indicated lower residual stresses in the DCL compared to a single-layer 8YSZ. The highest radial stresses were observed on the surface of the LZ, while axial and shear stresses concentrated at the interfaces' edges. Computational micro-mechanics analyses revealed that pores and microcracks locally increased the stresses but reduced them across the entire LZ layer. Overall, DCL LZ/8YSZ exhibits better resistance to residual stresses and a lower risk of cracking compared to 8YSZ, making it a promising material for high-temperature protective coatings.

Table 3. Summary of research on spraying techniques and coatings

No.	Spraying technique and coating configuration	Material	Thermal properties, cyclical durability and key conclusions
[14, 18]	Overview of techniques: APS, HVOF, LPPS, HVAF, CS. Process parameter control (gas flow, temperature, spraying speed) is crucial for the quality of the coatings. In the case of intermetallic coatings (MCrAlY), precise control of thermodynamic and kinetic phenomena is essential	Mainly MCrAlY materials (NiCoCrAlY, CoNiCrAlY), yttria-stabilized zirconia (YSZ), various single- and multilayer configurations	Standard spraying methods allow for the production of coatings with a strictly controlled microstructure. The proper selection of parameters determines the mechanical and thermal properties, as well as the durability of the coatings under high-temperature conditions
[53]	Atmospheric plasma spraying (APS). Single- and double-layer TBCs deposited on nickel-based superalloys (Rene 80) with a NiCoCrAlY bond coat. Additionally, tests were performed on an aluminum substrate (for measuring mechanical and thermal properties)	YSZ (8% Y_2O_3) in the form of powders with different morphologies: Hollow Sphere (HOSP) and Fused & Crushed (FC). Layer thicknesses: approximately 400 μm (single-layer) and 300 μm (two-layer)	Single-layer: durability of 600–800 cycles in the FCT test (1100°C). Two-layer: durability exceeding 1200 cycles (B6, B7). Coating B6 (with an inner layer of 60 μm) demonstrated the best compromise between durability and low thermal conductivity. Multilayer TBC significantly increases the number of cycles while maintaining favorable insulation properties

5. Impact of the use of multi-layer coatings on the reduction of structural defects and engine energy efficiency

Multilayer barrier coatings applied to thermally stressed components of piston engine combustion chambers offer an effective method for reducing structural defects such as cracks, erosion, and corrosion, while improving overall engine efficiency. These systems use ceramic, metallic, or hybrid layers arranged in two- or multilayer configurations, with each layer fulfilling a specific, engineered function. The following sections outline the general effectiveness and limitations of TBC coatings, along with proposals for their further development. The most common benefit of multilayer coatings is their ability to reduce heat transfer to the cooling system, thereby improving the utilization of energy from fuel combustion. Higher temperatures prevailing in the combustion chamber of reciprocating internal combustion engines lead to improved thermal efficiency. Unfortunately, this requires controlling changes in NO_x emissions. Proper material selection and layer design – using components such as YSZ, $La_2Zr_2O_7$, GZO, or MCrAlY – can significantly minimize the formation of material defects, e.g., microcracks. Two-layer or three-layer thermal-barrier coating systems allow for:

- Protection against erosion and corrosion
- Facilitation of thermal-expansion matching by means of an appropriate interlayer
- Good thermal-barrier performance while maintaining high mechanical strength (by employing differentiated surface roughness for the various layers within the system).

Such coating solutions protect not only the piston-crown structure or cylinder-head components but also improve their durability and reduce engine operating costs.

Summary

- Studies of multilayer coatings deposited on the combustion-chamber surfaces of reciprocating internal combustion engines have demonstrated their key importance in increasing thermal and mechanical efficiency, as well as in reducing emissions. The thermal barrier provided by appropriately selected coatings reduces heat losses to the cooling system. This, in turn, increases durability and resistance to erosion and corrosion under the high-temperature and medium mean-effective-pressure conditions prevailing in the combustion chamber.
- Multilayer coatings (two or three layered, etc.) effectively reduce the risk of microcracks and show high resistance to corrosion and erosion in critical working conditions of the engine. Reducing structural defects by multi-layer coatings allow you to improve thermal properties and reduce operating costs.
- TBC coatings reduce heat loss, enabling higher fuel-air mixture combustion temperatures. The cited studies showed that it is possible to reduce fuel consumption by over 10%using these systems. Higher temperatures and catalytic properties (e.g. $La_2Zr_2O_7$) reduce CO, HC and soot emissions, although they often lead to increased NO_x emissions. This is due to the higher combustion temperature, especially for a poor fuel-air mixture.
- Ceramic layers are made of materials such as YSZ, $La_2Zr_2O_7$, $Gd_2Zr_2O_7$, $MgZrO_3$, Al_2O_3, Cr_2O_3 and Multiphase Composites. More important parameters. These coatings include thermal and mechanical properties (thermal conductivity, thermal capacity, resistance to cracking, and matching thermal expansion coefficients to the ground). The intermediate layers used (e.g., McRaly) and double-layer structures help reduce residual stress. This increases the durability of coatings, especially in terms of dynamic temperature changes in the combustion process.

- The use of thicker coatings (above 0.5 mm) can cause problems with lubrication and increase the risk of premature ignition (in engines with spark plugs). Incorrect surface roughness and large differences in thermal expansion can lead to cracking of these coatings and even their detachment. In this case, higher combustion temperatures can increase the emissions of nitrogen oxides. In this case, you can modify fuel injection parameters or add appropriate catalytic layers to the multilayer coatings system (e.g. PT, RH).
- Multilayer thermal-barrier coatings (TBCs) offer an effective means of increasing the power and torque of reciprocating internal combustion engines while maintaining their durability. These coatings increase the longevity of combustion-chamber components and enhance energy efficiency. Major challenges remain the elevated NO_x emissions and the need to ensure stable mechanical properties. Multilayer thermal-barrier coating solutions represent the next step in advancing modern engine design, especially today, when high durability, excellent performance, and low exhaust emissions are paramount.

Nomenclature

APS	air plasma spraying
BSFC	brake-specific fuel consumption
CI/Diesel	compression-ignition engine
CO	carbon monoxide
CSOME	cotton seed oil methyl ester
DCL TBC	double ceramic layer TBC
EB-PVD	electron beam physical vapor deposition
FCT	furnace cycle test
HC	hydrocarbons
$La_2Zr_2O_7$	lanthanum zirconate (pyrochlore phase)
LHR	low heat rejection engine
LZ	$La_2Zr_2O_7$ (cyrkonian lantu)
MES	the method of finite elements
$MgZrO_3$	magnesium zirconate
MMC	metal matrix composite
NKOME	neem kernel oil methyl ester
NO_x	nitrogen oxides
SI	spark-ignition engine
TBC	thermal barrier coating
YSZ	yttria stabilized zirconia
ZrO_2	zirconium oxide

Bibliography

[1] Advanced polymer coatings. High performance protective coatings for industry. http://www.adv-polymer.com/index.asp

[2] Assanis DN, Heywood JB. Development and use of a computer simulation of the turbocompound diesel system for engine performance and component heat transfer studies. SAE Technical Paper 860329. 1986. https://doi.org/10.4271/860329

[3] Bai Y, Zhang B, Du H, Cheng L, Huiling D. Efficient multiscale strategy for toughening HfB_2 ceramics: a heterogeneous ceramic–metal layered architecture. J Am Ceram Soc. 2020;104:1841-1851. https://doi.org/10.1111/jace.17610

[4] Bannikov MG, Draper PH, Chattha JA, Vasilev IP, Gavrilenko PN. Reduction in NO_x emission of diesel engines by in-cylinder catalysis. P I Mech Eng A-J Pow. 2003;217:101-106. https://doi.org/10.1243/095765003321148745

[5] Bruns L, Bryzik W, Kamo R. Performance assessment of U.S. army truck with adiabatic diesel engine. SAE Technical Paper 890142. 1989. https://doi.org/10.4271/890142

[6] Cao S, Tietz F, Basu D, Stover D, Vassen R. Zirconates as new materials for thermal barrier coatings. J Am Ceram Soc. 2000;83(8):2023-2028. https://doi.org/10.1111/j.1151-2916.2000.tb01506.x

[7] Carslaw H. S. Introduction to the Mathematical Theory of the Conduction of Heat in Solids. Macmillan & Co. London 1921:268.

[8] CeramTec. The Ceramic Experts. http://www.ceramtec.com/ceramic-materials/aluminum-oxide/

[9] Chan SH, Khor KA. The effect of thermal barrier coated piston crown on engine characteristics. J Materi Eng and Perform. 2000;9:103-109. https://doi.org/10.1361/105994900770346358

[10] Chan SH. Performance and emissions characteristics of a partially insulated gasoline engine. Int J Therm Sci. 2001; 40(3):255-261. https://doi.org/10.1016/S1290-0729(00)01215-1

[11] Chattarki AR, Basavakumar KG. Thermal barrier coating on IC engines; a review. In: Narasimham GSVL, Babu AV, Reddy SS, Dhanasekaran R. (eds). Recent trends in mechanical engineering. Lect N Mech Eng. Springer. Singapore 2021. https://doi.org/10.1007/978-981-15-7557-0_5

[12] Cho SH, Andersson HM, White SR, Sottos NR, Braun PV. Polydimethylsiloxane-based self-healing materials. Adv Mater. 2006;18(8):997-1000. https://doi.org/10.1002/adma.200501814

[13] Cho SH, White S, Braun P. Self-healing polymer coatings. Adv Mater. 2009;21(6):645-649. https://doi.org/10.1002/adma.200802008

[14] Darolia R. Thermal barrier coatings technology: critical review, progress update, remaining challenges and prospects. Int Mater Rev. 2013;58:315-348. https://doi.org/10.1179/1743280413Y.0000000019

[15] Dziubak T. Research into a two-stage filtration system of inlet air to the internal combustion engine of a motor vehicle. Energies. 2024;17:6295. https://doi.org/10.3390/en17246295

[16] Erickson LC, Hawthorne HM, Troczynski T. Correlations between microstructural parameters, micromechanical properties and wear resistance of plasma sprayed ceramic coatings. Wear. 2001;250(1-12):569-575. https://doi.org/10.1016/S0043-1648(01)00608-1

[17] Gaffney J, Sapienza R, Butcher T, Krishna C, Marlow W, Hare TO. Soot reduction in diesel engines: a chemical approach. Combust Sci Technol. 1980;24:89. https://doi.org/10.1080/00102208008952427

[18] Ghadami F, Aghdam ASR, Ghadami S. A comprehensive study on the microstructure evolution and oxidation resistance of conventional and nanocrystalline MCrAlY coatings. Sci Rep. 2021;11:875. https://doi.org/10.1038/s41598-020-79323-w

[19] Goes WU, Markocsan N, Gupta M, Vaßen R, Matsushita T, Illkova K. Thermal barrier coatings with novel architectures

for diesel engine applications. Surf Coat Tech. 2020;396: 125950. https://doi.org/10.1016/j.surfcoat.2020.125950.

[20] Haubold T, Wigren J, Gualco C. Comparison of thermal cycling experiments on thick thermal barrier coatings. Proceedings of the 15th International Thermal Spray Conference, 25-29 May 1998, Nice, France.

[21] Havstad PH, Gervin IJ, Wade WR. A ceramic insert uncooled diesel engine. SAE Technical Paper 860447. 1986. https://doi.org/10.4271/860447

[22] Hegazy N, Shoeib M, Abdel-Samea S, Abdel-Kader H. Effect of plasma sprayed alumina coating on corrosion resistance. Aerospace Sciences & Aviation Technology, ASAT-13. 2009;13:1-10. https://doi.org/10.21608/asat.2009.23859

[23] Hejwowski T. Comparative study of thermal barrier coatings for internal combustion engine. Vacuum. 2010;85(5):610-616. https://doi.org/10.1016/j.vacuum.2010.08.020

[24] Hu Z, Ladommatos N. In-cylinder catalysts – a novel approach to reduce hydrocarbon emissions from spark-ignition engines. SAE Technical Paper 952419. 1995. https://doi.org/10.4271/952419

[25] Hu Z. A mathematical model for in-cylinder catalytic oxidation of hydrocarbons in spark-ignition engines. SAE Technical Paper 961196, 1996. https://doi.org/10.4271/961196

[26] Hultqvist A, Christiensen M, Johansson B. The application of ceramic and catalytic coatings to reduce the unburned hydrocarbon emissions from a homogeneous charge compression ignition engine. SAE Technical Paper 2000-01-1833. 2000. https://doi.org/10.4271/2000-01-1833

[27] Kamo R, Mavinahally NS, Kamo L, Bryzik W, Schwartz EE. Injection characteristics that improve performance of ceramic coated diesel engines. SAE Technical Paper 1999-01-0972. 1999. https://doi.org/10.4271/1999-01-0972

[28] Kamo R. Adiabatic diesel-engine technology in future transportation. Energy. 1987;12(10/11):1073-1080. https://doi.org/10.1016/0360-5442(87)90063-6

[29] Kamo R. Assanis DN. Bryzik W. Thin thermal barrier coating for engines. SAE Technical Paper 890143. 1989. https://doi.org/10.4271/890143

[30] Klyus O. The using of preliminary biofuel treatment in diesel engines. Combustion Engines. 2015;162(3):639-643.

[31] Leshchinsky E, Sobiesiak A, Maev R. Intermetallic Al-, Fe-, Co- and Ni-based thermal barrier coatings prepared by cold spray for applications on low heat rejection diesel engines. J Therm Spray Tech. 2018;27:456-470. https://doi.org/10.1007/s11666-017-0681-z

[32] Mahade S, Curry N, Björklund S, Markocsan N, Nylén P, Vaßen R. Functional performance of $Gd_2Zr_2O_7$/YSZ multilayered thermal barrier coatings deposited by suspension plasma spray. Surf Coat Tech. 2017;318:208-216. https://doi.org/10.1016/j.surfcoat.2016.12.062

[33] Mendera KZ. Effectiveness of thermal barrier coatings for combustion chamber of reciprocating internal combustion engine. Częstochowa University Press. Czestochowa 1998 (in Polish).

[34] Mittal N, Athony RL, Bansal R, Kumar CR. Study of performance and emission characteristics of a partially coated LHR SI engine blended with n-butanol and gasoline. Alexandria Engineering Journal. 2013;52:285-293.

[35] Morel T, Keribar R, Blumberg PN, Fort EF. Examination of key issues in low heat rejection engines. SAE Technical Paper 860316. 1986. https://doi.org/10.4271/860316

[36] Mruk A, Jordan W, Taler J, Lopata S, Weglowski B. Heat transfer through ceramic barrier coatings used in internal combustion engines. SAE Technical Paper 941779. 1994. https://doi.org/10.4271/941779

[37] Nash CP, Dupuis DP, Kumar A, Farberow CA, To AT, Yang, C et al. Catalyst design to direct high-octane gasoline fuel properties for improved engine efficiency. Appl Catal B-Environ. 2021;301:120801. https://doi.org/10.1016/j.apcatb.2021.120801

[38] Palaniswamy E, Manoharan N. Ceramic coated combustion chamber for improving IC engine performance. International Journal on Design and Manufacturing Technologies. 2008; 2(1):22-25. https://doi.org/10.18000/ijodam.70023

[39] Pitzer D, Pracht G, Vassen R, Stover D. Thermal conductivity and thermal expansion coefficients of the lanthanum rare-earth-element zirconate system. J Am Ceram Soc. 2003; 86(8):1338-1344. https://doi.org/10.1111/j.1151-2916.2003.tb03473.x

[40] Richerson DW. Modern ceramic engineering, 2nd ed., Dekker New York 1992.

[41] Schihl P, Schwartz E, Bryzik W. Performance characteristics of a low heat rejection direct-injection military diesel engine retrofitted with thermal barrier coating. J Eng Gas Turb Power. 2001;123:644-651.

[42] Sharma TK. Performance and emission characteristics of the thermal barrier coated SI engine by adding argon inert gas to intake mixture. Journal of Advanced Research. 2015;6(6): 819-826. https://doi.org/10.1016/j.jare.2014.06.005

[43] Shrigiri BM, Hebbal OD, Reddy KH. Performance, emission and combustion characteristics of a semi-adiabatic diesel engine using cotton seed and neem kernel oil methyl esters. Alexandria Engineering Journal. 2016;55(1):699-706. https://doi.org/10.1016/j.aej.2015.12.023

[44] Shrirao PN, Pawar AN. Evaluation of performance and emission characteristics of turbocharged diesel engine with mullite as thermal barrier coating. International Journal of Engineering and Technology. 2011;3:256-262. http://www.enggjournals.com/ijet/docs/IJET11-03-03-44.pdf

[45] Sivakumar G, Senthil Kumar S. Investigation on effect of Yttria Stabilized Zirconia coated piston crown on performance and emission characteristics of a diesel engine. Alexandria Engineering Journal. 2014;53(4):787-794. https://doi.org/10.1016/j.aej.2014.08.003

[46] Slawinski Z, Sobczak J, Sarnowski C, Nykiel J. Exploitation characteristics of engines with composite coatings. Journal of Kones. 2001;231-241.

[47] Specific heats: the relation between temperature change and heat. http://web.mit.edu/16.unified/www/FALL/thermodynamics/notes/node18.html

[48] Thermal Spray Materials Guide. Technical Guide. Sulzer Metco. http://www.oerlikon.com/metco/en/products-services/coating-materials/coating-materials-thermal-spray/

[49] Thring RH. Platinum improves economy and reduces pollutants from a range of fuels. Catalysis Engine. 1980;24:126-133.

[50] Uchida N. A review of thermal barrier coatings for improvement in thermal efficiency of both gasoline and diesel reciprocating engines. Int J Engine Res. 2020;23(1):1-17. https://doi.org/10.1177/1468087420978016

[51] Vinay Kumar D, Ravi Kumar P, Santosha Kumari M. Prediction of performance and emissions of a biodiesel fueled lanthanum zirconate coated direct injection diesel engine using artificial neural networks. Procedia Engineer. 2013;64: 993-1002. https://doi.org/10.1016/j.proeng.2013.09.176

[52] Vinayagamoorthy R, Mothilal T, Madhavan S. Performance enhancement of a diesel engine by providing insulations on engine parts. International Journal on Design and Manufacturing Technologies. 2009;3(2):63-72. https://doi.org/10.18000/IJODAM.70064

[53] Viswanathan V, Dwivedi G, Sampath S. Engineered multilayer thermal barrier coatings for enhanced durability and

functional performance. J Am Ceram Soc. 2014;97(9):2770-2778. https://doi.org/10.1111/jace.13033

[54] Wallace FJ, Way RJB, Vollmert H. Effect of partial suppression of heat loss to the coolant on the high output diesel engine cycle. SAE Technical Paper 790823. 1979. https://doi.org/10.4271/790823

[55] Wang L, Wang Y, Sun XG, He JQ, Pan ZY, Wang CH. Finite element simulation of residual stress of double-ceramic-layer $La_2Zr_2O_7$/8YSZ thermal barrier coatings using birth and death element technique. Comp Mater Sci. 2012;53(1):117-127. https://doi.org/10.1016/j.commatsci.2011.09.028

[56] Wang Y, Sayre G. Commercial thermal barrier coatings with a double-layer bond coat on turbine vanes and the process repeatability. Surface and Coatings Technology. 2009;203(16):2186-2192. https://doi.org/10.1016/j.surfcoat.2009.02.007

[57] Wong R, Kamo R, Woods M. Coatings for improving engine performance. SAE Technical Paper 970204. 1997. https://doi.org/10.4271/970204

[58] Zeng W, Xie M, Jia M. Numerical investigation on the application of catalytic combustion to HCCI engines. Chem Eng J. 2007;127(1-3):81-93. https://doi.org/10.1016/j.cej.2006.10.018

Prof. Piotr Wróblewski, DSc., DEng. – Faculty of Engineering, University of Technology and Economics H. Chodkowska in Warsaw; Faculty of Mechatronics, Armament and Aerospace, Military University of Technology, Poland.

e-mail: *piotr.wroblewski@uth.edu.pl*

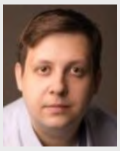

Przemysław Bratkowski, MSc. Eng. – Faculty of Engineering, University of Technology and Economics H. Chodkowska in Warsaw; Faculty of Mechatronics, Armament and Aerospace, Military University of Technology, Poland.

e-mail: *przemyslaw.bratkowski@uth.edu.pl*

Article citation info:
Szwajca F, Stępień Z, Pielecha I. The influence of alcohol-gasoline blends and deposit control additives on fuel injector contamination in SI DI engines. Combustion Engines. 2025;202(3):131-140. https://doi.org/10.19206/CE-207120

Filip SZWAJCA
Zbigniew STĘPIEŃ
Ireneusz PIELECHA

Combustion Engines
Polish Scientific Society of Combustion Engines

The influence of alcohol-gasoline blends and deposit control additives on fuel injector contamination in SI DI engines

ARTICLE INFO

Received: 9 May 2025
Revised: 11 June 2025
Accepted: 13 June 2025
Available online: 15 June 2025

The intense and multidirectional development of internal combustion engines, forced by tightening environmental regulations, has necessitated the verification and definition of new requirements for engine fuels. The article presents an experimental analysis of the ethanol or butanol admixture effect on the SI DI engine injectors contamination process based on engine and fundamental research. Injectors were evaluated after Keep-Clean only and Dirty-Up (Keep-Clean) tests, along with the Clean-Up test in accordance with CEC F-113-KC and CEC F-113-CU test procedures. The positive effect of the detergent additive on the ability to wash out injector deposits was demonstrated. A reduction of more than 80 percent in the duration of injection compared to the contaminated system was achieved. It was proven that the use of the detergent additive in the Clean-Up procedure makes it possible to return the injectors to full efficiency, which confirms the thesis of the leaching of injector nozzle deposits of SI DI engines.

Key words: *SI DI engine, fuel injector deposits, ethanol, butanol, DCA*

1. Introduction

Over the past three decades, internal combustion engines have undergone rapid, multidirectional development. This development has been driven by the systematic tightening of regulations to limit emissions of pollutants and greenhouse gases (GHG) and the associated need to increase engine efficiency [12]. As a result, modern combustion systems were introduced, high-pressure fuel injection systems became widespread in both CI and SI engines, and advanced exhaust aftertreatment systems were implemented. Consequently, novel requirements for fuels for contemporary internal combustion engines have been established. The utilization of biocomponents as fuel additives, particularly alcohol and biofuels, has emerged as a pivotal aspect in this context [3, 4]. The following is a list of the elements in question: As a result, new requirements for motor fuels were introduced. Some of these requirements (in terms of physicochemical properties) are contained in the European standards EN590 for diesel fuel and EN228 for motor gasoline. Much broader requirements, including performance characteristics with a breakdown by category of diesel fuel and motor gasoline, were included and subsequently revised and supplemented in subsequent editions of the Worldwide Fuel Charter, the latest edition of which was released on October 28, 2019 [5]. The testing and evaluation of fuel performance properties has become of particular importance to both fuel manufacturers, the additive packages used for them, and engine manufacturers who have begun to demand the introduction of standardized, generally recognized testing methodologies and criteria for evaluating fuel performance. In response to such demands, American procedures for testing specific fuel properties by engine methods were developed in the US under ASTM, and in Europe, similar procedures were developed by the Coordinating European Council for the Development of Performance Tests for Fuel, Lubricants and Other Fluids (CEC). Both U.S. and European procedures for testing motor fuels have been identified in the Worldwide Fuel Charter as required tests for specific properties for both various categories of diesel fuel and motor gasoline. In addition, the Worldwide Fuel Charter also includes the limiting requirements that evaluations of tested fuel properties should meet.

Fuel plays a central role in engine design and performance optimization. This role encompasses the selection process of construction materials, including lubricating oils. The limits of engine control parameters, which determine its efficiency and the optimization of exhaust emissions, performance, and utility-operating characteristics, are determined by the properties of the fuel. Consequently, the fuel should guarantee the technical functionality and adequate, unchanging performance characteristics of the vehicle. It is imperative to consider the maintenance of requisite emission standards throughout the engine's life cycle. This consideration must be in accordance with the stipulated regulations and the vehicle manufacturer's warranty period. Any change of fuels on the market must be adapted to the existing fleet of motor vehicles and the technical requirements arising from engine design. As early as the 1980s, it was found that the formation of harmful deposits in internal combustion engines had a major negative impact on the quantitative and qualitative course of combustion mixture formation, as well as the process of cargo preparation and its combustion in the engine combustion chambers. At the same time, it was noted that in the case of engines with CI, the most dangerous deposits are formed on components of the fuel injection system [16]. In SI engines with indirect gasoline injection, the most deleterious deposits are those that form in the engine's combustion chambers, on the intake valves, and on their stems. In SI engines with direct fuel injection, the deposits that pose the greatest threat to engine operation are those formed in high-pressure fuel injection injectors.

The global policy to reduce pollution from road transport requires the introduction of diversified powertrains, which in turn requires the development of entirely new or significantly modified technologies and design solutions already in use. In the automotive sector, the fundamental direction of these endeavors is to subordinate the development of motor vehicles and the fuels or other energy sources used for them to the overriding goal of reducing emissions of harmful components, including greenhouse gases, into the atmosphere. Given these expectations, alcohol emerges as a compelling alternative for commercial use as a fuel, either as a standalone fuel or in blends with gasoline or diesel. The utilization of alcohol fuels has the potential to play a significant role in reducing the emissions of harmful components from exhaust gases. However, it is imperative to possess a thorough comprehension of the properties inherent to these fuels and to utilize them in a manner that corresponds with the requirements of contemporary engine designs. Ethanol and butanol are alcohols that are regarded as the most promising biocomponents for current conventional fuels. It is imperative to acknowledge that the prevailing criterion for assessing the viability of fuel alternatives for vehicles in operation is their environmental sustainability, a characteristic that is exemplified by alcohol fuels. A substantial body of research has been dedicated to the study of blends of conventional fuels with various alcohols. Among other things, the fuel's effects on the performance, efficiency, and various performance parameters of SI engines powered by it with indirect injection [2, 8, 10, 20] and direct injection [10] have been evaluated. The present study aims to elucidate the effects of alcohol/gasoline blends on the propensity to form or leach preformed various injector deposits of SI DI engines and their impact on the quantitatively and qualitatively assessed fuel atomization process in the combustion chambers.

The results of this study contribute to a more complete understanding of the subject and provide a basis for further research in this area. The motivation for the authors to undertake research aimed at deepening and expanding the knowledge of the effect of alcohol-doped fuels (ethanol or butanol) in keeping the fuel injectors of SI DI engines clean was provided by this study. The study also addressed the effect of deposits produced in the injectors on fuel atomization quality processes. The novelty of the work lies in the hybrid combination of two different research methodologies for evaluating the fuel injection process. The first part of the study evaluated changes in fuel dose due to the formation of fuel injector deposits and was conducted using an engine-wide standardized test methodology. In the second part of the study, changes in fuel spray quality were evaluated based on studies of macroscopic indicators of fuel spray in a constant volume chamber using laser illumination. The engine test procedure was developed by CEC and bears the designation CEC F-113 and the name: VW EA111 DISI Injector Deposit Test. It is currently the only standardized and recognized procedure in Europe to reliably evaluate fuels in terms of their tendency to keep SI DI engine injectors clean and their ability to leach deposits after they have been previously produced [17].

Engine analyses do not provide a complete research diagnosis of injector quality, including fuel atomization. Complementary to such analyses are optical evaluations of fuel atomization. Their uniqueness lies in the optical registration of fuel atomization images, and on the basis of these images, a diagnostic evaluation of the atomization is possible. Depending on the complexity of these optical analyses, macroscopic and microscopic evaluation of the fuel spray is possible. Injector tips located in combustion chambers are directly exposed to extreme conditions during the combustion process, including high pressure, temperature, and chemical interaction of fuel components. These conditions result in the intensive formation of deposits, which significantly affect the injector performance and thus the quality of the fuel-air mixture formed [9, 14]. External deposits, forming mainly around the exhaust ports, come primarily from the fuel being burned and, to a lesser extent, from engine oil. They cause deformation of the fuel jet and its excessive elongation, washing out the walls of the combustion chamber and the bottom of the piston. This results in increased fuel consumption and emissions of pollutants, particularly hydrocarbons (HC) and particulate matter (PM). Internal deposits, on the other hand, formed in the flow channels of injectors due to thermal oxidation and polymerization of fuel components (e.g., in the form of lacquers and resins), come exclusively from the fuel itself. Their presence leads to a reduction in the cross-sectional area of the outlet channels, reducing fuel flow and worsening its atomization. As a result, the average diameter of fuel droplets increases, the homogenization of the mixture deteriorates (lower excess air ratio, λ), and the evaporation time increases. All these factors contribute to a decrease in engine efficiency, lower engine performance, and increased fuel consumption [15, 21].

2. Properties of ethanol and butanol relevant to engine applications

Applying alcohol as a fuel admixture provides several benefits, such as reducing greenhouse gas (GHG) emissions, decreasing toxic exhaust emissions, improving energy security, and enhancing many fuel performance properties, including resistance to knock combustion [6, 7]. Table 1 compares the selected properties of gasoline, n-butanol, and ethanol.

Table 1. Comparison of selected fuel properties [11]

Properties	Gasoline	n-butanol	Ethanol
Chemical formula	Blend	C_4H_9OH	C_2H_5O
RON (Research Octane Number)	95	94–96	110
Density [kg/m^3]	753	810	790
Molecular weight [g/mol]	114	74	46
Gravimetric lower heating value [MJ/kg]	42.9	33.3	26.8
Volumetric lower heating value [MJ/dm^3]	32.3	27.0	21.2
Enthalpy of vaporization [kJ/kg]	380–500	716	904
Mass fraction of carbon [%]	86	65	52
Mass fraction of hydrogen „H" [%]	14	13.5	13
Mass fraction of oxygen „O" [%]	0	21.5	35
Viscosity [mPa · s]	0.4–0.8	2.57	1.08
Boiling point [°C]	199	118	78
Stoichiometric air-to-fuel ratio	14.7	11.2	9.0

In blends with gasoline, butanol exhibits several significant advantages over ethanol. Butanol is much less hygroscopic, better mixable with gasoline, and has a higher specific calorific value, which translates into lower specific fuel consumption (butanol versus ethanol blends). When butanol is blended with gasoline, the vapor pressure of butanol is lower than that of ethanol, making it easier to meet the requirements of EN 228. The biggest disadvantages of butanol relative to ethanol in blends with gasoline are a lower octane number and lower heat of vaporization, as well as higher density and viscosity, which can contribute to a higher tendency than ethanol to form deposits. Like conventional motor gasoline, ethanol fuels are prone to form deposits on engine components, particularly in intake manifolds, injector tips, intake valves, and combustion chambers [13, 19].

3. Aim and scope of the research

The purpose of the study was to investigate the effect of ethanol or butanol admixture to gasoline on the fouling process of SI DI engine fuel injectors. In addition, the effectiveness of ethanol or butanol admixture with Deposit Control Additives (DCAs) on the ability to leach previously formed fuel injector deposits was evaluated. The scope of the study included two phases of research:

- Engine tests to evaluate the change in operating conditions of injectors as a result of deposit contamination and flushing capabilities using prepared gasoline blends with alcohol and with/without DCA. The main objective of the tests was to maintain a constant engine operating point regardless of the change in the level of injector fouling.
- Research on optical evaluation of fuel atomization geometric indicators. Conducted on a model test bench, leading to a macroscopic assessment of the injected fuel spray based on injectors from various phases of engine tests. Different fuels were not evaluated during static optical tests; instead, injectors from prior engine testing phases were used. The goal was to analyze the differences in injectors during tests using the same fuel.

4. Research methodology

4.1. Engine test procedure and bench equipment

The tests were conducted in accordance with European engine test procedures CEC F-113 and used two variations of the procedure, i.e., CEC F-113-KC "Keep-Clean" Test Procedure and CEC F-113-CU "Clean-Up" Test Procedure (VW EA111 BLG) [18]. The tests were performed with a VW EA111 BLG engine, the selected technical parameters of which are included in Table 2. The engine was equipped with wall-guided direct fuel injection and a combined supercharging system (mechanical supercharging + turbocharging). The injection system featured 6-hole solenoid controlled injectors.

In the "Keep-Clean" version of the CEC F-113-KC procedure, the time allocated for conducting the one-step test is 48 hours. Throughout the duration of the test, the engine functions under steady-state conditions, characterized by two fundamental parameters: constant speed (2000 rpm) and constant load (56 Nm). The primary objective of the test is to assess the propensity of the fuel to form injector deposits, thereby determining the efficacy of maintaining clean injectors.

In the CEC F-113-CU "Clean-Up" variant of the procedure, the test is divided into two stages. In the first stage, which lasts 48 h, a base fuel is applied, without DCA additives. In this stage, the "Dirty-Up" injector fouling process is carried out. In the second stage of the test, 24 h, refined fuel is used. That part of the test allows assessment of the cleaning properties of the "Clean-Up" fuel, and therefore the effectiveness of flushing out the deposits formed in the first stage.

Table 2. Technical data of VW EA111 BLG engine

Type	–	4-cyl., in-line (wall-guided mixture formation system)
Displacement	cm^3	1390
Cylinder bore.	mm	76.5
Piston stroke	mm	75.6
No. of valve/cyl.	–	4
Compression ratio	–	10:1
Max power	kW	125 kW at 6000 rpm
Max torque	Nm	220 Nm at 1750–4500 rpm
Aftertreatment systems	–	Three-way catalysts, closed feedback loop
Emission norm	–	Euro 4

The change in the width of the injector control impulse was used as a criterion for evaluating the intensity and magnitude of changes in deposits formed or flushed out. The injection time is extended as the amount of deposits accumulating outside and inside the injector gradually increases, or reduced as deposits are flushed out of the injectors. The tendency of a fuel to form injector deposits is a key criterion for distinguishing fuels in terms of their functional and operational characteristics.

The fuel tests were carried out on an engine test stand in accordance with the CEC F-113-KC "Keep-Clean" Test Procedure and the CEC F-113-CU "Clean-Up" Test Procedure (VW EA111 BLG) – 2022 edition. Figure 1 presents a general view of the test stand.

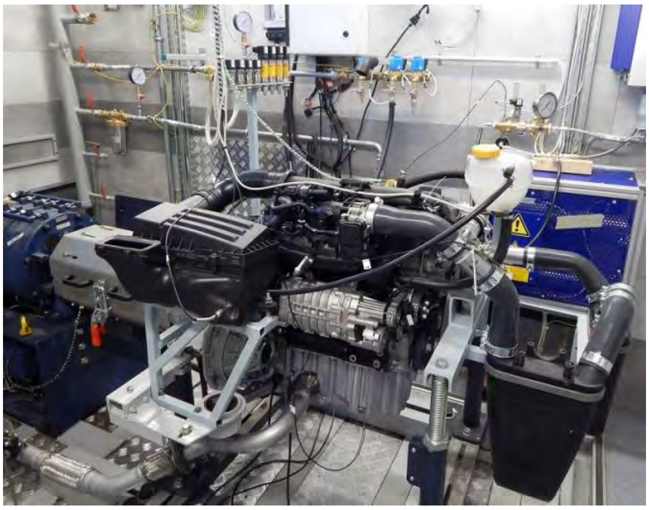

Fig. 1. View of the VW EA111 BLG engine test stand at INiG-PIB

4.2. DISI injector spray evaluation – optical test methodology

The second stage tests were carried out with a constant volume chamber (2.2 dm^3), which, along with the layout of the entire test stand, is shown in Fig. 2. Fuel was injected at a 10 MPa pressure with a 0.6 ms injector opening time. Spray pattern evaluation was performed as follows:

- a high-speed camera was used along with halogen illumination to evaluate geometric indicators of the spray
- a high-speed camera and NG:YAS 532 nm laser illumination system were used to evaluate the cross-sectional spray area of injected fuel.

The high-speed record process included:

- imaging frequency f = 10 kHz
- LaVision's HSS5 camera image size 512 × 512 px
- Nikkon AF Nikkor 24-85 mm 1:2.8-4 D lens
- image analysis was conducted using DaVis 10 software.

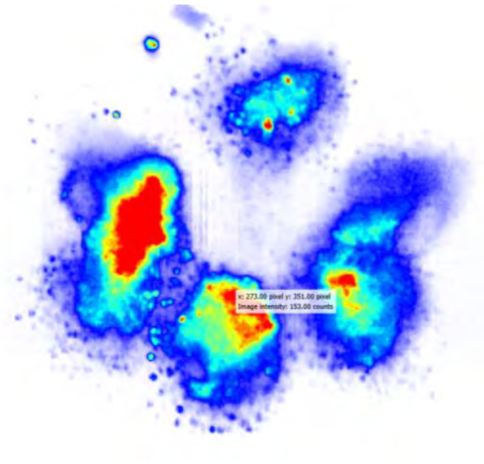

Fig. 3. View of raw images recorded with laser illumination

Data analysis was conducted using LaVision's DaVis 10 software. An example of a raw image is shown in Fig. 3. The program allowed the creation of macros for image analysis, including analysis of macroscopic indicators. The images were saved in a grayscale format that allowed individual assessment of each pixel's luminance (brightness). The choice of such an image processing form allowed the numerical representation of the results obtained.

The results were processed separately for halogen illumination and laser illumination. The first approach required the identification of macroscopic indicators of the spray (Fig. 4a), and the second – the area of the spray after it was cut with an optical cutter in a plane orthogonal to the fuel outflow (Fig. 4b).

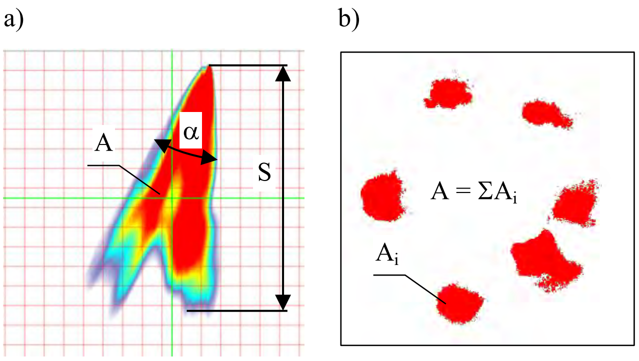

Fig. 4. Method of evaluating the fuel jet: a) with halogen lamps, b) with laser illumination

4.3. The fuel mixtures employed in the study

Five gasoline types with different physical and chemical properties were tested:

- RF-12-09 batch 11 used in CEC test procedures for checking, adjusting and calibrating test engines; it is often used for research or comparison purposes; this gasoline does not contain DCA and has a high tendency to form deposits on the intake valves of SI engines; in the tests it was the base fuel and at the same time (reference) fuel

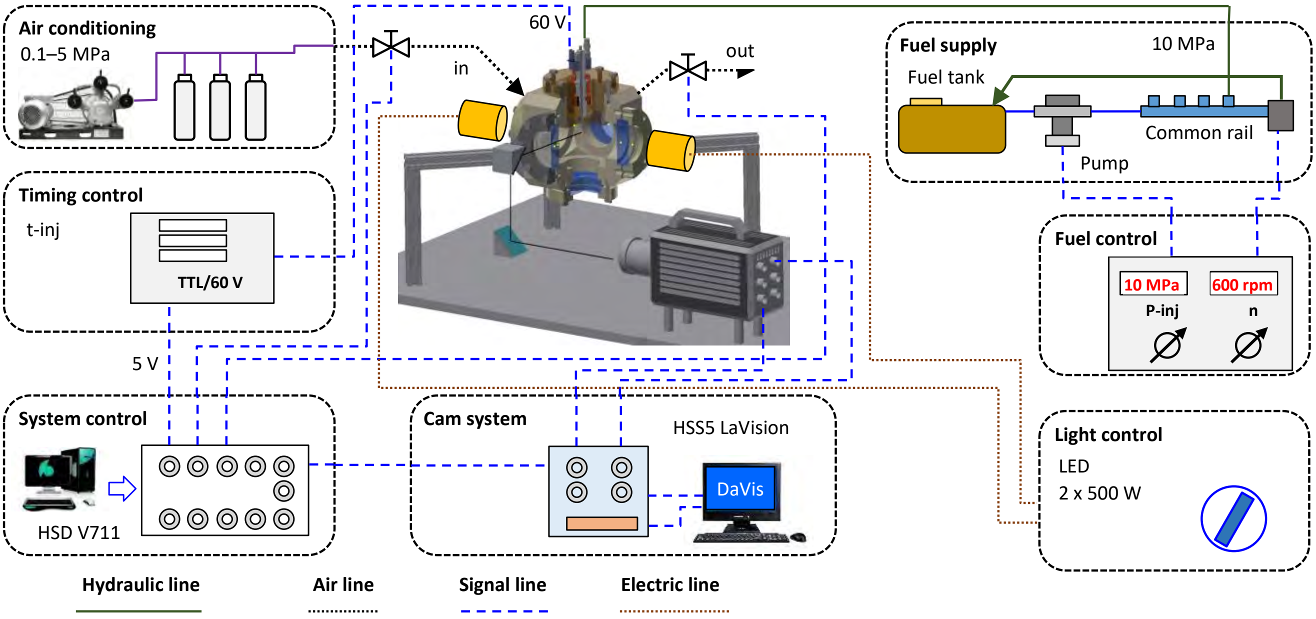

Fig. 2. Layout of fuel atomization studies under halogen illumination

- RF-12-09 batch 11 + 20% (v/v) ethanol
- RF-12-09 batch 11 + 20% (v/v) butanol
- RF-12-09 batch 11 + 20% (v/v) butanol refined with 500 ppm (m/m) DCA type additive
- gasoline RF-12-09 batch 11 doped with 20% (v/v) ethanol refined with 500 ppm (m/m) DCA-type additive.

The different fuel compositions (only 20%) resulted in similar (initial) fuel injection times – Table 3.

Table 3. Initial injection times of the tested fuels

Type of fuel	Initial injection time [ms]
RF-12-09 batch 11	1.577
RF-12-09 batch 11 + 20% (v/v) ethanol	1.575
RF-12-09 batch 11 + 20% (v/v) butanol	1.576
RF-12-09 batch 11 + 20% (v/v) butanol + 500 ppm (m/m) DCA	1.576
RF-12-09 batch 11 + 20% (v/v) ethanol + 500 ppm (m/m) DCA	1.577
The injection time values are average values	

The limitation of alcohol admixture to 20% (v/v) was due to the engine manufacturer's requirements for the maximum allowable alcohol content in gasoline. A DCA additive compatible with gasoline with alcohol content was used to refine the fuel blend. The amount of DCA additive was set at a level typical of fuels on the European market. The physicochemical properties of the fuel blends prepared for the tests are shown in Table 4.

All tests used the same set of injectors, which were subjected to a cleaning process strictly described in the CEC F-113 test procedure after each test. In addition, each injector was assigned to a specific engine cylinder and was therefore mounted to the same engine cylinder in each test.

5. Results

5.1. Assessing the tendency of fuels to generate injector deposits

Based on the engine tests carried out, the characteristics of the injection time variation in relation to the test duration were obtained. Figure 5 shows a comparison of the injection time changes of the tested fuels (base, base + 20E, base + 20B) obtained in tests conducted according to the CEC F-113-KC procedure. A test referred to as "Keep-Clean" (KC) in that case was equivalent to the "Dirty-Up" (DU) test due to the fact that the tested fuels cause the injectors to become more and more contaminated with deposits formed. The results (Fig. 5) represent the averaged difference in the electrical pulse width controlling the opening time of the injectors measured during engine operation in individual tests. As the measured pulse is unstable (it changes with a very high frequency and large amplitude over time), calculating the increase in pulse width (injection time) as the magnitude of its difference at the beginning and end of the test could be affected by a large error. Therefore, a methodology based on a trend function was used to calculate the change in pulse width that occurred during the test.

The averaged values calculated based on the trend are more representative than t based on the endpoints of the actual measurements. In this way, the average calculated width of the electrical pulse controlling the timing of a single injection during the test was obtained. The result is given in [%] of electric pulse width increase. The greater the difference, the greater the fuel's tendency to form deposits. Based on the CEC tests performed to date, based on the Student t-distribution, it was determined that a difference in the width of the electric control pulse of at least 1.8% is required to distinguish between the two results at the 90% confidence level.

Comparison of the test results for the three fuels tested (Fig. 5) divided the injection time increment up to 15 h and for the remainder of the test duration. The split is mainly due to the rapid increase in injection time, followed by its stabilization.

In relation to the reference RF-12-09 batch 11, the average calculated increase (during the first part of the test) in injection time was 3.06%, for the RF-12-09 batch 11 + 20% (v/v) ethanol – 3.94%, while for RF-12-09 batch 11 + 20% (v/v) butanol – 3.75%. The results so far have shown that the most important properties of unrefined fuel that have a major impact on injector deposit formation processes are T90, sulfur, olefins, and aromatics content, as well as vapor pressure, density, IBP, and octane number and upper distillation run [1, 21].

Table 4. Physicochemical properties of fuels used in engine tests

Property	Unit	RF-12-09 batch 11	RF-12-09 batch 11 +20% (v/v) ethanol	RF-12-09 batch 11 + 20% (v/v) ethanol + 500 ppm (m/m); DCA	RF-12-09 batch 11 + 20% (v/v) butanol	RF-12-09 batch 11 + 20% (v/v) butanol + 500 ppm (m/m); DCA	Test procedure
Notation	–	base	base + 20E	base + 20E + DCA	base + 20B	base + 20B + DCA	
Research octane number	–	96.3	98.3	98.2	98.8	98.8	EN ISO 5164
Motor octane number	–	87.1	87.7	87.6	88.7	88.7	EN ISO 5163
Sulfur content	mg/kg	5.0	3.7	3.3	3.5	3.4	EN ISO 20846
Content of hydrocarbon types:							
Olefinic	% (v/v)	5.5	< 4.0	< 4.0	< 4.0	< 4.0	EN 15553
Aromatic	% (v/v)	27.8	21.5	21.2	23.1	20.5	
Oxygen	% (m/m)	< 0.1	7.53	7.27	4.94	4.57	EN 1601
Organic compounds containing oxygen:							
Butanol	% (v/v)	< 0.80	< 0.17	< 0.17	20.2	20.1	EN 1601
Ethanol	% (v/v)	< 0.80	20.4	20.0	< 0.17	< 0.17	
Fractional composition:							
T10	°C	52.4	52.8	51.9	61.7	59.4	EN ISO 3405
T50	°C	106.8	72.7	72.0	102.6	101.9	
T90	°C	173.2	152.3	152.1	153.4	153.8	

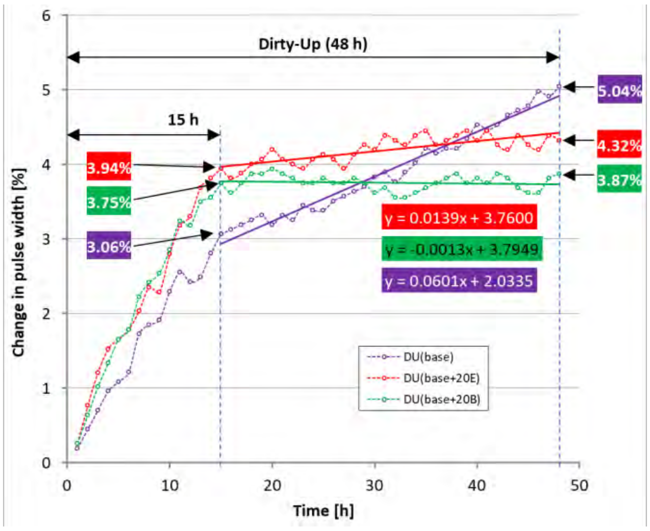

Fig. 5. Results comparison of the fuels ability to keep DISI engine injectors clean during the CEC F-113-KC (48 h) test

However, all the tested fuels were based on the same reference RF-12-09 Batch 11 fuel. Thus, the differences between their physicochemical properties were small and were mainly due to the admixture of ethanol or butanol – Table 2. In addition, the result is affected by the simultaneous interaction of different fuel properties, which can interact with each other. It is very difficult to determine the interactions that have different effects on the formation of injector deposits.

In the second part of the test, a continuous increase in injection time for the base fuel was observed. The final value of the injection time increment was 5.04%. The use of ethanol and butanol admixtures indicates that their share significantly reduces the fuel injection time. The use of butanol does not increase the injection time – a practically constant average value was obtained after 15 h of testing. The ethanol content increases the injection time, but the increment is only 0.5% of the base time.

The application of alcohol-enrichment fuels, after approximately 15 h of a test, caused deposit formation stabilization. The differences in the trends for different fuels are due to the intensity of the deposit precursor formation, the strength of their adhesion to the surface, and the simultaneous self-cleaning processes. Thus, the course of deposit formation is the result of their growth and flushing. It can be hypothesized that in that case, fuels that contain alcohol have a lower tendency to contaminate fuel injectors. As a result of the linear increase in injection time caused by non-alcohol-enrichment fuels, the level of contamination created will exceed that created by alcohol-containing fuels. The hypothesis put forward is confirmed by the trend lines in Fig. 5, which are plotted for each of the waveforms of changes in the size of the injection time control pulse width throughout the test. It can be seen that the trend lines have a flatter course for alcohol-doped fuel, including the flattest for fuel doped with 20% (v/v) butanol. In contrast, the course of the line showing the increase in injection time of a single dose of the base fuel during the test is much steeper.

5.2. Assessing the tendency of fuels to remove injector deposits

Figure 6 includes the results of the injection time changes of the tested fuels in a cycle including the "Dirty-Up" (DU) and "Clean-Up" (CU) phases. Each time, the DU phase was carried out with the reference fuel RF-12-09 Batch 11 fuel (base). Subsequently, four clean-up phases were carried out using alcohol-enriched fuels. Through this path, the effectiveness of flushing out injector deposits was evaluated by applying an admixture of alcohol without or with DCA to the reference fuel used in the "Dirty-Up" test.

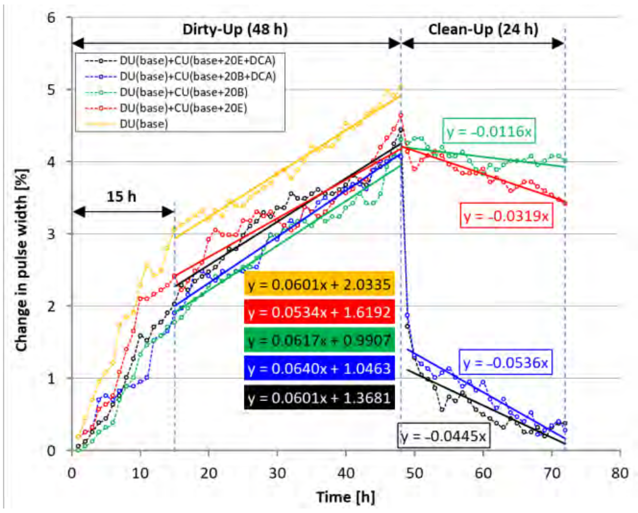

Fig. 6. Comparison of fuels' ability to remove DISI engine injector deposits according to CEC F-113-DU (48 h) and CEC F-113-CU (24 h) procedures

As in the previous test, the injection time increment period was divided into two groups: up to 15 h of the test and the rest of the 48 h of the test. This was due to a similar observation that the first part of the test generates a very large increase in injection time, and then a reduction in this phenomenon was observed. Mainly, the second part of the test was analyzed by linearizing the results obtained. The average slope of the curves is similar, which results from testing the same fuel (base).

The average increase in injection time extension was 0.6% for every 10 h of the test (this value is derived from the directional coefficient "a" in the equations in Fig. 6).

During the second part of the test – the "Clean-Up" – an addition of 20% (v/v) ethanol and the same concentration of butanol was applied to the base fuel. The use of the butanol additive resulted in a deposit washout rate of about 0.1% for every 10 h of the test. The use of the ethanol additive resulted in a higher rate of deposit washout, about 0.3% for every 10 h of test.

In the following part of the research, two more tests were carried out according to the F-113-CU procedure. In an effort to improve the efficiency of injector flushing, fuels with alcohol and DCA-type additive (performance additive) were used. When a reference fuel with a do-mix of 20% (v/v) ethanol + 500 ppm (m/m) DCA was used in the "Clean-Up" part of the test, a rapid reduction in injection time increment was achieved (within 1–2 h after the start of the test). A further phase of the test was able to achieve a 0.5% reduction in injection time increment for every 10 h.

By using a reference fuel admixed with 20% (v/v) butanol + 500 ppm (m/m) DCA in the "Clean-Up" part of the test, an average calculated reduction in injection time was also achieved by 0.5% for every 10 h of the test. In addition, it can be concluded that the efficiency of using the DCA additive is significantly higher than that of admixing ethanol or butanol.

5.3. Optical evaluation of spray indicators

Analysis of macroscopic indicators was carried out for all test cases. Fuel spray images under halogen illumination are shown in Fig. 7. The first three rows were dedicated to the effects of the DU phase, while the next four are a cycle covering the DU and CU phases.

Based on the camera images, analyses were made according to the data shown in Fig. 4a. The range of the spray, the flat area of the spray exposure, and the angle of the spray cone were taken for analysis (each jet was not analyzed separately). The results of this work are shown in Fig. 8, separately for contamination (DU) and leaching (CU) tests of injector orifices.

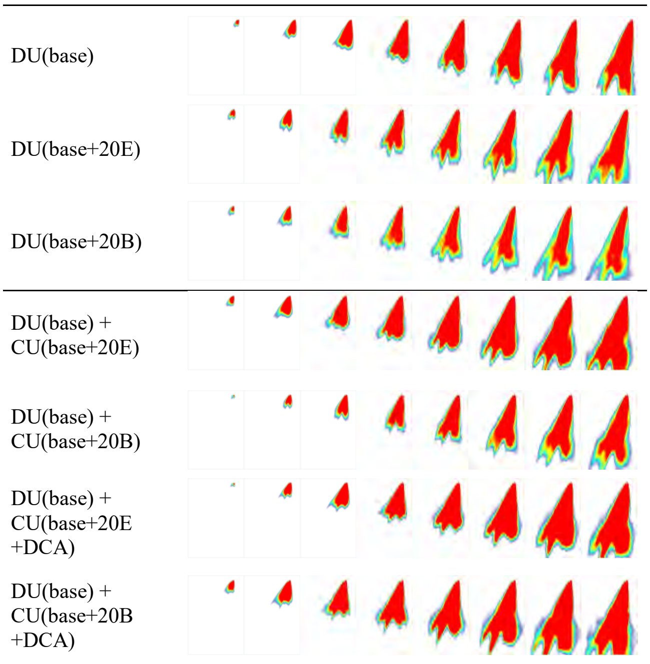

Fig. 7. Fuel spray images with halogen illumination (Δt = 100 μs; labels as shown in Table 2)

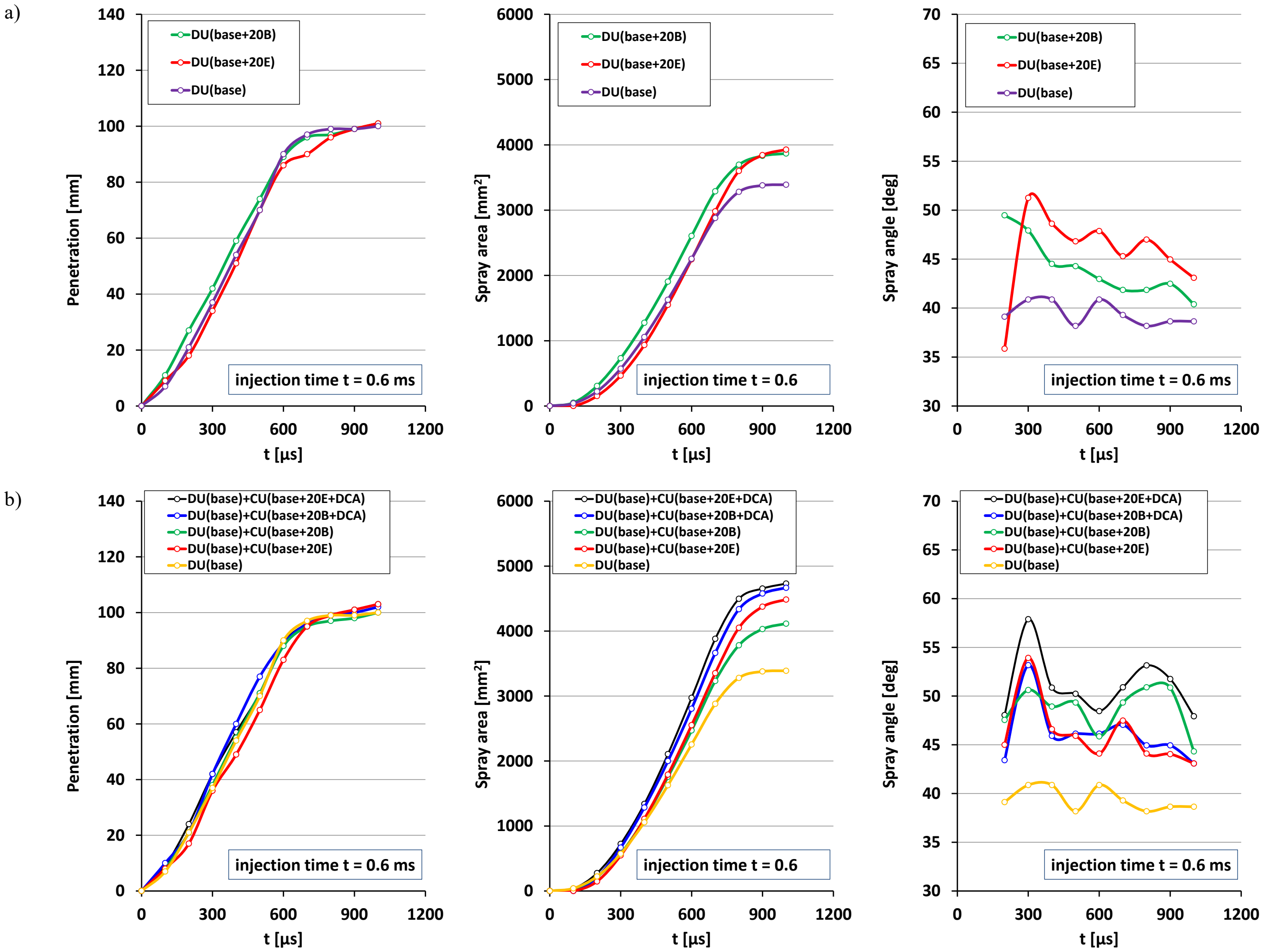

Fig. 8. Macroscopic indicators (penetration; spray area; spray angle) of the spray jet (t = 0.6 ms; p_{inj} = 10 MPa): a) after Dirty-Up test, b) after Dirty-Up and Clean-Up tests

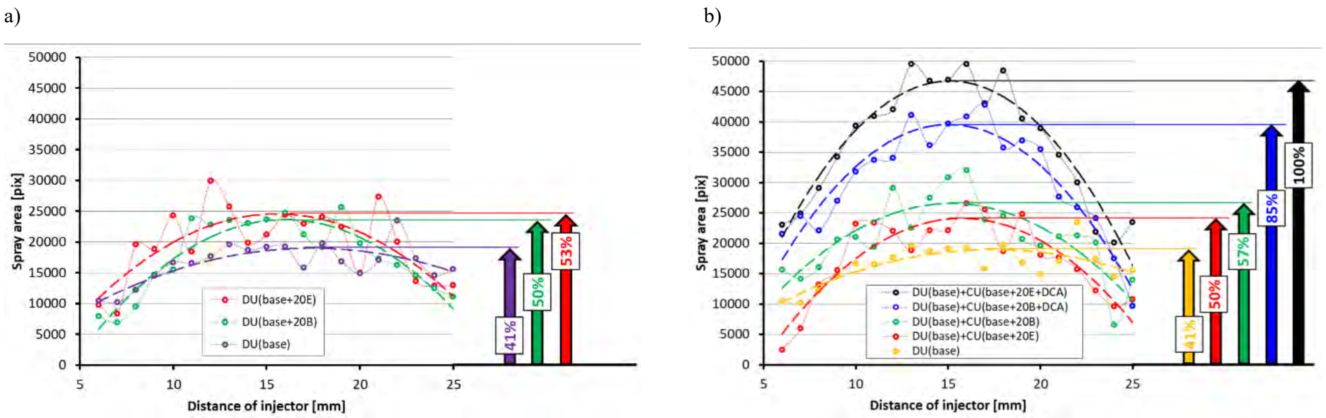

Fig. 9. Analysis of fuel atomization in the form of area fields under perpendicular laser light illumination of the jet: a) after Dirty-Up test, b) after Dirty-Up and Clean-Up tests

Analysis of fuel spray penetration indicates that there are no significant differences, regardless of the use of DU or DU + CU in the test. However, analysis of the fuel spray area already indicates some differences: significantly larger areas were obtained in the CU test. The application of ethanol and butanol increases the surface area in the DU test by approximately 15%. It means a reduction in injection time, which is also confirmed in Fig. 5. The shortest injection duration was recorded during the addition of butanol, which also confirms the area of the fuel jet from time 300 to approximately 800 µs after the start of injection. During the DU + CU test, the application of the DCA additive increases the jet area by 37% compared to the base fuel. It is difficult to identify a better system (butanol or ethanol additive), but the DCA additive is critical here.

The spray area is closely related to the angle of the spray cone. A small field correlates with a small spray angle (hole coking). Such correlations were noted during DU analysis, especially for the base fuel. Similarly, during DU + CU analysis, it can be clearly indicated that the use of DCA additives increases the spray cone angle. The use of DCA with ethanol allows for the largest spray cone angles. It follows that optical analyses are complementary to engine tests, but their results cannot determine the nature of the problem.

To further confirm the relationships obtained, cross-sections of fuel spray were analyzed according to Fig. 4b. On this basis, the individual areas of the plumes were summed, and their interpretation is included in Fig. 9.

In this part of the optical study, the area is presented as the number of pixels covering the spray. Basic research (DU) indicates that the maximum area occurs approximately 15 mm from the first measurement plane (which is half of the spray range – 50 mm). This means that the occurrence of the maximum area in the system containing the laser illumination takes place around 65 mm from the injector tip. It was confirmed that the sum of the cross-sectional area of the fuel plumes is the smallest at the base fuel (in the DU test) – Fig. 9a. Subsequent areas are larger and close to each other (also in the DU test with the addition of ethanol or butanol).

The analysis of the next part of the study during the leaching test (DU + CU) indicates that the lack of DCA addition results in similar cross-sectional area magnitudes. Such results are also confirmed by the data in Fig. 6. There, too, the lack of DCA addition does not result in large changes in injection time. The largest areas were obtained with the addition of DCA with both butanol – an increase of more than 40% over CU(base) and ethanol – an increase of as much as 60% – Fig. 9b. Although the individual areas do not represent exact relationships, the use of a trend line captures the trend of field changes very well.

Engine and non-engine fuel atomization tests were supported by photo material of the injector tips. The first test series (sample images of the injector tip) are shown in Fig. 10. Significant contamination of the injector nozzles, reducing the flow diameter, can be seen (after the Dirty-Up test). Such fouling is evident both for the reference fuel (base) and with the application of ethanol and butanol additives. The fouling indicates limitations in fuel atomization and, at the same time, the need to increase the percentage injection time during the test.


DU (base) DU (base + 20E) DU (base + 20B)

Fig. 10. View of unclean injector holes after Dirty-Up test

Figure 11 includes a view of the injector holes after the Clean-Up test. A view of the injector tip after the Dirty-Up test (first photo) is also included for comparison purposes. Significant differences in nozzle contamination were noted. The Clean-Up phases result in significant leaching of fouling.

6. Summary and conclusions

The combination of engine and non-engine tests, including optical studies, allows a wide-ranging (multi-directional) assessment of injector contamination and its effects during the application of varying base fuel additives (in the form of ethanol, butanol, and DCA additive).

Engine results analysis indicates an increase in injection time during Dirty-Up tests:

– by 5% in total for base fuel

- by approximately 4% with the application of fuels with 20% ethanol and butanol content, with a significant reduction in this increment observed after approximately 15 h of testing.

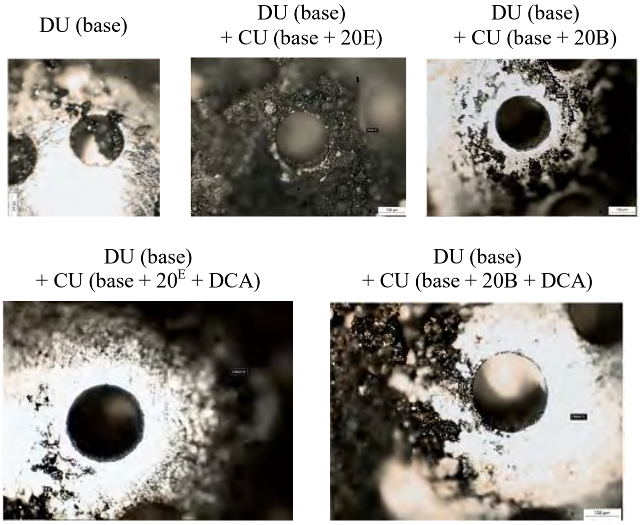
DU (base)

DU (base) + CU (base + 20E)

DU (base) + CU (base + 20B)

DU (base) + CU (base + 20^{E} + DCA)

DU (base) + CU (base + 20B + DCA)

Fig. 11. Images of the spray holes after Dirty-Up and Clean-Up tests

An investigation of the Clean-Up test (using various additives) after the Dirty-Up test (base fuel) resulted in:

- similar injection extension during the Dirty-Up test (absolute increase of about 4%)
- a minor reduction in relative injection time (0.5% in the test) during the use of ethanol additive and a slight reduction in this time during the use of butanol admixture
- significant reduction in injection time increase with DCA addition: after 1–2 h of test, absolute injection time was reduced by about 3%; after that, injection time reduction was significantly reduced
- the ability to achieve the original (baseline) injection time with the use of DCA additive; it follows that the contaminants formed during the 48 h Dirty-Up test are leveled in the 24 h Clean-Up test after the use of 20% ethanol or butanol additive with DCA additive; the leaching of contaminants occurs rapidly (1–2 h) after the start of the test, and then take on a linear, slow leaching character.

Among the optical metrics evaluated, only selected macroscopic parameters (spray area and angle) showed sensitivity to fuel composition. Although the spray penetration does not indicate differences, the other indicators in the form of spray area and spray angle significantly indicate changes due to the use of additives.

Acknowledgements

This article was prepared according to the statutory work 0415/SBAD/0351 and 0415/SBAD/0353 (Poznan University of Technology).

Nomenclature

20D	admixture of 20% (v/v) ethanol
20E	admixture of 20% (v/v) buthanol
CU	Clean-Up
DCA	500 ppm (m/m) Deposit Control Additives
DU	Dirty-Up
KC	Keep-Clean
SIDI	spark ignition direct injection

Bibliography

[1] Altin O, Eser S. Carbon deposition from thermal stressing of petroleum fuels. Am Chem Soc Div Fuel Chem. 2004;49(2): 764-766.

[2] Costagliola MA, De Simio L, Iannaccone S, Prati MV. Combustion efficiency and engine out emissions of a S.I. engine fueled with alcohol/gasoline blends. Appl Energy. 2013;111:1162-1171. https://doi.org/10.1016/j.apenergy.2012.09.042

[3] Directive 2003/30/EC of the European Parliament and of the Council of 8 May 2003 on the promotion and the use of biofuels or other renewable fuels for transport. 2003;123. https://eur-lex.europa.eu/legal-content/EN/ALL/?uri=CELEX:32003L0030

[4] Directive (EU) 2018/2001 of the European Parliament and of the Council of 11 December 2018 on the promotion of the use of energy from renewable sources. https://eur-lex.europa.eu/legal-content/EN/TXT/?uri=CELEX:32018L2001

[5] Elfasakhany A. Experimental study of dual n-butanol and iso-butanol additives on spark-ignition engine performance and emissions. Fuel. 2016;163:166-174. https://doi.org/10.1016/j.fuel.2015.09.059

[6] Elfasakhany A. Performance and emissions of spark-ignition engine using ethanol–methanol–gasoline, n-butanol–iso-butanol–gasoline and iso-butanol–ethanol–gasoline blends: A comparative study. Eng Sci Technol Int J. 2016;19(4): 2053-2059. https://doi.org/10.1016/j.jestch.2016.09.009

[7] Fournier S, Simon G, Seers P. Evaluation of low concentrations of ethanol, butanol, BE, and ABE blended with gasoline in a direct-injection, spark-ignition engine. Fuel. 2016; 181:396-407. https://doi.org/10.1016/j.fuel.2016.04.135

[8] Galloni E, Fontana G, Staccone S, Scala F. Performance analyses of a spark-ignition engine firing with gasoline–butanol blends at partial load operation. Energy Convers Manag. 2016;110:319-326. https://doi.org/10.1016/j.enconman.2015.12.038

[9] Henkel S, Hardalupas Y, Taylor A, Conifer C, Cracknell R, Goh TK, et al. Injector fouling and its impact on engine emissions and spray characteristics in gasoline direct injection engines. SAE Int J Fuels Lubr. 2017;10(2):287-295. https://doi.org/10.4271/2017-01-0808

[10] Kale R, Banerjee R. Optical investigation of flash boiling and its effect on in-cylinder combustion for butanol isomers and iso-octane. Int J Engine Res. 2021;22(5):1565-1578. https://doi.org/10.1177/1468087420917241

[11] Pielecha I, Szwajca F, Stępień Z. Potential of ethanol and butanol in reducing deposits of DISI engine injectors. Combust Engines. 2023;194(3):21-31. https://doi.org/10.19206/CE-167898

[12] Regulation (EU) 2019/631 of the European Parliament and of the Council of 17 April 2019 setting CO2 emission per-

formance standards for new passenger cars and for new light commercial vehicles, and repealing Regulations (EC) No 443/2009 and (EU) No 510/2011 (recast) (Text with EEA relevance)
http://data.europa.eu/eli/reg/2019/631/oj/eng. 2019.

[13] Schwahn H, Lutz U, Kramer U. Deposit formation of flex fuel engines operated on ethanol and gasoline blends. SAE Int J Fuels Lubr. 2010;3(2):22-37.
https://doi.org/10.4271/2010-01-1464

[14] Shuai S, Ma X, Li Y, Qi Y, Xu H. Recent progress in automotive gasoline direct injection engine technology. Automot Innov. 2018;1(2):95-113.
https://doi.org/10.1007/s42154-018-0020-1

[15] Song H, Xiao J, Chen Y, Huang Z. The effects of deposits on spray behaviors of a gasoline direct injector. Fuel. 2016;180:506-513. https://doi.org/10.1016/j.fuel.2016.04.067

[16] Stępień Z. A study of factors influencing the formation of harmful deposits in the diesel engine injectors. Eksploat Niezawodn. 2017;19(3):331-337.
https://doi.org/10.17531/ein.2017.3.3

[17] Stępień Z. Evolution of methods applied for assessing harmful engine deposits caused by gasoline combustion. Nafta-Gaz. 2021;77(5):340-347.
https://doi.org/10.18668/NG.2021.05.07

[18] Stępień Z, Pielecha I, Cieslik W, Szwajca F. The impact of alcohol admixture with gasoline on carbon build-up and fuel injectors performance. Eksploat Niezawodn. 2022;24(2):226-236. https://doi.org/10.17531/ein.2022.2.4

[19] Thewes M, Muther M, Brassat A, Pischinger S, Sehr A. Analysis of the effect of bio-fuels on the combustion in a downsized DI SI engine. SAE Int J Fuels Lubr. 2011;5(1):274-288. https://doi.org/10.4271/2011-01-1991

[20] Venugopal T, Ramesh A. Effective utilisation of butanol along with gasoline in a spark ignition engine through a dual injection system. Appl Therm Eng. 2013;59(1):550-558.
https://doi.org/10.1016/j.applthermaleng.2013.06.026

[21] Xu H, Wang C, Ma X, Sarangi AK, Weall A, Krueger-Venus J. Fuel injector deposits in direct-injection spark-ignition engines. Prog Energy Combust Sci. 2015;50:63-80.
https://doi.org/10.1016/j.pecs.2015.02.002

Filip Szwajca, DEng. – Faculty of Civil and Transport Engineering, Poznan University of Technology, Poland.
e-mail: *filip.szwajca@put.poznan.pl*

Prof. Zbigniew Stępień, DSc., DEng. – Performance Testing Department, Oil and Gas Institute – National Research Institute, Cracow, Poland.
e-mail: *stepien@inig.pl*

Prof. Ireneusz Pielecha, DSc., DEng. – Faculty of Civil and Transport Engineering, Poznan University of Technology, Poland.
e-mail: *ireneusz.pielecha@put.poznan.pl*

Article citation info:
Nakashima K, Yoshida M, Nishii K, Yoshida A, Okura N. Improving heat transfer of air-cooled cylinders with fins with slits. Combustion Engines. 2025;202(3):141-146. https://doi.org/10.19206/CE-207422

Kohei NAKASHIMA
Masao YOSHIDA
Kento NISHII
Ayanari YOSHIDA
Nobuyuki OKURA

Combustion Engines
Polish Scientific Society of Combustion Engines

Improving heat transfer of air-cooled cylinders with fins with slits

ARTICLE INFO

Received: 19 May 2025
Revised: 19 June 2025
Accepted: 22 June 2025
Available online: 12 July 2025

In finned cylinders with slits around the cooling fin circumference, thermocouples were attached at three positions in the radial direction on the surface of the fin, and fin surface temperatures were measured by rotating the cylinders relative to the flow direction in a wind tunnel to change the angular position of the attached thermocouples. The temperature distribution around the fin circumference and the average heat transfer coefficient were then investigated at air velocities from 20 km/h (5.6 m/s) to 60 km/h (16.7 m/s). Results indicated that, compared with fins without slits, fins with slits, either aligned or offset, decreased fin surface temperatures and increased the heat transfer coefficient. The fins with slits also resulted in a more uniform circumferential temperature at the fin root at a lower air velocity, but not at a higher air velocity, compared to fins without slits.

Key words: *air-cooled cylinder, cooling fin, slit, heat transfer, fin surface temperature*

1. Introduction

Air-cooled motorcycle engines are cooled by transferring waste heat from the cylinder through the cooling fins to the surrounding air. Therefore, increasing total fin surface area is generally effective in increasing cylinder cooling. Several studies have reported on the effect of fin dimensions and number of fins on cooling performance in conventional finned cylinders, in order to increase fin surface area [2, 5, 9–14]. For example, Biermann and Pinkel [2] investigated the surface heat transfer coefficient around the fin circumference under forced convection, using vertical steel cylinders with fins with various pitches, lengths, and thicknesses. They found that the space between the fins significantly affected the heat transfer coefficient. Thornhill and May [11] examined the surface heat transfer coefficient around the fin circumference under forced convection, utilizing vertical aluminium alloy cylinders with fins with various pitches and lengths. They also indicated that fin separation has a great effect on the heat transfer coefficient. Thornhill et al. [12, 13] also investigated the heat transfer coefficient around the fin root under forced convection, using vertical aluminium alloy cylinders with fins with various pitches and lengths. They clarified that there is a limit to the heat transfer coefficient for a given fin length, even with increased fin separation. The authors [14] used vertical aluminium alloy cylinders with different fin pitches and numbers of fins to investigate the heat transfer rate from the cylinder and the fin temperature under both natural convection and forced convection, and determined the optimal fin pitch for cooling. In addition to the above-mentioned studies, the numerical analysis by Mishra et al. [5] also revealed that, as more fins are mounted on the cylinder at too narrow a pitch in an effort to increase the total fin surface area, thermal boundary layers overlap between the upper and lower fins, reducing cylinder cooling [9].

Besides increasing total fin surface area, there have been practical examples of finned cylinders with slits [4]. However, even though 40 years had passed since the finned cylinder with slits was put into practical use, less research had been done on its cooling performance. Over the past 10 years or so, under natural convection, there have been some reports on the cooling performance of finned cylinders with slits where the slits promote a natural convection air flow. That is, for vertical aluminium alloy cylinders, the experiment in our previous study [6] or the numerical analysis by Dubey et al. [3] showed that there are optimal slit widths for cooling, while for a horizontal aluminium alloy cylinder, the numerical analysis by Angamuthu et al. [1] revealed that cooling is improved with a narrower slit width. On the other hand, under forced convection, there have been only our reports on the cooling performance of finned cylinders with slits [7, 8], where the slits disrupt the air flow between the fins, increasing cooling. In our previous studies [7, 8], using the vertical aluminium alloy cylinders with various slit widths around the circumference of the fins, both with slits set in line with cylinder axis, and with slits offset to the slits immediately above, the heat transfer rate from the cylinder was determined by measuring the temperature drop of the heat storage liquid in the cylinder. In addition, the air flow between the fins was observed with the smoke wire method and the air flow on the fin surface with the oil film method. Thus, the optimum slit width was identified for each slit arrangement. In general, it is important for an engine cylinder to be cooled uniformly around its circumference. However, the temperature distribution around the circumference of the finned cylinders with slits has not been clarified. This study set thermocouples to the fin surfaces of finned cylinders with slits around the fin circumference, and then investigated the temperature distribution around its circumference and average heat transfer coefficient under forced convection.

2. Experimental apparatus and method

Figure 1 shows the experimental finned cylinder with slits. For these finned cylinders, the cylinder bore diameter, the cylinder length, and the fin length were designed to approximate most actual single-cylinder motorcycle engines with displacement volumes of 150 cm^3 to 187 cm^3. The fins and cylinder were made of aluminium alloy (JIS A5052). In the fins, the slits were arranged in an equiangular 30° spiral around the circumference. The slit width was 14 mm, which achieved the greatest cooling when all the slits were set in line with the cylinder axis, in our previous study [7]. Six fins were fitted tightly in the cylinder at a fin pitch of 10 mm, either with slits set in line with cylinder axis, or with slits offset at a phase difference of 15° to the slits immediately above. These finned cylinders with slits were compared to a conventional finned cylinder without slits.

Figure 2 shows the experimental facilities, including an Eiffel-type wind tunnel, with a nozzle of height 680 mm and width 400 mm. The experimental cylinder was mounted on a support table, at a distance of 340 mm from the nozzle of the wind tunnel, with the cylinder axis perpendicular to the air flow.

Figure 3 shows the experimental apparatus. As shown in Fig. 3, a 300 W heater, a stirrer, and a K type thermocouple of 50 μm diameter wire were installed into the cylinder. The cylinder was filled with 290 cm^3 of ethylene glycol as heat storage liquid. On the upper surface of the fourth fin from the top, three K type thermocouples with a wire diameter of 50 μm were attached at positions 5 mm, 20 mm, and 33 mm radially from the fin root, as shown in Fig. 4.

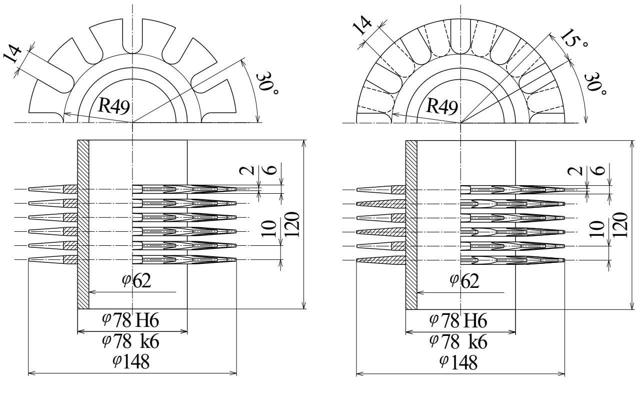

(a) Finned cylinder with aligned slits (b) Finned cylinder with offset slits

Fig. 1. Experimental finned cylinder with slits

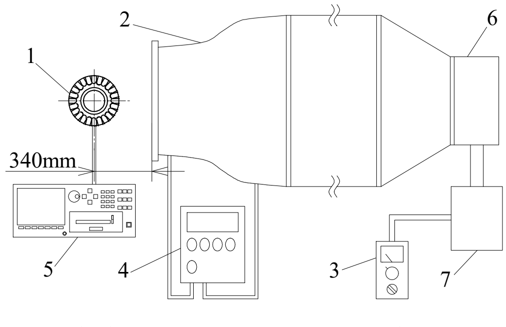

1 : Cylinder
2 : Wind tunnel
3 : Speed controller
4 : Manometer
5 : Data logger
6 : Blower
7 : Motor

Fig. 2. Experimental facilities

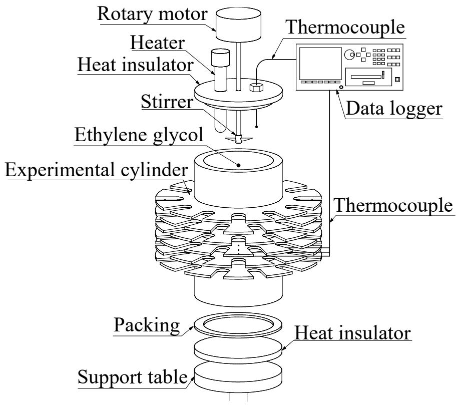

Fig. 3. Experimental apparatus

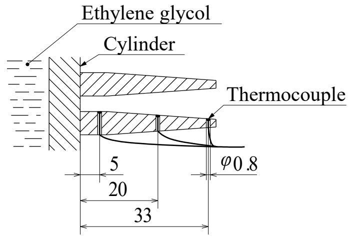

Fig. 4. Installation positions of thermocouples

In the experiment, the stirrer was run, the heat storage liquid was heated with the heater, and the wind tunnel was started. After the temperature of the heat storage liquid became constant, the temperatures of the fin surface and the heat storage liquid were recorded. Here, the cylinder was rotated so that the installation positions of the thermocouples in Fig. 4 were set at 15° intervals from 0° on the windward side (in front of the air flow) to 180° on the leeward side, and the temperatures were recorded for 5 minutes at each angular position of the thermocouple installation. In this case, the fins were located directly in front of the air flow, at 30° intervals from 0° to 180° in the angle position of the thermocouple installation, and the slits were located directly in front of air flow, at 30° intervals from 15° to 165° in the angle position (Table 1). Experiments were carried out at air velocities of 20 km/h (5.6 m/s), 40 km/h (11.1 m/s), and 60 km/h (16.7 m/s), and at an ambient temperature of 22.4 ±1.2°C. The measured temperature was accurate to within ±0.2°C.

Table 1. Slit arrangements

Aligned slits with front fin	Aligned slits with front slit	Offset slits with front fin	Offset slits with front slit
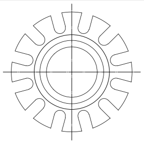	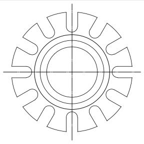	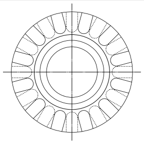	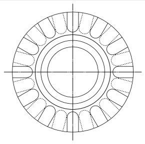

The heat rate used to calculate the average heat transfer coefficient was obtained by heating the heat storage liquid with the heater. Here, an insulated vessel (a double-layered stainless steel vacuum vessel wrapped with glass wool on the outside) was equipped with a 300 W heater, a stirrer, and a K type thermocouple with a wire diameter of 50 μm, and then filled with 290 cm^3 of heat storage liquid. The heat storage liquid in the insulated vessel was heated by a heater, while the stirrer ran, and the temperature of the heat storage liquid was measured without air blowing. The heat rate was determined from Eq. (1).

$$Q = \frac{c_m \cdot m \cdot (T_1 - T_2)}{t} \tag{1}$$

where Q is the heat rate [W], T_1 is 100°C (the approximate temperature of the heat storage liquid at an air velocity of 20 km/h (5.6 m/s)), T_2 is 70°C (the approximate temperature of the heat storage liquid at an air velocity of 60 km/h (16.7 m/s)), t is the time taken for the heat storage liquid to heat from 70°C to 100°C [s], c_m is the average specific heat of the heat storage liquid from 70°C to 100°C [J/(kg °C)], and m is the mass of the heat storage liquid [kg].

Here, the heat rate obtained in this experiment is the increased heat rate of both the heat storage liquid and the vessel from 70°C to 100°C. However, only the increased heat rate of the heat storage liquid was considered.

The average heat transfer coefficient was determined from Eq. (2).

$$h = \frac{Q}{(T_3 - T_4) \cdot A} \tag{2}$$

where h is the average heat transfer coefficient [W/(m^2 °C)], T_3 is the average fin surface temperature [°C], T_4 is the ambient temperature [°C], and A is the total surface area of the cylinder [m^2]. Here the fluctuation range of the heat transfer coefficient was within ±3%.

3. Results and discussion

Figures 5 and 6 show the fin surface temperatures at each angle position for the finned cylinder, without slits, with aligned slits, and with offset slits, at air velocities of 20 km/h (5.6 m/s) and 60 km/h (16.7 m/s), respectively. As shown in Table 1, in the slit arrangements in our previous studies [7, 8, 15], Figs. 5 and 6 also show the fin surface temperatures both in the aligned slits and in the offset slits, both separately with the front fin and with the front slit.

For all fins, the temperature difference from the windward side to the leeward side tended to decrease as air velocities increased. At all air velocities, the temperatures at each angle and radial position were lower for fins with slits aligned both with the front fin and with the front slit, and for slits offset both with the front fin and with the front slit, than for those without slits. The temperature drop in the fins with the aligned slits and the offset slits at each angle and radial position was greater when the air velocity was slower and smaller when the air velocity was faster. It appears that the air flow disturbance between the fins caused by the slits has a great effect at a lower air velocity. At all air velocities, the temperature differences between the fin root and the fin edge, at angle positions of 0° to 90° in the slits aligned and the slits offset with front fins, were larger than those without slits. The temperature differences between the fin root and the fin edge at angle positions of 15° to 105° in the aligned slits and the offset slits with front slits were also larger than those without slits. Thus, cooling is enhanced by slits, especially at angle positions of 0° to 105°.

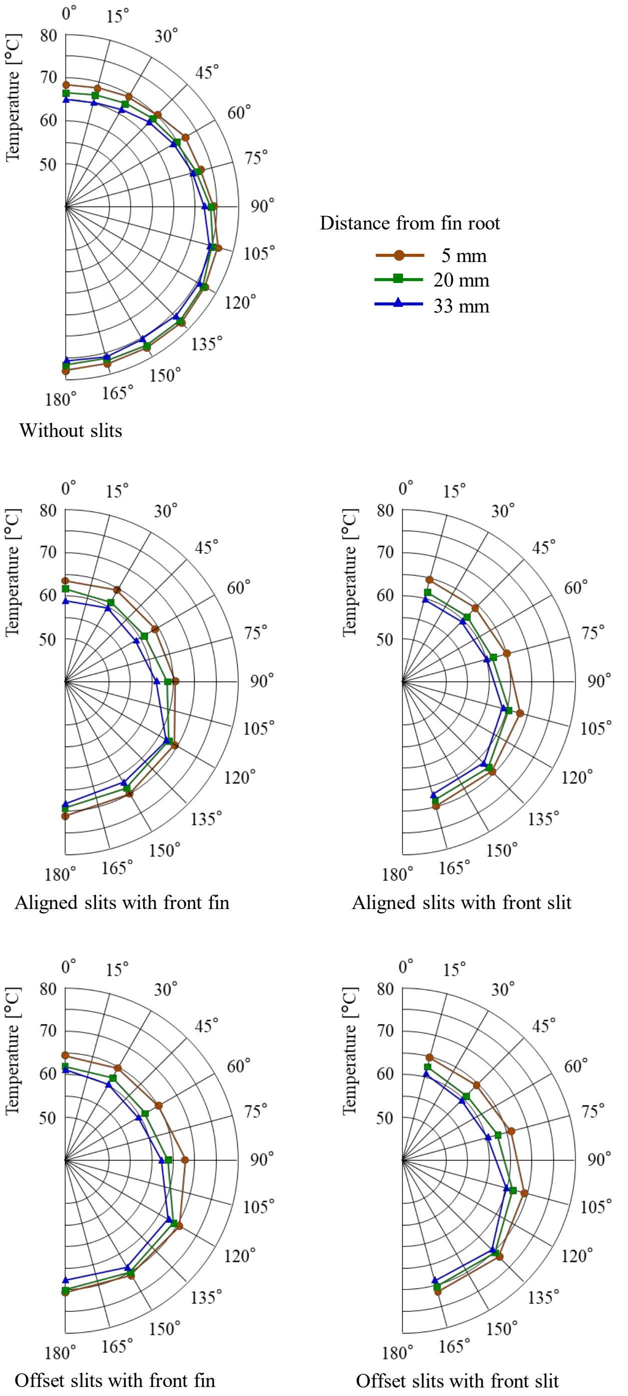

Without slits

Aligned slits with front fin

Aligned slits with front slit

Offset slits with front fin

Offset slits with front slit

Fig. 5. Fin surface temperatures at an air velocity of 20 km/h (5.6 m/s)

Compared to the slits offset with the front fin, in the slits aligned with the front fin, the temperature at an angle of 90° was lower at a lower air velocity, but the temperatures at all angles were similar at a higher air velocity. Compared to the slits offset with the front slit, in the slits aligned with the front slit, the temperatures at angles of 135° and 165° were also lower at a lower air velocity, but the temperatures at all angles were almost the same at a higher air velocity.

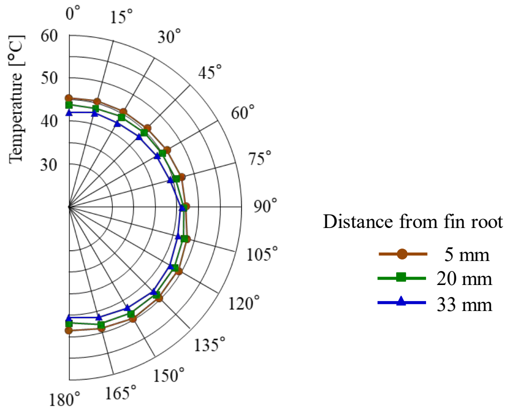

Without slits

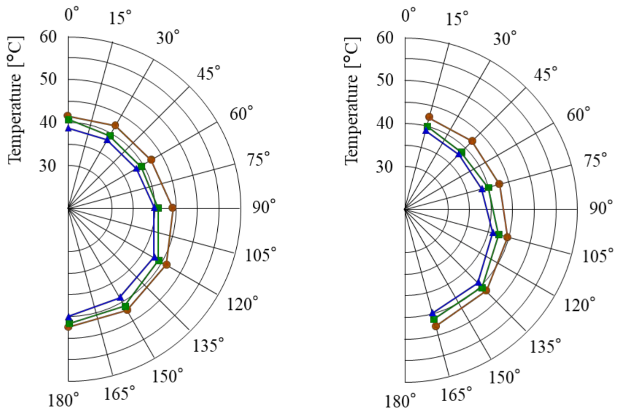

Aligned slits with front fin

Aligned slits with front slit

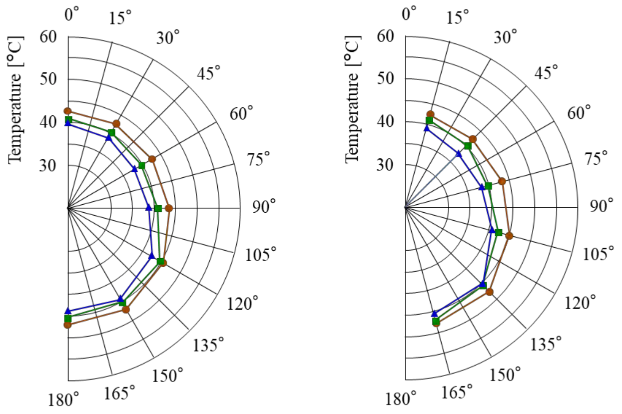

Offset slits with front fin

Offset slits with front slit

Fig. 6. Fin surface temperatures at an air velocity of 60 km/h (16.7 m/s)

In the fins without slits, the differences between the maximum and the minimum temperatures at the fin root were Δ10.0°C at an air velocity of 20 km/h (5.6 m/s), Δ6.6°C at an air velocity of 40 km/h (11.1 m/s) and Δ4.6°C at an air velocity of 60 km/h (16.7 m/s). Compared to the fins without slits, the differences between the maximum and the minimum temperatures at the fin root, with the slits aligned with the front fin and with the front slit, and with the slits offset with the front fin and with the front slit, were smaller at a lower air velocity, but tended to be almost the same or slightly larger at a higher air velocity. It seems that, at a lower air velocity, in all slit arrangements, air flow is disturbed between the fins, and the flow separation position moves to the rear side, decreasing the differences between the maximum and the minimum temperatures at the fin root. Figure 7 shows the flow pattern on the surface of the second fin from the top, at an air velocity of 60 km/h (16.7 m/s), observed using the oil film method in our previous study [15].

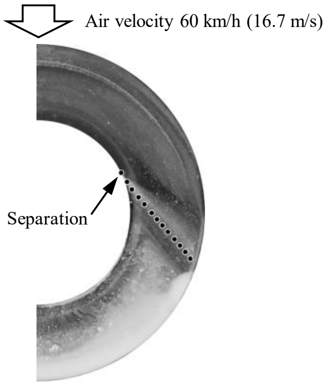

Without slits

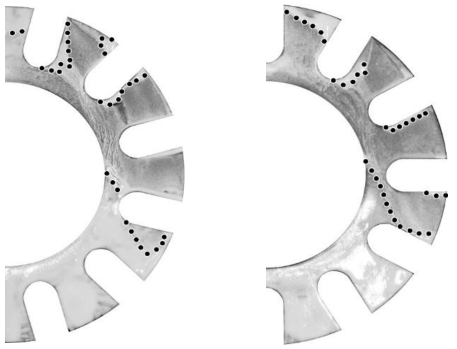

Aligned slits with front fin

Aligned slits with front slit

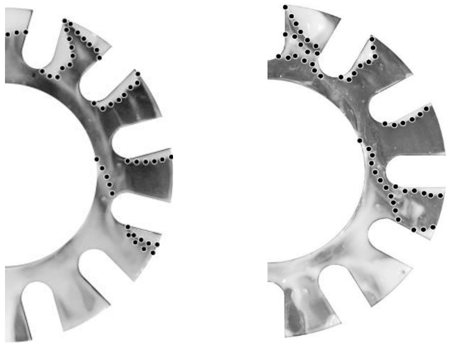

Offset slits with front fin

Offset slits with front slit

Fig. 7. Observed flow pattern on fin surface between fins at an air velocity of 60 km/h (16.7 m/s) [15]

As shown in Fig. 7, at a higher air velocity, the flow separation position is located at the rear side, even in fins without slits. The flow separation position moves further to the rear side, both in the slits aligned with the front fin and the front slit, and in the slits offset with the front fin and the front slit. These flow separation positions observed with the oil film method did not coincide with the angle positions where the temperature drop was smaller in the slits aligned with the front fin and the front slit, and in the slits offset with the front fin and the front slit, compared to the fins without slits. However, from our fin surface temperature measurements, compared to the fins without slits, the effect of the slits was greater at angle positions of 0° to 150°, but smaller at angle positions of 165° to 180°. As a result, at a higher air velocity, the differences between the maximum and the minimum temperatures at the fin root in all slit arrangements tended to be roughly the same or slightly larger than without slits.

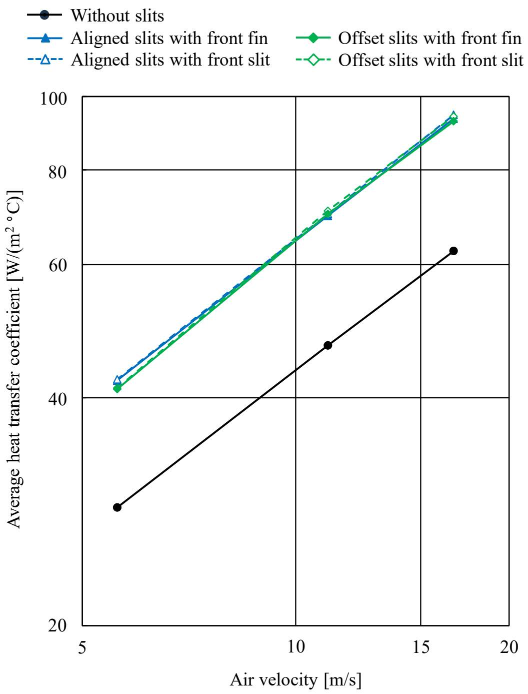

Fig. 8. Average heat transfer coefficient vs. air velocity

Figure 8 shows the average heat transfer coefficient versus air velocity for all slit arrangements and without slits. In all air velocities, the heat transfer coefficients for all slit arrangements were higher than those without slits. For example, the heat transfer coefficient with the slits aligned with the front fin was 47% to 49% higher than that without slits. However, there was no significant difference in the heat transfer coefficient between slits aligned with the front fin and with the front slit, and slits offset with the front fin and with the front slit.

The heat transfer rates from the cylinders with slits and without slits have been investigated by measuring the temperature drop of the heat storage liquid in the cylinder, in our previous study [15]. The result indicated that the heat transfer rate is in descending order of slits aligned with the front fin > slits offset > slits aligned with the front slit > without slits. The reasons why there was no significant difference in the heat transfer coefficient depending on the slit arrangements in this study, are thought to be as follows: First, the ambient temperature was higher than that in our previous study [15], second, the surface temperature on the root side of the slit was not measured, and third, the temperatures on the circumference were examined by attaching thermocouples to only three points on the surface of the fin and rotating the cylinder at 15° intervals from 0° on the windward side to 180° on the leeward side. Our future work will attach thermocouples on the circumferential surfaces of the root side of both the fins and the slits from the windward to leeward sides, in all slit arrangements, simultaneously measure the temperatures around the fin circumference, and then examine the heat transfer coefficient.

4. Conclusions

Using finned cylinders with slits around the fin circumference, the fin surface temperature distribution and the heat transfer coefficient were examined under forced convection. Results show the fin surface temperatures at each angle and radial position were lower, and the heat transfer coefficient was higher, for both fins with aligned slits and with offset slits, than for fins without slits. Compared to fins without slits, the fins both with aligned slits and with offset slits also had more uniform circumferential temperatures at the fin root at a lower air velocity, but not at a higher air velocity.

Bibliography

[1] Angamuthu K, Krishnan G, Gowrishankar M, Abraham JG. Modeling and simulation studies of 100 cc motor cycle engine cylinder with groove and perforated fin design using different materials. Mater Today-Proc. 2021;42:1447-1455. https://doi.org/10.1016/j.matpr.2021.01.249

[2] Biermann AE, Pinkel B. Heat transfer from finned metal cylinders in an air stream. NACA Report No.488. 1935.

[3] Dubey D, Singh D, Yadav A, Pal S, Thakur H. Thermal analysis of engine cylinder having thick tip with varying slot sizes and material. Mater Today-Proc. 2017;4:7636-7642. https://doi.org/10.1016/j.matpr.2017.07.097

[4] Howe H, Pischinger F. Der Luftgekühlte DEUTZ-Dieselmotor FL912. MTZ. 1968;29(4):132-138.

[5] Mishra AK, Nawal S, Thundil KRR. Heat transfer augmentation of air cooled internal combustion engine using fins through numerical techniques. Res J Engineering Sci. 2012; 1(2):32-40.

[6] Nakashima K, Toda T, Ishihara S, Yamamoto M. Optimizing the cooling effects of fins with slits on an air-cooled cylinder by increasing natural convection. SAE Int J Passeng Cars – Mech Syst. 2009;1(1):877-882. https://doi.org/10.4271/2008-01-1170

[7] Nakashima K, Mori Y, Yamada H, Yoshida M. Cooling characteristics of air-cooled cylinder with fins with slits under forced convection. Des Eng. 2019;54(8):551-558. https://doi.org/10.14953/jjsde.2019.2856

[8] Nakashima K, Mori Y, Yoshida M, Okura N. Cooling characteristics of air-cooled cylinder with fins with slits under forced convection (2nd Report, Fins with slits exhibiting a phase difference to slits immediately above). Des Eng. 2021; 56(5):241-250. https://doi.org/10.14953/jjsde.2020.2906

[9] Sachar S, Parvez Y, Khurana T, Chaubey H. Heat transfer enhancement of the air-cooled engine fins through geometrical and material analysis: a review. Mater Today-Proc. (in press). https://doi.org/10.1016/j.matpr.2023.03.447

[10] Sroka ZJ, Sufe G, Kejela E. Improving heat transfer in an air-cooled engine by redesigning the fins. Combustion Engines. 2025;201(2):14-21. https://doi.org/10.19206/CE-195440

[11] Thornhill D, May A. An experimental investigation into the cooling of finned metal cylinders, in a free air stream. SAE Technical Paper 1999-01-3307. 1999. https://doi.org/10.4271/1999-01-3307

[12] Thornhill D, Graham A, Cunnigham G, Troxler P, Meyer R. Experimental investigation into the free air-cooling of air-cooled cylinders. SAE Technical Paper 2003-32-0034. 2003. https://doi.org/10.4271/2003-32-0034

[13] Thornhill D, Stewart A, Cuningham G, Troxler P, Meyer R, Price B. Experimental investigation into the temperature and heat transfer distribution around air-cooled cylinders. SAE Technical Paper 2006-32-0039. 2006. https://doi.org/10.4271/2006-32-0039

[14] Yoshida M, Soichi Ishihara S, Murakami Y, Nakashima K, Yamamoto M. Air-cooling effects of fins on a motorcycle engine. JSME Int J B-Fluid T. 2006;49(3):869-875. https://doi.org/10.1299/jsmeb.49.869

[15] Yoshida M, Nakashima K, Nishii K, Hirai S, Ozaki S, Okura N. Cooling characteristics of air-cooled cylinder with fins with slits under forced convection (3rd Report, Cooling effects of number of slits in front). Des Eng. 2025;60(2):109-118 (in Japanese). https://doi.org/10.14953/jjsde.2024.3030

Prof. Kohei Nakashima, DEng. – Department of Vehicle and Mechanical Engineering, Meijo University, Nagoya, Japan.

e-mail: *nakasima@meijo-u.ac.jp*

Ass. Prof. Masao Yoshida, DEng. – Department of Vehicle and Mechanical Engineering, Meijo University, Nagoya, Japan.

e-mail: *yosida@meijo-u.ac.jp*

Kento Nishii, MEng. – Department of Vehicle and Mechanical Engineering, Meijo University Graduate School, Japan.

e-mail: *23343106@ccalumni.meijo-u.ac.jp*

Ayanari Yoshida, BEng. – Department of Vehicle and Mechanical Engineering, Meijo University Graduate School, Nagoya, Japan.

e-mail: *253431022@ccmailg.meijo-u.ac.jp*

Prof. Nobuyuki Okura, DEng. – Department of Vehicle and Mechanical Engineering, Meijo University, Nagoya, Japan.

e-mail: *ohkura@meijo-u.ac.jp*

Article citation info:
Czarnigowski J, Skiba K, Kida M, Jakliński P. Simple dynamic model of a PEM-type fuel cell. Combustion Engines. 2025;202(3):147-153. https://doi.org/10.19206/CE-207423

Jacek CZARNIGOWSKI
Krzysztof SKIBA
Marek KIDA
Piotr JAKLIŃSKI

Combustion Engines
Polish Scientific Society of Combustion Engines

Simple dynamic model of a PEM-type fuel cell

ARTICLE INFO

Received: 1 June 2025
Revised: 22 June 2025
Accepted: 22 June 2025
Available online: 12 July 2025

This paper presents a heuristic zero-dimensional model of a PEM-type fuel cell including dynamic states. The model is based on the static energy characteristics of the cell as a function of the voltage generated from the current drawn from the cell. The model was supplemented with a module of inertia under load change and the cleaning process. The phenomenon of cell efficiency decrease under the influence of water accumulation on the cathode side and purging of the cell, controlled by purging and short-circuiting, was also taken into account. The simulation and research results for the Horizon 300 W fuel cell are shown. Measurements and simulations were compared to demonstrate the model's high accuracy.

Key words: *fuel cell, model, static, dynamic, power*

1. Introduction

With the growing challenges of climate change, depletion of fossil fuel resources, and the need to reduce greenhouse gas emissions, the development of renewable energy technologies is becoming one of the key directions for research and technological innovation. Hydrogen, as a clean and high-energy fuel, is becoming increasingly important in the context of the energy transition. Its use in fuel cells, which enable emission-free conversion of chemical energy into electricity, is a promising alternative to conventional energy technologies.

Today, the European Union is pursuing its declared hydrogen strategy to achieve climate neutrality by 2050 [14, 22]. Hydrogen, especially so-called green hydrogen (produced using renewable energy sources), plays a key role in this transition. The strategy, also adopted by the member countries [23], includes the following actions [14]:

1. Increasing the share of hydrogen in the energy sources. Currently, hydrogen accounts for only about 2% of the EU's energy consumption, with most of it coming from fossil fuels. The Union's objective is to significantly increase the share of low-carbon hydrogen, primarily green hydrogen, in total energy consumption.
2. Green hydrogen development. The EU is emphasising the development of green hydrogen, which produces no CO_2 emissions. Although its production is currently more expensive than grey or blue hydrogen, the strategy includes investment in RES-powered electrolysers, reducing production costs through technology scaling, and support for research and innovation in electrolysis process efficiency.
3. Hydrogen applications in industry and transport. Hydrogen is expected to replace fossil fuels in sectors difficult to decarbonise, such as steel and chemical industries, heavy transport (trucks, railways, ships), energy storage, and grid stabilization.
4. Integration of energy systems. Hydrogen to act as an energy carrier and store, enabling seasonal integration of RES (e.g. surplus energy from photovoltaics in summer can be converted to hydrogen and used in winter).
5. Integration of energy systems. Hydrogen to act as an energy carrier and store, enabling seasonal integration of RES (e.g. surplus energy from photovoltaics in summer can be converted to hydrogen and used in winter).

Fuel cells are being considered as one of the key technological solutions [22]. Fuel cells, and in particular Proton Exchange Membrane Fuel Cell (PEMFC) hydrogen cells, are characterized by their high efficiency, low emissions, and ability to operate over a wide power range. Thanks to these properties, they find applications in both transport (cars, buses, trains) and stationary systems (emergency power, microgrids). However, despite their numerous advantages, the widespread deployment of fuel cells faces a number of technological and economic challenges, including production costs, component durability, and optimisation of the processes inside the cell [2, 7, 17].

Fuel cells as part of machine power systems are an important element in the energy efficiency of a machine. The static and dynamic characteristics of the cell make it necessary to adapt and optimise the power supply and control systems. This is easier with whole-machine (system-level) simulation methods. In most cases, it is not necessary to develop models describing the exact phenomena taking place in the cell (including physico-chemical phenomena, gas and heat flow), but they can be replaced by simplified models based on empirical data. This approach is often used in the development of system models [6, 10, 13, 20].

The aim of this article is to present a mathematical model describing the operation of a hydrogen fuel cell of the PEMFC type. A simple model has been developed, including the dependence of the current generated by the cell on the system voltage, taking into account not only its static characteristics, but also dynamic phenomena.

2. Simple fuel cell model

The basic assumption of the model was to obtain a simple form of the model that is as easy to identify as possible (with a small number of parameters), giving the model's response to the cell's operating conditions, which is correct in terms of both static and dynamic conditions. Due to the availability of measurement data, it was decided to use an empirical model instead of a physical model, which is an acceptable method for creating simplified models [10].

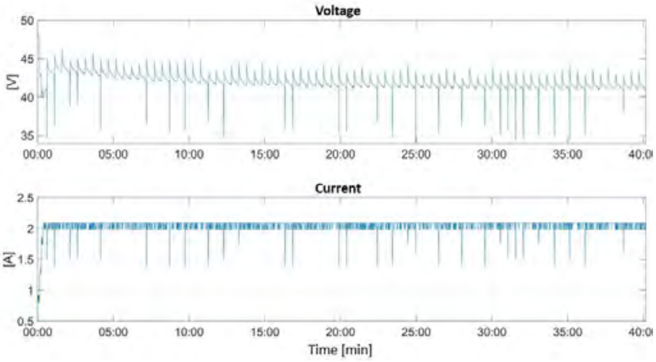

Fig. 1. Voltage and current flow for Spectronik Protium-450 fuel cell

From the testing of a Spectronik Protium-450 cell equipped with a control system that optimizes its performance (Fig. 1), it was noted that, in addition to the static characteristics of the voltage-current dependence of the cell's load, there are changes due to inertia during load spikes and changes due to the cell's cleaning process. This can be seen as periodic (with a frequency of about 60 s) voltage spikes.

It was therefore proposed that the model should take into account three phenomena: the static characteristics, the dynamic characteristics resulting from inertia under load change, and the cell cleaning characteristics. The components of the model are described below.

The simple fuel cell model is the relationship of the output voltage from the cell as a function of load (current) and time. The model, according to the assumption described above, is divided into three components:

$$\mathrm{U_{FC} = U_P + U_{Dyn} + U_{Purg}} \tag{1}$$

where: $\mathrm{U_P}$ – static fuel cell characteristic (polarization curve); $\mathrm{U_{Dyn}}$ – dynamic fuel cell characteristic; $\mathrm{U_{Purg}}$ – dynamic fuel cell characteristic during cleaning.

The first component of the model is the static characteristics of the cell. This is termed the polarization curve [1, 3]. This curve (Fig. 2) is characteristic of all PEM fuel cells and is divided into three regions: an initial activation region where the voltage decreases logarithmically with increasing current, a ohmic region where increasing current causes a linear decrease in voltage and a mass transport region where further increases in current lead to an exponential decrease in voltage. There are many simplified models describing these characteristics [1, 3, 9, 15]. These are based on a simple description of the physical phenomena occurring in the cell. The proposed model, however, adopts a much simpler approach based on an approximation of test results.

$$\mathrm{U_P = f(I)} \tag{2}$$

where: I – current, A.

The second component of the model is related to the dynamic response of the cell during a step change in load. As tests have shown (Fig. 3), with a step increase in load change, the system needs time to decrease the voltage (with respect to the polarization curve) and then asymptotically return to the polarization curve [11]. With a step decrease in load, the opposite occurs – a temporary increase in voltage relative to the polarization curve. As described in the articles [8, 11, 18, 20], this is due to the inertia of the phenomena occurring in the cell, mainly related to mass transport both to the membrane region and in the membrane structure. The phenomenon can therefore be described as:

$$\mathrm{U_{Dyn} = -k_{Dyn} \cdot \frac{dU}{dt}} \tag{3}$$

where: $\mathrm{k_{Dyn}}$– model parameters – fuel cell inertia.

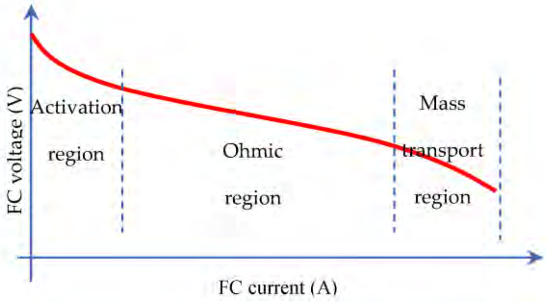

Fig. 2. Nonlinear U = f(I) characteristic of the fuel cell [3]

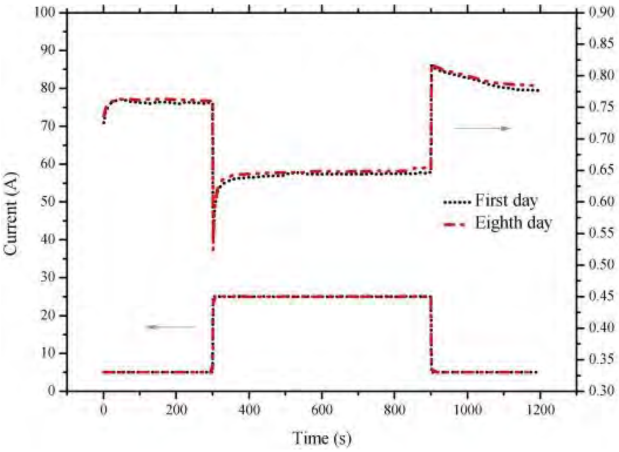

Fig. 3. Dynamic response of the fuel cell [11]

The final component of the model is the segment responsible for changing the polarization curve as a result of cleaning the cell. The effectiveness of the membrane depends, among other things, on the amount of accumulated water (or water vapor) on its surface and in its surroundings. This vapor is generated by the oxidation of hydrogen on the cathode side, but some of it enters the anode side, obstructing the flow of hydrogen to the membrane, reducing its efficiency. To prevent this phenomenon, periodic cleaning of the anode side is used [4, 5, 11, 16]. This is done by short-circuiting the cell (to evaporate the water) and opening the through-valve (purge) and blowing off a small amount of hydrogen with the water vapor. The result of this action is a temporary increase in the cell's efficiency, followed by a slow return to the basic polarity curve (Fig. 4). The frequency of purging and its intensity are selected to suit the design parameters and operating conditions of the cell.

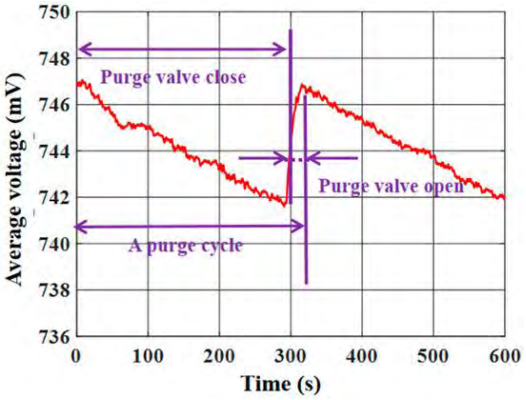

Fig. 4. The voltage variation of the average single cell under traditional long-cycle purge intervals [11]

In the developed model, the following function was adopted to describe this action:

$$U_{Purg} = \Delta U_{max} + \Delta U_{tot} \cdot \left(\frac{1}{e^{k_C \cdot t}} - 1\right) \tag{4}$$

where: ΔU_{max} – maximum increase over polarization curve; ΔU_{tot} – total possible drop of characteristic under polarization curve; k_C – model parameter; t – time form last cleaning process.

It should also be remembered that the implementation of cleaning causes a step change in the load of the cell. During a short-circuit, a much higher current flows through the cell (resulting from the low resistance of the cell). This change must therefore be taken into account in the calculation according to the formula:

$$I = \begin{cases} I_{Load}, & Purge = off \\ I_{Short}, & Purge = on \end{cases} \tag{5}$$

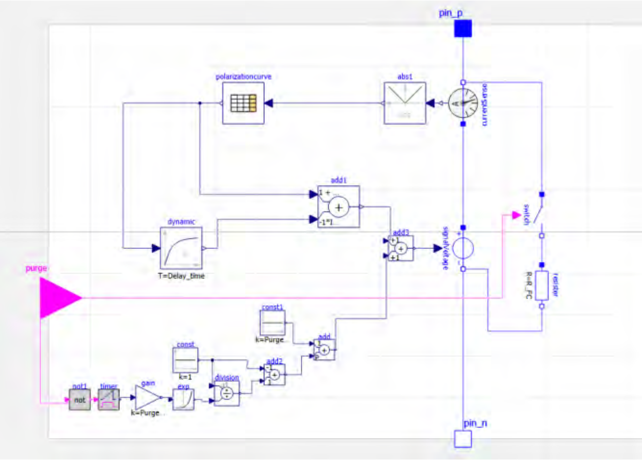

Fig. 5. Fuel cell model implementation in Modelica

The above model was implemented in the Modelica environment. Figure 5 shows the developed model, which is a component of an electrical circuit connected by pins (pin_p and pin_n) to an electrical circuit. A data matrix interpolation element using the continuous derivative method is responsible for the static model. Below this is the element responsible for the inertia of the system under dynamic load changes and at the bottom is the cell cleaning model. The model thus prepared was subjected to an identification process.

3. Model identification

3.1. Object research

The developed model, implemented in the Modelica environment, requires parameter identification. To this end, tests were carried out on a selected cell model equipped with an integrated control system performing the purification function automatically. Details are provided below.

The object of the study is a PEMFC Horizon 300 type cell from Horizon (Fig. 6). It is a cell consisting of 60 open-cathode cells with a nominal power of 300 W. Detailed data are provided in Table 1.

Table 1. Parameters of Horizon 300 fuel cell [21]

Fuel cell	Horizon 300
Type	PEM
No. of cells	60
Architecture	Open cathode
Coolant	Air cooled
Rated power	300 W
Rated current	8.3A
Voltage output	32–54 VDC
Start-up time	< 30 s
Hydrogen gas	Dry, 99.999% purity
Delivery pressure	0.4–0.5 bar
Fuel consumption	3.9 dm^3/min

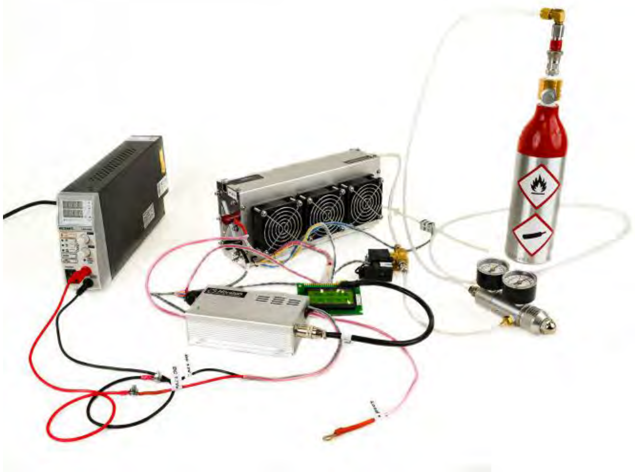

Fig. 6. Object of the research – Horizon-300W fuel cell [21]

3.2. Test stand

The research was carried out at the Lublin University of Technology. The hydrogen cell was supplied from a 0.4-litre bottle via a Spectronik EMPR regulator. The cell was connected to a current load EA-EL 3080-60 B, allowing the electrical load of the cell to be varied. Control of the cell was performed by a system that was an integral part of the cell. Current and voltage were measured using an oscilloscope, Tektronix TBS1052C 50 MHz, with a data recording card and current probe, Tektronix TCP0030A, plus an amplifier, Tektronix TCPA300. A schematic of the test bench is shown in Fig. 7 and Fig. 8. Measurements were taken at a frequency of 1 kHz. The measurement error of the voltage was 0.003 V, and the current was 0.01 A.

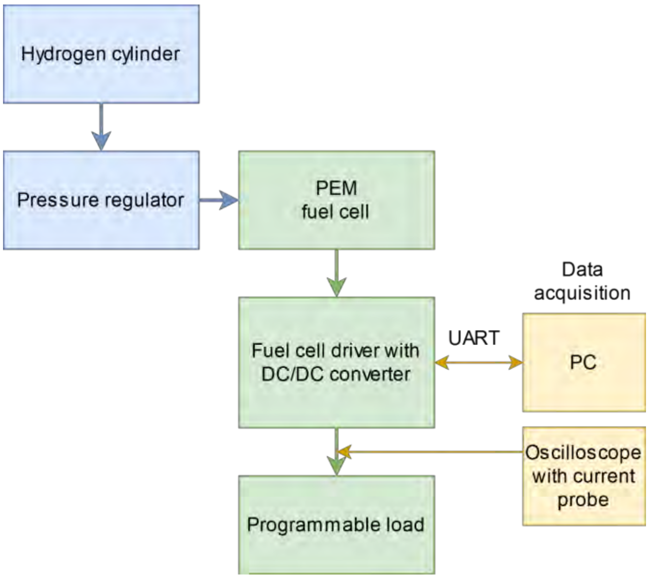

Fig. 7. Test stand block diagram

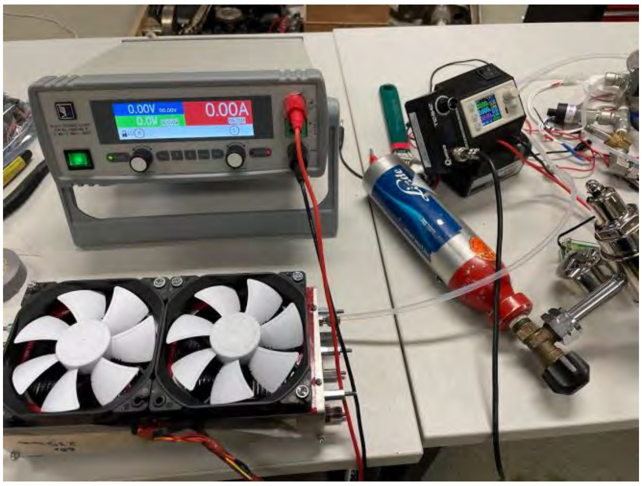

Fig. 8. Test stand

3.3. Methodology

The identification tests were divided into 2 parts. In the first, tests were carried out under steady-state conditions, and in the second, under dynamic conditions.

The first part involved determining the polarization curve of the cell when the purification system was switched off. For this purpose, the cell was loaded with a specific current and, after stabilization of its operation (a period of 1 minute), the voltage was measured. Measurements were carried out with increasing and decreasing load on then the average value was drawn.

The second part of the research was carried out in a set resistance system allowing for a step change in the load of the fuel cell between 65 and 130 W. Variations were performed with a current load on a 10 second cycle: 5 s – 65 W load, 5 s – 130 W load. In one cycle, there was both a step increase and a step decrease of the load. In addition, a purge circuit operating at 1 Hz was active in this experiment.

3.4. Analysis

The first part of the study involved the determination of the polarization curve. The result is shown in Fig. 9. The shape of the curve is consistent with the literature data [1, 3, 13, 16]. It should be noted that the power obtained is significantly less than that declared by the manufacturer. The maximum power, located at the end of the ohmic part of the curve (see Fig. 2), was 150 W (30 V · 5 A) against a rated 300 W (see Table 1). This is due to the high degradation of the cell. The test unit was used for six years as part of the activities of the Student Scientific Club of Aerospace Propulsion in the Shell Eco-marathon competition.

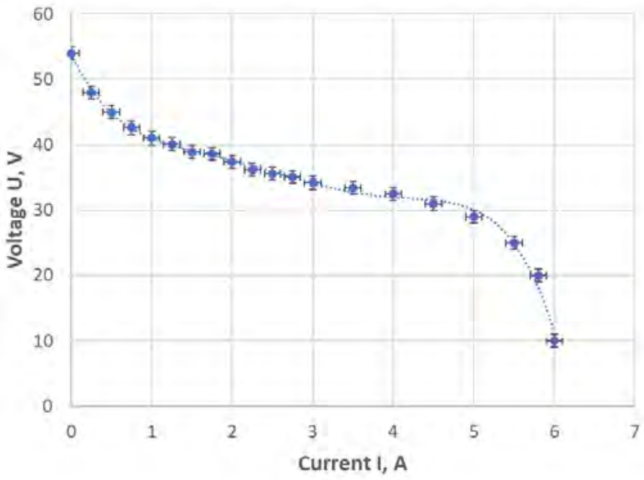

Fig. 9. Static characteristic of fuel cell – polarization curve

The second part of the research included load cycling and the operation of the cleaning system. Four load cycles were carried out. The results are presented in Fig. 10 and Fig. 11. The inertia of the system can be seen – when the load is activated, the voltage momentarily drops below the base value and the current increases, while when the load is deactivated, there is a momentary increase in voltage. The operation of the purge system causes, after the circuit output current drops due to a short circuit, a jump in the efficiency of the cell – an increase in both voltage and current, followed by a slow decrease in both values to the level of the polarization curve.

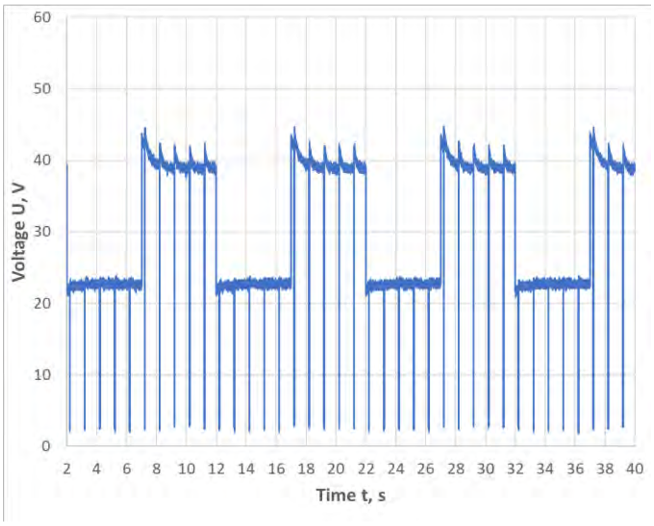

Fig. 10. Voltage during changed load conditions

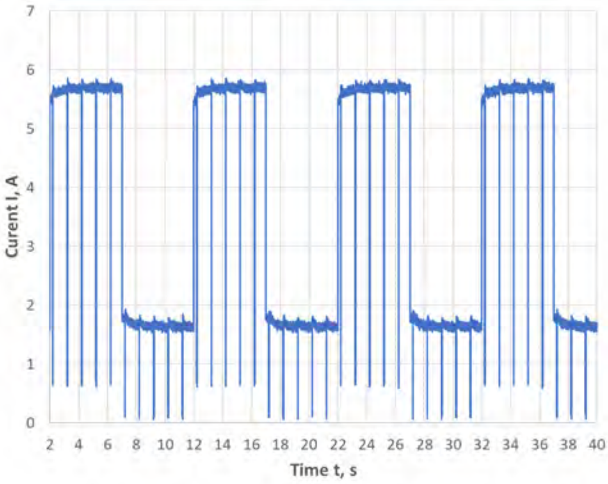

Fig. 11. Current during changed load conditions

3.5. Model parameters identification

As the model developed in Modelica used the derivative continuity approximation module to determine the polarization curve, it was therefore not necessary to determine the parameters of this model. The characteristics based on the test results shown in Fig. 9 were used for further calculations.

Figures 12–15 show the results of the measurements compared with the simulation results of the developed model. The blue line shows the bench measurements, the green line the model without the cleaning module (only with the dynamic module), and the orange line the results of the full model.

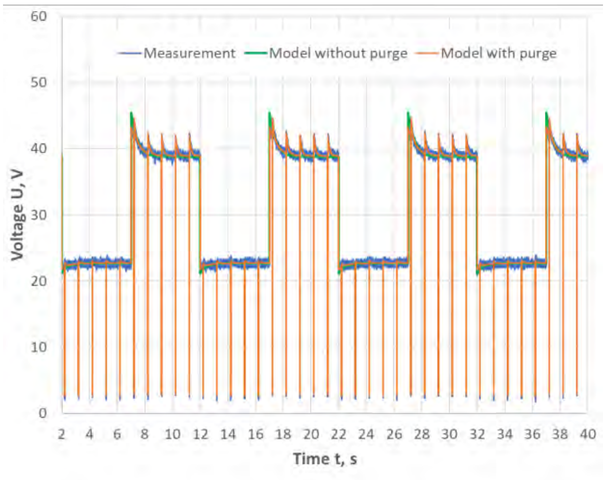

Fig. 12. Voltage measurement and simulation during changed load conditions

The identification of the dynamic model parameters and the cleaning were divided into two separate operations, but based on the same set of measurement data. Using the results of the bench tests described above, the identification of the dynamic model parameter was carried out using the least squares method, with the focus on obtaining a correct representation of the system inertia. A model with a concordance of R = 0.853 was obtained, although this was compared with the tests of the system with active cleaning. Figures 12–15 show the effect of the cell inertia.

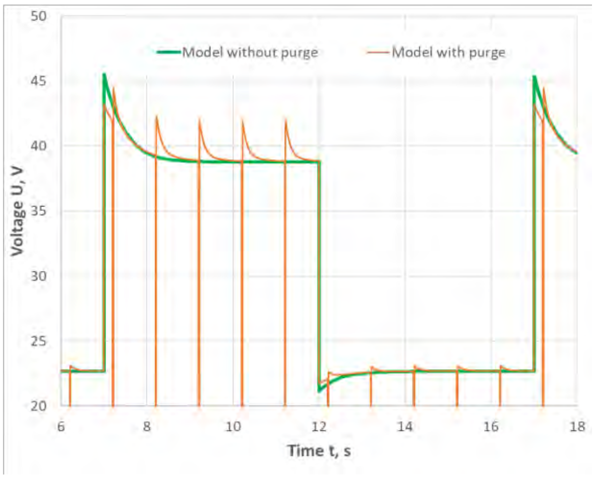

Fig. 13. Voltage simulation with and without active cleaning module during changed load condition

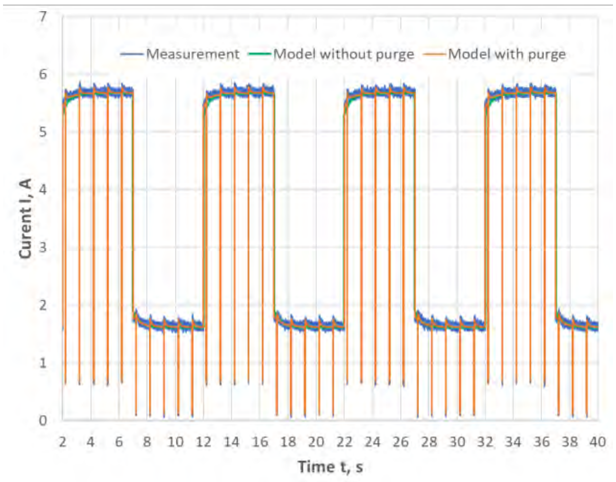

Fig. 14. Current measurement and simulation during a changed load condition

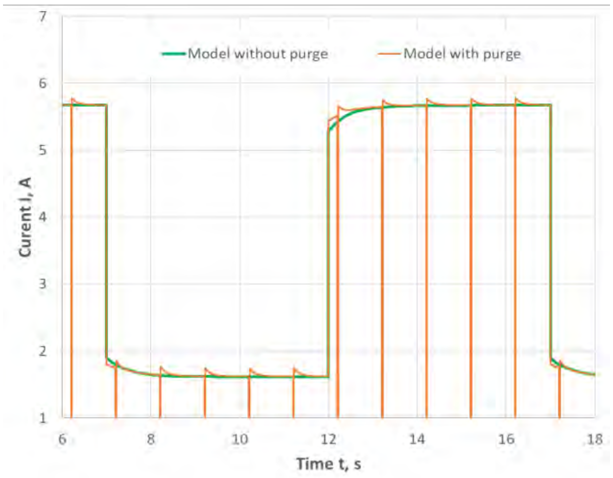

Fig. 15. Current simulation with and without active cleaning module during changed load condition

After the identification of the dynamic model, the identification of the cleaning model was performed. Again, the least squares method was used, with the simulation work performed on the model with the dynamic module parameters already identified. In this case, a much higher compliance performance R = 0.958 was obtained. Figures 13 and 15 show the difference in the behaviour of the model with the cleaning module on and off. Cleaning, as reported in the literature described in chapter 2 of this article, leads to a periodic increase in the capacity of the cell, despite the occurrence of temporary interruptions in the energy supply to external systems. The purpose of the purification process is to remove water accumulating on the cathode side. Water blocks the flow through the membrane, which causes a decrease in cell efficiency. Water accumulation also causes membrane degradation and a decrease in service life. Therefore, this process is carried out despite the fact that it causes fuel losses (fuel is blown into the atmosphere). According to publications [4, 5, 11, 16], this reduces the overall efficiency of the cell by about 10%, but extends its service life more than threefold.

The parameters of both models are shown in Table 2.

Table 2. Parameters of the dynamic and cleaning module

Parameter	Value
k_{Dyn}	0.541
ΔU_{max}	3.00
ΔU_{tot}	3.12
k_c	10.03

4. Summaries

A simple fuel cell model was developed, describing both the static characteristics of the polarization curve and also the dynamics of the model during load changes and the change in cell performance after the cleaning process. The model was developed as an empirical model by simplifying a physical description of the phenomena occurring inside the fuel cell. However, based on measurement data, a model with very high correlation with measurement results was obtained. A correlation of R = 0.958 was obtained.

The polarization curve obtained during the tests shows a significant reduction in cell performance resulting from wear and tear. The drop in power relative to the catalogue parameters is approximately 50%. During sudden load changes, there is a temporary deviation from the polarization curve of approximately 15% (with an increase in load, the voltage drops by 3.5 V from the nominal 23 V, and with a decrease in load, the voltage increases by 7.3 V from the nominal 28 V). Stabilization occurs after approximately 2 seconds.

Cleaning the cell causes a temporary increase in efficiency (increase in voltage relative to the polarization curve) of approximately 7%, with a return to the nominal value occurring after just 0.7 seconds.

Thanks to its simplicity, this model can be very easily identified for any fuel cell and thus provides a tool for simulation and optimizing control systems and powerplant systems using the cell as an energy source. The introduction of a cleaning model also allows the energy efficiency optimization of the cell by selecting the frequency of cleaning occurrence.

Acknowledgements

This work was supported by the Project 'Research platform of methods of optimizing the life cycle of modern vehicles' financed from the funds of the state budget, a specific subsidy of the Minister of Education and Science, contract no: MEiN/2023/DPI/2729 from 19.09.2023.

Nomenclature

PEM, PEMFC	proton exchange membrane fuel cell	I	current
U	voltage	t	time

Bibliography

[1] Andronie A, Stamatin I, Girleanu V, Ionescu V, Buzbuchi N. Simplified mathematical model for polarization curve validation and experimental performance evaluation of a PEM fuel cell system. Procedia Manuf. 2019;32:810-819. https://doi.org/10.1016/j.promfg.2019.02.289.

[2] Behling NH. Fuel cells: current technology challenges and future research needs. Newnes. 2012. https://doi.org/10.1016/C2011-0-04424-1

[3] Belhaj FZ, El Fadil H, El Idrissi Z, Intidam A, Koundi M, Giri F. New equivalent electrical model of a fuel cell and comparative study of several existing models with experimental data from the PEMFC Nexa 1200 W. Micromachines. 2021;12(9):1047. https://doi.org/10.3390/mi12091047

[4] Chen S, Tian A, Han C. Study on purging strategy of polymer electrolyte membrane fuel cell under different operation conditions. Processes. 2023;11(1):290. https://doi.org/10.3390/pr11010290

[5] Cheng Z, Luo L, Huang B, Jian Q. Dynamic analysis of internal reactants and water content distribution during anode purge in a proton-exchange membrane fuel cell. Int J Energy Res. 2021;45:10609-10629. https://doi.org/10.1002/er.6548

[6] Domke J. Generic methods for optimization-based modeling. Proceedings of the Fifteenth International Conference on Artificial Intelligence and Statistics, PMLR. 2012;318-326. http://proceedings.mlr.press/v22/domke12/domke12.pdf

[7] Faghri A, Guo Z. Challenges and opportunities of thermal management issues related to fuel cell technology and modeling. Int J Heat Mass Tran. 2005;48(19-20):3891-3920. https://doi.org/10.1016/j.ijheatmasstransfer.2005.04.014

[8] Friede W, Rael S, Davat B. Mathematical model and characterization of the transient behavior of a PEM fuel cell. IEEE T Power Electr. 2004;19(5):1234-1241. https://doi.org/10.1109/TPEL.2004.833449

[9] Georgakis D, Papathanassiou S, Manias S. Modeling and control of a small scale grid-connected PEM fuel cell system. IEEE 36th Power Electronics Specialists Conference, Dresden. 2005:1614-1620. https://doi.org/10.1109/PESC.2005.1581846

[10] Gosavi A. Simulation-based optimization. Springer New York 2015;62. https://doi.org/10.1007/978-1-4899-7491-4

[11] Guo W, Mu X, Shen W, Ma C, Yu J, Wang F et al. The purge characteristics and strategy in a proton exchange

membrane fuel cell with a linear segmentation-based anode recirculation system. Energies. 2025;18(9):2156. https://doi.org/10.3390/en18092156

[12] Guo Z, Chen H, Guo H, Ye F. Dynamic response and stability performance of a proton exchange membrane fuel cell with orientational flow channels: an experimental investigation. Energ Convers Manage. 2022;274:116467. https://doi.org/10.1016/j.enconman.2022.116467

[13] Hasikos J, Sarimveis, H, Zervas PL, Markatos NC. Operational optimization and real-time control of fuel-cell systems. J Power Sources. 2009;193(1):258-268. https://doi.org/10.1016/j.jpowsour.2009.01.048

[14] Koneczna R, Cader J. Hydrogen in the strategies of the European Union Member States. Gospodarka Surowcami Mineralnymi – Mineral Resources Management. 2021; 37(3);53-74. https://doi.org/10.24425/gsm.2021.138660

[15] Manoharan P, Ravichandran S, Kavitha S, Hashim TJT, Alsoud AR, Sin TC. Parameter characterization of PEM fuel cell mathematical models using an orthogonal learning-based GOOSE algorithm. Sci Rep. 2024;14:20979. https://doi.org/10.1038/s41598-024-71223-7

[16] Pei Y, Chen F, Jiao J, Liu S. Analysis and control strategy design for PEMFC purging process. Energy. 2024;290: 130233. https://doi.org/10.1016/j.energy.2024.130233

[17] Sazali N, Wan Salleh WN, Jamaludin AS, Mhd Razali MN. New perspectives on fuel cell technology: a brief review. Membranes. 2020;10(5):99. https://doi.org/10.3390/membranes10050099

[18] Sharifi Asl SM, Rowshanzamir S, Eikani MH. Modelling and simulation of the steady-state and dynamic behaviour of a PEM fuel cell. Energy. 2010;35(4):1633-1646. https://doi.org/10.1016/j.energy.2009.12.010

[19] Xue XD, Cheng KWE, Sutanto D. Unified mathematical modelling of steady-state and dynamic voltage–current characteristics for PEM fuel cells. Electrochim Acta. 2006; 52(3):1135-1144. https://doi.org/10.1016/j.electacta.2006.07.011

[20] Zhao H, Burke AF. Optimization of fuel cell system operating conditions for fuel cell vehicles. J Power Sources. 2009; 186(2):408-416. https://doi.org/10.1016/j.jpowsour.2008.10.032

[21] Horizon Education H-Series Fuel Cell Stacks, producer catalog. https://www.horizoneducational.com/h-300-pem-fuel-cell-300w/p1351 (accessed on 29.05.2025).

[22] EC 2020 A hydrogen strategy for a climate-neutral Europe. Communication from the Commission to the European Parliament. The Council, The European Economic and Social Committee and the Committee of the Regions. COM(2020) 301. Brussels, 8.7.2020.

[23] Polish Hydrogen Strategy until 2030 with a perspective until 2040. Ministry of Climate and Environment, Resolution 149 of the Council of Ministers of 2 November 2021 (pos. 1138) – in Polish.

Prof. Jacek Czarnigowski, DSc., DEng. – Faculty of Mechanical Engineering, Lublin University of Technology, Poland.

e-mail: *j.czarnigowski@pollub.pl*

Marek Kida, MEng. – Faculty of Electrical Engineering and Computer Science, Lublin University of Technology, Poland.

e-mail: *m.kida@pollub.pl*

Krzysztof Skiba, MEng. – Faculty of Electrical Engineering and Computer Science, Lublin University of Technology, Poland.

e-mail: *k.skiba@pollub.pl*

Prof. Piotr Jakliński, DSc., DEng. – Faculty of Mechanical Engineering, Lublin University of Technology, Poland.

e-mail: *p.jaklinski@pollub.pl*

Article citation info:
Wojciechowski H, Merkisz J. Results repeatability evaluation of exhaust emission data obtained in laboratory WLTC test conditions using stationary and PEMS analysers. Combustion Engines. 2025;202(3):154-161. https://doi.org/10.19206/CE-208399

Hubert WOJCIECHOWSKI
Jerzy MERKISZ

Combustion Engines
Polish Scientific Society of Combustion Engines

Results repeatability evaluation of exhaust emission data obtained in laboratory WLTC test conditions using stationary and PEMS analysers

ARTICLE INFO

Received: 10 June 2025
Revised: 4 July 2025
Accepted: 18 July 2025
Available online: 2 August 2025

The article presents an assessment of the repeatability of exhaust emission results in the WLTC test using two types of measurement systems: stationary laboratory analysers and a PEMS. The tests were conducted in laboratory conditions at BOSMAL Institute of Automotive Research and Development on a passenger car with a gasoline engine on a chassis dynamometer. The assessment included CO_2, CO, NO_x, THC emissions, and the particle number in each phase of the WLTC test and in the entire test. The coefficient of variation was used to assess the repeatability. The results showed greater repeatability of measurements in the case of laboratory analysers, especially for CO_2 and CO. The PEMS system showed greater variability, especially in the dynamic test phases. Despite this, the results validation confirmed the compliance of the PEMS system with regulatory requirements. The article emphasizes the importance of the precision of exhaust emission tests in the context of measurement technologies development and the implementation of more restrictive emission standards, and it indicates CO_2 as the most stable parameter for both systems.

Key words: *WLTC, PEMS, exhaust emissions, repeatability, analysers*

1. Introduction

Modern exhaust emission regulations require vehicle manufacturers to monitor the emissions more and more precisely in various operating conditions. Consequently, precise measurement and analysis of vehicle exhaust emissions are increasingly crucial in the context of reducing the negative impact of motorization on the environment. In addition to classic homologation tests on chassis dynamometers, emission tests in real conditions (RDE) are becoming increasingly important, carried out using smaller devices collectively classified as PEMS. Due to various environmental, operational, and hardware factors, these systems may show greater variability of measurement results compared to their stationary laboratory analyser counterparts. The aim of this article is to assess the repeatability of exhaust emission measurement results obtained in the WLTC test, performed using both of the above-mentioned measurement systems, with particular emphasis placed on the statistical analysis of the coefficient of variation. The issue of exhaust emission test results repeatability has been addressed in numerous research works, although it is still an area with a limited number of empirical analyses. Chłopek and Rostkowski [7] emphasized the importance of formalizing the repeatability assessment of combustion engines operating properties, including exhaust emissions. Studies have shown that CO and NO_x emission measurements are highly sensitive to random disturbances, which translates into difficulties in obtaining stable results. Jaworski et al. [13] conducted an emissions repeatability analysis in cold and hot engine start conditions in the NEDC test. The results confirmed the validity of using the coefficient of variation (CV) as an assessment tool for measuring reliability. Andrych-Zalewska et al. [2–4] focused on emission tests in dynamic conditions and in the RDE test. Their works emphasize the influence of engine operating states (e.g. torque, temperature) on the exhaust emission level, also paying attention to the differences resulting from the test methodology. One of the newer publications [2] analysed emission data from a full WLTC cycle and proposed methods for assessing the measurement data variability. The article by Merkisz et al. [14] is also particularly important, as it directly concerns the repeatability of WLTP test results. In this work, additional indicators were used besides CV (r – the ratio of extreme values to the mean and k – the cold/hot ratio), which allow for a broader interpretation of data variability.

The literature review shows that while the coefficient of variation remains the basic statistical measure of emissions repeatability, it is also important to take into account the environmental conditions, the thermal state of the engine, and the phase of the driving cycle in which the measurement was made.

2. Test method

The tests were carried out at the BOSMAL Automotive Research and Development Institute on the AVL Zoellner 48” Compact chassis dynamometer in laboratory no. 1 (Fig. 1). The dynamometer was fully integrated with the laboratory management system (AVL iGEM). The system was controlled by software that allowed not only to carry out exhaust emission tests in accordance with international test cycles (such as European cycles: WLTC, RTS95 – RDE, NEDC, WMTC; American: FTP-75, HWFET, US06; and the former Japanese cycle: JC08), but also allowed for measuring engine power in both static and dynamic conditions [6]. The laboratory system used the method of analysing diluted gases using the CVS system, collected in measuring bags, while the PEMS system recorded the emission of undiluted gases in real time. The coefficient of variation (CV), calculated separately for each phase of the cycle and the entire test, was used to assess repeatability. Each vehicle test that involves using portable exhaust measuring systems (PEMS) must be preceded by validation performed on a chassis dynamometer. The validation procedure is used to verify the correct installation and operation of the device. The PEMS system has been subjected to a validation procedure in accordance with Commission Regulation (EU) 2017/1151 and 2023/443 [9–12].

The air conditioning system in laboratory No. 1 enabled the following functions [1]:
- Temperature control in the range from +14°C to +28°C
- Maintaining a stable temperature during tests with an accuracy of ±2.0°C
- Regulating the humidity level from 5.5 to 12.2 grams of water per kilogram of dry air at temperatures between +14°C and +28°C
- Maintaining the target relative humidity with an accuracy of ±5% during tests.

The tests were conducted on a chassis dynamometer in accordance with the WLTP cycle procedures. The WLTP procedure has been used in Europe since September 2017, replacing the older NEDC cycle. As with the NEDC and EPA, the WLTP test is conducted in a laboratory setting. However, the WLTP cycle (Fig. 2) is divided into four parts, which correspond to different speed ranges: low, medium, high, and very high. The entire test lasts 30 minutes and covers 23.25 km of distance. The test route is a combination of urban and motorway conditions – 52% being city driving and 48% being on the motorway. The average test speed is 46.5 km/h, and the maximum speed is 131 km/h [5]. Unlike the NEDC, the WLTP test considers different vehicle equipment levels and tire and wheel configurations. The tire/wheel combination has an impact on the fuel consumption and vehicle range, as it changes the aerodynamics and increases the unsprung mass, depending on the wheel and tire size.

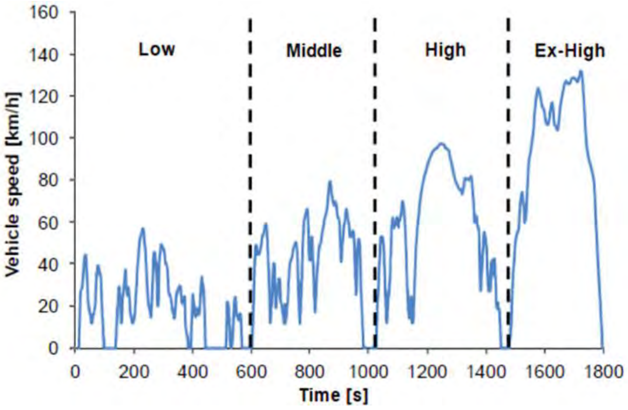

Fig. 2. The WLTP test cycle [5]

The vehicle used for the tests was a Skoda Scala with a 1.0 TSI petrol engine (Euro 6), equipped with a 5-speed manual gearbox. Emissions were measured simultaneously using a stationary laboratory system and PEMS. The test was performed five times by one experienced driver. Before each test, the car was thermally stabilized at a temperature of 21°C, as outlined by the regulations.

Table 1. Data of the vehicle used in the study

Vehicle designation	Car
Brand	Skoda
Model	Scala
Fuel type	Petrol
Engine type	TSI
Engine displacement [dm^3]	1
Power [kW]	81
Transmission	Manual 5-speed
Emission standard	Euro 6
Vehicle mileage [km]	7208

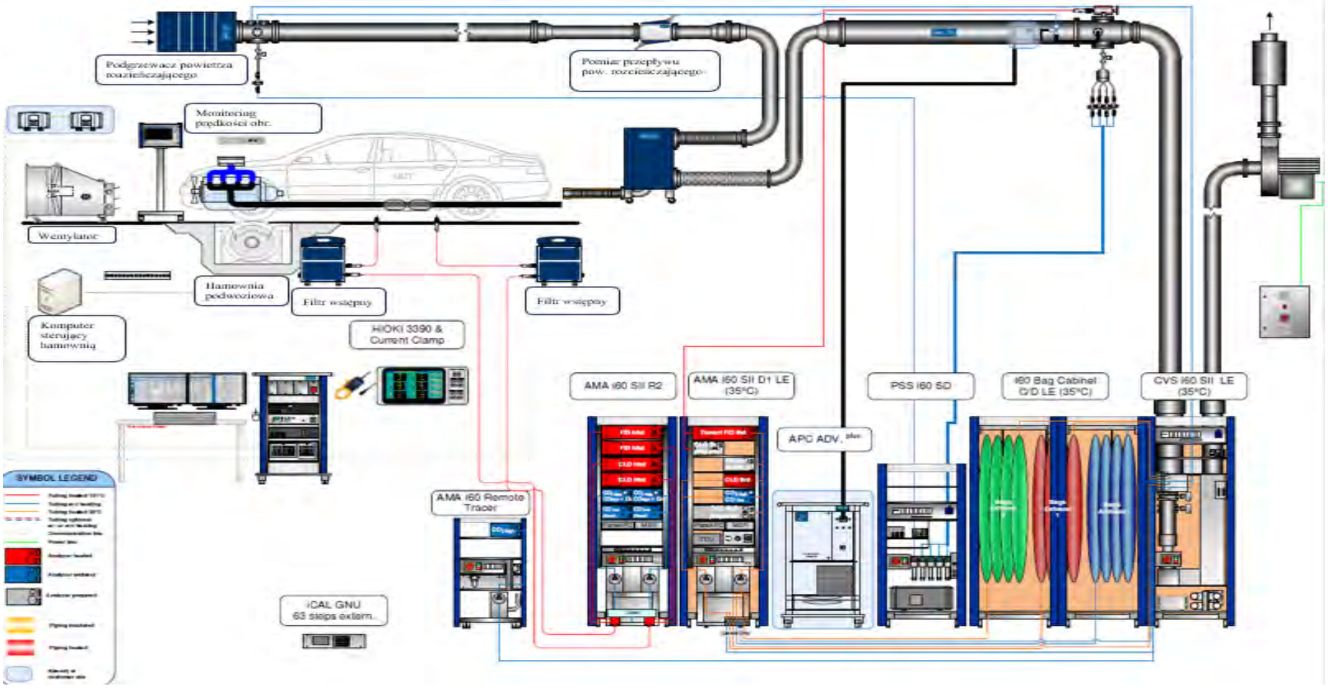

Fig. 1. Laboratory 1 equipment and setup schematic [1]

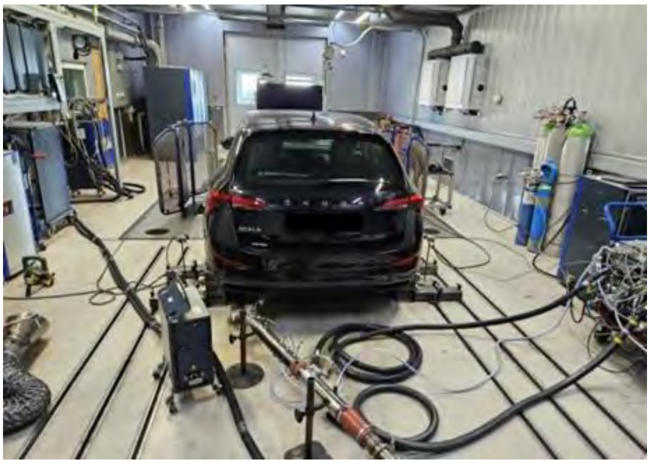

Fig. 3. The test vehicle during testing on the chassis dynamometer in the laboratory

To assess the repeatability of emission results, a detailed statistical analysis was performed. For each phase of the WLTC test, i.e. LOW, MIDDLE, HIGH, Ex-HIGH and the entire WLTC cycle, the arithmetic mean, standard deviation and coefficient of variation (CV) [15] were determined. The arithmetic mean was used to determine the typical emission level in each test phase, while the standard deviation was used to assess the dispersion of the results around the mean, indicating the stability of the measurements.

The main assessment method relied on the coefficient of variation (CV), which was calculated according to the formula:

$$CV = \frac{\sigma}{\mu} \cdot 100\ [\%] \tag{1}$$

where: σ – is the standard deviation, and μ is the arithmetic mean for a given phase; CV – shows the relative variability of the data, regardless of the mean emission scale, which allows for results repeatability comparison in phases with significantly different emission levels.

To assess the repeatability of measurement results in detail, a percentage-based classification of the coefficient of variation (CV) was used, in accordance with recommendations from statistical and technical literature [8, 14, 15].

- CV < 25% – Low variability (very good repeatability): Results are stable, and the data is distributed relatively close to the mean value
- 25% ≤ CV < 45% – Moderate variability (moderate repeatability): Data points show a moderate amount of scatter but are still acceptable in most cases
- 45% ≤ CV < 100% – Higher variability (low repeatability): Results are very widely distributed, requiring further analysis to identify sources of instability
- CV ≥ 100% – Very high variability (very low repeatability): Results are extremely widely distributed and should not be considered reliable without further verification.

3. Results

3.1. Repeatability of the stationary laboratory measurement results

Figures 4–8 show the results of THC, CO, NO_x, particle number (PN), CO_2, emission measurements obtained using stationary laboratory analysers. The graphs show the mean emission values and the corresponding coefficients of variation (CV) in the individual phases of the WLTC as well as overall values for the entire test.

Based on the analysis conducted using laboratory analyzers, it can be concluded that hydrocarbon emissions exhibit very good repeatability in all phases of the WLTC cycle. The coefficient of variation (CV) did not exceed 25% in any phase of the test.

In the analysis of carbon monoxide (CO) emissions, the coefficient of variation was lowest in the LOW phase (4.81%), confirming very good measurement repeatability, while the highest value (17.36%) was observed in the Ex-HIGH phase. For the entire test, the CV was 5.93%, which indicates very good repeatability overall (Fig. 5).

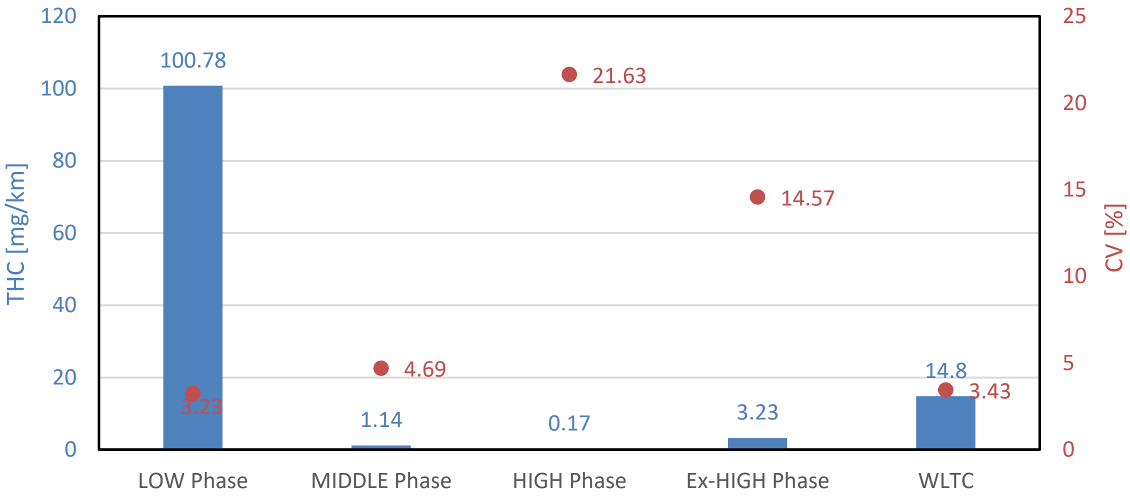

Fig. 4. Mean results of road emission of hydrocarbons with coefficient of variation in WLTC tests measured using stationary laboratory analysers

In the conducted analysis of nitrogen oxides (NO_x) emissions, the LOW phase showed the highest measurement stability, confirmed by a coefficient of variation (CV) of 1.77%, which indicates very good repeatability. This phase demonstrated the lowest data dispersion, making it the most reliable in terms of data quality. NO_x variability exceeded 25% in the HIGH (31.13%) and Ex-HIGH (27.91%) phases, which classifies them as having good repeatability. These results are consistent with the findings of Merkisz et al. [14], where dynamic WLTC phases led to increased NO_x dispersion – Fig. 6.

PN emission were characterized by very good repeatability in the LOW, MIDDLE, Ex-HIGH phases and the entire test, where the coefficient of variation did not exceed 25%. In contrast, the HIGH phase showed a CV of 43.58%, which, according to the adopted scale, places this result at the upper limit of good repeatability – Fig. 7. Increased variability is typical for this phase, especially under sudden load changes, as also noted in study [4].

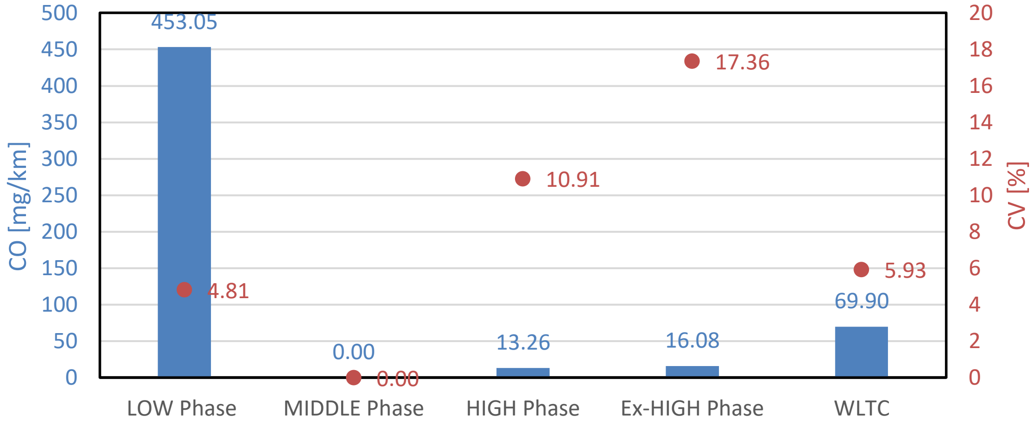

Fig. 5. Mean results of road emission of carbon monoxide with coefficient of variation in WLTC tests measured using stationary laboratory analysers

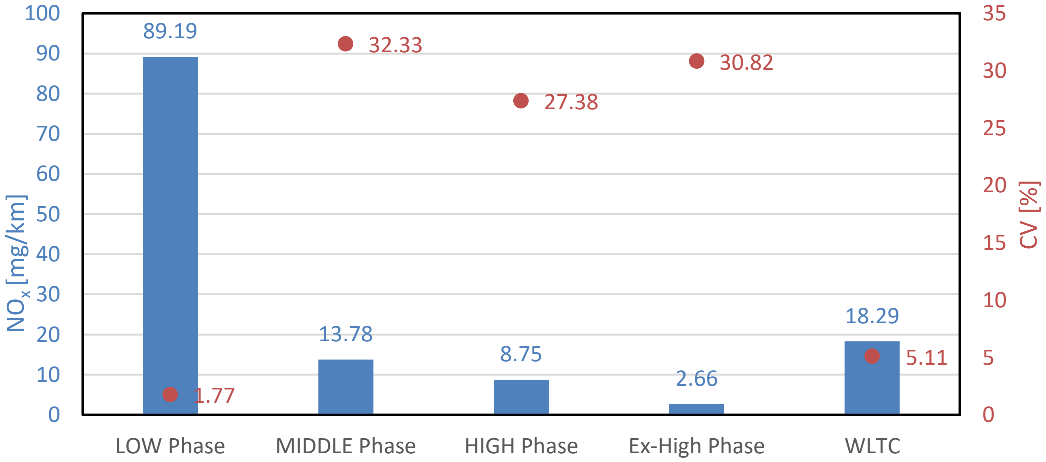

Fig. 6. Mean results of road emission of nitrogen oxides with coefficient of variation in WLTC tests measured using stationary laboratory analysers

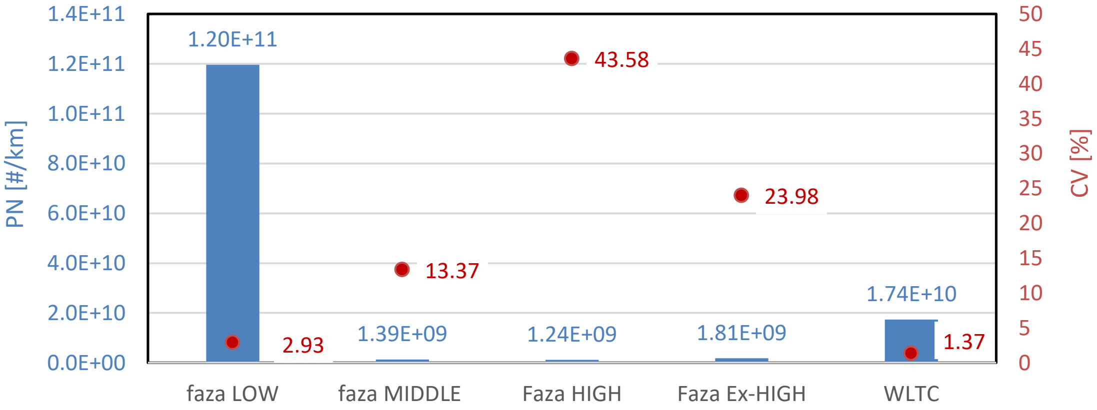

Fig. 7. Mean results of road emission of particle number with coefficient of variation in WLTC tests measured using stationary laboratory analysers

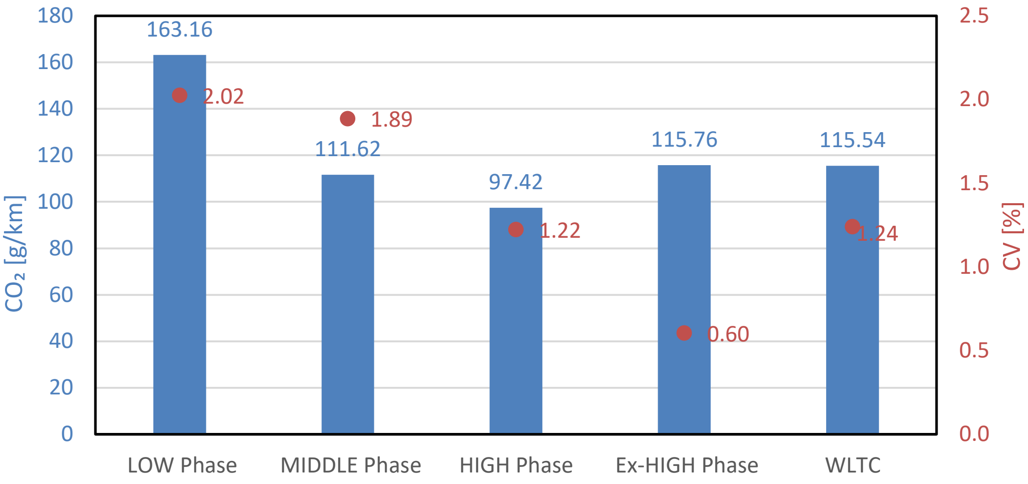

Fig. 8. Mean results of road emission of carbon dioxide with coefficient of variation in WLTC tests measured using stationary laboratory analysers

CO_2 emission demonstrated very good repeatability – CV did not exceed 2% in any phase, reaching a minimum of 0.42% in the LOW phase. This result aligns with the literature [14], where CO_2 was the least variable among all measured exhaust components. Such stable outcomes indicate high measurement quality for stationary CO_2 analyzers (Fig. 8).

Measurements performed at the laboratory using stationary laboratory analysers showed high emission results repeatability for most of the tested substances. The most stable was the CO_2 emission, for which the coefficient of variation (CV) did not exceed 2% in all WLTC phases. THC and CO emissions were also characterized by very good repeatability – in the entire cycle, CV values were 3.43% and 5.93%, respectively. NO_x emission was well repeatable in the LOW and MIDDLE phases of the test, while in the HIGH and Ex-HIGH phases the variability was notably increased (CV above 27%). The greatest variability was obtained for PN emissions – especially in the HIGH phase (CV = 43.58%), which indicates measurement difficulties related to the dynamic operation of the engine. However, for the entire WLTC cycle, CV values for PN and NO_x remained low, confirming generally very good repeatability of measurements.

3.2. Repeatability of the PEMS exhaust measurement results

Figures 9–12 present the test result data obtained using PEMS in a laboratory setting. These results show the mean emission levels and CV factors for all tested exhaust components in the four test phases of the WLTC as well as overall results for the entire test.

The hydrocarbon emission results obtained using the PEMS system indicate a very good level of repeatability across all phases of the WLTC test. The highest result stability was observed in the LOW phase, where the coefficient of variation reached 4.25%. In the HIGH phase, the CV value reached 20.48%, which still falls within the very good repeatability category, although the data already show a higher degree of variability.

Among the analyzed CO results, the highest measurement stability was observed in the LOW phase, where the coefficient of variation was 5.34%. In the MIDDLE and Ex-HIGH phases, CV values exceeded 25%, indicating good repeatability in these parts of the test. For the entire WLTC cycle, a CV of 8.59% was obtained, confirming very good overall repeatability of the results.

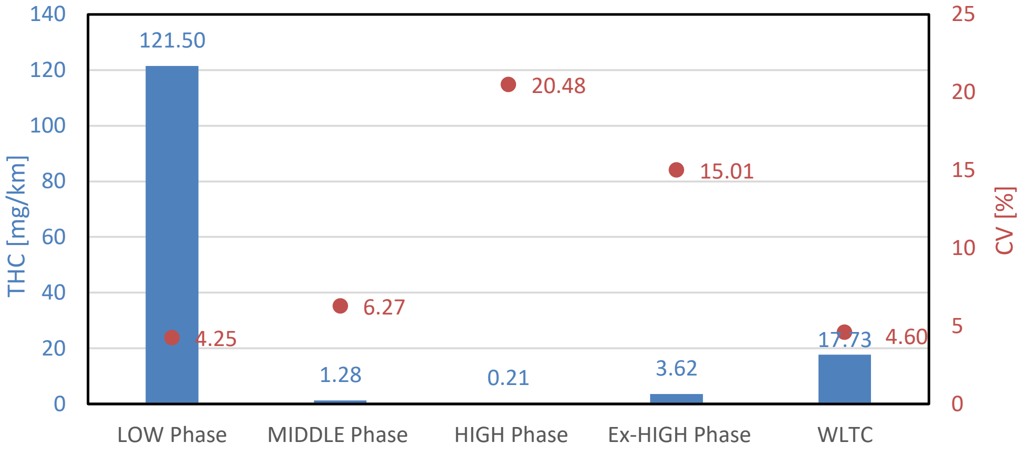

Fig. 9. Mean results of road emission of hydrocarbons with coefficient of variation in WLTC tests measured using PEMS

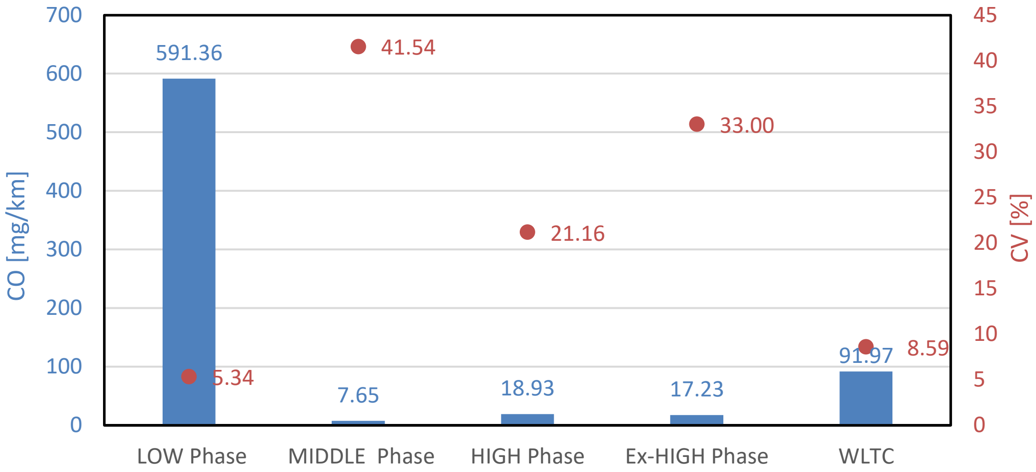

Fig. 10. Mean results of road emission of carbon monoxide with coefficient of variation in WLTC tests measured using PEMS

Nitrogen oxides (NO_x) emission measured using the PEMS system shows differences in repeatability levels depending on the WLTC phase. The most repeatable results were observed in the LOW phase, where the coefficient of variation (CV) was 2.62%. NO_x variability was noticeable in the Ex-HIGH phase (CV = 36.22%) and HIGH phase (29.87%), which indicates good repeatability. These results are consistent with similar studies [14], which indicated increased NO_x scatter in dynamic phases of WLTC, and with [7], where NO_x was shown to be highly sensitive to random disturbances in engine operating conditions.

The distribution of road PN emission results across individual WLTC phases shows clear differences in variability levels. The lowest coefficient of variation (CV), and thus the highest measurement repeatability, was observed in the LOW phase, where CV was 7.34%. In the MIDDLE phase, the CV reached 18.15%, also indicating very good repeatability. The highest data dispersion was recorded in the HIGH phase, with CV reaching 56.45%, which classifies this phase as having low repeatability. The Ex-HIGH phase had a CV of 26.91%, indicating moderate repeatability. The high PN variability confirms the observations in [4], which highlight the sensitivity of this exhaust component to the dynamic nature of the test.

The CO_2 emission data across individual WLTC phases indicate very good measurement repeatability in all analyzed stages of the test. The CV for the entire cycle was 3.27%. Although slightly higher than in laboratory conditions, the results confirm high measurement quality throughout the test range. Similar behavior of CO_2 as the most stable parameter was also observed in the study [14].

PEMS measurements generally showed very good repeatability of CO_2 and THC emission results over the entire WLTC test, with CV values of 3.27% and 4.60%, respectively. The LOW and MIDDLE phases were more stable than the dynamic phases of the test cycle. For CO and NO_x emissions, a clear increase in data variability was observed in the HIGH and Ex-HIGH phases, to CV = 33.00% and CV = 36.22%, respectively. The greatest data dispersion was obtained for PN emissions, especially in the HIGH phase (CV = 56.45%). Nevertheless, for the full WLTC cycle, the coefficient of variation value for all measured exhaust components was at a level characterized by very good repeatability. The results indicate that PEMS measurements under dynamic conditions may require further optimization in terms of stability and calibration.

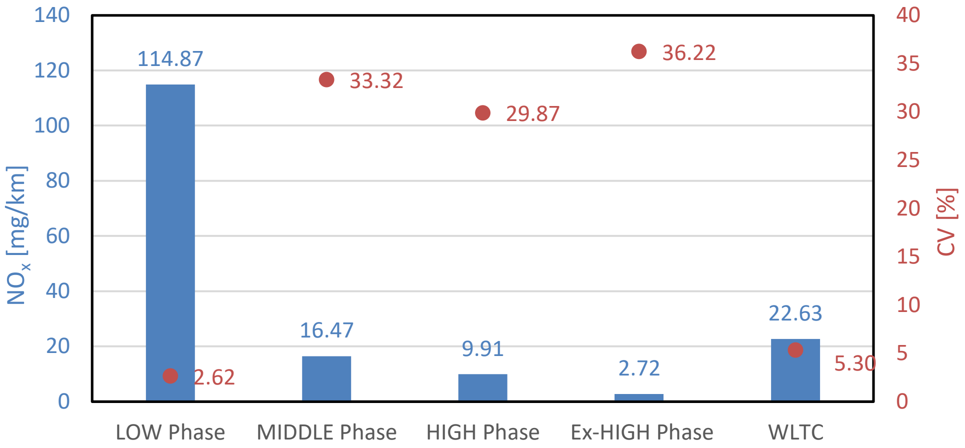

Fig. 11. Mean results of road emission of nitrogen oxides with coefficient of variation in WLTC tests measured using PEMS

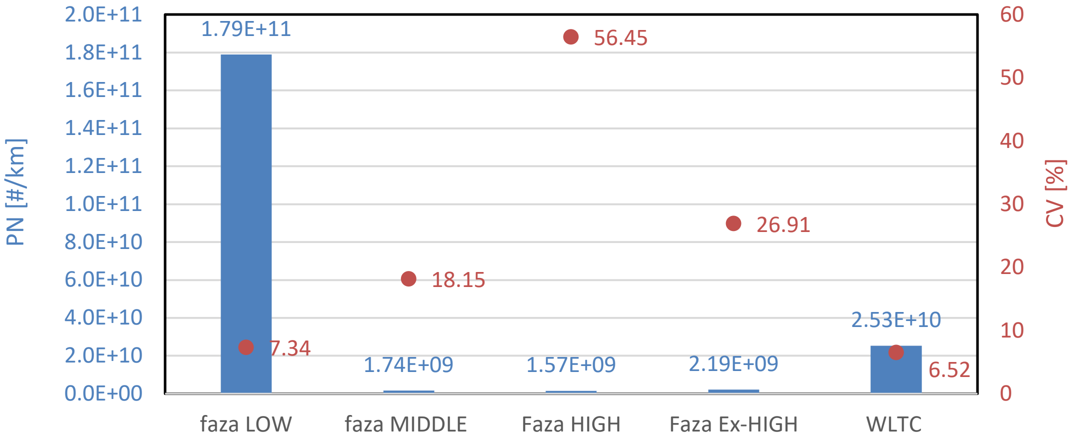

Fig. 12. Mean results of road emission of particle number with coefficient of variation in WLTC tests measured using PEMS

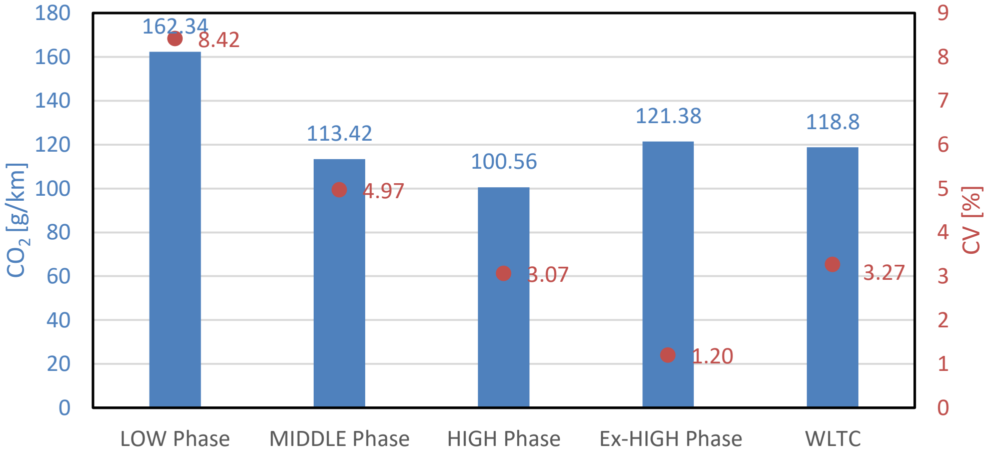

Fig. 13. Mean results of road emission of carbon dioxide with coefficient of variation in WLTC tests measured using PEMS

4. Conclusions

The conducted studies have shown that the repeatability of exhaust emission results in the WLTC test depends on both the measurement system used and the type of exhaust component analysed. Laboratory analysers generally provided higher stability of measurement results than PEMS devices, especially in dynamic test phases. CO_2 emissions were the most stable in both systems, while the greatest variability was noted for PN and NO_x emissions.

Main conclusions:

- For CO_2, CV values did not exceed 3.27% in the entire test in any of the systems used – this confirms the stability of this compound's emissions regardless of the test conditions
- THC showed very good repeatability in both systems, with slightly greater variability in the HIGH and Ex-HIGH test phases
- NO_x and CO results were more variable, especially in dynamic conditions, which indicates the sensitivity of the combustion process to variable loads and temperatures
- The greatest variability was shown by the PN emission results, reaching CV values exceeding 50% in the HIGH phase for the PEMS measurement
- The dynamic phases of the WLTC influenced the increase in the coefficient of variation, which suggests the need for further development of validation procedures and measurement technology for these test conditions
- Validation of the results showed that the absolute and relative differences for all analysed components were within acceptable limits. Despite the higher variability of the results, the PEMS measurements met the validation criteria set out in the EU regulations, which confirms its usefulness in measuring emissions in road traffic.

The impact of transport on the natural environment is multifaceted, and a full assessment of this impact requires detailed analyses that take into account various operating and technological conditions. The results of the research conducted in this work constitute a significant contribution to the field of analysis of the repeatability of exhaust emission results, but they do not answer all questions related to the construction and functionality of measurement systems. Therefore, the following directions for further research were proposed:

1. Expanding comparative analyses, conducting tests on a larger number of vehicles equipped with different types of engines:
    - Compression ignition engines (Diesel)
    - Vehicles powered by alternative fuels such as LPG, CNG, or hydrogen

   - Engines with different displacements, which would allow for assessing the impact of engine size on the repeatability of emission results
2. Tests in different atmospheric conditions:
   - Temperatures below 10°C and above 30°C, to determine the impact of atmospheric conditions on measurement results
   - Different levels of humidity and atmospheric pressure
3. Development of measurement technologies, development of new technological solutions that will increase the precision of mobile measurement systems in dynamic operating conditions:
   - Increasing the resistance of measurement systems to vibrations and changes in environmental conditions.
   - Improving the measurement methods for the particle number, especially in the dynamic test phases.

Nomenclature

CO	carbon monoxide
CO_2	carbon dioxide
CV	coefficient of variation
CVS	constant volume sampler
ECE	fuel consumption test in the urban driving cycle
GDI	gasoline direct injection
HDV	heavy duty vehicle
LDV	light duty vehicle
NEDC	New European Driving Cycle
NO_x	nitrogen oxides
PEMS	portable emissions measurement system
PM	particulate mass
PN	particulate number
RDE	real driving emissions
THC	total hydrocarbons
WLTC	Worldwide Harmonized Light Vehicles Test Cycles
WLTP	Worldwide Harmonized Light Vehicles Test Procedure
WMTC	World Motorcycle Test Cycle

Bibliography

[1] Adamiak B. Ocena mobilnych systemów badania emisji spalin w warunkach laboratoryjnych na hamowni podwoziowej [PhD dissertation]. Poznan University of Technology. Poznan 2024.

[2] Andrych-Zalewska M. Investigation of processes in the WLTC test of a passenger car with a diesel engine. Combustion Engines. 2023;194(3):52-62. https://doi.org/10.19206/CE-168328

[3] Andrych-Zalewska M, Chłopek Z, Merkisz J, Pielecha J. Exhaust emission from a vehicle engine operating in dynamic states and conditions corresponding to real driving. Combustion Engines. 2019;178(3):99-105. https://doi.org/10.19206/CE-2019-317

[4] Andrych-Zalewska M, Chłopek Z, Merkisz J, Pielecha J. Research on exhaust emissions in dynamic operating states of a combustion engine in a Real Driving Emissions test. Energies. 2021;14(18):5684. https://doi.org/10.3390/en14185684

[5] ArenaEV. Comparison of NEDC, EPA, and WLTP cycles. ArenaEV. 2022. https://www.arenaev.com/comparison_of_nedc_epa_and_wltp_cycles-news-419.php (accessed on 13.05.2025)

[6] Bielaczyc P, Klimkiewicz D, Woodburn J, Szczotka A. Exhaust emission testing methods – BOSMAL's legislative and development emission testing laboratories. Combustion Engines. 2019;178(3):88-98. https://doi.org/10.19206/CE-2019-316

[7] Chłopek Z, Rostkowski J. Non-repeatability of exhaust emission test results. Combustion Engines. 2015;163(4):92-100.

[8] Encyklopedia Zarządzania. Współczynnik zmienności (in Polish). Mfiles.pl. https://mfiles.pl/pl/index.php/Wsp%C3%B3%C5%82czynnik_zmienno%C5%9Bci (accessed on 13.05.2025).

[9] European Commission. Commission proposes new Euro 7 standards to reduce pollutant emissions from vehicles and improve air quality. Brussels: European Commission. 2022.

[10] European Commission. UN Regulation No. 168 – Approval of light duty vehicles with regard to real driving emissions. Off J Eur Union. 2024.

[11] European Union. Commission Regulation (EU) 2023/443 of 8 February 2023 amending Regulation (EU) 2017/1151. Off J Eur Union. 2023.

[12] Giechaskiel B, Melas A, Martini G, Dilara P. Overview of vehicle exhaust particle number regulations. Processes. 2021;9(12):2216. https://doi.org/10.3390/pr9122216

[13] Jaworski A, Kuszewski H, Ustrzycki A, Balawender K, Lejda K, Woś P. Analysis of the repeatability of the exhaust pollutants emission research results for cold and hot starts under controlled driving cycle conditions. Environ Sci Pollut R. 2018;25(18):17862-17877. https://doi.org/10.1007/s11356-018-1983-5

[14] Merkisz J, Chłopek Z, Sordyl A. Non-repeatability of the WLTP vehicle test results. Arch Transp. 2024;71(3):25-49. https://doi.org/10.61089/aot2024.fjw8a575

[15] Merkisz J, Pielecha J, Radzimirski S. Pragmatyczne podstawy ochrony powietrza atmosferycznego w transporcie drogowym (in Polish). Poznan University of Technology Publishing House. Poznan 2009.

[16] Tomalski P, Tomaszewski E. Metody statystyczne w analizach hydrologicznych środkowej Polski (in Polish). University of Lodz Publishing House. Lodz 2019.

Hubert Wojciechowski, Eng. – Faculty of Civil and Transport Engineering, Poznan University of Technology, Poland.

e-mail: *hubert.wojciechowski.1@student.put.poznan.pl*

Prof. Jerzy Merkisz, DSc., DEng. – Faculty of Civil and Transport Engineering, Poznan University of Technology, Poland.

e-mail: *jerzy.merkisz@put.poznan.pl*

Article citation info:
Brzeżański M, Mareczek M, Noga M. Conversion of an internal combustion engine to supply of hydrogen or other gaseous fuels. Combustion Engines. 2025;202(3):162-168. https://doi.org/10.19206/CE-207877

Marek BRZEŻAŃSKI
Michał MARECZEK
Marcin NOGA

Combustion Engines
Polish Scientific Society of Combustion Engines

Conversion of an internal combustion engine to supply of hydrogen or other gaseous fuels

ARTICLE INFO

Received: 20 June 2025
Revised: 2 July 2025
Accepted: 3 July 2025
Available online: 2 August 2025

The article contains practical knowledge on the process of converting a compression-ignition combustion engine to various types of gaseous fuels, including hydrogen. The content of the article is related to the completed project of this type of adaptation of an industrial engine. The process of preparing a gaseous fuel combustion system, the design of the ignition, power supply, safety, and power regulation systems are described. The basic functions of the adaptive engine control system are presented, which allow for the adjustment of its control parameters to the physicochemical properties of the gaseous fuel used. The preliminary results of tests of the engine powered by hydrogen or natural gas are also presented.

Key words: *hydrogen, spark ignition engine, conversion, adaptive control system, natural gas*

1. Introduction

In the era of searching for new sources of power for vehicles and machines, the use of hydrogen as a new energy carrier in transport is a very promising solution [14]. In the transition period, hydrogen can be used as a fuel in commonly known internal combustion engines (ICE), creating a bridge between traditional motorization and modern drive systems with hydrogen fuel cells. It can also help in building hydrogen distribution infrastructure and in shaping social awareness of the new energy carrier. A major advantage of hydrogen is the lack of geopolitical limitations, because hydrogen is not a fossil fuel dependent on local natural resources, but can be produced anywhere on the globe where we have access to water and electricity [5]. Hydrogen can be used in all transport sectors, both in wheeled [11, 12] and rail vehicles, in maritime transport [10], as a drive for industrial machines, and also as aviation fuel. When powered by hydrogen, the problem of vehicle range disappears, and its operation does not burden the environment. In practice, the conversion of IC engine to hydrogen fuel is a complex task, requiring interference in both the engine design and the control system, and this applies to all engines, both compression-ignition, spark-ignition, and engines powered by gaseous fuels. Due to the large scope of necessary changes, the conversion of an engine to hydrogen fuel is not possible using methods known from the practice of conversion to fuel with gaseous fuels such as natural gas, biogas, or propane-butane. In this case, the preparation of the engine to hydrogen fuel should be carried out in the process of its production [6, 7, 15].

In the Department of Automotive Vehicles of Cracow University of Technology, the first works on hydrogen fuel supply for ICE were carried out in the 1980s, a team of scientists led by Prof. Kordziński on the hydrogen drive of IC engines [8, 9]. Their continuation was the implementation in the years 2012–2018 of the project: "Use of waste hydrogen for energy purposes", in which a power plant with a rated power of 1 MW was developed and built, powered by waste hydrogen from the chemical industry [1]. The main difficulty in using this fuel to power engines was due to the contamination of hydrogen with various hydrocarbons and the frequent and rapid changes in the gas composition. For instance, the share of hydrogen varied from 60 to 90% in a time shorter than 1 minute [4]. The power plant consisted of three SI engines with a power of: 2 × 400 kW, 1 × 200 kW, equipped with an innovative hydrogen injection system, a system identifying the quality of the supplied hydrogen and a remote control and monitoring system [2, 3, 13]. The extension of this project is the work carried out since 2020, concerning the modernization of the hydrogen injection system of IC engines and the control system and operational safety systems, including the development of our own, electronically controlled systems of the mixing and injection system of the hydrogen engine supply system. The results of this work were used in the adaptation of a modern, 5-cylinder industrial engine from the Scania company to hydrogen supply.

2. Theoretical considerations

The basics of the operation of piston combustion engines powered by hydrocarbon fuels are based on the use of the exothermic oxidation reaction of hydrocarbon fuel, which supplies heat to the working medium. The main working medium of IC engine is always atmospheric nitrogen, regardless of the type of hydrocarbon fuel or alcohol used (Fig. 1). The share of the remaining components of the working medium, which are products of complete combustion, such as CO_2 and H_2O, varies depending on the share of carbon and hydrogen in the fuel molecule, and the share of oxygen is significant only in relation to compression-ignition engines. The gaseous toxic components included in the working medium do not play a major role in terms of its operating parameters.

In the case of fueling the engine with hydrogen, the composition of the working medium changes, with atmospheric nitrogen still being the main working medium, but the share of the remaining components changes, among which there is no CO_2, while the share of oxygen depends on the excess air coefficient used when fueling the engine with hydrogen (Fig. 2).

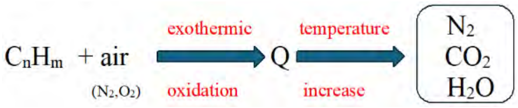

Fig. 1. Schematic diagram of the combustion process of hydrocarbon fuels in a combustion engine

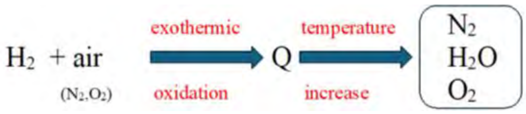

Fig. 2. Schematic diagram of the hydrogen combustion process in a combustion engine

An important factor influencing the heat flow rate released during combustion is the amount of oxygen in the cylinder. Therefore, the volume fraction of fuel in relation to the volume of air is very important (Fig. 3). In this case, hydrogen is not a good fuel compared to other fuels, especially gasoline. Therefore, a lower unit power of the engine should be expected.

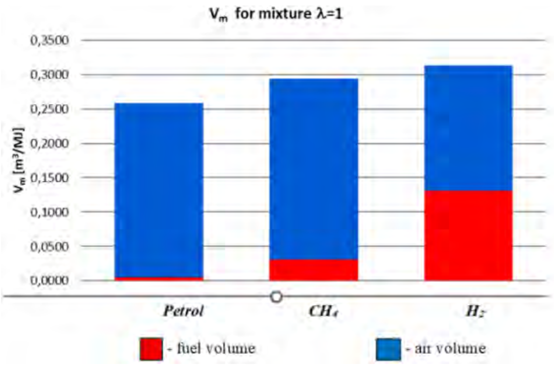

Fig. 3. Volumetric share of fuel in the stoichiometric mixture related to the energy unit

Another unfavorable feature of hydrogen is the course of the combustion process, which takes place at a very high speed and, in the internal combustion engine, leads to combustion anomalies and the impact effect of the gas force on the piston crown. Therefore, the only parameter that effectively influences the control of the flame movement in the combustion chamber of the piston internal combustion engine is the value of the excess air coefficient in the hydrogen-air mixture, and also, although to a lesser extent, the value of the ignition timing.

All of the above-mentioned features of hydrogen supply to the internal combustion engine create specific problems that must be addressed when undertaking the conversion of a specific type of engine.

3. Conversion of an internal combustion engine to hydrogen fueling

3.1. Research object

The object of the research and conversion to hydrogen power was an industrial engine type DI09 074M manufactured by Scania. It was a 4-stroke, turbocharged, diesel engine designed for marine applications. Basic technical data of the engine is as follows:

- Number of cylinders – 5
- Displacement – 9.3 L
- Cylinder bore × stroke – 130 mm × 140 mm
- Compression ratio – 18
- Rated power – 199 kW
- Pistons made of aluminum alloy
- Toroidal combustion chamber
- 4 valves per cylinder
- Fuel supply system – electronically controlled unit injector system
- Individual cylinder heads and wet cylinder liners
- Electrical installation voltage – 24 V
- Engine weight (with oil and coolant) – 1150 kg.

3.2. Combustion system

The basic task of converting the engine to hydrogen power is to develop a new combustion system. In the standard version, the engine is a compression ignition unit equipped with toroidal combustion chambers located in the piston. Changing the engine's operation from compression ignition to spark ignition requires significant design changes to the combustion system. In addition to the need to place a spark plug in the combustion chamber, it is necessary to reduce the compression ratio and use a combustion chamber with different geometric parameters. For this purpose, a design analysis of the existing combustion system in the engine was necessary, the result of which determined the possibility of converting the existing structure to power gas fuels, especially hydrogen.

This analysis required dismantling the engine, consisting of removing the heads and pistons. The measurements of the geometry of the channels in the cylinder head, intended for mounting the injectors, showed the possibility of mounting the spark plugs and placing integrated ignition system modules, consisting of spark plugs and high-voltage coils.

The piston structures of the converted engine were subjected to a detailed analysis. On the one hand, an analysis of the piston design was carried out, paying attention to the type of material, the location of the cooling channels, and the thickness of the walls subject to processing.

The standard engine piston (Fig. 4) was equipped with a typical, toroidal chamber combustion, commonly used in compression-ignition engines.

Due to the combustion process in the spark-ignition engine, it is necessary to design a new shape of the combustion chamber and reduce the compression ratio. Based on theoretical knowledge and design experience, a combustion chamber placed in a so-called cup-shaped piston was selected, which, thanks to the large surfaces of the squeezing zone in the final phase of the compression process, guarantees high charge swirl. At the same time, this type of conversion of the standard piston allows for selecting the appropriate compression ratio value. Figure 5 shows the design of the piston intended for the engine powered by gaseous fuels and an executive drawing showing the basic dimensions in relation to the standard version, necessary for the conversion process.

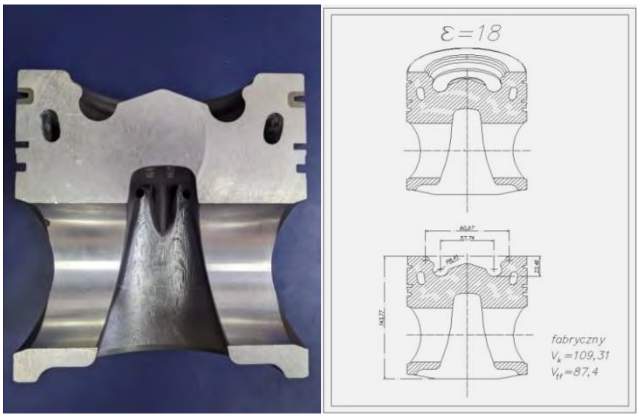

Fig. 4. Inventory of the standard engine version – the piston cross-section

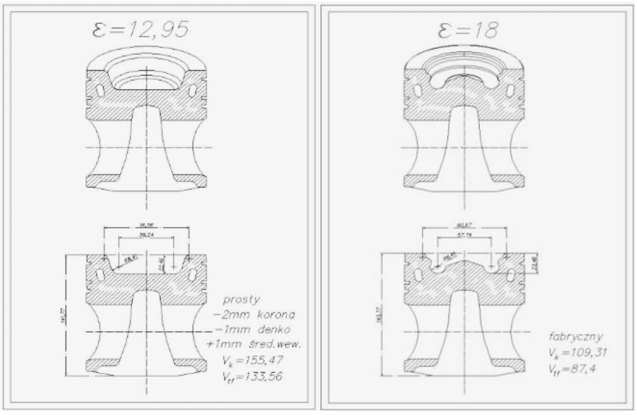

Fig. 5. Design of the engine piston for an engine powered by gas fuels, including hydrogen, and a production drawing for the conversion

Designing the shape of the combustion chamber required a series of theoretical analyses involving computer simulation of the thermal and mechanical loads of the combustion system, and in particular the piston (Fig. 6). An important element of the analysis was the selection of the appropriate geometric dimensions of the combustion chamber, which, on the one hand, met the requirements for the compression ratio, and on the other hand, the strength properties of the individual piston elements, especially the bottom, which transfers the highest value of gas force. This is important, especially when powering the engine with hydrogen, when the high speed of the combustion reaction causes large, momentary increases in pressure and temperature, loading the piston.

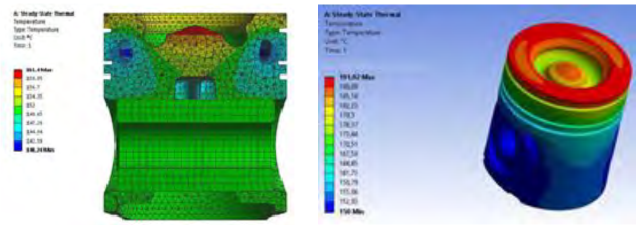

Fig. 6. Theoretical model analysis of thermal and mechanical loads of the standard version of the piston

Theoretical analyses showed the possibility of converting a standard compression-ignition engine piston after the above-mentioned design changes, using it in an engine powered by gaseous fuels. The designed piston met the requirements of an engine powered by gaseous fuels, including hydrogen.

3.3. Intake system

The compression-ignition engine, which is the object of conversion, is equipped with a classic power supply system implementing qualitative power regulation, which does not provide for throttling the air flow into the cylinders. In the case of spark-ignition engines, power is regulated by a quantitative method, and in engines powered by gaseous fuel with a large flammability range, also by a quantitative-qualitative method. Therefore, the intake system should be equipped with a valve to throttle the air flow.

In the designed engine designed to be powered by various gas fuels, including hydrogen, which is characterized by a very wide flammability limit, quantitative and qualitative power regulation is planned, which places special requirements on the accuracy of the selection of the excess air coefficient feeding the engine. In connection with this, the engine is planned to be equipped with a throttle module (Fig. 7), which is controlled by a stepper motor. Thanks to this solution, the degree of throttle opening can be included in the group of parameters constituting input signals to the electronic control module of the entire engine.

Fig. 7. Throttle module, during installation in the engine intake system (left), module with stepper motor controlling the throttle position

Placing the throttle module in the engine intake system changes its geometric dimensions, moving the original intake manifold away from the engine cylinder head body by a distance equal to the length of the module. In order to compensate for this dimension, elements fastening the gas fuel injectors with appropriately selected dimensions were designed (Fig. 8).

Fig. 8. Injector mounting body (in the photo – one of the prototypes printed using the 3D method from standard plastic)

These elements, called injector bodies, were designed using modern design tools and manufactured using the 3D printing method. An appropriately selected polymer material saturated with aluminum powder, which is resistant to high temperature and the chemical effects of hydrogen, was used to make the bodies. In addition, this material is characterized by plastic susceptibility and a controlled tearing process. This is a very positive feature from the point of view of operational safety, because in the event of the so-called flashback (backfire), depending on the intensity of this process, the body material may only undergo plastic deformation or crack without generating dangerous fragments.

3.4. Gas supply system

The engine, which was the subject of conversion to a gas fuel supply, was a compression ignition engine equipped with UIS (Unit Injector System) type pump injectors for diesel fuel injection. The entire standard power supply system was built into the engine. The developed concept of powering the engine with gas fuel assumed the use of an indirect gas fuel injection system to individual engine intake channels. The power supply system consists of a fuel rail in the form of a pipe made of acid-resistant steel, to which gas fuel is supplied at a pressure of not less than 4 bar (Fig. 9). The value of the gas fuel pressure in the fuel rail is controlled by a pressure sensor.

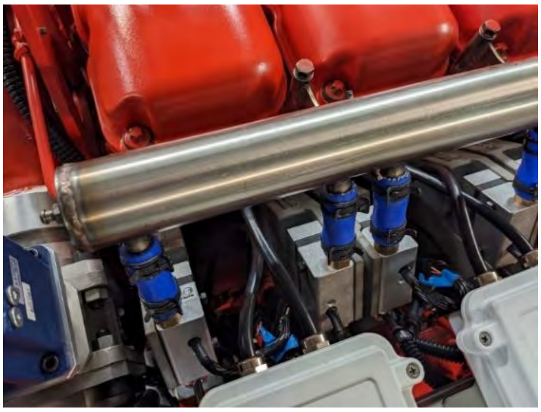

Fig. 9. A part of the fuel rail of the engine powered by gas fuels

From the fuel rail, gas fuel is transferred to the injectors through short pipes made of a plastic resistant to the chemical effects of the gas fuels used. Due to the design of the charge exchange system in the engine, which is equipped with two intake valves, and also due to the possibility of more precise selection of the dose of injected fuel, two injectors were used in the converted engine to supply each of the engine cylinders. These are serially produced, electronically controlled injectors designed for engines powered by natural gas (Fig. 10). For the needs of the implemented project, the injector dosing characteristics were made after previous calibration activities, thanks to which there was a guarantee of equal dosing of gas fuel in relation to the control signal.

The injectors were installed in developed injector mounting bodies (Fig. 11), which were made using the 3D printing method. In addition to the function of mounting the injectors, these bodies act as extensions of the intake channels, filling the space between the intake manifold and the heads, which changed after the introduction of the throttle body in the engine intake system.

Fig. 10. Electronically controlled gas fuel injector

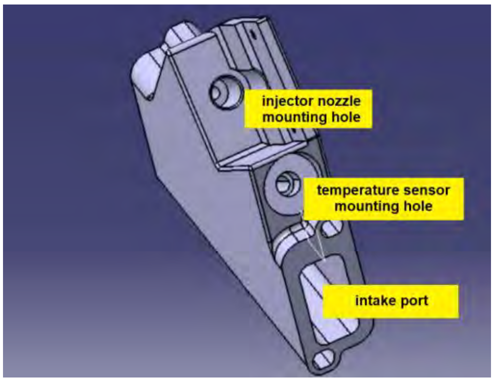

Fig. 11. Body of gas fuel injector

A characteristic feature of the bodies is the placement of special nozzles inside them, which are an extension of the injector nozzles, allowing gas fuel to be injected into the cylinder directly onto the intake valve. The developed power supply system provides for sequential gas fuel injection, synchronized with the position of the intake valves. Such a system largely prevents the risk of gas fuel accumulating in the engine intake channels, which may pose a risk of its explosion (Fig. 12).

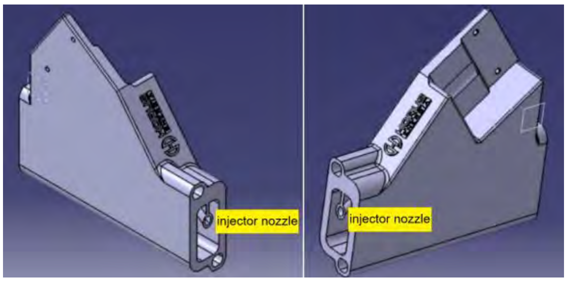

Fig. 12. Position of the gas fuel injector nozzles in the injector body

The arrangement of the injector bodies with injectors supplying gas fuel to the subsequent engine cylinders is shown in Fig. 13.

Fig. 13. Arrangement of gas fuel injectors in the engine (2 injectors per cylinder)

3.5. Ignition system

A conversion of the compression ignition engine to an engine powered by gas fuels involves developing an ignition system from scratch. Ignition modules from Denso, mass-produced for the automotive industry, were used. A single module consists of a spark plug integrated with an ignition coil. Modules of this type were placed in specially prepared sockets in the cylinder heads after the built-in injectors. Preparing the sockets required mechanical machining of the cylinder heads, together with the valve covers, and placing sleeves and seals protecting the ignition modules from external factors. The arrangement of the ignition modules in the engine is shown in Fig. 14.

Fig. 14. Arrangement of ignition modules in the engine

3.6. Control system

The control system designed and manufactured at the Cracow University of Technology is the most important system of the engine, designed to be powered by various gas fuels, including hydrogen. The engine uses an integrated electronic control system for individual processes that make up the full engine cycle in various operating conditions. This system uses the LabView software environment, which allows for multi-component regulation of all engine parameters in adaptive mode. It concerns both the control of basic systems necessary for the engine to operate, such as the power supply system and the ignition system, but also integrates signals from all sensors equipped with the engine. For this purpose, an electrical installation was developed, consisting of wiring harnesses creating a network of connections between the control parameters used.

The most important system of the engine powered by various gas fuels is the combustion process control system. In the developed solution, the basic role in controlling the operation of the combustion system is played by the value of the exhaust gas temperature exiting individual cylinders and signals from the knock sensors. These two parameters are linked in adaptive mode with the fuel supply system, which selects the appropriate value of the excess air coefficient, and with the ignition system, which selects the appropriate ignition timing. This type of system is also an element of the engine operation safety system, which can implement the engine shutdown procedure, e.g. in the event of a lack of combustion in one of the cylinders (exhaust gas temperature from a given cylinder is too low) or in the event of exceeding the set knock combustion threshold, which can no longer be corrected by appropriately setting the ignition advance angle. This system is also integrated with many other sensors transmitting signals related to operational safety. An example of this is the individual mixture temperature sensors, located in the engine intake channels, which decide to cut off the fuel supply in the event of the so-called backfire.

In the standard version, the engine was equipped with mechanically activated pump injectors by camshaft cams. During the adaptation of the engine to a gas fuel supply, it was necessary to make a new measurement system, requiring the installation of additional sensors necessary to synchronize many engine operating parameters. The developed system uses signals taken from the flywheel ring gear and the camshaft drive gear. The signal generated from them determines the instantaneous angular position of the crankshaft. Based on this parameter, the control system defines:

- fuel injection angle
- ignition timing
- knock detection zone
- engine speed
- and other engine parameters.

Figure 15 shows the location of both sensors. These are Honeywell LCZ260-30 sensors operating based on the Hall effect.

Fig. 15. Crankshaft and camshaft position sensors

Fig. 16. Cassettes with the main engine control system

The main control units are located in cassettes attached to the engine block (Fig. 16).

Injector operation is controlled by individual control units (Fig. 17), which support each of the two injectors per cylinder. The operation of these controllers is integrated and synchronized with the operation of the main control system.

Fig. 17. Cassettes with individual injector drivers for each cylinder

4. Preliminary tests

4.1. Start-up tests

The tested engine was equipped with a complete set enabling start-up tests and initial measurements of operating parameters. Start-up tests of the engine were carried out in the Laboratory of ICEs of the Cracow University of Technology on a test stand equipped with a 500 kW Zoellner eddy current brake (Fig. 18). It should be emphasized that the research did not provide for a change in the supercharging system, therefore the engine was equipped with a Holset turbocharger, used in the standard version of the engine.

Fig. 18. Engine on the test stand in the Laboratory of ICEs of the Cracow University of Technology

Start-up tests were carried out while fueled with two selected types of gas fuel (natural gas or hydrogen), which present different properties in terms of use as fuel for ICEs. The first tests were carried out while the engine was fueled with natural gas. During these tests, the functioning of individual engine components was checked, including mainly components and systems developed during the engine conversion. Tests of the functioning of the control system and safety systems were performed.

The next stage of the initial start-up tests was to feed the engine with hydrogen. In both cases, starting the engine powered by natural gas or hydrogen did not cause any problems, and the tests performed to check the operation of the control system, including the operation of the adaptive functions, were positive.

4.2. Initial bench measurements

The methodology of the measurements consisted of measuring selected operating parameters of the engine in operating conditions corresponding to its use in cooperation with a generator in a power generator. Therefore, measurements were carried out while the engine was running at a constant rotational speed of 1500 1/min and with variable load. The determination of engine control parameters, such as the excess air coefficient and the ignition advance angle in the initial tests, was selected individually to the engine operating conditions. During the measurements, all measured engine parameters were subject to control, while parameters important from the point of view of the conducted research, which were of an exploratory nature, were recorded. These parameters were:

- engine torque
- intake manifold absolute pressure
- excess air coefficient λ
- fuel consumption.

Based on these measured values, the following were calculated: engine effective power, specific fuel consumption and overall efficiency.

Initial tests of the engine control system operation and measurements of selected parameters, which were carried out while fueled with natural gas or hydrogen, were positive. In both cases, engine start-up did not cause any problems, and the tests performed to check the operation of the control system, including the operation of adaptive functions and the operation of safety systems, showed convergence with the design assumptions. Since the tested engine is designed to work with an electric generator, the engine speed was constant and amounted to n = 1500 1/min.

Initial tests have shown that when the engine is powered by natural gas and the ignition timing and excess air coefficient are adjusted, as determined by the developed controller, the effective power of the engine reaches the assumed value, while when the engine is powered by hydrogen, the effective power is approximately 30% lower. This significant difference in the obtained effective power value resulted from other physicochemical properties of the fuels used, and mainly from the calorific value of the mixture, which is significantly lower for the hydrogen-air mixture used, compared to the calorific value of the natural gas-air mixture. The second reason for the reduction in power when powered by hydrogen was the significantly lower energy of the exhaust gases flowing into the turbocharger, which significantly reduces the boost pressure and prevents the delivery of a larger mass of the hydrogen-air mixture. The turbocharger, which the engine is equipped with, was adapted to the exhaust gas flow generated in the process of diesel combustion, in which the thermodynamic parameters of the exhaust gas stream significantly differ from those parameters obtained when powered by natural gas or hydrogen.

5. Conclusions

The implementation of the project has shown that it is possible to convert a conventional combustion engine to be powered by various types of gas fuels with significantly different properties. This type of conversion is a complex issue that requires comprehensive technical analysis and development of an appropriate methodology for conducting work, taking into account the specific design features of the engine. In this case, it is not possible to develop a universal conversion system, similar to the methods used when adapting combustion engines to power, for example, natural gas or LPG. The necessary design changes should be introduced in the combustion system, ignition system, and power supply system. The most important thing here is the development of a control system that interactively combines the parameters of the ignition system and power supply system with the value of the engine's operating parameters. At the same time, the properties of the engine's construction materials should be taken into account, mainly in terms of exposure to thermal loads, mechanical loads resulting from the gas force, the course and dynamics of which depend on the properties of the fuel used. An important aspect of conversion is also the need to ensure the safety of engine operation. Therefore, an appropriate system should be introduced to monitor the change in pressure and temperature in the charge flow path, both on the inlet and outlet sides. The obtained engine operating parameters depend significantly on the physicochemical properties of the gas fuel used due to the existing limitations. Such limitations include, among others, the tendency to self-ignite, resistance to knocking combustion, backfire into the intake system, combustion process temperature, calorific value of the mixture, or the properties of the construction materials used. A significant improvement in the engine operating parameters can also be expected after conducting an analysis of the cooperation of the turbocharger with the engine, taking into account its flow characteristics, allowing it to be adapted to the type of fuel used.

Nomenclature

CI	compression ignition
ICE	internal combustion engine
LPG	liquified petroleum gas
n	engine speed
SI	spark ignition
UIS	unit injector system
V_m	volume of mixture per unit of energy
ε	compression ratio
λ	excess air coefficient

Bibliography

[1] Brzeżański M, Mareczek M, Marek W, Papuga T. Determination of operating parameters of industrial engine fuelled with post processing gases with high hydrogen content. IOP Conf Ser: Mater Sci Eng. 2016;148:012061. https://doi.org/10.1088/1757-899X/148/1/012061

[2] Brzeżański M, Mareczek M, Papuga T, Marek W. The use of gaseous fuels with variable chemical composition in the internal combustion engine. SAE Technical Paper 2020-01-2140. 2020. https://doi.org/10.4271/2020-01-2140

[3] Brzeżański M, Mareczek M, Marek W, Papuga T, Sutkowski M. The realized concept of variable chemical composition fuel gas supply systems, for internal combustion engines. Combustion Engines. 2017;170(3):108-114. https://doi.org/10.19206/CE-2017-318

[4] Brzeżański M, Marek W, Mareczek M, Papuga T. Application of gaseous fuels with variable chemical composition for energy purposes. IOP Conf Ser: Mater Sci Eng. 2018;421: 042007. https://doi.org/10.1088/1757-899X/421/4/042007

[5] Chi J, Yu H. Water electrolysis based on renewable energy for hydrogen production. Chinese J Catal. 2018;39(3):390-394. https://doi.org/10.1016/s1872-2067(17)62949-8

[6] Hassan HA, Nguyen T, Yousuf A, Patterson M, Duan C, Merchan-Merchan W et al. Performance and emissions of natural gas/hydrogen blends in large-bore spark-ignition engines. Int J Hydrogen Energ. 2025;125:168-180. https://doi.org/10.1016/j.ijhydene.2025.03.466

[7] Kim S, Lee J, Lee S, Lee S, Kim K, Min K. Effects of various compression ratios on a direct injection spark ignition hydrogen-fueled engine in a single-cylinder engine. Int J Automot Technol. 2024;25(5):1159-72. https://doi.org/10.1007/s12239-024-00096-6

[8] Kordziński C, Papuga T, Rudkowski M. Electronically controlled fuel supply system of hydrogen spark ignition engines. Advances in Hydrogen Energy Hydrogen Energy Progress. V Proceedings of the 5th World Hydrogen Energy Conference, Toronto, Canada. 15-20.06.1984;4:1649-1654.

[9] Kordziński C, Rudkowski M. Papuga T. An experimental investigation of the optimum air-to-fuel ratio of a two stroke high-speed hydrogen engine with spark ignition. Proceedings of the 3th World Hydrogen Energy Conference, Tokyo, Japan, 23-26.06.1980;3:1231.

[10] Krakowski R. Analysis of replacement of internal combustion engine with the hydrogen fuel cell in ship powertrain. Advances in Science and Technology Research Journal. 2024;18(5):385-399. https://doi.org/10.12913/22998624/190130

[11] Noga M, Moskal T. Hydrogen and ethanol co-combustion in a SI engine for CO_2 emission reduction. Proceedings of 28th International Scientific Conference Transport Means. 2024; 1:981-986. https://doi.org/10.5755/e01.2351-7034.2024.P981-986

[12] Paluch M, Noga M. Influence of hydrogen addition on performance and ecological parameters of a spark-ignition internal combustion engine at part load typical for urban traffic. Advances in Science and Technology Research Journal. 2025;19(3):262-270. https://doi.org/10.12913/22998624/199738

[13] Sutkowski M, Mareczek M. Operational experience and new developments for industrial gas engines fuelled with hydrogen fuels. Combustion Engines. 2024;197(2):146-151. https://doi.org/10.19206/CE-183185

[14] Tak YC, Paw JKS, Kadirgama K, Yusaf T, Ramasamy D, Sudhakar K et al. Decarbonizing the future for the transportation and aviation industries: green hydrogen as the sustainable fuel solution. Materials Today Sustainability. 2025;31: 101152. https://doi.org/10.1016/j.mtsust.2025.101152

[15] Tsujimura T, Suzuki Y. Development of a large-sized direct injection hydrogen engine for a stationary power generator. Int J Hydrogen Energ. 2018;44(22):11355-11369. https://doi.org/10.1016/j.ijhydene.2018.09.178

Prof. Marek Brzeżański, DSc., DEng. – Faculty of Mechanical Engineering, Cracow University of Technology, Poland.
e-mail: *marek.brzezanski@pk.edu.pl*

Michał Mareczek, DEng. – Faculty of Mechanical Engineering, Cracow University of Technology, Poland.
e-mail: *michal.mareczek@pk.edu.pl*

Marcin Noga, DSc., DEng. – Faculty of Mechanical Engineering, Cracow University of Technology, Poland.
e-mail: *noga@pk.edu.pl*

Politechnika Poznańska
Wydział Inżynierii Lądowej i Transportu
Wydział Technologii Chemicznej
Wydział Inżynierii Środowiska i Energetyki
ul. Piotrowo 3; 60-965 Poznań

Studia Podyplomowe

Inżynieria systemów zasilania wodorem

III edycja

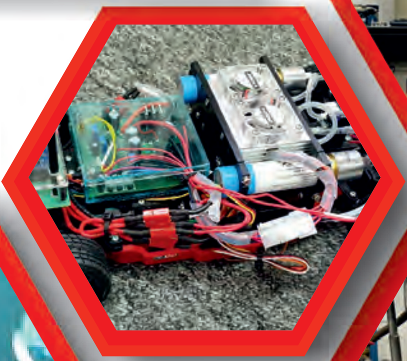

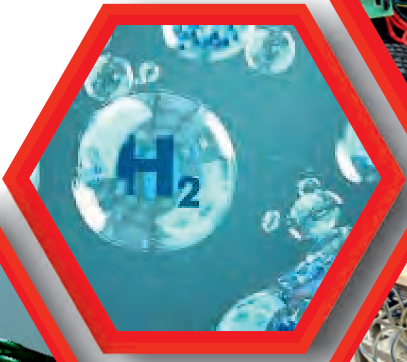

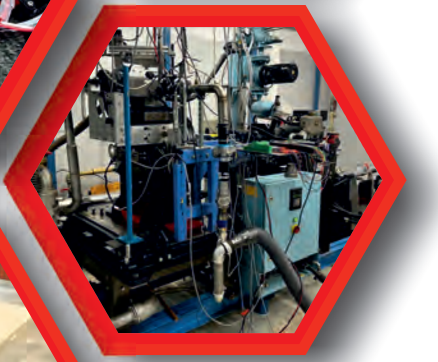

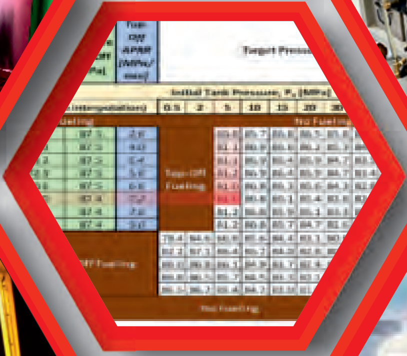

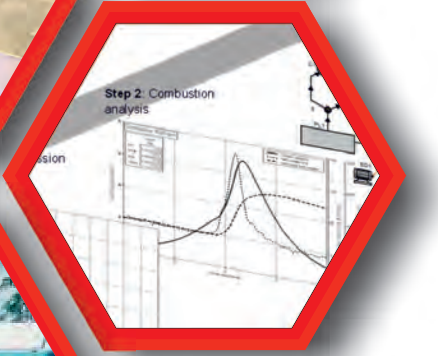

H2.put.poznan.pl

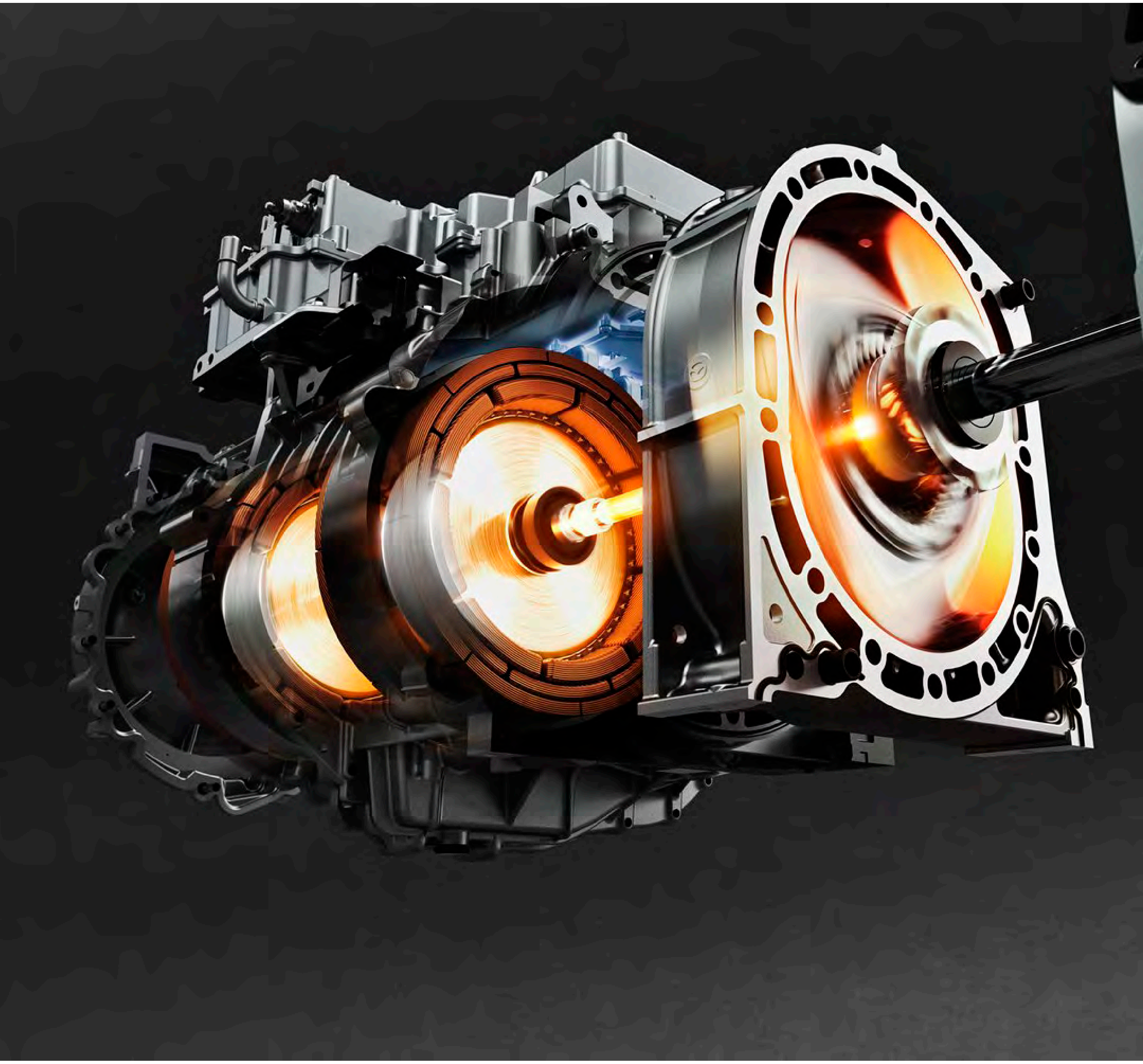

Publisher:

Polish Scientific Society of Combustion Engines

9 772300 989002

ISSN: 2300-9896
eISSN: 2658-1442

Combustion Engines
Polskie Towarzystwo Naukowe Silników Spalinowych

www.combustion-engines.eu